

École Doctorale de Physique et Chimie-Physique (ED182)
Institut de Physique et Chimie des Matériaux de Strasbourg
(UMR 7504 CNRS-Unistra)

THÈSE

présentée par :

Quentin EVRARD

Soutenue le : 12 décembre 2017

pour obtenir le grade de :

Docteur de l'Université de Strasbourg

Discipline/ Spécialité : Chimie-Physique des Matériaux

Hydroxydes Simples Lamellaires multifonctionnels : investigations structurales, fonctionnalisations et propriétés

THÈSE dirigée par :

M. ROGEZ Guillaume

Dr, IPCMS (UMR CNRS-Université de Strasbourg 7504)

RAPPORTEURS :

M. CARTERET Cédric

M. PAYEN Christophe

Pr, LCPME (UMR CNRS-Université de Lorraine 7564)

Pr, IMN (UMR CNRS-Université de Nantes 6502)

AUTRES MEMBRES DU JURY :

Mme TAVIOT-GUÉHO Christine

Mme GERARDIN Corine

M. PRELLIER Wilfrid

Mme BRENDLÉ Jocelyne

Pr, ICCF (UMR CNRS-Université Clermont Auvergne 6296)

Dr, ICG (UMR CNRS-Université de Montpellier 5253))

Dr, CRISMAT (UMR CNRS-ENSICAEN 6508)

Pr., IS2M (UMR CNRS-Université de Haute-Alsace 7361)

Remerciements

Je tiens tout d'abord à remercier Guillaume pour son soutien sans faille au cours de ces trois (5) années et la confiance qu'il m'a accordée. Il a su à la fois préserver intacte ma passion pour la science dans les difficiles années du master et me guider dans la voie des matériaux multifonctionnels pour la thèse. Sous sa tutelle j'ai pu rencontrer un grand nombre de personnes passionnantes en congrès, avec des collaborations, au laboratoire...

Parmi ces personnes figurent les membres du laboratoire, Émilie, Marina et Oleg dont les conseils m'ont permis d'apprendre la vie en laboratoire, les bonnes pratiques, m'ont transmis leur passion d'expérimentateurs. Je tiens aussi à remercier Pierre Rabu pour nos discussions portant aussi bien sur le magnétisme que sur la chimie des hydroxydes. Je remercie aussi tous les doctorants de l'équipe, Yanhui et Pierre, qui ont partagé le laboratoire et m'ont permis de voir qu'il n'y a pas que les hydroxydes dans la vie! Et enfin, je remercie le pilier du bon fonctionnement des labos du 3e étage : Céline pour son aide précieuse allant des solvants aux commandes de produits en passant par la synthèse de complexes de salen de platine insérés pendant cette thèse. Je remercie aussi Marie-Noëlle pour son aide à la synthèse des complexes de ruthénium tris-bipy qui ont bien fini par marcher! Je remercie aussi Sylvie pour son aide dans toutes les tâches administratives, les inscriptions aux congrès et les organisations des voyages. Je remercie aussi toutes les personnes du département pour leur aide, Cédric pour toutes ces belles images MEB, et même sur des échantillons moins beaux, Didier pour ma formation ATG, Marc pour son aide sur la diffraction sur poudre. Je remercie aussi Nicolas pour son assistance et sa disponibilité.

Je remercie bien évidemment aussi les membres du Jury pour avoir accepté d'examiner ma thèse, la discussion que nous avons tenue lors de ma soutenance ainsi que les rapports de soutenance ont été très instructifs.

Je tiens à remercier toutes les personnes de l'ANR pour leur travail et leur aide à l'aboutissement de ce projet, Paul-Alain Jaffrès, Charlotte Sevrain et Mélissa Roger pour la synthèse des très nombreuses molécules organiques servant de produit de départ à la synthèse des composés décrits dans cette thèse avec une réactivité qui a permis de dynamiquement changer de molécules organiques quasiment à façon.

Jean-Michel et Clarisse pour nos discussions sur l'aspect one-pot de l'ANR, les différentes similitudes entre nos deux approches et pour leur chaleureux accueil lors de mes séjours à Caen où il fait bon-vivre.

Olivier et Nicolas pour la résolution structurale de mes composés de départ, qui m'ont prouvé qu'après quasiment un an d'effort, il était possible d'obtenir des cristaux suffisamment bons pour pouvoir résoudre leur structure!

Alain et Tathamay pour leur dynamisme dans les très nombreuses et complexes mesures diélectriques de nos matériaux, ils m'ont permis de faire mes premiers pas dans le monde étonnant des matériaux à couplage magnétocapacitif.

Ziyad qui, par sa passion pour la simulation et la science, a été le moteur des simulations effectuées dans l'équipe du DCMI avec le soutien de Guido, Carlo Massobrio et Mauro Boero. Nos discussions sur la politique, la philosophie, la physique et la chimie aussi bien entendu m'auront marqué.

Mathieu pour les mesures des propriétés de luminescence de nos matériaux, ce qui m'a fait découvrir la difficulté des mesures sur échantillon solide.

Grégory et Honorat pour ma formation sur la mesure des propriétés d'optique non linéaire sur des échantillons capricieux...

Erik Elkaïm pour son aide à l'optimisation des conditions d'acquisition des données de diffraction des rayons X à Soleil.

Christine pour m'avoir fait découvrir le monde de la PDF, la puissance de cet outil dans les matériaux peu ordonnés, ainsi que pour ses longues heures de travail sur mes échantillons complexes.

Je tiens aussi à remercier bien évidemment Keltoum avec qui il a été un plaisir d'échanger et de l'encadrer lors de son stage, son travail rigoureux a été le bienvenu.

I would like to thank Deividas as well for his work during his internship, our discussions about Lithuanian culture and his thirst for knowledge that fueled the hard work.

I would also like to thank Varun Kumar and Yann Garcia for this interesting collaboration between our labs.

Je tiens à remercier aussi la "dream-team", Jérôme, Kassioyé, Mathilde, Andra, Élodie, Florian, Francis, Kübra, Kevin ainsi que les nouveaux arrivants Paula, Suvidyakumar, Nesrine et Florian(bis), ça a été un plaisir de travailler, fêter, jouer, manger, enfin bref, de partager ces années à l'IPCMS avec vous... J'espère que vous saurez maintenir l'esprit d'équipe qu'on nous jalouse dans tout l'institut!

Je remercie aussi tout les membres du DCMI que je n'ai pas encore cité, passé comme présent pour leur accueil, leur aide et leur bonne humeur, je pense particulièrement à Nathalie, Christophe, Damien, Oksana, Benoît, Silviu, Jean-Luc, Sylvie, Manu...

Je remercie aussi ma famille, mes parents et mes amis pour leur soutien et leur aide lors de ces trois intenses années de thèse, le temps où je faisais pousser du sulfate de cuivre dans le garage est maintenant bel et bien révolu!

Je remercie aussi l'ANR et le CNRS pour le financement de ces trois années de recherche qui m'on permis d'avancer.

Et enfin, je tiens à remercier ma deuxième famille (par ordre d'apparition) Dr Bobby, Dr Bobby et (bientôt Dr) Bobby!

Table of Contents

Introduction	1
1. Lamellar Hybrid Compounds and Experimental Conditions Used to Obtain Them.....	2
2. Layered Hydroxides.....	4
2.1. Layered Double Hydroxides	5
2.2. Layered Simple Hydroxides.....	6
3. Thesis Structure	8
4. Bibliography	11
Chapter I : New Insights on the Synthesis and Structural Investigations of Copper Hydroxide-Based Starting Compounds	17
1. Synthesis and Reactivity of $\text{Cu}_2(\text{OH})_3\text{OAc}\cdot\text{H}_2\text{O}$	17
1.1. Previous Synthesis Method : Coprecipitation via Drop-wise Base Addition	18
1.2. New Synthesis : Without Base Addition	19
1.3. Reactivity of $\text{Cu}_2(\text{OH})_3\text{OAc}\cdot\text{H}_2\text{O}$ Crystals.....	20
2. Synthesis of $\text{Cu}_2(\text{OH})_3\text{DS}$	22
2.1. Previous Synthesis Method : Ion-Exchange Reaction from $\text{Cu}_2(\text{OH})_3\text{OAc}\cdot\text{H}_2\text{O}$	22
2.2. « Secondary Discovery » : Ribbonlike Hydroxide Structure	23
2.3. New One-Pot Synthesis of $\text{Cu}_2(\text{OH})_3\text{DS}$	26
2.3.1. Synthesis and Crystal Structure.....	26
2.3.2. Comparison with Classical Ion Exchange Method	28
2.3.3. Morphology Control	28
2.3.4. Properties of $\text{Cu}_2(\text{OH})_3\text{DS}$	30
2.3.4.1. Non-Linear Optics : Second Harmonic Generation	30
2.3.4.2. Magnetic Properties	32
3. Conclusion.....	35
4. Bibliography	36
Chapter II : Characterization of the Structure of Layered Cobalt Simple Hydroxide Derivatives via Pair Distribution Function Analysis	39
1. Introduction	40
2. Experimental Procedure	41
3. Experimental Setup Optimization.....	42

4. PDF Extraction on Layered Cobalt Hydroxides.....	43
4.1. Signature of the Organic Part of the Cobalt Hydroxide Hybrids in Their Respective PDFs	43
4.2. Cell Parameter Determination.....	47
5. Structural Model Determination	49
5.1. Starting from a Purely Brucite Structure	50
5.2. Starting from a Nitrate Hydrozincite Structure.....	51
5.3. Starting from a Carbonate Hydrozincite Structure	51
6. Results of PDF Fits on the Selected Compounds and Comparison with the Literature.	54
6.1. Naming Nomenclature and Results of the Fitting Procedure.	54
6.2. Confrontation of the Model with the Literature.	59
7. Conclusion.....	63
8. Bibliography	64

Chapter III : Layered Hydroxides Hybrid Materials Obtained by Intercalation of Fluorene Derivatives67

1. Molecular Design.....	68
2. Intercalation Chemistry of the Phosphonic Acids	69
3. Insertion in Copper Hydroxide.....	69
3.1. Insertion Conditions : the Crucial Role of pH	69
3.2. Insertion Conditions : the Roles of Temperature, Excess Ratio of the Molecule of Interest and Reaction Time	72
3.3. Characterization of the Copper Hydroxide Hybrids.....	73
3.3.1. Powder X-Ray Diffraction.....	73
3.3.2. Packing of the Fluorenes in the Interlamellar Spacing.....	75
3.3.3. Infrared Spectroscopy	77
3.3.4. TGA/TDA, Micro-Analysis and EDX	79
4. Insertion in Cobalt Hydroxide	80
4.1. Structure of the Cobalt Hydroxide with PDF Analysis and UV-Visible Spectroscopy.....	81
4.2. Powder X-Ray Diffraction of Cobalt Hybrids	82
4.3. Infrared Spectroscopy of Cobalt Hydroxide Hybrids.....	84
4.4. TGA/TDA, Micro-Analysis and EDX	85
5. Properties of the Hybrid Compounds.....	87
5.1. Luminescence of Hybrid Compounds	87

5.2. Magnetic Properties of Hybrid Compounds.....	88
5.2.1. Magnetic Properties of Copper Hydroxide Hybrids.....	88
5.2.2. Magnetic Properties of Cobalt Hydroxide Hybrids.....	89
5.3. Magneto-Electric Properties of Layered Cobalt Hydroxide Hybrids.....	93
5.3.1. Magneto-Electric Properties of P ₂ -Fluo-C ₈ C _o	94
5.3.2. Magneto-Electric Properties of P ₂ -Fluo-C _c Co.....	97
6. Conclusion.....	99
7. Bibliography.....	100

Chapter IV : Layered Hydroxides Hybrid Materials Obtained by Intercalation of Benzene Derivatives 105

1. Introduction.....	105
2. General Chemistry of the System.....	106
2.1. Grafting Moiety.....	106
2.2. Lateral Functionalization.....	106
3. Lateral Functionalization Role.....	107
4. Insertion in Copper Hydroxide.....	108
4.1. With Phosphonic Acid.....	108
4.1.1. Typical Experimental Procedure.....	108
4.1.2. XRD and Infrared Spectroscopy.....	108
4.1.3. TGA/TDA, Micro-Analysis, SEM and EDX.....	112
4.1.4. Attempts to Vary the Insertion Rates.....	114
4.2. With Carboxylic Acid.....	115
4.2.1. Typical Experimental Procedure.....	115
4.2.2. XRD and Infrared Spectroscopy.....	115
5. Insertion in Cobalt Hydroxide.....	119
5.1. With Phosphonic Acid.....	119
5.1.1. Typical Experimental Procedure.....	119
5.1.2. XRD and Infrared Spectroscopy.....	120
5.1.3. TGA/TDA, Micro-Analysis, SEM and EDX.....	122
6. Properties of the Hybrids Compounds.....	123
6.1. Luminescence.....	123
6.2. Magnetic Properties of Cobalt Hybrid Compounds.....	124
6.3. Magnetoelectric Effect.....	128
7. Conclusion.....	128
8. Bibliography.....	129

Chapter V : Layered Hydroxides Hybrid Materials Obtained by Intercalation of Thiophene Derivatives	131
1. Introduction	131
2. Intercalation Chemistry.....	132
2.1. Oleyl Sulfate-Intercalated Copper Hydroxide.....	133
2.2. Oleyl Sulfate-Intercalated Cobalt Hydroxide	134
3. Insertion of Thiophene Derivatives in Copper Hydroxide.....	135
3.1. Reactions Conditions and Usefulness of the Oleyl-Sulfate-Intercalated Compound as an Alternative Pre-Intercalated Compound.	135
3.2. XRD and Infrared Spectra of the Thiophene Copper Hydroxide Hybrids	137
3.3. TGA/TDA, Micro-Analysis and EDX of the Thiophene Copper Hydroxide Hybrids.....	139
4. Insertion of Thiophene Derivatives in Cobalt Hydroxide	140
4.1. Reactions Conditions Used to Obtain Thiophene Cobalt Hydroxides Hybrids.....	140
4.2. XRD and Infrared Spectra of the Thiophene Cobalt Hydroxides Hybrids.....	141
4.3. TGA/TDA, Micro-Analysis and EDX of the Thiophene Cobalt Hydroxide Hybrids.....	144
5. Properties of the Hybrids Compounds.....	145
5.1. Luminescence Properties	145
5.2. Magnetic Properties.....	147
5.2.1. Magnetic Properties of P ₂ -diThioC ₂ Cu	147
5.2.2. Magnetic Properties of P ₂ -diThioC ₂ Co	148
6. Conclusion.....	149
7. Bibliography	149
Chapter VI : Layered Cobalt Hydroxides Obtained by Intercalation of Ruthenium and Platinum Complexes Derivatives	151
1. Introduction	151
2. Intercalation Chemistry.....	152
2.1. Intercalation Chemistry with Ru-trisbipy in Cobalt Hydroxide.....	152
2.2. Intercalation chemistry with Pt-Salen in cobalt hydroxide	153
3. Characterizations of the Obtained Hybrids	154
3.1. Ru-trisbipyC ₂ Co	154

3.1.1. X-Ray Diffraction and Infrared Spectroscopy	154
3.1.2. Micro-Analysis and UV/Vis Spectroscopy of Ru-trisbipy _c Co.....	155
3.2. Pt-Salen _c Co	156
3.2.1. X-Ray Diffraction and Infrared Spectroscopy	156
3.2.2. Micro-analysis and UV/Vis spectroscopy of Pt-Salen _c Co	157
4. Magnetic and Luminescence Properties.....	158
4.1. Magnetic Properties.....	159
4.1.1. Magnetic Properties of Ru-trisbipy _c Co	159
4.1.2. Magnetic Properties of Pt-salen _c Co	161
4.2. Luminescence Properties	162
4.2.1. Luminescence Properties of Ru-trisbipy _c Co.....	162
4.2.2. Luminescence Properties of Pt-salen _c Co	163
5. Conclusions	164
6. Bibliography	165
General Conclusion and Prospects.....	168
Bibliography	171
Appendix I : Theory about total scattering and Pair Distribution Function extraction	173
Appendix II : Complete IR Tables.....	175
Appendix III : Published Results	181
Appendix IV : Experimental protocols.....	195

Introduction

The field of material science is extremely wide and has always been of great interest from the first tailored silex to 14 nm photolithography on single crystal silicon wafers. If the tools at our disposal have vastly improved over time, the principle is still basically the same. For example, combining the compressive strength of concrete with the tensile resistance of steel allows us to build a material that possesses both tensile and compressive strength to build bridges or tall buildings. Of course in this example it is only the macroscopic combination of both materials that allows us to have better mechanical properties. But this principle is also viable at much lower scale, from composites like carbon fibre mixed with epoxy resin to an intrinsic mixing at the atomic scale.

These materials are then called hybrid materials, where the combination at a nanometric scale of at least two different materials allow the final compound to have either a mix of the properties of its initial components or new intrinsic properties due to synergistic effects between the two materials.

One of the most common materials of this type is called hybrid organic/inorganic material. Indeed, if the concept of mixing organic and inorganic materials dates back to pre-Columbian Mesoamerican cultures with the Maya blue, which is the mixing of clays (palygorskite and montmorillonite) with an organic molecule (indigotin obtained from añil leaves),¹ allowing the relatively fragile organic molecule to be preserved much longer (figure 1). Indeed its inclusion in clays leads to an exceptional resistance to acids, alkalis or biodegradation, making it effectively stable for many centuries. However, even today, being able to rationally design such materials is still a big challenge which raises interest in many fields with various applications such as membrane separation² or interesting optical properties³ such as solid-state dye laser,⁴⁻⁶ light-emitting diodes⁷ or hole transport.⁸



Figure 1 : Picture involving Maya Blue in the room 3 of the Bonampak Temple (Mexico) dating back to 791 AD.⁹

These hybrid materials have been classified in two distinct classes,¹⁰ the class I is said of hybrid materials where the cohesion between the two phases are weak (hydrogen bonding, Van der Waals or electrostatic) while class II hybrid exhibit much stronger cohesion (covalent or coordination bonds). The reason behind this classification is mainly because a stronger interaction can allow more physical interactions between the compounds thus allowing synergistic effects to occur, such as higher electrochemical capacitance¹¹ or enhanced luminescence¹² even if this condition is not necessary for all physical properties such as catalysis¹³ or luminescence.¹⁴

Most of these hybrids also possess the advantage of being obtainable *via* soft chemical/physical conditions, so-called *chimie douce*, and thus allowing easier synthesis at a lower energetic cost.

In the case of the Maya blue the property sought was the improved stability of the organic molecule, however, it is possible to seek many other properties than improved stability. They are many examples in the literature where hybrid materials exhibit peculiar luminescent,^{12, 14-16} magnetic,¹⁷⁻¹⁹ optical,^{3, 5, 6} electronic,²⁰⁻²² photo²³ or electro²⁴⁻²⁶ catalytic properties. And in some cases²⁷⁻³⁰ it is possible to effectively get multifunctional materials. Among the broad synthetic pathway choices to get hybrid compounds, the lamellar hybrid approach has raised a significant interest due to its wide array of available chemical-tuning and shaping protocols.

1. Lamellar Hybrid Compounds and Experimental Conditions Used to Obtain Them

As stated above, the lamellar hybrid compound approach is a well-suited path to obtain hybrid materials. This part will sum these techniques up and show the relevance of the chosen technique for this thesis.

The first and most natural way of obtaining lamellar hybrid compounds is when the system itself grows into a lamellar compound. Many hybrid systems have been obtained in that way and possess interesting properties such as ferroelectric order, ferromagnetic order or both like in the CuCl_4 -2-phenylethylammonium hybrid (figure 2).³¹ These systems are generally obtained *via* hydrothermal synthesis or even by simple mixing of metallic salt with organic molecules in solution at room temperature and letting it evaporate, which is the method used to obtain the CuCl_4 -2-phenylethylammonium hybrid discussed above.

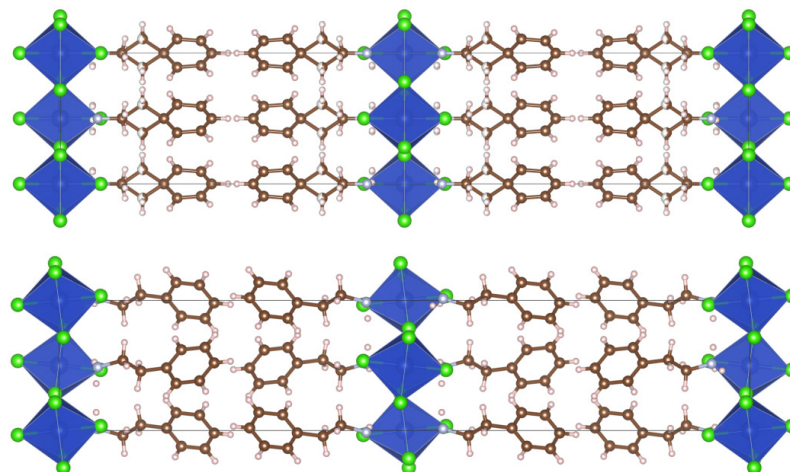


Figure 2 : Structure of the CuCl_4 -2-phenylethylammonium hybrid resolved at room temperature (top) and at 100 K (bottom), below its phase transition according to this work.³¹

This technique has the advantage of being straightforward once the synthetic conditions have been optimized, as well as to allow mixed metal compositions, but this optimization work is very likely to be required again if a single component is modified. Another limitation of this technique is that there is little to no control over the obtained material and that the eventual presence of remaining solvent molecule inside the material could lead to problematic stability concerns. Indeed in some cases, the loss of solvent inside the material or the addition of an external solvent such as water leads to a collapse of the structure. This phenomenon is well known in Metal-Organic Frameworks (MOFs). For instance, the famous MOF-5 becomes unstable if exposed to water.³² This can be mitigated *via* Ni-doping.³³ Hopefully in other cases the solvent can be used as structural modifier such as in the azido-bridged Co^{2+} layers that will either form square, honeycomb or Kagomé network depending on the solvent crystallization (figure 3).³⁴

All the other techniques are based on the same principle, which is to first build a 2D material and then use it as a scaffold for the hybrid material.

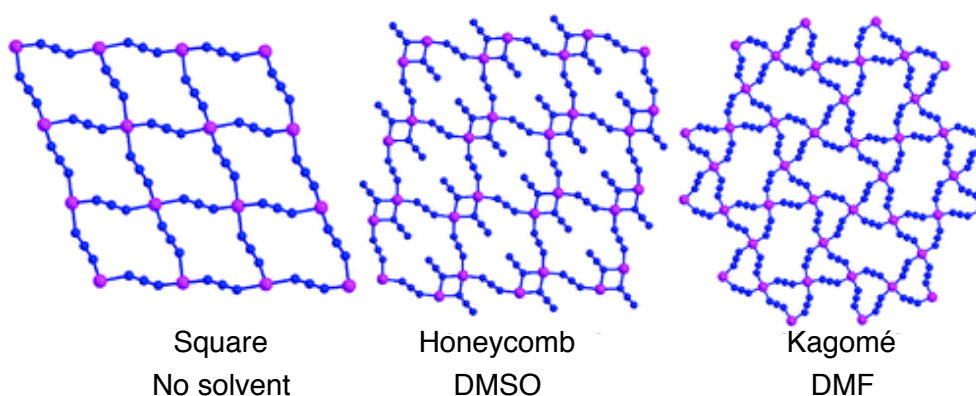


Figure 3 : Details of azido-bridged Co^{2+} layers structure depending on the solvent used.³⁵

With the main concern of stability, a logical approach has been to seek among the most resilient 2D starting block to build the hybrid material with, so the choice of oxides has often been made as a scaffolding unit for their mechanical properties as well as their other interesting physical properties. Indeed, on a detailed review³⁶ about oxides and oxides derivatives for hybrid materials applications it can be observed that they can have multiple properties going back from magnetic tapes protection coating based on CrO_2 films³⁷ to catalytic properties of oxy-methoxy compounds of molybdenum(VI) with selective oxidation properties of methanol to formaldehyde.³⁸

Oxides have a practically boundless reactivity with many covalent or ionic organic molecules moieties which allow a better substructure control *via* the organic modification. This approach was also studied in our lab with the functionalization of Aurivillius phases $\text{Bi}_2\text{SrTa}_2\text{O}_9$.^{39, 40}

This method takes full advantage of its versatility when it comes to the insertion of specific molecular entities with a directly aimed property in mind, but its chemistry is still widely uncovered due to synthetic challenges.

Another strategy is to play with the fact that several of these 2D layers possess a net charge, would that be positive for layered double hydroxides (LDH)⁴¹ or negative for titanoniobate⁴² or calcium niobate⁴³ oxides. It is possible to assemble the oppositely charged layers either *via* exfoliation and electrostatic self-reassembly²⁸ or *via* successive deposition on a surface *via* the so-called layer-by-layer method, as employed for the successive deposition of LDH and layered perovskites (figure 4).⁴⁴ The layer-by-layer method is a promising method for the earliest applications, it is indeed already shaped on a surface and thus easier to construct a device with it.

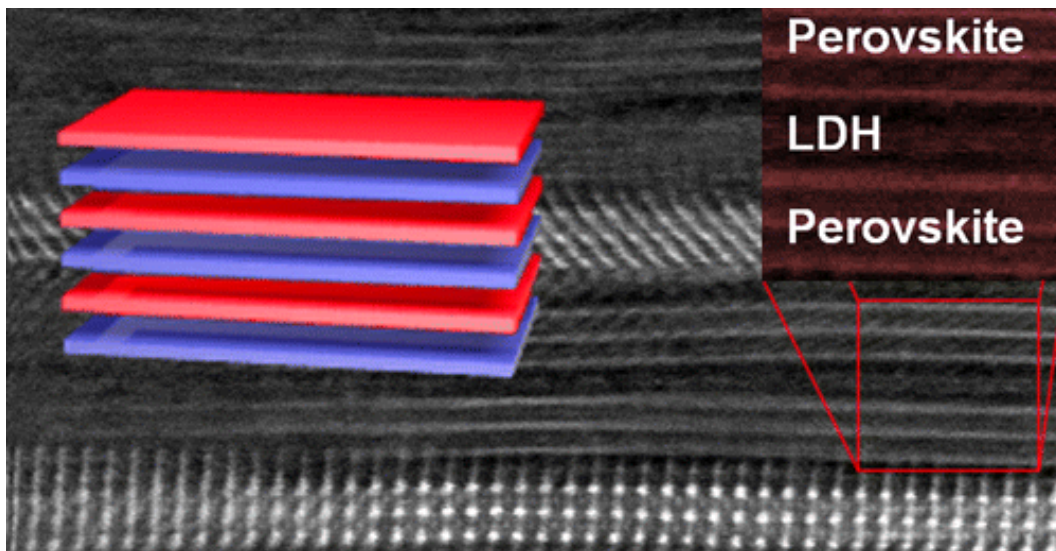


Figure 4 : Hybrid heterostructure made from Mn/Al LDH and $Ca_2Nb_3O_{10}$ assembled by layer by layer deposition.⁴⁴

On the other hand, this method is also quite difficult to master, from the difficulty of the exfoliation process to the stability of high aspect ratio nano platelets. Another difficulty of this chemistry is to take into account the net surface charge density incompatibility between the layers and the difficulty to have good surface coverage.

Among all the different scaffolding materials available, the most widely used are layered hydroxides, they have been extensively studied with their interesting magnetic,⁴⁵ mechanical and flame retardant,⁴⁶ photocatalytic⁴⁷ or water purification properties⁴⁸ and bounteous intercalation chemistry.^{41, 49-55}

2. Layered Hydroxides

In lamellar hydroxides, it is important to differentiate two types of hydroxides : i) layered double hydroxide (LDH), formed by positively charged layers of hydroxide or transition metal ions interleaved by anions held together *via* electrostatic forces ii) layered simple hydroxides (LSH) with neutral layers due to covalent bonding between the organic and inorganic phase. It can be observed in figure 5 the LDH structure (left) with Zn^{2+} and Al^{3+} forming the brucite-like layers (single layer of edge-sharing octahedra) and the carbonate anions present in a disordered fashion for charge balancing along with water molecules. Meanwhile the right part of the figure represents the LSH structure of copper hydroxy-acetate with covalent bonding of the Cu^{2+} brucite-like layers with the acetate molecules, along with an important hydrogen bonding network with the interlamellar water molecules.

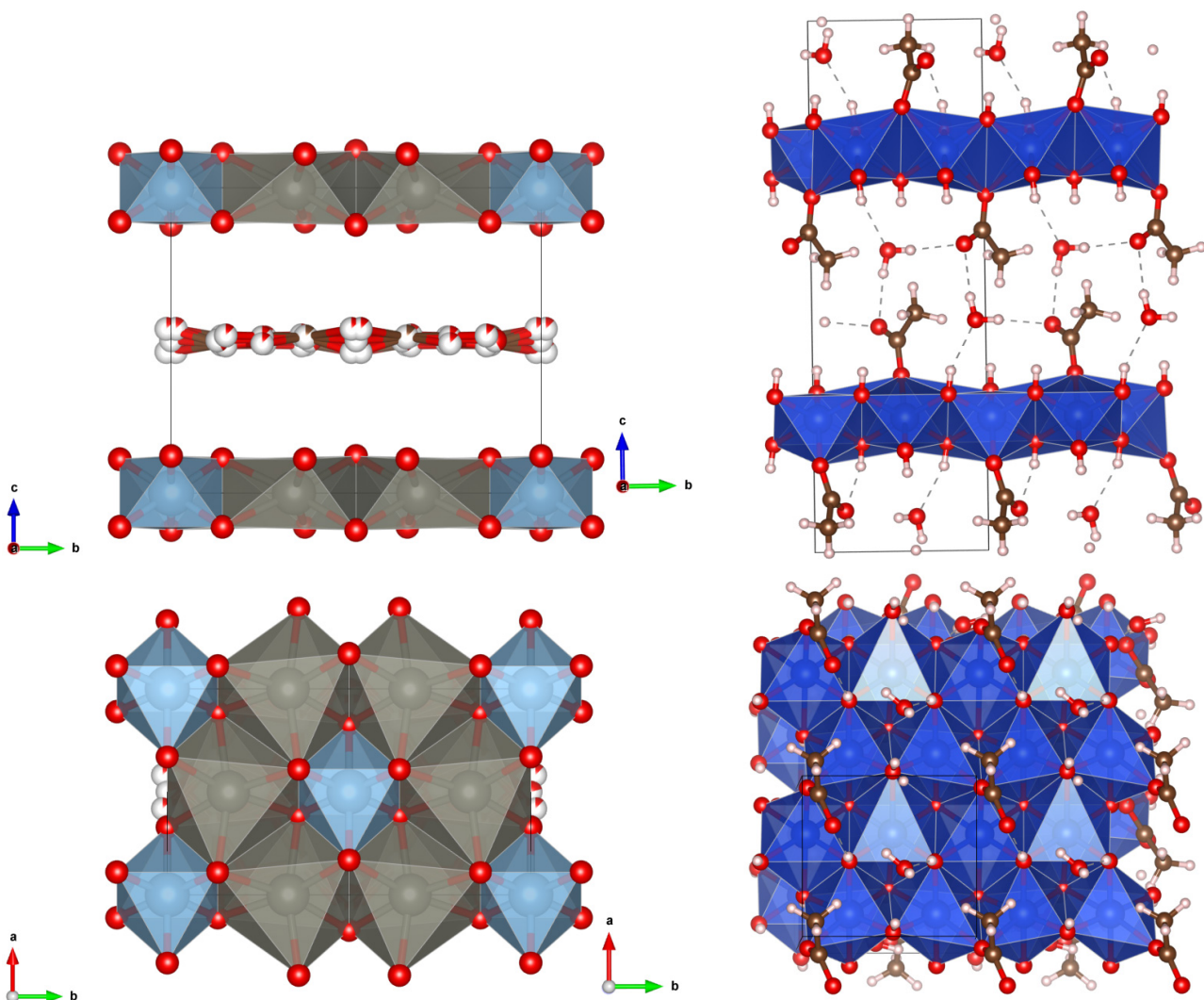


Figure 5 : Structure of Zn/Al-LDH-CO₃(left),⁵⁶ structure of copper hydroxy-acetate LSH (right).⁵⁷

Both these systems have their advantages and disadvantages towards functionalization and/or synergy of the organic/inorganic parts properties but it is important to note that the most studied systems are by far the LDHs^{41, 58} mainly due to their charged nature and thus somehow easier functionalization and exfoliation process.

2.1. Layered Double Hydroxides

The general formula of a LDH is $[M(II)_{1-x}M(III)_x(OH)_2]^{x+}(A^{n-})_{x/n} \cdot mH_2O$ where M=Al, Zn, Mg, Mn, Co, Fe...) and A is an exchangeable anion such as CO₃²⁻, Cl⁻, Br⁻, NO₃⁻, SO₄²⁻...

Due to the presence of two different oxidation states of the transition metals and the flexibility of the structure composition, it is possible to change the charge density of the layers in most of these systems.^{59, 60} The most studied system is the $[Mg^{2+}_{1-x}Al^{3+}_x(OH)_2]^{x+}(CO_3^{2-})_{x/2} \cdot yH_2O$ with x=0.10-0.33. It is widely represented as a model of LDH for many applications that have been extensively studied in fields ranging from CO₂ adsorption,⁵² catalyst precursor,^{61, 62} ions^{54, 63, 64} or organic molecules⁶⁵ capture in wastewater, flame-retardant,⁴⁶ chemiluminescence catalyst,⁶⁶ piezochromic luminescence⁶⁷ or as a nano-filler in polymers.⁶⁸⁻⁷⁰

It must be noted that even though the Mg/Al-LDH is the most studied system up to this day, they are many other LDH systems that can be synthesized with an Al³⁺ basis. Examples of such LDH systems are Zn/Al-LDH,^{50, 71} Ni/Al-LDH,⁷² Co/Al-LDH,⁷³ Cu/Al-LDH⁷⁴ and Ca/Al-LDH.⁴⁸ Other systems can be found in the literature with Fe³⁺ or Cr³⁺ basis. Examples of LDH with Fe³⁺ basis are Ni/Fe-LDH,⁷² Ca/Fe-LDH,⁵³ Co/Fe-LDH⁷⁵ and Mg/Fe-LDH⁷⁶ with various properties ranging from magnetism⁷² to water oxidation.⁷⁵

Examples of LDH with Cr³⁺ basis scarcely appear in the literature in the form of Cu/Cr-LDH,⁷⁷ Co-Cu/Cr-LDH⁷⁸ or Zn/Cr-LDH.⁷⁹ They are a few other LDH that has been studied in recent years with more « exotic » elements or properties, among them are Ni/Mn-LDH,⁸⁰ Mg/Ga-LDH⁸¹ that is capable of incorporating DNA fragments or even more unusual systems with Ni²⁺/Ti⁴⁺-LDH able to adsorb pentachlorophenol due to its enhanced hydrophobicity.⁸²

Another unusual system is the Li⁺/Al³⁺-LDH⁸³ with its ability to deintercalate lithium to desorb previously absorbed chromate.⁴⁹

A last system that differs a little bit compared to previous ones are layered rare earth hydroxides, they have a general chemical formula of Ln₂(OH)_{6-m}(A^{x-})_{m/x}·nH₂O (Ln: trivalent rare earth, A: guest anion; 0.5 ≤ m ≤ 2.0). They have been known for a long time⁸⁴ and regained interest more recently with improved crystallinity⁸⁵ and reactivity especially in their anion exchange behavior.⁸⁶ The most common ions found in the interlayer are nitrate,⁸⁶⁻⁸⁸ chloride,⁸⁹ sulfate⁹⁰ or even organic molecules such as acetate⁹¹ or alkylsulfates.⁸⁶ The addition of rare earth in these compounds can be very interesting because of the specific 4f shell bringing peculiar properties in photo physics^{92, 93} and magnetic anisotropy⁹⁴ for example. It must be noted that this last system contains two different series, the first one being of typical formula Ln₂(OH)₅(A^{x-})_{1/x}·nH₂O (m = 1) with positively charged layers and freely accommodated anionic species in the interlayer space and a lanthanide coordination number between eight and nine. The second series with typical formula Ln₂(OH)₄(A^{x-})_{2/x}·nH₂O (m = 2) possess a lanthanide coordination number of nine (generally) and coordinated guest anions. This series is very much alike to the one I have studied during my PhD, they are named layered simple hydroxides (LSH) or sometimes layered hydroxy salts (LHSs).

2.2. Layered Simple Hydroxides

As mentioned earlier, the main difference between layered simple hydroxides (LSH) and LDH is the grafting of the organic molecules to the inorganic layer, leading to a null net lamellae charge. They have a general formula of M(II)₂(OH)_{4-x}(A^{m-})_{x/m}·nH₂O with a divalent metal cation (Co²⁺, Cu²⁺, Ca²⁺, Cd²⁺, Zn²⁺, Ni²⁺, Mn²⁺ or Mg²⁺) and A an anion that can be any molecule bearing an anchoring function or a halide. The most common examples of anions are chloride,⁹⁵ nitrate,^{95, 96} sulfate⁹⁷ and carboxylate.⁹⁸

The chemical properties of these systems are well known and have been studied extensively along the years. One of the first examples is topotactic reactions of the zinc hydroxide nitrate⁹⁶ compound with aqueous metal chloride⁹⁵ leading to the anion exchange from nitrate to chloride as well as a partial exchange of the zinc with the cobalt or nickel salts. The most studied LSH are the M₂(OH)₃·H₂O with M = Cu, Co and X = NO₃ or OAc,⁹⁹ they are also being very well-known for their anion exchange properties with iodine,¹⁰⁰ n-alkylsulfonates,¹⁰¹ n-methylene (di)carboxylates,¹⁰² stilbazolium-carboxylate or -sulfonate,¹⁰³ α-α'oligothiophenecarboxylates¹⁰⁴ or even metal phthalocyanines tetrasulfonate^{26, 105} and salen type complexes with carboxylate or sulfonate anchoring groups.¹⁰⁶⁻¹⁰⁸

LSH can be classified in two categories, depending on the structure of the inorganic layers. Type I LSHs¹⁰⁹ corresponds to a simple brucite-like layer of metals in octahedral configuration sharing edges with each other and with the anion directly grafted to three octahedra shared vertices. Type II LSHs differs from the type I by the fact that the octahedral layers present vacancies, with tetrahedral sites above and below these vacancies (figure 6). It must be noted that these vacancies can be randomly distributed like in the case of cobalt hydroxy-chloride¹¹⁰ or have a specific ordering like in the zinc hydroxy-nitrate compound⁹⁶ depending on the material. But it must also be noted that due to general difficulties to obtain single crystals of these materials, the debate about the ordering or random distribution of these vacancies or even of the whole layer structure itself is still ongoing.¹¹¹⁻¹¹⁴

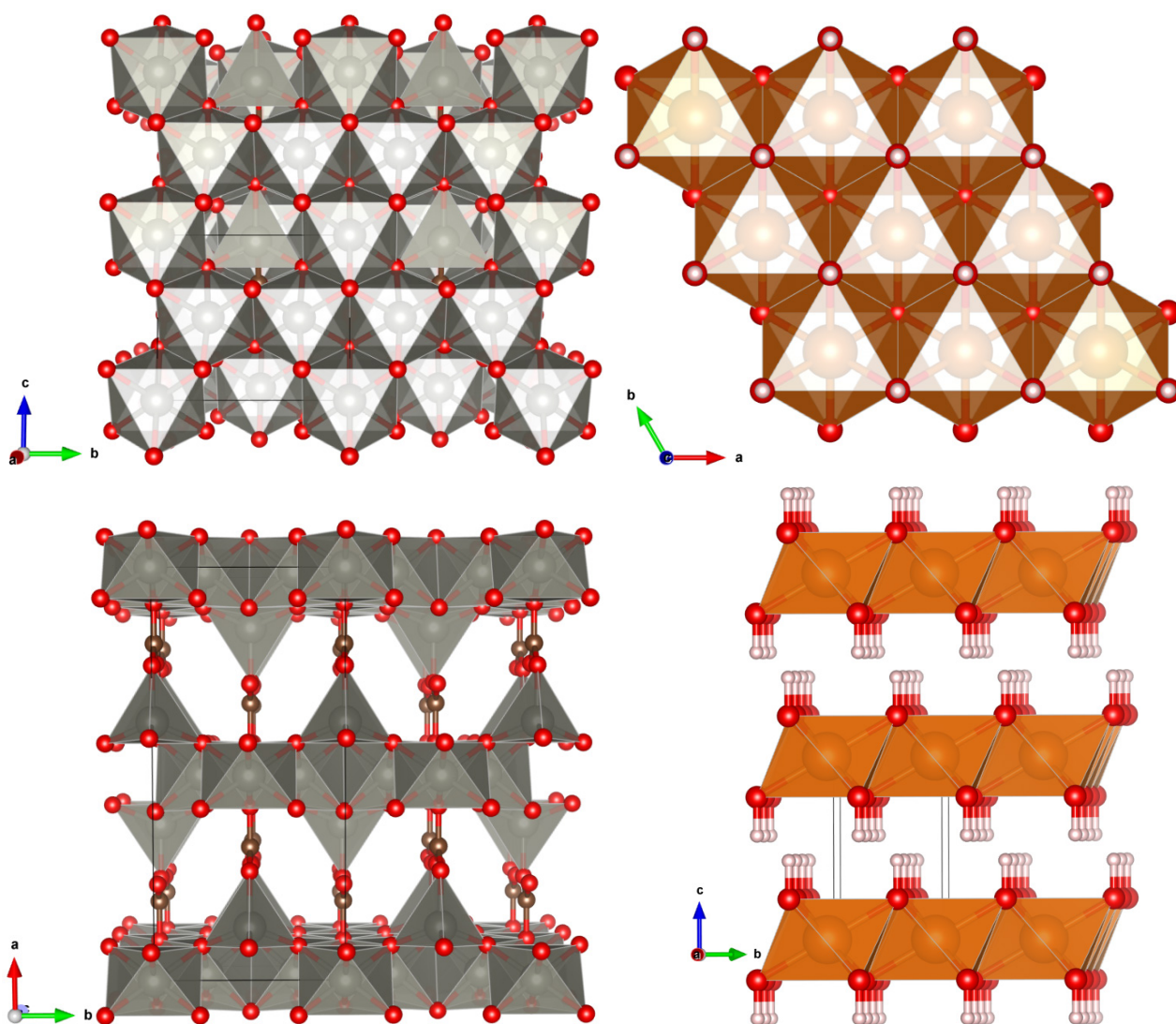


Figure 6 : Hydrozincite ($Zn_5(OH)_6(CO_3)_2$) structure¹¹⁵(left) brucite ($Mg(OH)_2$) structure (right).¹¹⁶

They are still many other LSH systems that have been less studied such as systems having two different metals like the $NiCu(OH)_{3.1}(CH_3COO)_{0.9} \cdot 0.9H_2O$ ¹¹⁷ known for his chromate intercalation properties¹¹⁸ or $Ni_{1-x}Zn_{2x}(OH)_2(CH_3COO)_{2x} \cdot n H_2O$ ¹¹⁹ with $(0.15 \leq x \leq 0.25)$,¹²⁰ $(Cu,Co)(OH)_3(NO_3)$ ¹²¹ or $Zn_xCu_{2-x}(OH)_3(NO_3)$ ¹²² $(0 < x \leq 1.8)$. These last systems are usually obtained by hydrothermal synthesis at high temperatures usually from 150°C¹¹⁷ to 220°C.¹²³

3. Thesis Structure

The main objective of my thesis consists in the addition of a new property to magnetic layered simple hydroxides *via* the addition of functional molecules. Out of the several interesting properties that can be added *via* molecular intercalation, we have chosen to focus on bringing electric ordering. The goal being to obtain a material that is multiferroic, meaning having both electric and magnetic ordering. This domain is largely covered by oxides with model materials such as BiFeO_3 or $\text{BaTiO}_3\text{-CoFe}_2\text{O}_4$ structures,^{124, 125} but hybrids and molecule-based materials have attracted increasing attention with MOFs for example.^{126, 127}

The two LSH that are used thoroughly as inorganic matrix during my PhD are $\text{Co}_2(\text{OH})_{3.2}(\text{OAc})_{0.8}\cdot 1.8\text{H}_2\text{O}$ and $\text{Cu}_2(\text{OH})_3(\text{OAc})\cdot 1\text{H}_2\text{O}$. The structure of the latter has been recently solved *via* mono crystal resolution in Švarcová's paper,⁵⁶ meanwhile the cobalt hydroxy-acetate structure has not been resolved at the time of writing. As for the magnetic properties, $\text{Cu}_2(\text{OH})_3(\text{OAc})\cdot 1\text{H}_2\text{O}$ presents an antiferromagnetic ordering ($T_N = 9 \text{ K}$),¹²⁸ whereas $\text{Co}_2(\text{OH})_{3.2}(\text{OAc})_{0.8}\cdot 1.8\text{H}_2\text{O}$ presents a ferrimagnetic ordering ($T_C = 12.6 \text{ K}$).¹²⁹

To be able to functionalize these two hydroxides with complex molecules, a technique called pre-intercalation has been developed in the laboratory.^{99, 103} This technique will be discussed in more details in chapter I of this thesis but the principle is to exchange the acetate with dodecylsulfonate or dodecylsulfate for cobalt and copper hydroxides respectively. This allows a wider interlamellar spacing as well as a more hydrophobic environment between the layers, this either enhance the crystallinity of the final compound with the molecule of interest or even allows the intercalation that could not be made *via* direct reaction from the acetate-intercalated hydroxide.

The first part of my work was devoted to the improvement the crystallinity of all the starting compounds as much as possible as well as to the optimization of the structural description for all the starting compounds. This work is described in chapter I for the copper hydroxide and in chapter II for the cobalt hydroxide. Due to major characterization method differences between the two systems these chapters have been split, indeed for the copper hydroxide, single crystal experiments have been made possible meanwhile the very low crystallite size, lack of long-range ordering and possible defects for cobalt made single crystal determination impossible. To that end, the chapter II will deal with pair distribution function (PDF) extracted from X-ray total scattering *via* experiments made at SOLEIL synchrotron (France), in close collaboration with Pr. Taviot-Guého (Institut de Chimie de Clermont-Ferrand).

Once the starting compounds syntheses has been optimized, it has been possible to work on the insertion of new compounds. The main difference compared to what has been made previously in the laboratory concerns the grafting moiety. We have used molecules with a phosphonic acid anchoring group, whereas the anchoring functions used up to now in layered simple hydroxides were carboxylate, sulfate and sulfonate. The molecules were designed within the frame of the ANR project HYMN (HYbrid Multiferroic Nanomaterials). They were synthesized in the gram scale by the group of Pr. P.-A. Jaffrès in the Laboratoire Chimie Electrochimie et Chimie Analytique in Brest. These molecules were used simultaneously for one-pot hydrothermal syntheses of hybrid compounds by the group of Dr. J.-M. Rueff in the Laboratoire CRISallographie et MATériaux in Caen.

The presence of a phosphonic acid next to an aromatic ring makes the molecules rigid and this grafting moiety also enables a symmetry breaking that is mandatory (but not sufficient) to obtain the sought property of ferroelectricity. Indeed, most of the molecules used in this PhD possess a low symmetry and some exhibit prochiral faces. We conjectured that this low symmetry

should favour the formation of chiral hybrid materials due to the distinction of the two prochiral faces during the synthesis of the hybrid, either by one pot approach performed in Caen or by the functionalization of layered magnetic hydroxides performed in this PhD. Racemic hybrid compounds can theoretically be formed but homochiral structures (non-centrosymmetric structure) can also be produced. In addition, the flexibility induced by the lateral chain on some molecules is likely to favour the non-centrosymmetric arrangement. Side functionalization may also be helpful to trigger the polarity of the compounds. The main idea behind this molecular design can be summarized in figure 7 below.

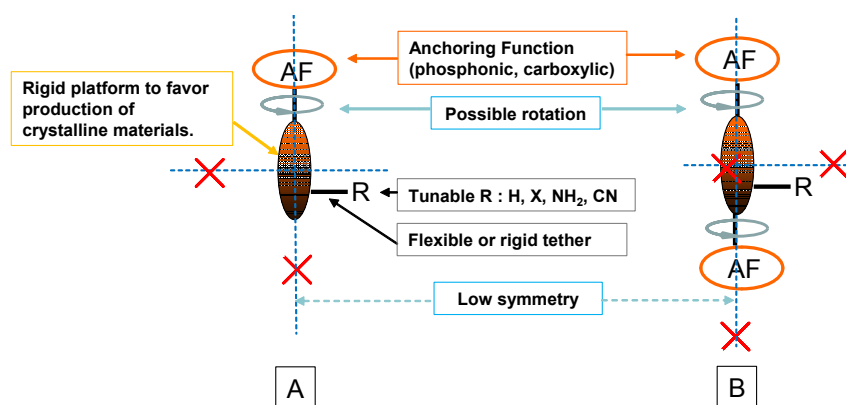


Figure 7 : Molecular design for mono (A) and di (B) functional molecules.

During my thesis I worked on the insertion on many molecules which could add a new property to the final hybrid material. The table below summarizes the different molecules inserted and presented in this thesis as well as the thought properties. This table excludes the dodecylsulfate-intercalated copper hydroxide discussed in detail in the chapter I due to the fact that it has been obtained *via* direct coprecipitation and not exchange reaction in an already formed inorganic matrix.

Goal	Structural analysis	Magneto-electric effect			Luminescence			
Grafting moiety	-COOH	-PO(OH) ₂ or -COOH		-PO(OH) ₂	-PO(OH) ₂	-SO ₂ (OH)		
Rigid platform								
Functionalization	None	R = NH ₂ , -N(CH)(CH ₂) ₂ CH ₃ , -N(CH)(CH ₂) ₃ CH ₃ , -N(CH)(CH ₂) ₄ CH ₃ , -N(CH)(CH ₂) ₁₀ CH ₃ or 4-(iminomethyl) benzotrile	R' = PO(OH) ₂ R'' = PO(OH) ₂ , COOH or H R''' = H, CH ₃ , -(CH ₂) ₃ -CH ₃ , or -(CH ₂) ₇ -CH ₃	R' = COOH or PO(OH) ₂ X = F, Cl, Br, I, O(CH ₂)CN or O(CH ₂) ₃ CN	R = PO(OH) ₂ R' = H or CH ₃	R = PO(OH) ₂	None	None
Chapter	II	III	IV	V	VI			

Table 1 : Molecules inserted into copper and cobalt layered simple hydroxides in this thesis.

Chapter I deals with the improvements made on the synthesis and structural characterization of layered copper hydroxide. The goal is to get as much structural information as possible about the dodecylsulfate-intercalated compound and to be able to obtain crystallites as big as possible for an eventual future shaping of the materials for deposition on electrodes for (di)electric measurements.

In chapter II, the compounds studied have been first synthesized by O. Palamarciuc during his post-doc in the laboratory, and prepared by myself.¹³⁰ In this chapter, the goal was two folds, first to prove the in-situ reaction of the 4-aminobenzoic acid (previously grafted into layered cobalt hydroxide) with different aldehydes *via* PDF analysis. Most of all, this study will allow to have a better insight of the structure of the cobalt hydroxide layers.

The molecules listed in chapter III, IV and V represents the « chemical core » of my work during these three years. Following the molecular design shown in figure 7, we played with both the nature of the rigid platform and the lateral functionalization. These molecules, additionally to the chemical challenge of inserting them in single phase hybrids are also interesting to study the influence of both the symmetry (or lack thereof) and the nature of the lateral functionalization on measurements of magneto-electric coupling.

Actually, as stated above, the initial goal of this project was to endow the magnetic layered hydroxides with ferroelectric properties. Yet, to probe the ferroelectric behaviour, good quality electrodes should be realized on the samples. This can be a difficult task especially on powder samples incompatible with high temperature sintering. Good ohmic electric pads can be difficult to realize on such samples. However, some measurements reported in the literature show that reproducible dielectric measurements can be realized on hybrid cold sintered materials (organic ferroelectrics or multiferroic MOFs for instance) with pressed electrodes and good choice of conducting paste.^{131, 132} Yet, up to now, it has not been possible to assess unambiguously the possible ferroelectric character of the samples prepared in this thesis because of strong leakage currents due to grain boundaries. Yet an interesting magneto-electric coupling effect was evidenced on several samples and will be discussed.

The series with fluorenes described in chapter III also underlines the differences observed between single and bi-functionalization of the molecules on the structure and properties of the obtained hybrids.

The benzene derivatives shown in the chapter IV have the great interest of changing only the nature of the halogen in meta position and therefore the polarity and polarizability of the C-X bond without greatly modifying the molecule shape. This could allow us to monitor the effect of this polarity/polarizability on the magnetoelectric properties.

The thiophene series described in chapter V add a heteroatom to the rigid platform and offer the possibility to be directly compared to their dicarboxylic counterparts previously studied in our laboratory.¹⁰⁴

The complexes inserted in cobalt hydroxide and described in chapter VI are somewhat different from the previous molecules on many aspects. They were used with luminescence properties in mind instead of looking for magnetoelectric effect. Indeed, the experience acquired to develop the insertions of molecules bearing phosphonic acid proved to be useful to insert a complex of ruthenium-trisbipyridine bearing the same anchoring groups. Indeed, work attempted previously in our laboratory gave promising results but problems of reproducibility and presence of important amounts of remaining starting molecules within the interlayer space were observed.¹³³ After a successful insertion, we decided to extend this research to a platinum-salen complex to evidence that sulfonate groups are also good candidates to avoid a quenching of the luminescence of the complex.

4. Bibliography

1. A. Doménech, M. T. Doménech-Carbó, M. Sánchez del Río, M. L. Vázquez de Agredos Pascual and E. Lima, *New Journal of Chemistry*, 2009, **33**, 2371-2379.
2. P. Kumar and V. V. Guliyants, *Microporous and Mesoporous Materials*, 2010, **132**, 1-14.
3. C. Sanchez, B. Lebeau, F. Chaput and J.-P. Boilot, *Advanced Materials*, 2003, **15**, 1969-1994.
4. Y. Kobayashi, Y. Kurokawa and Y. Imai, *Journal of Non-Crystalline Solids*, 1988, **105**, 198-200.
5. B. Dunn and J. I. Zink, *Journal of Materials Chemistry*, 1991, **1**, 903-913.
6. M. Casalboni, F. De Matteis, P. Proposito and R. Pizzoferrato, *Applied Physics Letters*, 1999, **75**, 2172-2174.
7. T. Dantas de Moraes, F. Chaput, K. Lahlil and J.-P. Boilot, *Advanced Materials*, 1999, **11**, 107-112.
8. T. Dantas de Moraes, F. Chaput, J.-P. Boilot, K. Lahlil, B. Darracq and Y. Lévy, *Advanced Materials for Optics and Electronics*, 2000, **10**, 69-79.
9. A. Espinosa, Mexico, 1987. « Conservation and restoration of the murals of the Temple of the Paintings in Bonampak, Chiapas »
10. C. Sanchez, B. Julián, P. Belleville and M. Popall, *Journal of Materials Chemistry*, 2005, **15**, 3559-3592.
11. J. Xu, K. Wang, S. Z. Zu, B. H. Han and Z. Wei, *ACS Nano*, 2010, **4**, 5019-5026.
12. L. Liu, Q. Wang, C. Gao, H. Chen, W. Liu and Y. Tang, *The Journal of Physical Chemistry C*, 2014, **118**, 14511-14520.
13. K. Zhou, Y. Zhu, X. Yang and C. Li, *Electroanalysis*, 2009, **22**, 259-264.
14. X. Gao, M. Hu, L. Lei, D. O'Hare, C. Markland, Y. Sun and S. Faulkner, *Chemical Communications*, 2011, **47**, 2104-2106.
15. E. Káfuňková, K. Lang, P. Kubát, M. Klementová, J. Mosinger, M. Šlouf, A.-L. Troutier-Thuilliez, F. Leroux, V. Verney and C. Taviot-Guého, *Journal of Materials Chemistry*, 2010, **20**, 9423-9432.
16. D. Yan, Y. Zhao, M. Wei, R. Liang, J. Lu, D. G. Evans and X. Duan, *RSC Advances*, 2013, **3**, 4303.
17. Z.-L. Huang, M. Drillon, N. Masciocchi, A. Sironi, J.-T. Zhao, P. Rabu and P. Panissod, *Chemistry of Materials*, 2000, **12**, 2805-2812.
18. P. Rabu, J. M. Rueff, Z. L. Huang, S. Angelov, J. Souletie and M. Drillon, *Polyhedron*, 2001, **20**, 1677-1685.
19. M. Drillon, P. Panissod, P. Rabu, J. Souletie, V. Ksenofontov and P. Gütllich, *Physical Review B*, 2002, **65**, 104404-104412.
20. A. García-Fernández, J. M. Bermúdez-García, S. Castro-García, R. Artiaga, J. López-Beceiro, M. A. Señarís-Rodríguez and M. Sánchez-Andújar, *Polyhedron*, 2016, **114**, 249-255.
21. X.-H. Lv, W.-Q. Liao, P.-f. Li, Z.-X. Wang, C.-Y. Mao and Y. Zhang, *Journal of Materials Chemistry C*, 2016, **4**, 1881-1885.
22. S. Chaouachi, B. Hamdi and R. Zouari, *Synthetic Metals*, 2017, **223**, 122-131.
23. X. Li, Y. Zhong, Q. Li and L. Wang, *Journal of colloid and interface science*, 2013, **405**, 226-232.
24. Y. Liang, Y. Li, H. Wang and H. Dai, *Journal of the American Chemical Society*, 2013, **135**, 2013-2036.

25. A. L. Wang, H. Xu, J. X. Feng, L. X. Ding, Y. X. Tong and G. R. Li, *Journal of the American Chemical Society*, 2013, **135**, 10703-10709.
26. S. Eyele-Mezui, P. Vialat, C. Higy, R. Bourzami, C. Leuvrey, N. Parizel, P. Turek, P. Rabu, G. Rogez and C. Mousty, *The Journal of Physical Chemistry C*, 2015, **119**, 13335-13342.
27. R. Marangoni, L. P. Ramos and F. Wypych, *Journal of Colloid and Interface Science*, 2009, **330**, 303-309.
28. E. Coronado, C. Marti-Gastaldo, E. Navarro-Moratalla, A. Ribera, S. J. Blundell and P. J. Baker, *Nature Chemistry*, 2010, **2**, 1031-1036.
29. B. W. Li, M. Osada, Y. Ebina, S. Ueda and T. Sasaki, *Journal of the American Chemical Society*, 2016, **138**, 7621-7625.
30. Y.-L. Liu, D.-H. Wu, Z. Wang and Y. Zhang, *New Journal of Chemistry*, 2017, **41**, 3211-3216.
31. A. O. Polyakov, A. H. Arkenbout, J. Baas, G. R. Blake, A. Meetsma, A. Caretta, P. H. M. van Loosdrecht and T. T. M. Palstra, *Chemistry of Materials*, 2012, **24**, 133-139.
32. J. A. Greathouse and M. D. Allendorf, *Journal of the American Chemical Society*, 2006, **128**, 10678-10679.
33. H. Li, W. Shi, K. Zhao, H. Li, Y. Bing and P. Cheng, *Inorganic Chemistry*, 2012, **51**, 9200-9207.
34. X. Y. Wang, L. Wang, Z. M. Wang and S. Gao, *Journal of the American Chemical Society*, 2006, **128**, 674-675.
35. X. Y. Wang, L. Wang, Z. M. Wang and S. Gao, *Journal of the American Chemical Society*, 2006, **128**, 674-675.
36. P. J. Hagrman, D. Hagrman and J. Zubieta, *Angewandte Chemie International Edition International Edition*, 1999, **38**, 2638-2684.
37. B. Bhushan, G. S. A. M. Theunissen and X. Li, *Thin Solid Films*, 1997, **311**, 67-80.
38. E. M. McCarron and A. W. Sleight, *Polyhedron*, 1986, **5**, 129-139.
39. Y. Wang, E. Delahaye, C. Leuvrey, F. Leroux, P. Rabu and G. Rogez, *Inorganic Chemistry*, 2016, **55**, 4039-4046.
40. Y. Wang, Ph. D., Université de Strasbourg, 2017.
41. V. Rives and M. a. Angeles Ulibarri, *Coordination Chemistry Reviews*, 1999, **181**, 61-120.
42. M. Osada, G. Takanashi, B.-W. Li, K. Akatsuka, Y. Ebina, K. Ono, H. Funakubo, K. Takada and T. Sasaki, *Advanced Functional Materials*, 2011, **21**, 3482-3487.
43. T. C. Ozawa, M. Onoda, N. Iyi, Y. Ebina and T. Sasaki, *The Journal of Physical Chemistry C*, 2014, **118**, 1729-1738.
44. C. Ziegler, S. Werner, M. Bugnet, M. Wörsching, V. Duppel, G. A. Botton, C. Scheu and B. V. Lotsch, *Chemistry of Materials*, 2013, **25**, 4892-4900.
45. H. Shimizu, M. Okubo, A. Nakamoto, M. Enomoto and N. Kojima, *Inorganic Chemistry*, 2006, **45**, 10240-10247.
46. C. M. Becker, A. D. Gabbardo, F. Wypych and S. C. Amico, *Composites Part A: Applied Science and Manufacturing*, 2011, **42**, 196-202.
47. J. L. Gunjekar, T. W. Kim, H. N. Kim, I. Y. Kim and S. J. Hwang, *Journal of the American Chemical Society*, 2011, **133**, 14998-15007.
48. P. Zhang, G. Qian, H. Shi, X. Ruan, J. Yang and R. L. Frost, *Journal of Colloid and Interface Science*, 2012, **365**, 110-116.
49. Y.-M. Tzou, S.-L. Wang, L.-C. Hsu, R.-R. Chang and C. Lin, *Applied Clay Science*, 2007, **37**, 107-114.

50. G. G. Arizaga, A. S. Mangrich, J. E. da Costa Gardolinski and F. Wypych, *Journal of Colloid and Interface Science*, 2008, **320**, 168-176.
51. D. Yan, J. Lu, L. Chen, S. Qin, J. Ma, M. Wei, D. G. Evans and X. Duan, *Chemical Communications*, 2010, **46**, 5912-5914.
52. J. Wang, L. A. Stevens, T. C. Drage and J. Wood, *Chemical Engineering Science*, 2012, **68**, 424-431.
53. Y. Wu, Y. Yu, J. Z. Zhou, J. Liu, Y. Chi, Z. P. Xu and G. Qian, *Chemical Engineering Journal*, 2012, **179**, 72-79.
54. X. Y. Yu, T. Luo, Y. Jia, R. X. Xu, C. Gao, Y. X. Zhang, J. H. Liu and X. J. Huang, *Nanoscale*, 2012, **4**, 3466-3474.
55. S. Dong, F. Liu and C. Lu, *Analytical Chemistry*, 2013, **85**, 3363-3368.
56. S. Švarcová, M. Klementová, P. Bezdička, W. Łasocha, M. Dušek and D. Hradil, *Crystal Research and Technology*, 2011, **46**, 1051-1057.
57. S. Marappa and P. V. Kamath, *Industrial & Engineering Chemistry Research*, 2015, **54**, 11075-11079.
58. G. Arizaga, K. Satyanarayana and F. Wypych, *Solid State Ionics*, 2007, **178**, 1143-1162.
59. Y. Zhao, F. Li, R. Zhang, D. G. Evans and X. Duan, *Chemistry of Materials*, 2002, **14**, 4286-4291.
60. C. Carteret, B. Grégoire and C. Ruby, *Solid State Sciences*, 2011, **13**, 146-150.
61. J. S. Valente, H. Pfeiffer, E. Lima, J. Prince and J. Flores, *Journal of Catalysis*, 2011, **279**, 196-204.
62. O. D. Pavel, D. Tichit and I.-C. Marcu, *Applied Clay Science*, 2012, **61**, 52-58.
63. L. Kentjono, J. C. Liu, W. C. Chang and C. Irawan, *Desalination*, 2010, **262**, 280-283.
64. D. Zhao, G. Sheng, J. Hu, C. Chen and X. Wang, *Chemical Engineering Journal*, 2011, **171**, 167-174.
65. L. Ai, C. Zhang and L. Meng, *Journal of Chemical & Engineering Data*, 2011, **56**, 4217-4225.
66. Z. Wang, F. Liu and C. Lu, *Chemical Communications*, 2011, **47**, 5479-5481.
67. D. Yan, J. Lu, J. Ma, S. Qin, M. Wei, D. G. Evans and X. Duan, *Angewandte Chemie International Edition*, 2011, **50**, 7037-7040.
68. K. Yano, A. Usuki, A. Okada, T. Kurauchi and O. Kamigaito, *Journal of Polymer Science Part A: Polymer Chemistry*, 1993, **31**, 2493-2498.
69. F. Leroux and C. Taviot-Guého, *Journal of Materials Chemistry*, 2005, **15**, 3628.
70. F. Kovanda, E. Jindová, K. Lang, P. Kubát and Z. Sedláková, *Applied Clay Science*, 2010, **48**, 260-270.
71. M. Z. B. Hussein, Z. Zainal and C. Y. Ming, *Journal of Materials Science Letters*, 2000, **19**, 879-883.
72. E. Coronado, J. R. Galan-Mascaros, C. Marti-Gastaldo, A. Ribera, E. Palacios, M. Castro and R. Burriel, *Inorganic Chemistry*, 2008, **47**, 9103-9110.
73. S. Sun and W. G. Hou, *Chinese Chemical Letters*, 2007, **18**, 1371-1373.
74. Y. Lwin, M. A. Yarmo, Z. Yaakob, A. B. Mohamad and W. Ramli Wan Daud, *Materials Research Bulletin*, 2001, **36**, 193-198.
75. S. J. Kim, Y. Lee, D. K. Lee, J. W. Lee and J. K. Kang, *Journal of Materials Chemistry A*, 2014, **2**, 4136.
76. I. M. Ahmed and M. S. Gasser, *Applied Surface Science*, 2012, **259**, 650-656.

77. C. Depège, C. Forano, A. d. Roy and J. P. Besse, *Molecular Crystals and Liquid Crystals Science and Technology. Section A. Molecular Crystals and Liquid Crystals*, 1994, **244**, 161-166.
78. K. Parida, L. Mohapatra and N. Baliarsingh, *The Journal of Physical Chemistry C*, 2012, **116**, 22417-22424.
79. K. Parida and L. Mohapatra, *Dalton Transactions*, 2012, **41**, 1173-1178.
80. C. Barriga, J. M. Fernández, M. A. Ulibarri, F. M. Labajos and V. Rives, *Journal of Solid State Chemistry*, 1996, **124**, 205-213.
81. L. Desigaux, M. B. Belkacem, P. Richard, J. Cellier, P. Leone, L. Cario, F. Leroux, C. Taviot-Gueho and B. Pitard, *Nano Letters*, 2006, **6**, 199-204.
82. Z. Gao, B. Du, G. Zhang, Y. Gao, Z. Li, H. Zhang and X. Duan, *Industrial & Engineering Chemistry Research*, 2011, **50**, 5334-5345.
83. C. J. Serna, J. L. Rendon and J. E. Iglesias, *Clays and Clay Minerals*, 1982, **30**, 180-184.
84. J. M. Haschke and L. Eyring, *Inorganic Chemistry*, 1971, **10**, 2267-2274.
85. F. Geng, Y. Matsushita, R. Ma, H. Xin, M. Tanaka, N. Iyi and T. Sasaki, *Inorganic Chemistry*, 2009, **48**, 6724-6730.
86. K.-H. Lee and S.-H. Byeon, *European Journal of Inorganic Chemistry*, 2009, **7**, 929-936.
87. L. J. McIntyre, L. K. Jackson and A. M. Fogg, *Chemistry of Materials*, 2008, **20**, 335-340.
88. Q. Zhu, J.-G. Li, C. Zhi, X. Li, X. Sun, Y. Sakka, D. Golberg and Y. Bando, *Chemistry of Materials*, 2010, **22**, 4204-4213.
89. F. Geng, H. Xin, Y. Matsushita, R. Ma, M. Tanaka, F. Izumi, N. Iyi and T. Sasaki, *Chemistry*, 2008, **14**, 9255-9260.
90. J. Liang, R. Ma, F. Geng, Y. Ebina and T. Sasaki, *Chemistry of Materials*, 2010, **22**, 6001-6007.
91. S. P. Newman and W. Jones, *Journal of Solid State Chemistry*, 1999, **148**, 26-40.
92. G. Blasse, *Journal of Alloys and Compounds*, 1993, **192**, 17-21.
93. J.-C. G. Bünzli and S. V. Eliseeva, *Basics of Lanthanide Photophysics*, 2010, **7**, 1-45.
94. J. D. Rinehart and J. R. Long, *Chemical Science*, 2011, **2**, 2078.
95. W. Stählin and H. R. Oswald, *Journal of Solid State Chemistry*, 1971, **3**, 256-264.
96. W. Stählin and H. R. Oswald, *Acta Crystallographica Section B Structural Crystallography and Crystal Chemistry*, 1970, **26**, 860-863.
97. D. Louër, J. Rius, P. Bénard-Rocherullé and M. Louër, *Powder Diffraction*, 2012, **16**, 86-91.
98. V. Laget, C. Hornick, P. Rabu and M. Drillon, *Journal of Materials Chemistry*, 1999, **9**, 169-174.
99. G. Rogez, C. Massobrio, P. Rabu and M. Drillon, *Chemical Society Reviews*, 2011, **40**, 1031-1058.
100. A. Jimenez-Lopez, E. Rodriguez-Castellon, P. Olivera-Pastor, P. Maireles-Torres, A. A. G. Tomlinson, D. J. Jones and J. Roziere, *Journal of Materials Chemistry*, 1993, **3**, 303.
101. S. H. Park and C. E. Lee, *The Journal of Physical Chemistry B*, 2005, **109**, 1118-1124.
102. C. Hornick, P. Rabu and M. Drillon, *Polyhedron*, 2000, **19**, 259-266.
103. É. Delahaye, S. Eyele-Mezui, J.-F. Bardeau, C. Leuvrey, L. Mager, P. Rabu and G. Rogez, *Journal of Materials Chemistry*, 2009, **19**, 6106-6115.
104. A. Demessence, A. Yassar, G. Rogez, L. Miozzo, S. De Brion and P. Rabu, *Journal of Materials Chemistry*, 2010, **20**, 9401-9141.
105. R. Bourzami, S. Eyele-Mezui, E. Delahaye, M. Drillon, P. Rabu, N. Parizel, S. Choua, P. Turek and G. Rogez, *Inorganic Chemistry*, 2014, **53**, 1184-1194.

106. E. Delahaye, S. Eyele-Mezui, M. Diop, C. Leuvrey, P. Rabu and G. Rogez, *Dalton Transactions*, 2010, **39**, 10577-10580.
107. E. Delahaye, S. Eyele-Mezui, M. Diop, C. Leuvrey, D. Foix, D. Gonbeau, P. Rabu and G. Rogez, *European Journal of Inorganic Chemistry*, 2012, **2012**, 2731-2740.
108. S. Eyele-Mezui, E. Delahaye, G. Rogez and P. Rabu, *European Journal of Inorganic Chemistry*, 2012, **2012**, 5225-5238.
109. M. Louër, D. Louër and D. Grandjean, *Acta Crystallographica Section B Structural Crystallography and Crystal Chemistry*, 1973, **29**, 1696-1703.
110. J. R. Neilson, D. E. Morse, B. C. Melot, D. P. Shoemaker, J. A. Kurzman and R. Seshadri, *Physical Review B*, 2011, **83**.
111. P. V. Kamath, G. H. Annal Therese and J. Gopalakrishnan, *Journal of Solid State Chemistry*, 1997, **128**, 38-41.
112. Z. P. Xu and H. C. Zeng, *Chemistry of Materials*, 1999, **11**, 67-74.
113. M. Rajamathi, P. V. Kamath and R. Seshadri, *Materials Research Bulletin*, 2000, **35**, 271-278.
114. R. Ma, Z. Liu, K. Takada, K. Fukuda, Y. Ebina, Y. Bando and T. Sasaki, *Inorganic Chemistry*, 2006, **45**, 3964-3969.
115. S. Ghose, *Acta Crystallographica*, 1964, **17**, 1051-1057.
116. M. Catti, G. Ferraris, S. Hull and A. Pavese, *Physics and Chemistry of Minerals*, 1995, **22**.
117. N. Kozai, H. Mitamura, H. Fukuyama, F. Esaka and S. Komarneni, *Microporous and Mesoporous Materials*, 2006, **89**, 123-131.
118. R. Rojas, M. Á. Ulibarri, C. Barriga and V. Rives, *Applied Clay Science*, 2010, **49**, 176-181.
119. R. Rojas, C. Barriga, M. Angeles Ulibarri, P. Malet and V. Rives, *Journal of Materials Chemistry*, 2002, **12**, 1071-1078.
120. S. Yamanaka, K. Ando and M. Ohashi, *MRS Proceedings*, 2011, **371**.
121. K. Petrov and L. Markov, *Journal of Materials Science*, 1985, **20**, 1211-1214.
122. S. Catillon-Mucherie, F. Ammari, J.-M. Krafft, H. Lauron-Pernot, R. Touroude and C. Louis, *The Journal of Physical Chemistry C*, 2007, **111**, 11619-11626.
123. S. Yamanaka, K. Ando and M. Ohashi, *MRS Proceedings*, 1995, **371**, 131-142.
124. J. Wang, J. B. Neaton, H. Zheng, V. Nagarajan, S. B. Ogale, B. Liu, D. Viehland, V. Vaithyanathan, D. G. Schlom, U. V. Waghmare, N. A. Spaldin, K. M. Rabe, M. Wuttig and R. Ramesh, *Science*, 2003, **299**, 1719-1722.
125. H. Zheng, J. Wang, S. E. Lofland, Z. Ma, L. Mohaddes-Ardabili, T. Zhao, L. Salamanca-Riba, S. R. Shinde, S. B. Ogale, F. Bai, D. Viehland, Y. Jia, D. G. Schlom, M. Wuttig, A. Roytburd and R. Ramesh, *Science*, 2004, **303**, 661-663.
126. R. Ramesh, *Nature*, 2009, **461**, 1218-1219.
127. G. Rogez, N. Viart and M. Drillon, *Angewandte Chemie International Edition*, 2010, **49**, 1921-1923.
128. N. Masciocchi, E. Corradi, A. Sironi, G. Moretti, G. Minelli and P. Porta, *Journal of Solid State Chemistry*, 1997, **131**, 252-262.
129. V. Laget, C. Hornick, P. Rabu, M. Drillon and R. Ziessel, *Coordination Chemistry Reviews*, 1998, **178-180**, 1533-1553.
130. O. Palamarciuc, E. Delahaye, P. Rabu and G. Rogez, *New Journal of Chemistry*, 2014, **38**, 2016-2023.
131. Q. Ye, D. W. Fu, H. Tian, R. G. Xiong, P. W. Chan and S. D. Huang, *Inorganic Chemistry*, 2008, **47**, 772-774.

132. Q. Ye, T. Hang, D.-W. Fu, G.-H. Xu and R.-G. Xiong, *Crystal Growth & Design*, 2008, **8**, 3501-3503.
133. S. Eyele-Mezui, Ph.D. Thesis, Université de Strasbourg, 2011.

Chapter I : New Insights on the Synthesis and Structural
Investigations of Copper Hydroxide-Based Starting Compounds

Chapter I : New Insights on the Synthesis and Structural Investigations of Copper Hydroxide-Based Starting Compounds

The systems that will be discussed in this chapter are the starting compounds derived from copper hydroxide. These starting materials are layered simple hydroxides (LSH) presenting brucite-like copper hydroxide sheets with acetate or dodecylsulfate grafted onto the layers.

Several strategies have been reported for the synthesis of functionalized LSH: insertion-grafting,¹⁻³ direct hydrothermal synthesis,^{4, 5} *in situ* synthesis,⁶ controlled hydrolysis⁷ or, very recently, confined condensation.⁸ The most widely used method is insertion-grafting, which consists in an anionic exchange between the starting layered hydroxy-acetate and the molecule of interest bearing an anchoring group (carboxylate, sulfonate or phosphonate). A pre-intercalation method has been shown to be very effective to allow the insertion-grafting of large, hydrophobic or prone to hydrolysis molecules, including coordination complexes in LSH.^{2, 3, 9, 10}

This method consists in the insertion-grafting of molecules bearing long-alkyl chains by anion-exchange from the starting layered hydroxy-acetate. In the case of layered copper hydroxide, dodecylsulfate can be readily inserted into copper hydroxy-acetate, much more easily than less flexible molecules. Compared to copper hydroxy-acetate, copper hydroxy-dodecylsulfate presents a much larger and more hydrophobic interlamellar spacing which enables the subsequent insertion of various molecules.

The precise understanding of the properties of the layered hybrid compounds (optical, magnetic or dielectric for instance) requires a deeper knowledge of their structure. To this aim, it is worth investigating the structures of the starting materials, which appears not to be an easy task. The single-crystal structure of copper hydroxy-acetate $\text{Cu}_2(\text{OH})_3(\text{OAc})\cdot\text{H}_2\text{O}$ was only reported in 2011, whereas research involving this compound has been performed for more than 25 years.^{1, 11-17} Concerning the dodecylsulfate analogue, now widely used as a starting compound for insertion, to the best of our knowledge, no precise description of its structure has ever been reported.

We describe here the synthesis of high crystallinity $\text{Cu}_2(\text{OH})_3(\text{C}_{12}\text{H}_{25}\text{SO}_4)$. Single-crystal structure determination shows that this compound crystallizes in the non-centrosymmetric space group $\text{P}2_1$. The non-centrosymmetry is confirmed by non-linear optical measurements.

Moreover, during the synthetic approach, we managed to isolate and to characterize by single-crystal X-ray diffraction a ribbon-like compound of formula $\text{Cu}_3(\text{C}_{12}\text{H}_{25}\text{SO}_4)_2(\text{CH}_3\text{COO})_2(\text{OH})_2(\text{H}_2\text{O})_2$ which can be considered as an intermediate in the synthesis of $\text{Cu}_2(\text{OH})_3(\text{C}_{12}\text{H}_{25}\text{SO}_4)$ from $\text{Cu}(\text{CH}_3\text{COO})_2\cdot\text{H}_2\text{O}$. Finally, the magnetic properties of $\text{Cu}_3(\text{C}_{12}\text{H}_{25}\text{SO}_4)_2(\text{CH}_3\text{COO})_2(\text{OH})_2(\text{H}_2\text{O})_2$ and of $\text{Cu}_2(\text{OH})_3(\text{C}_{12}\text{H}_{25}\text{SO}_4)$ are described in the section 2.3.3.2 of this chapter.

1. Synthesis and Reactivity of $\text{Cu}_2(\text{OH})_3\text{OAc}\cdot\text{H}_2\text{O}$

The first hydroxide that will be discussed here is copper hydroxy-acetate, $\text{Cu}_2(\text{OH})_3(\text{OAc})\cdot\text{H}_2\text{O}$. This material has been extensively used in our laboratory as a chemical model for intercalation reactions.^{2, 9, 18-20} Indeed, among LSH, it is the compound that is the easiest and fastest to synthesize, and it has long been efficiently used as starting material to obtain copper layered hybrid simple hydroxide functionalized with many organic molecules by insertion-grafting anion exchange reactions. All the reactions described below are stirred at 600 rpm in round bottom flasks and bubbled with argon for 15 minutes unless stated otherwise.

1.1. Previous Synthesis Method : Coprecipitation *via* Drop-wise Base Addition

The method¹³ used at the beginning of my PhD was to simply induce the copper hydroxy-acetate precipitation *via* addition of sodium hydroxide (30 mmol) to 100 mL aqueous copper acetate (20 mmol) solution heated at 70°C under nitrogen to avoid carbonate intercalation and oxide formation. This method is one of the most common methods in the literature, it allows to obtain the product in high yield in about 30 minutes albeit with a relatively low crystallinity (figure 1).

The compound possesses a lamellar structure, clearly evidenced in XRD pattern by the succession of 00 l harmonics, strongly enhanced because of preferential orientation of the crystallites. Indeed, the obtained crystallites present a platelet-like morphology with a very high aspect ratio, a lateral size of a few microns and a thickness of a few hundreds nanometres (figure 1). The interlamellar distance for $\text{Cu}_2(\text{OH})_3(\text{OAc})\cdot\text{H}_2\text{O}$ is measured around 9.6 Å.

The structuration of the IR spectrum in the O-H region (3200-3700 cm^{-1}) indicates that a complex H-bond network with water molecules, hydroxide moieties and acetate molecules is already present with this synthesis.

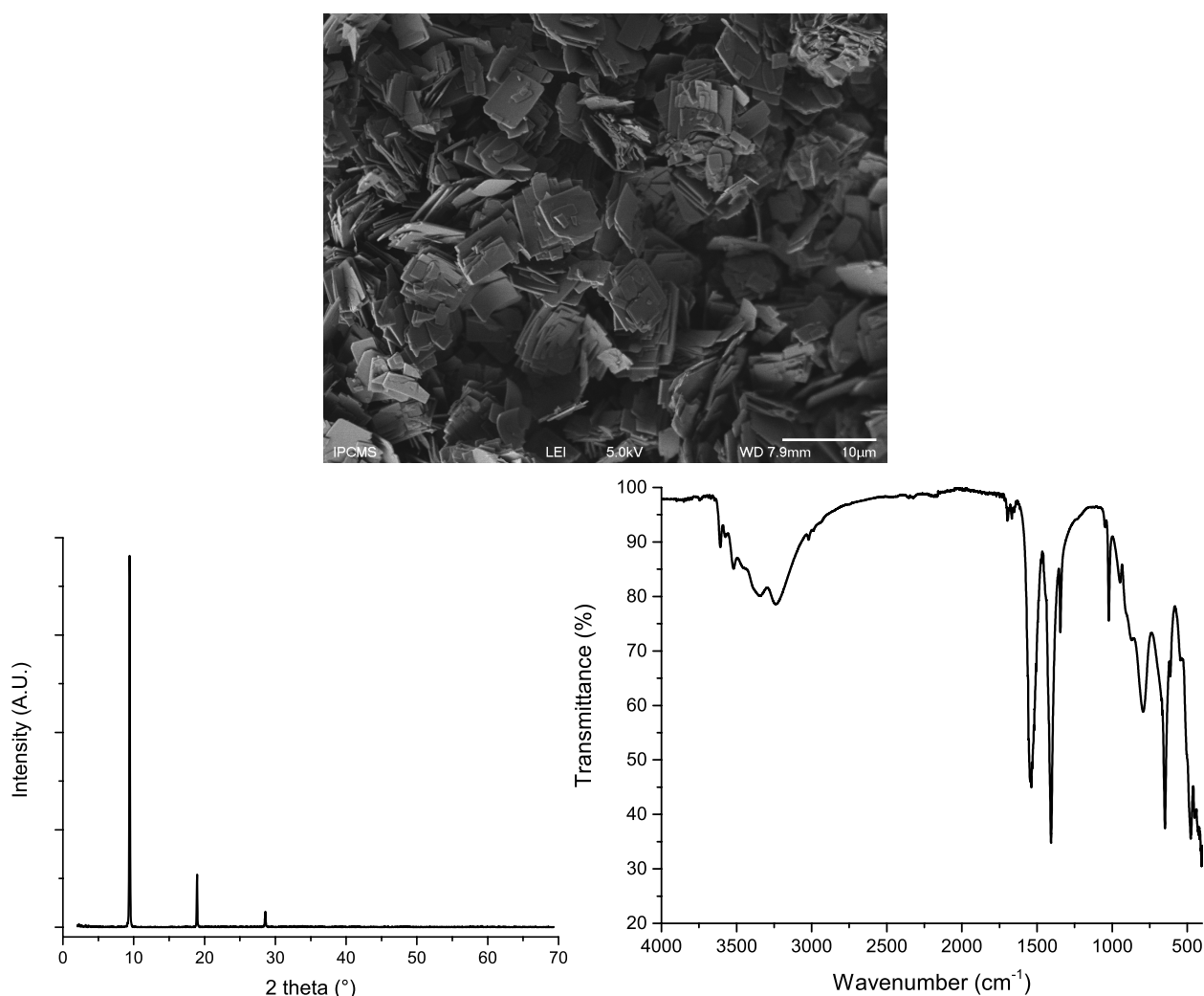


Figure 1 : SEM image (top), XRD pattern (left) and ATR-IR spectrum (right) of the copper hydroxy-acetate obtained via sodium hydroxide drop-wise addition.

$\text{Cu}_2(\text{OH})_3(\text{OAc})\cdot\text{H}_2\text{O}$ reacts well for the intercalation chemistry, but is prone to oxidation if the insertion conditions are too harsh or too long. From a practical point of view, obtaining higher

crystallinity of the starting compound is highly desirable for both potentially enhancing the crystallinity of the future hybrid and also for physical measurements. Indeed, having single crystals of suitable size instead of powders could greatly improve the accessibility to some properties such as ferroelectricity measured along several crystallographic axes. The measurements of such properties on powders indeed undeniably leads to important leakage currents as well as quite important grain boundaries that might affect the measurements. To that end, I worked on the optimization of the crystallite size of the starting compounds by doing the experiments described below.

1.2. New Synthesis : Without Base Addition

In a recent paper²¹ it has been shown that it was possible to synthesize single crystals of copper hydroxy-acetate big enough for single crystal diffraction. This strategy originated from an optimized synthesis described in Masciocchi's paper²² that consists in heating a 0.1M aqueous solution of copper acetate at 60°C without stirring and in contact with air to let the hydrolysis take place for 30 to 72 hours. This method indicates that the nitrogen bubbling and the addition of sodium hydroxide previously used are not mandatory to obtain pure compound. This reaction leads to a very well-crystallized compound with crystal perfectly suitable for mono-crystal diffraction (figure 2) but with a very low yield of 2.5%. To enhance this yield it is possible to heat the filtrate again to collect more material. This process is repeatable at least 5 times to attain a total yield of around 12% overall with the five reactions. The diffractogram shown in figure 2 also indicates a preferred orientation with very strong 002/ diffraction peaks and weaker out of plane reflexions as shown in the magnified insert.

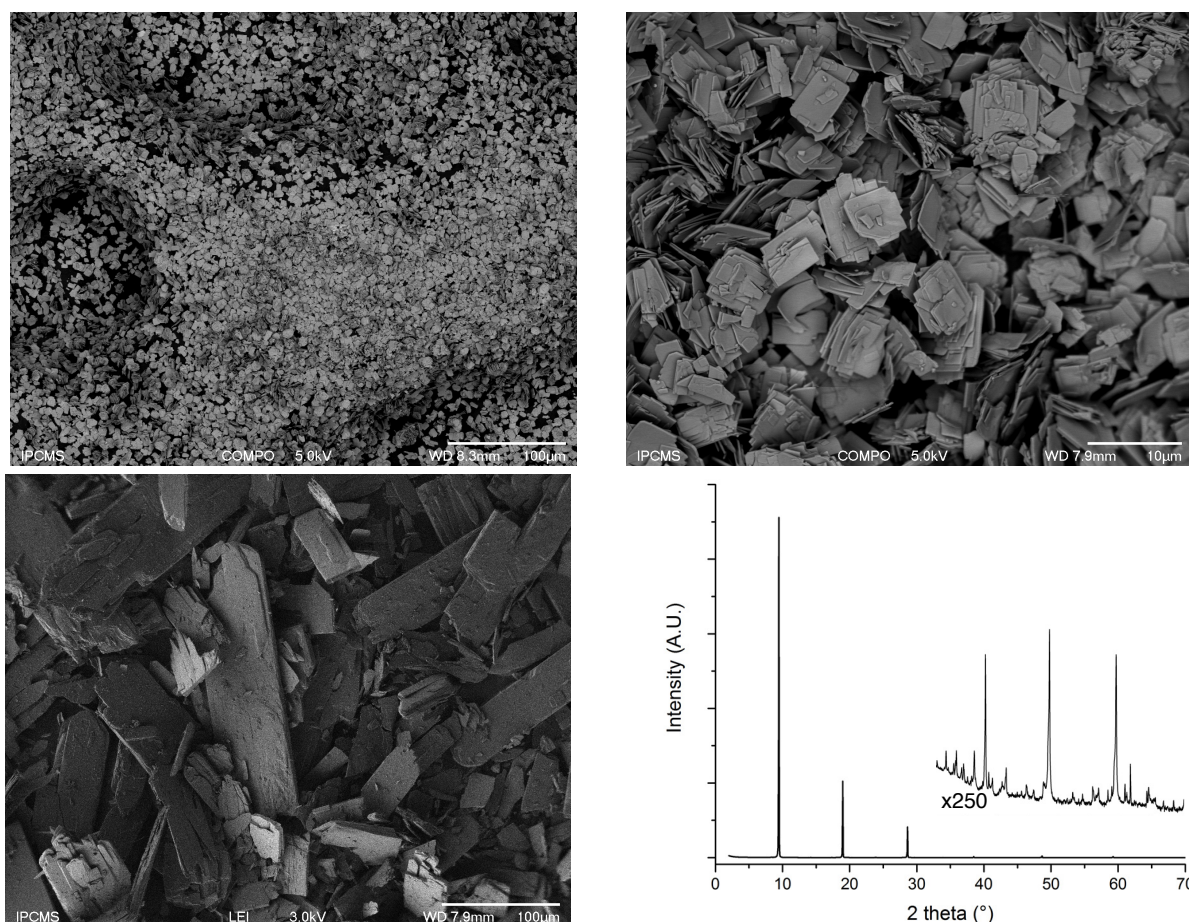


Figure 2 : SEM images showing cristallite size difference between with (top left and right) and without (bottom left) base addition. Diffractogram of the copper-hydroxy-acetate obtained without base addition (bottom right).

This reaction leads to the known structure shown below.

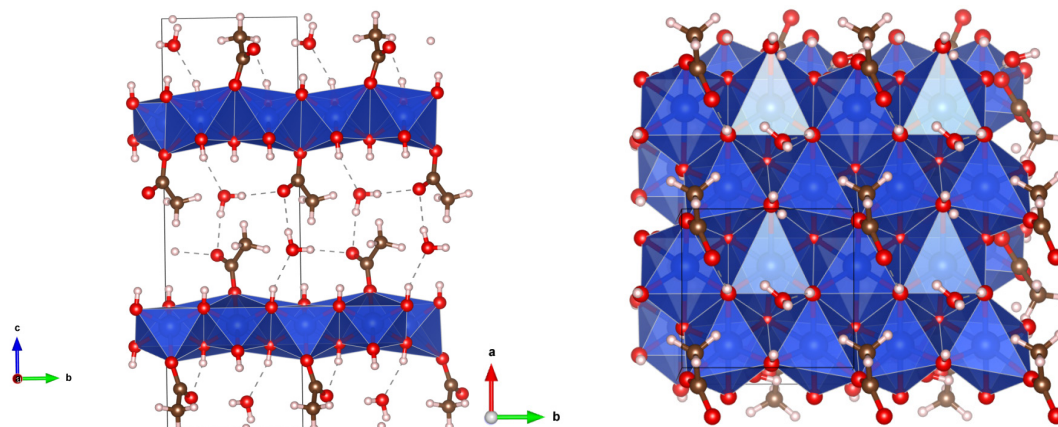


Figure 3 : Structure of $\text{Cu}_2(\text{OH})_3(\text{OAc})\cdot\text{H}_2\text{O}$ as described in Švarcová's work.²¹

This compound crystallizes in the $P2_1$ space group and has the following cell parameters :

Chemical formula	$\text{Cu}_2(\text{OH})_3(\text{CH}_3\text{COO})\cdot\text{H}_2\text{O}$
Molecular weight ($\text{g}\cdot\text{mol}^{-1}$)	510.37
Space group	$P2_1$
a (Å)	5.5875(4)
b (Å)	6.0987(4)
c (Å)	18.6801(10)
β (°)	91.934(5)
Cell volume (Å ³)	636.19(7)
Z	2
Density ($\text{g}\cdot\text{cm}^{-3}$)	2.70
μ (mm^{-1})	3.285
wavelength (Å)	0.71069
θ range	3.27-28.76
unique reflections with $I \geq 3\sigma(I)$	1521
# refinement parameters	210
$p_{\text{min}} / p_{\text{max}}$ ($e^l \text{ Å}^{-3}$)	-0.41/0.42

Table 1 : Crystallographic data of $\text{Cu}_2(\text{OH})_3(\text{CH}_3\text{COO})\cdot\text{H}_2\text{O}$.²¹

The botallackite type structure obtained consists of corrugated sheets of edge-sharing copper octahedra perpendicular to c direction with acetate and water molecules intercalated in the interlayer spacing. They are four different CuO_6 octahedra, they are all strongly distorted due to Jahn-Teller effect.²³ The bond valence calculated for these copper octahedra remains reasonable, indeed, they are ranging from 1.88 to 1.98.²¹

1.3. Reactivity of $\text{Cu}_2(\text{OH})_3\text{OAc}\cdot\text{H}_2\text{O}$ Crystals

It is worth mentioning that the reactivity of the crystals remains similar to the previously obtained powders. Yet, the crystals are less sensitive to oxidation as long as the reaction medium is not stirred, allowing for longer reaction times to occur. It is thus possible to use exchange properties of this material towards molecules of interest, as it was previously done with $\text{Cu}_2(\text{OH})_3(\text{OAc})\cdot\text{H}_2\text{O}$ prepared by precipitation in basic medium.

Yet, we have noted that even though the insertion is working on single crystals, the long-range ordering is broken, leading to crystallites unfit for single crystal diffraction. This long-range order breaking is clearly visible in the SEM image below (figure 4). For this specific experiment, the goal was to see if it was possible to do crystal to crystal modification from copper-hydroxy-acetate to copper-hydroxy-dodecylsulfate. It can also be observed that there is still a large amount of the starting copper hydroxy-acetate phase. This is likely due to the soft conditions used (25°C for 48 hours) compared to the regular 60°C for 72 hours. This experiment showed that even though the insertion in the crystals is indeed possible, keeping a crystalline structure on the entire crystallite is, however, impossible as shown in the SEM images below.

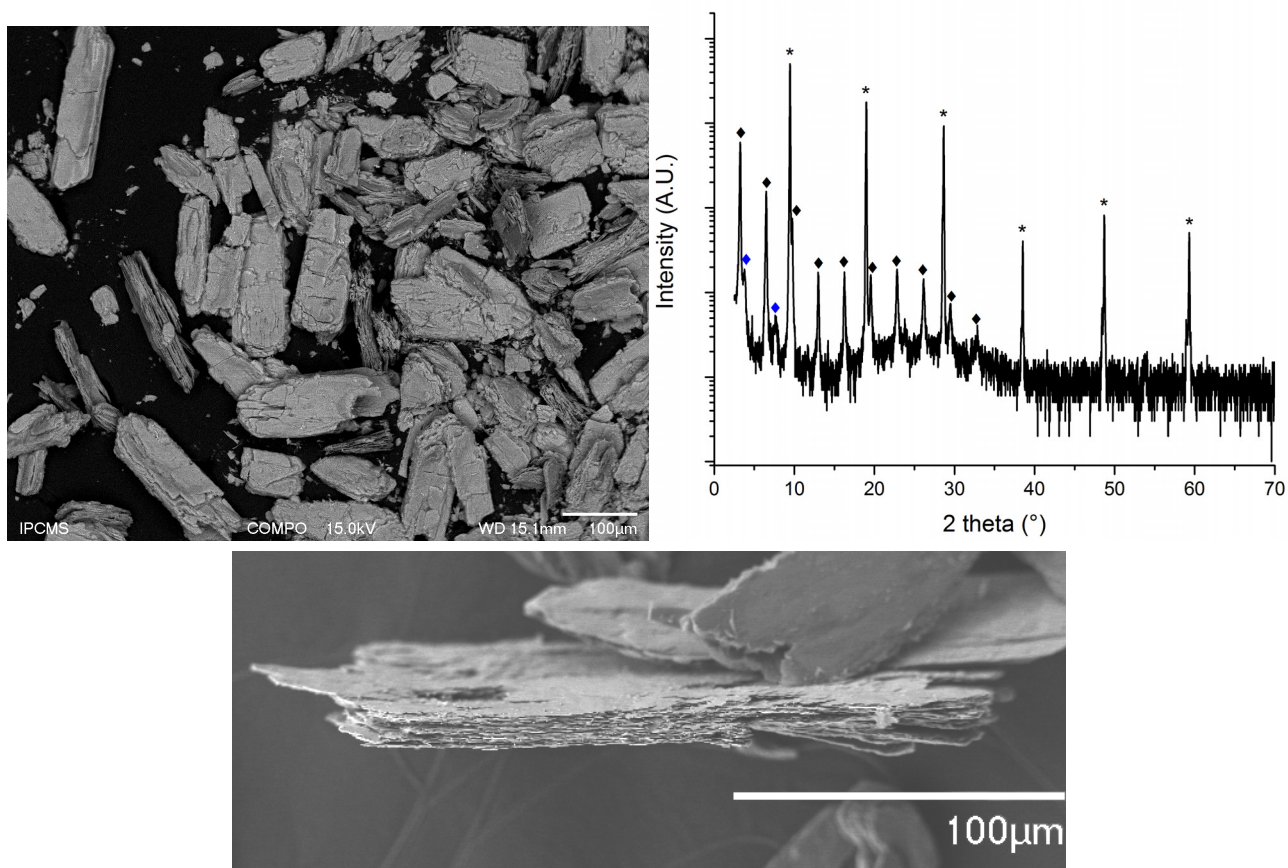


Figure 4 : SEM image of the copper-hydroxy-acetate crystallites after functionalization (top right), PXRD pattern of the obtained compound, stars represent remaining copper-hydroxy-acetate, black diamonds copper-hydroxy-dodecylsulfate and blue diamonds an hydrated phase of copper-hydroxy-dodecylsulfate (top left), magnification of top SEM image showing the bidimensional cleaving of the crystallite (bottom).

While copper hydroxy-acetate's reactivity with other molecules is generally allowing insertion-grafting, in some cases, this insertion-grafting is impossible or very difficult to achieve. This is mainly the case when the molecules or complexes to intercalate are larger than 6-8 Å in one of their dimensions or when they are hydrophobic.

The example given below describes an attempt to insert a thiophene bis-phosphonic acid derivative (figure 5) directly in copper-hydroxy-acetate with a two hours reflux in a water/ethanol mixture. This molecule was chosen because of its relatively small size, the very comparable interlamellar spacing between the starting compound (9.6 Å) and the hybrid compound obtained using the hydroxy-dodecylsulfate derivative $\text{Cu}_2(\text{OH})_3(\text{DS})$ as starting material (9.3 Å, see chapter V) and the presence of a lateral methyl to help solubilization. Figure 5 shows the reaction does not occur when using $\text{Cu}_2(\text{OH})_3(\text{OAc})\cdot\text{H}_2\text{O}$ as starting material. In chapter V, we will see that, using the same conditions but starting from $\text{Cu}_2(\text{OH})_3(\text{DS})$, the insertion is indeed possible.

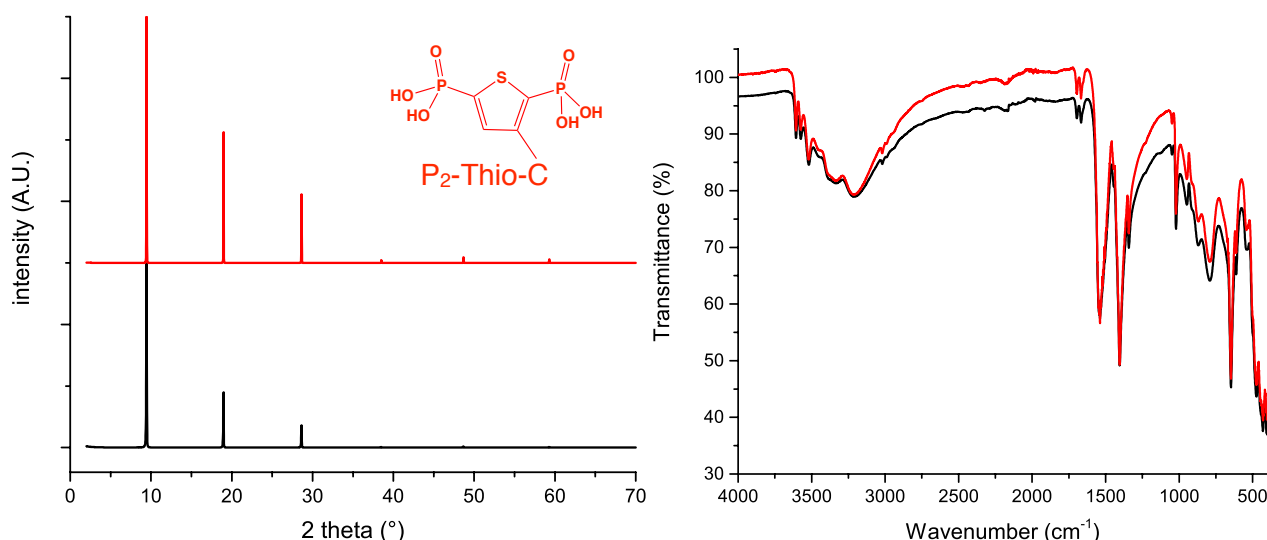


Figure 5 : PXRD pattern (left) and IR spectra (right) of $\text{Cu}_2(\text{OH})_3(\text{OAc})\cdot\text{H}_2\text{O}$ (black) and obtained compound after reaction of with $\text{P}_2\text{-Thio-C}$ (red) (left).

2. Synthesis of $\text{Cu}_2(\text{OH})_3\text{DS}$

A method has proved to be very effective to allow the insertion-grafting of large molecules, highly hydrophobic ones or even metallic complexes, as mentioned earlier, it is called the pre-intercalation method.² This method consists of the insertion of long alkyl chains in-between the layers *via*, in the copper hydroxy-acetate case, the insertion of dodecylsulfate (DS). The flexibility of the alkyl chains allows them to be inserted easily compared to rigid molecules, greatly increasing the interlamellar spacing as well as its hydrophobicity. We will thus deal in the last part of this chapter with the optimization of the synthesis of $\text{Cu}_2(\text{OH})_3(\text{DS})$ as well as with the structural characterization, and study of its magnetic properties.

2.1. Previous Synthesis Method : Ion-Exchange Reaction from $\text{Cu}_2(\text{OH})_3(\text{OAc})\cdot\text{H}_2\text{O}$

$\text{Cu}_2(\text{OH})_3(\text{DS})$ has been for a long time obtained *via* ion exchange from $\text{Cu}_2(\text{OH})_3(\text{OAc})\cdot\text{H}_2\text{O}$. It thus necessitates first the synthesis of $\text{Cu}_2(\text{OH})_3(\text{OAc})\cdot\text{H}_2\text{O}$, whether by precipitation in basic medium or by direct synthesis, then its use as a starting material for the intercalation of dodecylsulfonate chains.¹⁶ The first step of this synthesis lasts for roughly one hour by coprecipitation *via* sodium hydroxide addition meanwhile the second step takes three days. Compounds obtained *via* this synthetic pathway present a crystallite size not exceeding $5\ \mu\text{m}$ at best in the optimal synthesis conditions.

During my PhD, efforts have been made to obtain a better crystallinity of the starting $\text{Cu}_2(\text{OH})_3(\text{DS})$ in the scope of an optimization of the crystallinity of the hybrid compounds obtained from it, as well as in the scope of a future shaping of the crystallites on surfaces. In addition, as we will show, this study will allow a better understanding of the structure of $\text{Cu}_2(\text{OH})_3(\text{DS})$ that was still unknown due to the lack of enough reflexions in powder diffraction as well as to too small crystallite size for single crystal diffraction.

We mainly used protocols inspired by the recent one pot synthesis of $\text{Cu}_2(\text{OH})_3(\text{OAc})\cdot\text{H}_2\text{O}$ described in Švarcová's paper.²¹

2.2. « Secondary Discovery » : Ribbonlike Hydroxide Structure

In order to try to obtain single crystals of $\text{Cu}_2(\text{OH})_3(\text{DS})$, we adopted a method derived from the one described by Švarcová *et al.* which had led to obtain single crystals of $\text{Cu}_2(\text{OH})_3(\text{CH}_3\text{COO})\cdot\text{H}_2\text{O}$,²¹ or from the one used by Fujita to obtain single crystals of copper hydroxides with sulfonates, either with a layer structure or with a distorted diamond chain structure.

134, 135

In the present case, it consists in adding copper acetate (10 mmol) to a 100 mL solution of sodium dodecylsulfate (5 mmol) in a water/ethanol mixture and in heating the solution at 70°C for several days in air, with a condenser to avoid solvent evaporation. Despite the relative simplicity of this procedure, several observations can be made.

When the two reactants are mixed (either solid $\text{Cu}(\text{OAc})_2\cdot\text{H}_2\text{O}$ or concentrated (1 M) aqueous solution of $\text{Cu}(\text{OAc})_2\cdot\text{H}_2\text{O}$ added to 0.5 equivalent of a solution (0.05 M) of $\text{C}_{12}\text{H}_{25}\text{SO}_4\text{Na}$ in a water/ethanol (70/30 v:v) mixture, or the reverse, $\text{C}_{12}\text{H}_{25}\text{SO}_4\text{Na}$ poured onto solid $\text{Cu}(\text{OAc})_2\cdot\text{H}_2\text{O}$ or into concentrated aqueous solution of $\text{Cu}(\text{OAc})_2\cdot\text{H}_2\text{O}$) a blueish precipitate forms immediately. This precipitate is filtered after 1 h of stirring at room temperature. Powder X-ray diffraction and infrared spectroscopy (figure 6) clearly shows that this blueish precipitate is composed of sodium dodecylsulfate and at least one other phase which could not be identified and which corresponds neither to copper acetate nor to copper dodecylsulfate nor to the ribbon like structure which forms when the suspension is let to slowly evaporate (see below).

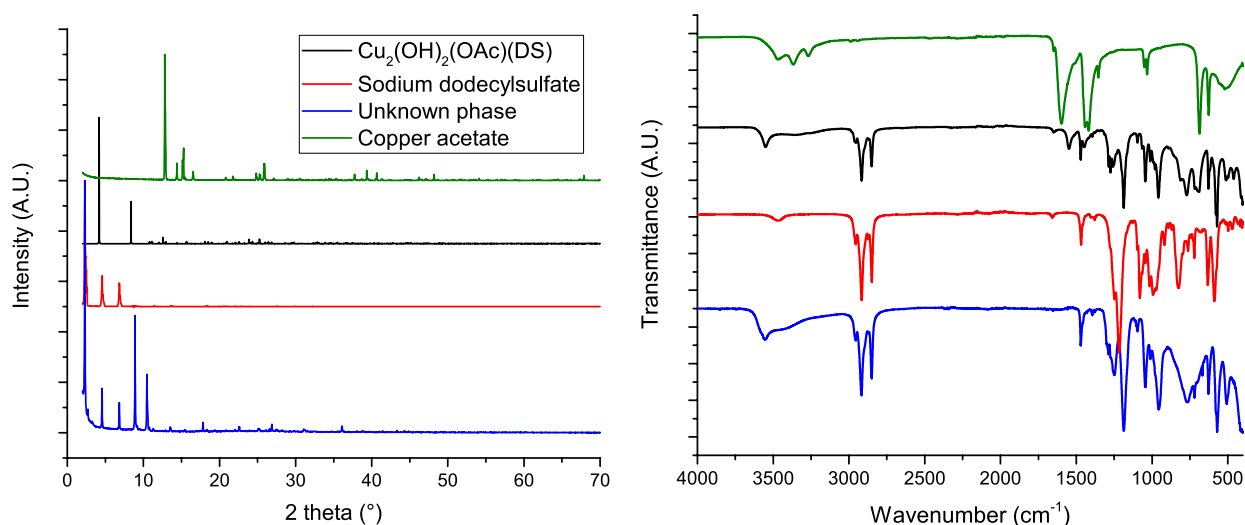


Figure 6 : Diffractograms and infrared spectra of the unknown phase (blue), sodium dodecylsulfate (red), copper acetate (green) and ribbon-like copper hydroxy-dodecylsulfate-acetate (black).

Indeed, when, instead of being filtered, this suspension is slowly evaporated at room temperature without stirring, crystalline needles form (compound **1**) (Figure 7 left) Interestingly, when the reactants are only mixed during 5 min, without full dissolution of $\text{Cu}(\text{OAc})_2\cdot\text{H}_2\text{O}$, similar needles appear to grow from the remaining $\text{Cu}(\text{OAc})_2\cdot\text{H}_2\text{O}$ crystals (compound **1'**) (Figure 7 right), which suggests that the corresponding compound may be an intermediate between $\text{Cu}(\text{OAc})_2\cdot\text{H}_2\text{O}$ and $\text{Cu}_2(\text{OH})_3(\text{DS})$.

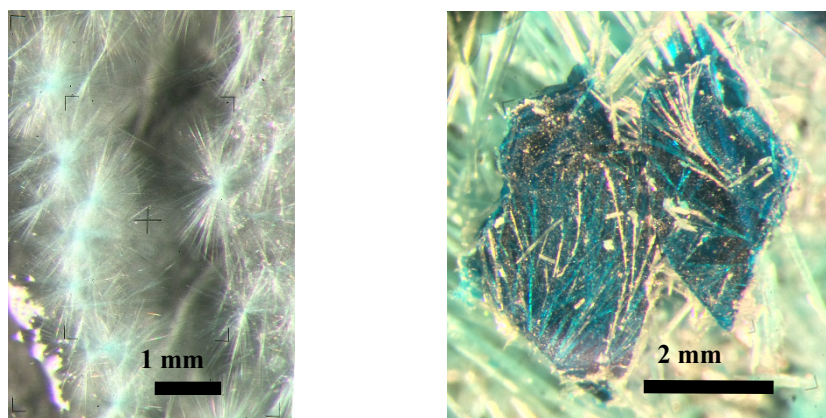


Figure 7 : Optical microscopy picture of the crystals of compound 1 (left) and of compound 1' (right)

Single-crystal structure determination on the needles showed that compounds 1 and 1' are in fact identical. The crystal structure of compound 1 has been solved by O. Pérez, from CRISMAT Laboratory in Caen.

It can be described by 2 Cu, 1 S, 8 O, 14 C independent atoms. All the atomic positions were refined and then atomic displacement parameters (ADP) were considered as anisotropic for copper and sulfur atoms and isotropic for all remaining atoms. At this step, 25 independent hydrogen atoms were introduced using geometric considerations to fill the carbon environment. Bond valence sum calculations performed for all the atoms lead to low value for two O atoms: O2 and O3 (0.4 and 1.3 respectively); these weak values can be attributed to the presence of H atoms. Two hydrogen atoms were then added around O2 and one hydrogen for O3; the position of the H atoms was determined based on geometrical considerations and restricted in link to their O first neighbour. The resulting model corresponds to the composition $\text{Cu}_3(\text{C}_{12}\text{H}_{25}\text{SO}_4)_2(\text{CH}_3\text{COO})_2(\text{OH})_2(\text{H}_2\text{O})_2$, where 2 water molecules and 2 hydroxide groups per formula are present. Final reliability factors and details of the refinement are reported in table 2 below.

Chemical formula	$\text{Cu}_3(\text{C}_{12}\text{H}_{25}\text{SO}_4)_2(\text{CH}_3\text{COO})$
Molecular weight ($\text{g}\cdot\text{mol}^{-1}$)	905.5
Space group	$P\bar{1}$
a (Å)	5.602(2)
b (Å)	8.314(3)
c (Å)	21.283(8)
α (°)	83.02(2)
β (°)	85.87(2)
γ (°)	81.85(2)
Cell volume (Å ³)	972.4(7)
Z	1
Density ($\text{g}\cdot\text{cm}^{-3}$)	1.546
μ (mm^{-1})	1.798
wavelength (Å)	0.71069
scan strategy / Dx (mm)	ω/ϕ scan / 50
Θ max	29.17

Reflections index limit	$-6 \leq h \leq 7$
unique reflections with $I \geq 3\sigma(I)$	1199
Absorption correction	multi-scan / SADABS
Internal R value before /after correction (%)	15.1% / 6.2%
# refinement parameters	119
ρ_{min} / ρ_{max} ($e/\text{\AA}^3$)	-1.72/1.21
F(000)	473
Reliability factors %	9.95%

Table 2 : Crystallographic data for $\text{Cu}_3(\text{C}_{12}\text{H}_{25}\text{SO}_4)_2(\text{CH}_3\text{COO})_2(\text{OH})_2(\text{H}_2\text{O})_2$.

This compound adopts a distorted diamond chain structure, analogous to that of azurite $\text{Cu}_3(\text{OH})_2(\text{CO}_3)_2$.²⁵ A similar arrangement has been recently described by Fujita *et al.* for sulfonate compounds of general formula $\text{Cu}_3(\text{OH})_2(\text{RSO}_3)_2(\text{CH}_3\text{COO})_2(\text{H}_2\text{O})_2$,²⁴ but, to the best of our knowledge, it is the first time such a structure is reported with sulfate groups. Although the general diamond-like structure of the chains remains essentially the same, it is worth underlining here that in the present case, the sulfate groups are mono-coordinated to one copper atom, whereas the sulfonate groups in the compounds described by Fujita *et al.* are, depending on the nature of the alkyl chain, either coordinated in μ_2 bridging mode to two copper ions or not coordinated (instead, water molecules are coordinated in μ_2 bridging mode). The chains of this compound are well separated from each other by the dodecyl groups, develop along the **a** direction.

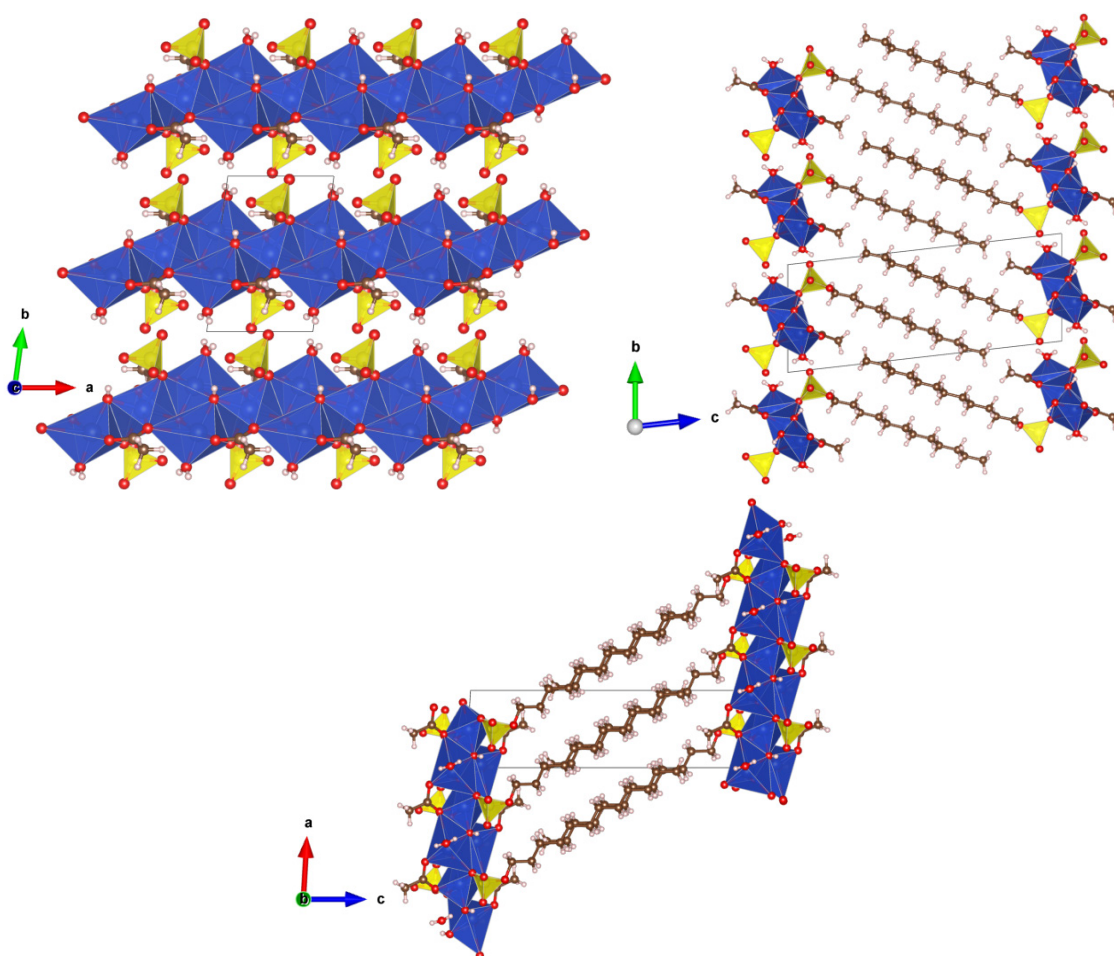


Figure 8 : Ribbonlike structure resulting from the evaporation viewed from **c** (top left), **a** (top right) and **b** (bottom left) (Cu (blue), O (red), S (yellow), C (brown), H (white)).

Both crystallographically independent copper atoms are octahedrally coordinated by oxygen atoms. Hydroxide groups are in μ_3 bridging coordination mode and bridge one Cu1 and two Cu2. Acetate groups in $(\kappa^1-(\kappa^1-\mu_2))-\mu_3$ bridging mode are coordinated to one Cu1 in κ^1 mode and bridge one Cu1 and one Cu2 in $\kappa^1-\mu_2$ mode. Finally, the sulfate groups are bridging one Cu1 and one Cu2 in $\kappa^1-\mu_2$ mode. One water molecule completes the coordination sphere of Cu2.

2.3. New One-Pot Synthesis of $\text{Cu}_2(\text{OH})_3\text{DS}$

2.3.1. Synthesis and Crystal Structure

If, using the same starting conditions *i.e.* the 70:30 $\text{H}_2\text{O}/\text{EtOH}$ solution of copper acetate (10 mmol) and sodium dodecylsulfate (5 mmol) is heated at 60°C without stirring and with a condenser during 3 days instead of being slowly evaporated, blue platelet-like crystals of the desired layered copper hydroxide of formula $\text{Cu}_2(\text{OH})_3(\text{DS})$ form, with a relatively high yield (around 40%) and with a crystallite size exceeding $100\ \mu\text{m}$. Despite the very thin plate-like shape, the structure could be solved on a single crystal, still by O. Pérez in CRISMAT Laboratory in Caen (figure 12).

$\text{Cu}_2(\text{OH})_3(\text{DS})$ crystallizes in the non-centrosymmetric space group $P2_1$. The crystal structure of this compound can be described by 2 Cu, 1 S, 7 O, 12 C independent atoms. All the atomic positions were refined and then atomic displacement parameters (ADP) were considered as anisotropic for copper and sulfur atoms and isotropic for all remaining atoms. In addition, 25 independent hydrogen atoms were further introduced using geometric considerations to fill the carbon environment. As for oxygen atoms, bond valence sum calculations indicated low values for O2, O3 and O7 attributed to the presence of H atoms. Each of these O is surrounded by 3 copper atoms and the hydrogen is building a OCu_3H tetrahedron. The position of the H atoms was determined based on these geometrical considerations and restricted in link to their O first neighbor. The model results in the elemental formula $\text{Cu}_2(\text{OH})_3(\text{C}_{12}\text{H}_{25}\text{SO}_4)$. Since the space group is non centrosymmetric, a twin law corresponding to an inversion centre has been introduced and the ratio of the possible twin domains (*i.e.* the Flack parameters) was refined to 0.26(9)/0.74(9).

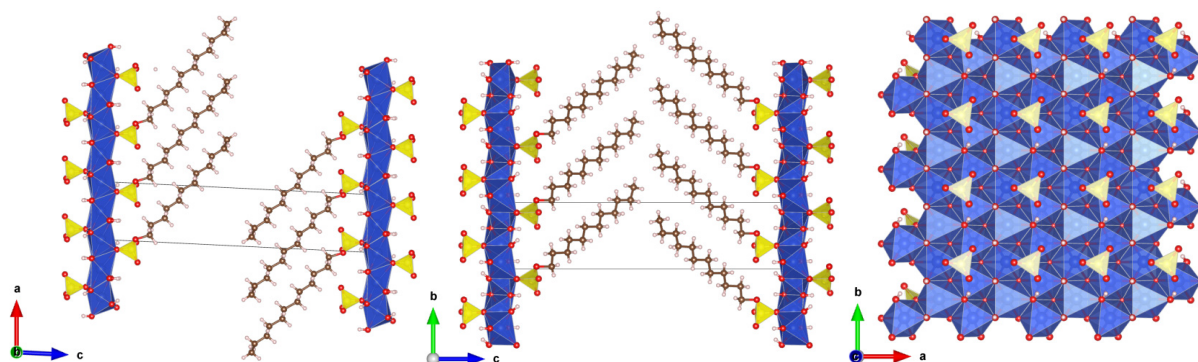


Figure 9 : Structure of $\text{Cu}_2(\text{OH})_3(\text{DS})$, space group $P2_1$, cell parameters : $a=5.591(10)\text{\AA}$, $b=6.108(11)\text{\AA}$, $c=26.96(5)\text{\AA}$, $\alpha=\gamma=90^\circ$ $\beta=92.76(3)^\circ$, R -factor : 7%.

Final reliability factors and details of the refinement are reported in the table below.

Chemical formula	$\text{Cu}_2(\text{OH})_3(\text{C}_{12}\text{H}_{25}\text{SO}_4)$
Molecular weight ($\text{g}\cdot\text{mol}^{-1}$)	444.5
Space group	$P2_1$
a (Å)	5.591(10)
b (Å)	6.108(11)
c (Å)	26.96(5)
α (°)	90
β (°)	92.76(3)
γ (°)	90
Cell volume (Å ³)	920(3)
Z	2
Density ($\text{g}\cdot\text{cm}^{-3}$)	1.6053
μ (mm^{-1})	2.452
wavelength (Å)	0.71069
scan strategy / Dx (mm)	ω/ϕ scan / 50
Θ max	29.03
Reflections index limit	$-7 \leq h \leq 7$
unique reflections with $I \geq 3\sigma(I)$	1093
Absorption correction	multi-scan / SADABS
Internal R value before /after correction (%)	15.3% / 4.9%
# refinement parameters	78
$\rho_{\text{min}} / \rho_{\text{max}}$ ($e / \text{Å}^3$)	-2.43/1.19
F(000)	460
Reliability factors %	6.98%

Table 3 : Crystallographic data for $\text{Cu}_2(\text{OH})_3(\text{C}_{12}\text{H}_{25}\text{SO}_4)$.

$\text{Cu}_2(\text{OH})_3(\text{DS})$ consists of layers of copper hydroxide of botallackite-type structure, separated by dodecylsulfate ions, with an interlamellar distance of 26.96 Å (table 2). The dodecylsulfate molecules are coordinated to the layers by the sulfate group in $\kappa^1\text{-}\mu_3$ position (figure 10). The structure resembles one recently reported with aromatic sulfonate molecules (see below), yet to the best of our knowledge, it is the first time the crystal structure of a sulfate-containing layered copper hydroxide is reported, although $\text{Cu}_2(\text{OH})_3(\text{C}_{12}\text{H}_{25}\text{SO}_4)$ is often used as a precursor for intercalation compounds.^{2, 3, 17}

One peculiar aspect of this structure is that it crystallizes in a non-centrosymmetric space group. The non-centrosymmetry comes from the Herringbone-like arrangement of the alkyl chains in the interlamellar spacing. This arrangement is different from the one which was classically and empirically drawn, where the alkyl chains were simply interdigitated in the interlamellar spacing.^{14, 26, 27} This compound constitutes one relatively rare example of chiral compounds obtained from achiral building blocks.²⁸⁻³⁰ Interestingly, $\text{Cu}_2(\text{OH})_3(\text{OAc})\cdot\text{H}_2\text{O}$ also crystallizes in a non-centrosymmetric space group ($P2_1$),²¹ with the acetate molecules forming a fish-bone arrangement, contrarily to what was initially inferred by calculations ($P2_1/m$).²² Here, even though it could not be obtained *via* a crystal to crystal transformation from $\text{Cu}_2(\text{OH})_3(\text{OAc})\cdot\text{H}_2\text{O}$, $\text{Cu}_2(\text{OH})_3(\text{C}_{12}\text{H}_{25}\text{SO}_4)$ crystallizes in the same non-centrosymmetry crystal space group as $\text{Cu}_2(\text{OH})_3(\text{OAc})\cdot\text{H}_2\text{O}$. It is worth noting here that layered copper hydroxides functionalized by sulfonate molecules, as

reported by Fujita *et al.*, crystallizes in centrosymmetric space groups, even though the synthetic procedure is similar to the one described here.⁷ Hence, functionalizing the hydroxide layers with sulfate instead of sulfonate has a significant influence on the structure that can lead to different properties.

2.3.2. Comparison with Classical Ion Exchange Method

The method used to synthesize $\text{Cu}_2(\text{OH})_3(\text{DS})$ (0.1M $\text{Cu}(\text{OAc})_2$ and 0.05M NaDS in 70:30 $\text{H}_2\text{O}/\text{EtOH}$ mixture heated at 60°C for 72h) enables to obtain more than 800 mg for each synthesis, with a yield of about 40%. This synthesis does not involve any pH adjustment like the one used by Okazaki *et al.*¹³⁶ Compared to the « classical » ion-exchange method from $\text{Cu}_2(\text{OH})_3(\text{OAc})\cdot\text{H}_2\text{O}$,⁹⁸ this one-step hydrolysis method enables to increase greatly the crystallite size (Figure 10).

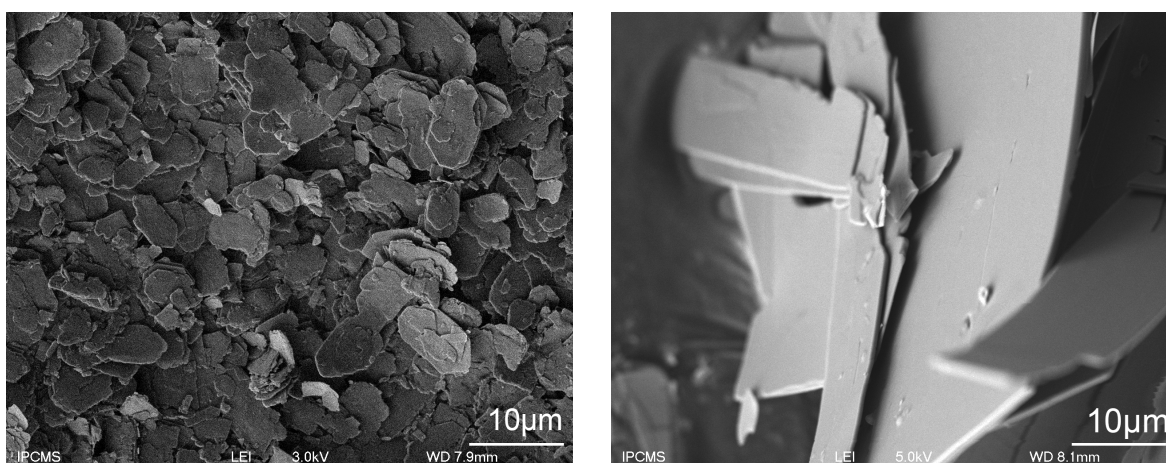


Figure 10 : SEM image of $\text{Cu}_2(\text{OH})_3\text{DS}$ obtained via ion exchange (left) and one pot synthesis (right).

In addition, the reaction has the great advantage of being made in a single step instead of two, hence saving time and solvents. This one pot synthesis also has the advantage of simplicity, indeed, in this case no addition of sodium hydroxide is required, lowering the chances of failure due to the drop-wise addition.

It is noteworthy that this reaction is likely to be rather general. The reaction with cobalt acetate in a solution of dodecylsulfonate, leads to a layered cobalt hydroxide, incorporating dodecylsulfonate. However, contrarily to the case of copper, in the case of cobalt, the obtained compound is very poorly crystallized. Due to lack of time a thorough optimization of the synthesis conditions for the cobalt analogue could not be achieved.

2.3.3. Morphology Control

A last point that has been observed during this study is the possibility to control the morphology of the $\text{Cu}_2(\text{OH})_3(\text{DS})$ crystallites. Playing with the water/ethanol ratio allows us to go from the regular platelet shape to a « butterfly » shape. The platelets are formed with a solution containing up to 30% ethanol in volume, on the other hand, the butterfly shape is obtained with solutions containing more than 43% ethanol in volume, associated a lower reaction temperature (30°C instead of 60°C). The difference between the two morphologies is clearly shown in figure 11 below.

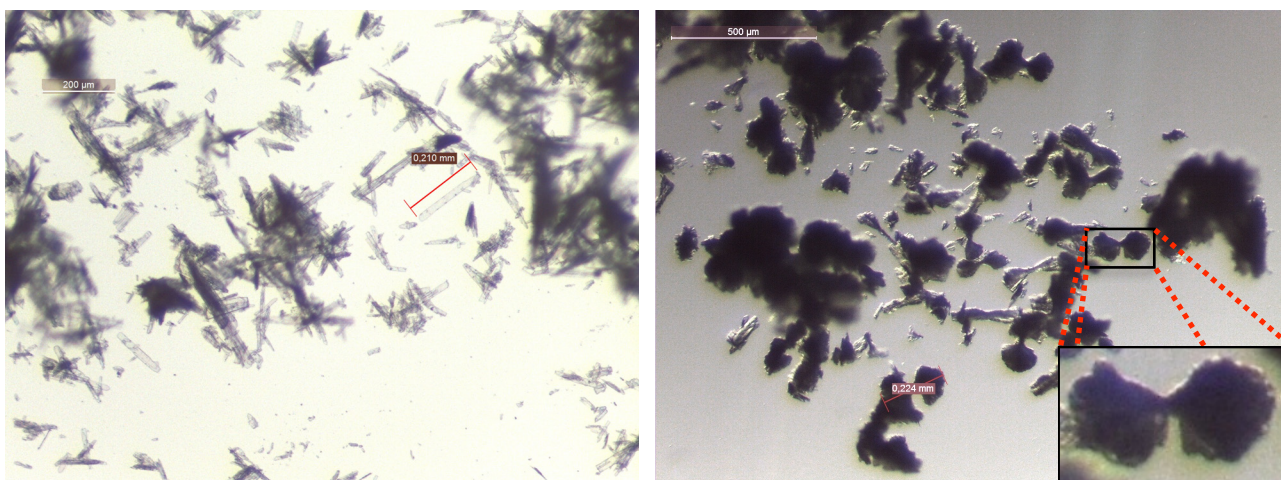


Figure 11 : Optical images of the regular $\text{Cu}_2(\text{OH})_3(\text{DS})$ platelet morphology (left) and butterfly morphology (right).

Moreover, to be certain that this was only a morphology change and no additional structural changes were observed we compared PXRD patterns and IR spectra of both the butterfly and platelet morphology. The IR spectra (figure 12) shows that the only difference between the morphologies is in the O-H region (3200-3700 cm^{-1}) with different O-H vibrations. These vibrations can only be due to the hydroxide layers as both these compounds shows no water content *via* TGA analysis.

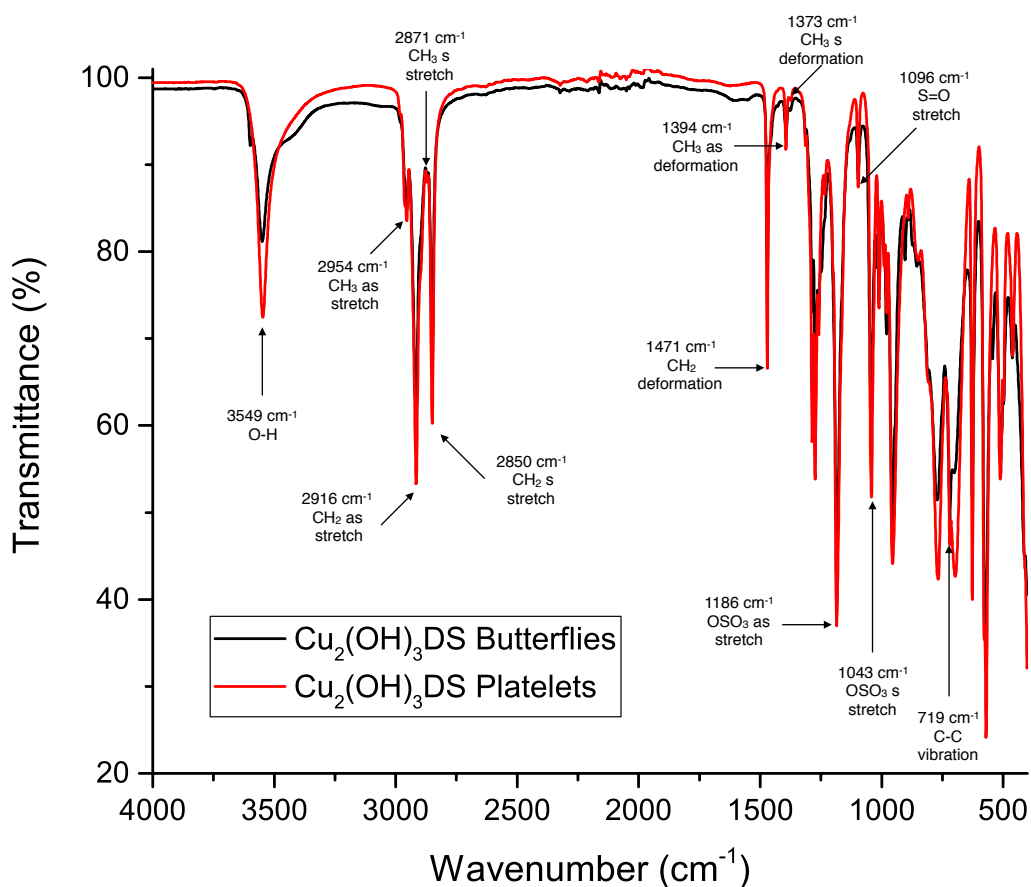


Figure 12 : IR spectra of the two morphologies of $\text{Cu}_2(\text{OH})_3(\text{DS})$ and band attributions.³¹⁻³³

In collaboration with Nicolas Barrier, CRISMAT, Caen, we performed capillary X-ray diffraction measurements followed by Rietveld refinement on the butterfly morphology. This study shows that there are no significant crystallographic changes between the two morphologies (figure 13).

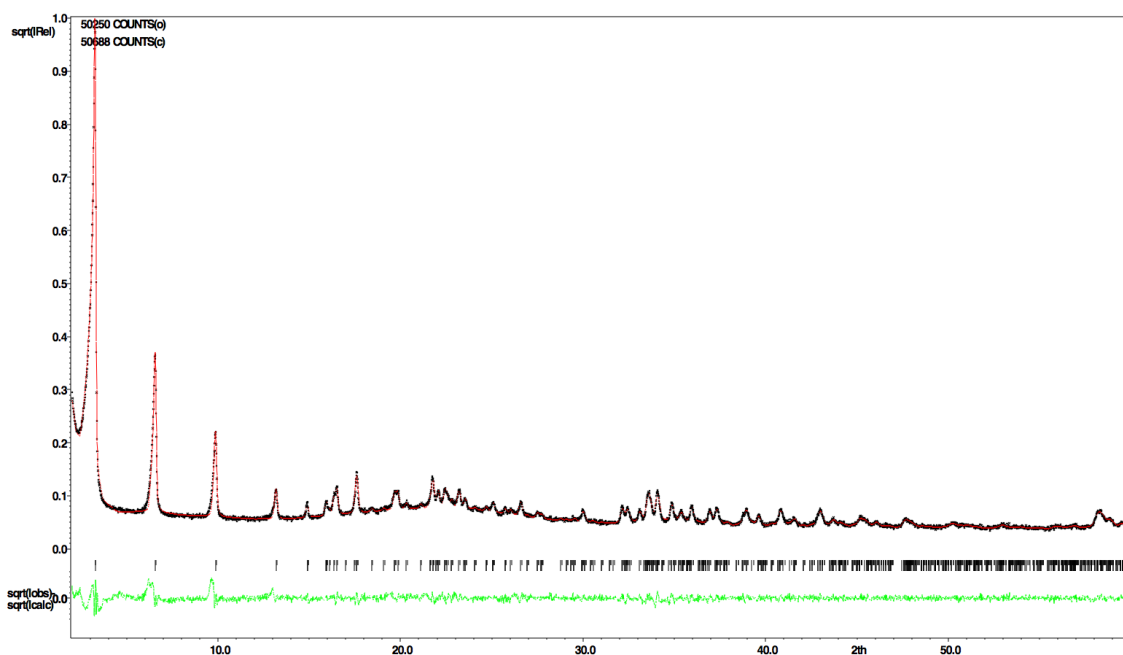


Figure 13 : Capillary Xray diffractogram and Rietveld refinement on the $\text{Cu}_2(\text{OH})_3(\text{DS})$ crystals butterfly morphology using the single crystal platelet structure as reference (green line is the difference between calculated and observed values).

2.3.4. Properties of $\text{Cu}_2(\text{OH})_3\text{DS}$

2.3.4.1. Non-Linear Optics : Second Harmonic Generation

In the scope of the observation of a possible ferroelectric behaviour, one mandatory requirement is the non-centrosymmetry of the obtained hybrid. Due to the nature of our compounds and the difficulty to obtain single crystals of even good crystallinity, a pre-screening of all starting compounds and our hybrids has been done with a technique called Second Harmonic Generation (SGH thereafter).³⁴

This technique allows for a fast characterization of all the obtained compounds without having the need for accurate structural characterization. Observation of a SHG signal can only occur for non-centrosymmetric compounds (except for possible artifacts described below).

This study was carried out in collaboration with Grégory Taupier and Honorat Dorkenoo at the IPCMS. The apparatus design allows the minimization of any possible artifact signals, especially surface SHG³⁵⁻³⁷ by using a perpendicular excitation compared to a grazing incidence measurement (figure 14).

We were able to screen all the hybrid compounds as well as the starting compounds as reference. Unfortunately, if the 50 mW average intensity of the laser doesn't seem big enough to damage the samples, I must stress that the power of the pulse translated to a continuous laser would correspond to a power of 125 kW. In our case, all samples, except $\text{Cu}_2(\text{OH})_3\text{DS}$ described below, burnt under illumination (it is worth noticing that for other molecular compounds obtained as single crystals the destruction of the sample appeared to be much slower, allowing for SHG measurements). Even in the case of $\text{Cu}_2(\text{OH})_3\text{DS}$, some black circular spots can be observed on the optical image after illumination (Figure 15), which correspond to local destruction of the

material due to small crystallites ignition. Only big crystals were able to withstand the laser beam probably due to their sheer size.

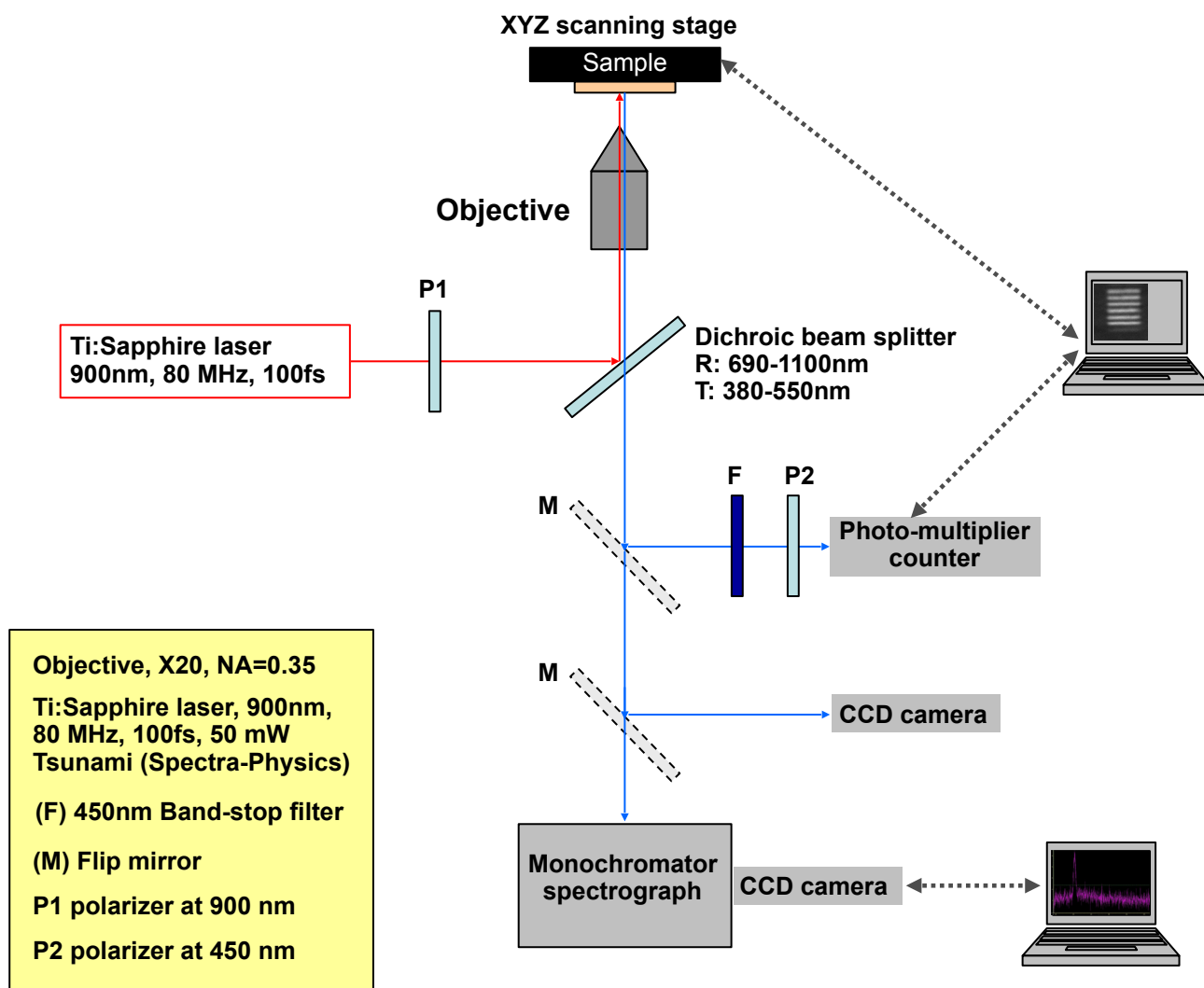


Figure 14 : Experimental apparatus used to observe SHG signals from all samples.

It must be noted that at the time of the measurements on $\text{Cu}_2(\text{OH})_3\text{DS}$, we did not have the crystallographic structure of this compound and no knowledge of the specific crystal symmetry. We were thus rather surprised to observe a SHG signal for $\text{Cu}_2(\text{OH})_3\text{DS}$ crystals that had *a priori* no reason to exhibit such behaviour. To investigate this behaviour we performed measurements with a variation of the excitation with linear polarization as well as a mapping of the SHG signal strength on a suitable crystal (figure 15). The variation of the excitation polarization showed a very important modulation of the signal strength. For the mapping of the SHG signal strength, we used ethanol and ultrasound to disperse the crystals to then drop cast them onto a microscope slide. The optical image below (figure 15), shows a single crystal, partly cleaved by the ultrasonic treatment. The SHG signal appeared to be stronger on the thicker part of the crystal and weaker on the thinner one, tending towards a volumetric effect and not a surface effect. Ultimately, we tried to do a measurement along the z axis (along the thickness of the crystals) but, due to a voxel size of about $1 \mu\text{m}^3$ and the thinness of the platelets, we were unable to obtain truly indisputable results. Yet, the structural resolution proved that the system was indeed non-centrosymmetric.

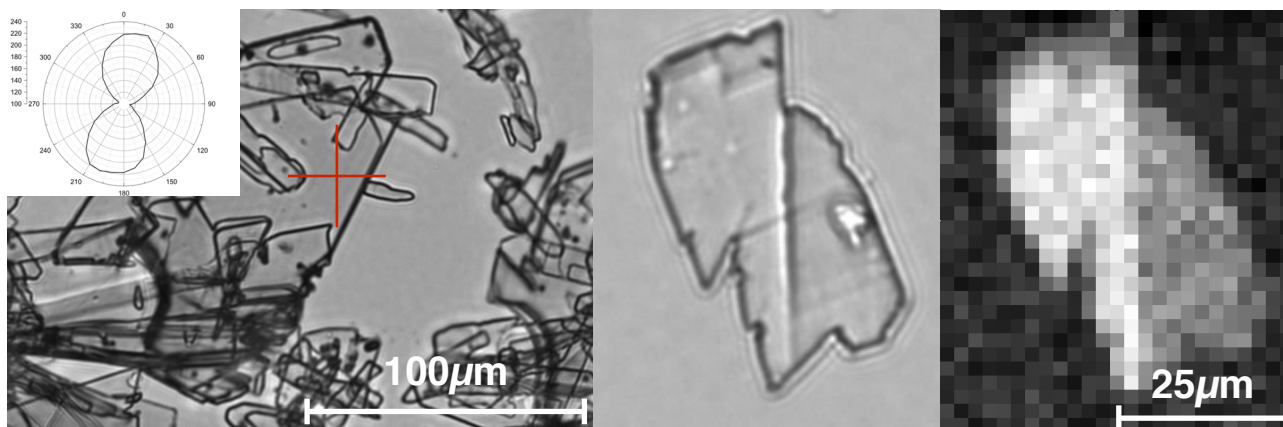


Figure 15 : Optical image of the $\text{Cu}_2(\text{OH})_3\text{DS}$ crystal, insert shows polarization response of the sample and red cross the laser position. (left) Optical image (centre) and SHG mapping of the same crystal (right).

2.3.4.2. Magnetic Properties

The magnetic properties of $\text{Cu}_3(\text{DS})_2(\text{OAc})_2(\text{OH})_2(\text{H}_2\text{O})_2$ (1) and $\text{Cu}_2(\text{OH})_3\text{DS}$ (2) were recorded in the range 1.8-300 K under a DC magnetic field of 5000 G.

The magnetic properties of $\text{Cu}_3(\text{DS})_2(\text{OAc})_2(\text{OH})_2(\text{H}_2\text{O})_2$ are presented on figure 17. The fit of the $1/\chi = f(T)$ curve in the high temperature region (above 200 K) leads to a Curie constant of $1.73 \text{ emu}\cdot\text{K}\cdot\text{mol}^{-1}$ (i.e. $0.58 \text{ emu}\cdot\text{K}\cdot\text{mol}^{-1}$ per Cu(II) ion, within the range of expected values¹³⁷) and negative Weiss temperature of -77 K, which indicates dominant antiferromagnetic interactions. The $\chi = f(T)$ for $\text{Cu}_3(\text{DS})_2(\text{OAc})_2(\text{OH})_2(\text{H}_2\text{O})_2$ indicates a paramagnetic behaviour on the whole temperature range with short-range interactions. The curve presents a sharp maximum at 10.5 K with a very broad shoulder centred around 70 K. This peculiar shape, with two, more or less defined, peaks in $\chi = f(T)$ has already been observed in other diamond-like Cu(II) hydroxide chains, with sulfonate and acetate ligands,¹³⁵ or for the related $\text{Cu}_3(\text{OH})_2(\text{CO}_3)_2$ azurite.²⁵

The $\chi = f(T)$ curve for 1 could be fitted above 7 K, considering isolated chains (separated by long dodecylsulfate molecules), and the spin topology schematized on figure 16. Below 7 K, the model used is too simplified to be valid, because other intrachain or 3D interchain interactions are likely to be taken into account in this temperature range and because of the finite size of the model.

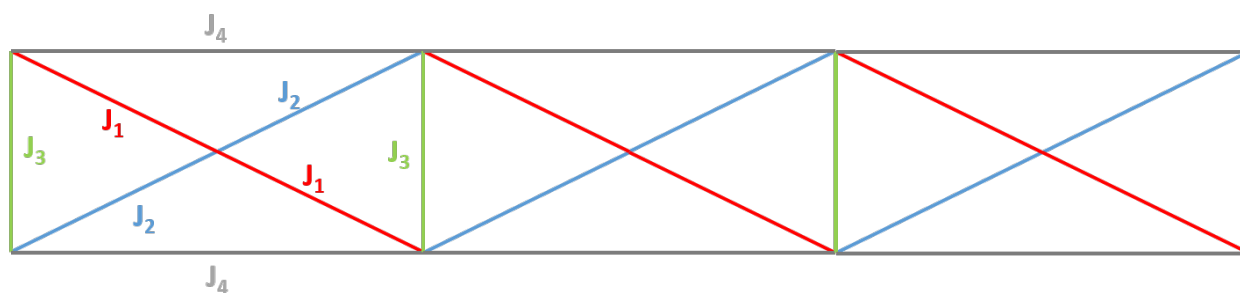


Figure 16 : Spin topology considered for $\text{Cu}_3(\text{DS})_2(\text{OAc})_2(\text{OH})_2(\text{H}_2\text{O})_2$ above 7 K. This topology is identical to the one used by Fujita et al. for related diamond-like chain compounds bearing sulfonate molecules.²⁴

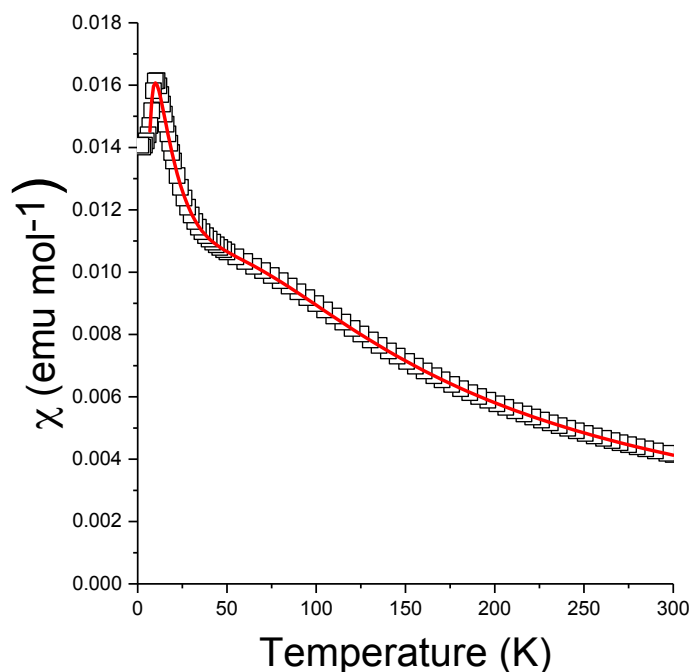


Figure 17 : $\chi = f(T)$ curve at 5000 G for $\text{Cu}_3(\text{DS})_2(\text{OAc})_2(\text{OH})_2(\text{H}_2\text{O})_2$
(open squares : experimental points, full red line : best fit).

The fit was performed considering the following Hamiltonian for spin-spin interactions :

$\hat{H} = \sum - J_{ij} \hat{S}_i \hat{S}_j$. We considered a ring of twelve spins to reproduce the chain behaviour without edge effect. The numerical resolution of the Hamiltonian was carried out by using the program SPIN including a refinement routine.³⁹ A very good adjustment of the experimental data was obtained with the refined values : $J_1 = 11(6) \text{ cm}^{-1}$, $J_2 = -75(1) \text{ cm}^{-1}$, $J_3 = -52(2) \text{ cm}^{-1}$, $J_4 = 28(2) \text{ cm}^{-1}$ and $g = 2.29(3)$. The fit was performed with a single g factor for the two different copper ions avoiding over-parameterization. Standard deviations on J_i values are quite high due to important correlations between parameters. Given the fact that several exchange pathways exist between two spin carriers, it is here difficult and beyond the scope of this study to perform a clear correlation between the J values determined and the structure of the compound. Yet it is worth noticing that the J values are moderate, and within the usually observed range for Cu-O-Cu (OH, $(\kappa^1-\mu_2)$ -sulfate or $(\kappa^1-\mu_2)$ -carboxylate) or Cu-OCO-Cu ($((\kappa^1-\kappa^1)-\mu_2)$ -carboxylate) motives.^{24, 40, 41} Clearly, the peculiar behaviour of $\text{Cu}_3(\text{DS})_2(\text{OAc})_2(\text{OH})_2(\text{H}_2\text{O})_2$, can be explained by the competition between ferromagnetic and antiferromagnetic nearest neighbour exchange interactions.

As for $\text{Cu}_2(\text{OH})_3\text{DS}$, the fit of the $1/\chi = f(T)$ curve in the high temperature region (above 200 K) leads to a Curie constant of $0.89 \text{ emu}\cdot\text{K}\cdot\text{mol}^{-1}$ (*i.e.* $0.45 \text{ emu}\cdot\text{K}\cdot\text{mol}^{-1}$ per Cu(II) ion, within the range of expected values³⁸) and very small negative Weiss temperature of -0.3 K , which indicates dominant antiferromagnetic interactions. Approximating the triangular magnetic lattice as being regular, the $\chi = f(T)$ can be fitted using the high temperature series expansion for a $S = \frac{1}{2}$ Heisenberg 2D triangular lattice (figure 21) for $T > 20 \text{ K}$.^{42, 43}

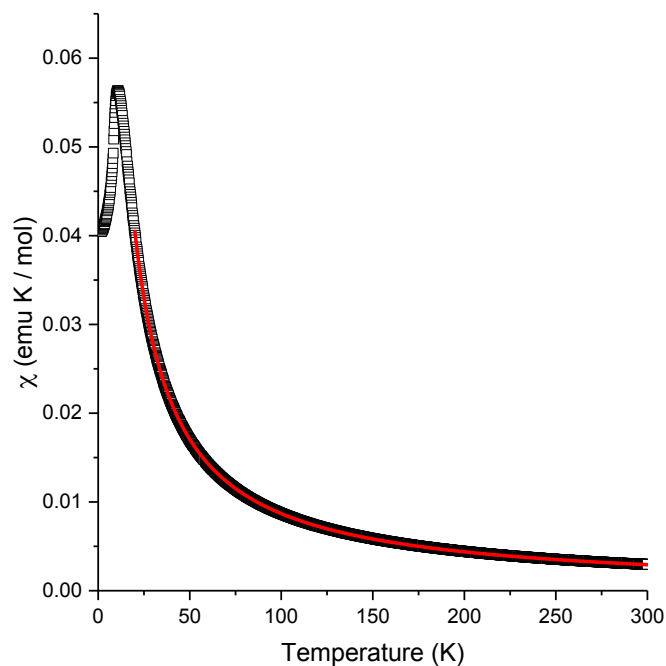


Figure 18 : $\chi = f(T)$ curve at 5000 G for $\text{Cu}_2(\text{OH})_3\text{DS}$ (open squares : experimental points, full red line : best fit).

The best fit provides $J = -0.40(1) \text{ cm}^{-1}$ and $g = 2.17(1)$. The exchange interaction is significantly smaller (by two orders of magnitude) than the ones obtained by Fujita for a series of layered hydroxides containing aromatic sulfonates.⁷ The sharp maximum observed around 11 K in the $\chi = f(T)$ curve and the very abrupt decrease of $\chi T = f(T)$ (figure 19), can be associated with the occurrence of a long range (3D) antiferromagnetic ordering. The ordering temperature can be determined precisely from the maximum of the in phase susceptibility (figure 19), leading to $T_N = 10.8 \text{ K}$. This value is slightly higher than the one determined recently for an analogous compound (synthesized by confined condensation, a totally different approach, and for which no crystal structure could be obtained) ($T_N = 8 \text{ K}$).⁸

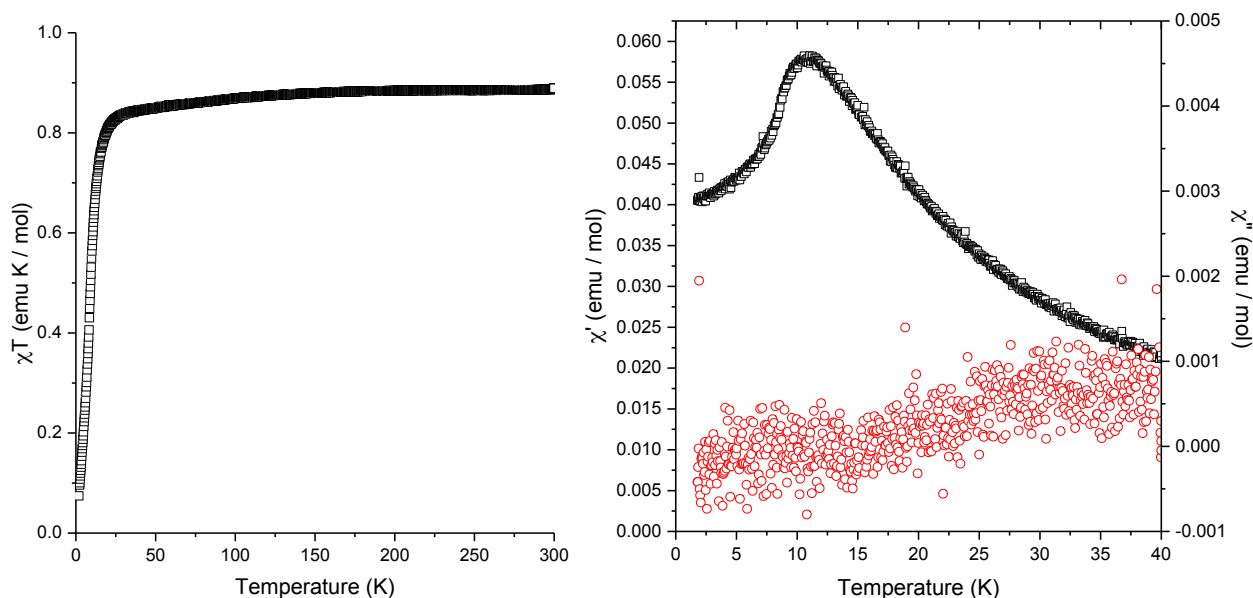


Figure 19 : $\chi T = f(T)$ curve at 5000 G (left) and ac susceptibility (left) ($\mu_0 H_{ac} = 0.1 \text{ mT}$, $f = 95 \text{ Hz}$) (open black squares : in-phase susceptibility χ' , open red circles : out-of-phase susceptibility χ'') for $\text{Cu}_2(\text{OH})_3\text{DS}$.

The magnetization vs. field curve at 1.8 K shows a clear spin-flop transition for a critical field of 2 T (figure 20) which supports an antiferromagnetic ordering at low temperature.

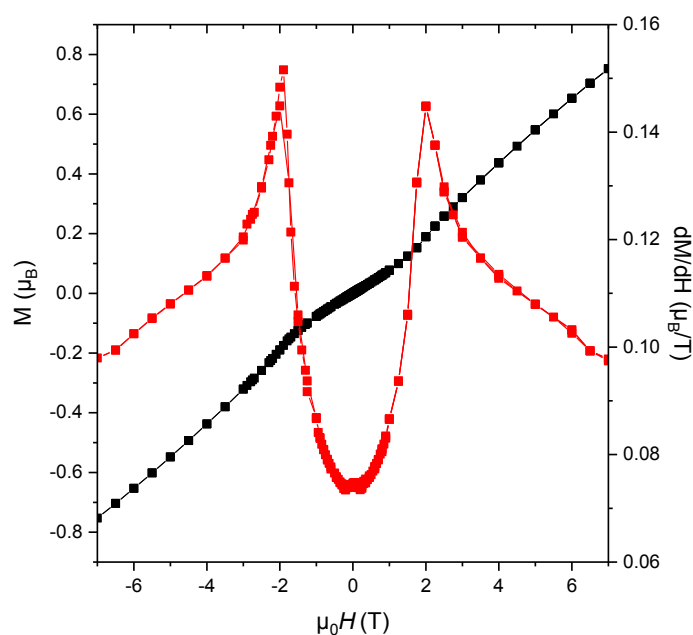


Figure 20 : $M = f(H)$ (black squares) and $dM/dH = f(H)$ (red squares) at 1.8 K for $\text{Cu}_2(\text{OH})_3\text{DS}$. Full lines are just guides for the eye.

3. Conclusion

In this chapter we show the interest of $\text{Cu}_2(\text{OH})_3\text{DS}$ and the wide possibilities now available to synthesize the starting compound and control the crystallite size or morphology. The inorganic scaffold synthesis now mastered, the following chapters will cover the functionalization of such systems with organic molecules *via* the insertion of other molecules or even coordination complexes *via* the insertion-grafting by ion exchange.

The following chapter is devoted to the structural characterization of the other layered hydroxide that has been used during this thesis which is the cobalt hydroxy-acetate. This cobalt hydroxy-acetate exhibit a type II LSH structure but with a lot of turbostratic disorder as well as defaults in the layers, hence the use of a specific characterization technique described thereafter.

4. Bibliography

1. W. Fujita and K. Awaga, *Inorganic Chemistry*, 1996, **35**, 1915-1917.
2. É. Delahaye, S. Eyele-Mezui, J.-F. Bardeau, C. Leuvrey, L. Mager, P. Rabu and G. Rogez, *Journal of Materials Chemistry*, 2009, **19**, 6106.
3. R. Bourzami, S. Eyele-Mezui, E. Delahaye, M. Drillon, P. Rabu, N. Parizel, S. Choua, P. Turek and G. Rogez, *Inorganic Chemistry*, 2014, **53**, 1184-1194.
4. M. Kurmoo, H. Kumagai, S. M. Hughes and C. J. Kepert, *Inorganic Chemistry*, 2003, **42**, 6709-6722.
5. A. Demessence, A. Yassar, G. Rogez, L. Miozzo, S. De Brion and P. Rabu, *Journal of Materials Chemistry*, 2010, **20**, 9401.
6. O. Palamarciuc, E. Delahaye, P. Rabu and G. Rogez, *New Journal of Chemistry*, 2014, **38**, 2016-2023.
7. W. Fujita, *CrystEngComm*, 2015, **17**, 9193-9202.
8. S. H. Park, M. H. Jung, Y. J. Lee and Y. D. Huh, *Dalton Transactions*, 2017, **46**, 3363-3368.
9. E. Delahaye, S. Eyele-Mezui, M. Diop, C. Leuvrey, P. Rabu and G. Rogez, *Dalton Transactions*, 2010, **39**, 10577-10580.
10. S. Eyele-Mezui, E. Delahaye, G. Rogez and P. Rabu, *European Journal of Inorganic Chemistry*, 2012, **2012**, 5225-5238.
11. S. Yamanaka, T. Sako and M. Hattori, *Chemistry Letters*, 1989, **18**, 1869-1872.
12. S. Yamanaka, *Solid State Ionics*, 1992, **53-56**, 527-533.
13. P. Rabu, S. Rouba, V. Laget, C. Hornick and M. Drillon, *Chemical Communications*, 1996, **0**, 1107-1108.
14. V. Laget, M. Drillon, C. Hornick, P. Rabu, F. Romero, P. Turek and R. Ziessel, *Journal of Alloys and Compounds*, 1997, **262-263**, 423-427.
15. W. Fujita, *Applied Clay Science*, 1999, **15**, 281-303.
16. V. Laget, C. Hornick, P. Rabu and M. Drillon, *Journal of Materials Chemistry*, 1999, **9**, 169-174.
17. G. Rogez, C. Massobrio, P. Rabu and M. Drillon, *Chemical Society Reviews*, 2011, **40**, 1031-1058.
18. E. Delahaye, S. Eyele-Mezui, M. Diop, C. Leuvrey, D. Foix, D. Gonbeau, P. Rabu and G. Rogez, *European Journal of Inorganic Chemistry*, 2012, **2012**, 2731-2740.
19. S. Eyele-Mezui, P. Vialat, C. Higy, R. Bourzami, C. Leuvrey, N. Parizel, P. Turek, P. Rabu, G. Rogez and C. Mousty, *The Journal of Physical Chemistry C*, 2015, **119**, 13335-13342.
20. P. Rabu, E. Delahaye and G. Rogez, *Nanotechnology Reviews*, 2015, **4**, 557-586.
21. S. Švarcová, M. Klementová, P. Bezdička, W. Łasocha, M. Dušek and D. Hradil, *Crystal Research and Technology*, 2011, **46**, 1051-1057.
22. N. Masciocchi, E. Corradi, A. Sironi, G. Moretti, G. Minelli and P. Porta, *Journal of Solid State Chemistry*, 1997, **131**, 252-262.
23. H. A. Jahn and E. Teller, *Proceedings of the Royal Society A: Mathematical, Physical and Engineering Sciences*, 1937, **161**, 220-235.
24. W. Fujita, A. Tokumitsu, Y. Fujii and H. Kikuchi, *CrystEngComm*, 2016, **18**, 8614-8621.
25. H. Kikuchi, Y. Fujii, M. Chiba, S. Mitsudo, T. Idehara, T. Tonegawa, K. Okamoto, T. Sakai, T. Kuwai and H. Ohta, *Physical Review Letters*, 2005, **94**, 227201.
26. M. Okazaki, K. Toriyama, S. Tomura, T. Kodama and E. Watanabe, *Inorganic Chemistry*, 2000, **39**, 2855-2860.

27. S. H. Park and C. E. Lee, *The Journal of Physical Chemistry. B*, 2005, **109**, 1118-1124.
28. C. Janiak, *Dalton Transactions*, 2003, **0**, 2781.
29. L. Ma, C. Abney and W. Lin, *Chemical Society reviews*, 2009, **38**, 1248-1256.
30. B. Gil-Hernandez, H. A. Hoppe, J. K. Vieth, J. Sanchiz and C. Janiak, *Chemical Communications*, 2010, **46**, 8270-8272.
31. F. Holler and J. B. Callis, *The Journal of Physical Chemistry*, 1989, **93**, 2053-2058.
32. R. P. Sperline, *Langmuir*, 1997, **13**, 3715-3726.
33. S. H. Park and C. E. Lee, *Journal of Physical Chemistry B*, 2005, **109**, 1118-1124.
34. R. C. Miller, *Applied Physics Letters*, 1964, **5**, 17-19.
35. C. K. Chen, A. R. B. de Castro and Y. R. Shen, *Physical Review Letters*, 1981, **46**, 145-148.
36. T. F. Heinz, C. K. Chen, D. Ricard and Y. R. Shen, *Physical Review Letters*, 1982, **48**, 478-481.
37. Y. R. Shen, *Nature*, 1989, **337**, 519-525.
38. R. L. Carlin, *Magnetochemistry*, Springer-Verlag Berlin Heidelberg, 1986.
39. P. Legoll, M. Drillon, P. Rabu and F. Maingot, *SPIN 2.3*, 1996, Université Louis Pasteur, Strasbourg.
40. V. H. Crawford, H. W. Richardson, J. R. Wasson, D. J. Hodgson and W. E. Hatfield, *Inorganic Chemistry*, 1976, **15**, 2107-2110.
41. C. J. Gomez-Garcia, E. Escriva, S. Benmansour, J. J. Borrás-Almenar, J. V. Folgado and C. Ramirez de Arellano, *Inorganic Chemistry*, 2016, **55**, 2664-2671.
42. G. S. Rushbrooke and P. J. Wood, *Proceedings of the Physical Society. Section A*, 1955, **68**, 1161-1169.
43. R. Navarro, in *Magnetic Properties of Layered Transition Metal Compounds*, L. J. de Jongh ed. Kluwer Academic Publishers; Dordrecht, 1990.

Chapter II : Characterization of the Structure of Layered Cobalt
Simple Hydroxide Derivatives via Pair Distribution Function Analysis

Chapter II : Characterization of the Structure of Layered Cobalt Simple Hydroxide Derivatives via Pair Distribution Function Analysis

The work shown here is the result of the characterization of compounds obtained by functionalization of $\text{Co}_2(\text{OH})_{3.2}(\text{OAc})_{0.8}$ (the structure of which is considered to present type II or hydrozincite-like layers^{1, 2}) by ion exchange with *p*-amino benzoic acid, and of the compounds obtained by subsequent *in-situ* reaction of $\text{Co}_2(\text{OH})_{3.35}(4\text{-NH}_2\text{-BzAc})_{0.65}$ with various aldehydes following the work previously done in our laboratory.³

These compounds, like, as far as we know, all compounds obtained by ion exchange from $\text{Co}_2(\text{OH})_{3.2}(\text{OAc})_{0.8}$, including cobalt hydroxy acetate itself, present disordered inorganic layers, with very small crystallite size, which prevents precise structural characterization. Unfortunately, strategies used previously for the copper hydroxy acetate or the copper hydroxyl dodecylsulfate described in the previous chapter are inefficient here. The growth of crystals large enough for a structural determination on single crystals appears to be impossible up to now. The crystallinity of the obtained powders is also largely insufficient to allow for Rietveld refinement of the structure.

As stated above, the structure generally admitted for the inorganic layers of cobalt layered simple hydroxide hybrids can be described as a triple-deck sheet deriving from the structure of the analogous hydrozincite $\text{Zn}_5(\text{OH})_8(\text{NO}_3)_2 \cdot 2\text{H}_2\text{O}$ (figure 1).^{1, 2} It is formed of a monolayer of octahedral Co(II) hydroxide (brucite type structure), with metal vacancies counterbalanced by the occurrence of tetrahedral Co(II) sites on both sides of the octahedral monolayer. In this kind of structure, it is generally assumed that the exchange reactions proceed *via* a dissolution-recrystallization mechanism, and that each carboxylate (or sulfate or sulfonate) group is linked to one cobalt ion in a tetrahedral environment.^{4, 5} Therefore the number of coordinating groups corresponds to the number of tetrahedral Co(II) ions.

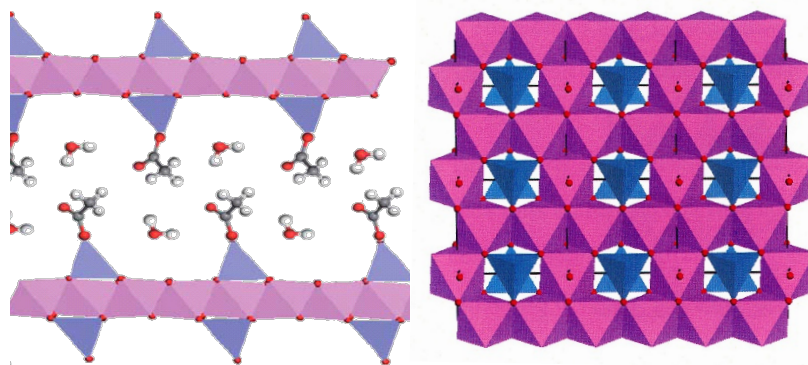


Figure 1 : View of the generally accepted structure of $\text{Co}_2(\text{OH})_{3.2}(\text{OAc})_{0.8}$ parallel (left) and perpendicular (right) to the inorganic layers, adapted from the structure of $\text{Zn}_5(\text{OH})_8(\text{NO}_3)_2 \cdot 2\text{H}_2\text{O}$.¹

This hydrozincite-like structure is further supported by the structure of $\text{Co}_5(\text{OH})_8(\text{chdc}) \cdot 4(\text{H}_2\text{O})$ this compound was obtained by hydrothermal one-pot method, and the structure solved on a monocrystal.⁶

Therefore, some authors use the formulation $\text{Co}_5(\text{OH})_8(\text{OAc})_2$ for cobalt hydroxy acetate, and more generally $\text{Co}_5(\text{OH})_{10-x}(\text{A})_x$, with A a monoanionic species. This notation is convenient in that it underlines the similarity of the proposed structure with that of $\text{Zn}_5(\text{OH})_8(\text{NO}_3)_2 \cdot 2\text{H}_2\text{O}$. In addition, it allows to point out the maximum possible value for the insertion ratio, $x = 2$. If we consider that the interlayer molecule is grafted only of tetrahedral cobalt ions, values of x larger than 2 would indicate an excess of tetrahedral sites with respect to octahedral ones, incompatible

with the proposed structure. Yet, in the following of this manuscript and for a sake of comparison with the insertion rates in copper hydroxide, we will be using the same formulation as the one used for copper hydroxide-based hybrids *i.e.* $\text{Co}_2(\text{OH})_{4-y}(\text{A})_y$. This notation is chemically strictly equivalent to the $\text{Co}_5(\text{OH})_{10-x}(\text{A})_x$. With this notation $\text{Co}_2(\text{OH})_{4-y}(\text{A})_y$, the maximum insertion rate is $y = 0.8$.

The work described in this chapter had two main goals, the first and main one being to analyse as finely as possible the structure of the inorganic layers of functionalized cobalt hydroxide. Very few studies have been reported so far on the structural determination of layered cobalt hydroxide salts. Previous works done by Morse *et al.*⁷ or Sasaki *et al.*⁸ published powder X-ray Rietveld refinements on the $\text{Co}_{2-x}^{\text{Oct}}\text{Co}_x^{\text{Tet}}(\text{OH})_{4-x}\text{Cl}_x \cdot y \text{H}_2\text{O}$ system considering an averaged rhombohedral structure first described by Ma, *et al.* in which tetrahedral sites are statistically disordered. Morse *et al.* also performed refinements of PDF data (total X-ray scattering experiments) and concluded that the local structure is better described by a weighted average of different phases consisting of symmetrically distributed metal polyhedra rather than a random distribution of metal polyhedra on average. They also clearly demonstrated that the tetrahedrally coordinated cobalt sites require an octahedral vacancy in the layers. However, the structural data obtained from PDF refinements show an unreasonable value of the isotropic atomic displacement parameter $u = 0.2484(9) \text{ \AA}^2$ ($B \sim 19.5 \text{ \AA}^2$) for the water molecules siting aside the fourth apex of Co^{Tet} occupied by Cl. This certainly allowed the authors to reach a good fit but does not seem to us correctly attributed.

The second goal was to try to get evidence of the *in-situ* reaction *via* the differences observed in the PDF. This aspect is clearly a side project of this PhD work. All the work shown here has been performed in close collaboration with Pr. C. Taviot-Guého from the Institut de Chimie of Clermont-Ferrand (ICCF).

1. Introduction

X-ray diffraction is known to bring very important structural information in well-ordered materials *via* the use of the Bragg peaks in Rietveld method for structure determination.¹³⁸⁻¹⁴⁰ However, as previously described, in the case of hybrid layered hydroxides it is very difficult to have access to other information than space group, lattice constants, and interlamellar distance spacing using the Bragg peaks. Indeed, the very small crystallite size as well as the strong turbostratic disorder and the generally accepted random tetrahedron distribution in the case of triple-layered cobalt hydroxide^{12, 13} only generate relatively weak $\{00\}$ reflections as well as asymmetric $hk0$ peaks showing the typical shape indicative of turbostratic disorder.¹⁴¹ Several layered compounds are known to present defects, both within each layer and between the layers which disrupts the long-range periodicity even more.¹⁴⁻¹⁶

Total X-ray scattering and pair distribution function analysis is a powerful approach well suited for disordered materials because it takes into account diffuse scattering in addition to Bragg scattering. Using this technique, we can get an accurate description of short-range structure, paving the way for a deeper understanding of the local structuration of the present materials. Theoretical details about PDF analysis are given in appendix I.

This method has been successfully applied alone for the structural resolution of ferrihydrite,¹⁷ $\text{V}_2\text{O}_5 \cdot n\text{H}_2\text{O}$ xerogel¹⁸ or the observation¹⁹ of lattice polaron formation in $\text{La}_{1-x}\text{Ca}_x\text{MnO}_3$ upon modification of $0.12 < x < 0.25$. This method can also be applied in

combination with other techniques to the local structural study of numerous disordered materials such as a positive electrode material²⁰ $\text{Li}(\text{NiMn})_{0.5}\text{O}_2$ or the lithiation of iron fluoride for example.²¹

As stated in the introduction of the present chapter, there are also a few studies on layered double hydroxides and layered hydroxide salts. In particular, Morse *et al.* investigated the structure of α -type cobalt hydroxides incorporating Cl^- anions into the layers by synchrotron X-ray diffraction ($Q_{\text{max}} 25 \text{ \AA}^{-1}$) and atomic pair distribution function analysis.^{7, 13} These real space analyses allowed them to reveal local clustering of cobalt hydroxide polyhedra within the layers modelled by the weighted average of different ordered phases with fixed fractions of tetrahedrally coordinated cobalt sites. These authors said that this structural description provides insights into the mechanisms of formation of these materials and a better understanding of their magnetic behaviours. In this chapter we investigated the local structure of a series of cobalt hydroxide based hybrids using total X-ray scattering data and pair distribution function analysis. Our PDF approach and the results we obtained will be discussed in comparison with those of Morse *et al.*

2. Experimental Procedure

From an experimental point of view, this method is very sensitive to data collection and correction effects. Indeed, it is crucial to carefully collect and precisely extract the data.

To that end, we obtained a six-day run at SOLEIL synchrotron on the CRISTAL beamline. We used an energy of 28 keV ($= 0.436 \text{ \AA}$) and an XPAD hybrid pixel detector. During this run, we optimized the collection of the X-ray total scattering data using the XPAD 2D detector¹⁴² (hybrid pixel area detectors). Using this detector, we got a better signal to noise ratio than with the multi-analyser detector, and as a consequence a better resolution of the pair distribution functions. The first objective of this run was to develop and optimize the use of the new XPAD 2D detector to replace the previous multi-analyser detector for PDF extraction. Indeed, for PDF extraction experiment, as it is not the diffraction peaks that are analysed but the scattering background therefore having the highest possible signal to noise ratio is the key to achieve the best PDF resolution and thus, extracting the best PDF possible.

For these experiments, we had first to optimize the data collection conditions in close interaction with the line coordinator Erik Elkaïm, from slit sizes or blade position to the optimal collection mask to convert the 2D images collected by the XPAD to the final exploitable diffractogram (figure 1). After this optimization work, all samples were analysed in the same way described as follows :

The samples were packed in 0.7 mm quartz sealed capillaries. Data was collected at room temperature, in the $1-125.88^\circ 2\theta$ angular range with a total collection time of 30 min. Instrument calibration was done using a reference standard, LaB_6 . The signal from the empty capillary was subtracted as a background. All diffraction data were Fourier transformed to PDF data using the PDFgetX2 program²³ and data simulation was performed using the PDFgui program.²⁴ Breit-Dirac correction was applied to remove Compton scattering. The upper limit of the Q value used for the calculation of PDF data (Q_{max}) was equal to 20 \AA^{-1} .

3. Experimental Setup Optimization

As explained above we first worked on the optimization of the collection of total X-ray scattering data. We first compared the datasets collected using the 2D hybrid detector (XPAD) and the multi-analyser (figure 1). The comparison is made with the PDF extracted from the two datasets using two different programs PDFgetX2 and PDFgetX3. The treatment of the data using these two programs allowed us to check the influence of the detector. In particular, the data collected using the XPAD detector must be corrected from Compton scattering. PDFgetX2 allows a precise control of numerous parameters for correcting the signal while PDFgetX3 “requires fewer inputs and less user experience and it can be readily adopted by novice users”, as indicated by the authors.²⁵

During the run, it is necessary to measure accurately the instrumental background including air scattering and also scattering from the sample holder *i.e.* the capillary. All the data were thus first corrected from air and capillary contributions to scattering, as well as absorption and multiple scattering and normalized using the program PDFgetX2/3. The reliability of the PDF data depends greatly on the way the corrections are applied. In case of a beam line interruption, the background needs to be recollected before doing further experiments.

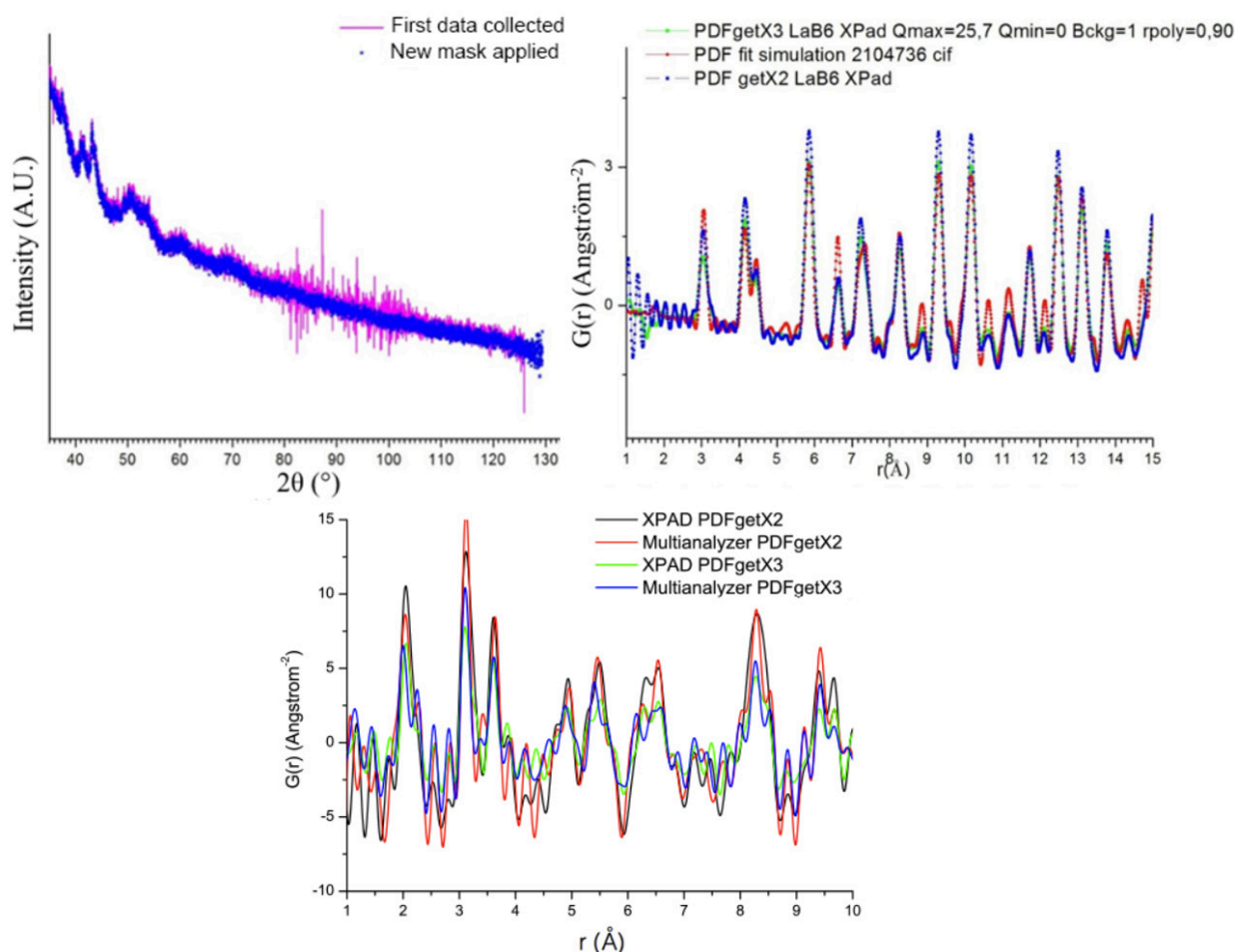


Figure 1 : Raw data input with mask enhancements (top left), LaB₆ PDFs and simulation comparison (top right), multi-analyser versus XPAD detectors on Co₂(OH)_{3,2}(OAc)_{0,8} (bottom).

The reliability of the data sets acquired from both the multi-analyser and the XPAD has been challenged with the comparison between a reference and simulated LaB₆ material while

using both PDFgetX2 and PDFgetX3 (figure 1). The collection of the raw data for the XPAD detector was also optimized with a specific mask able to filter the noise seen between 80-105 ° in 2θ.

The first indication of the quality of our data and data correction is given by checking if the limits of the different functions are in agreement with their physical limits. Indeed, the normalized total scattering structure function $S(Q)$, Q being the value of the diffusion vector ($Q = 4 \pi \sin(\theta)/\lambda$) where λ is the wavelength of the incident X-rays and θ half of the diffusion angle 2θ , should be 0 when $Q = 0$. Moreover, $S(Q)$ should oscillate around 1 for $Q \rightarrow \infty$ as this scattered intensity is normalized.

$S(Q)$, defined in the reciprocal space is linked *via* a Fourier transform to a function called $G(r)$ which is defined in real space. Experimental $G(r)$ obtained from total X-ray scattering data is defined as :

$$G(r) = \frac{2}{\pi} \int_0^{\infty} Q [S(Q) - 1] \sin(Qr) dQ$$

$$\lim_{r \rightarrow \infty} G(r) = 0$$

This $G(r)$ is commonly called normalized pair distribution function, it represents the probability to find in the structure a pair of atoms at an r distance of each other. It is a monodimensional function that possesses Dirac peaks for values of r equal to interatomic distances. Consequently, this function is 0 for $r < r_c$ with r_c being the value of the shortest interatomic distance in the material and it should oscillate around 1 when $r \rightarrow \infty$ because of the normalization. The theoretical $G(r)r$ calculated from a structural model is described as :

$$G(r) = \frac{1}{r} \sum_j \sum_{k \neq j} \frac{b_j b_k}{\langle b^2 \rangle} \delta(r - r_{jk}) - 4\pi r \rho_0$$

To test the data reliability, we had to check if they were in good agreement with these limits, it was also important to extract the data for different values of Q to make sure that all the observed peaks were real and not just due to residual signals from the Fourier transform.

4. PDF Extraction on Layered Cobalt Hydroxides

4.1. Signature of the Organic Part of the Cobalt Hydroxide Hybrids in Their Respective PDFs

As mentioned above, one of the goals of this study was to investigate the structure of the starting compound *i.e.* $\text{Co}_2(\text{OH})_{3.2}(\text{OAc})_{0.8}$, the functionalized phase obtained by ion exchange with *p*-aminobenzoic acid and the phases obtained by subsequent *in-situ* reaction of the *p*-aminobenzoic with various aldehydes as described in a previous work done in our laboratory.³

Using the PDF analysis, we aimed to obtain a direct proof of the *in-situ* reaction on the interatomic distances observed in the PDF. Unfortunately, due to the high contrast between the organic molecules (low Z) and the cobalt hydroxide layers (high Z), it was not possible to observe interatomic distances attributed to the organic part. Indeed, the coherent scattering of atomic species such as carbon/nitrogen atoms with low Z numbers is quite weak and is completely hidden

by the high-Z part of the structure. On the other hand, as shown below, we observed indirect effects on the interatomic distances reported for the hydroxide layers.

To demonstrate this contrast effect between the two scattering components, we calculated the PDF profiles of the average structure obtained by Kepert *et al.*²⁶ via Rietveld refinement and repeated the calculations by sequentially removing the organic molecules then the interlamellar water. This structure is made of pillaring *trans*-1,4-cyclohexanedicarboxylates into layered cobalt hydroxide ($\text{Co}_5(\text{OH})_8(\text{chdc})\cdot 4\text{H}_2\text{O}$) and the cobalt hydroxide layers exhibit the triple-deck structure similar to our expected layer structure. The comparison of the three simulated PDFs clearly shows a very weak contribution of the interlayer species to the total scattering signal leading to only subtle variations in the intensities and probably reliable only for data collected to very high Q (figure 2).

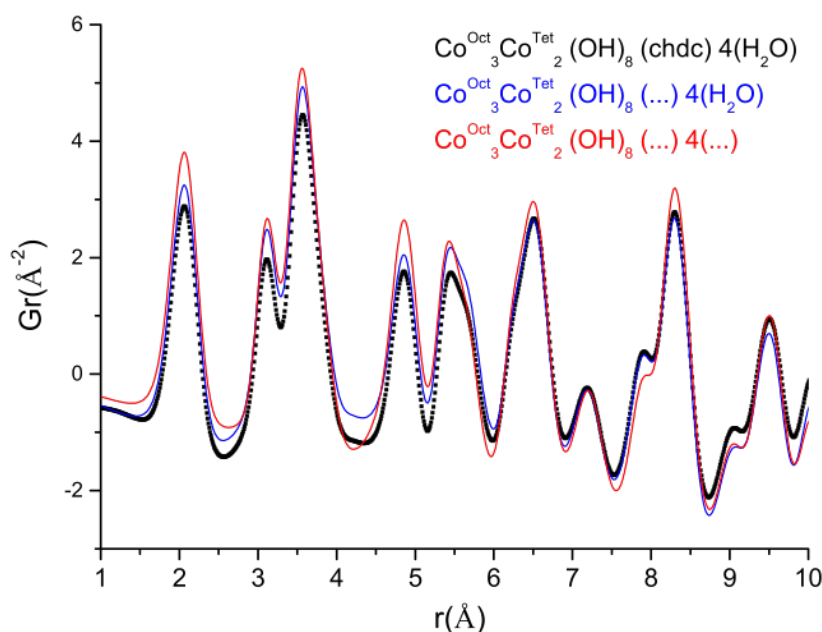


Figure 2 : Comparison between the three PDFs calculated from the structure of $\text{Co}_5(\text{OH})_8(\text{chdc})\cdot 4\text{H}_2\text{O}$ with sequential removal of organic molecules and water.

These results indicated that it was not possible to investigate the arrangement of the organic molecules located in the interlamellar spacing, and neither the formation of a C=N bond by *in-situ* reaction. Therefore, in the second part of this chapter we mainly focus on the structural changes observed on the inorganic hydroxide layers resulting from the functionalization process. We also performed a PDF refinement of the data to get an accurate description of the local structure of the layers for selected compounds.

In addition, incoherent scattering (Compton) is expected with atomic species with low-Z number. The Compton signal is not eliminated by the XPAD hybrid detector we used which makes more difficult the derivation of experimental PDF from experimental XRD patterns. However, the application of the Breit-Dirac Factor allowed us to take into account Compton intensities and obtain PDFs of relatively good quality.

The experimental structure functions $S(Q)$ and the PDFs obtained by a direct sine Fourier transformation of $S(Q)$ are presented in figures 3 and 4 respectively. The quality and low noise level of the data is visible on the structure factors. In addition, a significant modulation of the scattering data (diffuse scattering) can be observed at high Q. The data were terminated at $Q_{\text{max}} = 20 \text{ \AA}^{-1}$ to obtain the corresponding PDF.

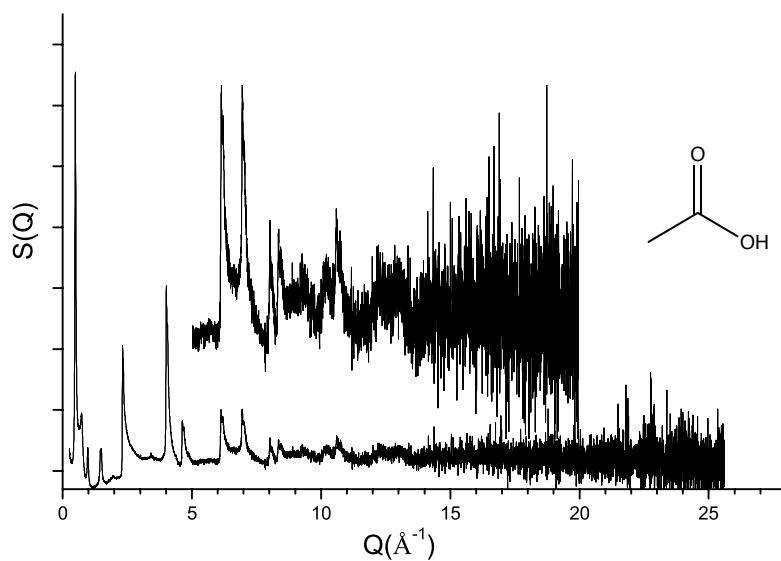
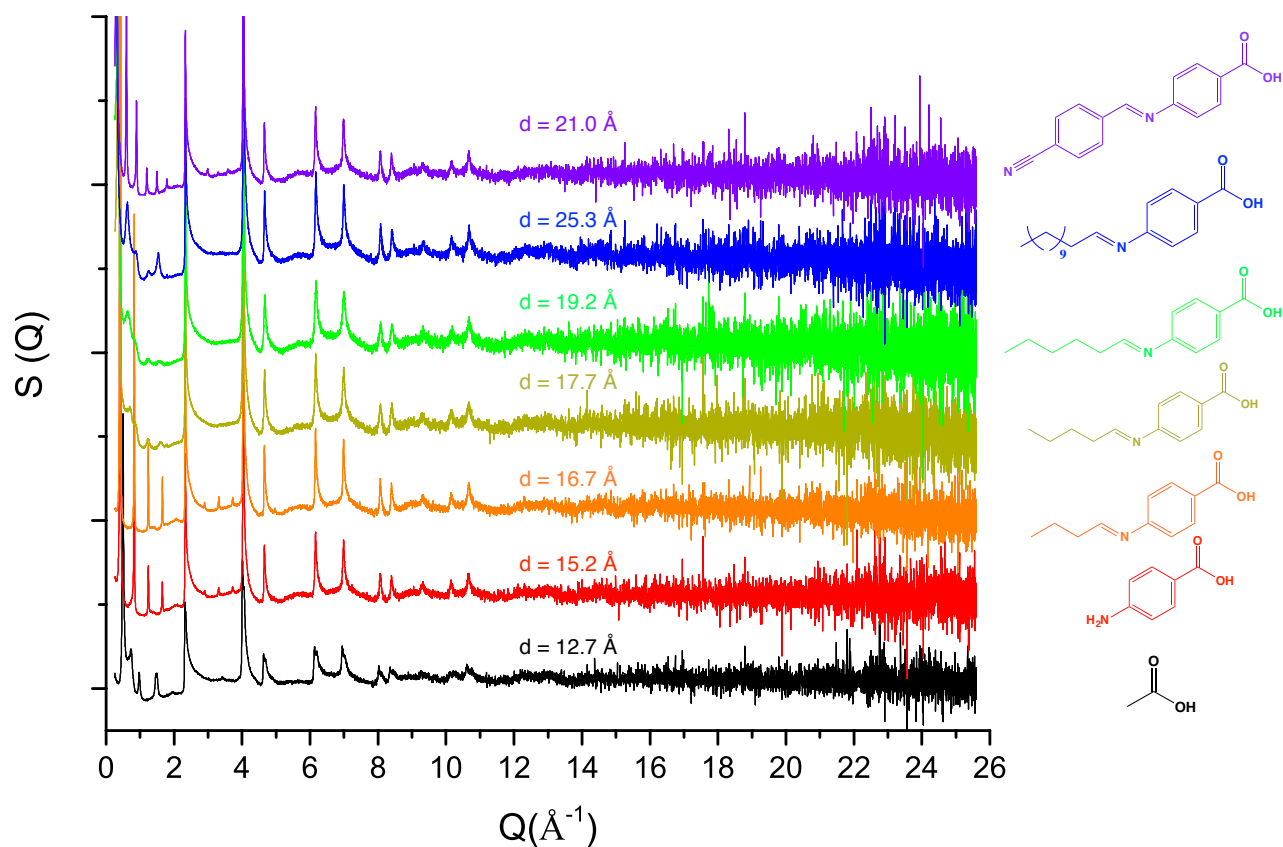


Figure 3 : Structure functions of the studied hybrid compounds and their interlamellar spacing (top)(the inserted molecule is shown on the right side) and emphasis on the substantial diffuse scattering on cobalt hydroxy acetate.(bottom)

The obtained $S(Q)$ functions in the reciprocal space are then Fourier transformed to $G(r)$ or more commonly called PDF. The results of this transformation are shown in figure 4 below.

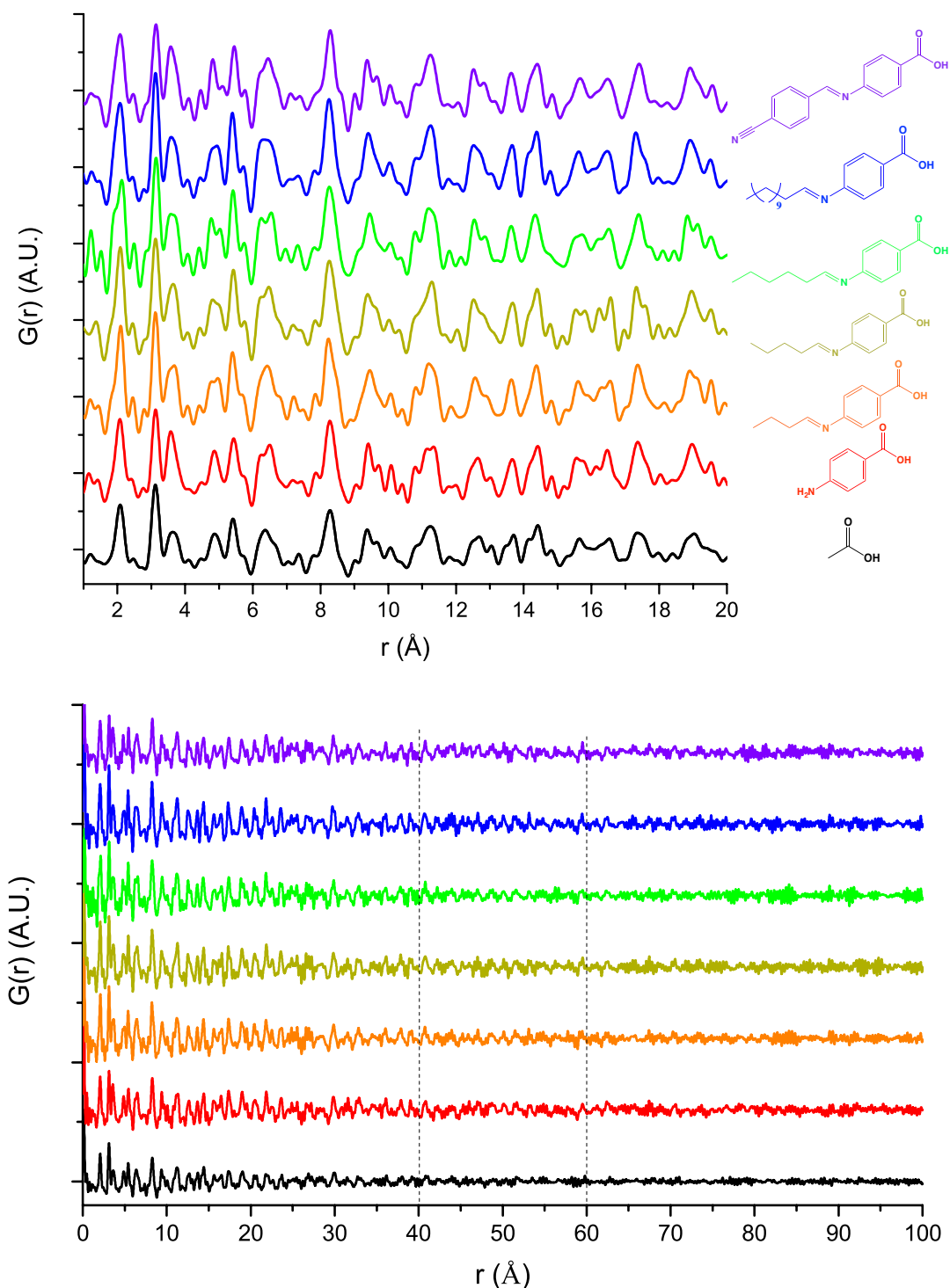


Figure 4 : PDFs of all the compounds studied and the molecule present in the interlamellar spacing (top) and high r PDFs showing coherence domains (bottom)

Figure 4 shows explicitly the differences (or in this case, lack thereof) with the extracted PDFs of all the compounds we studied at low r . In all cases, the atomic pair correlations extend to distances of approximately 40 Å. For rigid molecules, the loss of correlation occurs at slightly larger distance (around 60 Å) suggesting an increased order for such compounds (figure 4). The PDF can provide information on both the local structure in the low r region and the average structure in the high r region. In the present case, we will focus mainly on the low r region in which solely intralayer pairwise interactions are observed as verified above.

Compared to the experimental PDF reported by Morse *et al.*⁷ extracted from data collected up to 25 Å⁻¹, our PDFs are better resolved. In order to confirm that all the small correlation peaks

and shoulders observed in the low r region are not the result of truncation artifacts, the data were Fourier transformed over two Q ranges, $Q_{\max} = 20 \text{ \AA}$ and $Q_{\max} = 23 \text{ \AA}$, the peak positions were found unchanged confirming the existence of these correlation peaks. The results suggest a greater local order for our materials. compared to what has been previously found in Morse *et al.*⁷

4.2. Cell Parameter Determination

As seen from section 4.1 the PDF of the obtained compounds are very similar between all the samples tested. Differences are, in the other hand, very visible in the XRD patterns obtained at SOLEIL (figure 5). There are specifically three regions where these differences are clearly visible.

To discuss the cell parameters of the different samples and their variation along the series, we consider the Bragg peaks referring to the long-range averaged structure. In the XRD patterns presented Figure 5, noticeable difference are observed.

Considering the classical rhombohedral cell, the first region is at low angle with intense peaks corresponding to $00l$ reflections allowing a direct determination of the interlayer distance $d = d_{001}$ and the c parameter. The average on all harmonics are reported directly in figure 5.

The second region with higher angles at around 16° (2θ) allows for the determination of the unit cell parameter $a = 2 * d_{110}$

Finally, the third region with the reflection at intermediate angles (8 - 12° in 2θ) corresponding to $(01l)$ and $(10l)$ reflections.

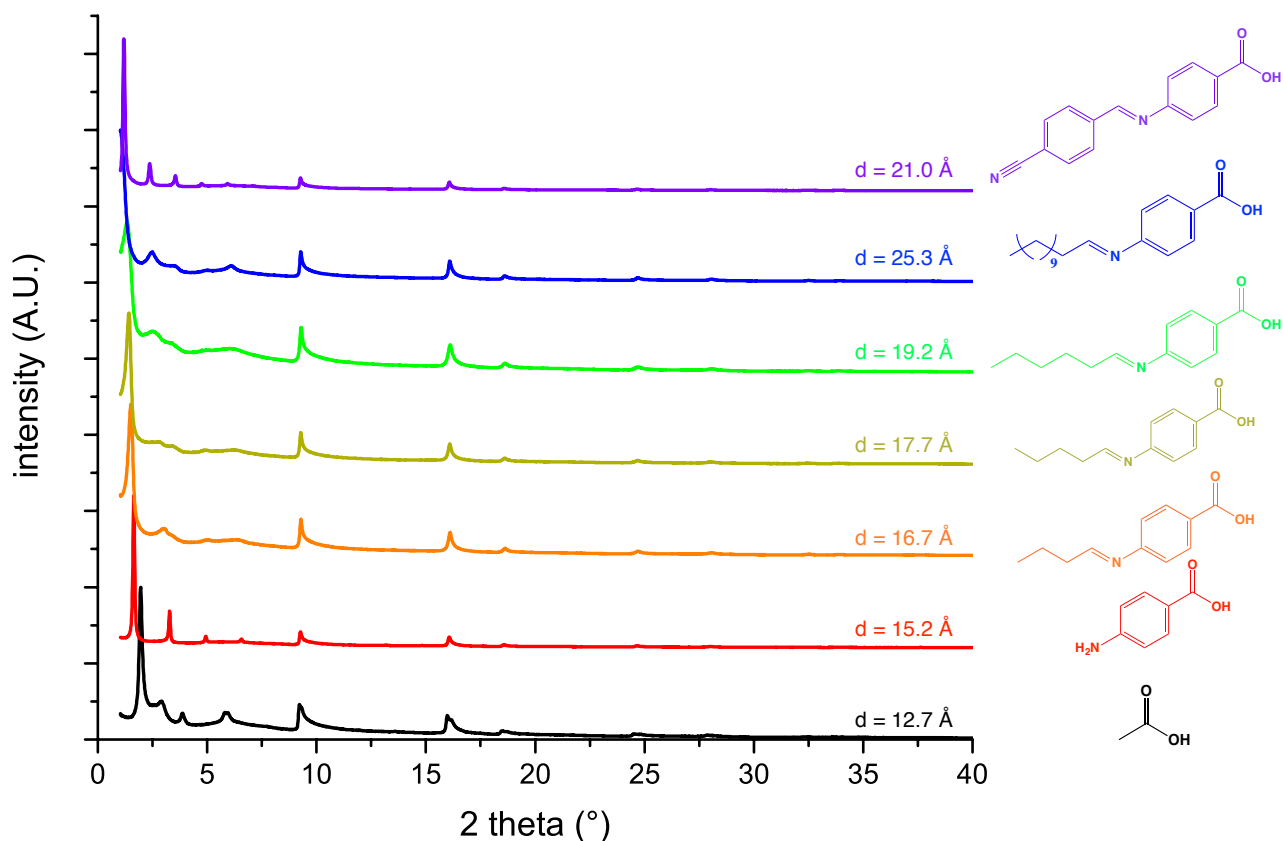


Figure 5 : X-ray diffractograms of several hybrids with their corresponding molecule and interlamellar distance.

Concerning the cell parameter **a**, we observed a slight shift of the position of the 110 reflection towards high 2θ angles (figure 6) that causes the double peak to evolve into a single peak. This may be attributed to a decrease of the value of the cell parameter **a**. Indeed, as observed in the literature, a decrease of fractional occupancy of tetrahedral cobalt sites leads to a lattice contraction along the **a** axis.⁷ However, the increase of the interlayer distance is also expected to lead to a shift of the 11/ reflections towards low 2θ angles, overlapping the 110 reflection and we think that it is what can be observed here. These results show that the unit cell parameter **a** and the Co_{tet}/Co_{oct} ratio does not change drastically, result which is also supported by chemical analysis and UV-Vis measurements.³

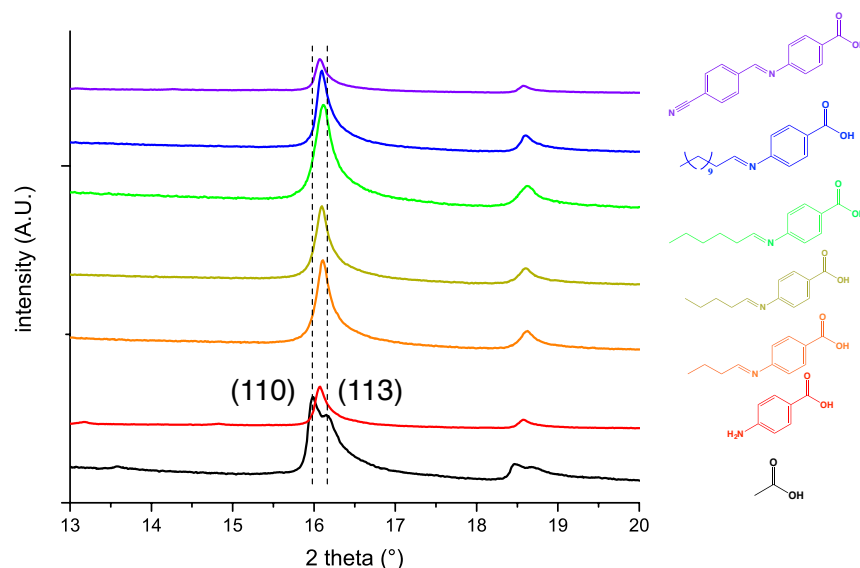


Figure 6 : Detail of the 110 and 113 reflection (assuming rhombohedral symmetry) as a function of interlayer distance.

The value of the unit cell parameter assuming a rhombohedral symmetry was estimated from the position of the 110 reflection in $Co_2(OH)_{3.2}(OAc)_{0.8}$ because in that case it clearly distinguishes from the 11/ reflection : $a = 2 \cdot d_{110} = 2 \cdot 1.5665 = 3.1330 \text{ \AA}$. This value is very close to that reported by Morse *et al.*⁷ for a cobalt hydroxide compound containing 26.6% of tetrahedrally coordinated cobalt ions : $a = 3.13677(7) \text{ \AA}$.

The anisotropic width of the reflection is consistent with the platelet-like morphology of the crystal but supplementary broadening effect may occur due the presence of defects (static or dynamic atomic disorder, stacking faults...) which decrease the size of the coherent domains and/or lead to the presence of microstrains. In the present case, only the 00/ reflections show significant broadening effects indicating the predominance of staking faults and probably important structural disorders in the interlayer space. It is interesting to note that this disorder does not proportionally increases with the interlayer distance. The molecular structure of the interlayer species as well as the rigidity of the inserted molecule must be determinant in the observed effects.

An additional comment should be made with the diffractogram of $Co_2(OH)_{3.2}(OAc)_{0.8}$ compound. Indeed, at low angle it is possible to see the presence of two distinct 00/ reflections families. This phenomenon is attributed to dehydration of our sample under the beam (figure 7), both phases has been previously observed and identified in the lab. This phase with an interlamellar distance of 9.7 \AA , however, does not influence the extracted PDFs as the structure of the lamella remains untouched. The difference in the amount of water between the two phases has been determined *via* TGA/TDA analysis to be going down from 1.8 H_2O per formula unit to 0.7.

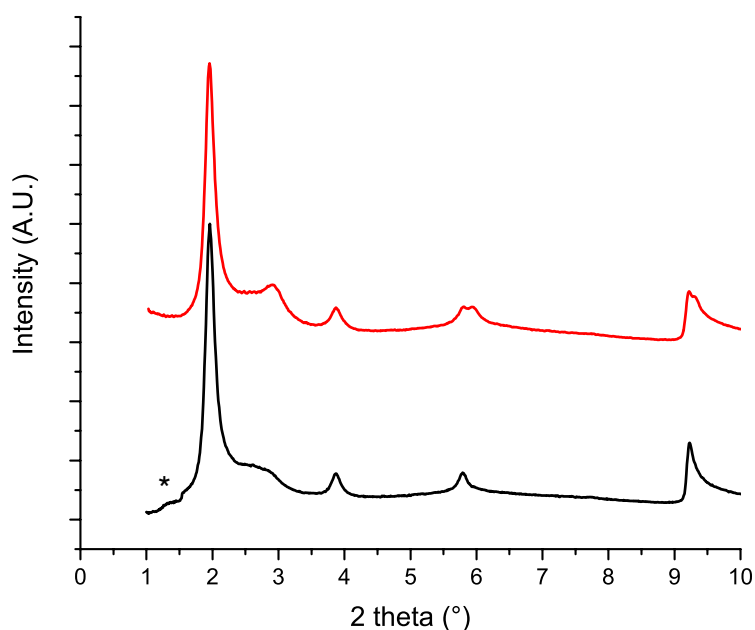


Figure 12 : Diffractograms of $\text{Co}_2(\text{OH})_{3.2}(\text{OAc})_{0.8}$ measured multiple times, black first then red (star represents the anomaly due to the use of a different blade size in the data collection)

This section has shown that the PDFs extracted from all the compounds are essentially similar to each other, the signature of the organic part being too small to be clearly identified. Nonetheless, it has been noted that the XRD patterns allowed us to get access to cell parameters. The following section will focus on the structure of the inorganic layers on selected compounds.

5. Structural Model Determination

In the case of the cobalt hydroxide based hybrid compounds studied in this chapter, we chose to focus on three specific compounds (Table 1). These three compounds are chosen because they represent the starting compounds of the exchange reaction ($\text{Co}_2(\text{OH})_{3.2}(\text{OAc})_{0.8}$ (1)) and of the *in-situ* reaction (aminobenzoic acid intercalated cobalt(2)) to obtain a compound that reacted with hexanal(3). Apart from their significant chemical differences, they also represent the most different crystallinities obtained out of the entire series of hybrids measured. Since we have shown in the previous part that it is not possible to observe the organic moiety directly, the goal here is to be able to observe the difference in the local structure of the layers induced by the functionalization, while retaining an identical grafting function (carboxylate) and in the last case, even keeping the same molecule in place but modifying it *in-situ*.

Name of the compound	(1)	(2)	(3)
Molecule present in the interlamellar space			
Formula unit	$\text{Co}_2(\text{OH})_{3.2}(\text{OAc})_{0.8}$	$\text{Co}_2(\text{OH})_{3.35}(4\text{-NH}_2\text{-BzAc})_{0.65}$	$\text{Co}_2(\text{OH})_{3.53}(\text{BzAc-N=CH-C}_4\text{H}_9)_{0.47}$

Table 1 : Name and nomenclature of the three selected compounds.

The first experimental step was to define the PDF signature of the inorganic layers alone. Once the quality of the datasets is ascertained, a reverse Monte-Carlo method developed principally by McGreevy and Pusztai²⁷ must be applied *via* the PDFgui program. Indeed, this program can be used to calculate PDF of adjusted structures in order to fit experimental PDF data. This method uses random number sequences and a simulation box containing all the atoms allowed to move according to parameters depending on the user input. This method is not *ab initio* so having a relatively good idea of the initial structure is required.

The fitting procedure remains identical for all the compounds, we first adjust the interlayer distance of the starting model to match the observed interlamellar spacing of the hybrid compound, then we perform PDF fitting using several parameters ranging from scale factor, Q_{damp} (value of the damping of the FT oscillations), cell parameters, atomic positions and finally atomic anisotropy.

To that end three starting models have been chosen, a brucite $\text{Co}(\text{OH})_2$, an hydrozincite containing nitrate anions and finally a carbonate containing hydrozincite containing carbonate ions in order to reproduce the experimental PDF of $\text{Co}_2(\text{OH})_{3.2}(\text{OAc})_{0.8}(1)$.

5.1. Starting from a Purely Brucite Structure

The first starting model used is a brucite-type hydroxide $\text{Co}(\text{OH})_2$ similar to the one shown in the first chapter, containing layers made of edge-sharing cobalt octahedra. In order to be able to compare the structure of the inorganic layers of $\text{Co}(\text{OH})_2$, whose structure is given in the cif file number 1010267²⁸ with the one of the layers of $\text{Co}_2(\text{OH})_{3.2}(\text{OAc})_{0.8}$, we first needed to modify it artificially in order to have the same interlamellar spacing as $\text{Co}_2(\text{OH})_{3.2}(\text{OAc})_{0.8}$ (12.7 Å). This enables to avoid any additional peak in the 1-10 Å region due to interatomic distances of atoms coming from different sheets. The structural refinement of the modified (in the **c** direction) brucite model structure derived from $\text{Co}(\text{OH})_2$ in order to fit the experimental PDF of $\text{Co}_2(\text{OH})_{3.2}(\text{OAc})_{0.8}$ is given in figure 13. As it can be observed, the intense peak present at 2.74 Å in the model structure is not present at all in $\text{Co}_2(\text{OH})_{3.2}(\text{OAc})_{0.8}$. This peak corresponds to the O-O distance of a quasi-undistorted octahedral cobalt. The fact that this peak is not present in the experimental PDF of $\text{Co}_2(\text{OH})_{3.2}(\text{OAc})_{0.8}$ indicates that the octahedral cobalt environment is highly distorted. This distortion is also very visible with the narrow peaks at 3.80 Å (Co-O), 4.19 Å (O-Co-O) and 4.95 Å (Co-O), corresponding to a narrow distribution of distances which are clearly visible on the fitted structure and which are either completely absent or much broader in $\text{Co}_2(\text{OH})_{3.2}(\text{OAc})_{0.8}$ (figure 13). The 3.17 Å (Co-Co) and 2.09 Å (direct Co-O of the same octahedron) distances are, however, also observed in $\text{Co}_2(\text{OH})_{3.2}(\text{OAc})_{0.8}$.

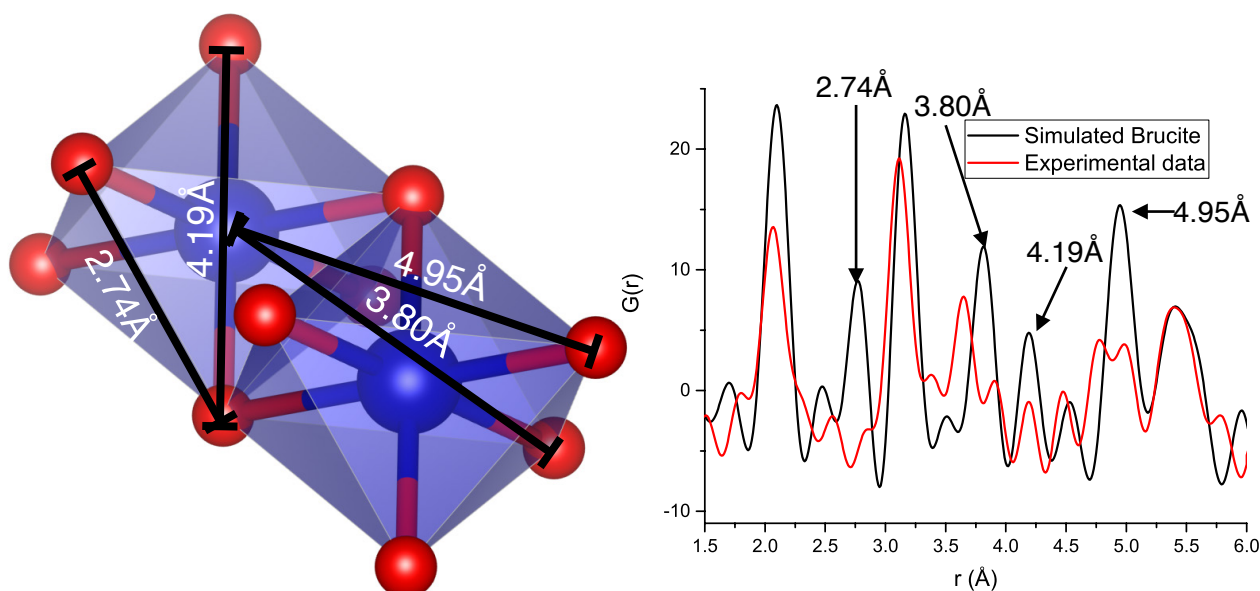


Figure 13 : (Left) Typical distances observed the brucite $\text{Co}(\text{OH})_2$ model (for clarity reasons, only 2 octahedra are shown) (Right) comparison of calculated PDF of the brucite layers and superposition with the experimental PDF of the cobalt-hydroxy-acetate.

5.2. Starting from a Nitrate Hydrozincite Structure

The second starting model we used is more elaborated, and definitely closer to the expected and generally admitted structure of $\text{Co}_2(\text{OH})_{3.2}(\text{OAc})_{0.8}$ the hydrozincite containing nitrate anions in the interlamellar spacing (without any grafting).²⁹

Using this nitrate hydrozincite model (after adjusting the interlamellar distance to the experimental one and, of course, replace Zn by Co) appears to be irrelevant because it leads to a distance between the two tetrahedral cobalt which are too close to be physically reasonable (2.56 Å). Indeed, this distance between the two tetrahedral cobalt means that they would be inside the octahedral vacancy.

5.3. Starting from a Carbonate Hydrozincite Structure

Finally, we used as a starting point for the fit of the experimental PDF the structure of carbonate-intercalated hydrozincite (figure 14), in which, contrarily to the previous case, the carbonate is coordinated to both tetrahedra and octahedral metal ions.³⁰

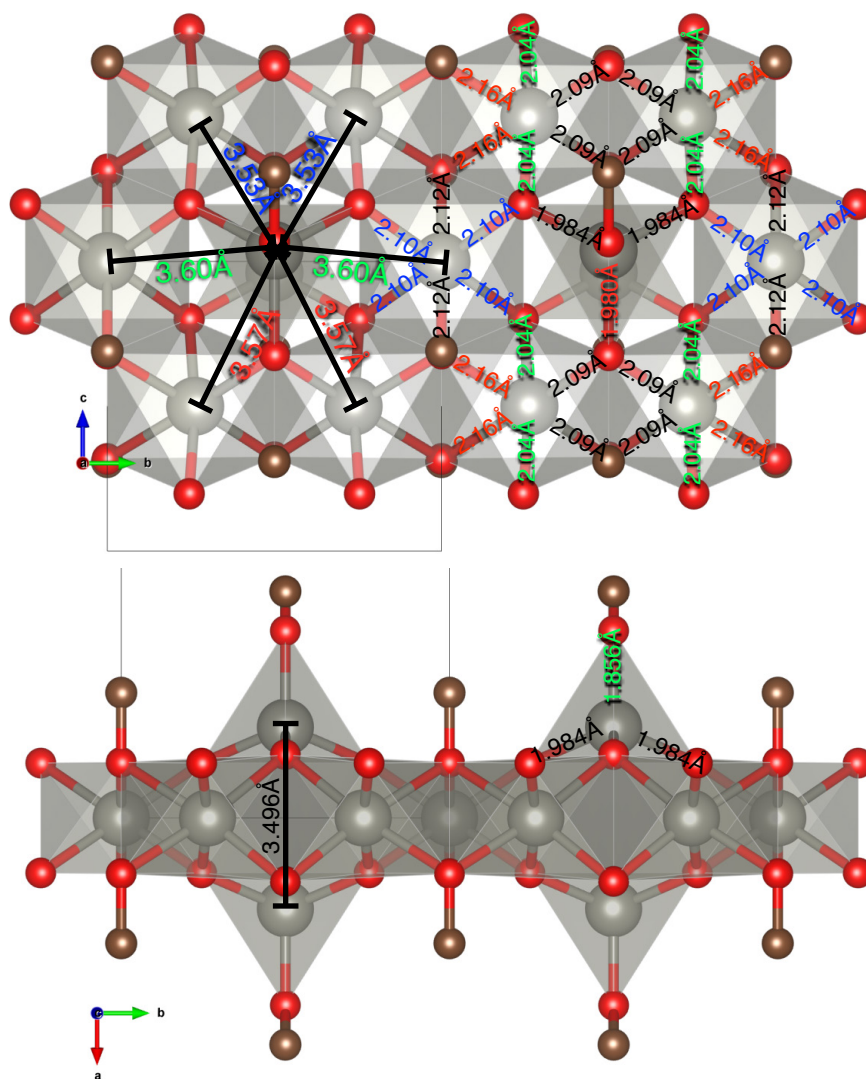


Figure 14 : Selection of distances in the hydrozincite-carbonate structure as reference (CIF n°9007481) (top) and view parallel to the inorganic layers which emphasizes on the lack of network distortion of the layers. For clarity reasons, only the carbon directly grafted to the layer via the oxygen is displayed.

The fitting shown on figure 15 leads to the structure presented figure 16. We achieved a good agreement with the experimental PDF as well as a more reasonable distance of 2.93 Å between the two tetrahedral cobalt compared to the short 2.56 Å distance found using the previous starting model.

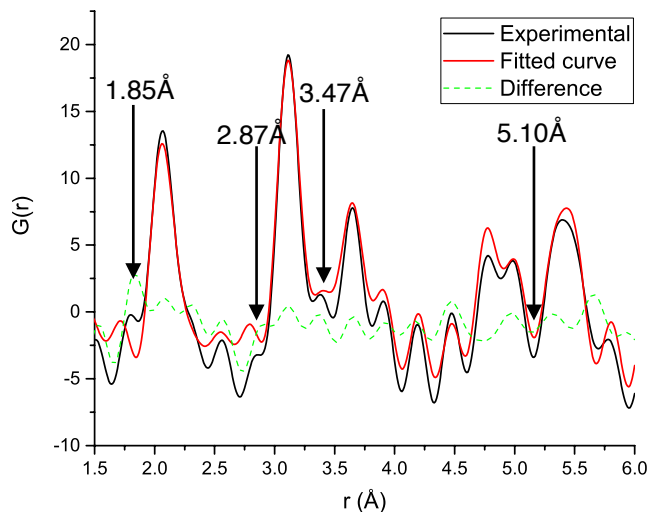


Figure 15 : Experimental and fitted PDF using the hydrozincite carbonate as starting model for the sheet structure.

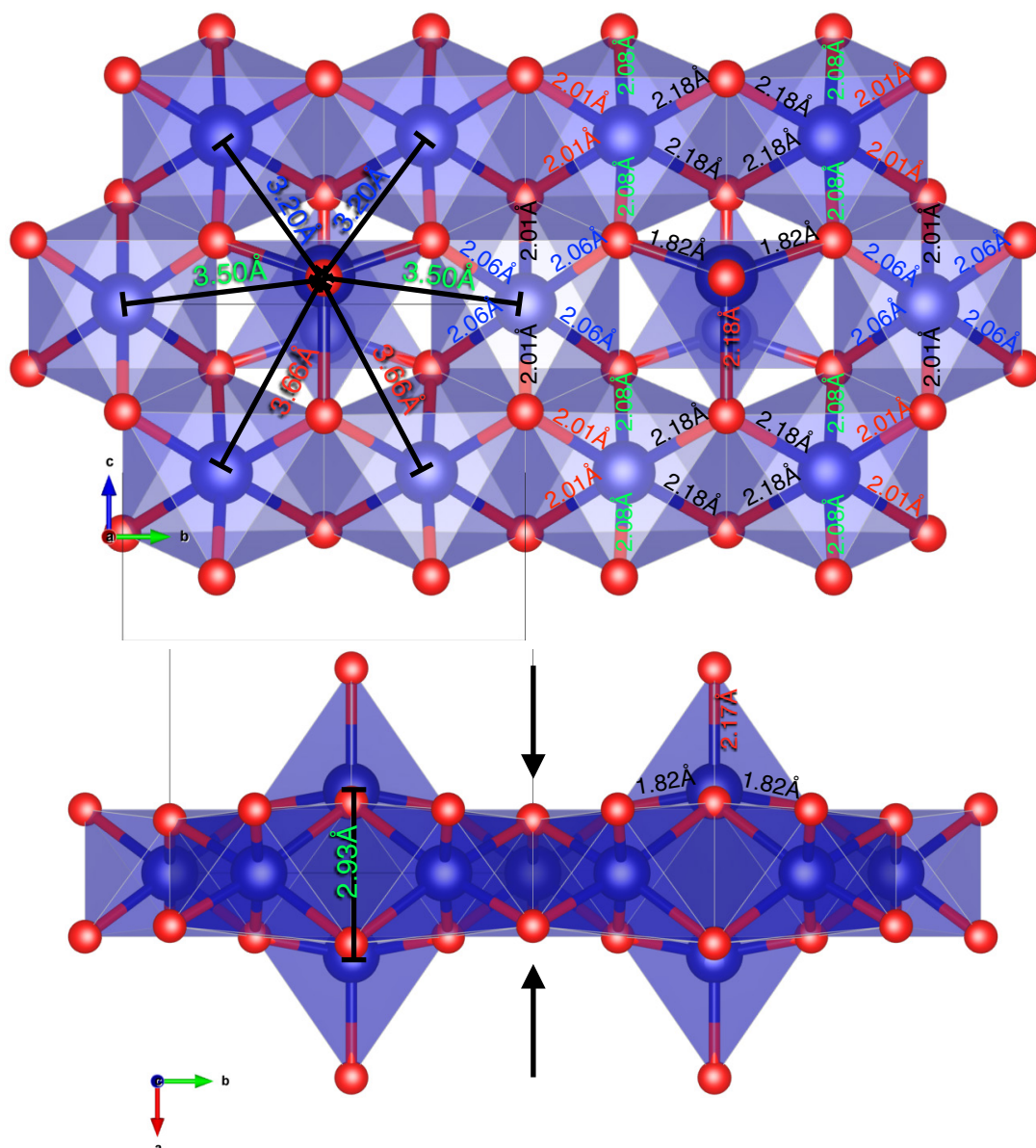


Figure 16 : Distances obtained via PDF fitting from the hydrozincite carbonate structure (top) and emphasis on the strong distortion of the whole network. (bottom)

As seen in figure 16 above, they are two specific types of octahedra, the first one bridges four tetrahedral cobalt along the three octahedra axes (« cis-octahedron ») and the second one is connecting four tetrahedral cobalt only along two axes (« trans-octahedron »). The tetrahedron itself is also distorted with two pairs of Co-O distances, the metallic centre is almost coplanar with the upper oxygen layer of the octahedral sheet. This allows us to monitor the interesting distances that might change on the compounds after reaction, these distances are pointed in figure 16, showing the obtained fitting made from 1.5 to 6 Å corresponding to the structure described above. Most of them cannot be observed on the PDF above, but appear in compounds once the functionalization has occurred. They are related to the even stronger octahedron distortion as well as the tetrahedra modification.

Once this first fit gave satisfying results shown in figure 16, we then proceeded to the same exact procedure with the compounds after reaction with the *p*-amino-benzoic acid, the starting compound of our *in-situ* reaction.

6. Results of PDF Fits on the Selected Compounds and Comparison with the Literature.

To interpret the slight differences observed in the PDFs at short distances, we focus here on the comprehensive analysis of the PDF of the three samples described above. The goal being to be able to observe the difference in the local structure of the layers with the difference of functionalization, while retaining an identical grafting function (carboxylate).

The fitting procedure remains identical for all the compounds, we first adjust the interlayer distance of the hydrozincite model to match the observed interlamellar spacing of the hybrid compound, then we perform PDF fitting using several parameters ranging from scale factor, lower and higher boundaries to analyse, Q_{damp} (value of the damping of the FT oscillations), cell parameters, atomic positions and finally atomic anisotropy.

6.1. Naming Nomenclature and Results of the Fitting Procedure.

For the sake of simplicity, figure 17 below indicates the positions of the different cobalt sites as well as the naming nomenclature of the oxygen that are discussed thereafter.

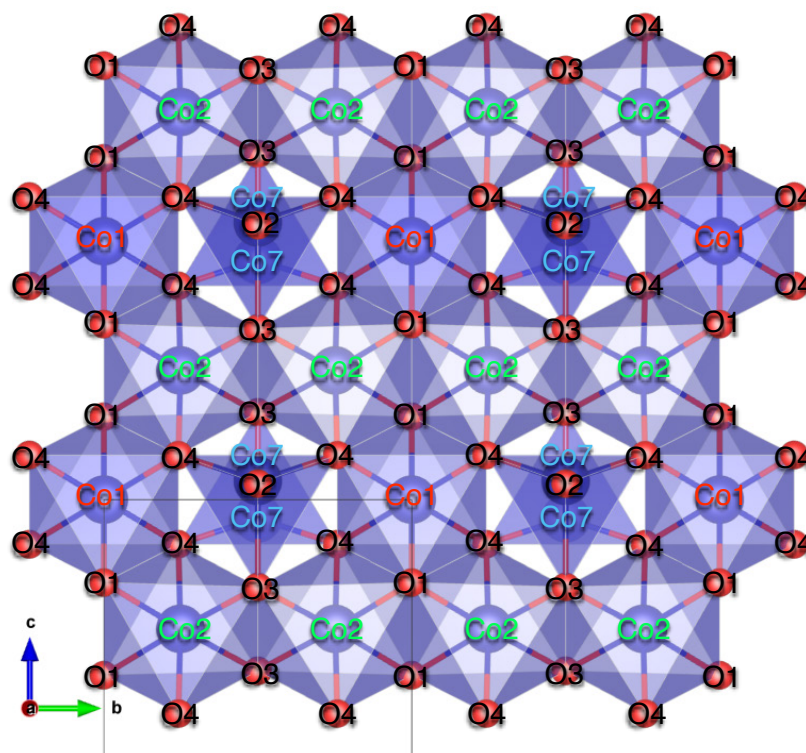


Figure 17 : Equivalent sites due to symmetry and naming nomenclature used in the tables below.

The two following tables show the complete results of this fitting procedure on the three compounds.

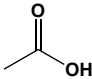
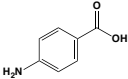
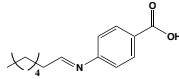
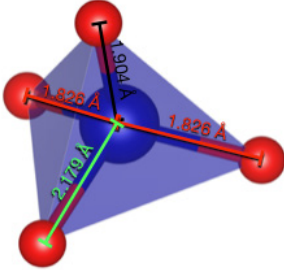
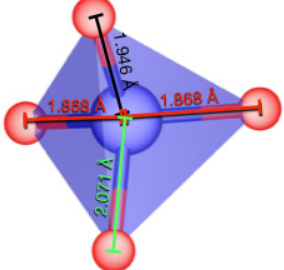
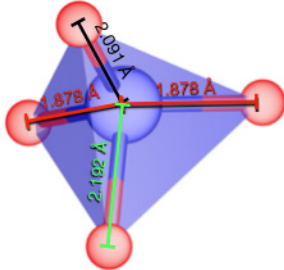
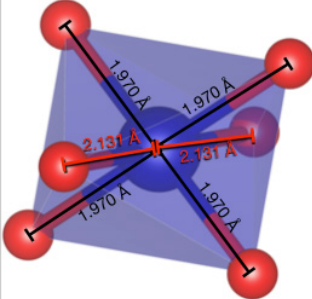
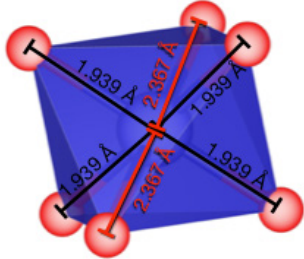
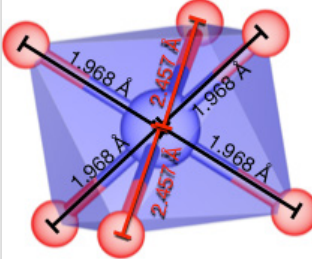
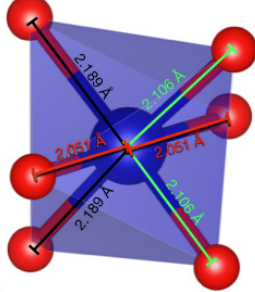
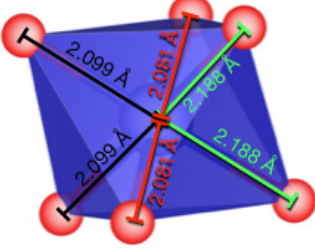
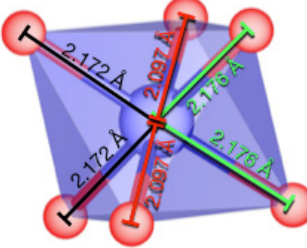
Molecule present in the interlamellar space			
Space group and cell parameters obtained	Monoclinic C2/m a = 24.278 Å b = 6.3245(7) Å c = 5.34(1) Å β = 95.41° Rw: 0.19	Monoclinic C2/m a = 28.685 Å b = 6.3207(2) Å c = 5.3308(3) Å β = 95.83° Rw: 0.28	Monoclinic C2/m a = 38.087 Å b = 6.1967(8) Å c = 5.4208(2) Å β = 96.00° Rw: 0.31
Tetraedral cobalt « Co7 »			
	Valence : 2.18 Average Co-O : 1.934 Å	Valence : 2.10 Average Co-O : 1.927 Å	Valence : 1.80 Average Co-O : 2.010 Å
Octahedral cobalt 1 « Co1 »			
	Valence : 2.49 Average Co-O : 2.024 Å	Valence : 2.37 Average Co-O : 2.102 Å	Valence : 2.15 Average Co-O : 2.126 Å
Octahedral cobalt 2 « Co2 »			
	Valence : 1.93 Average Co-O : 2.115 Å	Valence 1.89 Average Co-O : 2.124 Å	Valence 1.78 Average Co-O : 2.148 Å
Calculated average valence on the structure	2.14	2.07	1.86
Calculated layer thickness	6.71 Å	6.85 Å	7.55 Å

Table 2 : Results of PDF fitting on the selected compounds (valence calculated from Brese and O'Keeffe work).³¹

It must be noted that due to the fact that as the hydrozincite model we used crystallizes in the monoclinic C2/m space group we used the same space group to fit our structure.

The table above gives several informations, the first information is that the relatively high deformation noticed in the compound (1) is maintained in compounds (2) and (3). The *in-situ* functionalization seems to have amplified this deformation even further. This point is of particular interest because in the case of the reaction of (2) with hexanal to give (3) the grafted molecule is even not exchanged.

A hypothesis for this deformation and especially the one observed between (2) and (3) is that intermolecular interactions in the interlayer space are more important in the case of (3) with alkyl-alkyl interactions for example. These interactions thus may have a structural consequence on the inorganic layer. They may also explain the increase of the layer thickness from 6.85 Å to 7.55 Å.

The calculated bond-valence parameters using Brese and O’Keeffe work³¹ show relatively large variations of valence even if the average valence calculated for all the structure is still comparable with values of similar systems found in the literature (see section 6.2 of this chapter). The average length of the Co-O bond appears to also be generally lengthened with the replacement of the acetate molecule with bulkier ones.

Table 3 below shows a different aspect of these deformations *i.e.* the variations of the atomic displacement parameters (adp). Indeed, it is worth noting that the refinement of the atomic displacement parameters was essential to reach a good fit for the three phases. The adp parameters were refined isotropically for the oxygen atoms and anisotropically for the cobalt atoms. (except Co7 for (3) due to very high disorder)

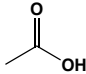
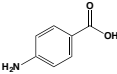
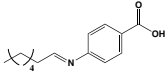
																	
Rw - value : 0.19 Lin. corr. factor : 1.97 (5) Low r sigma ratio : 0.008 (4) R cutoff: 4 Å						Rw - value : 0.28 Lin. corr. factor : 2 (1) Low r sigma ratio : 0.3 (1) R cutoff: 4 Å						Rw - value : 0.31 Lin. corr. factor : 1.87 (3) Low r sigma ratio : 0.19 (6) R cutoff: 4 Å					
Cell parameters a=24.278 Å b=6.3245(7) Å c=5.34(1) Å β=95.41°						Cell parameters a= 28.685 Å b=6.3207(2) Å c= 5.3308 (3) Å β=95.41°						Cell parameters a=38.087 Å b=6.1965(8) Å c=5.4208(2) Å β=96.00°					
Atomic parameters						Atomic parameters						Atomic parameters					
Atom	Wyck. (sym)	x	y	z	U _{iso} (Å ²)	x	y	z	U _{iso} (Å ²)	x	y	z	U _{iso} (Å ²)				
Co1	2a (2/m)	0	0	0		0	0	0		0	0	0					
Co2	4h (2)	0	0.2486(1)	0.5		0	0.2494(1)	0.5		0	0.2541(1)	0.5					
Co7	4i (m)	0.0614(1)	0.5	0.0723(6)		0.053(1)	0.5	0.068(3)		0.0457(1)	0.5	0.0639(2)	0.0431				
O1	4i (m)	0.454(2)	0.5	0.320(7)	0.0111	0.453(3)	0.5	0.336(9)	0.0059	0.464(2)	0.5	0.350(6)	0.0000				
O2	4i (m)	0.139(2)	0.5	0.062(7)	0.0062	0.121(3)	0.5	0.12(1)	0.0057	0.0993(1)	0.5	0.0088(6)	0.0001				
O3	4i (m)	0.4458(1)	0.5	0.3375(1)	0.0002	0.4618(1)	0.5	0.3202(4)	0.0000	0.4637(1)	0.5	0.3419(3)	0.0005				
O4	8j (1)	0.0379(2)	0.2420(2)	0.1728(3)	0.0072	0.0327(4)	0.239(1)	0.168(1)	0.0004	0.0239(1)	0.2489(3)	0.1688(1)	0.0005				
Anisotropic displacement parameters (Å ²)						Anisotropic displacement parameters (Å ²)						Anisotropic displacement parameters (Å ²)					
Atom	U ₁₁	U ₂₂	U ₃₃		U ₁₁	U ₂₂	U ₃₃		U ₁₁	U ₂₂	U ₃₃						
Co1	0.0467	0.0025	0.0025		0.0000	0.0002	0.0002		0.0005	0.0000	0.0000						
Co2	0.0467	0.0036	0.0036		0.0000	0.0000	0.0000		0.0000	0.0000	0.0000						
Co7	0.0220	0.0255	0.0255		0.0042	0.0046	0.0046		0.0000	0.0000	0.0000						

Table 3 : Structure parameters obtained from the real-space refinements in a monoclinic P2/m cell of the pair distribution functions.

Before going into details about the different adp for each atom, it is important to underline that these parameters have a very strong influence on the simulated PDF as illustrated in the figure below for the calculated PDF from the structure of Co₅(OH)₈(chdc)•4(H₂O).

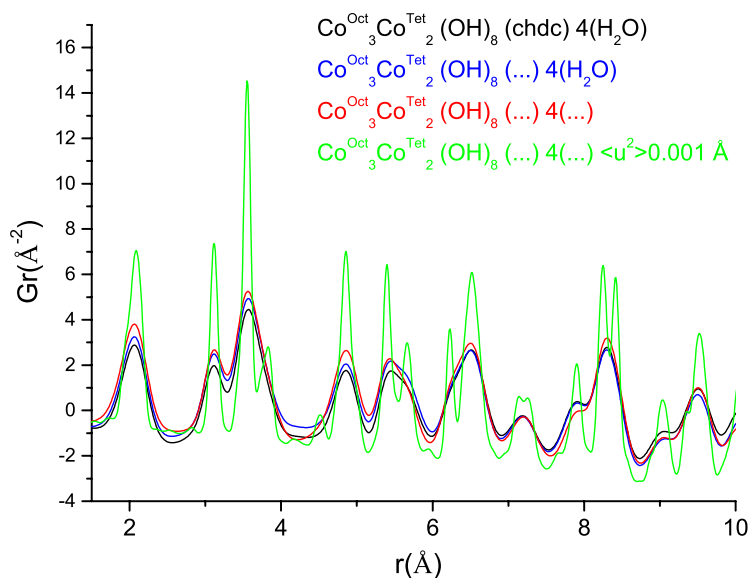


Figure 18 : Effect of the atomic displacement parameter on the calculated PDF from Kepert structure.²⁶

PDF peak width is influenced by correlated motions δ and atomic displacement parameters $\langle u^2 \rangle$. The presence of static disorder leads to large anisotropic parameters in Rietveld refinement which are not required in the PDF analysis of short range atomic correlations. The PDF profile calculated with large anisotropic parameters inevitably display broad peaks. To avoid a misinterpretation of the simulated PDF in the short range, the atomic displacement parameters were set to a value of 0.001 \AA^2 and the corresponding simulated PDF are displayed in Figure 18. The other simulations have been made with the much higher adp published in Kepert *et al.* work⁶ that are ranging from 0.006 to 0.0135 \AA^2 depending on the considered atom. The PDF profiles thus obtained are better resolved allowing us to see more easily the individual correlations. For instance, the PDF peak observed at $1,7 \text{ \AA}$ in the case of Morse *et al.*⁷ results from $\text{Co}_{\text{oct}}\text{-Co}_{\text{tet}}$ correlation is due to the statistical occupancy of the vacancy. This feature was actually not observed in the experimental PDF and is conclusive with the impossibility of an octahedral cobalt to be present between two tetrahedral cobalt. This feature could have been hidden by too large atomic displacement parameters.

As for the values obtained in compound (1), they indicate a positional disorder both for cobalt atoms and bridging oxygen atoms. For Co1 and Co2 atoms U_{11} values are larger than U_{22} and U_{33} values indicating more important out-of-plane displacements for these two sites. This is consistent with the fact that the layers are topologically more constrained in the b, c plane.

The adp values obtained for O1, O2 and O4 oxygen atoms are also indicative of positional disorder for these atoms. Co1 atoms surrounded by two O1 and four O4 oxygen atoms are the most affected, Co7 tetrahedral sites also but to a lesser extent. This positional disorder may partly explain the difference observed for Co1 between the sum of the valence of individual bonds (table 2) and the formal valence *i.e.* +2.

It is worth noting that in the hydrozincite structure, the carbonate groups bind the layers by sharing the corner of Zn7 tetrahedra pointing away from the layer occupied by O2 and the corner of Zn1 octahedra occupied by O1. As a consequence of the grafting process, in the cobalt compounds studied here, the positional disorder observed on O2 and O1 sites could be due to the presence of a second grafting site on O1. There is, however, no direct proof for this observation. This positional disorder could be due to strong water interactions between the free oxygen of the acetate and the hydroxyl group in O1 in a similar fashion to what has been observed with copper-hydroxy-acetate.³²

This positional disorder is also observed for the two other compounds but is less important. This seems to be consistent with their better crystallinity according to the XRD patterns. In the compound (2), adp values indicate a positional/occupational disorder for Co7 tetrahedral site only, and for O1/O2 oxygen atoms. Meanwhile in the compound (3), only the Co1 octahedral site is affected as well as O1 oxygen atoms.

This structural accommodation is also visible on the variation of the cell parameters. Of course, **a** increases with the size of the intercalated guest but changes are also observed on **b** and **c** revealing a structural accommodation also in the y-z plane.

The variation of **b** and **c** cell parameters is quite significant in the case of (3) with $\Delta b/b = -0.020$ and $\Delta c/c = +0.015$. The expansion along the **c** direction is related to the increase of Co1-O1 bond length resulting in distorted Co1 octahedra strongly elongated in the **a** axial direction. The contraction in the **b** direction is more related to a combination of Co2 octahedra rotation *via* the movement of O4 along **a** and a shortening of the tetrahedral edge O4-O4 in **b** direction. The relative position of the Co7 tetrahedra is also altered as it moves both along **c** and closer to the horizontal plane formed by Co1 and Co2 octahedra.

The figures below emphasizes the important positional changes observed between the different compounds

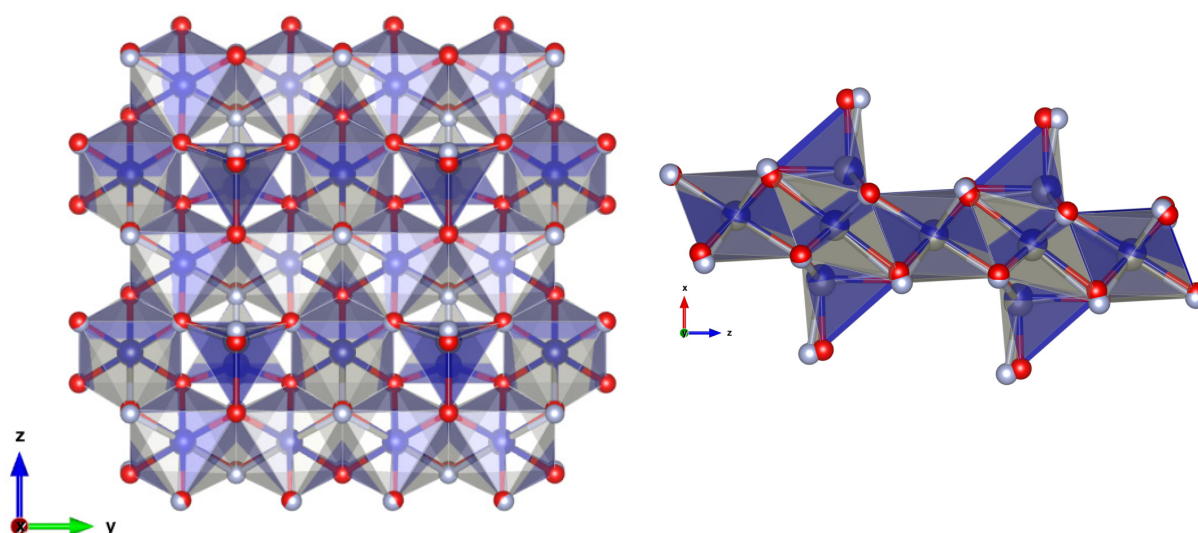


Figure 19 : Structural comparison between (1) (in blue/red) and (2) (in grey/silver) obtained via PDF refinement.

It can be observed in the figure above that apart from the rather strong deformation of the tetrahedral sites, the O1 position is also moving further away from the layers. This could be due to side effect of the force exerted on the tetrahedra by the grafting/intermolecular interactions within the interlamellar space. Another hypothesis would be specific interactions *via* a carboxylate-water-hydroxide bridge due to a different geometry of the amino-benzoic acid within the layers.

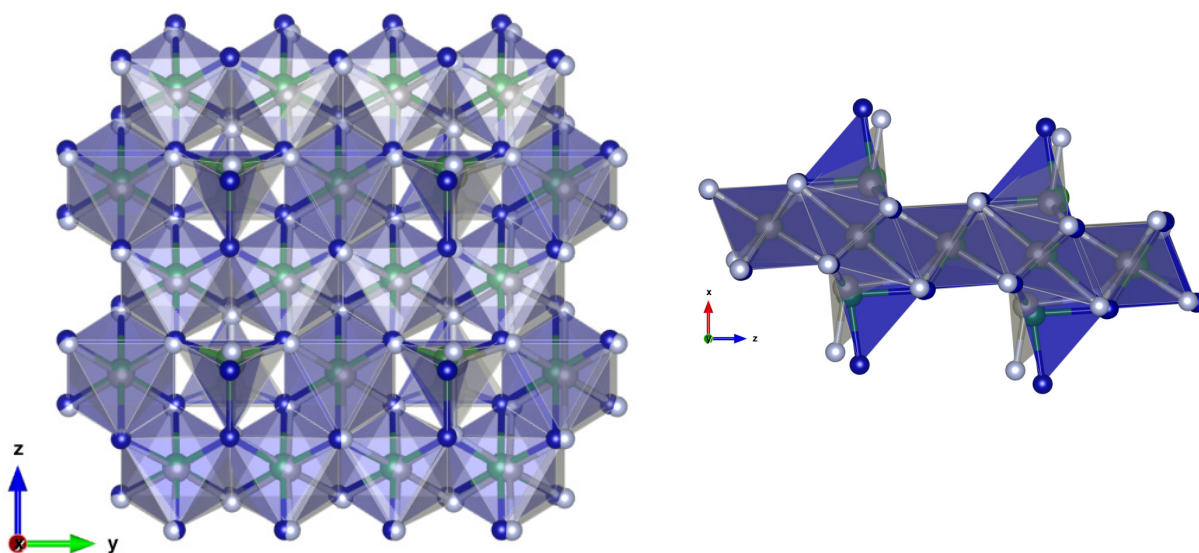


Figure 20 : Structural comparison between (2)(in grey/silver) and (3) (in green/blue).

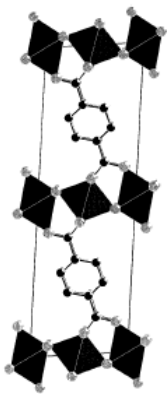
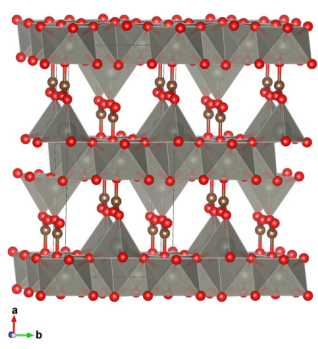
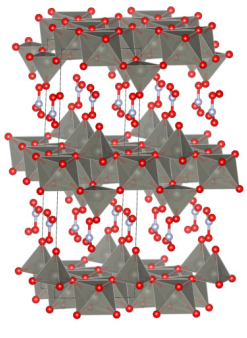
These figures must, however, be taken with the caveat that this superposition not strictly representative of the structure of the compounds, the cell parameters having slightly changed, some displacements on the outer part of the sketch are induced by this cell change. Nonetheless, it is possible to see in figure 20 that the deformation of the tetrahedra in (3) is even more pronounced than for (2) but the direction is opposed to the one previously observed. The position of the tetrahedral cobalt is also strongly affected as it becomes in (3) closer to its position in (1). The distortion previously observed with O1 (in (2)) seems to be less important as well.

These results must now be compared with what has been previously described in the literature. This comparison with several systems already mentioned previously as well as other systems is presented in the following section.

6.2. Confrontation of the Model with the Literature.

Once our model was obtained it seemed important to compare it with the other models present in the literature. To that end, the table below collects different related systems reported in the literature.

Reference	Structural parameters	Main distances in the polyhedra	Structural representation
COD number 1010267 Co(OH) ₂ P-3m a = 3,173(2) Å c = 4,640(5) = d	Co ^{Oct} (OH) ₂	Co ^{Oct} - OH 2 x 2,0970 Å 4 x 2,0972 Å BV sum = 2.00 v.u.	

Reference	Structural parameters	Main distances in the polyhedra	Structural representation
<p>Huang <i>et al.</i> Chem. Mater. 2000, 12, 2805-2812</p> <p>C2/m a = 19,943(1) Å ~ 2d b = 3,2895(1) Å c = 6,2896(3) Å β = 95,746(3)°</p>	<p>Co₂(OH)₂(C₈H₄O₄)</p> <p>C₈H₄O₄ : trans-1,4- clohexanedicarboxylate</p> <p>terephthalate pillars bridging COO- groups</p> <p>Co^{Oct} (OH)₂</p>	<p>Co₁^{Oct} - OH 4 x Co-OH : 2,1821 Å <u>2 x Co-O₂ (O-C...) : 2,1060 Å</u> BV sum = 1.71 v.u.</p> <p>Co₂^{Oct} - OH 4 x Co-OH : 2,2046 Å <u>2 x Co-O₂ (O-C...) : 1,9985 Å</u> BV sum = 1.87 v.u.</p> <p>Average : 1.79 v.u.</p> <p>O₁-C-O₂</p>	
<p>Ghose Acta Cryst. (1964). 17, 1051</p> <p>Hydrozincite</p> <p>C2/m a=13.6200 Å = 2d b=6.3000 Å c=5.4200 Å β=95.8330°</p>	<p>Zn^{Oct}₃Zn^{Tet}₂(OH)₆(CO₃)₂</p> <p>2 oxygen atoms of CO₃ are bonded to 1 Zn^{Oct} and 1 Zn^{Tet}</p> <p>% Tet =40</p>	<p>Zn₁^{Oct} 4 x Zn-OH : 2.1050 Å <u>2 x Zn-O(CO3) : 2.1226 Å</u> BV sum = 2.00 v.u.</p> <p>Zn₂^{Oct} 2 x Zn-OH : 2.0431 Å 2 x Zn-OH : 2.0986 Å <u>2 x Zn-O(CO3) : 2.1588 Å</u> BV sum = 2.07 v.u.</p> <p>Zn₃^{Tet} Zn-OH : 1.9799 Å 2 x Zn-OH : 1.9844 Å <u>Zn-O(CO3) : 1.8564 Å</u> BV sum = 2.07 v.u.</p> <p>Average : 2.05 v.u.</p>	
<p>zinc hydroxide nitrate ICSD number : 16023</p> <p>C2/m a=25.4000 Å = 2d b=6.238(1) Å c=5.517(1) Å β=93.2800°</p>	<p>Zn^{Oct}₃Zn^{Tet}₂ (OH)₈(NO₃)₂(H₂O)₂</p> <p>Unbounded NO₃ anion Coordinated water molecules</p>	<p>Zn₁^{Oct} 2 x Zn-OH : 2.0206 Å 4 x Zn-OH : 2.1934 Å BV sum =1.91 v.u.</p> <p>Zn₂^{Oct} 2 x Zn-OH : 2.0900 Å 2 x Zn-OH : 2.1178 Å 2 x Zn-OH : 2.1600 Å BV sum = 1.94 v.u.</p> <p>Zn₃^{Tet} 2 x Zn-OH : 1.9371 Å Zn-OH : 1.9642 Å <u>Zn-OH : 1.9553 Å (free apex)</u></p> <p>BV sum = 2.07 v.u.</p> <p>Average : 1.95 v.u.</p>	

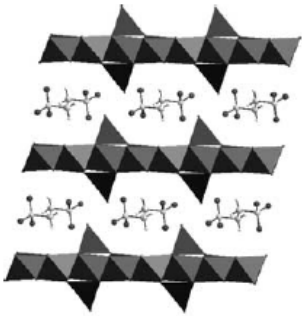
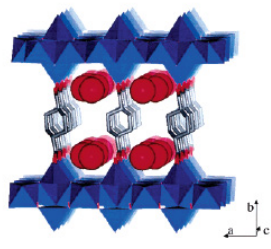
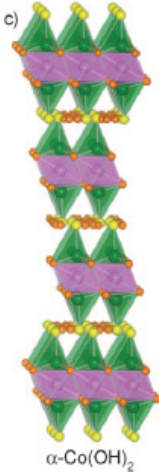
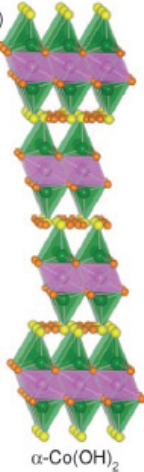
Reference	Structural parameters	Main distances in the polyhedra	Structural representation
<p>Anthony K. Cheetham <i>et al.</i> Journal of Physics and Chemistry of Solids 65 (2004) 11-16</p> <p>$\text{Co}_7(\text{OH})_{12}(\text{C}_2\text{H}_4\text{S}_2\text{O}_6)(\text{H}_2\text{O})_2$</p> <p>P-1 $a = 6,2752(19) \text{ \AA}$ $b = 8,361(3) \text{ \AA}$ $c = 9,642(3) \text{ \AA} \sim d$ $\alpha = 96,613(5)^\circ$ $\beta = 98,230(5)$ $\gamma = 100,673(5)$</p>	<p>Unbounded ethanedisulfonate anion Coordinated water molecules</p> <p>$\text{Co}_5^{\text{Oct}}\text{Co}_2^{\text{Tet}}(\text{OH})_{12}$ % Tet ~28,6</p>	<p>Co^{Oct} - OH Co1 : 2,0576-2,1495 Å Co2 : 2,058-2,1554 Å Co3 : 2,0784 - 2,1548 Å BV sum = 1.92-1.99 v.u.</p> <p>Co^{Tet}-OH Co4 - O1 : 1,9504 Å O2 : 1,9477 Å O6:1,9421 Å O7 (H₂O): 2,0920 Å free <u>apex</u> BV sum = 1.91 v.u.</p>	
<p>Cameron J. Kepert Inorg. Chem. 2003, 42, 6709-6722</p> <p>Imma $a = 12,456(3) \text{ \AA}$ $b = 29,027(7) \text{ \AA} = 2d$ $c = 5,3996(13) \text{ \AA}$</p>	<p>$\text{Co}_5(\text{OH})_8(\text{chdc}) \cdot 4(\text{H}_2\text{O})$</p> <p>chdc : $\text{C}_8\text{H}_{10}\text{O}_4$: trans-1,4-clohexanedicarboxylate</p> <p>chdc pillars Non coordinated water molecules</p> <p>$\text{Co}_3^{\text{Oct}}\text{Co}_2^{\text{Tet}}(\text{OH})_8$ % Tet =40</p>	<p>Co^{Oct} - OH Co1 : 2,0560-2,1791 Å Co2 : 2,0631-2,1610 Å BV sum = 1.85-2.20 v.u.</p> <p>Co^{Tet} - OH Co3 : 1,9298-2,0075 Å O11 (O-C.): 2,0176 Å BV sum = 1.98-2.10 v.u. Average : 2.01 v.u.</p>	
<p>Daniel E. Morse <i>et al.</i> Chem. Eur. J. 2010, 16, 9998-10006</p> <p>Structure 1 (PDF refinement) $R3 m$ $a = 3,14155(6) \text{ \AA}$ $c = 24,165(5) \text{ \AA} = 3d$</p> <p>Structure 2 (Rietveld refinement) $R3 m$ $a = 3,1466(23) \text{ \AA}$ $c = 24,0731(24) \text{ \AA} = 3d$</p>	<p>Free water molecules Cl anion coordinated to Co^{Tet}</p> <p>Statistical occupation</p> <p>$\text{Co}_{2,39}^{\text{Oct}}\text{Co}_{1,22}^{\text{Tet}}(\text{OH})_6\text{Cl}_1$.22. 1,51 H₂O % Tet ~33,8</p> <p>$\text{Co}_{2,58}^{\text{Oct}}\text{Co}_{0,87}^{\text{Tet}}(\text{OH})_6\text{Cl}_0$.87. 1,78 H₂O</p> <p>$\text{Co}_{2,48}^{\text{Oct}}\text{Co}_{1,04}^{\text{Tet}}(\text{OH})_6\text{Cl}_{1,04}$.1,36H₂O. % Tet ~25,2</p>	<p>Structure 1 :</p> <p>Co^{Oct} - OH Co-O : 2.136 Å BV sum = 1.81 v.u.</p> <p>Co^{Tet} - OH Co-O : 1.980 Å Co-Cl :2.351 Å BV sum = 2.15 v.u. Average : 1.86 v.u.</p> <p>Structure 2 :</p> <p>Co^{Oct} - OH Co-O : 2.093 Å BV sum = 2.03 v.u.</p> <p>Co^{Tet} - OH Co-O : 1.918 Å Co-Cl :2.397 Å BV sum = 2.11 v.u. Average : 2.04 v.u.</p>	
<p>Takayoshi Sasaki <i>et al.</i> Inorg. Chem. 2006, 45, 3964-3969</p> <p>(Rietveld refinement) $R3 m$ $a = 3,1439(5) \text{ \AA}$ $c = 24,058(6) \text{ \AA} = 3d$</p>	<p>Cl anion /H₂O coordinated to Co^{Tet}</p> <p>$\text{Co}_{2,48}^{\text{Oct}}\text{Co}_{1,04}^{\text{Tet}}(\text{OH})_6\text{Cl}_{1,04}$.1,36H₂O. % Tet ~29,5</p>	<p>Co^{Oct} - OH : Co-O : 2,124 Å BV sum = 1.87 v.u.</p> <p>Co^{Tet} - OH Co-O : 1,898 Å Co-Cl : 2,32 BV sum = 2.08 v.u. Average : 1.93 v.u.</p>	

Table 4 : Comparison with other structures found in the literature.

The hydroxide layers in β -Co(OH)₂ are brucite type built up from edge sharing cobalt hydroxyl octahedra. In the other materials, cobalt ions present on both octahedral and tetrahedral coordination geometries in different ratios. In Kepert *et al.*²⁶ one in four of the Co octahedral sites are removed and a pair of Co tetrahedral sites is generated above and below each octahedral vacancy, sharing three hydroxyl ions neighbouring octahedral. The tetrahedral fourth apex pointing into the interlayer space is completed by the unidentate carboxylate groups of the 1,4-cyclohexanedicarboxylate pillars. The resulting tetrahedral-octahedral layer structure is similar to hydroxy nitrate Zn₅(OH)₈(H₂O)₂(NO₃)₂ or hydroxyl carbonate Zn₅(OH)₆(CO₃). In Zn₅(OH)₈(H₂O)₂(NO₃)₂, a water molecule completes the tetrahedral zinc coordination sphere and unbound nitrate anions are located between the layers. On the other hand, in Zn₅(OH)₆(CO₃), one oxygen atom of the CO₃ group is bonded to a tetrahedral zinc while another oxygen atom is coordinated to an octahedral zinc ion. In Morse *et al.*³³ the authors considered disordered structures with all Co_{oct} sites sandwiched by two Co_{tet} sites and a statistic occupation of both sites. This being the result of an « intimate mix » of three phases with different occupations for the tetrahedral sites. In Sasaki *et al.*⁸ the tetrahedral fourth apex is occupied by the chloride anion and the authors consider a statistical distribution of the tetrahedral site and an inversely proportional octahedral site occupation.

The table above shows that the results obtained in this chapter are compatible with previous findings on analogous systems. It is also observed that the relative variations of the bond valence³¹ calculated for all the compounds is in line with the bond valence obtained from the literature. Indeed, even for structures obtained *via* mono-crystal diffraction such as the one described in Kepert paper²⁶ a relatively important variation of the bond valence parameters can be seen with values ranging from 1.85 to 2.20 valence units. It can also be observed that in most cases of unbound layers, such as the chloride or ethanedisulfonate-intercalated cobalt hydroxide, the tetrahedron is likely to be only marginally distorted with a bond length variation of less than 0.01 Å for the three oxygen shared with neighbouring octahedra. Meanwhile, for bound tetrahedra, the bond length variation is greater than 0.07 Å, similar to what has been observed in our compounds.

A direct comparison with the closest system available is of course greatly desirable. To that end, in Figure 21, we compare the PDF of Co₂(OH)_{3.2}(OAc)_{0.8} we obtained with the PDF simulated from the structure of cobalt hydroxyl chlorides with different ratios between tetrahedral sites and octahedral sites proposed by Morse *et al.* which represent the most in-depth analysis of a α -type cobalt hydroxide so far.⁷ The PDF profiles were calculated from the structural parameters obtained either by Rietveld refinement (average structure) or refinement of the PDF (local structure).

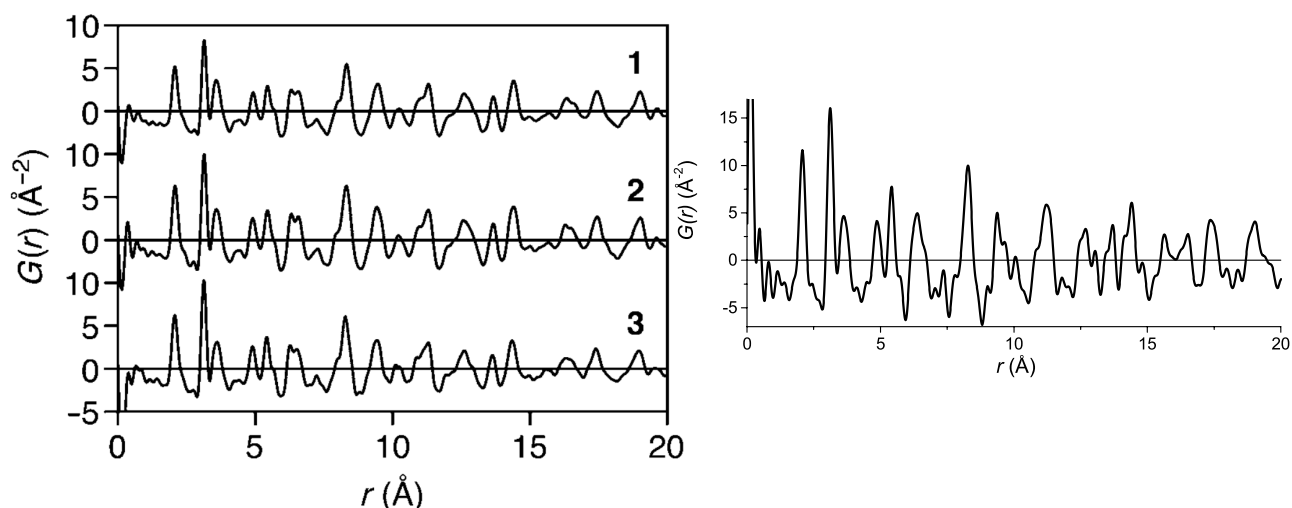


Figure 21 : Comparison between PDFs extracted for Morse *et al.*⁷ for three of their syntheses containing 40% (1) 33% (2) and 23% (3) of Co_{tet} ($Q_{max} = 25 \text{ \AA}^{-1}$) (left) and the extracted PDF for $Co_2(OH)_{3.2}(OAc)_{0.8}$ (40% Co_{tet}) collected at $Q_{max} = 20 \text{ \AA}^{-1}$ (right).

This comparison allows us to see that the PDFs we obtained are logically similar but qualitatively better, indeed the high atomic displacement parameters and the intrication of three phases with different tetrahedra/octahedra ratios used by Morse *et al.*⁷ tend to reduce the overall quality of the fitting procedure, even with data collected at higher Q_{max} (25 \AA^{-1}) than ours (20 \AA^{-1}), the better statistics can also be the source for this better structural resolution.

7. Conclusion

In this chapter we have first demonstrated the efficiency of the hybrid X-Pad detector over the previously used multi-analyser, which allows better statistics while reducing the collection time by more than eight times. Ideal experimental conditions for X-ray total scattering experiments have been found and output signal treatment has been optimized.

The X-ray total scattering analysis *via* the pair distribution function showed that the contrast between the high-Z (cobalt) and low-Z (carbon/nitrogen) was too great to be able to have an accurate position of the organic molecules. But it has helped us to get a rather unusual insight about the local structure of a series of cobalt layered hydroxides as well as a few advances in the understanding of the layered cobalt hydroxide itself.

From this analysis we made several observations, the first being the measurement of rather strong deformations of the layers upon functionalization. It has also been noted that these deformations are not related to the chemical nature of the grafting moiety, all the organic molecules present on the hybrids having a carboxylate. These deformations are also anisotropic, most of these being perpendicular to the layers for the octahedra and along the **c** axis for the tetrahedra.

All these local deformations lead to a total layer thickness that varies from 6.7 \AA up to 7.5 \AA depending on the internal functionalization. The interactions between organic molecules might play a role on this layer structuration, especially alkyl-alkyl interactions that could add strain to the layers themselves.

We also observed a rather intriguing movement of O1 (the oxygen shared by three octahedra) out of the layer plane depending on the grafted molecule, this movement could be due to several factors ranging from the accommodation of the layer due to the tetrahedra deformation to the presence of either a direct carboxylate grafting onto an octahedral site (yet rather unlikely) or

interactions with water bridging the carboxylate grafted to the tetrahedra and the neighbouring hydroxyl group.

This run at SOLEIL having been made at the beginning of my Ph.D., it could not be applied to the hybrids synthesized and described thereafter. This study, in parallel with simulations however, could prove very useful to at least locate the position of the newly studied grafting moiety, the phosphonic acid. Indeed, the higher Z of the phosphorus could help to locate the anchoring moiety.

8. Bibliography

1. M. Louër, D. Louër and D. Grandjean, *Acta Crystallographica Section B Structural Crystallography and Crystal Chemistry*, 1973, **29**, 1696-1703.
2. M. Kurmoo, *Philosophical Transactions of the Royal Society A: Mathematical, Physical and Engineering Sciences*, 1999, **357**, 3041-3061.
3. O. Palamarciuc, E. Delahaye, P. Rabu and G. Rogez, *New Journal of Chemistry*, 2014, **38**, 2016-2023.
4. V. Laget, P. Rabu, C. Hornick, F. Romero, R. Ziessel, P. Turek and M. Drillon, *Molecular Crystals and Liquid Crystals Science and Technology. Section A. Molecular Crystals and Liquid Crystals*, 1997, **305**, 291-302.
5. V. Laget, C. Hornick, P. Rabu, M. Drillon and R. Ziessel, *Coordination Chemistry Reviews*, 1998, **178-180**, 1533-1553.
6. M. Kurmoo, H. Kumagai, S. M. Hughes and C. J. Kepert, *Inorganic Chemistry*, 2003, **42**, 6709-6722.
7. J. R. Neilson, J. A. Kurzman, R. Seshadri and D. E. Morse, *Chemistry*, 2010, **16**, 9998-10006.
8. R. Ma, Z. Liu, K. Takada, K. Fukuda, Y. Ebina, Y. Bando and T. Sasaki, *Inorganic Chemistry*, 2006, **45**, 3964-3969.
9. C. J. B. Clews, E. N. Maslen, H. M. Rietveld and T. M. Sabine, *Nature*, 1961, **192**, 154-155.
10. H. M. Rietveld, *Acta Crystallographica*, 1967, **22**, 151-152.
11. H. M. Rietveld, *Journal of Applied Crystallography*, 1969, **2**, 65-71.
12. F. Cavani, F. Trifirò and A. Vaccari, *Catalysis Today*, 1991, **11**, 173-301.
13. J. R. Neilson, D. E. Morse, B. C. Melot, D. P. Shoemaker, J. A. Kurzman and R. Seshadri, *Physical Review B*, 2011, **83**, 094418-094425.
14. L. Poul, N. Jouini and F. Fiévet, *Chemistry of Materials*, 2000, **12**, 3123-3132.
15. M. Taibi, S. Ammar, N. Jouini, F. Fiévet, P. Molini and M. Drillon, *Journal of Materials Chemistry*, 2002, **12**, 3238-3244.
16. A. Viani, A. F. Gualtieri and G. Artioli, *American Mineralogist*, 2002, **87**, 966-975.
17. F. M. Michel, L. Ehm, S. M. Antao, P. L. Lee, P. J. Chupas, G. Liu, D. R. Strongin, M. A. A. Schoonen, B. L. Phillips and J. B. Parise, *Science*, 2007, **316**, 1726-1729.
18. V. Petkov, P. N. Trikalitis, E. S. Bozin, S. J. L. Billinge, T. Vogt and M. G. Kanatzidis, *Journal of the American Chemical Society*, 2002, **124**, 10157-10162.
19. S. J. L. Billinge, R. G. DiFrancesco, G. H. Kwei, J. J. Neumeier and J. D. Thompson, *Physical Review Letters*, 1996, **77**, 715-718.
20. J. Bréger, N. Dupré, P. J. Chupas, P. L. Lee, T. Proffen, J. B. Parise and C. P. Grey, *Journal of the American Chemical Society*, 2005, **127**, 7529-7537.

21. N. Yamakawa, M. Jiang, B. Key and C. P. Grey, *Journal of the American Chemical Society*, 2009, **131**, 10525-10536.
22. E. Wenger, S. Dahaoui, P. Alle, P. Parois, C. Palin, C. Lecomte and D. Schaniel, *Acta Crystallographica Section B, Structural Science, Crystal Engineering and Materials*, 2014, **70**, 783-791.
23. X. Qiu, J. W. Thompson and S. J. L. Billinge, *Journal of Applied Crystallography*, 2004, **37**, 678-678.
24. C. L. Farrow, P. Juhas, J. W. Liu, D. Bryndin, E. S. Bozin, J. Bloch, T. Proffen and S. J. Billinge, *Journal of physics. Condensed matter : an Institute of Physics journal*, 2007, **19**, 335219.
25. P. Juhás, T. Davis, C. L. Farrow and S. J. L. Billinge, *Journal of Applied Crystallography*, 2013, **46**, 560-566.
26. M. Kurmoo, H. Kumagai, S. M. Hughes and C. J. Kepert, *Inorganic Chemistry*, 2003, **42**, 6709-6722.
27. R. L. McGreevy and L. Pusztai, *Molecular Simulation*, 1988, **1**, 359-367.
28. W. Lotmar and W. Feitknecht, *Zeitschrift für Kristallographie - Crystalline Materials*, 1936, **93**.
29. W. Stählin and H. R. Oswald, *Acta Crystallographica Section B Structural Crystallography and Crystal Chemistry*, 1970, **26**, 860-863.
30. S. Ghose, *Acta Crystallographica*, 1964, **17**, 1051-1057.
31. N. E. Brese and M. O'Keeffe, *Acta Crystallographica Section B Structural Science*, 1991, **47**, 192-197.
32. S. Švarcová, M. Klementová, P. Bezdička, W. Łasocha, M. Dušek and D. Hradil, *Crystal Research and Technology*, 2011, **46**, 1051-1057.
33. J. R. Neilson, B. Schwenzer, R. Seshadri and D. E. Morse, *Inorganic Chemistry*, 2009, **48**, 11017-11023.

Chapter III : Layered Hydroxides Hybrid Materials Obtained by
Intercalation of Fluorene Derivatives

Chapter III : Layered Hydroxides Hybrid Materials Obtained by Intercalation of Fluorene Derivatives

As discussed before, the main objective of my thesis consists in the addition of a new property to layered simple hydroxides, *via* the addition of functional molecules. Out of the several interesting properties that can be added *via* molecular intercalation, we have chosen to focus on bringing electric ordering. The goal is to obtain a material that is multiferroic, meaning having both electric and magnetic ordering. This domain is largely covered by oxides, but hybrids and molecule-based materials have attracted an increasing attention.^{1, 2} The best known molecule-based materials are coordination polymers³ and Metal-Organic Frameworks⁴ or the series of compounds $[(\text{CH}_3)_2\text{NH}_2]\text{M}(\text{HCOO})_3$ (with $\text{M} = \text{Mn}, \text{Co}, \text{Ni}, \text{Fe}$) which illustrates one of the most exhaustively studied systems in the MOFs approach to obtain multiferroic materials.⁵⁻⁷ This system exhibit a non-collinear magnetic ordering below 8.5 K to 35.6 K depending on the transition metal ion^{8, 9} and an antiferroelectric order which appears at 170 K.⁶ The modification of the central cation allows to tune the properties and ordering temperature of the material.¹⁰ For some compounds of this system, it is also possible to have an electric control of the magnetization, a very interesting property for advanced memory devices for instance.¹¹

There is another example of hybrid multiferroic compounds that uses the hosting behaviour and magnetic properties of oxalate-bridged two-dimensional networks.¹² This material exhibit a ferromagnetic behaviour below 3.9 K and is ferroelectric in the entire temperature range, but no magneto-electric coupling could be evidenced in this material.

A last example of multiferroic hybrid compounds are the materials based on layered perovskites. These layered perovskites are excellent candidates to obtain multiferroic properties because they have a good structural flexibility as well as robust magnetic and electrical properties.¹³⁻¹⁵ The study of CuCl_4 -based hybrids with ethyl ammonium or phenyl-ethyl ammonium counter ions reveals that these systems exhibit the coexistence of ferromagnetic ordering below 9 K and 13 K respectively, coming from the inorganic part as well as an improper ferroelectric ordering below 347 K and 340 K respectively, originating from the hydrogen-bonding promoted by the organic part.^{16, 17}

This chemical organic-inorganic hybrid approach to multiferroics and magnetoelectrics is still scarcely explored. This method has many advantages compared to the solid state chemistry approach, including an easier modulation of the structure and properties of the hybrid material *via* the synthetic pathway. In organic-inorganic hybrid materials, the two sub-networks responsible for the magnetic and electric properties are deeply interwoven and are more likely to exhibit magneto-electric coupling properties compared to nanostructured composite materials, the potential magneto-electric coupling being mainly bound to the surface interactions between the two sub-networks.

With this in mind, the layered intercalation compounds are particularly well suited for an easier tuning of the different properties sought. This chemical flexibility in multifunctional hybrids has been widely used with layered bimetallic trioxalatometalates,^{18, 19} hexathiohypodiphosphates,²⁰ or magnetic layered double hydroxides,²¹ because of their rich functionalization by various ligands *via* versatile reactions. Noteworthy results have been recently reported concerning the combination of magnetism with chirality,²² ferroelectricity,¹² superconductivity,²¹ or non-linear optics.²³

The majority of the compounds described earlier, possesses a weak organic-inorganic interaction, *via* hydrogen-bonding,¹⁷ or electrostatic interactions for example.²⁴ This weak bonding between the sub-networks might limit the synergy between properties.

To help mitigate this problem, we adopt a different approach, which is the insertion and grafting of functional organic molecules into magnetic layered transition-metal hydroxides. In the literature, it can be found that the grafting functions used for this type of hydroxide are carboxylate, sulfate or sulphonate moieties. In my PhD however, we used phosphonic acid which has been, to the best of our knowledge, never used for a layered single hydroxide system, and seldom in the closely related compounds which are Layered Double Hydroxides.²⁵

Phosphonic acids, due to their coordination properties, are widely employed to prepare crystalline hybrid materials²⁶ that are studied for their ionic conduction,^{27, 28} porosity^{29, 30} magnetic^{31, 32} or fluorescent^{33, 34} properties, sometimes even for their bactericidal effects.³⁵

1. Molecular Design

The choice of the phosphonic acid comes from recent years experience. Indeed, efforts to use of phosphonic acids, especially rigid phosphonic acids for solvothermal one-pot synthesis of hybrid compounds were made recently to study the influence of this rigidity on the topology of the obtained system.³⁶ The source of this rigidity comes from a direct connection of the phosphonic acid to the aromatic³⁷ or hetero-aromatic³⁸ ring, making what is assimilated to a rigid molecular platform. An example of the use of this rigidity combined with low symmetrical phosphonic acids gives the non-centrosymmetric crystals that are obtained *via* the reaction of 3-phosphonobenzoic acid (which possesses an aromatic ring with pro-chiral faces) and a copper salt in solvothermal conditions.³⁹ It is noteworthy that non-centrosymmetric crystals can also be obtained with diposphonic acid as organic precursors.³⁸ These results made us explore further diposphonic acids as precursors of hybrid materials based on Layered Simple Hydroxides, the rigidity of the molecule being another important parameter to keep in mind.

In this respect, fluorene is an interesting rigid platform in which the presence of a 5-membered ring lowers the symmetry of the obtained compound.^{40, 41} This is the reason why this chapter will cover extensively the fluorene as a rigid platform as well as different functionalizations of this fluorene shown in figure 1. All these molecules have been provided by our colleagues from the CEMCA CNRS UMR 6521 of Brest, France (Melissa Roger, Charlotte Sevrain, Paul-Alain Jaffres).

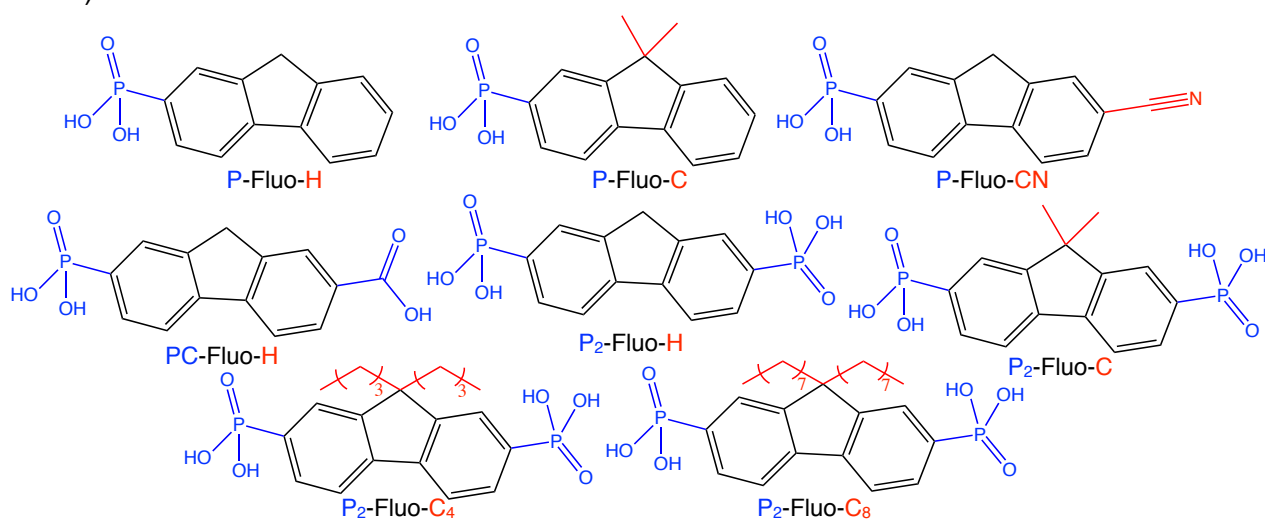


Figure 1 : Fluorene-based molecules used as well as their nomenclature used throughout this chapter.

These fluorene molecules may bring two properties within the hybrid, the first being electric polarization and the second being the luminescence of the aromatic skeleton. As mentioned

before, the grafting of phosphonic acid in layered simple hydroxides have, to the best of my knowledge, not yet been reported so during my PhD I had to adapt the already existing protocols for carboxylates and sulfate/sulfonates to this new moiety.

2. Intercalation Chemistry of the Phosphonic Acids

It must be noted that a direct intercalation from the cobalt or copper hydroxy-acetate compounds is impossible for these molecules. However, as discussed in chapter I, there is a possibility to enable grafting of such molecules *via* a preintercalation method.

Indeed, this technique is often used in the literature to help or enable the functionalization of layered materials such as hexathiohypodiphosphates (MPS₃),^{42, 43} zirconium phosphate,⁴⁴⁻⁴⁶ Layered Double Hydroxides (LDH),⁴⁷ or layered oxides.⁴⁸⁻⁵⁰ In all these cases, the preintercalation drastically modifies the interlayer spacing, hydrophobicity/hydrophilicity of the interlayer space and changes the reactivity of the compounds. In our case, the preintercalation strategy developed in the laboratory consists in functionalizing the starting cobalt or copper hydroxy-acetate with dodecylsulfonate and dodecylsulfate respectively. This strategy is very efficient to allow the insertion-grafting of large or fragile molecules.⁵¹⁻⁵³

Without this preintercalation strategy, it is impossible to graft the fluorene derivatives in the layers without having either no reaction at all, multiphasic compounds or oxides. The complete insertion on the preintercalated compounds is made with different conditions but disregarding the molecule to insert, it must be put in excess in the reactive medium, the same phenomenon is observed for other molecules bearing carboxylate or sulfonate anchoring moieties.

The first part of this chapter will deal with the insertion-grafting of fluorene derivatives in copper hydroxide and the second part will show how the insertion in cobalt hydroxide happened and especially focus on the difficulties encountered in this system.

3. Insertion in Copper Hydroxide

The first system I used is the copper hydroxide, as seen in the first chapter, this system is a layered brucite-type sheets of copper hydroxide with a direct grafting of the molecules inside the layers. This system has been extensively used as a chemical model for the grafting of the molecules, as it is generally an easier system to functionalize.

3.1. Insertion Conditions : the Crucial Role of pH

If there is a general procedure to exchange the molecules, there are wild variations in the temperatures, times and ratios on a molecule to molecule basis. The common point of all these insertion reactions is that the fluorene must be first dissolved in water *via* pH adjustment up to 8.3-8.8 values. These values are chosen because of two parameters, first the solubility of the fluorene itself that can be, depending on the functionalization, completely insoluble in distilled water, and also because this pH range corresponds to the stability domain of the copper hydroxide. For some fluorenes, this dissolution process may take up to three hours due to the high hydrophobicity of fluorene, and also because the large concentration used ($5.5 \cdot 10^{-2}$ M, which is probably very near saturation). This high concentration is due to the use of a 4-fold excess ratio (number of grafting functions of the molecule to insert *per* dodecylsulfate) used. Indeed, in the case

of 4:1 ratios, after reaching pH = 8.8, the upper stability limit of the hydroxide, the water solutions are still slightly turbid. On the other side, any attempt to leave the phosphonic acid protonated leads to the formation of layered copper phosphonates, the copper hydroxide being in this case used as a metal source and being dissolved within a few seconds in the reaction medium leading to the diffractogram and IR spectrum given in figure 2.

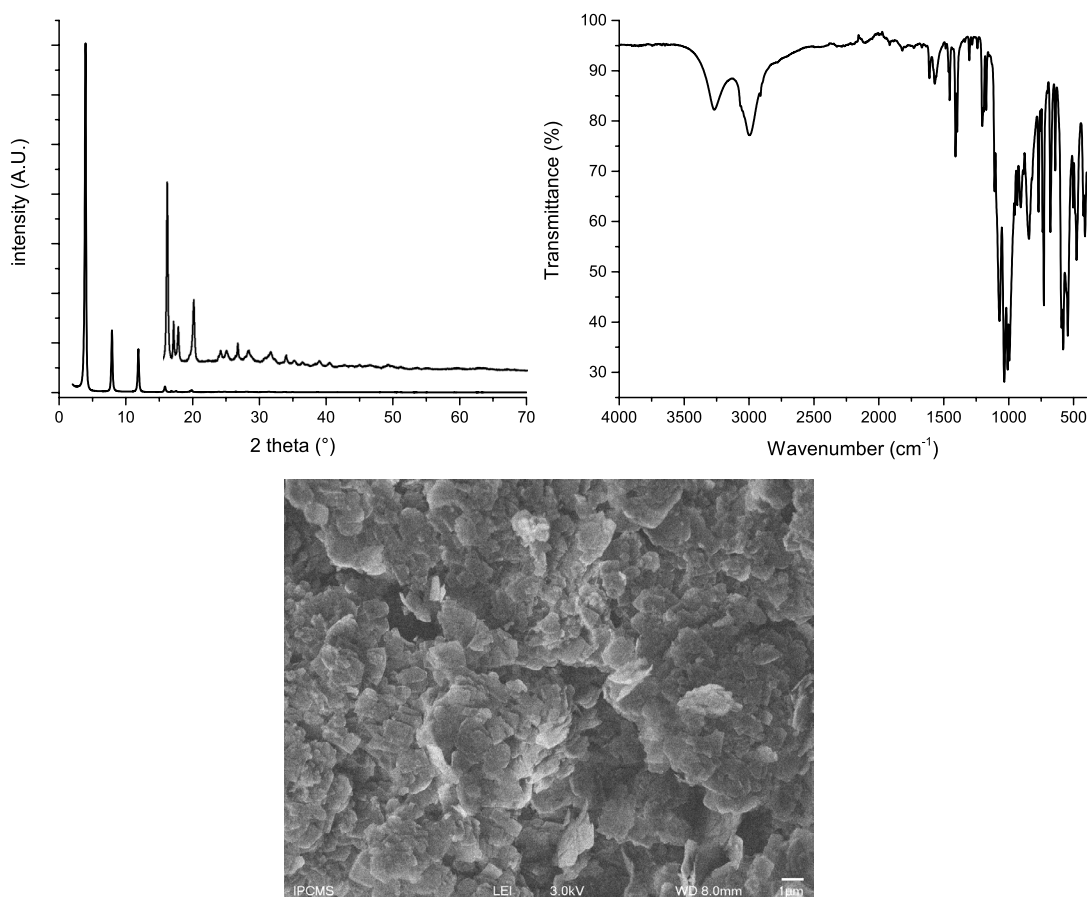


Figure 2 : Diffractogram, infrared spectrum and SEM image of a typical compound obtained with the reaction of protonated P-Fluo-H (0.33 mmol) and dodecylsulfate-intercalated layered copper hydroxide (0.165 mmol) in 12 mL/12 mL (H₂O/EtOH) medium heated at 70°C for 1 hour.

As it can be observed in the figure above, the compound obtained without pH control remains lamellar albeit with additional in-plane diffraction peaks, but the infrared spectrum and SEM picture are indicating that the hydroxide typical IR fingerprint and morphology are lost, revealing the loss of the hydroxide structure. This compound is very similar to the one found by our colleagues from Caen obtained in hydrothermal conditions.⁴⁰ The diffractograms of our compound and the copper-fluorenephosphonate obtained by our colleagues have also been compared in figure 3 below. It must be stressed that the differences observed for other than 00l reflexions are due to the difference in crystallinity (our colleagues have slightly grinded mono crystals when we have a powder) as well as the change of data collection method from capillary transmission to our regular Bragg-Brentano configuration.

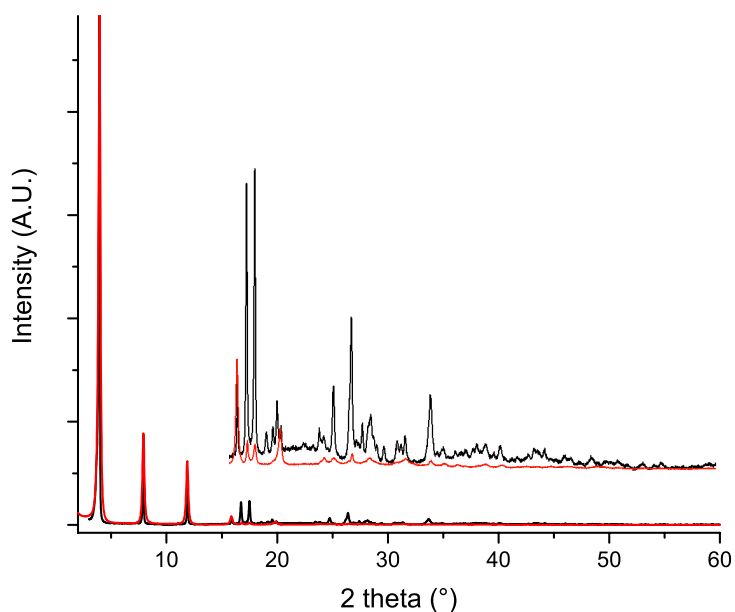


Figure 3 : Comparison of our colleague's diffractogram⁴⁰ (black) compared to the one obtained in our laboratory (red) using protonated P-Fluo-H and dodecylsulfate-intercalated layered copper hydroxide.

As can be seen in figure 4 below, the structure is made of two edge-sharing $\text{CuO}_3(\text{H}_2\text{O})$ pyramids that are sharing six oxygen apices with four PO_3C groups and has two free apices occupied by H_2O and a double layer of fluorene molecules.

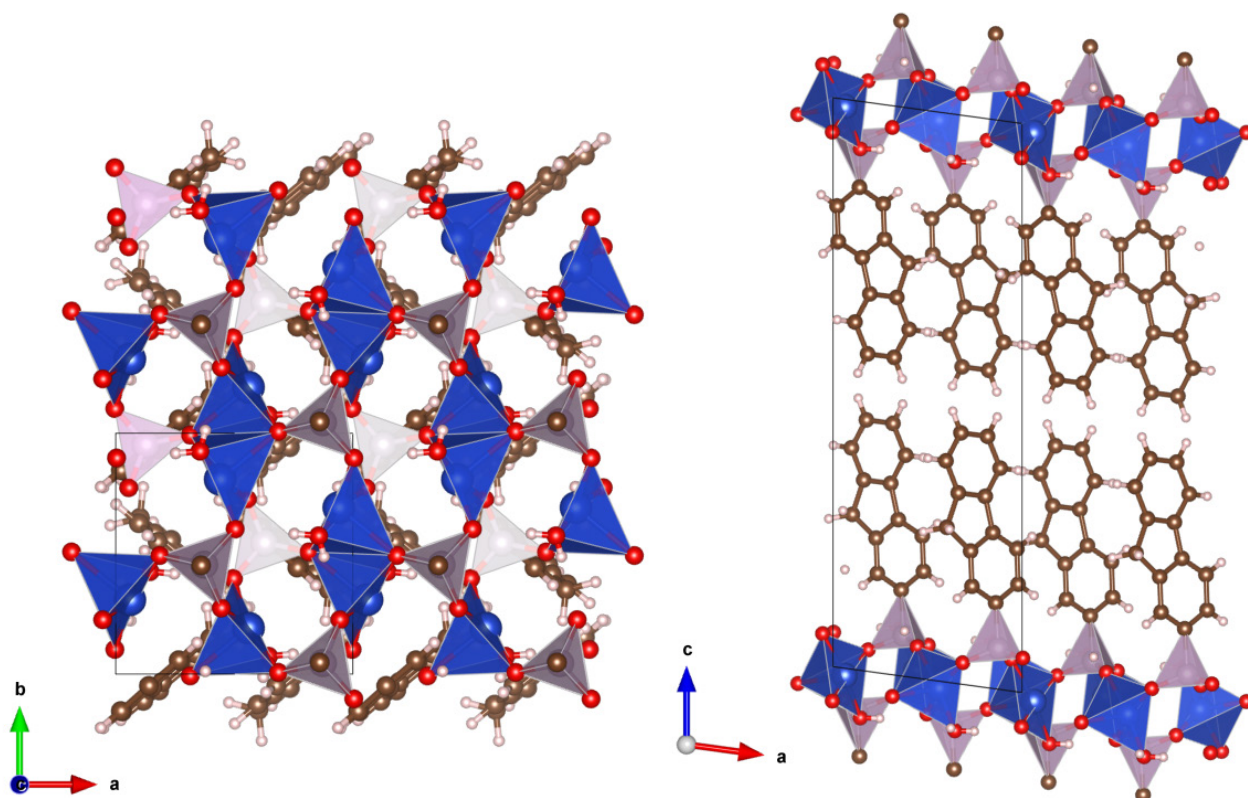


Figure 4 : Structure of the P-Fluo-H hybrid (one pot hydrothermal approach).⁴⁰

3.2. Insertion Conditions : the Roles of Temperature, Excess Ratio of the Molecule of Interest and Reaction Time

For this first series the reaction conditions to obtain pure, single phase and totally exchanged hybrid materials are listed on the table below :

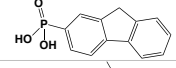
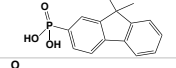
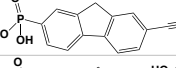
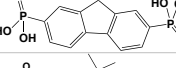
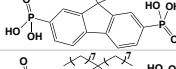
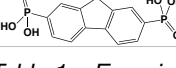
Molecule inserted	Reference	Ratio PO ₃ :DS (1 = 0.165 mmol)	pH	Temperature	Time (h)
	P-Fluo-HCu	4:1	8.8	Reflux (82°C)*	0.25
	P-Fluo-CCu	2:1	8.3	R.T.	70
	P-Fluo-CNCCu	2:1	8.3	Reflux (82°C)*	4
	P ₂ -Fluo-HCu	8:1	8.8	Reflux (82°C)*	0.25
	P ₂ -Fluo-CCu	4:1	8.3	Reflux (82°C)*	1
	P ₂ -Fluo-C ₈ CCu	4:1	8.3	70°C	2

Table 1 : Experimental conditions used to obtain single phase copper-based hybrid compounds. *The reflux temperature is calculated from the phase diagram for a 50/50 H₂O/EtOH mixture, this temperature may slightly vary due to partial solvent evaporation on the reflux condenser walls.

As can be seen from the figure above, the reactivity of the fluorenes is dependent on both the lateral chains and the presence (or absence) of a second grafting moiety. In general, the presence of protons on the 9 position makes the molecule harder to insert and thus requires an increased pH. That pH increase unfortunately lowers the stability of the hydroxide, only allowing for shorter reaction times before the oxides are formed. It is, however, possible to obtain single-phase materials from these very short reaction times that are quite uncommon for carboxylate and sulfonate moieties where reaction times tend to be around 1.5 to 24 hours generally.⁵²⁻⁵⁴

The molecule functionalization also drastically modifies the solubility in the reaction mixture, especially in water when the pH needs to be adjusted. Indeed, some fluorenes are readily soluble in water (P-Fluo-C) meanwhile some others are completely hydrophobic and insoluble (P-Fluo-H). It must be noted that at this pH (8.3-8.8) the phosphonic acids are totally deprotonated as the pK_{a1} is expected to be around 3.0 and pK_{a2} to 7.3 for these fluorenes. The addition of ethanol serves several purposes, the first one is to lower the boiling point of the reaction mixture to avoid a fast oxidation of the hydroxide due to local overheating while keeping an easy control on the temperature, and the second one is to help to disperse the quite hydrophobic dodecylsulfated hydroxide. Additionally, it also has an antioxidant effect along with a facilitator role towards dodecylsulfate leaving the hydroxide, hence helping the exchange reaction.

The last parameter that is modified is the ratio of the molecule of interest. Typically for the 2:1 ratio, 0.33 mmol of fluorene is solubilized in 12 mL of water *via* the pH adjustment discussed before and then 12 mL of ethanol is added along with the 0.165 mmol of copper-hydroxy-dodecylsulfate. For some molecules, such as the fluorenes bearing no lateral moieties (only protons), it is important to note that this ratio needs to be increased to 0.66 mmol of fluorene to get a pure single phase, as shown in figure 5 below.

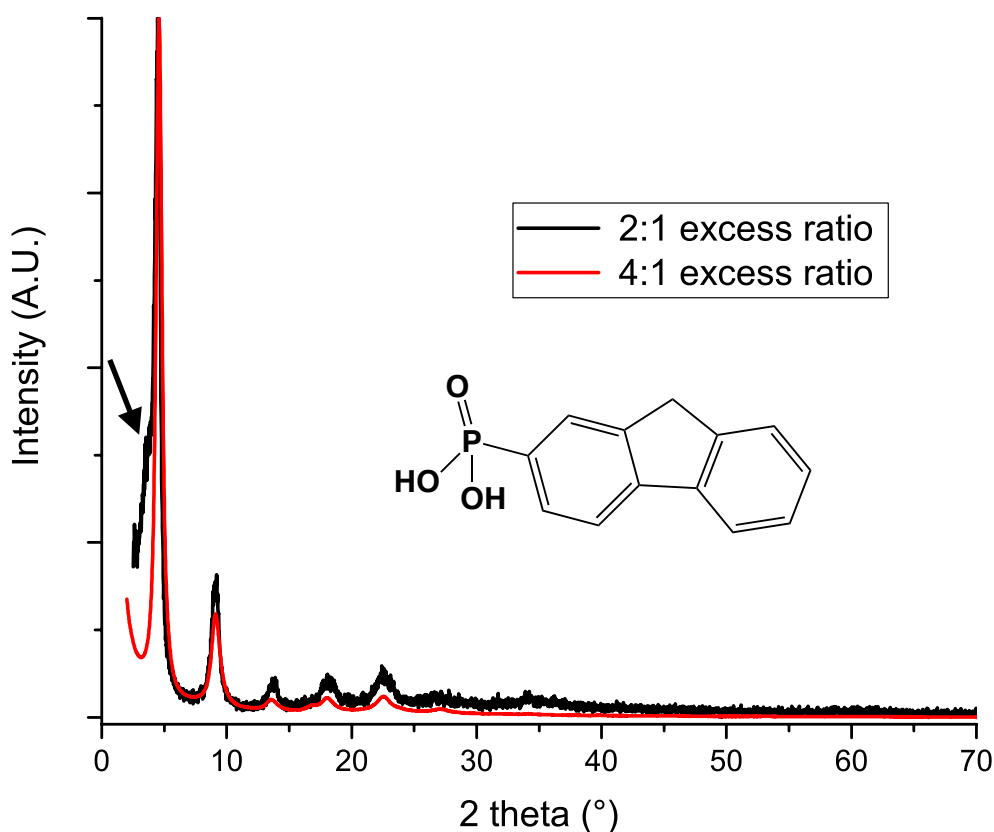


Figure 5 : Diffractograms of fluorene monophosphonic acids copper hydroxide hybrids with different excess ratio.

3.3. Characterization of the Copper Hydroxide Hybrids

3.3.1. Powder X-Ray Diffraction

The powder X-ray diffraction patterns of the obtained hybrids (figure 6) show a typical lamellar structure with the presence of 001 diffraction peaks at low angle but high disorder between planes (major broadening) as well as a complete loss of in-plane information. This indicates that the functionalization reaction resulted in an increased disorder of the material.

Moreover, there are clearly two types of hybrid obtained. The first ones present an interlamellar spacing of about 19.5 Å and corresponds to the hybrids obtained with fluorenes bearing only a single phosphonic acid. There is a slight deviation (enlargement of the interlamellar spacing by 1 Å) for P-Fluo-CN₂Cu. The second series is constituted by hybrids based on fluorenes with two phosphonic acids moieties, showing a smaller interlamellar spacing at around 18 Å. This distance is incompatible with the first supposed pillaring structure that would lead to an interlamellar spacing of roughly 16 Å. This apparent discrepancy will be treated in the section 3.3.2 of this chapter.

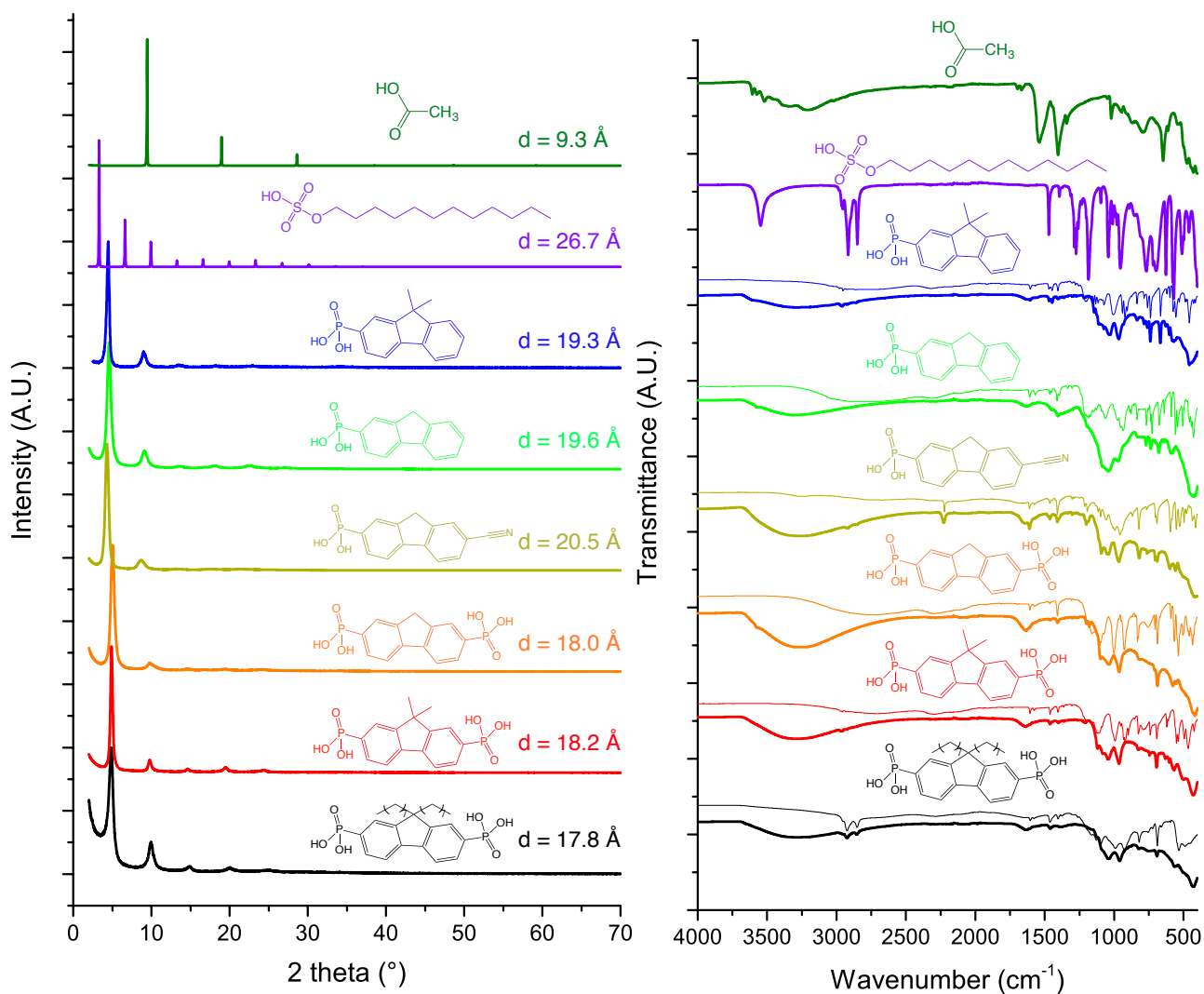


Figure 6 : Diffractograms (left) and corresponding infrared spectra of the different hybrids (right) the thin lines corresponds to the molecules alone.

This loss of long-range ordering is also « visible » with the hybrid morphology. As can be seen in figure 7, the functionalization leads to a change of morphology from a flat slab to a slab with a silky surface, probably similar to the failed crystal to crystal experiment described in chapter I. If the crystallites are still looking like platelets, the long-range ordering is somehow reduced.

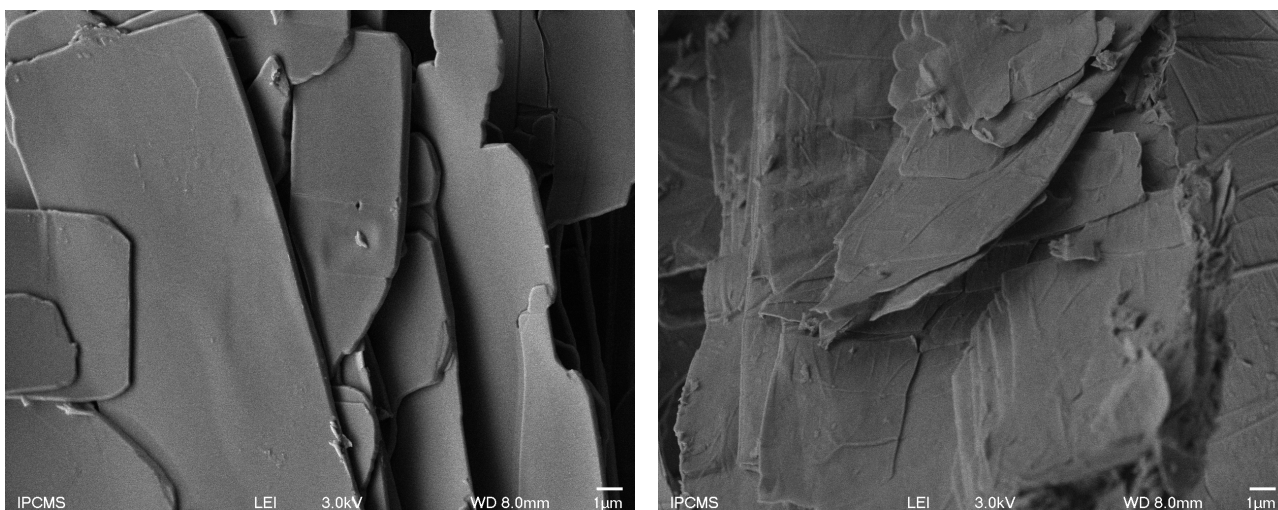


Figure 7 : SEM image of $\text{Cu}_2(\text{OH})_3(\text{DS})$ (left) and of P-Fluo-H-Cu (right).

3.3.2. Packing of the Fluorenes in the Interlamellar Spacing

An important question about how the molecules are packed within the layer still remains unanswered. Indeed, the impossibility to have single crystals as well as the poor general crystallinity of the products prohibits any attempts of powder structure resolution. A technique that has been used at the beginning of my PhD is the extraction of Pair Distribution Function from the diffuse scattering obtained at Soleil Synchrotron on the Cristal beamline as discussed in the chapter II. Unfortunately, our experience led us to believe that the contrast between the organic and the inorganic layers might be too important to propose a model of the local structure but maybe would be enough to get an idea about the phosphorus position onto the layers. Due to a lack of Synchrotron availability we could not obtain any data to test this hypothesis for the hybrids described in this chapter.

To try to get some insight about the packing of the fluorenes between the layers nonetheless, we worked with the only available structural information *i.e.* the interlamellar spacing with the caveat that the results obtained by this study are just naive calculations and might not *in fine* describe the real system.

The two main conceivable packing for this system with fluorenes bearing only one grafting function are either interdigitated molecules or tilted molecules forming a double layer (figure 8). There is also another possible packing that will be discussed in the next section of this chapter where the molecules seems to be flat on the hydroxide surfaces. In the case of copper hydroxide however, as this situation has not been encountered, only the interdigitated and the tilted double layer will be taken into account.

The first case is the interdigitated one where the molecules have a value of θ (tilt angle) close to zero. With this hypothesis the outer benzoic ring should be near the 5-member centre ring of the next fluorene as shown in figure 8 with water filling the remaining space. In the case of the tilted bilayer the calculated tilt angle is around 50° with water filling the void once again.

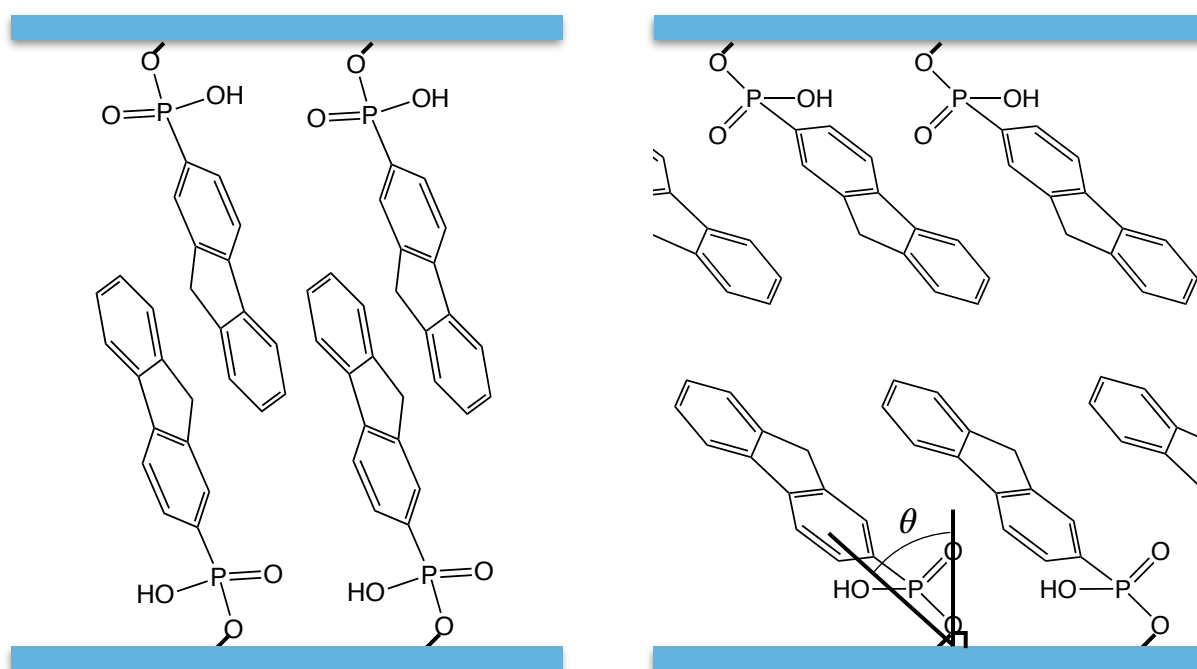


Figure 8 : Illustrations of the proposed interdigitated (left) and tilted double layer (right), θ being defined as the angle made by the molecule with the hydroxide layer normal.

To try to get a better idea of the packing and bonding within the interlamellar space, thorough simulations have been made by the simulation team in IPCMS-DCMI Ziyad Chaker, Guido Ori, Mauro Boero and Carlo Massobrio.⁵⁵ Their approach was to mix a quantum approach (Density Functional Theory) and a classical one (Molecular Dynamics) into a so-called Car-Parrinello Molecular Dynamics (CPMD) methodology to obtain viable simulations of our system. Their major difficulty was to find a good starting model as we do not have any structural information for the interlamellar ordering to begin with. To that end, they started with the most probable model we had at our disposal *i.e.* the structure of layered copper hydroxide taken from the copper-hydroxy-acetate and an interdigitated doubly deprotonated fluorene packing. The results and exact methodology of these simulations will not be extensively discussed here as they are the product of the PhD of Ziyad Chaker and beyond the scope of this thesis. The main point can, however, be seen in figure 9 below.

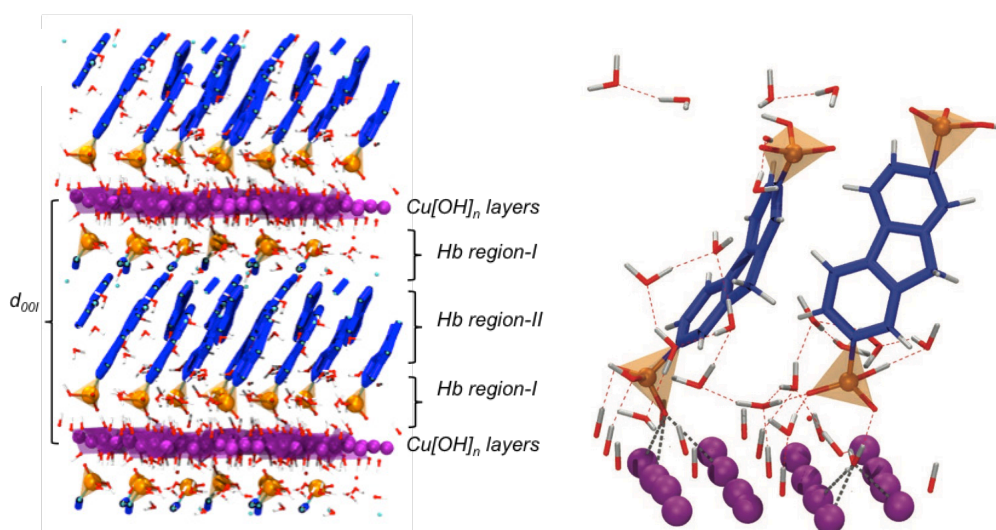


Figure 9 : Snapshot of the most stable configuration of P-Fluo-H-Cu (left) and P₂-Fluo-H-Cu (right). The latter underlines the two different types of phosphonic acid group, one coordinated to the layers the other in interaction with the layers via a network of water molecules (right) as calculated by First Principles Molecular Dynamics.⁵⁵

As can be observed from the picture above, the most stable structure appears to be a packing of the fluorenes with a vast network of hydrogen interactions with both the hydroxide, the phosphonic acids and the water in the Hb region-I. Meanwhile, in the Hb region-II, the hydrogen interactions are made only with water. These simulations also indicate that the doubly deprotonated phosphonic acid stabilization goes by the capture of a neighbouring proton. Comforting the idea that only one oxygen is covalently bound to the layer.

For the case of hybrids with fluorenes having two phosphonic acids, as stated above, a grafting for each moiety has shown to be incompatible with the observed interlamellar distance. The simulations led to a system where one phosphonic acid is bound to one layer (Cu-O distance in the range of 2.6-3.2 Å) meanwhile the other phosphonic acid exhibits a Cu-O(phosphonic) distance of about 5.5 Å to the other hydroxide layer. This configuration allows for the coordination of water by the copper atoms, effectively replacing the stabilizing role of the phosphonic acid group (figure 9).

3.3.3. Infrared Spectroscopy

Another important aspect of the simulations described in the previous paragraph would be for the infrared interpretation to get a much needed insight about the grafting type of the phosphonic acids in the absence of precise structure.

Infrared spectra of the hybrid compounds (figure 6) all show the signature of the C-C rings stretching modes of the fluorene aromatic skeleton visible at 1570, 1469, 1446, 1402 cm^{-1} ,^{56, 57} as well as a complete disappearance of the signature of the dodecylsulfate molecules.⁵⁸ Indeed, the bands present at 2954, 2916, 2871, 2850, 1470 and 1350-1250 cm^{-1} , signature of the alkyl chains, disappears as well as the bands of the sulfate group at 1186 and 1043 cm^{-1} (figure 10).

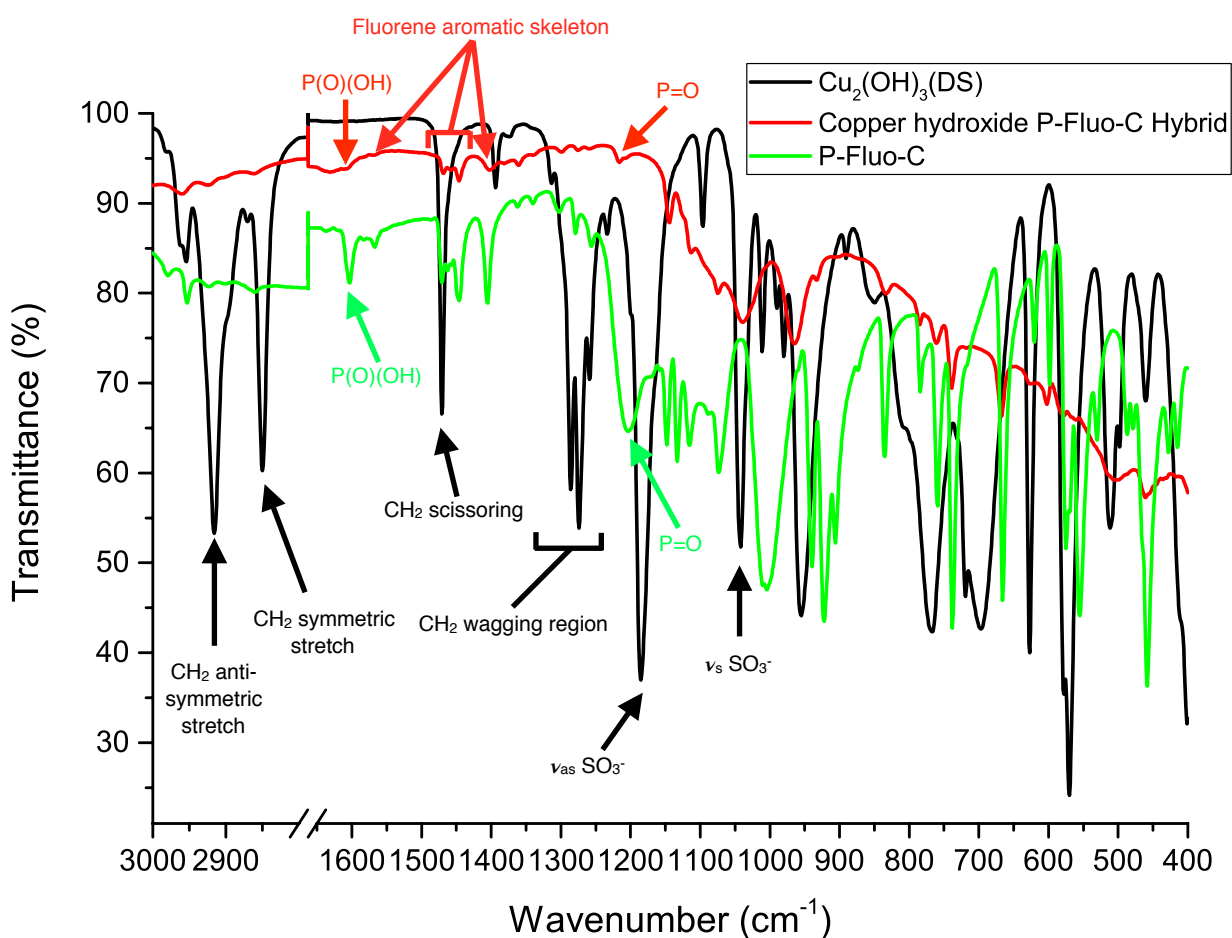


Figure 10 : Comparative spectrum between starting compound (black), P-Fluo-C alone (green) and P-Fluo-C=Cu hybrid (red).⁵⁶⁻⁵⁸

Another very important question is, as mentioned before, the description of the grafting mode of the phosphonates onto the hydroxide layers. To that end the only observable readily available to us is their infrared signature. This kind of moiety has seldom been found in the literature : rare examples can be found in the case of layered double hydroxide^{59, 60} but are of limited usefulness in the present case due to the essential differences between layered double and single hydroxides (*i.e.* charge balance in one case and covalent bonding in the other). In addition, all these band attributions are prone to errors, due to the large number of bands present in this region.

As can be seen on the figure above and reported on the table below, the bands around 1200-1220 cm^{-1} have been ascribed to the P=O bond⁶¹⁻⁶³ and the band around 1600 cm^{-1} to the P(O)(OH) group.⁶⁴ The grafting of phosphonic acids onto several surfaces and in very different system have been described previously, but several discrepancies are observed when it comes to their interpretation.⁶²⁻⁶⁸ In the present work, I tried to assign as many bands as possible *via* direct comparison between all the samples obtained with all the molecules bearing a phosphonic acid anchoring group. The result of this empirical work is, for convenience reasons, only available in appendix 2 but a condensed version (yet with several unattributed bands) is shown in the table below (table 2).

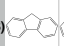
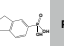
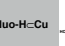
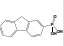
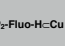
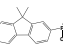

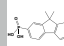
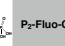
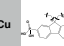
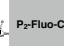
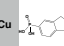

															
P(O)(OH) group		1606	1609	1607	1634	1603	1633	1606	1633	1604	1633	1609	1610		
C-C ring stretch		1575	1579/ 1567	1570/ 1561(w)	1574/ 1557	1575/ 1557	1583/ 1567		1577	1574	1577	1573	1574/ 1562(w)	1572/ 1535	
C-C ring stretch	1471	1478	1482/ 1464	1462	1475/ 1464	1462	1470/ 1462	1469/ 1458	1461	1461	1463	1459	1476/ 1464	1476/ 1462	
C-C ring stretch		1447	1452	1450	1449		1456/ 1446	1446	1444	1444	1440	1438(w)	1447	1436(w)	
C-C ring stretch		1402	1411	1407	1409	1407	1405	1402	1405	1402	1404	1398	1409	1408/ 1396	
	1374	1384	1397		1391			1383	1383	1384	1376	1377	1398/ 1382(w)		
PO ₃ asymmetric stretching (1330 cm^{-1})			1334	1338	1333	1337	1340	1339	1337	1339	1339		1332(w)	1332	
	1286	1300	1303	1299	1306	1299	1302	1299	1304	1299	1301	1299	1303	1301	
	1274		1284	1276	1283	1275/ 1265	1278	1275	1261(w)	1262		1262(w)	1289	1286	
C-H inplane bending	1259	1234	1265(w) 1239	1233(w)	1244	1240(w)	1255	1259			1217			1250	1243/ 1234(w)
C-H inplane bending and P=O (1200-1220 cm^{-1})	1233	1192	1208/ 1195/ 1184/ 1171	1198/ 1188/ 1171	1198/ 1180/ 1160	1200/ 1179	1203/ 1158(w)	1217/ 1207	1161	1208	1162		1212/ 1206/ 1193	1210(w) 1201/ 1188	
C-H inplane bending	1199/ 1185/ 1164(w)		1146		1140		1148	1145	1140			1162	1180		
C-H inplane bending			1126		1121		1133	1127	1124	1120	1128	1126	1145/ 1132	1133(w)/ 1110(w)	
PO ₃ symmetric stretching (1110 cm^{-1})	1096	1108	1103	1103	1106	1099	1115	1112	1109				1115		
P-O Probable zone		1092	1091	1087	1095		1088		1086	1082	1094	1092	1098	1092	
			1064		1072		1073	1074	1073(w)	1070(w)			1057		
	1042	1019	1022	1039		1038		1036		1044	1039	1042	1021	1044	
	1011	1000	1001		1001		1011/ 1005		993	1010	991	1009	1009/ 995	1008	
	808		834/ 820	832/ 818	832/ 825		835	834	825	824	820	823	821	819	
PO ₃ Symmetrical deformation (605 cm^{-1})				592	604		598	602	609/ 601	603	596	600	594	599	

Table 2 : IR bands of all hybrids and all starting molecules.

To support this work, the simulations done by Ziyad Chaker to help to identify more accurately which band corresponds to which bond vibration mode is still under way at the moment of this writing.

3.3.4. TGA/TDA, Micro-Analysis and EDX

A last parameter that has not been discussed so far is the insertion rate of the different molecules in the layered copper hydroxide. To have some ideas of this insertion rate, we combined micro-analysis, thermogravimetric analysis as well as energy-dispersive X-ray analysis. The TGA/TDA technique has been used to have an estimation of the water content of the hybrids, indeed, in our case a net water loss could not be observed (see figure below) but a rough estimate of the water content could be obtained. This water content was calculated with the mass lost at 130°C.

In the case of hybrids having phosphonic acid moieties the TGA technique was unfortunately unfit to have an accurate metal content, indeed, the product of the TGA/TDA that normally leads to a pure CuO at 900°C in the case of hybrids obtained with carboxylic anchoring groups, leads in our case in a mixture of CuO and Cu₃(PO₄)₂. The very small quantity and the relatively poor crystallinity did not allow for an accurate profile matching and quantitative analysis and trying to get rid of the phosphorous *via* further heating would have been technically impossible as heating to temperatures up to 1400°C would still lead to various Cu_xP_y compounds.⁶⁹

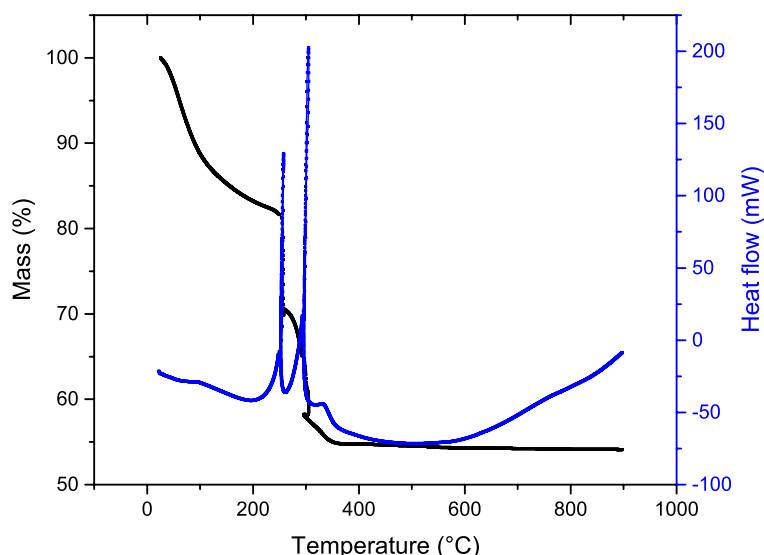


Figure 11 : Typical TGA/TDA curves obtained with P-Fluo-C≡Cu, typical of all fluorene-copper-hybrids.

To help mitigate this problem, we have used two other techniques at our disposal. The first is the EDX analysis, allowing us to get an estimate of the Cu:P ratio within reasonable margins as well as a crucial information about the absence of other amorphous phases of different composition. Finally, the micro-analysis allowed us to have the titration of copper, carbon, phosphorus and hydrogen (as well as nitrogen if necessary). The obtained results are listed in the table below :

TGA/TDA water content measured (calculated)	Cu:P ratio <i>via</i> EDX measured (calculated)	Micro-analysis results measured (calculated)	Obtained formula
7.2% (19.7%)	6.35 (4.54)	Cu : 36.80 (36.88), C : 20.15 (19.94) H : 3.63 (4.04), P : 3.79 (3.95)	P-Fluo-H≡Cu Cu ₂ (OH) _{3.56} (C ₁₃ H ₁₀ O ₃ P) _{0.44} ·2.7H ₂ O
13.6% (11.3%)	3.85 (4.00)	Cu : 34.64 (34.91), C : 24.72 (24.74) H : 4.03 (4.18), P : 3.82 (4.26)	P-Fluo-C≡Cu Cu ₂ (OH) _{3.5} (C ₁₅ H ₁₄ O ₃ P) _{0.5} ·2.3H ₂ O
9.0% (7.7%)	5.39 (4.76)	C : 23.95 (23.61), H : 3.22 (3.44), N : 1.57 (1.69)	P-Fluo-CN≡Cu Cu ₂ (OH) _{3.5} (C ₁₄ H ₈ O ₃ PN) _{0.42} (DS) _{0.08} ·1.5H ₂ O

TGA/TDA water content measured (calculated)	Cu:P ratio via EDX measured (calculated)	Micro-analysis results measured (calculated)	Obtained formula
9.5% (19.4%)	4.99 (4.34)	Cu : 38.99 (39.29), C : 11.18 (11.1) H : 3.03 (4.00), P : 4.19 (4.41)	P ₂ -Fluo-HcCu Cu ₂ (OH) _{3.54} (C ₁₃ H ₁₀ O ₆ P ₂) _{0.23} ·3.5H ₂ O
17.0% (15.8%)	5.97 (10.00)	Cu : 41.4 (40.80), C : 11.74 (12.00) H : 3.74 (3.17), P : 4.04 (3.23)	P ₂ -Fluo-CcCu Cu ₂ (OH) _{3.6} (C ₁₅ H ₁₄ O ₆ P ₂) _{0.2} ·2.7H ₂ O
9,2% (14,0%)	3.80 (6.25)	Cu : 39.11 (39.54), C : 17.32 (17.34) H : 3.86 (4.83), P : 3.94 (3.09)	P ₂ -Fluo-C ₈ cCu Cu ₂ (OH) _{3.68} (C ₂₉ H ₄₂ O ₆ P ₂) _{0.16} ·2.5H ₂ O

Table 3: Different insertion ratios of the copper hybrids.

As can be seen in the table above, some discrepancies between the different methods can be found. Each method having its own accuracy and error, it is difficult to try to interpret these differences as there is no noticeable trend. It can be noted that the only compound where the exchange is not absolutely complete (*i.e.* traces of dodecylsulfate remains) is with the fluorene bearing a nitrile moiety, P-Fluo-CNcCu. Due to the fact that this could not be detected with the XRD, infrared or EDX analyses where it showed a sulfur value that was within half the uncertainty of the measurement, only the micro-analysis gave us conclusive result about the small amount of remaining dodecylsulfate. Due to this late detection, harsher synthetic conditions could not be tested to try to obtain a purely exchanged hybrid.

Once these hybrids have been obtained, their different properties have been studied and will be discussed in the section 5 of this chapter.

4. Insertion in Cobalt Hydroxide

The second system studied during this thesis is the layered cobalt hydroxide. As mentioned in the second chapter, the exact structure of this compound is unknown but is considered to be similar to the hydrozincite *i.e.* a purely octahedral sheet with vacancies and tetrahedrally coordinated cobalt on top and below these vacancies. During my PhD, some efforts have been made to try to have a description of our system as accurate as possible (see chapter II). This system has been chosen for its magnetic properties, indeed this hydroxide presents a ferrimagnetic ordering at temperatures in the range of 10-15K.⁷⁰ The insertion conditions have been adapted from the conditions determined by the experiments done on copper hydroxide, with the reaction parameters listed in the table below.

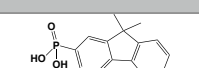
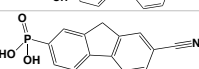
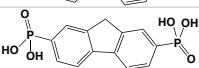
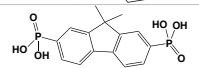
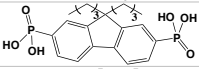
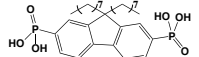
Molecule inserted	Reference	Ratio PO ₃ :DS (1 = 0.165 mmol)	pH	Temperature	Time (h)
	P-Fluo-CcCo	1.4:1	8.3	R.T.	24
	P-Fluo-CNcCo	1.4:1	8.8	Reflux (82°C)	2
	P ₂ -Fluo-HcCo	2.8:1	8.6	Reflux (82°C)	1
	P ₂ -Fluo-CcCo	2.8:1	8.3	Reflux (82°C)	2
	P ₂ -Fluo-C ₄ cCo	2.8:1	8.5	Reflux (82°C)	2.5
	P ₂ -Fluo-C ₈ cCo	2.8:1	8.3	Reflux (82°C)	1.5

Table 4 : Experimental conditions used to obtain single phase cobalt-based hybrid compounds.

As it can be seen from the table above, the compounds bearing lateral protons (P-Fluo-CN and P₂-Fluo-H) do not require harsher insertion conditions contrarily to what was observed for insertion into copper hydroxide.

Yet, the insertion with the fluorene bearing only one phosphonic acid moiety P-Fluo-H has proven to be tougher. The insertion is possible, but we did not succeed in obtaining a single phase material despite many attempts using different conditions. The interlamellar spacing obtained varied from 21 Å to 17.6 Å with in most of the cases a mixture of these two phases depending on the starting compound. This may be due to the difficulty to obtain a single packing of the fluorenes, indeed, the flatness of the molecule might not help to separate energetically a double layer packing from an interdigitated one.

4.1. Structure of the Cobalt Hydroxide with PDF Analysis and UV-Visible Spectroscopy

As mentioned before, the exact structure of the cobalt-hydroxy-acetate is still unknown, but the Pair Distribution Function experiments shown in chapter II gives us an insight about the local structure. As a reminder, the figure below shows the local structure we managed to obtain in collaboration with Pr. Christine Taviot-Guého.

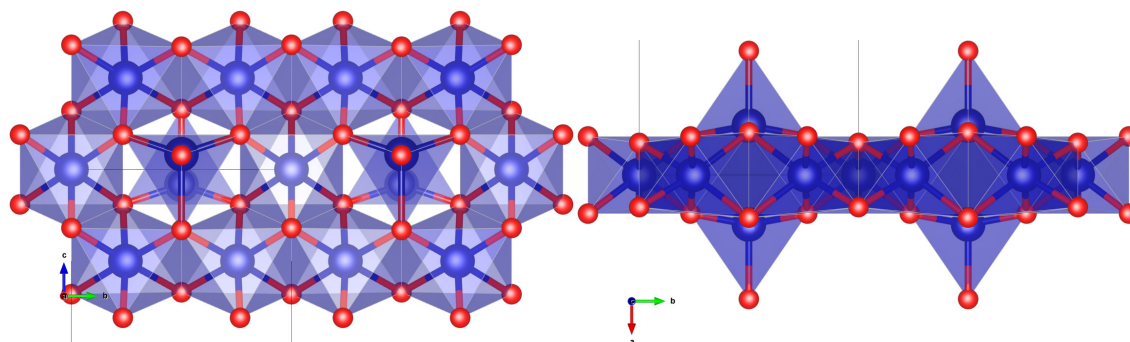


Figure 12 : Local structure of the layered cobalt hydroxide obtained via fitting of PDF (chapter II).

Another technique used to characterize the hybrid hydroxides is the UV-visible reflectance spectroscopy. Indeed, this technique allowed us to identify the transition bands of high spin d⁷ cobalt II in tetrahedral and octahedral sites (see figure 13).

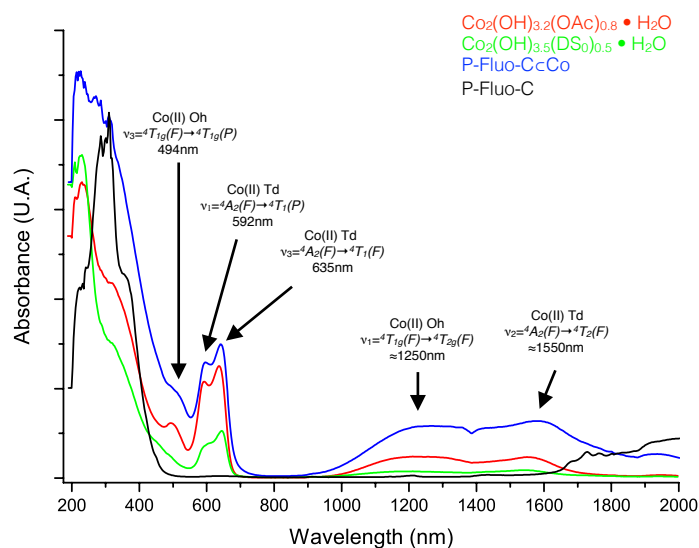


Figure 13 : Kubelka-Munk corrected UV-Vis spectra of layered cobalt hydroxides before and after P-fluo-C intercalation. The other hybrid compounds exhibit similar spectra.

The UV part of the spectra is dominated by the O → Co charge transfer band and the $\pi \rightarrow \pi^*$ bands of the fluorene moiety. At lower energies, two series of bands can be observed. The bands observed at 1550, 635, and 592 nm can be attributed respectively to ${}^4A_2(F) \rightarrow {}^4T_2(F)$, ${}^4A_2(F) \rightarrow {}^4T_1(F)$, and ${}^4A_2(F) \rightarrow {}^4T_1(P)$ transitions of high spin d^7 Co(II) in tetrahedral sites, whereas the bands observed at 1250 and 494 nm can be attributed respectively to ${}^4T_{1g}(F) \rightarrow {}^4T_{2g}(F)$ and ${}^4T_{1g}(F) \rightarrow {}^4T_{1g}(P)$ transitions of high spin d^7 Co(II) in octahedral sites.

It is also visible in these spectra that the octahedral/tetrahedral band intensity ratio does not change drastically before and after the functionalizations. This shows that the layered hydroxide is not drastically modified by the organic exchange. Yet, as demonstrated in chapter II, it is likely that distortions of the inorganic layers are modified upon functionalizations. Unfortunately, it was not possible during the time of this PhD to obtain synchrotron beam time to perform further PDF analyses on these hybrids.

4.2. Powder X-Ray Diffraction of Cobalt Hybrids

As stated previously, the paracrystallinity⁷¹ (*i.e.* structural distortion in which the individual vectors between adjacent unit cells can vary in magnitude and direction subject to the constraint that the cells are uniquely defined⁷²) of the layered cobalt hydroxide⁷³ greatly reduces the available structural information obtained from diffraction peaks. As in the case of the layered copper hydroxide, the information given by powder X-ray diffraction will be limited to the interlamellar spacing ($(00l)$ peaks) and to the in-plane diffraction peaks (100) and (110) if observable. These last two peaks are an important proof that the structure of the lamellae is not drastically modified as they are the only out of plane information we have (see figure 14).

After prefunctionalization by dodecylsulfonate molecules, the interlamellar spacing goes from 12.7 Å to 25.4 Å.

Then, after this prefunctionalization, like what observed in the case of copper hydroxide, two groups can be distinguished, the number of phosphonic acid moieties being directly related to the interlamellar spacing of the obtained hybrid.

The smaller interlamellar spacing (18.8 Å) is obtained with fluorenes having two phosphonic acids regardless of the lateral functionalization (except for P_2 -Fluo-H \subset Co, see below). Unlike what has been observed with copper hydroxide, this corresponds well with a grafting of the two phosphonic acids to the tetrahedral cobalt. The inorganic layer being 7.5 Å large (from apical oxygen from one tetrahedral cobalt to the opposite one) and the fluorene being 12 Å long, it corresponds well to a grafting of the fluorenes with both phosphonic acids with a pillaring arrangement and a tilt angle of about 15°.

For fluorenes bearing a single phosphonic acid moiety the interlamellar spacing swells to distances of around 20 Å. This is in agreement with interdigitated fluorenes or a double layer of fluorenes with a more pronounced tilt angle of 58° to the normal compared to the copper hydroxide. It can be noted that the interlamellar spacing for P-Fluo-C \subset Co is 1 Å larger than for P-Fluo-CN \subset Co. This is probably due to the difference of packing between the two systems.

The case of P_2 -Fluo-H \subset Co does not match the previous categories. Indeed, the interlamellar distance goes down to 11.8 Å, that is almost 1 Å smaller than $Co_2(OH)_3OAc \cdot H_2O$. A major peak broadening is also noticeable compared to all the other hybrids, which seems to indicate that this compound has smaller crystal domains than the others and/or that the interlamellar distance is more widely distributed than in any other hybrid. This behaviour is also observed in other flat molecules such as thiophenes and bithiophenes that will be discussed in chapter V.

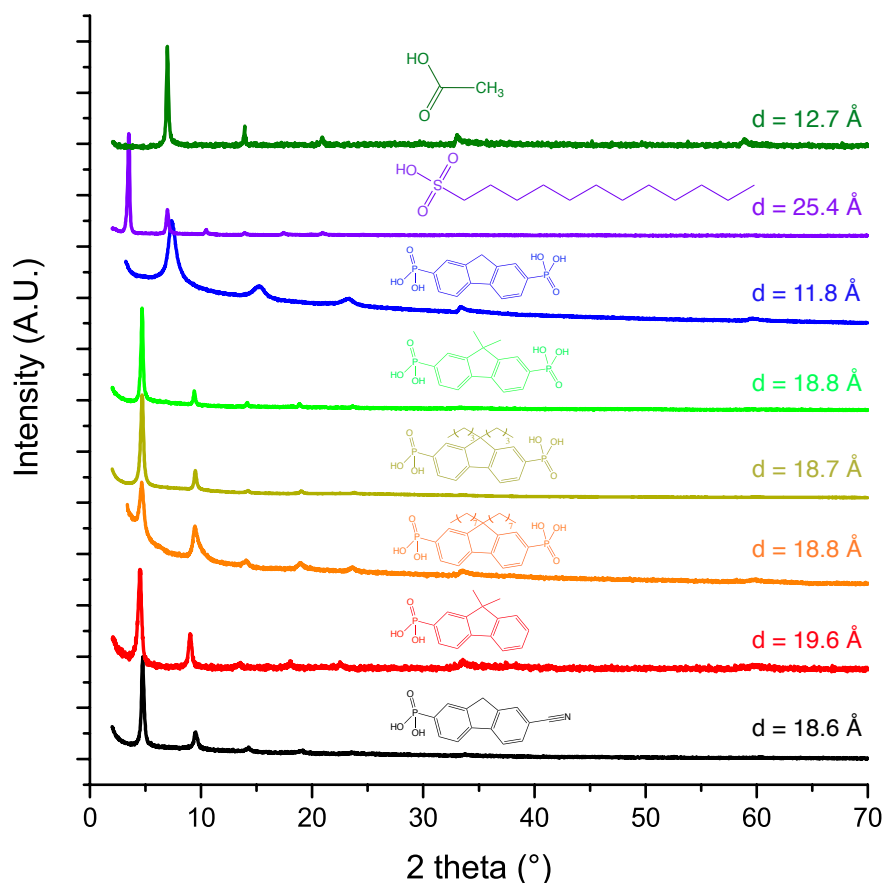


Figure 14 : powder X-ray diffractograms of the hybrids obtained with cobalt hydroxide.

With the assistance of Ziyad Chaker, we have been able to study one (purely hypothetical) possible configuration of the fluorene molecules within the layers (see figure 15). This illustration also helped us determine which was the expected insertion rate of fluorene for a « flat » configuration. The observed insertion rate of 0.17 fluorenes per formula unit appeared to be compatible with this configuration. The absence of lateral functionalization coupled with the two grafting moieties might be the source of this odd behaviour.

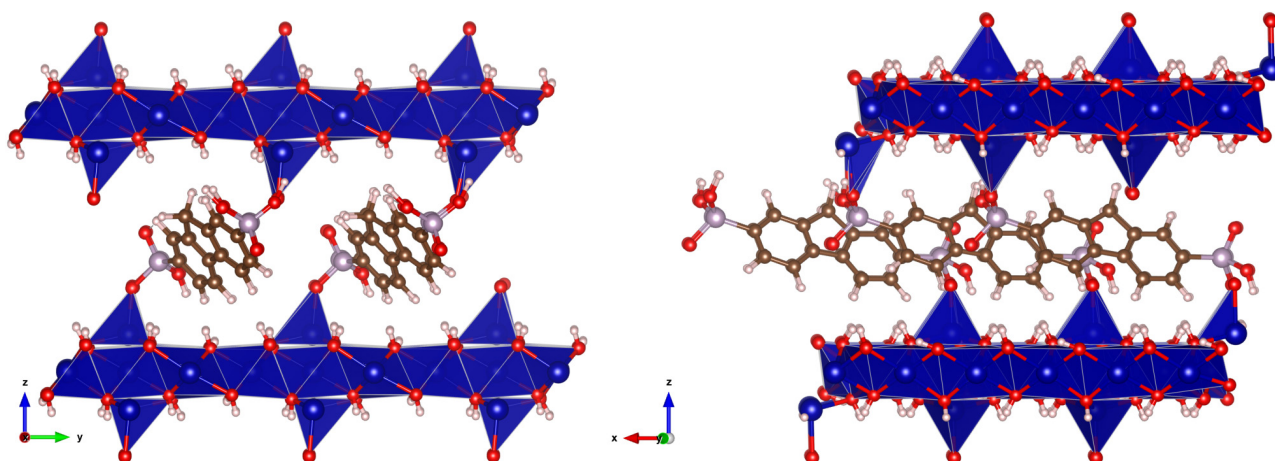


Figure 15 : Illustration of a possible configuration of the fluorenes inside the layers.

Of course, further structural analyses such as diffuse scattering for PDF extraction may give us additional hints about the real interlayer packing of the fluorenes.

4.3. Infrared Spectroscopy of Cobalt Hydroxide Hybrids

All the hybrids also underwent infrared spectroscopy, the approach is the same as for the copper hydroxide. Infrared spectroscopy indicates that the exchange is complete and the signatures of the different molecules are also clearly visible in spectra of the resulting hybrids.

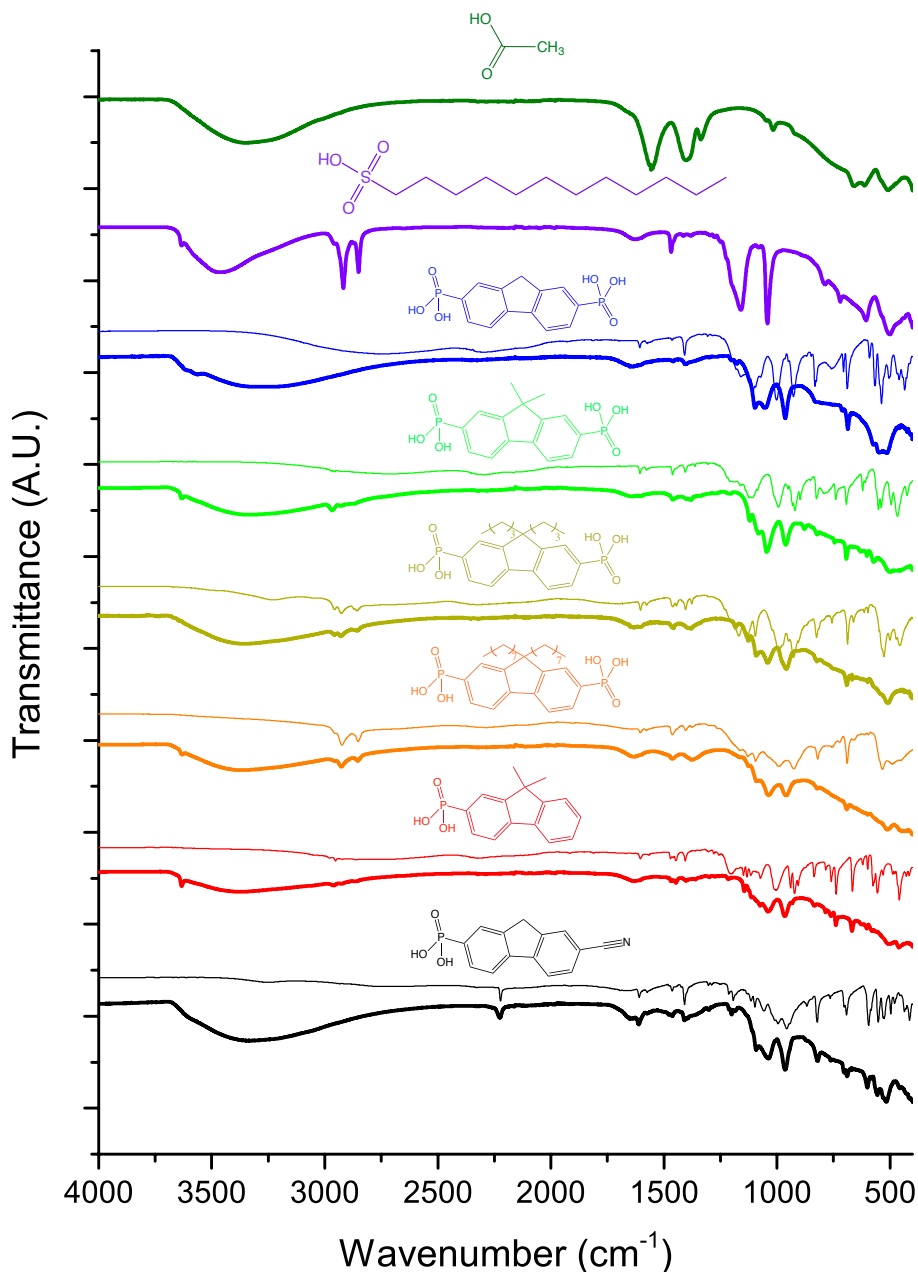


Figure 16 : Infrared spectra of the hybrids obtained with cobalt hydroxide (thin lines represent the molecules alone while bold lines correspond to the hybrids).

As shown above, in each case the signature of the molecule is present in the hybrid compound and the signature of the alkyl chains from dodecylsulfate disappears (at least for compounds without alkyl lateral chains). The table below is an attempt of peak attribution equivalent to the one performed with the copper hydroxide.

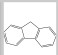
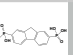
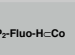
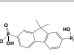
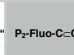
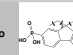
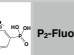
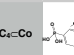
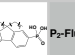
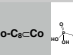
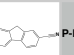
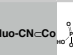
	Co ₂ (OH) ₂ s (D ₂ O) ₂ s													
P(O)(OH) group			1607	1601	1606	1643/ 1604	1603	1604	1604	1633/ 1604	1609	1611	1603	1633/ 1607
C-C ring stretch		1575	1574/ 1557	1571/ 1556/ 1540/ 1517/ 1504	1577	1575	1575		1577		1574/ 1562(w)	1574/ 1558/ 1540/ 1506	1583/ 1567	
C-C ring stretch	1467	1478	1475/ 1464	1488/ 1472/ 1461	1461	1481/ 1460	1461	1460	1463	1460	1476/ 1464	1477/ 1463	1470/ 1462	1469
C-C ring stretch	1456	1447	1449		1444	1446	1445		1440		1447		1456/ 1446	1457/ 1446
C-C ring stretch	1379	1384	1391	1384	1383	1382	1376	1380	1376	1377	1398/ 1382(w)	1397/ 1394		1382
PO ₃ asymmetric stretching (1330 cm ⁻¹)		1311	1333		1337	1337	1343(w)		1339		1332(w)	1334(w)	1340	1339
	1293	1300	1306	1300	1304	1299	1303	1299	1301	1297(w)	1303	1302	1302	1299
	1277		1283	1277		1274	1268(w)	1264			1289	1289	1278	1275
C-H inplane bending	1249/ 1223/ 1195(w)	1234	1244	1260/ 1237	1261(w)		1230	1228			1250	1245(w)	1255	1259
C-H inplane bending and P=O (1200-1220cm ⁻¹)	1159	1192	1198/ 1180/ 1160	1200/ 1179	1161	1218/ 1207	1205	1206	1162	1166	1212/ 1206/ 1193	1211/ 1200/ 1187	1203/ 1158(w)	1216/ 1205
C-H inplane bending			1140		1140		1185/ 1168	1183			1180	1181	1148	1143
C-H inplane bending			1121	1123(w)	1124	1121	1138	1138(w)	1128	1126	1145/ 1132	1137(w)	1133	1126
PO ₃ symmetric stretching (1110cm ⁻¹)	1104(w)	1108	1106		1109		1128	1125			1115	1111(w)	1115	1112
		1092	1095	1097	1086	1081	1095	1090	1094	1090	1098	1092	1088	
P-O		1079	1072		1073(w)						1057		1073	1073
Probable zone	1042	1019	1028(w)	1050		1045	1021	1041	1039	1038	1021	1037		1039
		1000	1001	1007	993		1007(w)/ 992	1006	(1010)/ 991		1009/ 995	1005	1011/ 1005	
	831(w)		832/ 825	831	825	822	824/ 813	822	820	822	821	820	835	833
PO ₃ Symmetrical deformation (605cm ⁻¹)	606		604		609/601	602	614/ 597	599	596	598	594	600	598	601

Table 5 : IR bands of all hybrids and all starting molecules.

As can be observed from the table above and figure 16, the fingerprints of the different molecules are clearly visible in the hybrid compounds. The exchange between the molecule of interest and the dodecylsulfonate seems to be complete as we don't see dodecylsulfate signature especially the strong CH₂ bands at 2918 and 2850 cm⁻¹ corresponding to the antisymmetric and symmetric stretching respectively. Further analysis has been made to get more information about the insertion ratio and the water content.

4.4. TGA/TDA, Micro-Analysis and EDX

As for copper hybrids, the cobalt hybrids underwent the same procedure with TGA/TDA, micro-analysis and EDX. It can be seen in figure 17 the TGA/TDA analyses of P-Fluo-C≡Co which is typical of the behaviour of all the other hybrids. As with the copper hybrid, there is no clear water loss followed by the decomposition but a gradual mass loss followed by a first event at 160°C that could be corresponding to a partial catalytic oxidation of the cobalt as described in the work of Markov, Petrov and Petkov in a similar system.⁷⁴

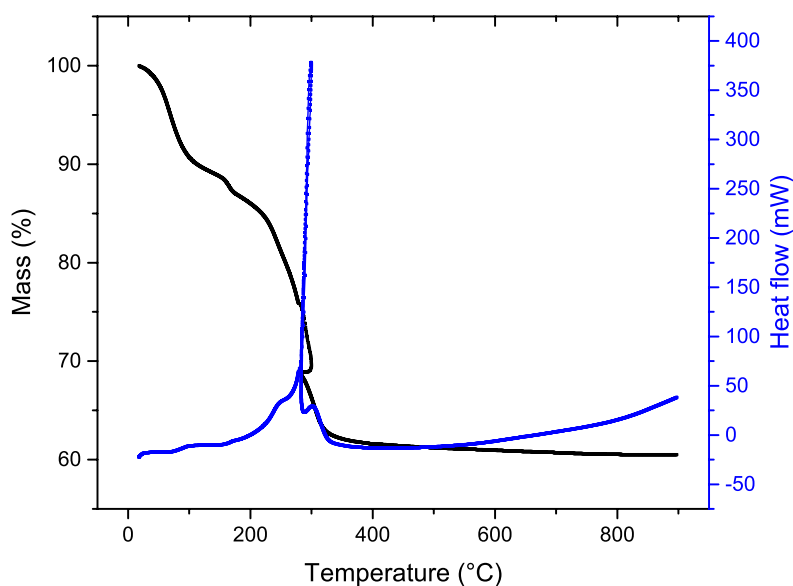


Figure 17 : Typical TGA/TDA obtained for P-Fluo-C≡Co, typical of all fluorene-cobalt-hybrids.

The result of this degradation leads to a mixture of $\text{Co}_3(\text{PO}_4)_2$ and Co_3O_4 , the ratio between the two phases being dependent on the insertion ratio. As the crystallinity of the obtained ashes was much higher than with copper we tried to perform a quantitative analysis from one sample to compare it to the micro-analysis results. However, the ratio given after refinement made by Marc Lenertz (32.0(2)% of $\text{Co}_3(\text{PO}_4)_2$ and 68.0(6)% of Co_3O_4) were unrealistic compared to our understanding of the system. Indeed, this ratio corresponds to an insertion rate of 0.91 per formula unit, which is impossible as it is above the theoretical maximum of 0.8 for 100% of grafting onto cobalt in tetrahedral sites. Indeed, to maintain the geometry of the layer, the ratio of octahedral to tetrahedral cobalt must be 1.2 to 0.8 respectively. A difference in the crystallinity of the two phases could explain the failure of the quantitative analysis. Another potential explanation would be the grafting on the octahedral cobalt, even if this hypothesis is unlikely, but more evidence should be gathered first. The results are displayed in the table below with the same caveats as discussed earlier.

TGA/TDA water content measured (calculated)	Co:P ratio <i>via</i> EDX measured (calculated)	Micro-analysis results measured (calculated)	Obtained formula
10.7% (8.0%)	5.43 (5.88)	Co : 39.53 (39.82), C : 21.01 (20.69) H : 3.63 (3.75), P : 3.73 (3.56)	P-Fluo-C≡Co $\text{Co}_2(\text{OH})_{3.66}(\text{C}_{15}\text{H}_{13}\text{O}_3\text{P})_{0.34} \cdot 1.3\text{H}_2\text{O}$
12.1% (11.4%)	4.32 (5.40)	Co : 45.9 (37.35), C : 19.77 (19.71) H : 3.38 (3.50), P : 2.24 (3.63)	P-Fluo-CN≡Co $\text{Co}_2(\text{OH})_{3.63}(\text{C}_{14}\text{H}_8\text{O}_3\text{PN})_{0.37} \cdot 2\text{H}_2\text{O}$
-	6.50 (5.88)	C : 10.61 (10.53) H : 3.21 (2.94)	P ₂ -Fluo-H≡Co $\text{Co}_2(\text{OH})_{3.66}(\text{C}_{13}\text{H}_{10}\text{O}_6\text{P}_2)_{0.17} \cdot 1\text{H}_2\text{O}$
10.5% (10.0%)	5.97 (3.45)	Co : 38.24 (38.01), C : 16.95 (17.47) H : 3.37 (3.53), P : 5.83 (4.65)	P ₂ -Fluo-C≡Co $\text{Co}_2(\text{OH})_{3.42}(\text{C}_{15}\text{H}_{14}\text{O}_6\text{P}_2)_{0.29} \cdot 1.7\text{H}_2\text{O}$
-	-	Co : 40.80 (41.31), C : 15.74 (15.91) H : 4.24 (4.00), P : 3.36 (3.91)	P ₂ -Fluo-C ₄ ≡Co $\text{Co}_2(\text{OH})_{3.64}(\text{C}_{21}\text{H}_{26}\text{O}_6\text{P}_2)_{0.18} \cdot 1.5\text{H}_2\text{O}$
10.0% (18.0%)	6.87 (10.00)	Co : 40.35 (40.79), C : 12.06 (12.13) H : 3.58 (4.81), P : 2.67 (2.15)	P ₂ -Fluo-C ₈ ≡Co $\text{Co}_2(\text{OH})_{3.8}(\text{C}_{29}\text{H}_{42}\text{O}_6\text{P}_2)_{0.10} \cdot 2.9\text{H}_2\text{O}$

Table 6 : Different insertion ratios of the cobalt hybrids.

After these analyses of the obtained hybrid, it was also important to see if the sought properties were still present after functionalization. To that end, we performed several measurements described in the section below.

5. Properties of the Hybrid Compounds

5.1. Luminescence of Hybrid Compounds

The first property we investigated was the luminescence of the hybrids, in collaboration with Mathieu Gallart. Indeed, the fluorene is well known for its luminescence^{75, 76} and the changes of its properties upon functionalization inside double layered hydroxide for example.⁷⁷ For our compounds, despite all the fluorenes used being actively luminescent (emission around 385 nm for an excitation at 340 nm) only the hybrids with the fluorenes bearing long lateral chains retain this property (see figure 18).

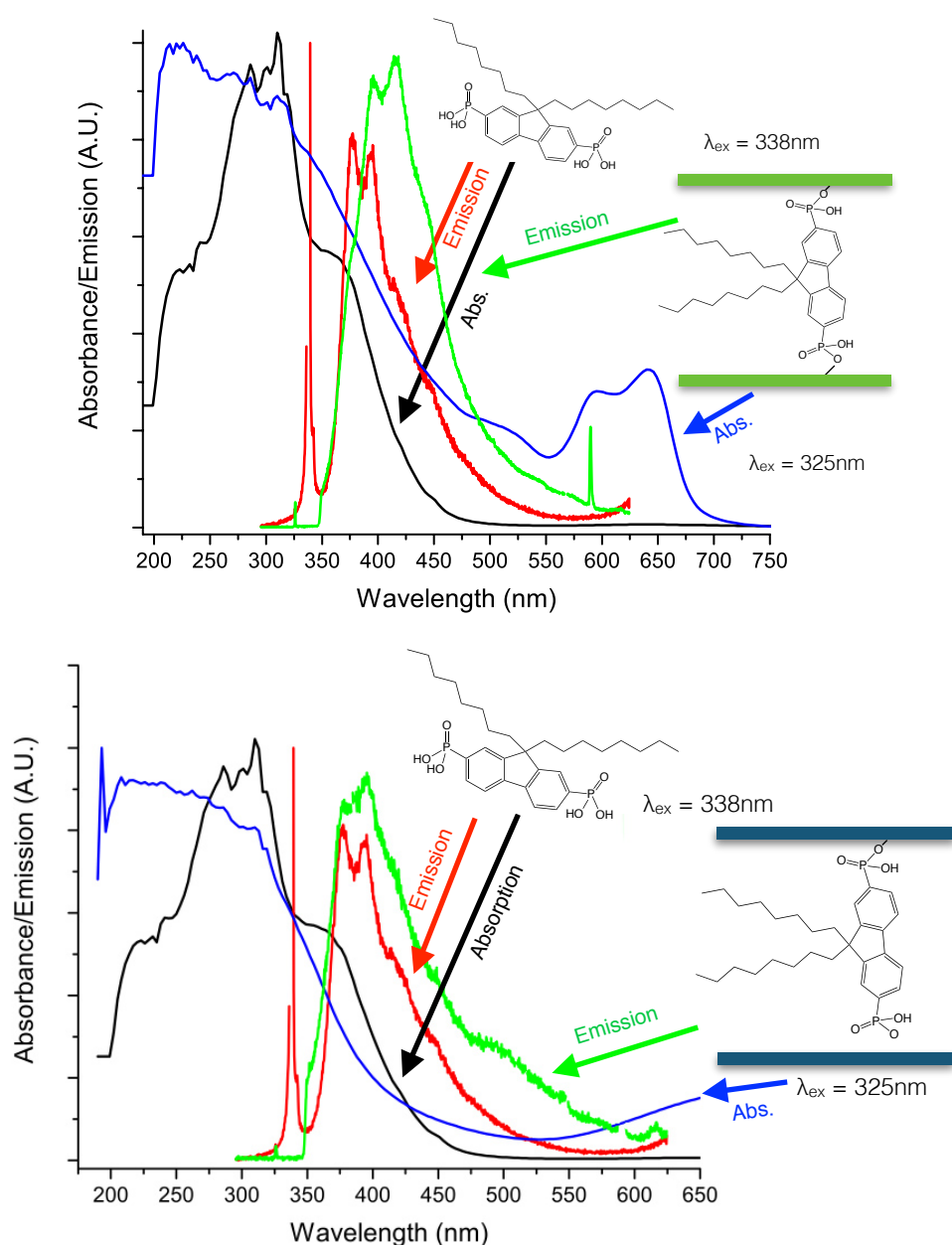


Figure 18 : Kubelka Munk corrected UV-Visible absorption and emission spectra of $P_2\text{-Fluo-C}_8$ superposed with the ones of $P_2\text{-Fluo-C}_8\text{Co}$ (top) and $P_2\text{-Fluo-C}_8\text{Cu}$ (bottom).

A hypothesis is that the quenching observed for the other hybrids is mostly due to intermolecular interactions between fluorene moieties in the interlamellar spacing as observed for oligothiophenes⁷⁸ and oligophenylenevinyls.⁷⁹ As seen in figure 18, the emission for bulky fluorenes are nearly identical as the emission observed with the fluorene alone in solid state. The slight shift observed with the cobalt hydroxide hybrid could be explained by the reabsorption of the inorganic matrix that is more important in the 375 nm region compared to copper hydroxide.

Further measurements could be done on such systems, such as time resolved spectroscopy to see if the lifetimes significantly vary between the organic molecules alone and the hybrid systems.

Among the properties of our hybrid systems, the magnetic properties of the hybrid compounds have also been measured, the results are shown below.

5.2. Magnetic Properties of Hybrid Compounds

5.2.1. Magnetic Properties of Copper Hydroxide Hybrids

As stated before the general magnetic behaviour of the copper compounds is antiferromagnetic. The inverse of the susceptibility varies linearly with the temperature above 200 K and is fitted by the Curie-Weiss law and the results are listed in the table below.

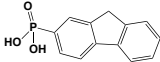
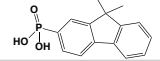
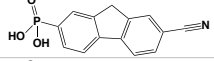
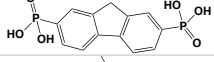
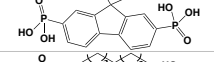
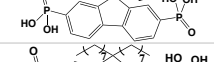
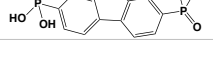
Molecule in the interlamellar space	Reference	Curie Constant ($\text{emu}\cdot\text{K}\cdot\text{mol}^{-1}$)	Weiss temperature θ (K)	Magnetization at 7 T (μ_B) (at 1.8 K)
	P-Fluo-HCCu	0.72	-12.9	0.39
	P-Fluo-CCCu	0.94	-31.7	0.49
	P-Fluo-CNCCu	0.62	-11.1	0.32 ($\mu_0H = 5$ T)
	P ₂ -Fluo-HCCu	0.76	-30.1	0.30
	P ₂ -Fluo-CCCu	0.71	-3.3	0.50 ($\mu_0H = 5$ T)
	P ₂ -Fluo-C ₄ CCu			
	P ₂ -Fluo-C ₈ CCu	0.95	-19.9	0.57

Table 7 : Magnetic properties of the layered copper hydroxide hybrids.

The Curie constants found are in the expected range for two copper(II) ions^{51, 80} in this configuration, except for P-Fluo-CNCCu which presents a somehow too small Curie constant. The results have been obtained at the very end of this PhD and could not be investigated further. The χT products decrease regularly with the temperature decrease, indicating an overall antiferromagnetic behaviour, without any magnetic ordering down to the lowest accessible temperature tested (1.8 K).

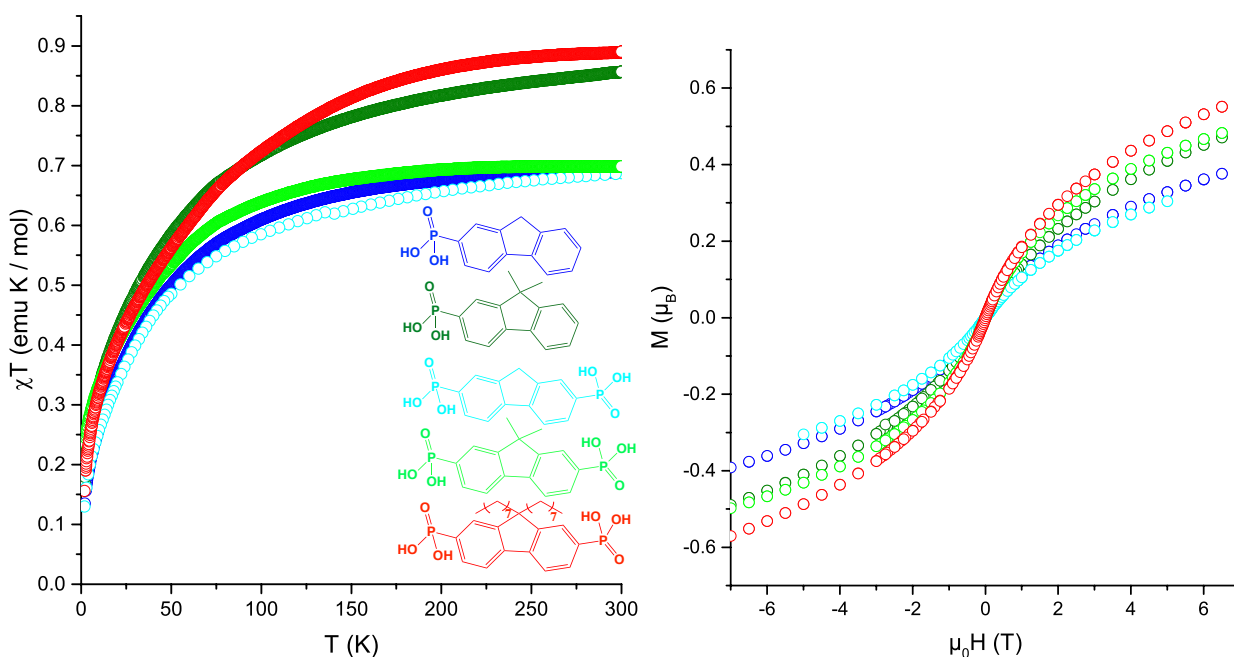


Figure 19 : Magnetic behaviour of copper hybrids as χT vs. T plots under an applied dc field of 5000 Oe (left) and magnetization vs. field at 1.8 K (right).

The functionalization does not modify the antiferromagnetic behaviour of the hydroxides for the copper hybrids, as expected for our chemical model. The cobalt hydroxide, however, was the main system studied to obtain more interesting magnetic properties.

5.2.2. Magnetic Properties of Cobalt Hydroxide Hybrids

The cobalt hydroxide compounds all behave like ferrimagnets, with the characteristics shown in the following table :

Molecule in the interlamellar space	Reference	Curie Constant (emu·K·mol ⁻¹)	Weiss temperature θ (K)	Curie Temperature T_c (K)	Magnetization at 7 T (μ_B) (at 1.8 K)	Coercive field at 1.8 K (T)
	P-Fluo-C≡Co	6.09	-21.7	11.8	2.43	0.20
	P-Fluo-CN≡Co	5.70	-31.4	8.5	2.46	0.10
	P ₂ -Fluo-C≡Co	5.95	-22.4	11.9	2.43	0.33
	P ₂ -Fluo-C ₄ ≡Co	5.73	-63.4	13.5	1.95*	-
	P ₂ -Fluo-C ₈ ≡Co	6.02	-13.6	17.8/11.0/6.3	2.92	0.22

Table 8 : Magnetic properties of layered cobalt hydroxides hybrids (* Magnetization obtained at 2 K and 5 T).

As can be observed in the table above the Curie constants are ranging between 5.70 and 6.09 emu·K·mol⁻¹ which is in good agreement with a mixture of tetrahedral and octahedral high spin cobalt(II) ions. Indeed the values found in the literature^{80, 81} are ranging from 2.2 to 2.8 emu·K·mol⁻¹ for a tetrahedral cobalt(II) ion and from 2.8 to 3.4 emu·K·mol⁻¹ for an octahedral cobalt (II) ion. As seen in figure 20, upon cooling the χT product of all the cobalt hybrids go through a minimum around 80 K. This small decrease is described as a consequence of the spin-orbit coupling and/or antiferromagnetic interactions between the cobalt(II) moments.⁸³

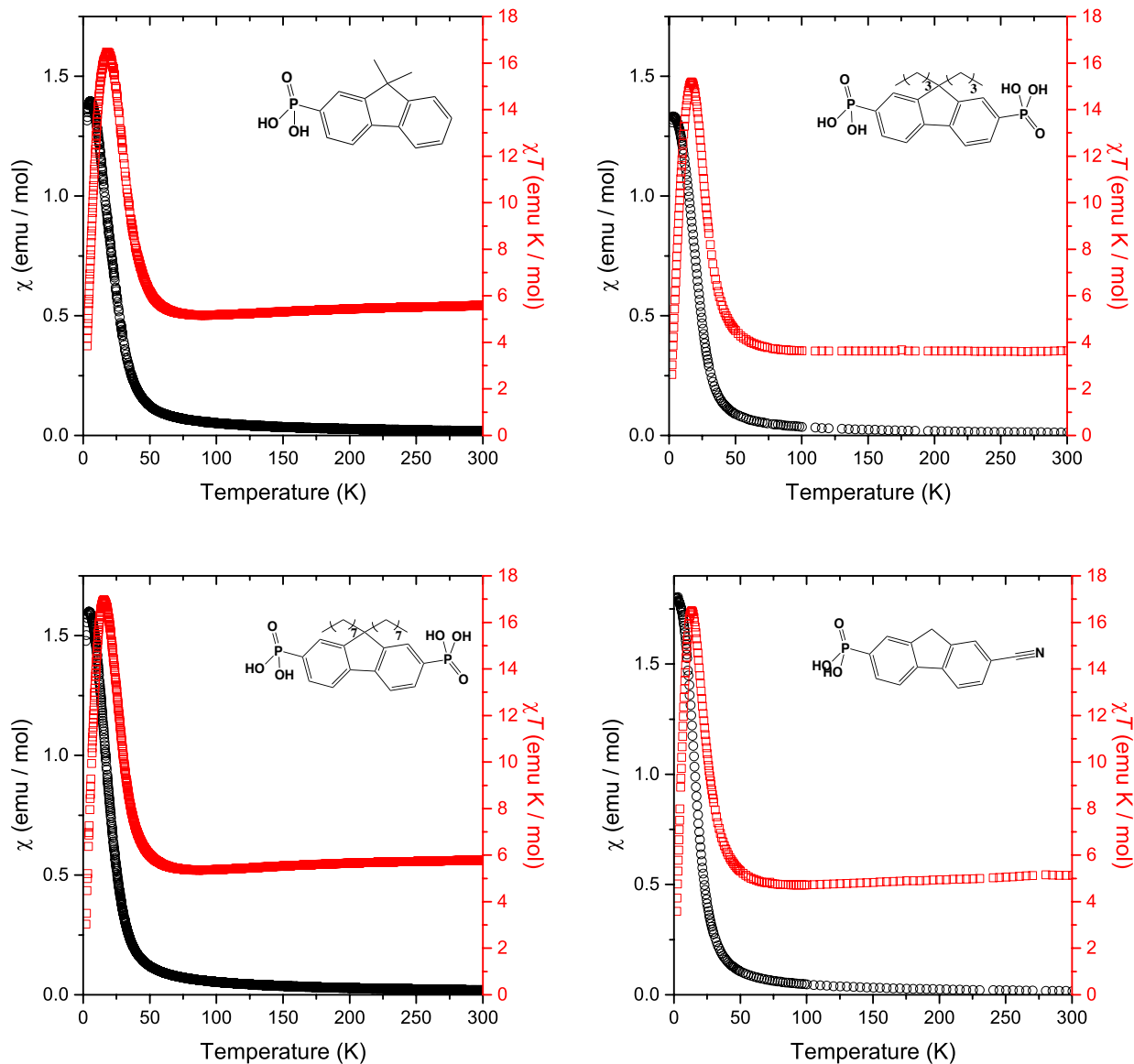


Figure 20 : χ and χT products of several cobalt fluorene derivative hybrids measured at 5000G.

Below 80 K an increase of the χT product is observed and related to the occurrence of short range ferromagnetic-like interactions, leading to a ferrimagnetic ordering supported by the occurrence of an out of phase signal in the imaginary part of the ac susceptibility, χ'' (see figure 21) and by the low values of the saturation magnetization (see below). The ordering temperatures were determined from the maximum of the real part χ' of the ac susceptibility measurements.

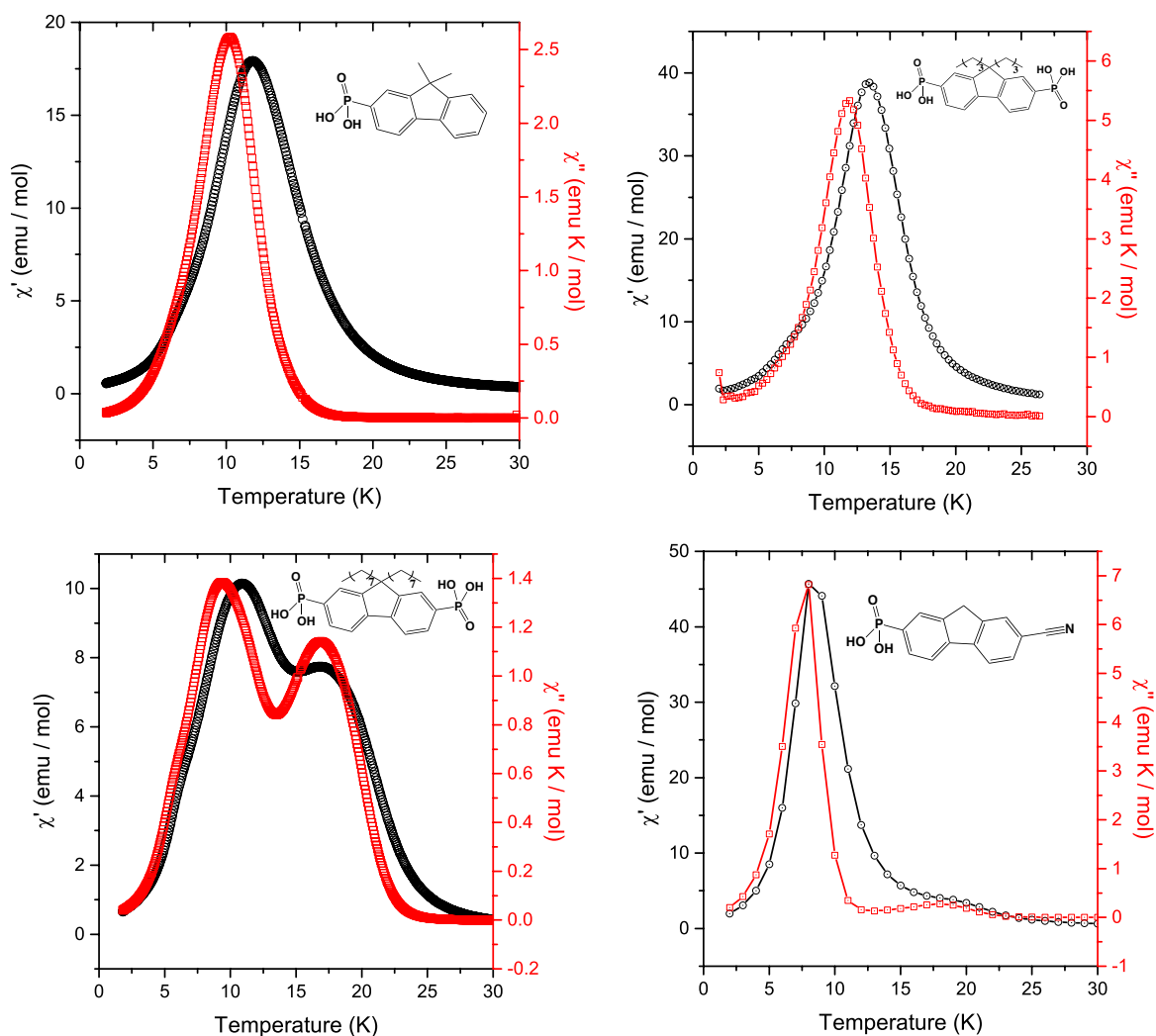


Figure 21 : ac susceptibility measurements of several layered cobalt hybrids ($f = 95$ Hz, $\mu_0 H_{ac} = 0.3$ mT).

As seen from the figure above, the presence of a higher temperature magnetic ordering (17 K) is observed in some compounds and especially present in P_2 -Fluo- C_8 -Co. To investigate further this behaviour, we tried to perform multiple measurements of the same sample. The results of these experiments are shown in figure 22, for clarity reasons, only the imaginary part of the ac measurements is shown.

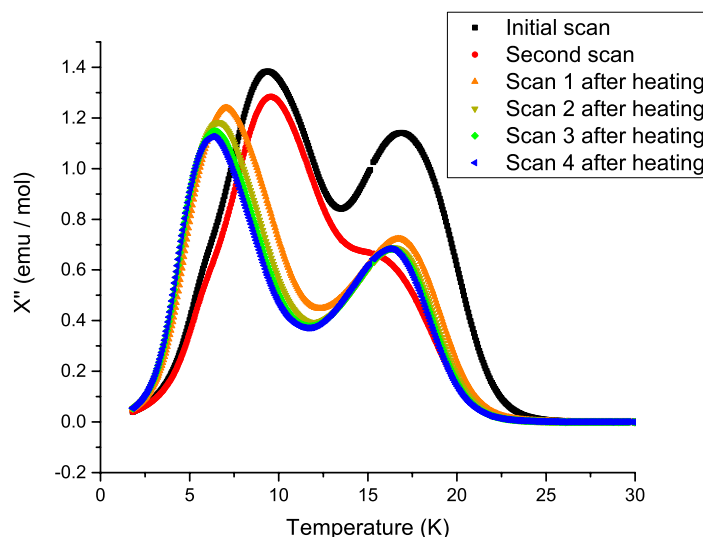


Figure 22 : ac susceptibility measurements performed on P_2 -Fluo- C_8 -Co.

The difference between the first and second scan from the figure above is a period of a few weeks, during which the sample was removed from the SQUID machine. The differences observed for this period can be due to hydration of the compound.

After the second measurement, the next four scans have been performed after heating the sample at 60°C for 30 minutes in the SQUID, indeed, at first the presence of water was thought to be the cause of these multiple phases. The heating only suppresses the phase around 9 K and greatly amplifies the phase present at 6 K while maintaining the high temperature phase unchanged. The presence of several peaks in ac magnetometry has been observed in other cases for layered magnets such as cyanide-bridged bimetallic assemblies⁸³ or bimetallic oxalates⁸⁴ or also in cobalt hydroxide hybrid functionalized with thiophenecarboxylates.⁷⁸

The presence of multiple local structures inducing different couplings might be an explanation of this behaviour. It must be stressed that this property is also very much synthesis dependent, as can be seen from figure 23 below. For one synthesis, about only one magnetic phase is visible, whereas for the other two, the ratio between the phases at low and high temperatures varies greatly. The compounds have been prepared from the same batch of starting compound which indicates that these changes are not due to the starting cobalt hydroxy dodecylsulfonate but rather linked to the intercalation process.

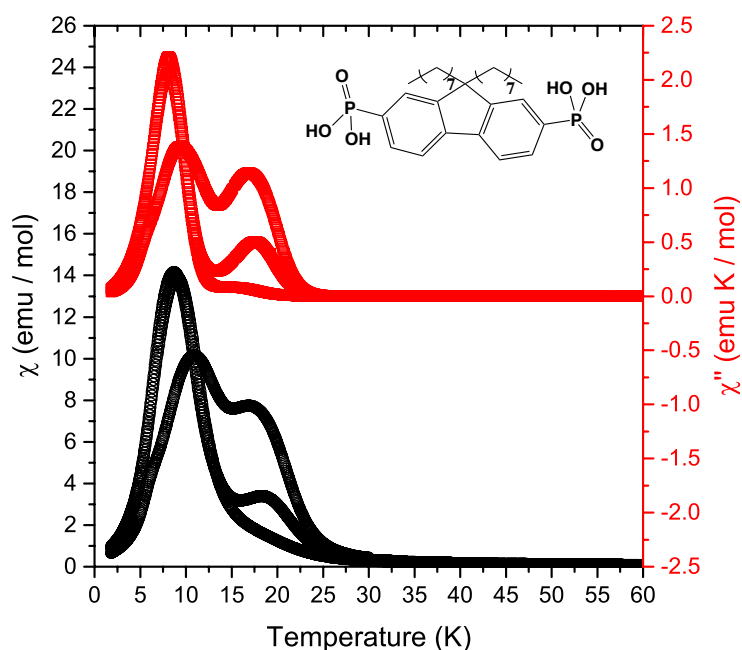


Figure 23 : ac susceptibility measurements of several samples of cobalt of $P_2\text{-Fluo-C}_8\text{-Co}$.

Finally, the magnetization versus field curves that have been measured at 1.8 K and confirm the ferromagnetic-type ordering of the cobalt hydroxides hybrids with the presence of hysteresis loops and coercive fields ranging from 0.10 to 0.33 T. As can be seen in figure 24, the low value of the moments at high field (5-7 T) ranging from 2.43 to 2.92 μB compared to the expected value for a total alignment of the moments (4-6 μB for two cobalt (II) ions) confirms the ferrimagnetic ordering. This ordering results from the antiparallel alignment of the moments leads by tetrahedral and octahedral cobalt ions.⁸² Indeed, for octahedral $S = 3/2$, $L = 1$ cobalt (II) the magnetization saturation value $MS = 2.87 \mu\text{B}$ is found in $\text{Co}_2(\text{OH})_3(\text{NO}_3)$ which contains exclusively octahedral sites,⁸⁵ and for a tetrahedral $S = 3/2$ cobalt (II) ion, this value is around 3 μB .

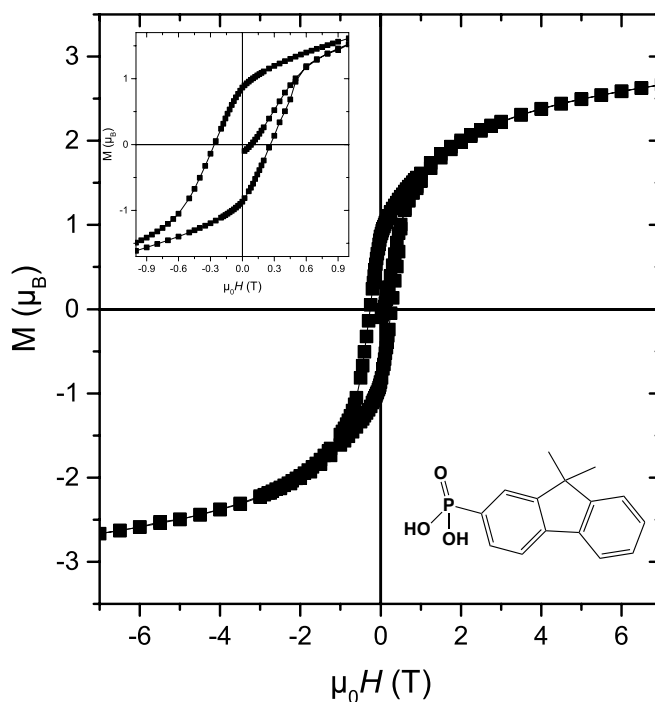


Figure 24 : Magnetization vs. field curve of P-Fluo-CcCo hybrid (magnification of the opening in insert).

We can see in this section that the magnetic properties of the cobalt hybrid compounds are preserved *via* the functionalization, even if their ordering temperatures have been altered compared to the starting compound. These results show that these materials were suitable for the next phase towards multi-functionality that is the measurement of a magneto-electric effect described thereafter.

5.3. Magneto-Electric Properties of Layered Cobalt Hydroxide Hybrids

As stated above, the goal of my PhD was to add a second ferro order into the hydroxide *via* the insertion of polar molecules. One of the challenges of this PhD was to be able to measure, out of a powder, the dielectric properties of our samples. This study was performed in collaboration with Alain Pautrat from CRISMAT in Caen. Due to the nature of our compound and the potential variation of structural and magnetic properties upon heating, thermal annealing of the pellets was ruled out. The pellets were simply obtained *via* cold-pressing of the pure powders. The use of a binder to improve the mechanical properties of the pellet such as Rhodoviol was also ruled out due to the difficulty to obtain a control sample. These measurements are, to the best of my knowledge, the first ones made on such cobalt hydroxide. This field is indeed dominantly covered by oxide systems such as BaTiO_3 ^{86, 87}, BiFeO_3 ^{88, 89} or $\text{Ba}_{1-x}\text{Sr}_x\text{TiO}_3$ composites⁹⁰ for example. Some scarce measurements have been described in the case of hydroxides such as rare earth hydroxides⁹¹ or more recently in iron oxy-hydroxide composite.⁹²

The pellets obtained after cold-pressing of the pure powders were 5 mm in diameter and with a thickness of 40 to 90 μm depending on the mechanical properties of each pellet. Once the pellet is made, silver electrodes are applied *via* silver paste DuPont 4929 and the copper wires are soldered to the sample holder wires with an indium solder (see figure 25). The choice of indium is due to its excellent malleability and ductility at low temperatures, allowing to compensate for the thermal fatigue due to thermal expansion-shrinking cycles, as well as having good electrical conductivity.

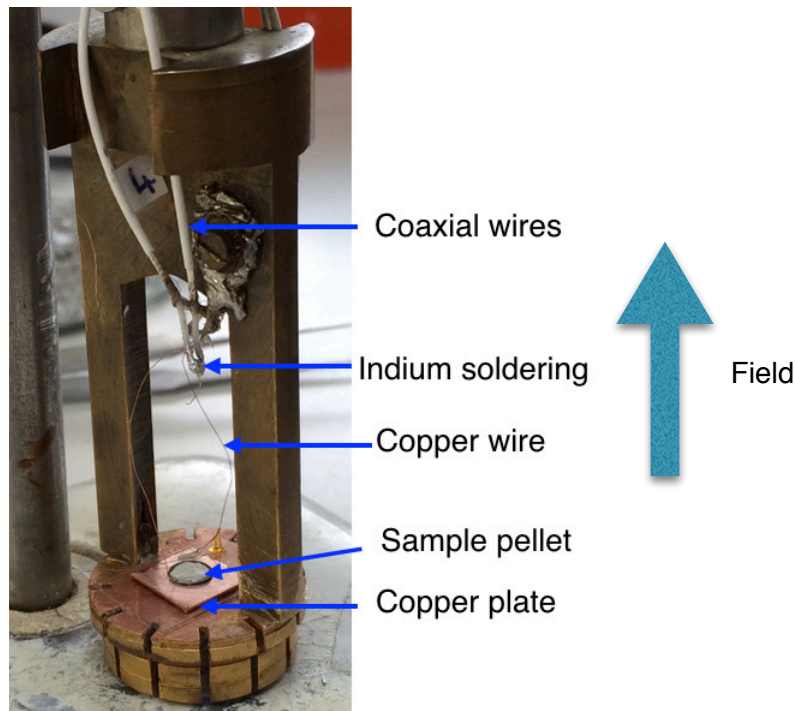


Figure 25 : Sample holder and field direction once installed in the cryostat (copper plate not used in measurements).

The sample holder is then put in a cryostat with supra-conducting magnets and connected to an Agilent RLC impedance analyser *via* coaxial cables. The first measurement that must be done is a measurement impedance versus frequency measurement. Indeed, the impedance signal can be hidden behind multiple intrinsic contributions such as electronic or ionic conduction or even grain boundaries. To that end a working tension inferior to 0.5 V is applied with a frequency ranging from 100 Hz to 800 kHz. The « slowest » phenomena such as free charges movements being visible only at the lower frequency while only the « fastest » such as ionic or electronic movements can be observed at high frequency. Once the good working frequency range is found (quasi-purely capacitive regime at 1-10 kHz) several experiments have been done on the pellets.

Unfortunately, due to very strong leakage currents, it has not been possible to measure unambiguously the ferroelectric properties of the compounds. Yet we managed to evidence a strong and interesting magneto-electric coupling on several samples. Due to the time required to perform the experiments we have not been able to measure all the samples described in this chapter within the time of this PhD.

5.3.1. Magneto-Electric Properties of $P_2\text{-Fluo-C}_8\text{Co}$

The magneto capacitance was measured for two different geometries, *i.e.* $E_{ac} // B$ and $E_{ac} \perp B$ (figure 26), while the $E_{ac} // B$ configuration was the most studied.

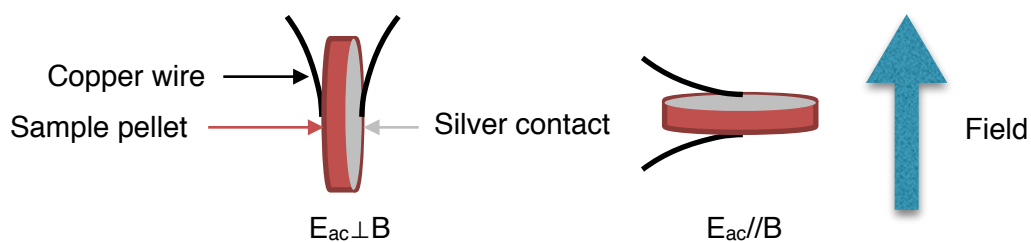


Figure 26 : Geometries used for impedance measurements.

As shown in figure 27, the variation of C_p as function of temperature in the low temperature range and measured at different isotherms when warming the sample. Within our experimental resolution, no dielectric anomaly was detected that would correspond to the temperature of long range magnetic ordering.

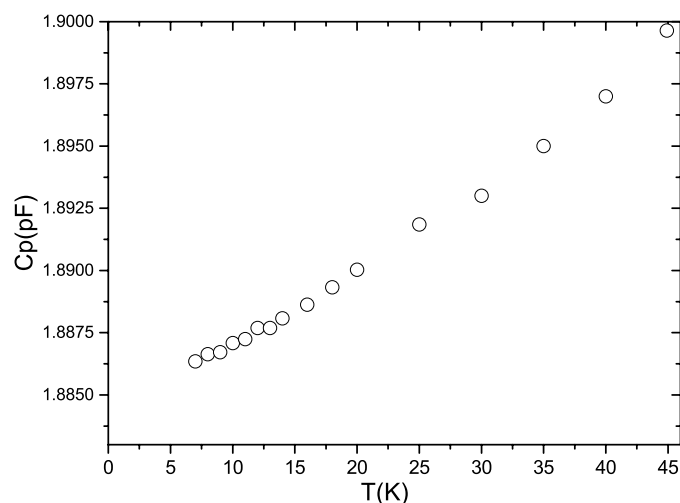


Figure 27 : Capacitance of $P_2\text{-Fluo-C}_8\text{-Co}$ hybrid as a function of temperature measured at a 100 kHz frequency.

However, as shown in figure 28, we do observe a positive magneto capacitance ($ME = C_p(B)/C_p(0) - 1 = 0.16\%$ at 10 K and 7 T) as well as its variation as function of temperature.

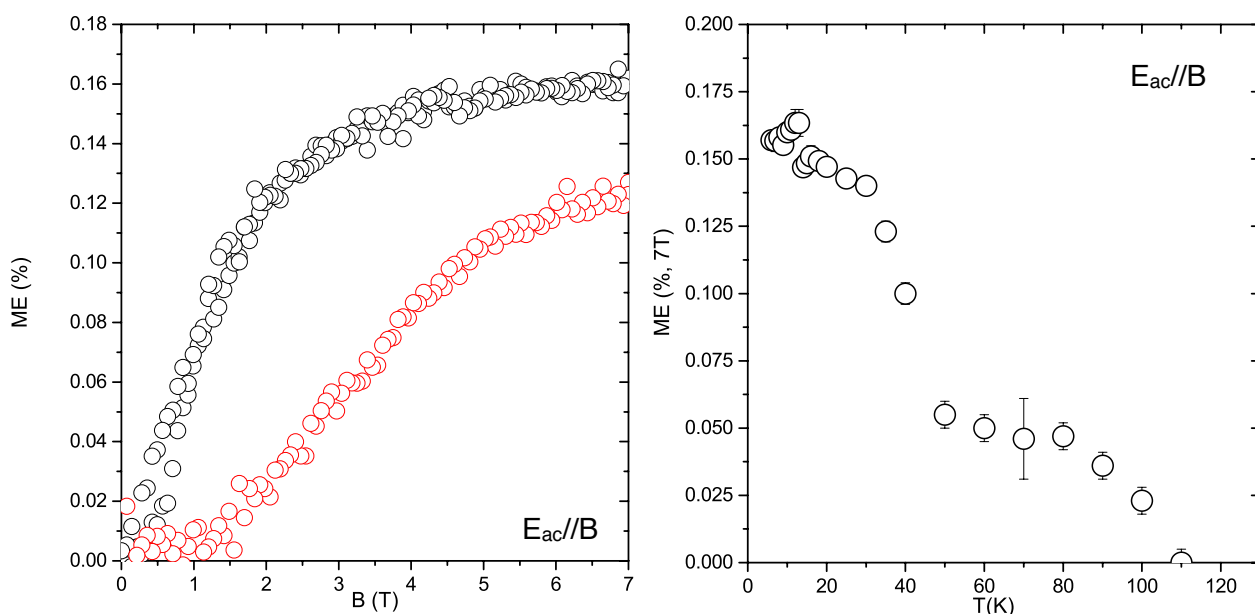


Figure 28 : Relative magneto capacitance as a function of the magnetic field at 10K (open black circles) and 35K (open red circles) (left) and relative magneto capacitance at 7 T as a function of temperature (right) of $P_2\text{-Fluo-C}_8\text{-Co}$.

The magneto capacitance effect seen from figure 28 persists up to large temperature around 110 K, well over the magnetic ordering temperature of the material. There are two other specific temperatures that can be observed, the first one at 50 K where the magneto-electric effect changes by a factor of 2.6 and at 17 K where a smaller but clear anomaly can be observed. A comparison with the thermal variation of magnetic susceptibility indicates some interesting similarities. The highest temperature corresponds to the departure from a pure Curie-Weiss susceptibility (figure 29) and the probable appearance of short range magnetic correlations which seems to trigger the magneto-electric effect in this compound.

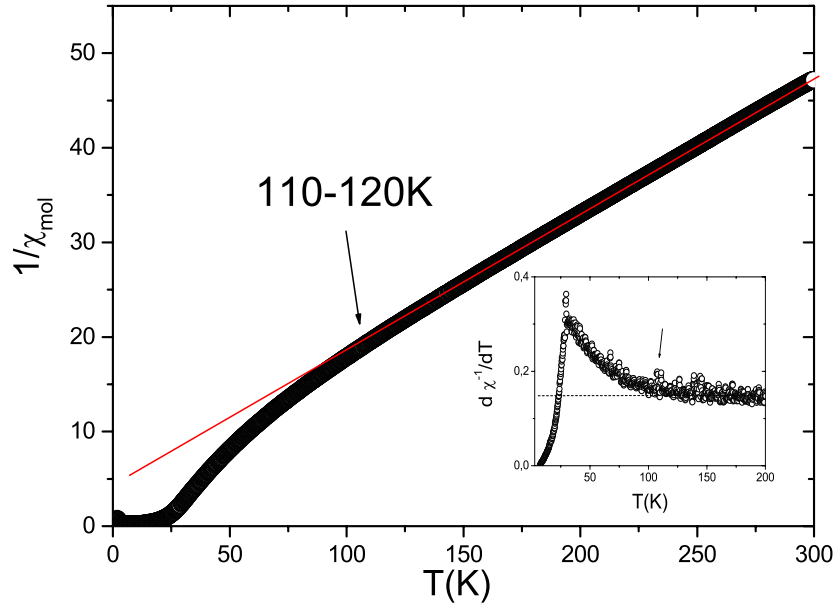


Figure 29 : Plot of the reverse susceptibility as a function of temperature of $P_2\text{-Fluo-C}_8\text{Co}$.

The two other anomalies correspond respectively to the change of dimensionality of the magnetic behaviour of the hybrid compound, from 2D to 3D short range magnetic correlations (around 50K) and the long-range magnetic ordering (around 17 K).

Unfortunately, as discussed in the previous section, our compound having a distribution of ordering temperatures (figure 23), it was not possible to perform an accurate dimensionality analysis of the magnetic behaviour. However, this transition from 2D to 3D is reported in the literature in a similar temperature range.^{93, 94}

Another interesting characteristic of this material is that the magnetic threshold field necessary for the magneto-electric effect to appear becomes zero below the magnetic ordering temperature of the compound (figure 30), indicating that the internal field of the sample can also trigger the effect.

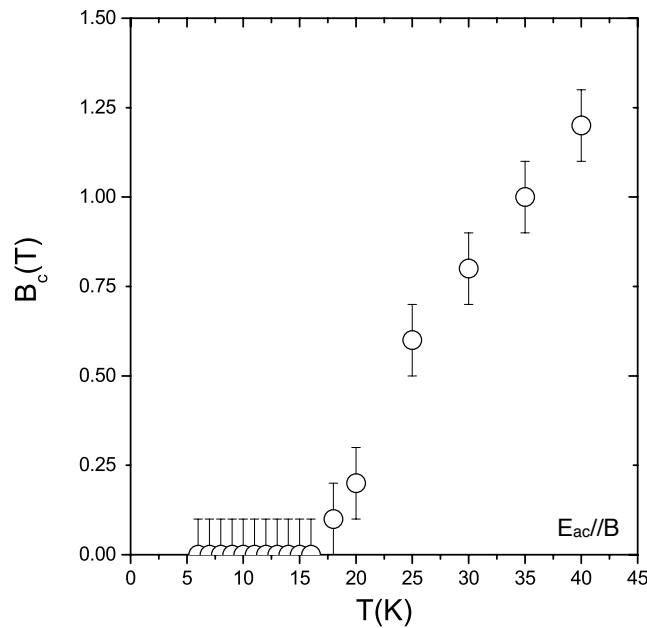


Figure 30 : Magneto-electric threshold field as a function of temperature of $P_2\text{-Fluo-C}_8\text{Co}$.

The second geometry, $E_{ac}\perp B$, was also tested and a magneto capacitance effect was observed, but with opposite sign and a lower intensity, as shown in figure 31, where the magneto-electric effects are measured at the same temperature for both geometries. This anisotropic effect is likely related to the preferred local orientation of the microcrystalline platelets that compose the pellets.

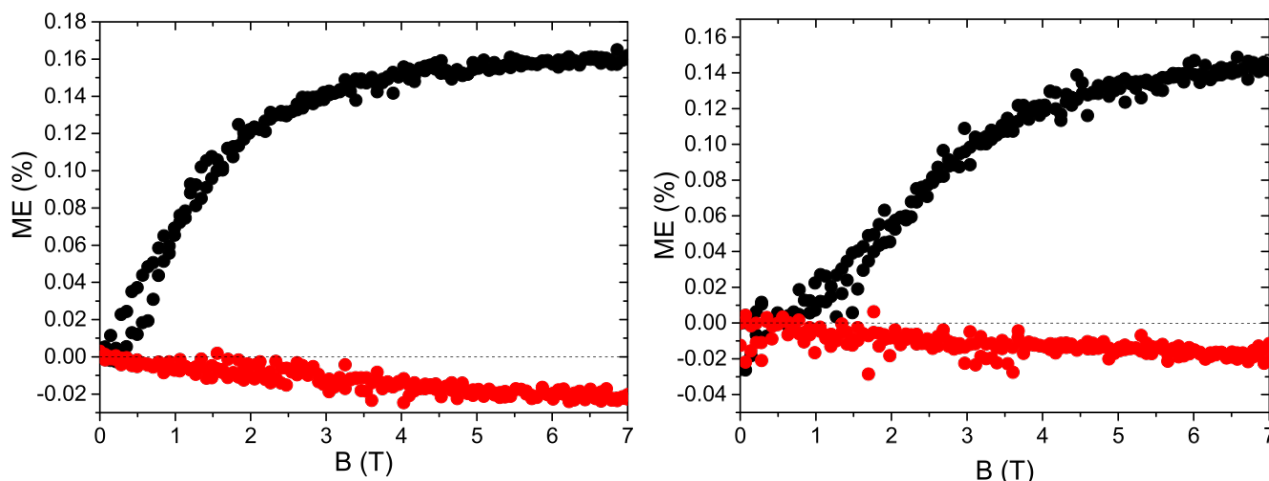


Figure 31 : Relative magneto capacitance as a function of temperature for $E_{ac}\parallel B$ (black points) and $E_{ac}\perp B$ (red points) at 10 K (left) and 25 K (right).

5.3.2. Magneto-Electric Properties of P_2 -Fluo- $C\subset Co$

For this sample, the magneto-electric properties were only measured for the $E_{ac}\perp B$ configuration due to the extremely time consuming measurements. We observe in figure 32 a small negative magneto capacitance with the same magnitude as the P_2 -Fluo- $C_8\subset Co$ hybrid which disappears near 60 K.

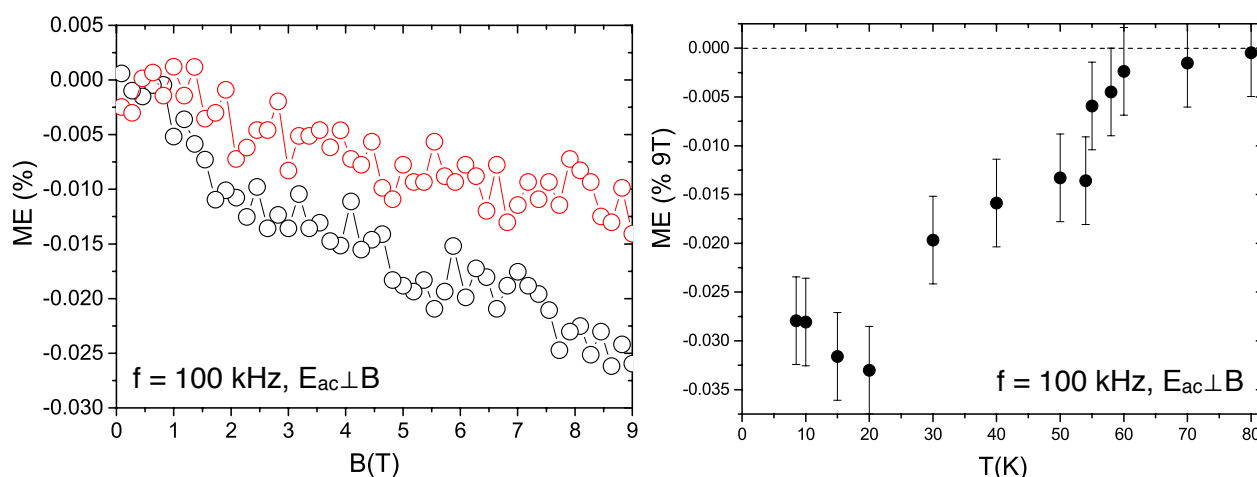


Figure 32 : Relative magneto capacitance of P_2 -Fluo- $C\subset Co$ as function of the magnetic field at 10 K (open black circles) and 30 K (open red circles) (left) and as a function of temperature at 9 T (right).

For this hybrid a dielectric anomaly is observed at the temperature where the magneto capacitance appears. This anomaly is observed both when sweeping the temperature and after a long stabilization time at different isotherms (figure 33), excluding any thermalization effects that could be due to the very bad thermal conductivity of our hybrid compounds.

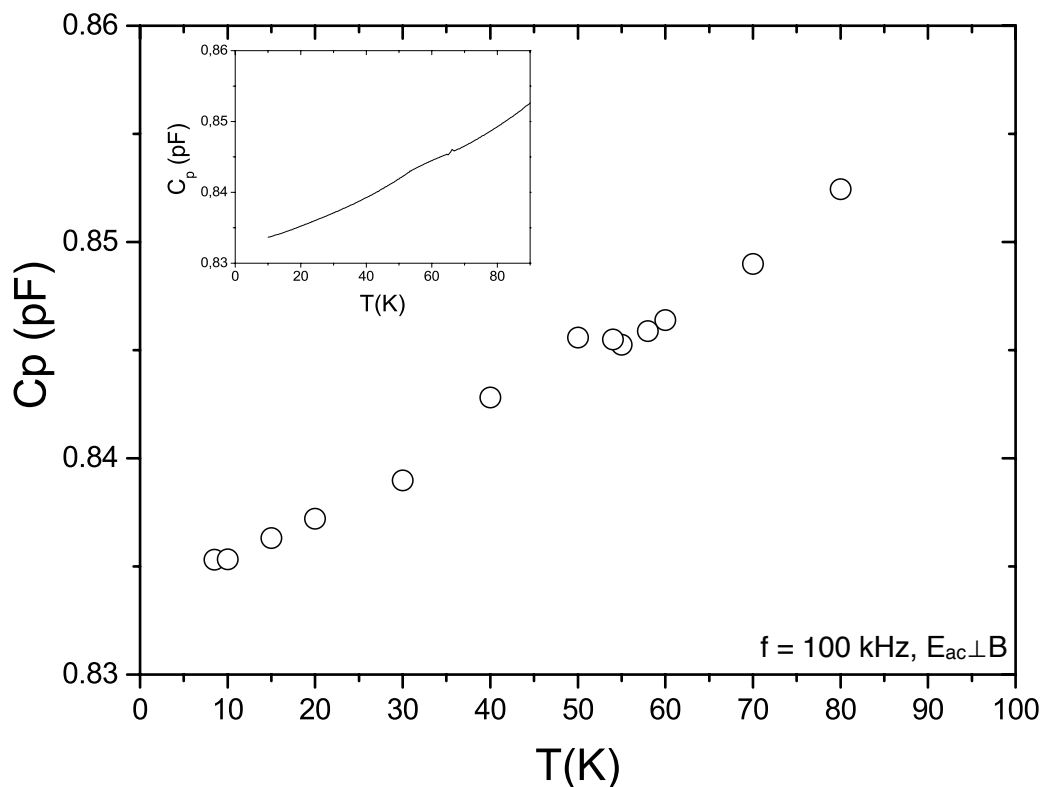


Figure 33 : Capacitance of P₂-Fluo-C-Co as a function of temperature, the insert show the same data measured with a sweep mode (0.5 K / min, warming).

Similarly to what has been observed for the previous hybrid, a clear magneto-electric coupling is present at temperatures below 60 K. This temperature is, once again, much higher than the temperature where the long magnetic range ordering appears ($T_N \approx 11$ K) and rather corresponds to the temperature where short range magnetic correlations occur.

This behaviour *i.e.* the emergence of magnetoelectricity in a paramagnetic state has only been seldom reported. Indeed, a first example would be the piezoelectric paramagnet $\text{NiSO}_4 \cdot 6\text{H}_2\text{O}$ where a small magneto-electric effect was reported and principally attributed to crystal field splitting.⁹⁵ In a more recent example, a nonlinear magneto-electric effect was shown to remain in the paramagnetic regime in CsCuCl_3 .⁹⁶ The coincidence of magneto-electric effect starting precisely at the temperature where short-range magnetic correlation can be deduced from the Curie-Weiss susceptibility is also scarcely reported. To the best of my knowledge the only case reported concerns a Metal Organic Framework $[(\text{CH}_3)_2\text{NH}_2]\text{Mn}(\text{HCOO})_3$.⁹⁷ In general, such a change in absence of long-range magnetic ordering implies a local spin lattice interaction where elastic energy plays a significant role. This indicates that a magneto elastic interaction is likely the driving force of the measured magneto-electric effects.

6. Conclusion

In this chapter we demonstrated that the phosphonic acid moiety can be successfully used to insert organic molecules inside layered copper- and cobalt-based hydroxides to create new layered hybrid materials. Propositions about the internal structure and the bonding nature *via* a thorough set of characterization techniques has been made.

For the copper-based hybrids, several interesting findings has been observed. The first one corresponds to the non-bridging mode adopted by the fluorenes bearing two grafting moieties. First-principles molecular dynamics calculations enables us to propose possible interlayer arrangements corresponding to the experimental findings. The role of the hydrogen-bonding network promoted within the surrounding of the phosphonate groups has been especially underlined. We also observed that the intrinsic luminescence of the fluorene can still be present within the interlayer if the lateral functionalization is bulky enough to forbid deactivation.

For the cobalt hydroxide, the functionalization with phosphonic acids led to compounds for which the ferrimagnetic behaviour has been preserved, with ordering temperatures around 15 K. We also observed clear magneto-electric effects *i.e.* the application of a magnetic field to the material modifies its capacitance significantly. This effect appears above a threshold magnetic field, which is null below the magnetic ordering temperature, and persists even in the paramagnetic regime, which is rather rare.

This work paves the way to get a better understanding of the influence of the organic and inorganic matrix interactions for new magneto-electric hybrid compounds with potential ferroelectric properties. The next step would be to have polarization versus electric field measurement for example. This kind of measurement, however, is very hard to acquire on non-dense powders. Indeed the polarization *vs.* electric field that has been obtained up to now can be described as a banana shape⁹⁸ due to high current leakage, and is therefore meaningless. Efforts will be made for instance on low temperature sintering of the samples including flash sintering for example.

Nevertheless, an important question now arises from these results, it is the question of the origin of the measured magneto-electric effect. To give some additional elements to answer this question, a complete series of halogen-substituted benzene-phosphonic acids ranging from fluorine to iodine has been inserted into layered copper and cobalt hydroxides. The main idea behind this experiment is to study the potential influence of the C-X bond polarity and the polarizability of the halogen on the magneto-electric effect (if any). This work is presented in the following chapter even if at the time of writing no dielectric measurements could be performed yet.

7. Bibliography

1. R. Ramesh, *Nature*, 2009, **461**, 1218-1219.
2. G. Rogez, N. Viart and M. Drillon, *Angewandte Chemie International Edition*, 2010, **49**, 1921-1923.
3. H. R. Wen, Y. Z. Tang, C. M. Liu, J. L. Chen and C. L. Yu, *Inorganic Chemistry*, 2009, **48**, 10177-10185.
4. S.-i. Ohkoshi, H. Tokoro, T. Matsuda, H. Takahashi, H. Irie and K. Hashimoto, *Angewandte Chemie International Edition*, 2007, **119**, 3302-3305.
5. P. Jain, N. S. Dalal, B. H. Toby, H. W. Kroto and A. K. Cheetham, *Journal of the American Chemical Society*, 2008, **130**, 10450-10451.
6. P. Jain, V. Ramachandran, R. J. Clark, H. D. Zhou, B. H. Toby, N. S. Dalal, H. W. Kroto and A. K. Cheetham, *Journal of the American Chemical Society*, 2009, **131**, 13625-13627.
7. Y. Tian, A. Stroppa, Y. Chai, L. Yan, S. Wang, P. Barone, S. Picozzi and Y. Sun, *Scientific Reports*, 2014, **4**, 6062-6066.
8. X. Y. Wang, L. Gan, S. W. Zhang and S. Gao, *Inorganic Chemistry*, 2004, **43**, 4615-4625.
9. X.-Y. Wang, Z.-M. Wang and S. Gao, *Chemical Communications*, 2008, **3**, 281-294.
10. M. Maćzka, A. Gaćgor, M. Ptak, W. Paraguassu, T. A. da Silva, A. Sieradzki and A. Pikul, *Chemistry of Materials*, 2017, **29**, 2264-2275.
11. A. Stroppa, P. Jain, P. Barone, M. Marsman, J. M. Perez-Mato, A. K. Cheetham, H. W. Kroto and S. Picozzi, *Angewandte Chemie International Edition*, 2011, **123**, 5969-5972.
12. E. Pardo, C. Train, H. Liu, L. M. Chamoreau, B. Dkhil, K. Boubekour, F. Lloret, K. Nakatani, H. Tokoro, S. Ohkoshi and M. Verdaguer, *Angewandte Chemie International Edition*, 2012, **51**, 8356-8360.
13. D. B. Mitzi, in *Synthesis, Structure, and Properties of Organic-Inorganic Perovskites and Related Materials*, eds. Karlin, K. D., John Wiley & Sons, Inc., 1999, pp.1-121.«»
14. D. B. Mitzi, *Journal of the Chemical Society, Dalton Transactions*, 2001, **1**, 1-12.
15. D. B. Mitzi, in *Functional Hybrid Materials*, eds. P. Gómez-Romero and C. Sanchez, Wiley-VCH, 2004, DOI: 10.1002/3527602372.ch10, pp. 347-386.
16. B. Kundys, A. Lappas, M. Viret, V. Kapustianyk, V. Rudyk, S. Semak, C. Simon and I. Bakaimi, *Physical Review B*, 2010, **81**, 224434-224440.
17. A. O. Polyakov, A. H. Arkenbout, J. Baas, G. R. Blake, A. Meetsma, A. Caretta, P. H. M. van Loosdrecht and T. T. M. Palstra, *Chemistry of Materials*, 2012, **24**, 133-139.
18. M. Clemente-Leon, E. Coronado, C. Marti-Gastaldo and F. M. Romero, *Chemical Society reviews*, 2011, **40**, 473-497.
19. C. Train, M. Gruselle and M. Verdaguer, *Chemical Society Reviews*, 2011, **40**, 3297-3312.
20. R. Clément and A. Léaustic, in *Magnetism: Molecules to Materials II: Models and Experiments*, eds. J. S. Miller and M. Drillon, Wiley-VCH, 2003, DOI: 10.1002/3527600590.ch12, pp. 397-423.
21. E. Coronado, C. Marti-Gastaldo, E. Navarro-Moratalla, A. Ribera, S. J. Blundell and P. J. Baker, *Nature Chemistry*, 2010, **2**, 1031-1036.
22. R. Gheorghe, L. M. Chamoreau, J. Kapitan, N. S. Ovanesyan, S. M. Aldoshin, L. Hecht, L. D. Barron, C. Train and M. Gruselle, *Chirality*, 2008, **20**, 1085-1091.
23. P. G. Lacroix, I. Malfant, S. Bénard, P. Yu, E. Rivière and K. Nakatani, *Chemistry of Materials*, 2001, **13**, 441-449.

24. S. Marappa and P. V. Kamath, *Industrial & Engineering Chemistry Research*, 2015, **54**, 11075-11079.
25. V. Prévot, C. Forano and J. P. Besse, *Applied Clay Science*, 2001, **18**, 3-15.
26. K. Gopal, S. Ali and R. E. P. Winpenny, in *Structural Studies of Paramagnetic Molecular Phosphonates*, eds. Clearfield, A. and Demadis, K., RCS publishing, 2011, DOI: 10.1039/9781849733571-00364, pp. 364-419.
27. J. M. Taylor, R. K. Mah, I. L. Moudrakovski, C. I. Ratcliffe, R. Vaidhyanathan and G. K. Shimizu, *Journal of the American Chemical Society*, 2010, **132**, 14055-14057.
28. S. Pili, S. P. Argent, C. G. Morris, P. Rought, V. Garcia-Sakai, I. P. Silverwood, T. L. Easun, M. Li, M. R. Warren, C. A. Murray, C. C. Tang, S. Yang and M. Schroder, *Journal of the American Chemical Society*, 2016, **138**, 6352-6355.
29. M. Taddei, F. Costantino, F. Marmottini, A. Comotti, P. Sozzani and R. Vivani, *Chemical Communications*, 2014, **50**, 14831-14834.
30. B. S. Gelfand, R. P. Huynh, R. K. Mah and G. K. Shimizu, *Angewandte Chemie International Edition*, 2016, **55**, 14614-14617.
31. S. Chausson, J.-M. Rueff, M. B. Lepetit, O. Perez, R. Retoux, C. Simon, L. Le Pluart and P.-A. Jaffrès, *European Journal of Inorganic Chemistry*, 2012, **2012**, 2193-2202.
32. C. Bloyet, M. Roger, J.-M. Rueff, B. Raveau, J.-F. Lohier, G. Rogez and P.-A. Jaffrès, *European Journal of Inorganic Chemistry*, 2016, **2016**, 4643-4648.
33. J. M. Rueff, N. Barrier, S. Boudin, V. Dorcet, V. Caignaert, P. Boullay, G. B. Hix and P. A. Jaffrès, *Dalton Transactions*, 2009, **47**, 10614-10620.
34. B. Mutelet, S. Boudin, O. Perez, J. M. Rueff, C. Labbe and P. A. Jaffrès, *Dalton Transactions*, 2015, **44**, 1186-1192.
35. M. Berchel, T. L. Gall, C. Denis, S. L. Hir, F. Quentel, C. Elléouet, T. Montier, J.-M. Rueff, J.-Y. Salaün, J.-P. Haelters, G. B. Hix, P. Lehn and P.-A. Jaffrès, *New Journal of Chemistry*, 2011, **35**, 1000-1003.
36. J. M. Rueff, O. Perez, V. Caignaert, G. Hix, M. Berchel, F. Quentel and P. A. Jaffrès, *Inorganic Chemistry*, 2015, **54**, 2152-2159.
37. J.-M. Rueff, O. Perez, A. Leclaire, H. Couthon-Gourvès and P.-A. Jaffrès, *European Journal of Inorganic Chemistry*, 2009, **2009**, 4870-4876.
38. J. M. Rueff, O. Perez, A. Pautrat, N. Barrier, G. B. Hix, S. Hernot, H. Couthon-Gourves and P. A. Jaffrès, *Inorganic Chemistry*, 2012, **51**, 10251-10261.
39. J.-M. Rueff, V. Caignaert, A. Leclaire, C. Simon, J.-P. Haelters and P.-A. Jaffrès, *CrystEngComm*, 2009, **11**, 556-559.
40. N. Hugot, M. Roger, J.-M. Rueff, J. Cardin, O. Perez, V. Caignaert, B. Raveau, G. Rogez and P.-A. Jaffrès, *European Journal of Inorganic Chemistry*, 2016, **2016**, 266-271.
41. C. Bloyet, J.-M. Rueff, V. Caignaert, J.-F. Lohier, J. Cardin, P.-A. Jaffrès and B. Raveau, *Zeitschrift für Anorganische und Allgemeine Chemie*, 2017, **643**, 250-255.
42. P. G. Lacroix, R. Clément, K. Nakatani, J. Zyss and I. Ledoux, *Science*, 1994, **263**, 658-660.
43. T. Coradin, R. Clément, P. G. Lacroix and K. Nakatani, *Chemistry of Materials*, 1996, **8**, 2153-2158.
44. J. L. Colon, C. Y. Yang, A. Clearfield and C. R. Martin, *The Journal of Physical Chemistry*, 1988, **92**, 5777-5781.
45. J. L. Colon, C. Y. Yang, A. Clearfield and C. R. Martin, *The Journal of Physical Chemistry*, 1990, **94**, 874-882.

46. Q. Wang, D. Yu, Y. Wang, J. Sun and J. Shen, *Langmuir*, 2008, **24**, 11684-11690.
47. G. Huang, S. Ma, X. Zhao, X. Yang and K. Ooi, *Chemical Communications*, 2009, **3**, 331-333.
48. A. Shimada, Y. Yoneyama, S. Tahara, P. H. Mutin and Y. Sugahara, *Chemistry of Materials*, 2009, **21**, 4155-4162.
49. S. Akbarian-Tefaghi, E. Teixeira Veiga, G. Amand and J. B. Wiley, *Inorganic Chemistry*, 2016, **55**, 1604-1612.
50. Y. Wang, E. Delahaye, C. Leuvrey, F. Leroux, P. Rabu and G. Rogez, *Inorganic Chemistry*, 2016, **55**, 4039-4046.
51. É. Delahaye, S. Eyele-Mezui, J.-F. Bardeau, C. Leuvrey, L. Mager, P. Rabu and G. Rogez, *Journal of Materials Chemistry*, 2009, **19**, 6106-6115.
52. E. Delahaye, S. Eyele-Mezui, M. Diop, C. Leuvrey, P. Rabu and G. Rogez, *Dalton Transactions*, 2010, **39**, 10577-10580.
53. R. Bourzami, S. Eyele-Mezui, E. Delahaye, M. Drillon, P. Rabu, N. Parizel, S. Choua, P. Turek and G. Rogez, *Inorganic Chemistry*, 2014, **53**, 1184-1194.
54. E. Delahaye, S. Eyele-Mezui, M. Diop, C. Leuvrey, D. Foix, D. Gonbeau, P. Rabu and G. Rogez, *European Journal of Inorganic Chemistry*, 2012, **16**, 2731-2740.
55. Q. Evrard, Z. Chaker, M. Roger, C. M. Sevrain, E. Delahaye, M. Gallart, P. Gilliot, C. Leuvrey, J.-M. Rueff, P. Rabu, C. Massobrio, M. Boero, A. Pautrat, P.-A. Jaffrès, G. Ori and G. Rogez, *Advanced Functional Materials*, 2017, **27**, 1703576-1703589.
56. A. Bree and R. Zwarich, *The Journal of Chemical Physics*, 1969, **51**, 912-920.
57. S. Y. Lee and B. H. Boo, *The Journal of Physical Chemistry*, 1996, **100**, 8782-8785.
58. R. P. Sperline, *Langmuir*, 1997, **13**, 3715-3726.
59. H. Nakayama, K. Takeshita and M. Tshako, *Journal of Pharmaceutical Sciences*, 2003, **92**, 2419-2426.
60. T. Kameda, T. Shinmyou and T. Yoshioka, *Applied Surface Science*, 2016, **366**, 523-528.
61. H. Nijs, A. Clearfield and E. F. Vansant, *Microporous and Mesoporous Materials*, 1998, **23**, 97-108.
62. G. Guerrero, P. H. Mutin and A. Vioux, *Chemistry of Materials*, 2001, **13**, 4367-4373.
63. C. S. Kim, R. J. Lad and C. P. Tripp, *Sensors and Actuators B: Chemical*, 2001, **76**, 442-448.
64. K. D. Demadis and S. D. Katarachia, *Phosphorus, Sulfur, and Silicon and the Related Elements*, 2004, **179**, 627-648.
65. G. R. Williams and D. O'Hare, *Solid State Sciences*, 2006, **8**, 971-980.
66. R. Luschtinetz, G. Seifert, E. Jaehne and H. J. P. Adler, *Macromolecular Symposia*, 2007, **254**, 248-253.
67. S. Yagyu, M. Yoshitake, N. Tsud and T. Chikyow, *Applied Surface Science*, 2009, **256**, 1140-1143.
68. S. Shori, P. J. Pellechia, H. C. zur Loye and H. J. Ploehn, *Journal of Colloid and Interface Science*, 2015, **437**, 97-110.
69. C. E. Bamberger, E. D. Specht and L. M. Anovitz, *Journal of the American Ceramic Society*, 2005, **80**, 3133-3138.
70. V. Laget, S. Rouba, P. Rabu, C. Hornick and M. Drillon, *Journal of Magnetism and Magnetic Materials*, 1996, **154**, L7-L11.
71. F. Cavani, F. Trifirò and A. Vaccari, *Catalysis Today*, 1991, **11**, 173-301.
72. C. Wright, *Journal of Catalysis*, 1982, **78**, 257-261.

73. J. R. Neilson, B. Schwenzer, R. Seshadri and D. E. Morse, *Inorganic Chemistry*, 2009, **48**, 11017-11023.
74. L. Markov, K. Petrov and V. Petkov, *Thermochimica Acta*, 1986, **106**, 283-292.
75. G. Weber and F. W. J. Teale, *Transactions of the Faraday Society*, 1958, **54**, 640-648.
76. J. F. Kauffman, M. J. Coté, P. G. Smith and J. D. McDonald, *The Journal of Chemical Physics*, 1989, **90**, 2874.
77. D. Yan, Y. Zhao, M. Wei, R. Liang, J. Lu, D. G. Evans and X. Duan, *RSC Advances*, 2013, **3**, 4303.
78. A. Demessence, G. Rogez and P. Rabu, *Chemistry of Materials*, 2006, **18**, 3005-3015.
79. A. Demessence, A. Yassar, G. Rogez, L. Miozzo, S. De Brion and P. Rabu, *Journal of Materials Chemistry*, 2010, **20**, 9401.
80. R. L. Carlin, *Magnetochemistry*, Springer-Verlag Berlin Heidelberg, 1986.
81. O. Kahn, *Molecular Magnetism*, VCH Publishers, 1993.
82. J. R. Neilson, D. E. Morse, B. C. Melot, D. P. Shoemaker, J. A. Kurzman and R. Seshadri, *Physical Review B*, 2011, **83**.
83. F. Bellouard, M. Clemente-León, E. Coronado, José R. Galán-Mascarós, Carlos J. Gómez-García, F. Romero and Kim R. Dunbar, *European Journal of Inorganic Chemistry*, 2002, **2002**, 1603-1606.
84. E. Coronado, J. R. Galan-Mascaros, C. J. Gomez-Garcia and V. Laukhin, *Nature*, 2000, **408**, 447-449.
85. P. Rabu, S. Angelov, P. Legoll, M. Belaiche and M. Drillon, *Inorganic Chemistry*, 1993, **32**, 2463-2468.
86. H. Zheng, J. Wang, S. E. Lofland, Z. Ma, L. Mohaddes-Ardabili, T. Zhao, L. Salamanca-Riba, S. R. Shinde, S. B. Ogale, F. Bai, D. Viehland, Y. Jia, D. G. Schlom, M. Wuttig, A. Roytburd and R. Ramesh, *Science*, 2004, **303**, 661-663.
87. M. Etier, V. V. Shvartsman, Y. Gao, J. Landers, H. Wende and D. C. Lupascu, *Ferroelectrics*, 2013, **448**, 77-85.
88. J. Wang, J. B. Neaton, H. Zheng, V. Nagarajan, S. B. Ogale, B. Liu, D. Viehland, V. Vaithyanathan, D. G. Schlom, U. V. Waghmare, N. A. Spaldin, K. M. Rabe, M. Wuttig and R. Ramesh, *Science*, 2003, **299**, 1719-1722.
89. G. Catalan and J. F. Scott, *Advanced Materials*, 2009, **21**, 2463-2485.
90. M. M. Sutar, A. N. Tarale, S. R. Jigajeni, S. B. Kulkarni, V. R. Reddy and P. B. Joshi, *Solid State Sciences*, 2012, **14**, 1064-1070.
91. A. Nørlund Christensen, R. M. Hornreich and B. Sharon, *Solid State Communications*, 1973, **13**, 963-966.
92. P. Martins, A. Larrea, R. Goncalves, G. Botelho, E. V. Ramana, S. K. Mendiratta, V. Sebastian and S. Lanceros-Mendez, *ACS Applied Materials & Interfaces*, 2015, **7**, 11224-11229.
93. P. Rabu, J. M. Rueff, Z. L. Huang, S. Angelov, J. Souletie and M. Drillon, *Polyhedron*, 2001, **20**, 1677-1685.
94. J. Souletie, P. Rabu and M. Drillon, *Magnetism : Molecules to Materials V*, Wiley-VCH, Weinheim, 2005.
95. S. L. Hou and N. Bloembergen, *Physical Review*, 1965, **138**, A1218-A1226.
96. A. I. Kharkovskiy, Y. V. Shaldin and V. I. Nizhankovskii, *Journal of Applied Physics*, 2016, **119**, 014101.
97. W. Wang, L. Q. Yan, J. Z. Cong, Y. L. Zhao, F. Wang, S. P. Shen, T. Zou, D. Zhang, S. G. Wang, X. F. Han and Y. Sun, *Scientific Reports*, 2013, **3**, 2024-2028.

98. J. F. Scott, *Journal of Physics: Condensed Matter*, 2008, **20**, 021001.

Chapter IV : Layered Hydroxides Hybrid Materials Obtained by
Intercalation of Benzene Derivatives

Chapter IV : Layered Hydroxides Hybrid Materials Obtained by Intercalation of Benzene Derivatives

As stated in the previous chapter, one important question is the origin of the observed magneto-electric effect. In order to try to obtain some elements to answer that question, we decided to insert a new series of molecules (see figure 1) bearing a phosphonic acid grafting moiety as well as several meta-substituted halogens (F, Cl, Br, I). This series is completed with a cyano-propoxy moiety that brings additional flexibility and mobility to the polar end of the chain. All these molecules were synthesized by the group of Paul-Alain Jaffrès in Brest. The expected polarizabilities for such a series is $H < F < Cl < Br < I < O(CH_2)_3CN$, indeed, polarizability is more related to the ability of the electronic cloud to move than to the difference of electronegativity. The biggest electronegativity difference is indeed obtained with the C-F bond but the valence electrons are tightly connected to the nucleus. In the case of the C-I bond, the difference of electronegativity is negligible but the polarizability is very high due to the nucleus shielding from the core electrons which makes the valence electrons much looser. In our case it is interesting to study the influence of both polarizability and polarity on the magneto-electric effect, and, if possible if such molecules could add a ferroelectric behaviour to the obtained hybrid compounds.

1. Introduction

The work described in this chapter is about the functionalization of copper and cobalt hydroxides with benzene derivatives. The molecular design concept remains the same as discussed in the previous chapter with a rigid platform as well as a lateral moiety bringing potential polarization to the system. We have also been able to compare directly the reactivity of carboxylic versus phosphonic acid with otherwise identical molecules. In this chapter I will discuss the insertion of the molecules shown in figure 1 below.

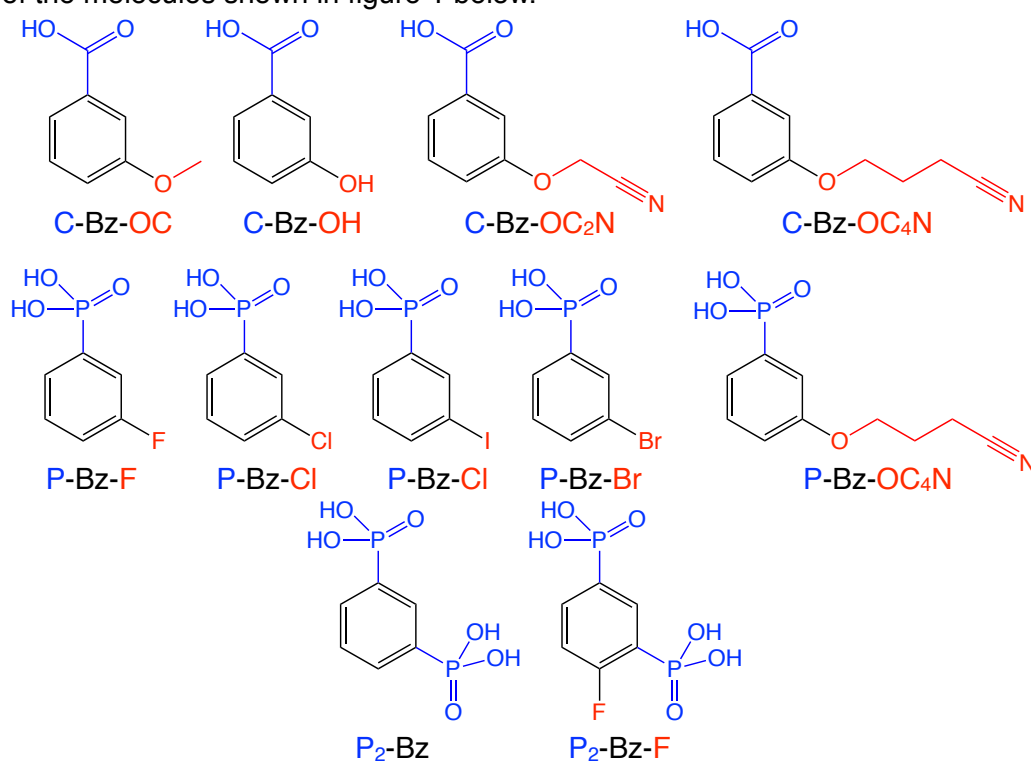


Figure 1 : Benzene derivatives and naming nomenclature used throughout this chapter.

These molecules have the advantage of being good candidates to bring the required non-centrosymmetry on the system. Indeed, previous work done with difunctional meta-substituted phosphonobenzoic acid shows the ability of such meta-substituted molecules to form non-centrosymmetric helical structures using a one pot synthetic approach.¹ For my PhD this meta-substitution is used to break the symmetry of the benzene ring even further.

2. General Chemistry of the System

The hybrid compounds were generally obtained from $\text{Cu}_2(\text{OH})_3(\text{DS})$ and $\text{Co}_2(\text{OH})_{3.5}(\text{DS}_0)_{0.5}$ as starting materials, in water/ethanol mixture as described in the previous chapter. The precise reaction conditions are detailed below. Yet, some peculiar points concerning the reactivity of the molecules deserve a few comments.

2.1. Grafting Moiety

To test the difference of reactivity between carboxylate and phosphonic acid, we have been provided with a molecule bearing lateral propoxy nitrile moiety and having either a carboxylate or a phosphonic acid. One of the main observations is that the reactivity of these two moieties is, as expected, very different. In the case of the phosphonic acid, after the same pH adjustments as previously discussed (insertion at pH between 8 and 8.8) a total insertion in copper hydroxide can be achieved within 1h30 at 90°C meanwhile with the carboxylate, only partial insertion can be achieved with 2 to 15h at 90°C in the copper hydroxide. Allowing the reaction to last longer than 15 hours lead to the formation of oxides. This difference might be due to the poorer solubility and the worse pH control with the carboxylate compared to the phosphonic acid.

This phenomenon is also observed in the case of cobalt hydroxide where 1 hour at 90°C is enough to obtain fully inserted phosphonic hybrid meanwhile the carboxylic moiety requires a reaction of 15 hour at 90°C to obtain a co-inserted compound.

2.2. Lateral Functionalization

Another issue with the carboxylate series is with the hydroxyl terminated molecule C-Bz-OH. Indeed the reactivity appears to be quite different than from the nitrile terminated molecules C-Bz-OC₂N and C-Bz-OC₄N.

With copper hydroxide, the reaction leads to the presence of oxides in less than 2 hours, limiting the range of obtainable hybrids. Allowing the reaction to occur without any pH control generates a compound that is also a « one pot » equivalent as what is described in the section 3.1 of the chapter III concerning the fluorenes. This unknown « one-pot phase » can be evidenced by the presence of additional peaks different than 00l peaks on the diffractogram (black circles in figure 2) as well as a drastically modified IR spectrum, especially in the hydroxy region ($\approx 3600 \text{ cm}^{-1}$). Indeed, the usual large band attributed to water is almost absent and two sharp peaks are visible around 3600 cm^{-1} . The SEM images are also an additional proof of the destruction of the hydroxide with the loss of the typical lamellar morphology (figure 2).

The slow reactivity of the carboxylic moiety in our synthesis conditions is also observed for the cobalt hydroxide although, due to the higher resistance to oxidation, the time for the appearance of an unwanted phase is noticeably longer (24h) while still not making full insertion possible.

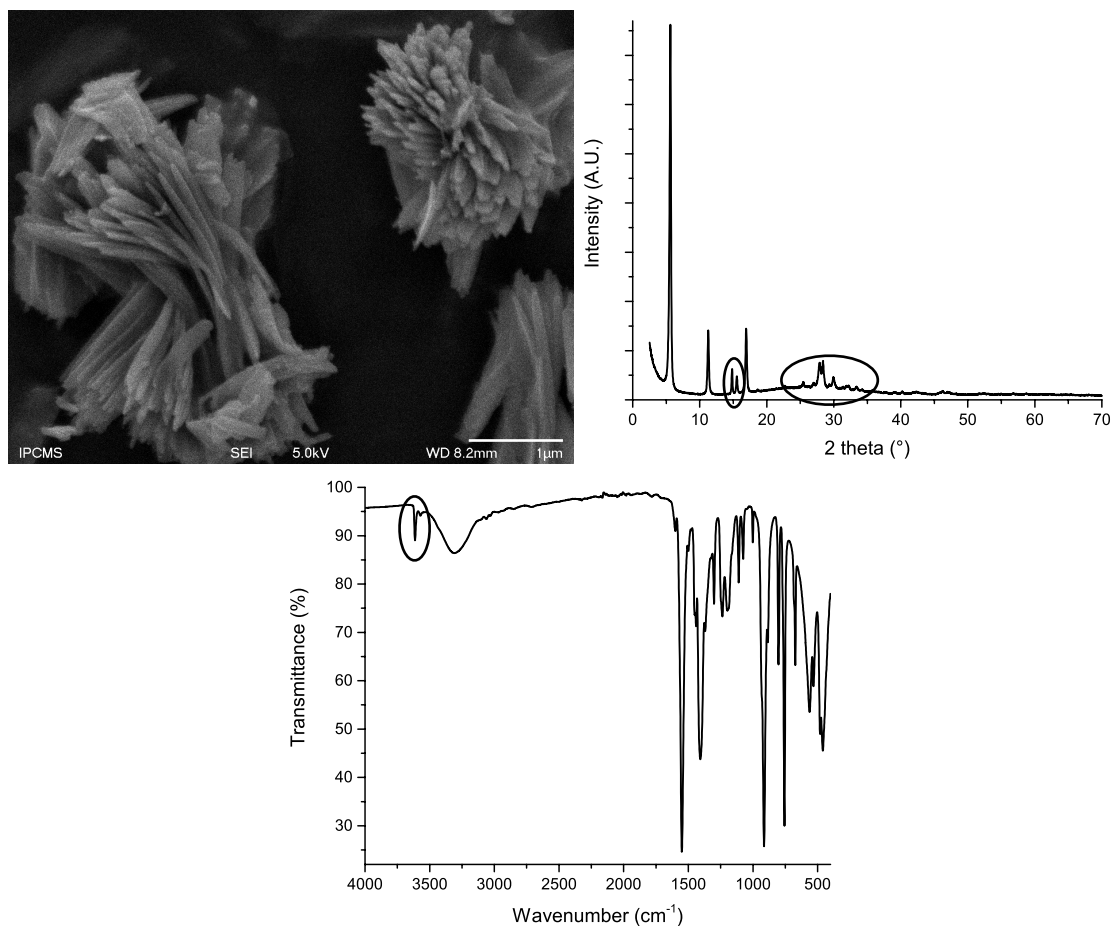


Figure 2 : SEM image (top left) XRD pattern (top right) and infrared spectrum (bottom) of the product of the reaction between C-Bz-OH and $\text{Cu}_2(\text{OH})_3(\text{DS})$ hybrid obtained without pH control. Black circles evidence the “abnormal” peaks with respect to what was expected of a ion-exchange reaction.

Finally, a last series with benzenes having two phosphonic acids grafting moieties has been used ($\text{P}_2\text{-Bz}$ and $\text{P}_2\text{-Bz-F}$). The purpose of this series is to have both polarity and a pillaring of the hydroxide sheets. As will be described in the section 4.1.2 of this chapter, the close interlamellar spacing obtained for cobalt hydroxide (11.2 Å) as well as the polarity of the molecules might bring interesting magnetoelectric effects. Similar pillaring systems have been studied in the past in our laboratory with terephthalate for example.²

3. Lateral Functionalization Role

As seen in the previous section, the role of the lateral functionalization is to bring a potential electrical polarization to the hybrid material. As such, we found well suited the use of halogens in meta position, to keep the low symmetry of the system but allow a gradual change of the polarity of the molecule. The addition of propoxy nitrile chain to that series allowed us to add some flexibility to the polar group in order and to see the potential influence of this flexibility on dielectric properties.

The polarizability is also an important factor to take into account with this series. A quantitative analysis of the magnetoelectric effect could also give us hints about the source of this effect and the influence of polarizability vs polarity for the observation of this effect. The polarizability being roughly inversely proportional to the polarity of the different molecules, in our case, we might be able to get a definitive answer with the measurements of all these compounds.

4. Insertion in Copper Hydroxide

4.1. With Phosphonic Acid

4.1.1. Typical Experimental Procedure

The typical procedure remains similar to the one previously used. First the molecule of interest is solubilized in 12 mL of water with NaOH addition, then when the desired pH is obtained, ethanol is added and the solution is bubbled with argon for 15 minutes. The hydroxide of interest is then added to the solution and the whole system is heated at the desired temperature while being stirred at 600 rpm and under static argon pressure. The first hydroxide studied was the copper hydroxide, the synthesis conditions for these insertions are listed in the table below. The case of difunctional molecules will be described in section 4.1.2 of this chapter.

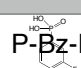
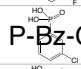
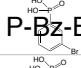
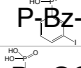
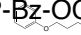
Molecule of interest	PO ₃ :DS ratio (1 = 0.165 mmol)	pH	Temperature	Time	Solvent (H ₂ O/EtOH)
 P-Bz-F	2:1	8.8	70°C	3h	12/12 mL
 P-Bz-Cl	2:1	8.8	70°C	3h	12/12 mL
 P-Bz-Br	2:1	8.8	70°C	3h	12/12 mL
 P-Bz-I	2:1	8.9	70°C	3h	12/12 mL
 P-Bz-OC ₄ N	2:1	8.8	82°C	1h30	12/12 mL

Table 1 : Experimental conditions used to obtain single phase copper-based hybrid compounds.

The experimental conditions for the full insertion are not dependent on the halogen type. However, when it comes to the propoxy-nitrile lateral moiety, the reaction time must be shorter, and temperature must be raised accordingly. With the conditions which work for the halogen series (70°C/3h), the reaction with P-Bz-OC₄N leads to multiphasic compounds.

4.1.2. XRD and Infrared Spectroscopy

The halogen series interlamellar distances observed are 15.3, 15.8, 15.7 and 15.8 Å for P-Bz-FcCu, P-Bz-ClcCu, P-Bz-BrCu and P-Bz-IcCu hybrids respectively. The slightly lower interlamellar spacing observed for the fluorinated compound might be due to the smaller size of fluorine and a shorter bond length while the three other interlamellar spacings are effectively identical within experimental error due to the variability observed from a sample to the other and the relative broadness of the peaks.

From the figure 3 below it can be seen that the different hybrids are obtained as single phase compounds. The signature of each molecule of interest is visible in the IR spectra of the corresponding final hybrid as well.

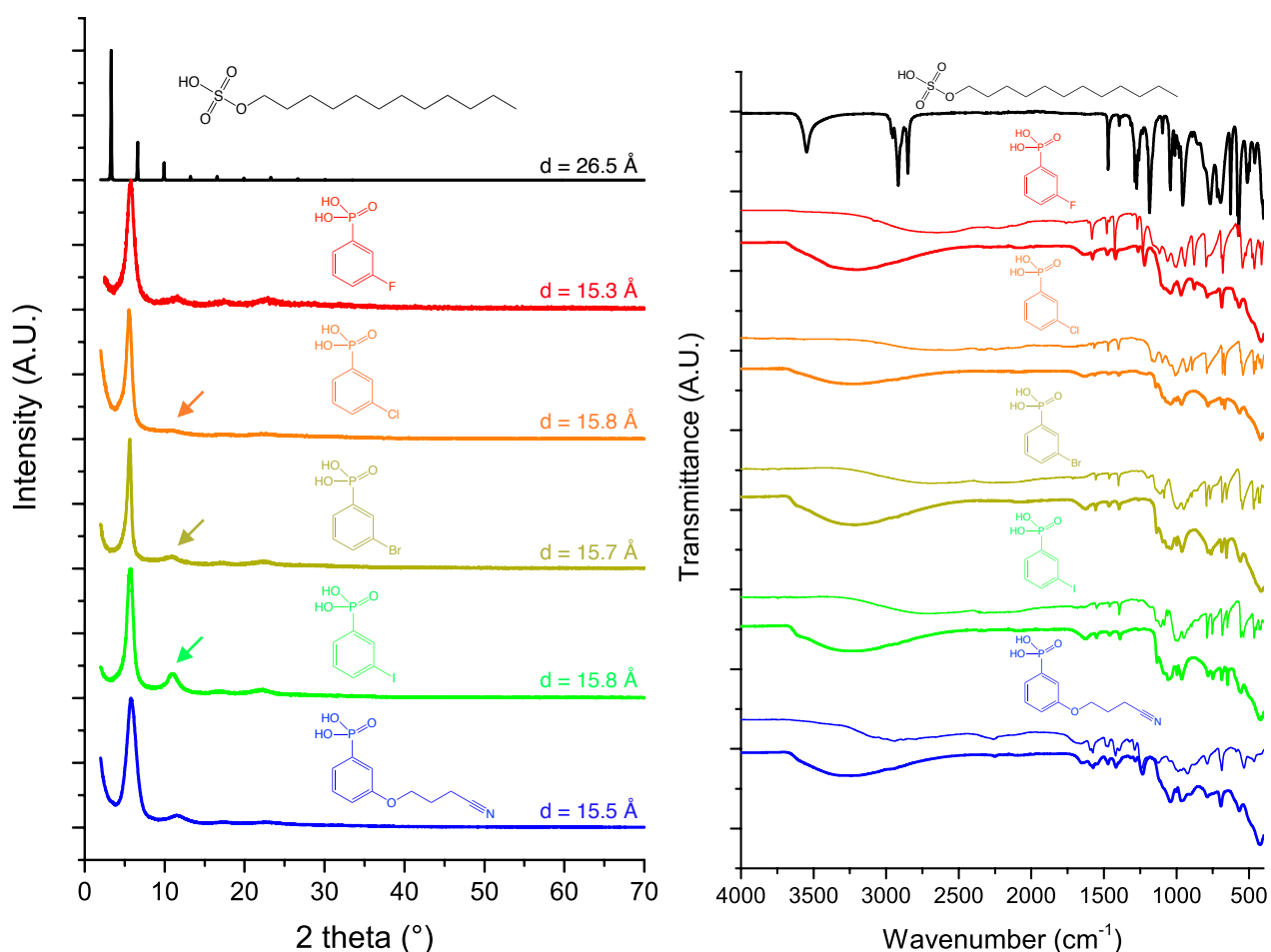


Figure 3 : Powder X-ray diffraction patterns (left) and infrared spectra (right) of the different hybrids obtained with copper hydroxide (bold line) and the organic molecule alone (thin line).

As shown in the diffractograms above, an intensity « anomaly » for the 002 peak can be observed. Indeed, the intensity of the 00 l diffraction peaks does not follow the general expected regular intensity decrease as 2θ increases. Indeed, the atomic scattering factor is decreasing as theta increases due to destructive interference of scattered X-rays.³ The larger intensity of the 00 l peaks (l even) can be linked to the larger electronic density in the interlamellar space due to the presence of heavy halogen atoms. The intensity anomaly is indeed more pronounced as the meta-substituted halogen is heavier. Unfortunately, as for the fluorene case, the quality of these diffractograms does not allow for a proper unidimensional electron density analysis of the system.

In IR spectroscopy the signature of each molecule of interest is well visible in the hybrid especially the benzene ring signature in the 1400-1700 cm^{-1} range. The signature of the alkyl chains from the dodecylsulfate are barely observed as trace amounts but the interlamellar spacing is anyway incompatible with co-insertion. The table 2 below is a listing and potential attribution of the IR bands observed for the hybrids obtained in copper hydroxide.

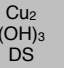
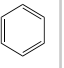
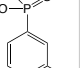
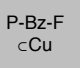
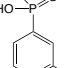
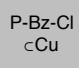
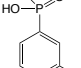
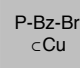
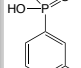
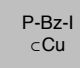
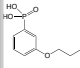
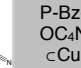
												
P(O)(OH)			1608		1588						1594	1591
C-C ring stretch		1528	1583	1579	1565/ 1540/ 1506	1562	1556/ 1505	1557/ 1539/ 1505	1550/ 1505	1551/ 1505	1577	1574 /1555 /1549
C-C ring stretch	1471	1479	1480/ 1462	1477	1471	1469/ 1457	1488/ 1464	1465	1462	1463/ 1455	1485/ 1471	1487s/ 1471
C-C ring stretch		1393			1399	1397	1399	1395	1393	1389	1393	1393s
PO ₃ asymmetric stretching (1330cm ⁻¹)	1313		1306		1337		1338		1339		1322	1314
C-H inplane bending	1274		1270	1265	1273		1287/ 1262	1261	1261	1261	1288	1284
C-H inplane bending and P=O (1200-1220cm ⁻¹)	1233/ 1199		1162	1159		1207	1198		1187		1195(w)	1196s
C-H inplane bending	1185	1176			1171/ 1158/ 1147	1142	1168/ 1143	1171(w)	1174	1170	1165	1164(w)
PO ₃ symmetric stretching (1110 cm ⁻¹)	1096		1117	1105	1097	1095	1086	1092	1086	1088	1091(w)	1090s
P-O Probable zone and C-H inplane bending (1040 cm ⁻¹)				1084	1084					1078/ 1074		
			1062	1062		1072	1070	1067	1061	1059		
	1042	1036		1042	1045	1040		1037		1044	1047	1041
	1011		1011/ 1001	1005	1007/ 994	1000	1002(w)/ 994	999	1003/ 991/ 980(w)	1011/ 996	1002/ 988	1001
	990/ 980		952	968		966		962		963	965	968
PO ₃ Symmetrical Deformation (605 cm ⁻¹)				604						596(w)	607	604s

Table 2 : IR bands of all hybrids and starting molecules obtained in copper hydroxide according to the literature⁴⁻⁷ and the spectral database for organic compounds (SDBS No.: 898).

As listed above, P₂-Bz and P₂-Bz-F were also at our disposal. These molecules have the interest of bringing a potential short bridging of the layers while maintaining a low symmetry *via* the meta phosphonic acid substitution. Indeed, similar systems such as a terephthalate (benzene ring and para-substituted carboxylic acids) hybrids obtained via hydrothermal synthesis² led to very interesting magnetic properties with high magnetic ordering temperatures of 48 K and giant hysteric effect with a coercive field of 5.9 T at 2 K. A comparison between the carboxylic and the phosphonic system could be interesting.

Unfortunately, the insertions of P₂-Bz and P₂-Bz-F into layered copper hydroxide led only to relatively well crystallized co-inserted compounds with the presence of copper oxide as shown in figure 4 below. Any attempt to apply harsher synthesis conditions led to a destruction of the hydroxide. The co-insertion is obvious in this case where the interlamellar distance is incompatible with interdigitated or even bilayer stacking (the molecule being at best 7.8 Å long) and the signature of the CH₂ groups of the alkyl chains is still strong in the infrared spectra (2919 and 2851 cm⁻¹). The alternate pre-intercalation strategy based on oleyl sulfate that will be discussed in the following chapter could not be used on these hybrids due to the lack of oleyl sulfate availability.

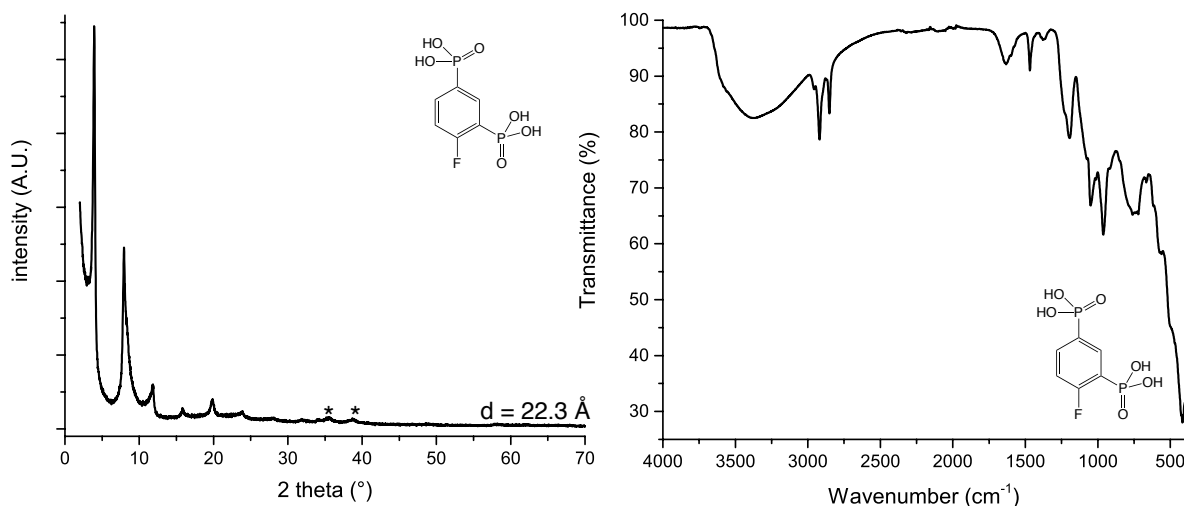


Figure 4 : Powder X-ray diffraction pattern (left) and infrared spectrum (right) of the compound obtained by reaction between $P_2\text{-Bz-F}$ and $\text{Cu}_2(\text{OH})_3(\text{DS})$ (the stars indicate the major peaks of CuO impurity).

For the $\text{P-Bz-OC}_4\text{N-Cu}$ hybrid compound two different types of packing are observed (see figure 5) depending on the reaction duration. A 1h30 reaction time leads to a compound with an interlamellar spacing of 15.5 \AA whereas a 2 h reaction time leads to a compound with an interlamellar spacing of 18.0 \AA . Due to the flexibility of the molecule, the geometrical rigid approach used in the previous chapter cannot be applied here to distinguish if this is an interdigitated or a bilayer packing, although a bilayer seems more plausible in regards to the obtained interlayer spacing. No other difference than the interlamellar spacing has been found between the two hybrids. Therefore, in the rest of the text, the compound referred to will be the one synthesized during 1h30 (15.5 \AA).

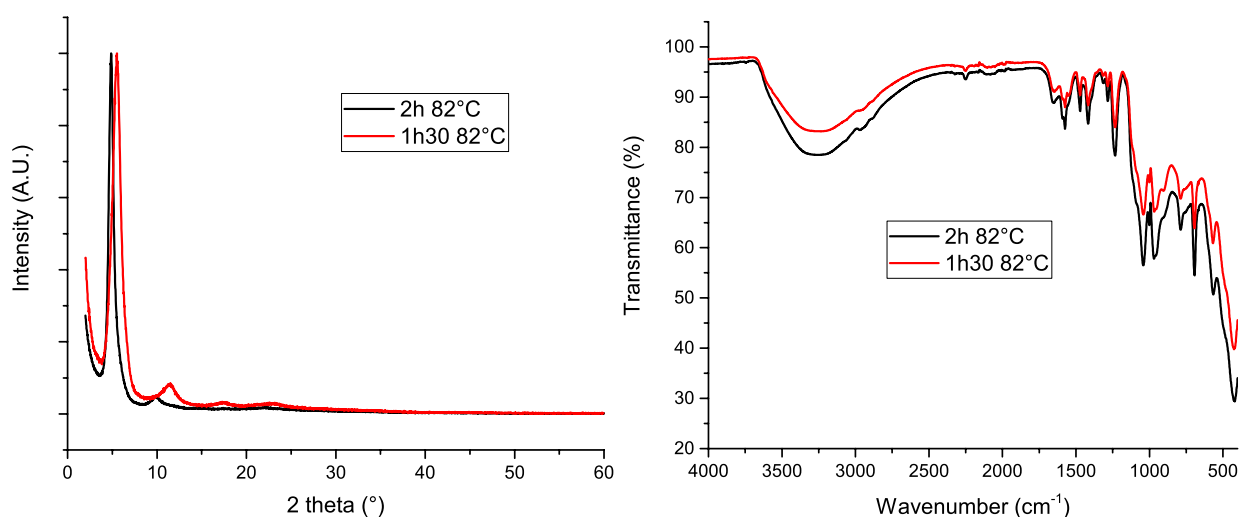


Figure 5 : Both $\text{P-Bz-OC}_4\text{N-Cu}$ hybrids PXRD (left) and IR spectra (right).

4.1.3. TGA/TDA, Micro-Analysis, SEM and EDX

The compounds were analysed by TGA/TDA, micro-analysis and scanning electron microscopy in order to determine the insertion rate of each molecule inside the copper hydroxide (table 3). The same procedure is applied to all the hybrids, the water content is calculated as weight loss at 130°C.

TGA/TDA water content measured (calculated)	Cu:P ratio via EDX measured (calculated)	Micro-analysis results measured (calculated)	Obtained formula
11.0% (6.8%)	5.24 (8.00)	Cu : 48.80 (47.95), C : 9.71 (9.52) H : 3.12 (2.76), P : 2.80 (2.92) F : 1.88 (1.79)	C-Bz-FcCu $\text{Cu}_2(\text{OH})_{3.7}(\text{C}_6\text{H}_5\text{FO}_3\text{P})_{0.25}(\text{DS})_{0.05} \cdot 1\text{H}_2\text{O}$
-	5.60 (5.40)	Cu : 45.70 (45.47), C : 9.41 (9.54) H : 3.12 (2.77), P : 3.76 (4.10) Cl : 4.35 (3.69)	C-Bz-ClcCu $\text{Cu}_2(\text{OH})_{3.63}(\text{C}_6\text{H}_5\text{ClO}_3\text{P})_{0.37} \cdot 1.1\text{H}_2\text{O}$
10.3% (9.3%)	5.88 (6.25)	Cu : 42.30 (41.47), C : 10.37 (9.88) H : 2.83 (3.18), P : 2.86 (3.23) Br : 8.75 (8.34)	C-Bz-BrCu $\text{Cu}_2(\text{OH})_{3.63}(\text{C}_6\text{H}_5\text{BrO}_3\text{P})_{0.32}(\text{DS})_{0.05} \cdot 1.6\text{H}_2\text{O}$
-	4.63 (5.13)	Cu : 37.8 (39.00), C : 10.3 (8.62) H : 2.73 (2.65), P : 2.58 (3.71) I : 10.68 (15.19)	C-Bz-IcCu $\text{Cu}_2(\text{OH})_{3.61}(\text{C}_6\text{H}_5\text{IO}_3\text{P})_{0.39} \cdot 1.5\text{H}_2\text{O}$
8.3% (9.1%)	6.50 (5.88)	Cu : 42.90 (42.97), C : 13.26 (13.40) H : 3.32 (3.51), P : 2.09 (3.46) N : 1.04 (1.56)	C-Bz-OC ₄ NcCu $\text{Cu}_2(\text{OH})_{3.67}(\text{C}_{10}\text{H}_{11}\text{NO}_4\text{P})_{0.39} \cdot 1.5\text{H}_2\text{O}$

Table 3 : Different insertion ratios calculated from analysis for copper hydroxide-based compounds.

The insertion rates determined in table 3 are very similar for all hybrids (between 0.25 and 0.39 phosphonic groups per formula unit), which is rather logical, considering that the molecules have essentially the same size.

The elemental analyses of P-Bz-BrcCu and P-Bz-FcCu hybrids reported in the table above can be reproduced by considering the presence of remaining dodecylsulfate molecules. EDX analyses confirms the presence of traces of sulfur in these two compounds, whereas no traces of sulfur could be detected in P-Bz-ClcCu, P-Bz-IcCu and P-Bz-OC₄NcCu. However, the hypothesis of a co-insertion in the case of P-Bz-BrcCu and P-Bz-FcCu seems unlikely as the alkyl chain (in « all-trans » configuration) is about 15 Å long in and thus incompatible with the observed interlamellar spacings. The remaining dodecylsulfate molecules are likely to be grafted onto the surface of the crystallites, but this hypothesis would be very difficult to prove, surface infrared spectroscopy on the platelets would be required.⁸

The small discrepancy observed for some compounds between the calculated water content and the experimental one can be ascribed to the different storage conditions of the compounds before the TGA measurements are done or before the elemental analyses are performed, which probably leads to evolution of the hydration level. As for the Cu:P ratio, they are within the experimental error. For P-Bz-IcCu and P-Bz-CNcCu, the elemental analyses show a relatively important discrepancy for the I and P analysis respectively. We do not understand the

origin of this discrepancy. New batches are currently being synthesized in order to check the obtained values.

The crystallinity enhancements of the starting compound discussed in chapter I have led to a higher crystallite size in the final compounds. The SEM images (figure 6) reveal the different morphologies of the surfaces of the hydroxide platelets. The hybrids obtained with benzenes functionalized by halogens tend to exhibit parallel lines and relatively monolithic platelets. On the other hand, functionalization with P-fluo-C₈ (Chapter III) or with P-Bz-OC₄N appear to show more disorganized silky surfaces. The flexibility of the lateral chain seems to play an important role in these morphology changes. Indeed, it can be observed in the majority of the pictures and more clearly in P-Bz-BrCu and P-Bz-ICu the appearance of unidimensional lines on the crystallites surface along with a rounding of the crystallite edges.

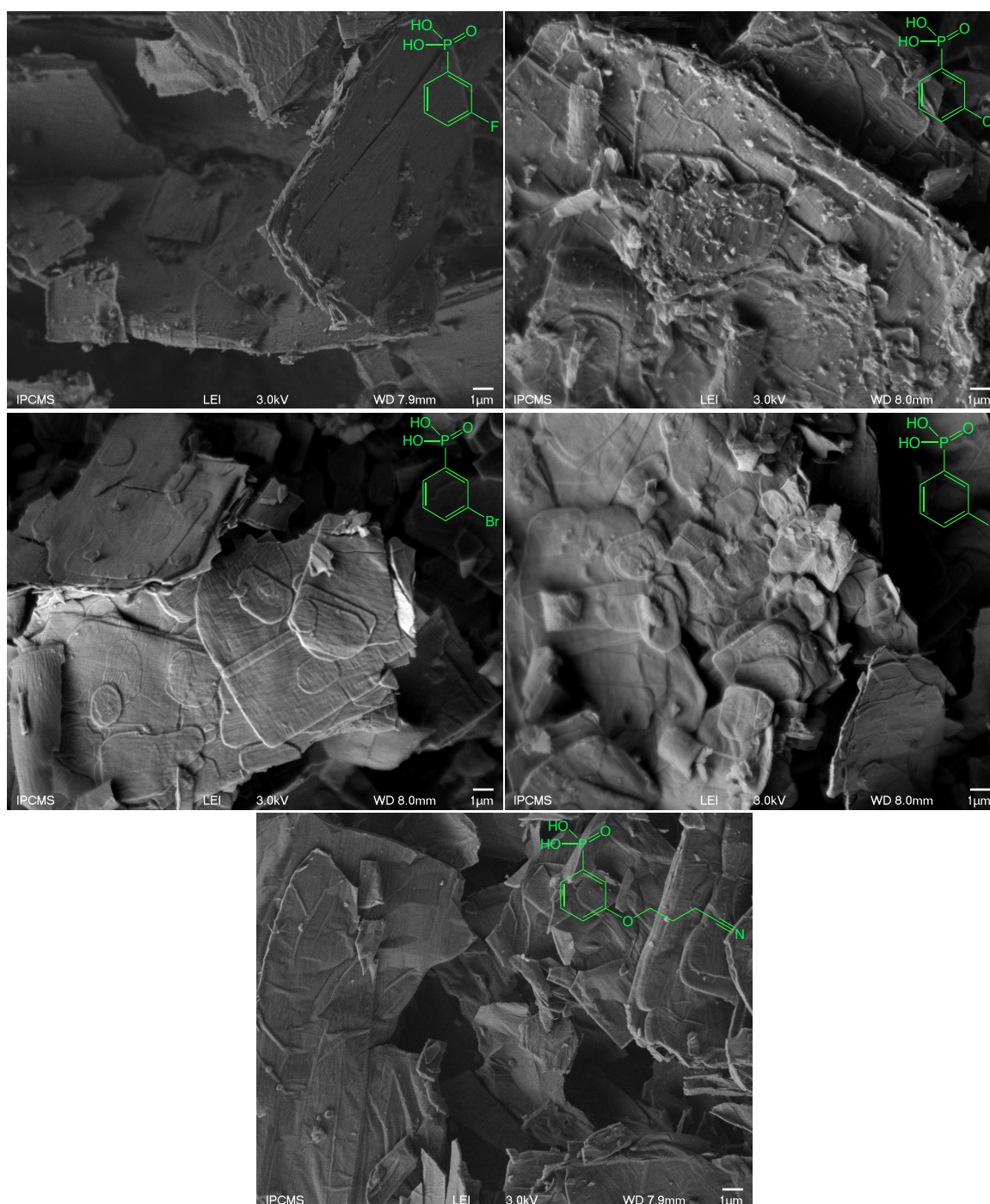


Figure 6 : SEM images of P-Bz-FcCu, P-Bz-ClcCu, P-Bz-BrccCu, P-Bz-IccCu and P-Bz-OC₄NcCu hybrids.

4.1.4. Attempts to Vary the Insertion Rates

An interesting issue was to determine whether the insertion rates obtained were determined by our synthetic procedure or by the system itself, either kinetically or thermodynamically. To that end, we chose to study P-Bz-OC₄N_CCu. This specific system was chosen because of the high solubility of the molecule, its availability and the presence of an easily obtainable experimental probe in the nitrogen that could be easily dosed locally by the analysis service of the university.

This work has been performed under my supervision by Keltoum Balbzioui during her master I internship. The tested parameters to achieve the insertion were time and temperature with parameters ranging from 30 minutes to up to 15 hours for time and between 60°C to reflux (82°C) for the temperatures. All these experiments have led to single phase hybrids and with a sulfur content (from the dodecylsulfate) below the detection threshold of the EDX measurements.

The table 4 below indicates the different experimental conditions and the obtained insertion rate for a formula such as Cu₂(OH)_{4-x}(C₁₀H₁₁PO₄N)_x·H₂O, all these experiments were done with a two-fold excess of the molecule to insert to limit the variables.

Reaction time (h)	Temperature (°C)	Insertion rate (calculated from nitrogen)
0.5	82	0.35 ± 0.04
1	82	0.31 ± 0.04
2	82	0.26 ± 0.05
4	82	0.18 ± 0.06
2	80	0.22 ± 0.05
1	70	0.27 ± 0.05
2	70	0.19 ± 0.06
2	60	0.21 ± 0.05
4	60	0.29 ± 0.04

Table 4 : experimental conditions and calculated insertion rates from nitrogen.

Several informations can be extracted from these experiments, the first and most obvious one is that the temperature range from 60 to 82°C does not seem to greatly influence the insertion rate (insertion does not work at room temperature). The main trend appears to be a slight decrease of the insertion rate with an increased reaction time. Indeed, all the series show a moderate decrease of the insertion rate for longer reaction times that seems to indicate the kinetic formation of a metastable compound before a thermodynamically stable compound. A hypothesis for this is the possible leaching of the molecules with longer reaction times. But further research about the plausible mechanism such as hydration/dehydration processes for example should be done to determine the driving force of this reaction and if these findings can apply to other molecules. Tests with modification of the solvent ratio, quantity of molecule used or even use of other solvents could also be performed.

4.2. With Carboxylic Acid

As stated above, the main goal for the use of molecules bearing a carboxylic acid was to be able to compare the reactivity of the phosphonic acid versus the carboxylic acid. Parts of this work have also been made by Keltoum Balbzioui during her master I internship.

4.2.1. Typical Experimental Procedure

Various experimental conditions have been applied for this series, the main observation that can be drawn from these experiments is that in all the cases, the insertion was more difficult than for phosphonic acid benzene derivatives, *i.e.* leading to co-inserted compounds in most of the cases or in certain cases to multiphasic compounds. This underlines the role of the phosphonic acid moiety which appears to be more favourable than carboxylate for formation of pure compounds.

The typical procedure is the following :

- Dissolution of the molecule of interest in two-fold excess (0.33 mmol) *via* pH adjustment to around 8 in a 12 mL aqueous solution in order to both dissolve the molecule and to assure the maximum stability of the hydroxide as discussed in part 2.1.1. of this chapter. The typical concentration of the obtained solution is about $2.75 \cdot 10^{-2}$ M and is most of the time turbid.
- Addition of 12 mL of ethanol to the solution in order to enable the dispersion of the hydroxide and eventually help solubilize the molecules. The clear solution is then bubbled under argon for 5 minutes.
- Addition of the $\text{Cu}_2(\text{OH})_3\text{DS}$ (0.165 mmol) to the solution with a maintained argon bubbling and stirring until complete dispersion.

It must be noted that for C-Bz-OH the pH change is able to deprotonate the phosphonic acid twice, but is not high enough to lead to a deprotonation of the phenol group (pKa around 9.9). For this series of compounds, apart from temperature, reaction time and volume of solvents, the ratio of molecule to insert with respect to the starting hydroxide has also been modified up to a 6:1 excess (depending on the solubility of the molecule of interest).

4.2.2. XRD and Infrared Spectroscopy

The case of C-Bz-OH insertion is typical of what can be observed with the carboxylic acids bearing molecules C-Bz-OC, C-Bz-OC₂N and C-Bz-OC₄N. The conditions used previously on P-Bz-X with halogens (3h/70°C) that allowed insertion with an interlamellar spacing of 15.8 Å are now leading to an almost purely co-inserted compound as seen in figure 7 below, with an interlamellar spacing of 22.3 Å. The arrow shows the presence of another phase with an interlamellar spacing of 15.8 Å, quite similar to the one observed for the P-Bz-X series. This phase probably corresponds to a complete substitution of the dodecylsulfate molecules. Efforts were thus devoted to try to favour the formation of this totally substituted phase with respect to the coinserted one.

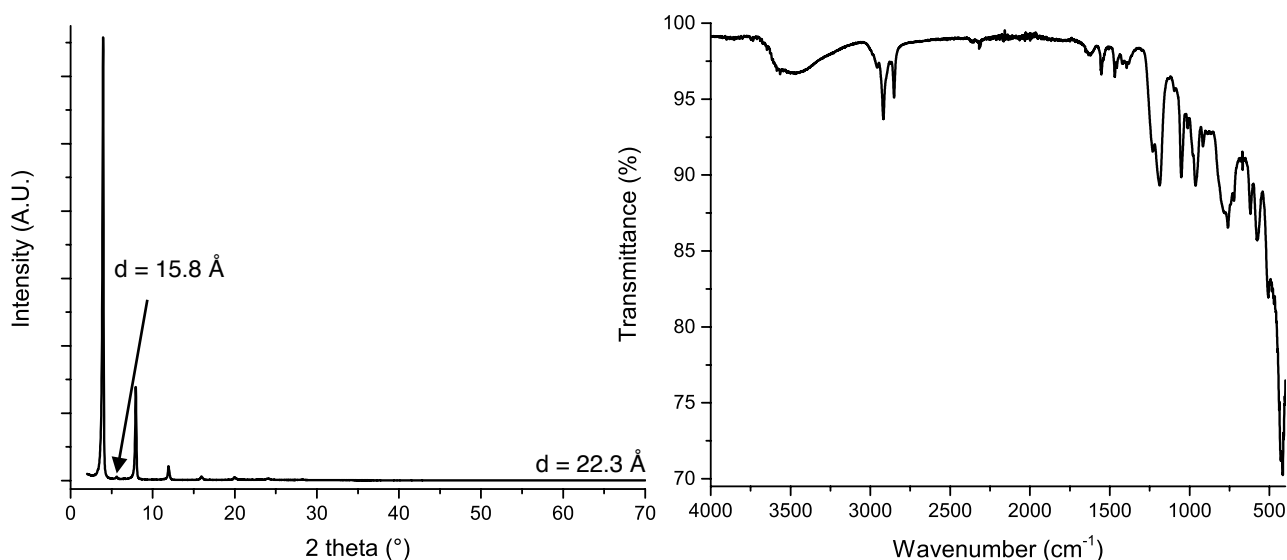


Figure 7 : XRD patterns (left) and infrared spectra of C-Bz-OH in copper hydroxide in 3h/70°C conditions.

Several parameters have then been modified. At 70°C, the increase of the reaction time does not lead to any increase of the proportion of the 15.8 Å phase. The increase of temperature leads to the formation of oxides, which in turn can only be limited by reducing the reaction time.

The volume of solvent used, while keeping the same concentrations of molecule and hydroxide was also changed. This might appear counter-intuitive, but we indeed observed that this parameter had an influence, most of all on the formation of oxides, likely because of the time needed to increase the temperature of the whole reacting mixture. Therefore, it appeared interesting to test if this parameter could also have an influence on the nature of the phases formed. Figure 8 below shows that a 30-minute reflux (82°C), still with a 2:1 excess ratio, leads to the formation of three phases, the first one being not well crystallized at low 2θ and another one with a major peak around 22.2 Å (likely the coinserted phase) and a third, unknown one with a major peak around 11.1 Å (we checked that this peak was not a harmonic of the major peak of the second phase). The ratio between these phases changed when the volume of solvent changed, but unfortunately, we could not observe any growth of the desired 15.8 Å phase.

In IR spectroscopy, the structuration of the O-H bands (3000-3600 cm^{-1}) is more pronounced when the volume of solvent increases (so when the 11.1 Å phase is dominant). It seems to indicate a better ordering of the hydroxides/water molecules/phenol groups is achieved. This could correspond to the interactions of the alcohol moiety with water/hydroxides of the opposite layer, even if a truly « pillaring-like » behaviour is unlikely in regards to the molecule size (6 Å). A hypothesis, highly speculative at this stage, is that this 11.1 Å phase corresponds to a fully inserted phase, but with a different arrangement than the expected 15.8 Å phase.

Further increase of the volumes (up to 24 mL H_2O / 24 mL EtOH) leads to the formation of oxides as well as dominant phase 22.2 Å, without any 11.1 Å phase. Another further increase of the volumes (34 mL H_2O / 34 mL EtOH) while maintaining the quantity of molecule and hydroxide as before leads to the quick formation of oxide as well as a disappearance of the lamellar structure of the compound. The optimal synthesis volumes have been deduced to be around 12/12 mL and 17/17 mL.

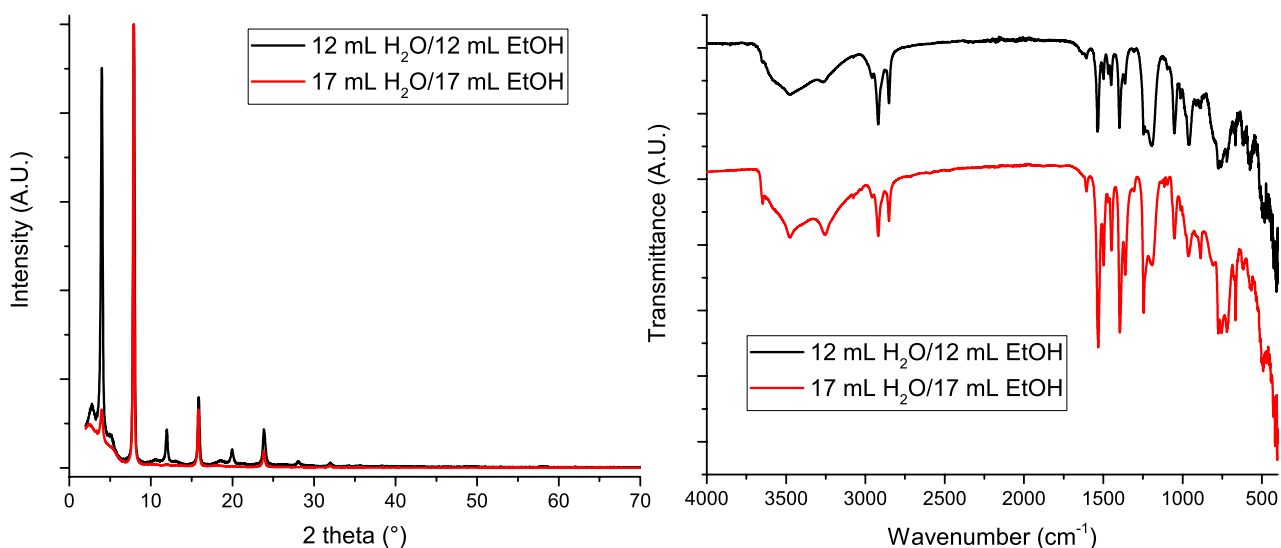


Figure 8 : XRD patterns (left) and infrared spectra of C-Bz-OH in copper hydroxide obtained in 30 min/reflux conditions with a 2:1 excess ratio.

Reducing the temperature reaction to 70°C allows the low 2θ phase to be less visible but also does not facilitate the formation of the pure phase at 11.1 Å or of the one at 15.8 Å as seen in figure 9. As previously observed, the structuration in the O-H region tends to disappear as the phase at 11.1 Å is less present, along with stronger bands for the CH₂ of the alkyl chains (2850-2919 cm⁻¹) and sulfate group (1189-1098-1050 cm⁻¹) indicative of the dodecylsulfate presence in the 22.2 Å phase.

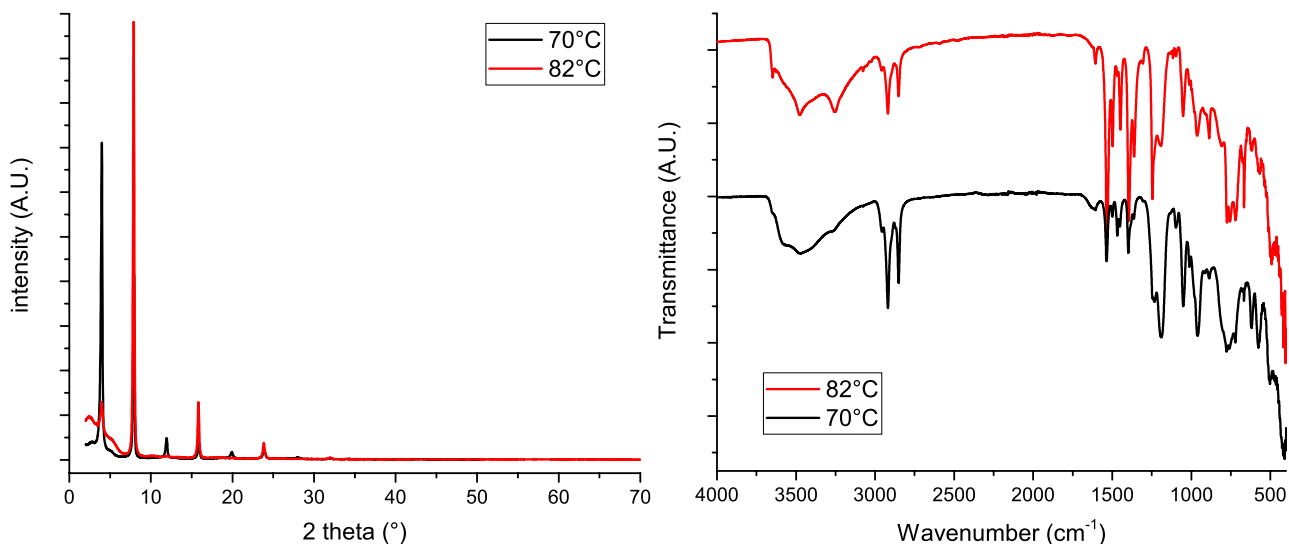


Figure 9 : XRD patterns (left) and infrared spectra of C-Bz-OH in copper hydroxide obtained in 30 minutes in a 17 mL H₂O/17 mL EtOH mixture with a 2:1 excess ratio.

A further warming of the reacting medium *i.e.* going above reflux temperature with closed microwave vessels (90°C and very short reaction times around 5 minutes) leads to the total destruction of the hydroxide and formation of oxides, so it is clearly an inappropriate method for this synthesis.

The last parameter that has been modified during Keltoum's internship was the ratio of molecule with respect to the amount of dodecylsulfate in the hydroxide. Thanks to the high solubility of the C-Bz-OH molecule we were able to make tests with 4:1 and 6:1 ratios instead of

the usual 2:1 ratio. The results shown in figure 10 indicate that this ratio increase leads to a higher quantity of the phase with a shorter inter lamellar spacing. Interestingly for very large ratio, 6:1, the interlamellar distance of this phase becomes slightly larger (11.6 Å).

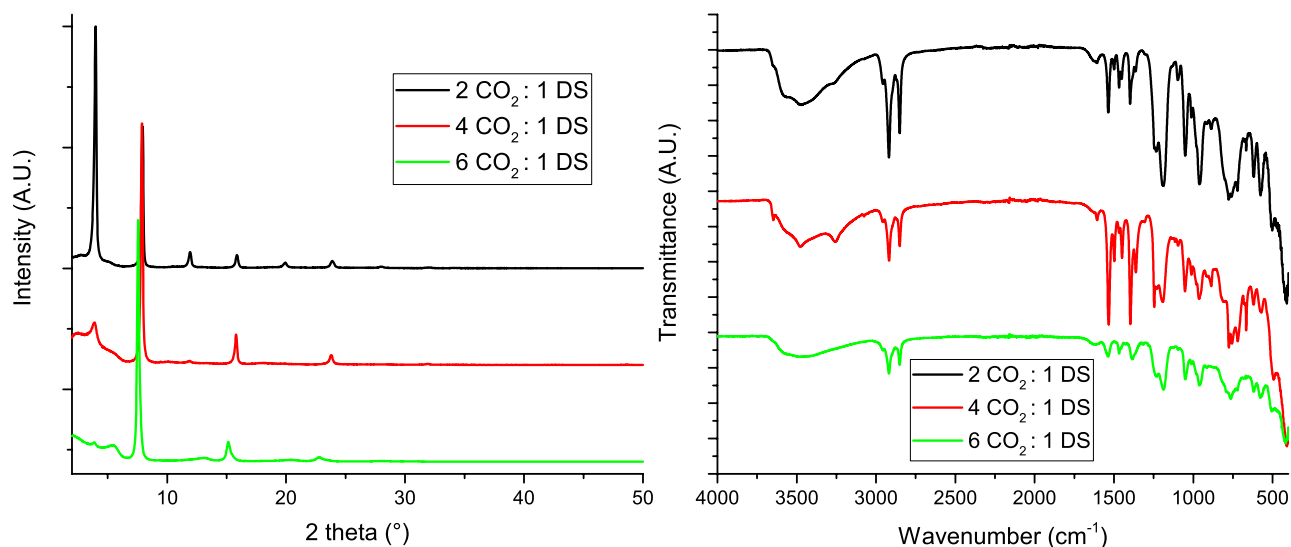


Figure 10 : XRD patterns (left) and infrared spectra of C-Bz-OH in copper hydroxide obtained in 30 minutes in a 12 mL H₂O/12 mL EtOH mixture heated at 70°C.

Willing to investigate the role of the alcohol moiety, we also tried to insert the C-Bz-OC molecule in the copper hydroxide system. We ran into many problems, the main ones being the poor pH control of the solution along with a very low solubility of C-Bz-OC. It was thus necessary to use a higher pH, and consequently the reacting medium became very favourable to the formation of oxides. These limits made us only obtain a single phase co-inserted hybrid with an interlamellar spacing of 22.3 Å by using a 30 minute refluxing of a 12 mL H₂O/ 12 mL EtOH solution with a two-fold excess of the molecule to insert (figure 11). We were not able to observe any totally inserted phase within the various tested experimental conditions.

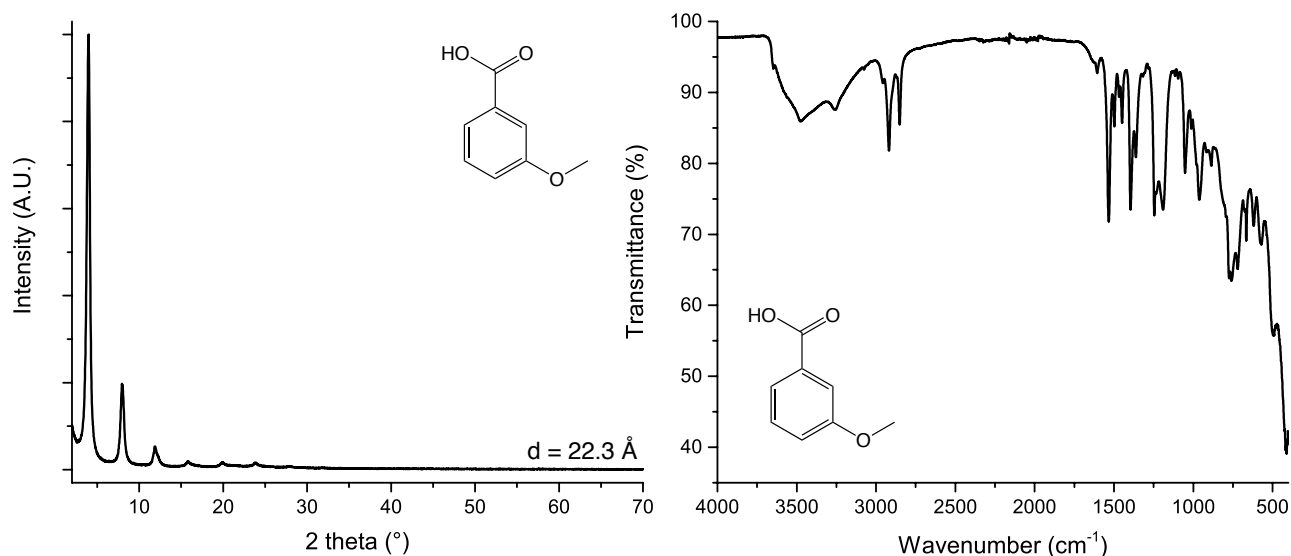


Figure 11 : XRD pattern (left) and infrared spectra(right) of C-Bz-OC hybrid in copper hydroxide.

Unfortunately, despite all our attempts, we have not been able to successfully obtain pure and totally inserted compounds with the other carboxylate based molecules P-Bz-C₂N and P-Bz-C₄N in copper hydroxide.

5. Insertion in Cobalt Hydroxide

Using the same methodology as described previously, we tried to insert all the benzene derivatives in layered cobalt hydroxide. These hybrids are particularly interesting for their potential magneto-electric properties along with the potential study of the role of the polarity versus polarizability on the characteristics of the magneto-electric effect.

5.1. With Phosphonic Acid

5.1.1. Typical Experimental Procedure

For this series (Table 5), the reactivity is rather different than from what has been observed with the copper hydroxide for which the conditions were identical for P-Bz-F, P-Bz-Cl, P-Bz-Br and P-Bz-I (Table 1).

Molecule of interest	PO ₃ :DS ratio (1 = 0.165 mmol)	pH	Temperature	Time	Solvent (H ₂ O/EtOH)
P-Bz-F	2:1	8.3	82°C	4h	12/12 mL
P-Bz-Cl	2:1	8.3	82°C	2h	12/12 mL
P-Bz-Br	2:1	8.6	82°C	1h	12/12 mL
P-Bz-I	2:1	8.6	82°C	1h	12/12 mL
P-Bz-OC ₄ N	2:1	8.4	82°C	4h	12/12 mL

Table 5 : Experimental conditions to obtain single phase hybrids in cobalt hydroxide.

In the case of cobalt hydroxide, the conditions for the insertion are not identical for all the molecules to insert. Whereas the small pH changes are due to the difference in solubility, the reaction times are, however, quite different for each hybrid. It seems to be more difficult to insert the molecules having a lighter halogen than bromine or iodine, even if the latter have a poorer solubility.

These hybrids have been obtained from the dodecylsulfonate-intercalated hydroxide Co₂(OH)_{3.5}(DS)_{0.5} but it is noteworthy to mention that for P-Bz-F it has been possible to have insertion from Co₂(OH)_{3.2}(OAc)_{0.8} leading to a compound with an interlamellar spacing of 12.8 Å compared to the 12.7 Å for Co₂(OH)_{3.2}(OAc)_{0.8}·1.7H₂O. The caveat being the presence of a small second phase at around 15.3 Å (figure 12) and the technical impossibility to detect if the intercalation is complete or not due to the absence of the sulfur atom probe from the dodecylsulfonate. The infrared spectrum (figure 12) suggests that if the acetate is still present in the hybrid, it is below the detection limit of the infrared spectroscopy.

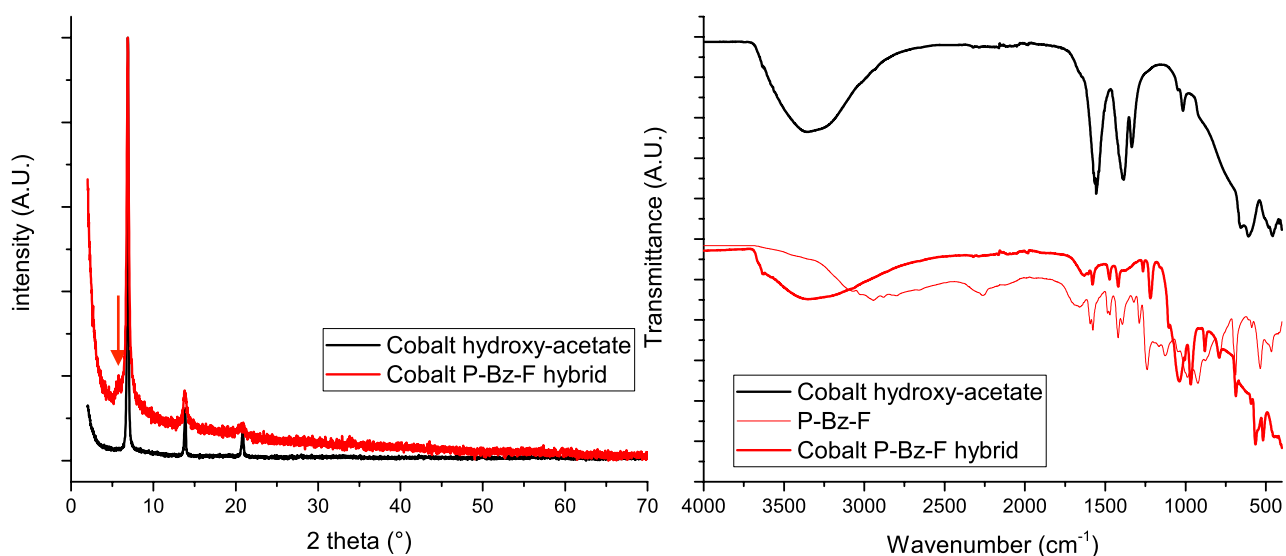


Figure 12 : XRD patterns (left) and infrared spectra (right) of P-Bz-FcCo.

In the rest of this chapter, the hybrids referred to are synthesized from $\text{Co}_2(\text{OH})_{3.5}(\text{DS}_0)_{0.5}$.

5.1.2. XRD and Infrared Spectroscopy

For the halogen series the interlamellar distances observed were of 12.7, 12.8, 13.0 and 12.6 Å for P-Bz-FcCo, P-Bz-ClcCo, P-Bz-BrCco and P-Bz-IcCo hybrids respectively. The interlamellar distance for the P-Bz-OC₄N hybrid is slightly larger (14.6 Å) (figure 13). Several observations have been made, among them the fact that all these compounds share very bad crystallinity with only at best a weak 002 diffraction peak. Despite our efforts, it has not been possible to optimize the crystallinity. In addition, the observed interlamellar distance itself is very short, indeed, the individual inorganic lamella has a thickness of 7.5 Å for the cobalt hydroxide compared to 3 Å for copper hydroxide and yet the interlamellar distance is even reduced by 3 Å compared to copper hydroxide hybrids analogue hybrids.

These short interlamellar distances could be compatible with an almost flat arrangement of the benzene derivatives in the interlamellar spacing assuming they are grafted to the tetrahedral cobalt. The possibility to study theoretically this possible arrangement by means of First Principles Molecular Dynamics, as it has been reported in Chapter III in the case of copper hydroxide-based fluorene hybrids is currently being questioned, but for the moment it is still seriously hampered by the difficulty to treat the structure of the cobalt hydroxide layers.

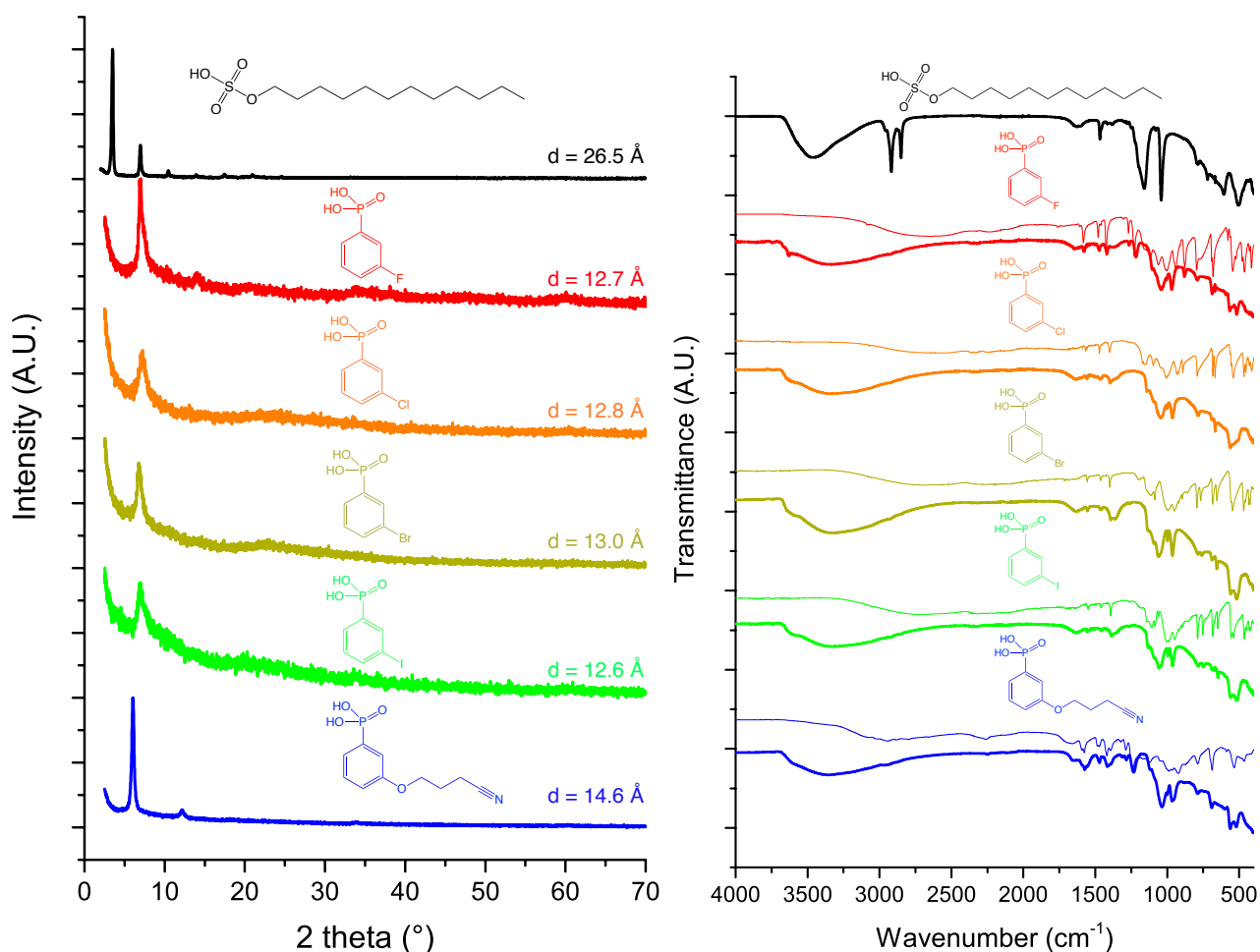


Figure 13 : XRD patterns (left) and infrared spectra (right) of the different hybrids obtained with cobalt hydroxide (bold line) and the organic molecule alone (thin line).

The table below is an attempt in peak attribution from the infrared spectroscopy with the same empirical method as used previously.

	<chem>Co2(OH)3.5(DSO)0.5</chem>	<chem>c1ccccc1</chem>	<chem>O=P(O)(O)c1ccc(F)cc1</chem>	P-Bz-F c Co	<chem>O=P(O)(O)c1ccc(Cl)cc1</chem>	P-Bz-Cl c Co	<chem>O=P(O)(O)c1ccc(Br)cc1</chem>	P-Bz-Br c Co	<chem>O=P(O)(O)c1ccc(I)cc1</chem>	P-Bz-I c Co	<chem>O=P(O)(O)c1ccc(OCCCN)cc1</chem>	P-Bz-OC4N c Co
	1626			1626	1634	1622		1629		1626	1656	1656
P(O)(OH) group			1608		1588						1594	1591
C-C ring stretch		1528	1583	1579/ 1558/ 1539	1565/ 1540/ 1506	1560/ 1540/ 1505	1556/ 1505	1556/ 1540/ 1505	1550/ 1505	1550/ 1505	1577	1574/ 1557
C-C ring stretch	1467	1479	1480/ 1462	1474/ 1472	1471	1488/ 1465	1488/ 1464	1462	1462	1455	1485/ 1471	1471
C-C ring stretch	1456		1425	1420/ 1418			1436					1442
C-C ring stretch		1393			1399	1397	1399	1393	1393	1387	1393	1397
PO3 asymmetric stretching (1330cm ⁻¹)			1306		1337		1338		1339		1322	1312
	1277		1270	1265	1273	1260	1287/ 1262	1261	1261	1262	1288	1284
C-H inplane bending	1249/ 1223		1231	1218	1237						1239	1234

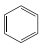
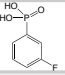
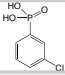
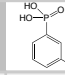
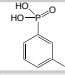
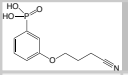
	Co ₂ (OH) _{3.5} (DSO) _{0.5}			P-Bz-F c Co		P-Bz-Cl c Co		P-Bz-Br c Co		P-Bz-I c Co		P-Bz-OC ₄ N c Co
C-H inplane bending and P=O (1200-1220cm ⁻¹)	1159		1162	1160			1198		1187		1195(w)	1197
C-H inplane bending		1176			1171/ 1158/ 1147	1140	1168/ 1143	1168(w)	1174	1170(w)	1165	1163(w)
C-H inplane bending							1126(w) /1112	1134	1139/ 1107	1133	1127	1118
PO ₃ symmetric stretching (1110 cm ⁻¹)	1104(w)		1117	1105	1097	1092	1086	1091	1086	1090	1091(w)	1089
P-O Probable zone and C-H inplane bending (1040 cm ⁻¹)					1084							
	1079		1062	1077			1070	1061	1061	1059		
	1042	1036		1042	1045	1044		1044(w)		1046	1047	1037
			1011/ 1001	1004	1007/ 994	1000	994	997	1003/ 991	996	1002/ 988	999
PO ₃ Symmetrical Deformation (605 cm ⁻¹)	606								597	607	602	
PO ₃ Asymmetrical deformation (510 cm ⁻¹)	503			518		506		518		515		523/ 519

Table 6 : IR bands of all hybrids and starting molecules obtained in cobalt hydroxide according to the literature⁴⁻⁷ and the spectral database for organic compounds (SDBS No.: 898).

As it can be seen from the table above, the different signatures of the molecules can be observed in the hybrid materials. Further analyses have been made to get more information about the water content and insertion ratios of the obtained hybrids.

5.1.3. TGA/TDA, Micro-Analysis, SEM and EDX

The same series of analyses than for copper hydroxide hybrids has been made for the hybrid compounds based on cobalt hydroxide. For the same reasons as discussed before (mixture of Co₃(PO₄)₂ and Co₃O₄ from the ashes), TGA/TDA could not be used to get an accurate metal content of the hybrids. The table below gives the proposed formulae for each compound with these different analyses.

TGA/TDA water content measured (calculated)	Co:P ratio via EDX measured (calculated)	Micro-analysis results measured (calculated)	Obtained formula
8.6% (6.8%)	5.47 (5.40)	Co : 58.9 (44.9), C : 10.19 (10.16) H : 3.12 (2.87), P : 2.41 (2.68) F : 2.41 (2.68)	P-Bz-FcCo Co ₂ (OH) _{3.63} (C ₆ H ₅ O ₃ PF) _{0.37} ·1H ₂ O
9.1% (13.1%)	5.81 (6.67)	Co : 42.97 (42.18), C : 7.88 (7.92) H : 3.38 (2.96), P : 3.39 (3.37) Cl : 2.71 (3.88)	P-Bz-ClcCo Co ₂ (OH) _{3.7} (C ₆ H ₅ O ₃ PCl) _{0.3} ·2H ₂ O
9.0% (0%)	6.50 (5.88)	Co : 47.7 (47.3), C : 8.65 (8.38) H : 2.95 (2.09), P : 2.92 (3.60) Br : 7.69 (9.29)	P-Bz-Br c Co Co ₂ (OH) _{3.71} (C ₆ H ₅ O ₃ PBr) _{0.29}
-	4.65 (5.71)	Co : 43.1 (40.4), C : 8.59 (8.65) H : 2.95 (2.35), P : 3.16 (3.72) I : 7.53 (15.23)	P-Bz-IcCo Co ₂ (OH) _{3.65} (C ₆ H ₅ O ₃ PI) _{0.35} ·0.7H ₂ O
9.1% (8.9%)	5.34 (5.00)	Co : 41.8 (39.0), C : 15.8 (15.9) H : 3.36 (3.67), P : 2.48 (4.10) N : 1.04 (1.85)	P-Bz-OC ₄ NcCo Co ₂ (OH) _{3.6} (C ₁₀ H ₁₁ O ₄ PN) _{0.4} ·1.5H ₂ O

Table 7 : Insertion ratios obtained in the cobalt hybrids.

The general insertion ratio is around 0.3-0.4 per formula unit, similar to the copper analogues. Yet, there are still some discrepancies between the calculated and the obtained elemental ratios, especially with the halogen titration. A rupture of the benzene-halogen bond is unlikely due to the relatively soft synthesis conditions. The question of the halogen titration methodology was also asked, but at the time of writing these lines, remains unanswered.

The size of the crystallites for the cobalt hybrids remains similar to the previously obtained hybrids and no obvious morphology changes could be observed from the small flakes (figure 14) obtained.

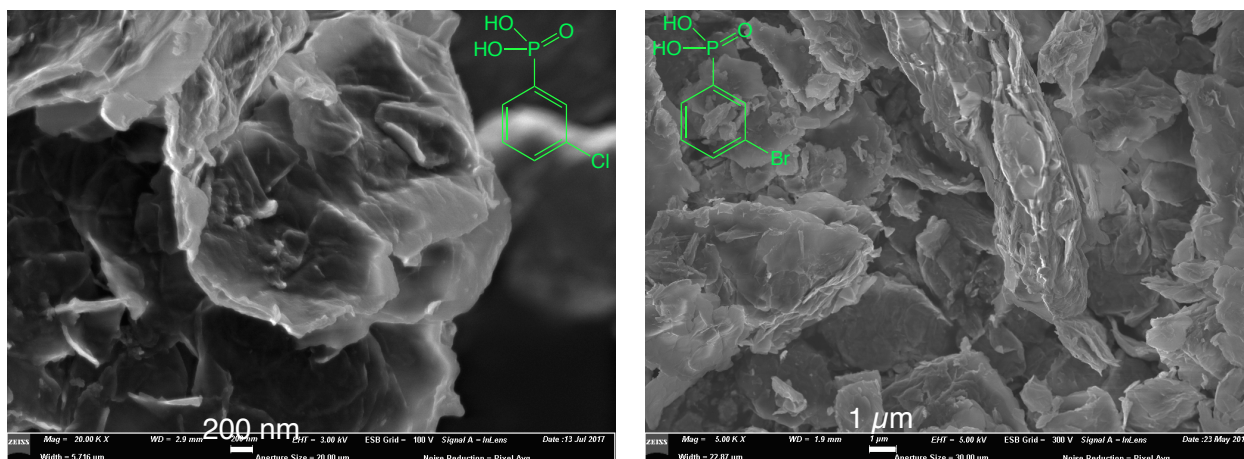


Figure 14 : Typical SEM images of cobalt hydroxide hybrids of P-Bz-ClCo (left) and P-Bz-BrCo (right).

6. Properties of the Hybrids Compounds

6.1. Luminescence

The first property that has been studied on the hybrids is the luminescence in the solid state. Only P-Bz-OC₄NCo and P-Bz-OC₄NCu have been studied yet. These first results indicate that luminescence appears to be present in P-Bz-OC₄NCo but seems to be quenched for P-Bz-OC₄NCu (figure 15). Indeed, the remaining luminescence observed for P-Bz-OC₄NCu is attributed to the tape present in the apparatus to hold the sample.

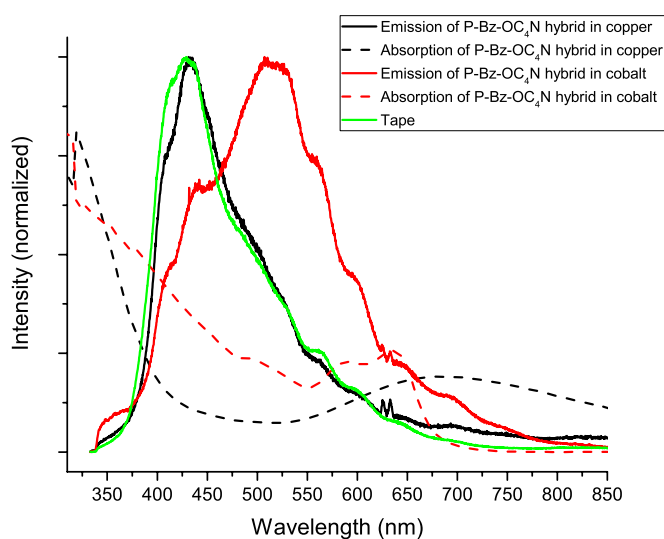


Figure 15 : Kubelka-Munk corrected and normalized solid state luminescence ($\lambda_{exc} = 320 \text{ nm}$) and absorption spectra of P-Bz-OC₄NCu and P-Bz-OC₄NCo.

Ignoring the intensities that have been normalized for all the spectra, the shape of the P-Bz-OC₄NcCu emission spectrum and the one of the scotch tape used are almost identical, which indicates that the main source of luminescence is coming from light scattered by the sample and hitting the tape instead of coming from the sample itself. The case of the P-Bz-OC₄NcCo hybrid is different as it exhibits a clear luminescence with a peak emission centred at 517 nm. The absence of luminescence for P-Bz-OC₄NcCu could be due to a difference in the packing of the molecules. Unfortunately, due to the physical form of P-Bz-OC₄N (viscous paste) we could not study the luminescence of the molecule alone.

Similar suggestions as stated in the previous chapter can be done to try to improve our understanding of the fluorescence properties, such as time resolved spectroscopy for example.

The magnetic properties of the hybrids have also been measured and the results are presented below.

6.2. Magnetic Properties of Cobalt Hybrid Compounds

Due to technical issues with our magnetometer and the expected antiferromagnetic behaviour of copper hybrids we focused our efforts on magnetic characterization of cobalt hybrids. The results of the measurements are listed on the table below.

Molecule in the interlamellar space	Curie Constant (emu·K·mol ⁻¹)	Weiss temperature θ (K)	Curie Temperature T _c (K)	Magnetization at 5 T (μ_B) (at 1.8K)	Coercive field at 1.8 K (T)
P-Bz-F	5.54	-3.4	10.9/8.0/2.9	2.90	0.09
P-Bz-Cl	5.43	-22.1	12.7/7.4	2.32	0.14
P-Bz-Br	5.41	-26.8	10.3/7.4	2.43	0.07
P-Bz-I	5.45	-17.9	10.1/7.4	2.75	0.05
P-Bz-OC ₄ N	5.41	-11.5	10.6	2.97	0.20

Table 8 : Magnetic properties of the layered cobalt hydroxide hybrids.

As can be seen in the table above the Curie constants range between 5.41 and 5.54 emu·K·mol⁻¹ which is in good agreement with a mixture of tetrahedral and octahedral high spin cobalt(II) ions. Indeed the values found in the literature range from 2.2 to 2.8 emu·K·mol⁻¹ for a tetrahedral cobalt(II) ion and from 2.8 to 3.4 emu·K·mol⁻¹ for an octahedral cobalt (II) ion.^{9, 10} As presented in figure 16, upon cooling the χT product of all the cobalt hybrids go through a minimum around 80 K. This small decrease is described as a consequence of the spin-orbit coupling and/or antiferromagnetic interactions between the cobalt(II) moments.¹¹

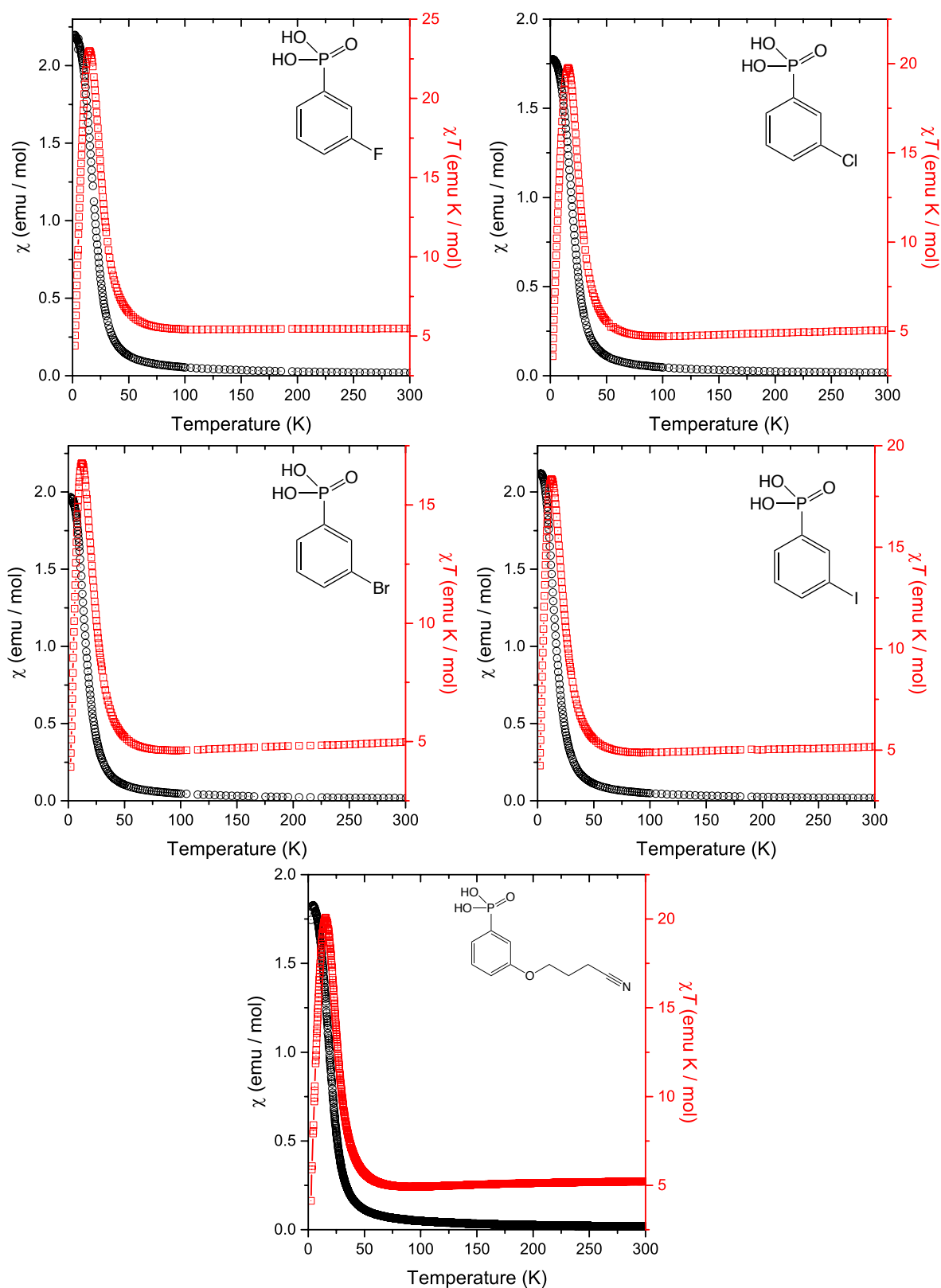


Figure 16 : χ and χT products of several cobalt hybrids measured at 5000G.

Below 80 K an increase of the χT product is observed and is related to the presence of short-range ferromagnetic-like interactions which leads to a long range ferrimagnetic ordering, supported by the occurrence of an out of phase signal in the imaginary part of the ac susceptibility, χ'' (figure 17). The ordering temperatures were determined from the maximum of the real part χ' of the ac susceptibility measurements.

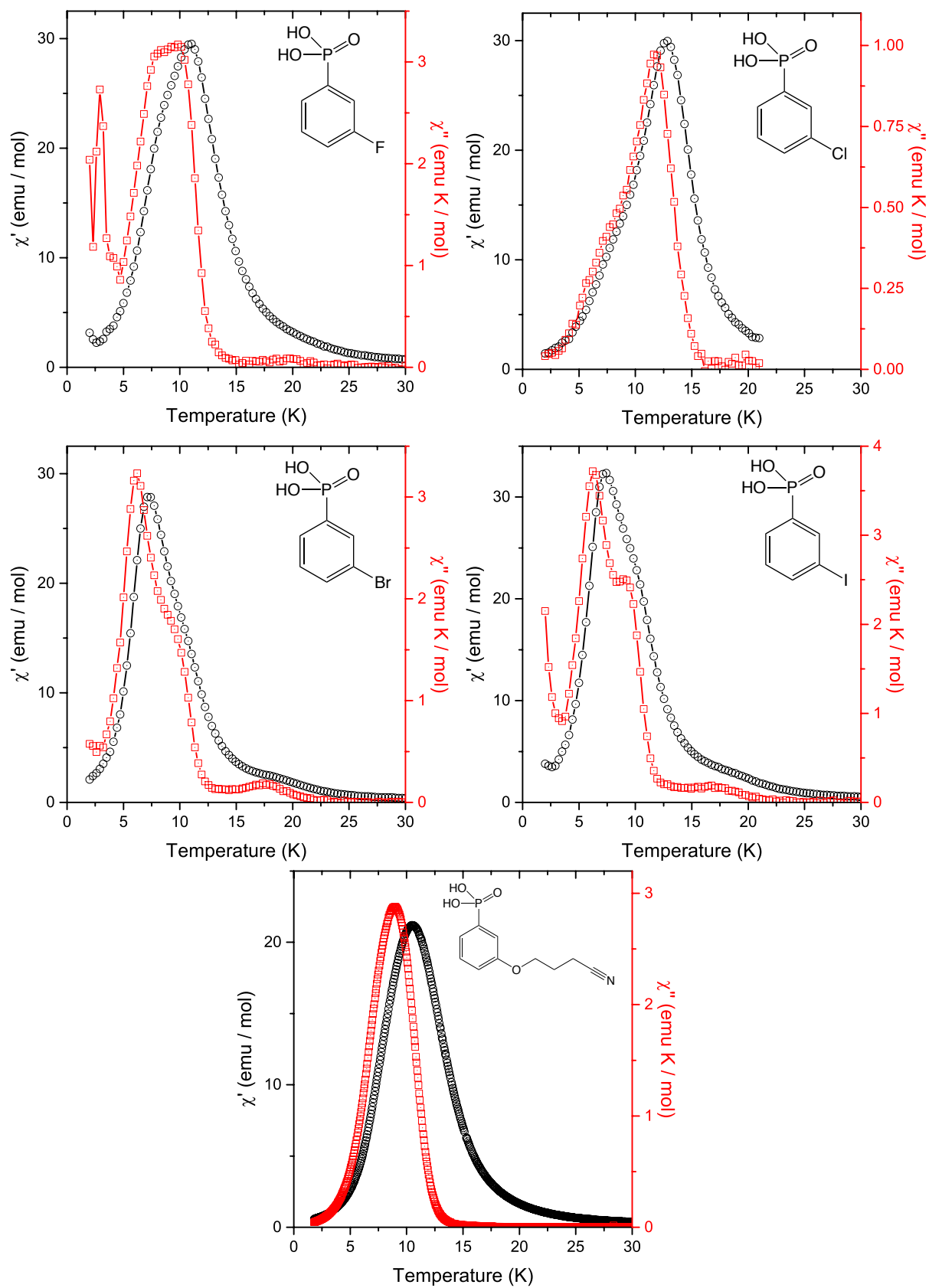


Figure 17 : ac susceptibility measurements of the cobalt-hydroxide-based hybrids ($f = 95$ Hz, $\mu_0 H_{ac} = 0.2$ mT).

As seen from the figure above, the presence of many peaks in ac susceptibility is observed in most of the hybrids with the exception of the most crystallized one (P-Bz-OC₄N₄Co) that keeps

a single phase with an ordering temperature of 10.5 K. This kind of magnetic behaviour has already been observed in the past as described in the chapter III. If there is no clear explanation about this behaviour, its dependence upon of the nature of the inserted molecule is even clearer with this series than with the fluorene series described in the previous chapter. It is noteworthy to see that, for hybrids presenting several peaks in ac susceptibility, the peaks appear at the same temperature ranges : one peak being at high temperature (around 17 K), another one around 10 K and the third one around 7 K. The presence of a lower ordering temperature in this series at 2 K or even less has, however, never been observed before. Complementary measurements such as AC measurements at multiple frequencies or different heating cycles to get rid of most of the interlamellar water should be done to see how these phases evolve and should help us to have a better understanding of these behaviours.

Finally, the magnetization versus field curves that have been measured at 1.8 K and confirm the ferrimagnetic ordering of the cobalt hydroxide hybrids with the presence of hysteresis loops and coercive fields of 0.05 to 0.20 T, values marginally lower than those obtained with fluorene-based hybrids. As seen in figure 18 the low moment values at high field (5 T) ranging from 2.32 to 2.97 μ_B compared to the expected value for a total alignment of the moments (4 to 6 μ_B for two cobalt (II) ions) is explained by the ferrimagnetic ordering identical as the one explained in chapter III.¹¹

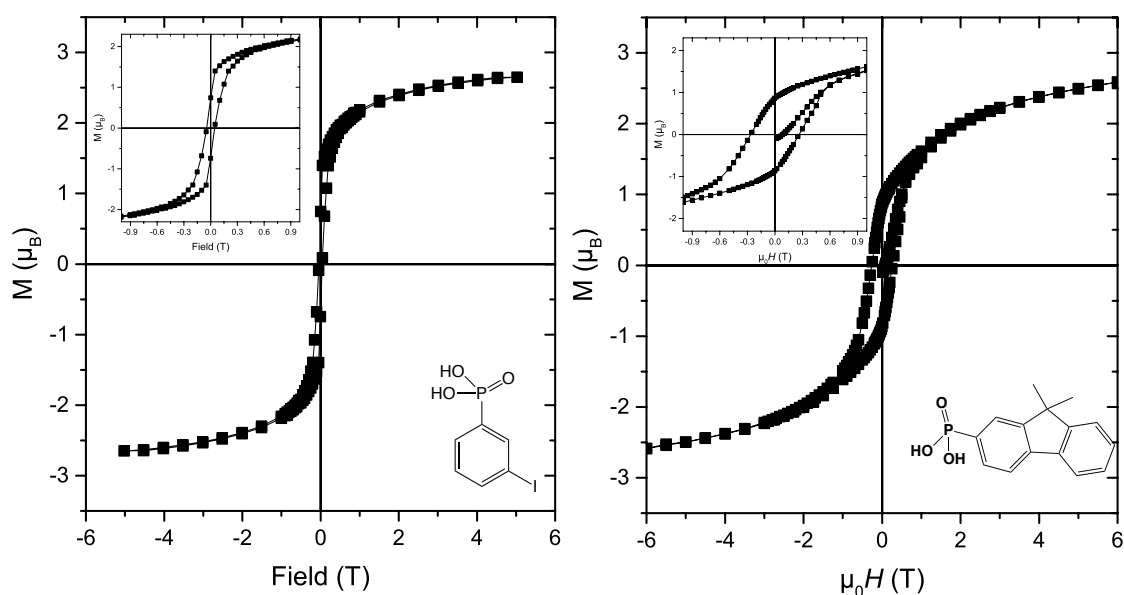


Figure 18 : comparison of magnetization vs. field curve of P-Bz-Ic Co and P-Fluo-Cc Co hybrids (magnification of the opening in insert).

As illustrated in figure 18, the benzene derivative series present significantly smaller coercive fields than the fluorene series described in the previous chapter. The remanent magnetization, however, is comparable between the benzene and fluorene based hybrids. In all cases, these coercive fields are much weaker than the ones observed in an analogous compound I synthesized before this PhD (a layered cobalt hydroxide functionalized by a terephthalate molecule). This terephthalate hybrid presents a much stronger coercive field of 0.43 T at 2 K (with $T_c = 18$ K). A hybrid obtained by hydrothermal synthesis and presenting purely octahedral cobalt layers, functionalized by terephthalate has an even stronger coercive field with values in excess of 5.9 T.²

6.3. Magnetoelectric Effect

All the samples are currently under study for their possible magnetoelectric effects. The first results are showing that a strong magnetoelectric effect is present in the P-Bz-Cl₂Co hybrid but appears to be weaker for P-Bz-I₂Co and P-Bz-Br₂Co hybrids meanwhile it seems to be absent in P-Bz-F₂Co.

7. Conclusion

In this chapter we have shown the successful insertion of a series of benzene phosphonic molecules into layered copper and cobalt hydroxides. The possibility to modify the insertion rates along with the reaction conditions was investigated, and we determined that we can modify only slightly the insertion rate (0.3 to 0.4) while maintaining a single phase. Additionally it has been shown that it was possible to insert smaller molecules without the need for pre-intercalation strategy on P-Bz-F₂Co hybrid.

The difference of reactivity of carboxylic and phosphonic acids has also been studied, shedding light upon the ability of carboxylic acid to form co-inserted phases with dodecylsulfate instead of purely inserted hybrids observed with most phosphonic acid based hybrids. Some aspects of the kinetics of this insertion reaction are also studied for the P-Bz-OC₄N hybrids in copper hydroxide but more efforts should be made, in particular from the excess ratio influence.

The magnetic measurements indicate that the cobalt-based products all keep their general ferrimagnetic behaviour but the observed coercive fields are substantially lower than those observed with fluorene based hybrids. The remanent magnetization remains similar between the hybrids.

Preliminary results of the ongoing measurements of magneto-electric effects in cobalt-based hybrids show that they are substantial variations of the magneto-electric effect with change of the halogen, further measurements and crosschecking are in progress to quantify these changes accurately.

8. Bibliography

1. J.-M. Rueff, V. Caignaert, A. Leclaire, C. Simon, J.-P. Haelters and P.-A. Jaffrès, *CrystEngComm*, 2009, **11**, 556-559.
2. Z.-L. Huang, M. Drillon, N. Masciocchi, A. Sironi, J.-T. Zhao, P. Rabu and P. Panissod, *Chemistry of Materials*, 2000, **12**, 2805-2812.
3. B. D. Cullity and S. R. Stock, *Elements of X-ray diffraction*, Pearson, 3rd Edition, 2001.
4. H. Nijs, A. Clearfield and E. F. Vansant, *Microporous and Mesoporous Materials*, 1998, **23**, 97-108.
5. G. Guerrero, P. H. Mutin and A. Vioux, *Chemistry of Materials*, 2001, **13**, 4367-4373.
6. C. S. Kim, R. J. Lad and C. P. Tripp, *Sensors and Actuators B: Chemical*, 2001, **76**, 442-448.
7. K. D. Demadis and S. D. Katarachia, *Phosphorus, Sulfur, and Silicon and the Related Elements*, 2004, **179**, 627-648.
8. Y. J. Chabal, *Surface Science Reports*, 1988, **8**, 211-357.
9. R. L. Carlin, *Magnetochemistry*, Springer-Verlag Berlin Heidelberg, 1986.
10. O. Kahn, *Molecular Magnetism*, VCH Publishers, 1993.
11. J. R. Neilson, D. E. Morse, B. C. Melot, D. P. Shoemaker, J. A. Kurzman and R. Seshadri, *Physical Review B*, 2011, **83**.

Chapter V : Layered Hydroxides Hybrid Materials Obtained by
Intercalation of Thiophene Derivatives

Chapter V : Layered Hydroxides Hybrid Materials Obtained by Intercalation of Thiophene Derivatives

The main objective of this chapter was to insert molecules based on a thiophene rigid platform instead of a benzene or fluorene. The addition of a heteroatom in the rigid body brings an additional potential polarization and may contribute to lower the symmetry of the system.

1. Introduction

The molecules used in this chapter are described in figure 1. They are composed of either single or bis-thiophene rigid bodies, a methyl group is also added on one of them to break the molecule symmetry.

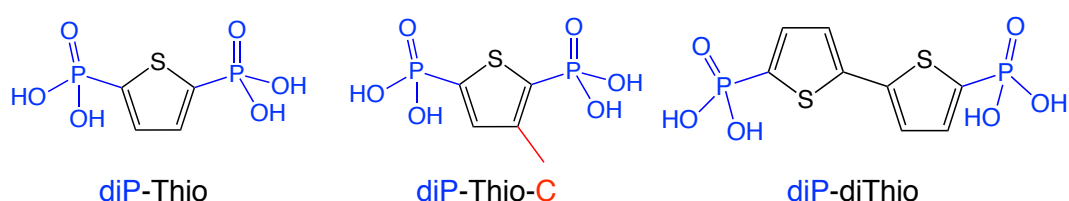


Figure 1 : Molecules and nomenclature used in this chapter.

It must be noted that for this specific series of compound, previous experience acquired during the PhD of Aude Demessence¹ in our laboratory led to many hybrids based on thiophene molecules albeit with carboxylic acid as a grafting moiety (figure 2).²⁻⁵ The main difference (other than reactivity) between a carboxylic and phosphonic acid based thiophenes derivatives being the disappearance of the conjugation between the two layers in the phosphonic acid system.

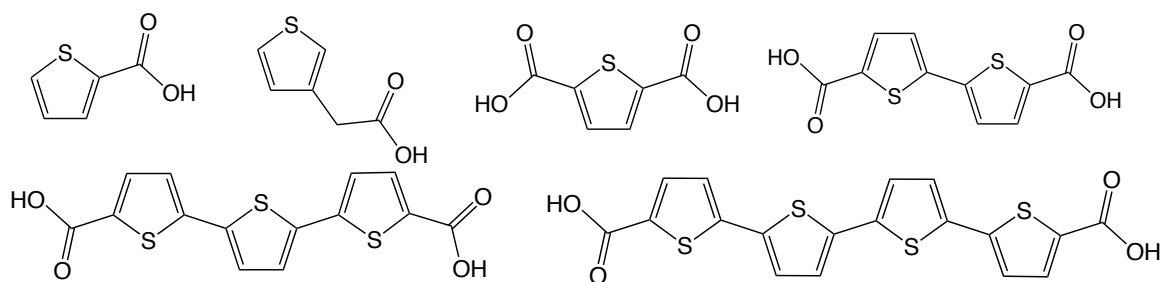


Figure 2 : Molecules used previously in our laboratory.

The layered hybrid materials studied during Aude Demessence's PhD were obtained either by exchange reactions from a layered hydroxide or by direct (« one pot ») synthesis in hydrothermal conditions. This allowed the synthesis of many layered hybrid materials. Among them the hybrids obtained with monothiophene molecules by anionic exchange led to interesting magnetic properties with 3D ferrimagnetic behaviours with high ordering temperatures around 55 K. Unfortunately, the luminescence of the system was completely quenched.² This quench was also observed for oligothiophene containing hybrids, obtained *via* hydrothermal method, and was attributed to strong intermolecular interactions within the interlamellar spacing and to a fast photoinduced electron transfer from the fluorophore to the metal hydroxide layers, which deactivates the oligothiophene singlet excited state (S1) before luminescence can occur.⁵

This quenching appears to be favoured by the coordination of paramagnetic ions (with unpaired d electrons) to carboxylates directly linked to the chromophore. This hypothesis is supported by the fact that the luminescence of another chromophore, oligophenylene vinylene, is indeed preserved when inserted into layered hydroxides using carboxylate anchoring functions separated from the conjugated fluorophore by long alkyl chains.⁶ The use of other grafting functions, such as sulfate, sulfonate or phosphonate, which does not allow electron delocalization between the aromatic moieties and the coordinated metal ion, may be an alternative to isolate the chromophore and to prevent the quenching of fluorescence.

Other thiophene carboxylate systems have been studied for several interesting properties such as intense metal to ligand charge transfer with 2-thiophenecarboxylate or 2,5-thiophenedicarboxylate coordinated to molybdenum or tungsten quadruple-bonded metallic centers.^{7, 8} Coordination chemistry of thiophenedicarboxylate towards transition metals such as copper, zinc, cobalt or manganese has been also studied with or without the presence of a nitrogen ligand.^{9, 10} Many other examples can be found in the literature concerning thiophene carboxylates complexes.¹¹⁻¹³

Examples with thiophene phosphonic acids are, however, much less present in the literature. Our colleagues in Caen, involved in the ANR project supporting the PhD, obtained a manganese containing layered MOF with thiophene diphosphonic acid with an interesting change of the orientation of the thiophenes upon dehydration.¹⁴ Another hybrid has been obtained with copper-layered phosphonate forming dimeric entities ($\text{Cu}_2\text{O}_6(\text{H}_2\text{O})_2$) linked with each other *via* phosphonic acids moieties.¹⁵ (Oligo)thiophenes has been mostly studied for phosphonate derivatives with zirconium¹⁶ or zinc¹⁷ in the past.

One interesting and recent work is the generation of chirality based on the prochiral character of the thiophene diphosphonic acid associated with cobalt ions and 4,4'-bipyridines demonstrating the potential gain of switching from carboxylic to phosphonic acid to get the non-centrosymmetry character, required to have ferroelectric properties.¹⁸

2. Intercalation Chemistry

The previously used conditions *i.e. via* the pre-intercalation method used with fluorenes and benzene could also be used with only slight variations to insert P₂-Thio-C and P₂-diThio in layered cobalt and copper hydroxides.

This insertion has, however, proved to be more difficult with the P₂-Thio molecule, both in copper and cobalt hydroxide. It was hinted that the alkyl-alkyl packing interactions might be inhibiting the insertion of such small molecules. To that end, we attempted to shorten the chains by inserting ethyl sulfate first as a pre-intercalation compound. All attempts to synthesize copper or cobalt hydroxides functionalized by ethyl-sulfate have unfortunately been unsuccessful. The idea was then changed to use an unsaturation in the chain to disrupt the packing as much as possible, while maintaining a high enough cohesion force between the lamellae while having a large interlamellar spacing. Due to availability and pricing reasons, the chosen molecule was oleyl-sulfate, a sulfate having an unsaturation in the middle of the chain (9th position) for a total chain length of 18 (figure 3) and which is yet rather difficult to obtain from chemical companies.

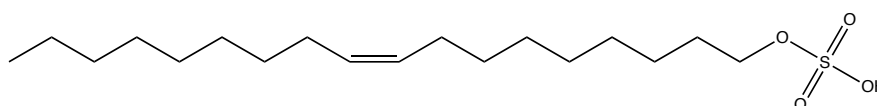


Figure 3 : Scheme of the oleyl-sulfate.

2.1. Oleyl Sulfate-Intercalated Copper Hydroxide

The first attempt to intercalate oleyl-sulfate in the copper hydroxide was performed with the following conditions :

- A two-fold excess solution of oleyl-sulfate was prepared in a 15 mL/10 mL (H₂O/EtOH) without any pH adjustments due to the moderate acidity of the sulfate group.
- This solution was bubbled under argon for 15 minutes to avoid any unwanted contamination from carbonates for example.
- Copper hydroxy acetate was then added to the solution and the obtained mixture was thermostated at 25°C for 3 days.
- The bluish powder was then filtered and washed thoroughly with water and ethanol.

The XRD of the obtained compound shows the presence of the starting compound (9.3 Å), indicating that the reaction temperature was probably too low to allow the exchange to fully take place, and several other peaks (37.5, 31.4 and 28.6 Å), which might be related to different degrees of hydration of the desired compound (figure 4). In order to confirm or infirm this last hypothesis, the sample was then dried at 80°C for 10 minutes. This thermal treatment allowed to get rid of the hydrated phase at 31.4 Å but unfortunately still led to a two-phase compound with the two extreme distances remaining unchanged (figure 4). The presence of the starting compound was also visible in the IR spectra showing clearly carboxylate moieties along with the oleyl-sulfate alkyl chains.

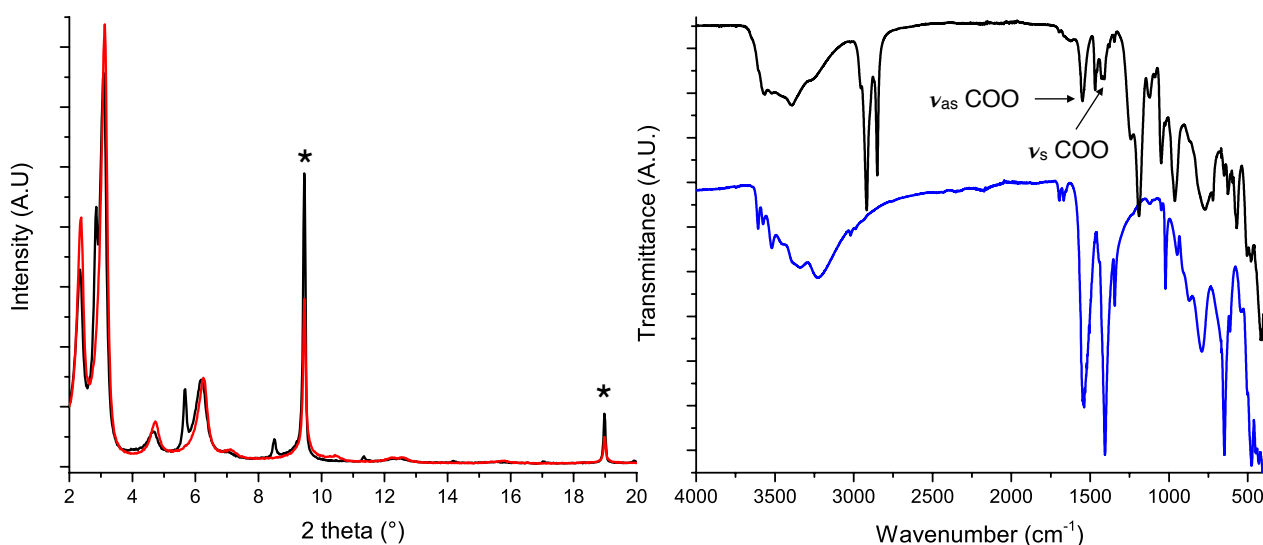


Figure 4 : XRD (left) of the obtained compound (black) and after heating (red) and infrared spectra of Cu₂(OH)₃OAc (blue) and the obtained compound (black). Stars represent the unreacted starting compound.

To obtain a single phase compound, the obtained multiphasic product was put in its reactive medium again and heated at 60°C for one hour and a half (figure 5). The XRD obtained just after the reaction shows a clear peak asymmetry. The compound was then heated at 80°C for 15 minutes, which enhanced the crystallinity slightly and suppressed the peak asymmetry.

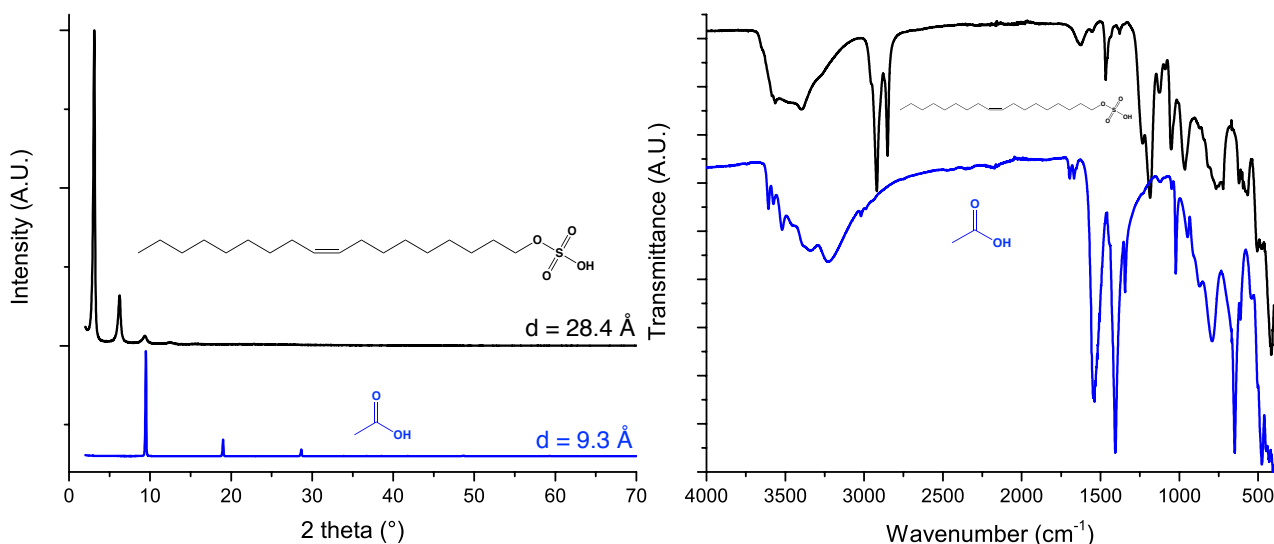


Figure 5 : XRD (left) and infrared spectra (right) of the heated oleyl-sulfate intercalated in copper hydroxide (black) and the starting compound $\text{Cu}_2(\text{OH})_3(\text{OAc})$ (blue).

As seen from the figure above, the obtained compound is single phase and corresponds to the one previously observed with the shortest interlamellar distance (28.4 Å). Interestingly, it is possible that the previously observed phase with $d = 37.5$ Å corresponds to a staging phenomenon, with an alternance of oleyl and acetate intercalation. This staging phenomenon was often observed in Layered Double Hydroxides¹⁹ but also in cobalt layered simple hydroxide.²⁰

To investigate whether this is purely incidental or if this staging state can be seen as an intermediary compound would require further investigations and a better availability of oleyl-sulfate.

Once the synthesis of pre-intercalated compound with oleyl-sulfate in copper hydroxide has been mastered, the experience acquired has been applied to the cobalt hydroxide and the results of these experiments are discussed in the following section.

2.2. Oleyl Sulfate-Intercalated Cobalt Hydroxide

The experimental conditions to obtain a single phase oleyl-sulfate intercalate cobalt hydroxide were set with the heating at 60°C of a 12/12 mL ($\text{H}_2\text{O}/\text{EtOH}$) solution of two-fold excess of oleyl-sulfate in presence of 0.165 mmol of cobalt hydroxy acetate for 6 hours. This reaction led to a compound having a relatively low crystallinity and an interlamellar spacing of 26.7 Å (figure 6). The compound was then heated at 70°C in water during 30 minutes to increase the crystallinity. Indeed, as it was noticed in previous syntheses of our compounds, the hydration (whenever possible) led to compounds having a better crystallinity, mainly noticeable by the increase of the numbers of 00l diffraction peaks observed and a small narrowing of the width at half-maximum of the peaks. This procedure led to a better crystallized compound and with a larger interlamellar spacing of 30.6 Å (figure 6).

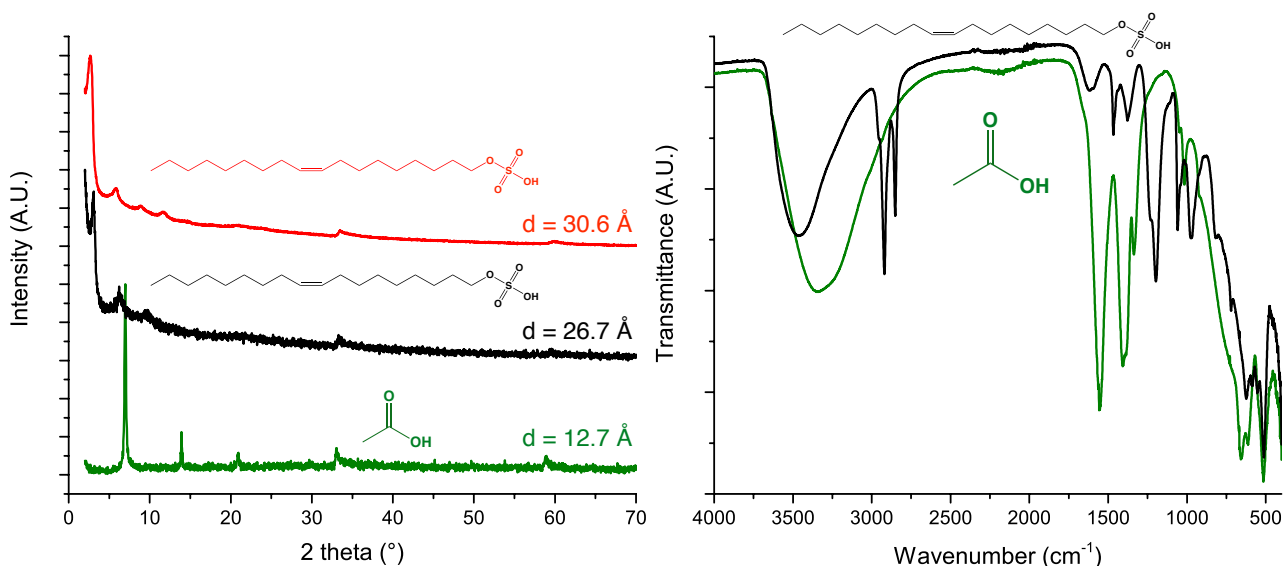


Figure 6 : XRD (left) and infrared spectra (right) of $\text{Co}_2(\text{OH})_3(\text{OAc})$ (green), pristine oleyl-intercalated cobalt hydroxide (black) and hydrated oleyl-intercalated cobalt hydroxide (red).

It must be noted that the hydrated compound presents up to 7 001 harmonics visible, which is quite unusual for cobalt hydroxide based materials and might allow us to perform unidimensional analysis of the electron density in the future to further investigate the packing of the oleyl-sulfate in the interlamellar space.

Once these two pre-intercalated hybrids were obtained, the insertions of the P₂-Thio molecule could be performed with copper and cobalt hydroxides as developed in the next section.

3. Insertion of Thiophene Derivatives in Copper Hydroxide

3.1. Reactions Conditions and Usefulness of the Oleyl-Sulfate-Intercalated Compound as an Alternative Pre-Intercalated Compound

As seen previously, several methods have been developed to allow the insertion of such molecules in layered simple hydroxides, the experimental conditions for successful insertion in copper hydroxides are listed in the table below :

Inserted molecule	PO ₃ :DS ratio (1 = 0.165mmol)	pH	Temperature	Time	Solvent (H ₂ O/EtOH)
P ₂ -Thio	3:1 (PO ₃ :Oleyl)	8.3	82°C	1h	12/12 mL
P ₂ -Thio-C	3:1	8.9	82°C	6h	12/12 mL
P ₂ -diThio	2:1	8.7	82°C	4h	12/12 mL

Table 1 : Experimental conditions used to obtain single phase hybrids based on copper hydroxide.

As shown in the table above, only the P₂-Thio molecule required the use of oleyl-sulfate, indeed for this specific compound, the reaction seemed vastly incomplete when starting from Cu₂(OH)₃(DS) even in rather harsh conditions with 2 hours reflux (85°C) in a 20/12 (H₂O/EtOH) and a 4:1 excess ratio at pH 8.7 (figure 7).

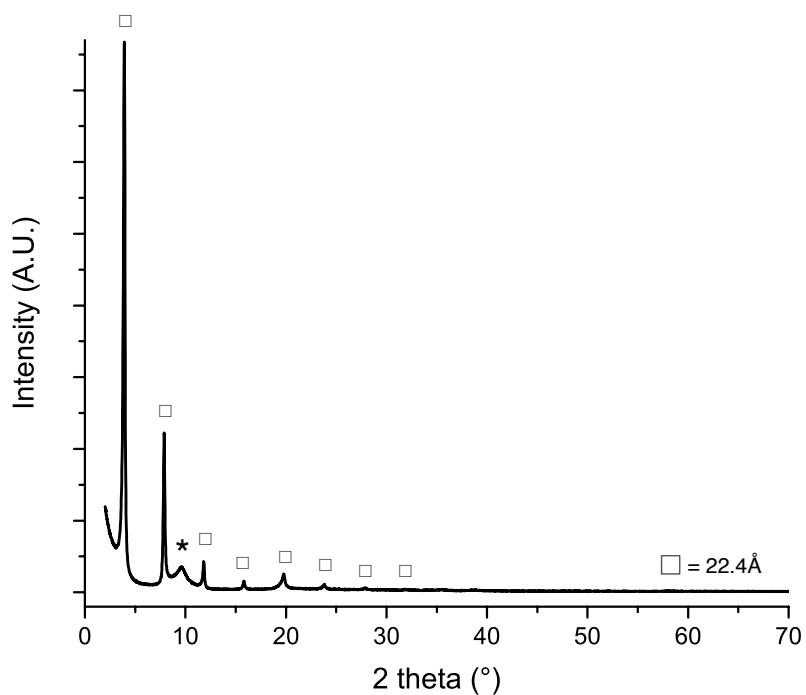


Figure 7 : XRD pattern of the reaction of P_2 -Thio with $Cu_2(OH)_3(DS)$ (Star represents the purely inserted compound, squares represents a co-inserted compound).

Under these harsh conditions, reaction times that are longer than two hours lead to the formation of oxides, while only marginally improving the ratio of purely inserted (star) and co-inserted compound (squares) as seen in figure 8.

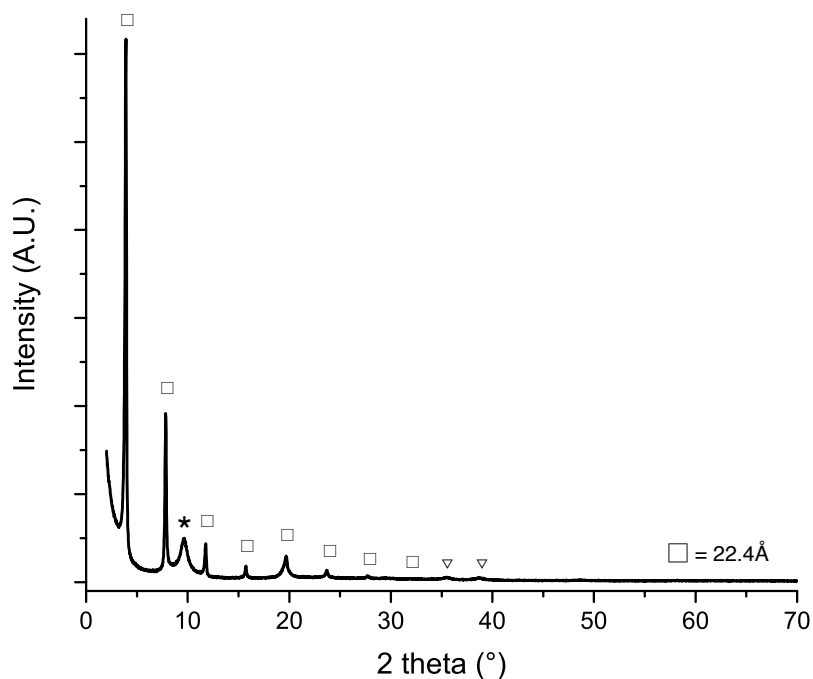


Figure 8 : XRD pattern of the reaction of P_2 -Thio with $Cu_2(OH)_3(DS)$ with 4 hours reaction time (Star represents the purely inserted compound, squares represents a co-inserted compound and triangles the copper oxide).

3.2. XRD and Infrared Spectra of the Thiophene Copper Hydroxide Hybrids

The experimental condition described earlier produced hybrids with interlamellar spacing of 9.0, 9.3 and 17.2 Å for P₂-Thio_CCu, P₂-Thio-C_CCu and P₂-diThio_CCu respectively.

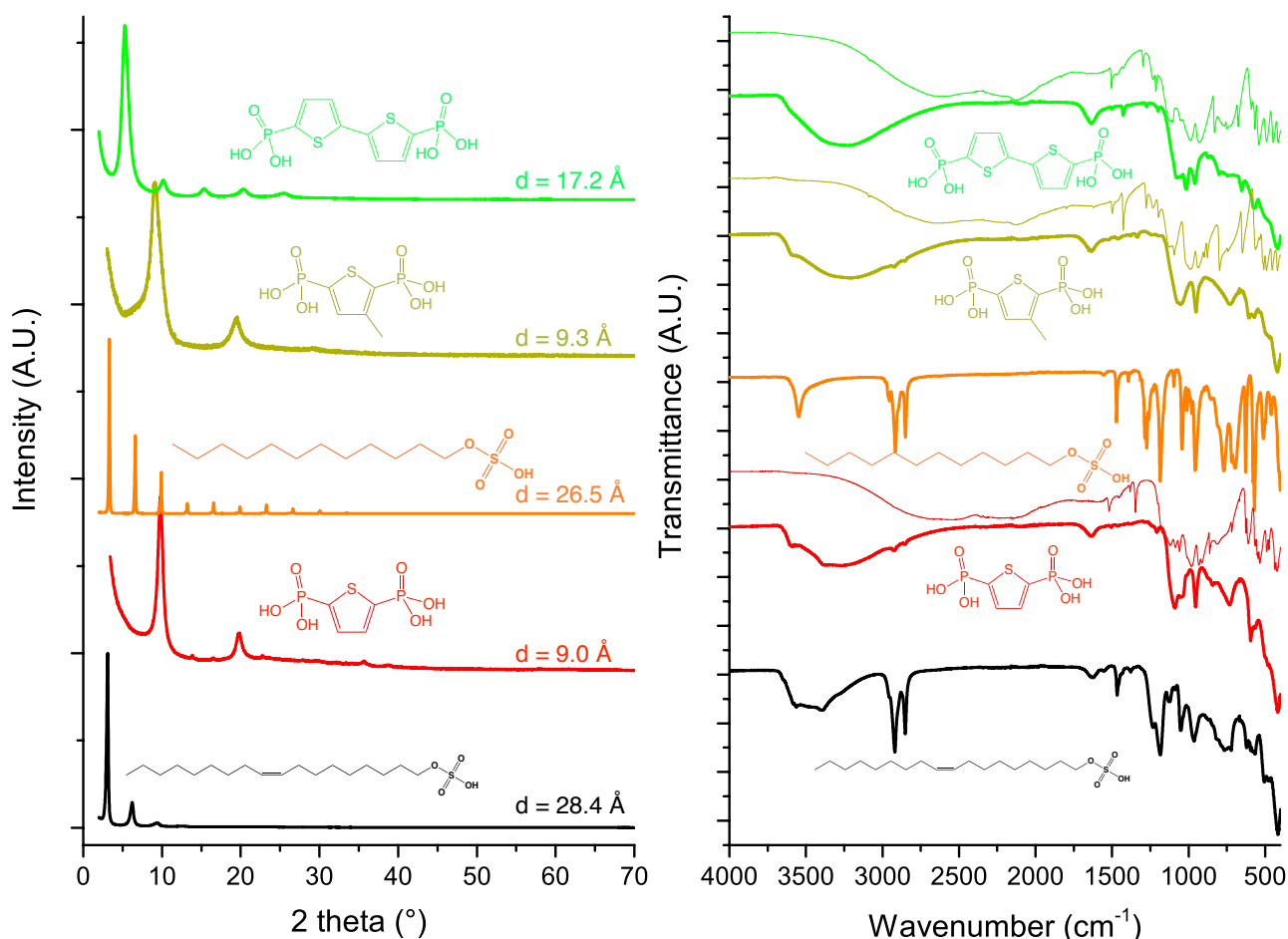


Figure 9 : XRD (left) and infrared spectra (right) of thiophene hybrids (bold lines), molecules alone (thin lines) and starting compounds.

According to IR spectra presented in figure 9 (right), all the hybrids exhibit traces of alkyl chains except the P₂-diThio_CCu hybrid. Yet, the interlamellar distance in P₂-Thio_CCu and P₂-Thio-C_CCu (around 9 Å) is incompatible with the one expected for co-intercalated compounds. The most probable explanation is that the difficulty to wash the compounds leads to some of the oleyl or dodecyl sulfate to remain on the surface of the crystallites.

The observed interlamellar spacing for in P₂-Thio_CCu and P₂-Thio-C_CCu are compatible with a bridging of the thiophene between two layers, the molecule being 7.6 Å long at best (figure 10). By taking the other extreme example (the two closest oxygen of the two phosphonic acids) with 6 Å it gives either a purely perpendicular grafting or a small 37° tilt with respect to the normal of the layers for the P₂-Thio_CCu and P₂-Thio-C_CCu hybrids respectively.

The case of P₂-diThio_CCu is in accordance with a non-bridging configuration similar to the P₂-Fluo-H_CCu, indeed, considering the length of the molecule (around 11 Å) a bridging would be incompatible with the observed interlamellar spacing of 17.2 Å. At this stage, two hypotheses can be proposed, either the formation of a bilayer configuration with a tilt angle of approximately 50° or

the existence of a water network between the uncoordinated phosphonate moiety and the inorganic layer, similarly to what was described in chapter III for the P_2 -Fluo- $H\text{-Cu}$. Experimental and theoretical investigations are under way to discriminate between these two hypotheses.

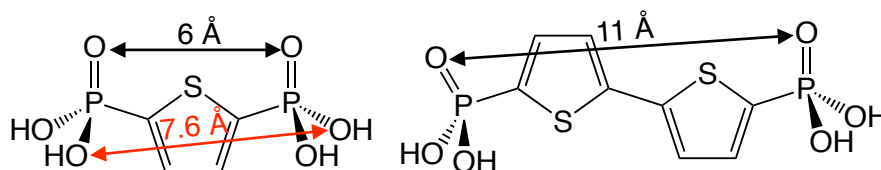


Figure 10 : Typical distances for the P_2 -Thio and P_2 -diThio molecules (calculated from Chem3D program).

The table below is an attempt of attributing the IR bands. Due to the high number of bands present in the 1600-600 region, these attributions are coming with the same caveat as explained for the benzene and fluorene hybrids.

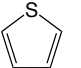
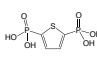
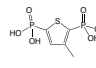
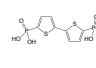
	$\text{Cu}_2(\text{OH})_3(\text{DS})$	$\text{Cu}_2(\text{OH})_3(\text{Oleyl})$			$P_2\text{-Thio-Cu}$		$P_2\text{-Thio-CcCu}$		$P_2\text{-diThio-Cu}$
C-C ring stretch		1554		1504	1506	1520	1527	1499	1500
C-C ring stretch	1471	1467/ 1456		1460	1466/ 1456	1456	1467/ 1456		
C-C ring stretch	1394	1409	1408	1423		1420		1427	1427
PO_3 asymmetric stretching (1330 cm^{-1})							1335		1339(w)/ 1317
P=O ($1200\text{-}1220\text{ cm}^{-1}$)	1259/ 1233	1232		1233/ 1214	1235/ 1208		1237	1232	1215
		1185		1188		1201	1197	1197	1199
C-H inplane bending		1126		1119/ 1104		1119		1127	
PO_3 symmetric stretching (1110 cm^{-1})	1096	1089	1081	1081	1090	1086		1094	
P-O probable zone		1052		1056	1050	1060	1068		1077
	1042	1035	1034	1047/ 1020	1038		1052		1048
	1011	1009		988	1011	1009		1015	1016
	990/ 980	964			982	981		987	
PO_3 Symmetrical Deformation (605 cm^{-1})		605				610/ 597	605		
PO_3 Asymmetrical déformation (510 cm^{-1})	512	505				525		515/ 509	

Table 2 : IR bands of starting molecules and all corresponding copper hydroxide-based hybrids.

As seen in the table above, the signature of the molecules can be seen in the hybrids, along with traces of dodecylsulfate or oleyl-sulfate with the exception of the P₂-diThio_CCu hybrid which does not show any traces of dodecylsulfate.

3.3. TGA/TDA, Micro-Analysis and EDX of the Thiophene Copper Hydroxide Hybrids

As done previously, the different analyses have been performed using the same methodology described for the benzene and fluorene derivatives. The results are shown in the table below :

TGA/TDA water content measured (calculated)	Cu:P ratio via EDX measured (calculated)	Micro-analysis results measured (calculated)	Obtained formula
-	9.14 (x)	-	P ₂ -Thio _C Cu Cu ₂ (OH) _{3,x} (C ₄ H ₄ O ₆ P ₂ S) _{0,x} ·yH ₂ O
12.5% (6.8%)	5.76 (4.54)	Cu : 50.6 (48.5), C : 6.00 (5.04) H : 3.11 (2.65), P : 4.25 (5.20) S : 1.87 (2.69)	P ₂ -Thio-C _C Cu Cu ₂ (OH) _{3,56} (C ₅ H ₆ O ₆ P ₂ S) _{0,22} ·1H ₂ O
15.0% (9%)	4.43 (3.70)	Cu : 43.4 (42.3), C : 8.89 (8.63) H : 2.87 (2.71), P : 3.39 (5.76) S : 3.38 (5.57)	P ₂ -diThio _C Cu Cu ₂ (OH) _{3,73} (C ₈ H ₆ O ₆ P ₂ S ₂) _{0,27} ·1.5H ₂ O

Table 3 : Calculated formula for the different copper hybrid compounds. Unfortunately, due to the very small quantity of P₂-Thio-Cu obtained, the TGA and micro-analysis could not be performed on this compound.

As observed from the table above, the insertion rates are in line with the ones observed with the previous fluorene or benzene derivatives. The discrepancy on the TGA/TDA analysis could be due to a lack of thermal stability of these compounds upon heating, indeed, as seen from figure 11, there is a rather continuous mass loss until an unknown exothermic reaction leading to a gain of mass at 225°C probably due to a first decomposition of the organic molecules.

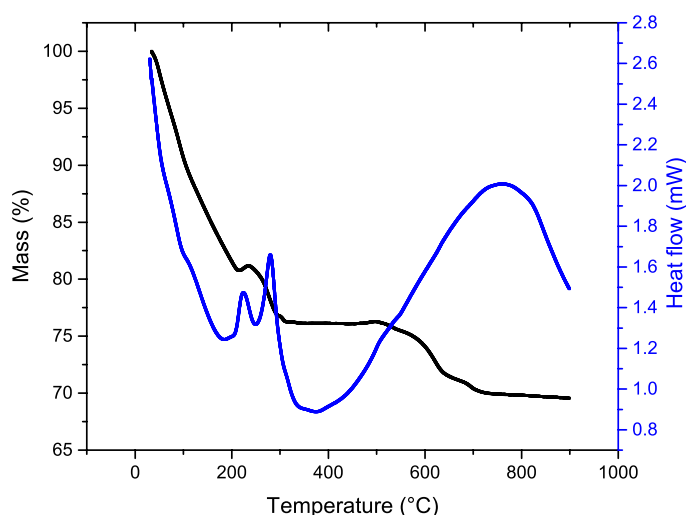


Figure 11 : TGA/TDA of P₂-diThio_CCu hybrid, typical of all thiophene hybrids.

The morphologies of the platelets are relatively different between P₂-Thio-C_CCu and P₂-diThio_CCu, as shown in figure 12 below. The same texturation of the surface of the platelets with parallel stripes and sharp edges is clearly visible for P₂-diThio_CCu meanwhile the P₂-Thio-C_CCu

platelets exhibit much smoother edges along with a silky surface texturation similar to what has been observed with P-Bz-OC₄N_cCu (chapter IV). The platelet size of P₂-Thio_cCu was unfortunately too small due to the additional synthetic step so the morphology could not be accurately compared to the other two hybrids.

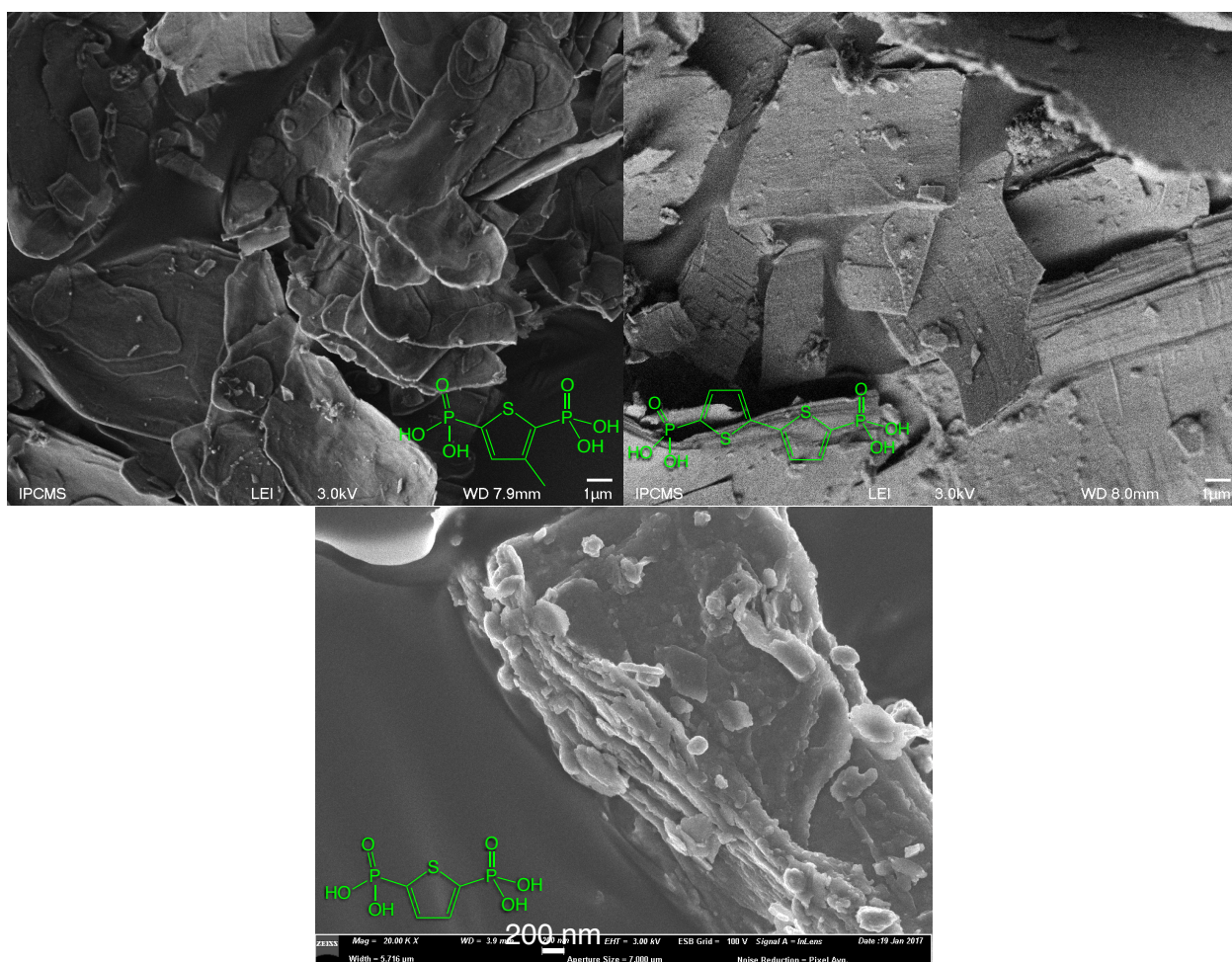


Figure 12 : SEM images of P₂-Thio-CcCu (top left) and P₂-diThioC Cu (top right) and P₂-ThioC Cu (bottom).

Hybrids were also made from cobalt hydroxide, the results of these experiments are described below.

4. Insertion of Thiophene Derivatives in Cobalt Hydroxide

4.1. Reactions Conditions Used to Obtain Thiophene Cobalt Hydroxides Hybrids

As described in the section 3.1 concerning copper hydroxide, the same experimental procedure can be applied to cobalt hydroxide. The pre-intercalation of oleyl-sulfate is mandatory for the P₂-Thio_cCo hybrid but remains optional for P₂-Thio-C_cCo and P₂-diThio_cCo. The reaction conditions used to obtain single phase hybrids are described in the following table.

Inserted molecule	PO ₃ :DS ratio (1 = 0.165 mmol)	pH	Temperature	Time	Solvent (H ₂ O/EtOH)
P ₂ -Thio	≈ 3:1 (PO ₃ :Oleyl)	8.1	82°C	1h	12/12 mL
P ₂ -Thio-C	2:1	8.8	82°C	4h	12/12 mL
P ₂ -diThio	2:1	8.7	84°C	3.25h	20/12 mL

Table 4 : Experimental conditions used to obtain single phase hybrids based on cobalt hydroxide.

The experimental procedures are similar to the one used with copper hydroxide. The use of a different water/ethanol ratio for the synthesis of P₂-diThio corresponds to an attempt to increase slightly the reaction temperature in order to reduce the reaction time. This temperature increase is indeed possible due to a better resistance to oxidation of the cobalt hydroxide compared to the copper hydroxide possible due to the higher resistance to oxidation from the cobalt hydroxide compared to the copper hydroxide. Yet the temperature variation is too limited to provide a significant gain on the reaction time. These conditions led to the hybrids described in the section below.

4.2. XRD and Infrared Spectra of the Thiophene Cobalt Hydroxides Hybrids

All hybrids have been obtained as single phase materials albeit with a very low crystallinity, as unfortunately often observed for cobalt hydroxide based hybrids.

However, according to its diffractogram made right after the end of the reaction (figure 13) P₂-Thio-C₆₀ does not seem to be a single phased material. According to our previous experience, this might be due to a partial dehydration process. To test this hypothesis, the same thermal treatment applied to oleyl-sulfate-cobalt hydroxide *i.e.* heating at 70°C for 30 minutes in water has been performed on P₂-Thio-C₆₀ leading to a single phase compound (figure 13). This hydration process was chosen over the dehydration one due to the fact that the compound crystallinity was already low and that usually dehydrated forms exhibit even lower crystallinity than their hydrated parent material. The acquisition conditions, sample and sample holder are identical in the two diffractograms, the hydration being done on the sample holder by putting water on the sample and heating it to 70°C. The difference in signal-to-noise ratio is purely indicative of the crystallinity of the material. The hydrated P₂-Thio-C₆₀ has an interlamellar spacing of 11.0 Å meanwhile the dehydrated form has an interlamellar spacing of 9.4 Å.

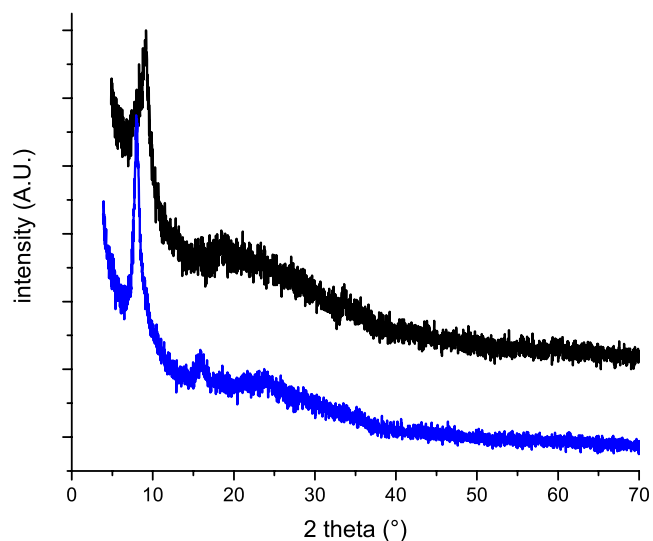


Figure 13 : XRD of P_2 -Thio- $CcCo$ as obtained at the end of the reaction (black) and hydrated (blue).

The figure 14 shows the very low crystallinity of the obtained compounds as well as the very low interlamellar spacing.

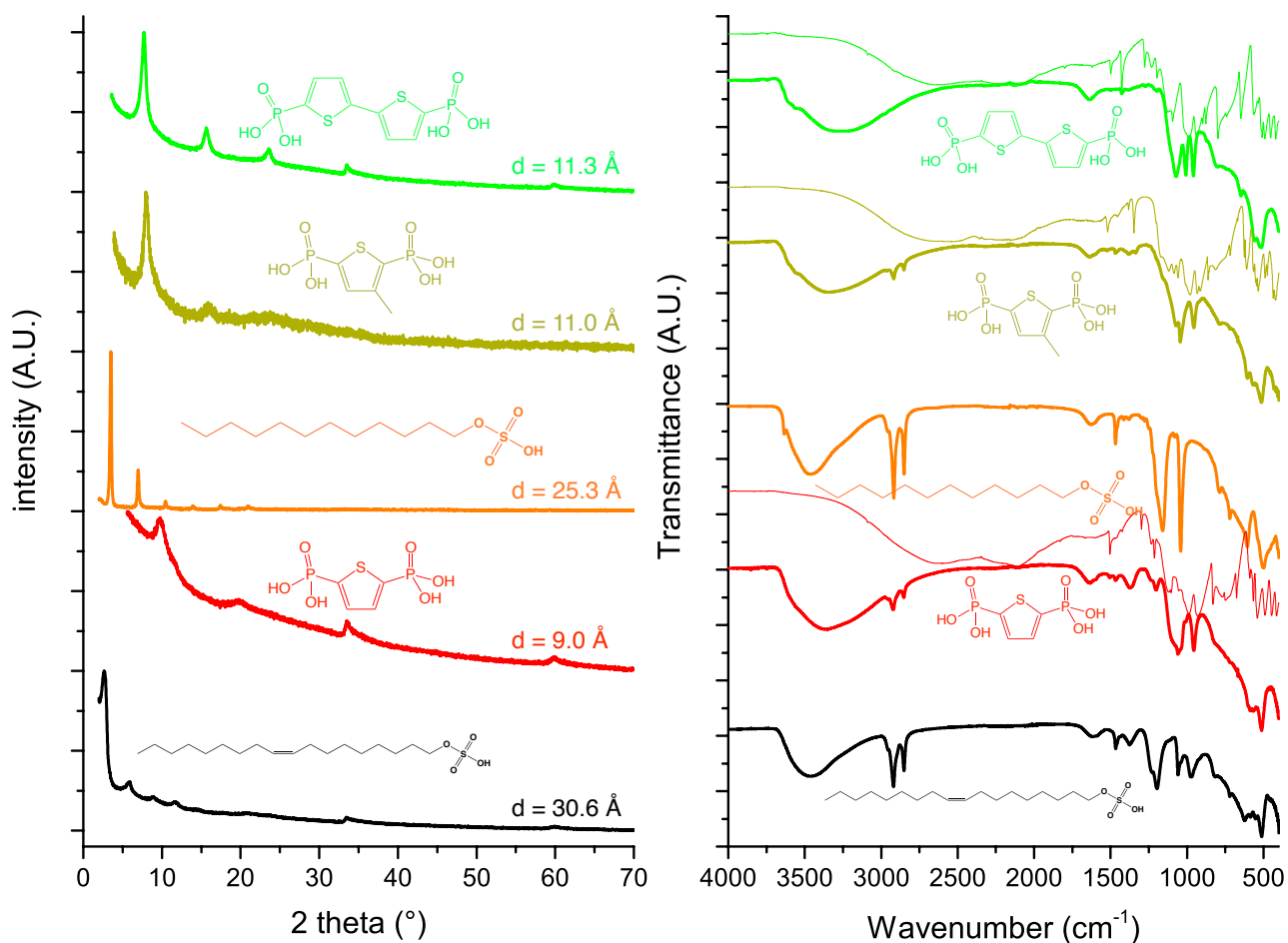
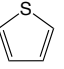
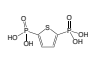
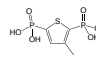
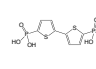


Figure 14 : XRD (left) and infrared spectra (right) of thiophene hybrids (bold lines), molecules alone (thin lines) and starting compounds.

The observed interlamellar distances are very short. They are shorter than the ones of the analogous compounds made from copper hydroxide, even if the inorganic layers are much thicker (about 7 Å for cobalt hydroxide triple layer, compared to about 3 Å for copper hydroxide where copper atoms are all in octahedral environment). Moreover, the interlamellar distances of P₂-Thio-C_cCo and of P₂-diThio_cCo are extremely close despite the additional thiophene ring. A hypothesis to explain these surprising results is to consider a flat, or almost flat arrangement of the molecules in the interlayer spacing. This feature has been observed in the past in the case of the insertion of a carboxylate azo dye into a layered Mg-Al LDH for low dye/LDH ratios.¹⁹ It has also been observed in metal disulfides (MoS₂) with amino-bithiophene²¹ but to the best of my knowledge, has very seldom been described in the case of layered simple hydroxides. One example reports the flat insertion of ethanedisulfonate anions in a Co LSH, leading to a basal spacing of 9.6 Å.²²

These results also greatly contrast with the results previously obtained in our laboratory. Indeed, a hybrid compound obtained with a [2,2']-bithiophene-5,5'-dicarboxylic acid, the equivalent of P₂-diThio with carboxylic instead of phosphonic acids, showed an interlamellar spacing of 13.4 Å.⁵ This compound was obtained *via* one pot hydrothermal synthesis and presents a purely octahedral cobalt layer, the obtained interlamellar spacing thus corresponds to a « normal » packing of the dithiophene with a tilt angle of 28°. This confirms that the phosphonic acid geometry offers wider grafting possibilities than a carboxylic acid.

The infrared spectroscopy (table 5) shows relatively significant traces of the alkyl chains from the starting compound for all the hybrids. The explanation might be similar to the one observed from copper hybrids *i.e.* the relative difficulty to properly wash the compounds. This phenomenon might be amplified here due to the difference in morphology between cobalt and copper hydroxides. Indeed, in the case of copper hydroxide, the platelets can have lateral sizes of around 100 μm meanwhile for cobalt hydroxide, this lateral size is often less than 2 μm leading to a powder even more difficult to wash. The co-insertion hypothesis can also be ruled out due to the fact that this generally creates phases with an interlamellar spacing of 22±1 Å which is clearly incompatible with the 9-11 Å distances observed here.

	Co ₂ (OH) _{3.5} (DSO) _{0.5}	Co ₂ (OH) _{3.5} (oleyl) _{0.5}			P ₂ -Thio _c Co		P ₂ -Thio-C _c Co		P ₂ -diThio _c Co
C-C ring stretch				1504	1505	1520	1522/ 1505	1499	1501
C-C ring stretch	1467	1467/ 1458		1460	1467/ 1455	1456	1470/ 1455		1454
C-C ring stretch	1413		1408	1423		1420	1411	1427	1427/ 1416
PO ₃ asymmetric stretching (1330 cm ⁻¹)							1336		1336/ 1315
P=O (1200-1220cm ⁻¹)	1223	1229/ 1197		1233/ 1214	1234/ 1202	1201	1222	1232/ 1197	1213/ 1198
C-H inplane bending		1110		1119/ 1104		1119		1127	1118(w)
PO ₃ symmetric stretching (1110 cm ⁻¹)	1104(w)		1081	1081	1086	1086		1094	
P-O probable zone	1079	1059		1056	1060	1060	1071		1072
	1042	1039/ 1010	1034	1047/ 1020	1040		1045		
				988	1008	1009		1015	1008

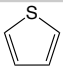
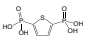
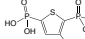
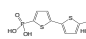
	$\text{Co}_2(\text{OH})_{3.5}(\text{DSO})_{0.5}$	$\text{Co}_2(\text{OH})_{3.5}(\text{oleyl})_{0.5}$			$\text{P}_2\text{-Thio}\text{C}\text{Co}$		$\text{P}_2\text{-Thio}\text{-C}\text{C}\text{Co}$		$\text{P}_2\text{-diThio}\text{C}\text{Co}$
P-O probable zone		974				981		987	959
PO_3 symmetrical deformation (605 cm^{-1})	606					610/597	605		
PO_3 asymmetrical deformation (510 cm^{-1})	503	512			513	525	514	515/509	524/514

Table 5 : IR bands of starting molecules and all corresponding cobalt hydroxide-based hybrids.

The table above indicate that the signature of starting compounds can be observed in the hybrids as well as the signature of some oleyl-sulfate or dodecyl-sulfonate depending on the starting compound.

4.3. TGA/TDA, Micro-Analysis and EDX of the Thiophene Cobalt Hydroxide Hybrids

Once again, the hybrids were analysed using different techniques following the same procedure, the results are summarized in the table below :

TGA/TDA water content measured (calculated)	Co:P ratio via EDX measured (calculated)	Micro-analysis results measured (calculated)	Obtained formula
-	-	-	$\text{P}_2\text{-Thio}\text{C}\text{Co}$ $\text{Co}_2(\text{OH})_{3.x}(\text{C}_4\text{H}_4\text{O}_6\text{P}_2\text{S})_{0.x}\cdot x\text{H}_2\text{O}$
12.5% (6.8%)	5.76 (4.54)	Co : 58.8 (44.58), C : 7.94 (7.72) H : 3.59 (3.08), P : 2.11 (5.15) S : 2.2 (5.15)	$\text{P}_2\text{-Thio}\text{-C}\text{C}\text{Co}$ $\text{Co}_2(\text{OH})_{3.56}(\text{C}_8\text{H}_6\text{O}_6\text{P}_2\text{S})_{0.22}(\text{DSO})_{0.05}\cdot 1\text{H}_2\text{O}$
12.7% (10.3%)	6.19 (5.88)	Co : 57.1 (44.94), C : 6.24 (6.23) H : 3.03 (2.95), P : 2.41 (4.02) S : 3.00 (4.16)	$\text{P}_2\text{-diThio}\text{C}\text{Co}$ $\text{Co}_2(\text{OH})_{3.66}(\text{C}_8\text{H}_6\text{O}_6\text{P}_2\text{S}_2)_{0.17}\cdot 1.5\text{H}_2\text{O}$

Table 6 : Calculated formula for the different cobalt hybrid compounds.

The table above indicates that the insertion rates are in line with the ones observed in the case of copper analogues, or with the previous fluorene or benzene derivatives. It is worth noticing that $\text{P}_2\text{-Thio}\text{-C}\text{C}\text{Co}$ still presents a measurable amount of dodecylsulfonate, confirming what has been observed in the infrared spectra (figure 15). As for $\text{P}_2\text{-Thio}\text{C}\text{Co}$, unfortunately, due to supply problems with the sodium oleyl-sulfate along with the very low quantity of the final product, it was not possible to synthesize enough material to carry out the analyses. The TGA/TDA analysis indicates similar behaviour previously obtained with copper hybrids with an even higher mass gain (2.1%) at $307\text{ }^\circ\text{C}$ along with a sharp exothermic peak.

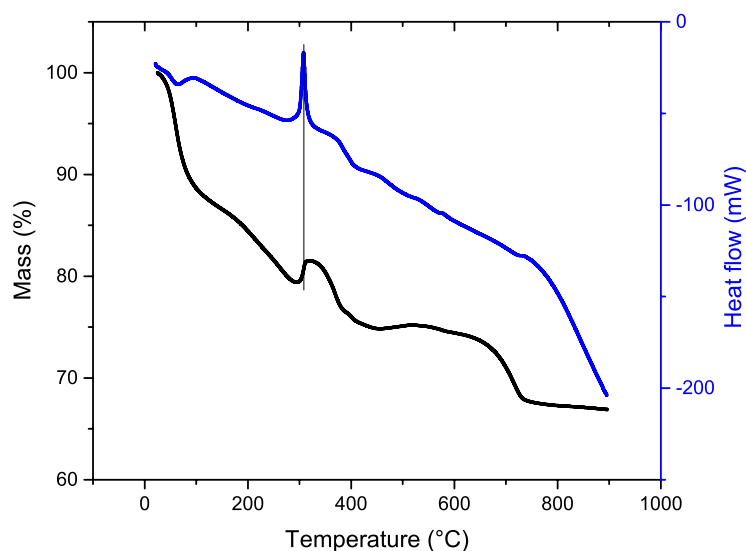


Figure 15 : TGA/TDA analysis of P_2 -Thio-Cc Co.

After this functionalization, some properties of these materials have been studied, the results are shown thereafter.

5. Properties of the Hybrids Compounds

5.1. Luminescence Properties

Thiophene is very well known for its luminescence properties, for instance, in the liquid state with nitrophenyl-nitrophenylethynyl oligothiophenes derivatives where the solvent as well as the nature of the functional group allows to cover a wide part of the visible spectrum.²³ There are also examples in the solid state where several substitutions are able to fine-tune the system luminescence in the entire visible spectrum.²⁴

From our previous experience in the laboratory,⁵ luminescence is quenched when the thiophene possesses carboxylic acid grafting moieties directly linked to the fluorophore. This absence of luminescence has also been reported in several perovskite hybrids systems based on bithiophenes²⁵ or quaterthiophenes.²⁶ Among the possible explanations the authors propose the presence of an exciton band M coming from the inorganic part and being between the S_1 and T_1 states of the organic part as described in figure 16.²⁷ This M band allows intersystem crossing ($S_1 \rightarrow T_1$) to occur and leads to a generally non-radiative (at room temperature) $T_1 \rightarrow S_0$ transition so no phosphorescence (or fluorescence) is observed.²⁸

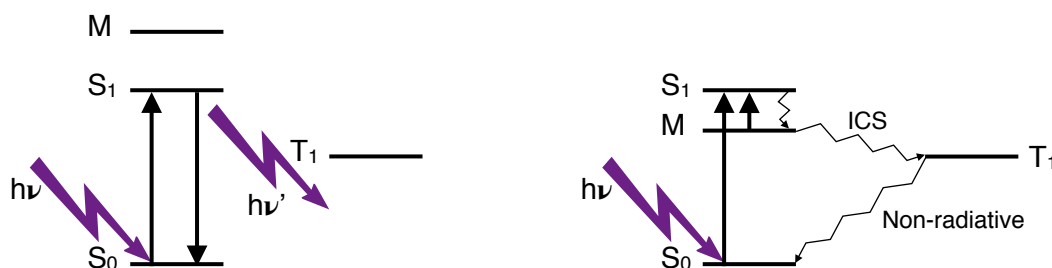


Figure 16 : Possible interpretation for the absence of luminescence in thiophenes bearing carboxylate grafting moieties.²⁷

In the case of the hybrids compounds described in this chapter, the results are difficult to interpret, some hybrids exhibit luminescence (P_2 -Thio_CCu, P_2 -Thio-C_CCu, P_2 -diThio_CCu and P_2 -diThio_CCo) meanwhile the others (P_2 -Thio_CCo and P_2 -Thio-C_CCo) do not show any sign of luminescence with a laser excitation at 320 nm and a power of approximately 2.5 mW.

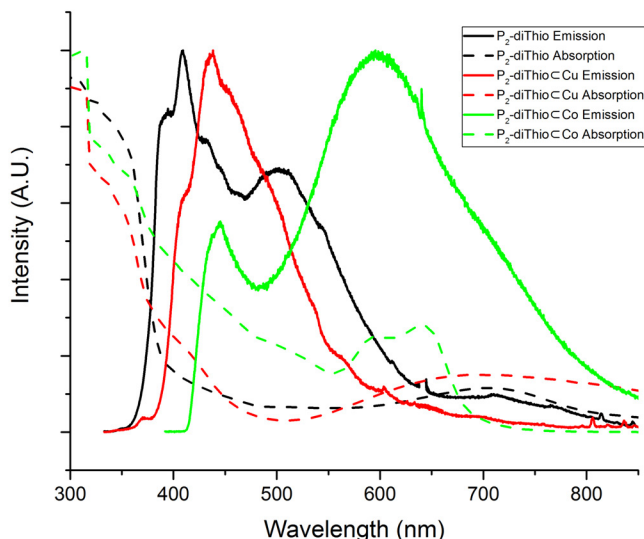


Figure 17 : Kubelka-Munk corrected and normalized solid state absorptions and luminescence with 320 nm excitation of P_2 -diThio_CCu, P_2 -diThio_CCo and of P_2 -diThio alone.

The absorption of P_2 -diThio at 700 nm might be due to the formation of the radical cation *via* self-doping²⁹ meanwhile the absorption at 270 nm is attributed to the $S_1 \leftarrow S_0$ transition between the fundamental state S_0 and the first excited state S_1 corresponding to a $\pi - \pi^*$ transition.

For P_2 -diThio emission with an excitation at 320 nm, we can observe an emission at 408 nm relatively close to the expected one for an unsubstituted dithiophene (362 nm)²⁸ and another one at 500 nm that is close to what has been observed for the bis-carboxylate dithiophene with an emission at 520 nm.¹

The emission of the P_2 -diThio_CCu is slightly broader than for the molecule alone and is centred at 438 nm, this shift of 30 nm could be explained by reabsorption of emitted light by the inorganic matrix. For the P_2 -diThio_CCo emission, an emission at 444 nm is observed. There is, however, a second broad peak centred at 597 nm whose origin is not yet understood.

The other two hybrids, P_2 -Thio_CCu and P_2 -Thio-C_CCu, exhibit relatively similar behaviours as shown in figure 18 below with a small emission band around 450 nm, and a much broader emission centred around 600 nm. In the present case, no clear blue shift of the emission wavelength upon decreasing the number of thiophene rings was observed, contrarily to what has been reported in the literature for other bis and oligothiophene systems.^{5, 28, 29} The presence of the phosphonic acids might be the reason for this peculiar behaviour.

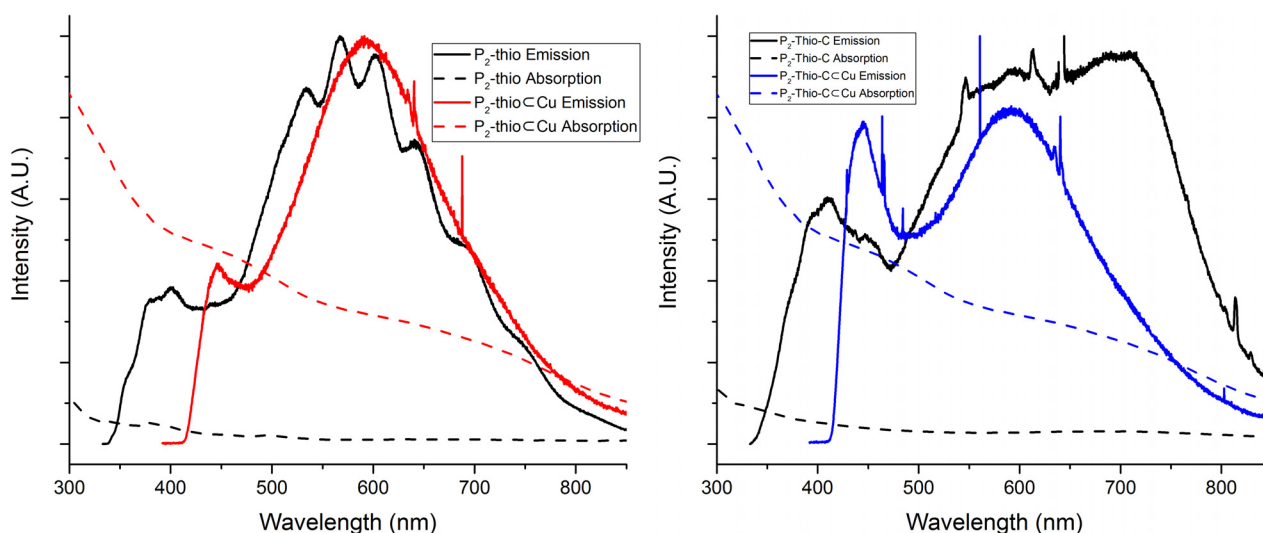


Figure 18 : Kubelka-Munk corrected and normalized solid state absorptions and luminescence with 320 nm excitation of P_2 -Thio, P_2 -ThioC Cu, P_2 -Thio-C and P_2 -Thio-Cc Cu.

The P_2 -Thio-C also exhibits an additional intense and large emission centred at 703 nm that is also unknown. Additional work should be done as well as a change of the excitation wavelength to get a better understanding of the luminescence mechanism.

5.2. Magnetic Properties

Due to long-lasting technical issues with our magnetometers, only P_2 -diThioC Cu and P_2 -diThioC Co have been analysed, in the CRISMAT laboratory.

5.2.1. Magnetic Properties of P_2 -diThioC Cu

The behaviour of P_2 -diThioC Cu is identical to all the other copper-based hybrids obtained previously. The compound presents an overall antiferromagnetic behaviour, without any magnetic ordering down to 1.8 K (figure 19). P_2 -diThioC Cu possesses a Curie constant of $0.67 \text{ emu}\cdot\text{K}\cdot\text{mol}^{-1}$, a Weiss temperature of -15.9 K and a magnetization at 5 T and 1.8 K of $0.31 \mu_B$.

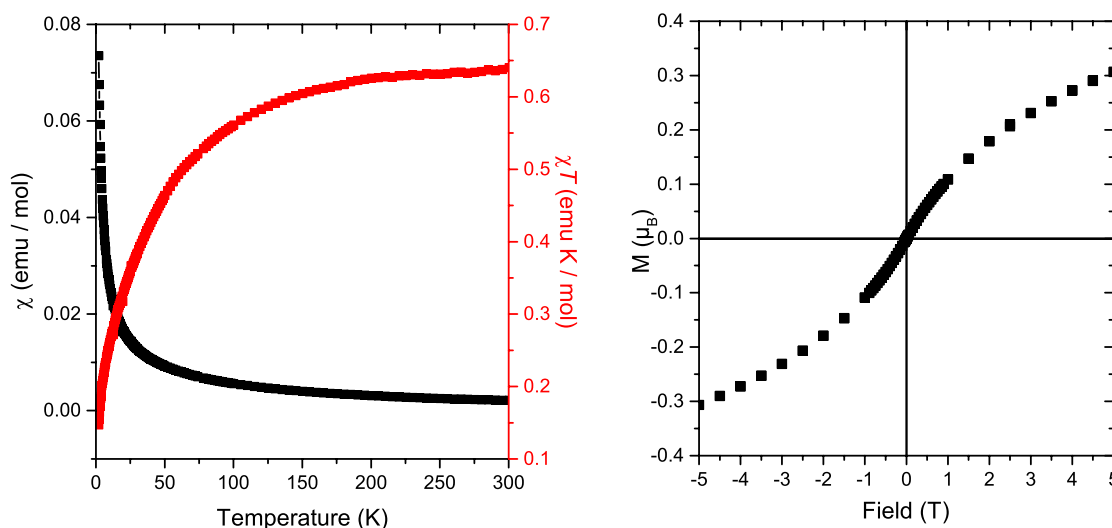


Figure 19 : χ and χT product measured at 5000G (left) and magnetization curve (right) of P_2 -diThioC Cu.

5.2.2. Magnetic Properties of P₂-diThioCo

As previously reported, the functionalization, even with the peculiar packing obtained here, does not modify the magnetic properties with respect to other Co-based hybrids. P₂-diThioCo exhibits a ferrimagnetic behavior. The Curie constant is 5.56 emu·K·mol⁻¹ which is in line with the expected values for a mixture of tetrahedral and octahedral high spin cobalt(II) ions. Indeed the values found in the literature^{30, 31} are ranging from 2.2 to 2.8 emu·K·mol⁻¹ for a tetrahedral cobalt(II) ion and from 2.8 to 3.4 emu·K·mol⁻¹ for an octahedral cobalt (II) ion. Additionally, P₂-diThioCo shows a Weiss temperature of -14.0 K. Ac susceptibility measurements allow to determine the ordering temperature, around 9.3 K. Like for many other cobalt hydroxide-based hybrids, or for other layered magnets,^{2, 32, 33} these measurements also reveals the existence of another magnetic phase, with an ordering temperature around 20 K.

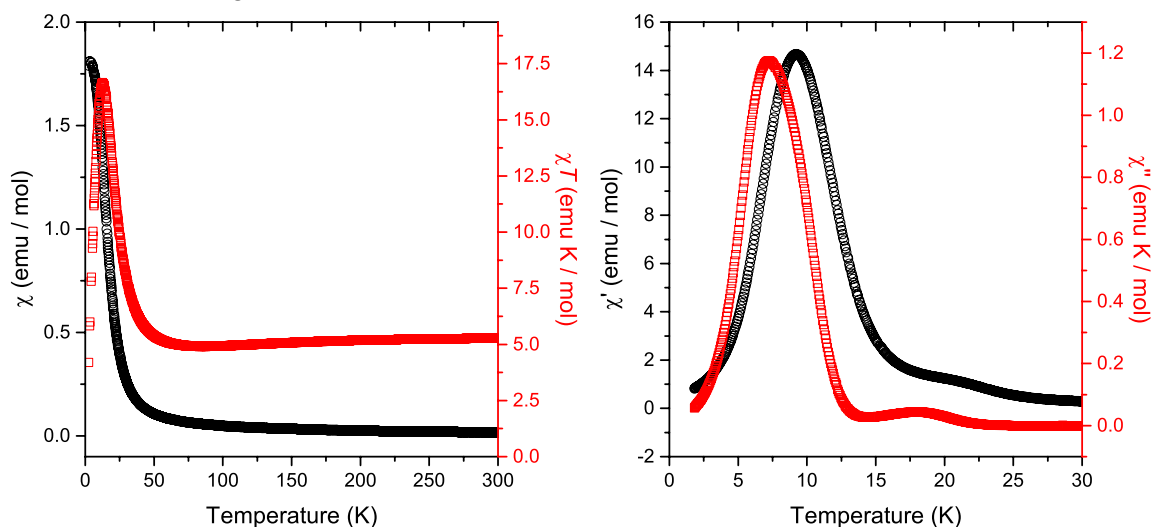


Figure 20 : χ and χT measured at 5000G (left) and AC susceptibility ($f = 95$ Hz, $\mu_0 H_{ac} = 0.3$ mT)(right) of P₂-diThioCo.

The coercive field measured for this hybrid is 0.12 T with a magnetization at 7 T and 1.8 K of $2.7 \mu_B$ as seen in figure 21 below. These values are also similar to the previously obtained hybrids.

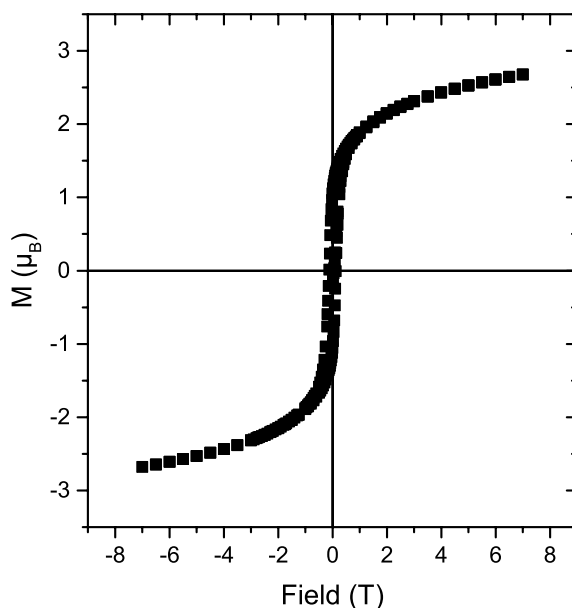


Figure 21 : Magnetization curve of P₂-diThioCo measured at 1.8K.

6. Conclusion

In this chapter we have shown that the modification of the rigid centre of the molecule to insert also modifies the intercalation chemistry of this system. To help mitigate insertion problems, a variation of the previously used pre-intercalation method has been developed. It is believed that the alkyl-alkyl interactions present in the dodecyl hybrids were partially responsible for the lack of desired reactivity for intercalation with these peculiar molecules. The addition of an unsaturation in the chains, using oleyl-sulfate instead of dodecylsulfate, seems to impact greatly the reactivity of the hybrids towards new functionalization.

The new oleyl-sulfate-intercalated hybrids have been characterized and their behaviour with respect to hydration and dehydration processes has been studied. The lack of availability of commercial oleyl-sulfate was the main limiting factor for a more thorough study of the properties and chemical behaviour of these hybrids.

The functionalization of copper hydroxide led to « classical » compounds with expected interlamellar spacing meanwhile the insertions in cobalt hydroxide have shown that a flat orientation of the molecules in the interlamellar spacing was favoured.

The magnetic properties of the obtained hybrids are classical, enabling the possibility of performing magneto-electric measurements that will be done in the future. The role and effect of the heteroatom in the ring being potentially interesting to investigate in respect to the magneto-electric properties of the final compound.

7. Bibliography

1. A. Demessence, Ph.D. Thesis, Université Louis Pasteur, Strasbourg I, 2006.
2. A. Demessence, G. Rogez and P. Rabu, *Chemistry of Materials*, 2006, **18**, 3005-3015.
3. A. Demessence, G. Rogez, R. Welter and P. Rabu, *Inorganic Chemistry*, 2007, **46**, 3423-3425.
4. A. Demessence, A. Mesbah, M. François, G. Rogez and P. Rabu, *European Journal of Inorganic Chemistry*, 2009, **2009**, 3713-3720.
5. A. Demessence, A. Yassar, G. Rogez, L. Miozzo, S. De Brion and P. Rabu, *Journal of Materials Chemistry*, 2010, **20**, 9401-9414.
6. J.-M. Rueff, J.-F. Nierengarten, P. Gilliot, A. Demessence, O. Cregut, M. Drillon and P. Rabu, *Chemistry of Materials*, 2004, **16**, 2933-2937.
7. M. J. Byrnes and M. H. Chisholm, *Chemical Communications*, 2002, **0**, 2040-2041.
8. M. J. Byrnes, M. H. Chisholm, R. J. Clark, J. C. Gallucci, C. M. Hadad and N. J. Patmore, *Inorganic Chemistry*, 2004, **43**, 6334-6344.
9. B.-L. Chen, K.-F. Mok, S.-C. Ng and M. G. B. Drew, *New Journal of Chemistry*, 1999, **23**, 877-883.
10. X.-Z. Sun and B.-H. Ye, *Acta Crystallographica Section E Structure Reports Online*, 2004, **60**, 878-880.
11. P. Kopel, Z. Trávníček, J. r. Marek, M. Korabik and J. Mrozinski, *Polyhedron*, 2003, **22**, 411-418.

12. T. Kuroda-Sowa, T. Nogami, H. Konaka, M. Maekawa, M. Munakata, H. Miyasaka and M. Yamashita, *Polyhedron*, 2003, **22**, 1795-1801.
13. J. M. Lim, Y. Do and J. Kim, *European Journal of Inorganic Chemistry*, 2006, **2006**, 711-717.
14. J. M. Rueff, O. Perez, A. Pautrat, N. Barrier, G. B. Hix, S. Hernot, H. Couthon-Gourves and P. A. Jaffres, *Inorganic Chemistry*, 2012, **51**, 10251-10261.
15. C. Bloyet, M. Roger, J.-M. Rueff, B. Raveau, J.-F. Lohier, G. Rogez and P.-A. Jaffrès, *European Journal of Inorganic Chemistry*, 2016, **2016**, 4643-4648.
16. H. E. Katz, M. L. Schilling, C. E. D. Chidsey, T. M. Putvinski and R. S. Hutton, *Chemistry of Materials*, 1991, **3**, 699-703.
17. P. Gerbier, C. Guérin, B. Henner and J. R. Unal, *Journal of Materials Chemistry*, 1999, **9**, 2559-2565.
18. C. Y. Gao, F. Wang, H. R. Tian, L. J. Li, J. Zhang and Z. M. Sun, *Inorganic Chemistry*, 2016, **55**, 537-539.
19. N. Iyi, K. Kurashima and T. Fujita, *Chemistry of Materials*, 2002, **14**, 583-589.
20. Y. Du and D. O'Hare, *Inorganic Chemistry*, 2008, **47**, 11839-11846.
21. M. A. Ibrahim, B. G. Lee, N. G. Park, J. R. Pugh, D. D. Eberl and A. J. Frank, *Synthetic Metals*, 1999, **105**, 35-42.
22. P. M. Forster, M. M. Tafoya and A. K. Cheetham, *Journal of Physics and Chemistry of Solids*, 2004, **65**, 11-16.
23. S. Hachiya, K. Asai and G.-i. Konishi, *Tetrahedron Letters*, 2013, **54**, 3317-3320.
24. G. Barbarella, L. Favaretto, G. Sotgiu, M. Zambianchi, A. Bongini, C. Arbizzani, M. Mastragostino, M. Anni, G. Gigli and R. Cingolani, *Journal of the American Chemical Society*, 2000, **122**, 11971-11978.
25. X. H. Zhu, N. Mercier, P. Frere, P. Blanchard, J. Roncali, M. Allain, C. Pasquier and A. Riou, *Inorganic Chemistry*, 2003, **42**, 5330-5339.
26. D. B. Mitzi, *Journal of the Chemical Society-Dalton Transactions*, 2001, **1**, 1-12.
27. D. B. Mitzi, K. Chondroudis and C. R. Kagan, *Inorganic Chemistry*, 1999, **38**, 6246-6256.
28. R. S. Becker, J. Seixas de Melo, A. L. Maçanita and F. Elisei, *The Journal of Physical Chemistry*, 1996, **100**, 18683-18695.
29. V. Wintgens, P. Valat and F. Garnier, *The Journal of Physical Chemistry*, 1994, **98**, 228-232.
30. R. L. Carlin, *Magnetochemistry*, Springer-Verlag Berlin Heidelberg, 1986.
31. O. Kahn, *Molecular Magnetism*, VCH Publishers, 1993.
32. E. Coronado, J. R. Galan-Mascaros, C. J. Gomez-Garcia and V. Laukhin, *Nature*, 2000, **408**, 447-449.
33. F. Bellouard, M. Clemente-León, E. Coronado, José R. Galán-Mascarós, Carlos J. Gómez-García, F. Romero and Kim R. Dunbar, *European Journal of Inorganic Chemistry*, 2002, **2002**, 1603-1606.

Chapter VI : Layered Cobalt Hydroxides Obtained by
Intercalation of Ruthenium and Platinum Complexes Derivatives

Chapter VI : Layered Cobalt Hydroxides Obtained by Intercalation of Ruthenium and Platinum Complexes Derivatives

After the experience acquired with the functionalization by various molecules bearing phosphonic acid described in the previous chapters, it seemed interesting to continue the work done by a former PhD student in the laboratory, Séraphin Eyele-Mezui which dealt with insertion of ruthenium tris-bipyridine complexes with phosphonic acid grafting moieties into layered single hydroxide.¹ During his PhD, Séraphin was indeed interested in the insertion of transition metal complexes into layered hydroxides such as Cu, Ni, Co or Zn phthalocyanines or salen-type complexes into Co, Cu or Zn layered simple hydroxides.^{2,3}

The ruthenium tris-bipyridine complex is one of the most studied luminescent complexes in the literature.^{4,9} A derivative complex has already been studied in confined space such as in a Mg-Al LDH and shows an interesting enhancement of their emission lifetimes *via* controlled dilution inside the layers.¹⁰ Other examples are the insertion of ruthenium tris-bipyridine into layered zirconium phosphate either *via* solution processing¹¹ or layer by layer deposition.¹² Our approach consists in obtaining multifunctional systems associating the magnetic properties of the hydroxide and luminescence of the complex.

The main challenge of this work was to optimize the poor crystallinity and low reproducibility of the past experiments as well as to avoid the presence of remaining dodecylsulfonate (co-inserted) in the final compound.

It seemed of great interest to extend this approach to the functionalization with another fluorescent complex based on platinum and salen ligand. Indeed, the functionalization of layered single hydroxides with salen-based complexes bearing sulfonate grafting moieties has previously been done in our laboratory^{13,14} albeit without salen-platinum complexes. The main focus on this work is not on the multiferroic properties aspect but rather in the coexistence of magnetism and luminescent properties within the same hybrid material by the insertion of a luminescent complex within the layers of the magnetic hydroxide.

1. Introduction

As explained above, the focus being in the coexistence of magnetism and luminescence, experiments have only been made with cobalt hydroxide. The complexes used in this chapter are described in figure 1.

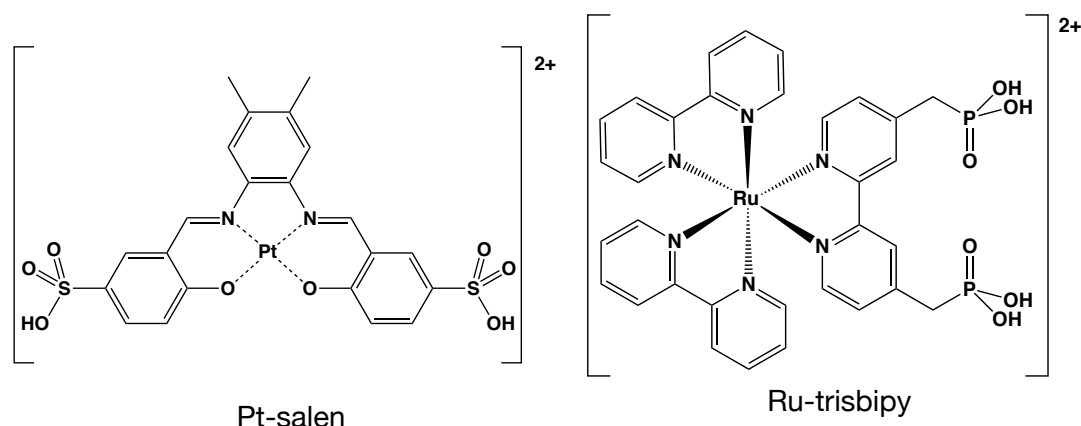


Figure 1 : Complexes and names used throughout this chapter.

Ruthenium-trisbipyridine excited states are probably the most studied among any inorganic complexes, the starting point being their very rich and strong luminescence in solution as well as in solid state.⁶ Lifetimes, quantum yields, energy levels description and charge transfer studies started in the late 60's⁴ early 70's^{5, 15, 16} up to until recently for non-luminescent methylated derivatives.¹⁷ This system can also be used as a probe for oxygen uptake,⁷ DNA binder¹⁸ or the study of electron-transfer reactions with viologen.⁸

The Pt-salen complex is part of the so-called Schiff base complexes, they have been studied for different applications such as phosphorescent organic light-emitting devices,¹⁹ DNA binder and luminescent probe,²⁰ luminescent oxygen sensing,²¹ and other OLED applications²² using rich photophysics.²³⁻²⁵

These two systems have a rich luminescence that could be also studied in a confined system, similarly to what was made in Mg:Al layered double hydroxides and tris(4,7-diphenyl-1,10-phenanthroline)ruthenium(II).¹⁰ The flexibility of this system has been demonstrated by the increase of the emission lifetimes *via* the modification of the ratio between Zn and Ru complexes, effectively diluting the active Ru complexes and enhancing the luminescence lifetime up to similar levels obtained in solution.

2. Intercalation Chemistry

2.1. Intercalation Chemistry with Ru-trisbipy in Cobalt Hydroxide

First, the synthesis of the Ru-trisbipy has been optimized from the literature,¹⁴³ the synthetic pathway used to obtain the complex is detailed below.

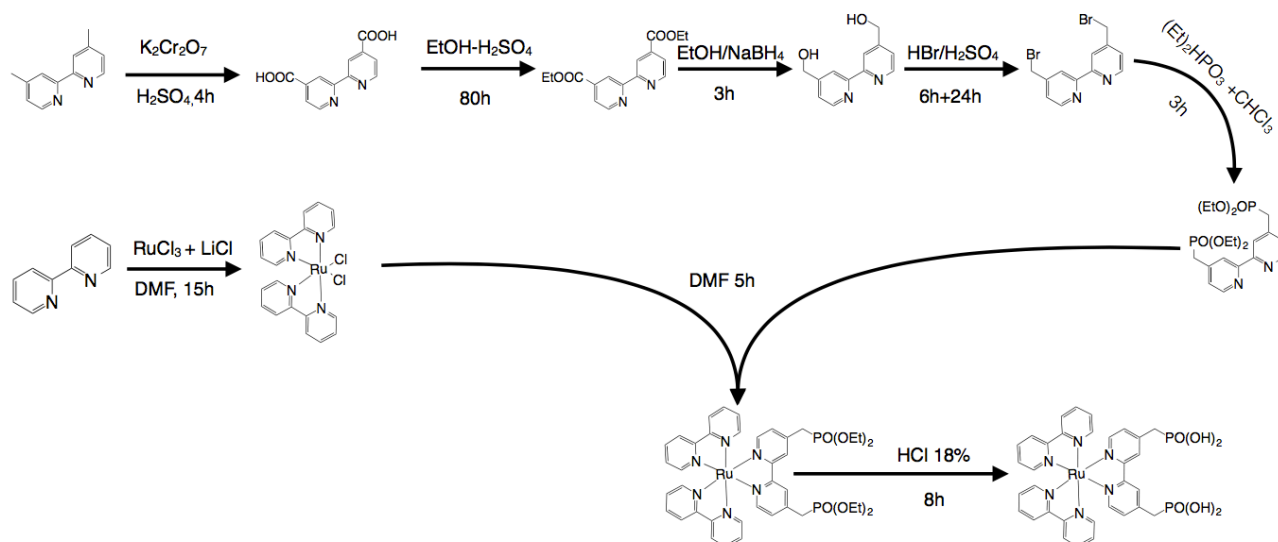


Figure 2 : Synthetic pathway used to obtain Ru-trisbipy complex.

The experience acquired from the previous functionalizations of cobalt hydroxide with Ru-trisbipy made by Seraphin Eyele Mezui¹ added to the experience I gathered from previous intercalation using phosphonic acids anchoring groups was used to obtain hybrids that are purely inserted. Indeed, previous work done by Seraphin led to Ru-trisbipy₃Co that were co-inserted *i.e.* dodecylsulfonate was also present in the interlamellar spacing. The experimental condition used by Seraphin was as follows :

- 0.36 mmol of Ru-trisbipy is solubilized in 60 mL of water and the pH is adjusted to 8
- 0.5 mmol of $\text{Co}_2(\text{OH})_{3.5}(\text{DSO})_{0.5}$ is dispersed in the solution along with 40 mL of ethanol
- The suspension is then heated under argon at 80°C for 15 hours

This led to a co-inserted compound with an interlamellar spacing of 26.5 Å, the co-insertion is notably characterized by the vibration bands of the remaining alkyl chains in the infrared spectroscopy.

The conditions I used for a pure insertion are as follows :

- 0.148 mmol of Ru-trisbipy is solubilized in 12 mL of water and the pH is adjusted to 8.6
- 0.073 mmol of $\text{Co}_2(\text{OH})_{3.5}(\text{DSO})_{0.5}$ is dispersed in the solution along with 12 mL of ethanol
- The suspension is then heated under argon at 80 °C for 15 hours

These rather small changes of ratio of molecules to insert and volume of reaction allows us to obtain a purely inserted hybrid with an interlamellar spacing of 24.7 Å, this corresponds to a bilayer stacking with slight interdigitation of the complexes.

2.2. Intercalation Chemistry with Pt-Salen in Cobalt Hydroxide

The Pt-Salen complex has been synthesized using adaptations of published work¹⁴⁴ according to the figure below :

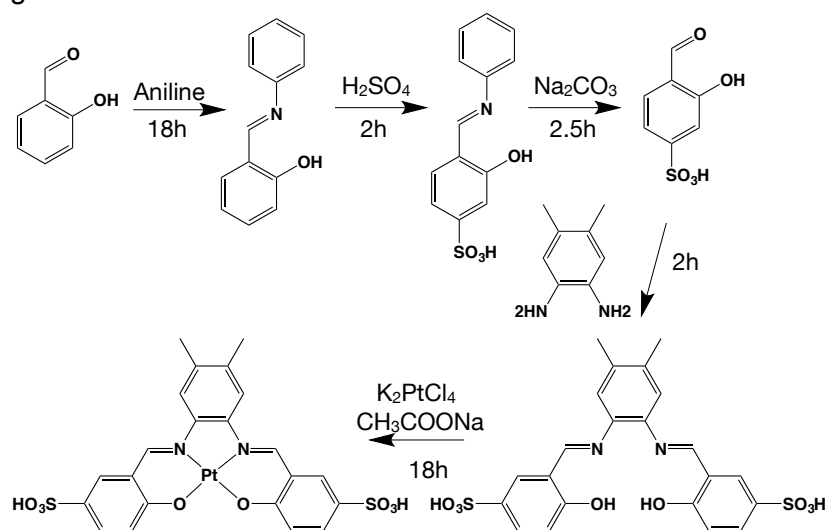


Figure 3 : Synthetic pathway used to obtain Pt-Salen complex.

This complex has been obtained with a yield of 5%. The use of methylated bisamino benzene has been made to improve the rather low solubility of the complex.

For this salen complexes, the past experiences are mainly coming from the work done Emilie Delahaye, at the time of her postdoc in the laboratory and her work on the synthesis and insertion of Co/Cu/Zn/Ni-salen into layered hydroxides.^{13, 14, 28} From this experience of functionalization of LSH by similar complexes several observations have been made for such systems. For example, the luminescence appears to be quenched if the grafting moiety is a carboxylate. In addition, when chiral complexes are used (figure 4), the chirality of the inserted complex is preserved once it has been inserted into the layers.

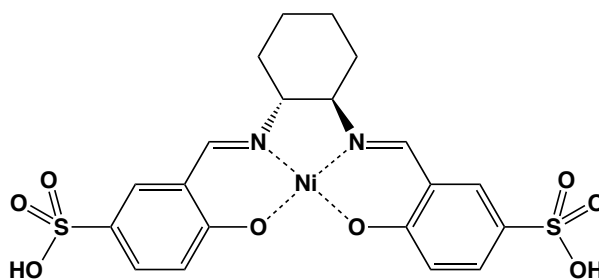


Figure 4 : Ni-salen complex previously used for intercalation.¹³

Yet, it is worth underlining that, when the salen type complex is not stable enough, or too labile in solution during the insertion process, the metal ion complexes can be leached, and gets involved to react directly with the inorganic layers.²⁸

This reaction was, however, never attempted with Pt-salen complexes nor with salen having methylated benzene ring as a linker.

Previous synthesis conditions for Ni-salen_cCo are as follows :

- 0.46 mmol of Ni-salen is dissolved in 50 mL of a 50/50 (v/v) mixture of water and ethanol
- 0.31 mmol of Co₂(OH)_{3.5}(DSO)_{0.5} is dispersed in the solution
- The mixture is then heated at 90°C for 6 hours under argon

This leads to a compound having an interlamellar spacing of 22.0 Å and a clear signature of the complex in its IR spectrum.¹³

These conditions have been slightly modified with the Pt-salen_cCo due to the relatively short amount of molecule I had at my disposal, the conditions I used are as follows :

- 0.185 mmol of Pt-salen is dissolved in 24 mL of a 50/50 (v/v) mixture of water and ethanol
- 0.165 mmol of Co₂(OH)_{3.5}(DSO)_{0.5} is dispersed in the solution
- The mixture is then refluxed for 24 hours under argon

The obtained product has the same interlamellar spacing as the Ni-salen_cCo *i.e.* 22.0 Å which is coherent with the previously obtained hybrids with a pillaring configuration of the salen complex between the layers.

3. Characterizations of the Obtained Hybrids

3.1. Ru-trisbipy_cCo

3.1.1. X-Ray Diffraction and Infrared Spectroscopy

Ru-trisbipy_cCo has been studied *via* X-ray diffraction and IR spectroscopy, it reveals an interlamellar spacing of 24.7 Å. The product is fully inserted without any visible remaining traces of dodecylsulfonate (figure 5).

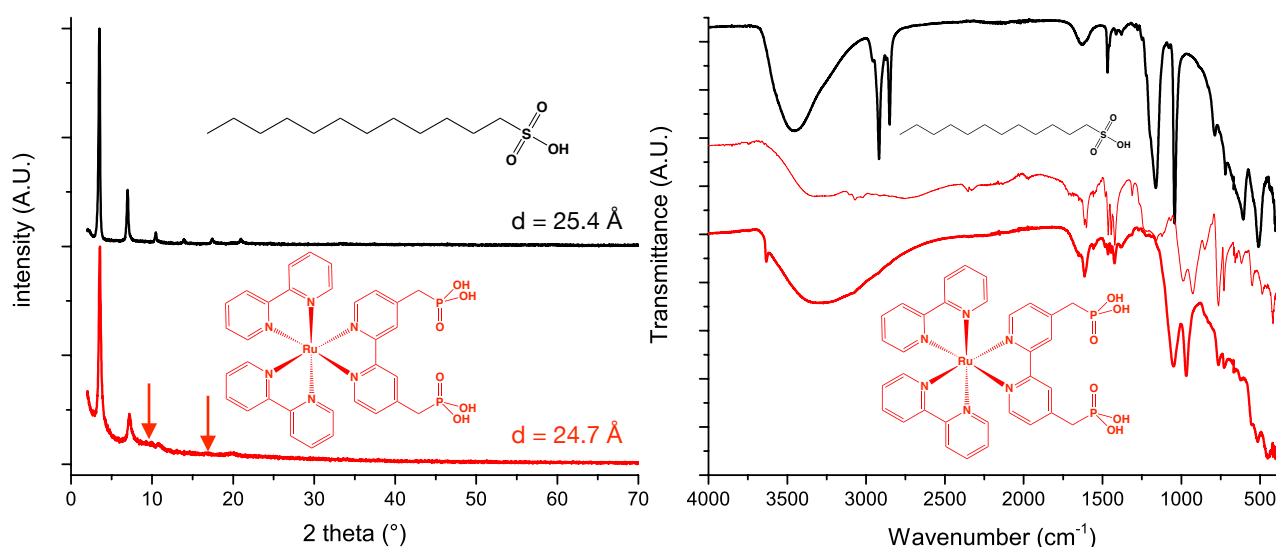


Figure 5 : XRD (right) and infrared spectra (left) of the starting compound (black), Ru-Trisbipy alone (red thin line) and Ru-Trisbipy c Co (red bold line).

The infrared spectroscopy indicates a clear signature of the complex in the spectrum of the hybrid. The diffractogram shows two unattributed very broad peaks centred at around 9.0 and 5.2 Å. These peaks are present in all the syntheses, even done with different experimental conditions. To try to get rid of these peaks, the pristine hybrid was heated at 80°C for 4 hours. This led to a compound with a slightly lower interlamellar spacing of 23.2 Å but left the unidentified peaks unchanged.

3.1.2. Micro-Analysis and UV/Vis Spectroscopy of Ru-trisbipy_cCo

The micro-analysis results are shown in the table below :

Micro-analysis results measured (calculated)	Obtained formula
Co : 42.4 (42.69), C ; 13.83 (13.92), H : 3.54 (3.14) P : 2.41 (2.24), N : 2.64 (3.04), Ru : 0.79 (3.66)	Ru-trisbipy _c Co Co ₂ (OH) _{3.8} (C ₃₂ H ₂₈ N ₆ O ₆ P ₂ Ru) _{0.1} •1H ₂ O

Table 1 : Micro-analysis results of Ru-trisbipy_cCo.

The calculated insertion ratio (0.1) is in line with previous findings made by Seraphin Eyele who obtained insertion rates ranging from 0.06 to 0.17 depending on the position of the anchoring moieties. These low insertion rates are common for such bulky molecules. There is however a discrepancy with the ruthenium titration that indicates an amount of ruthenium being five times lower than expected but considering the stability of the Ru-trisbipy complex and the good matching values with all the other elements, a measurement methodology problem is plausible. At the time of writing, unfortunately, we have not been able to prepare another batch for analysis.

The UV/Vis spectroscopy (figure 6) indicates that the tri-layer structure is also maintained after functionalization. For absorption bands at lower wavelength, due to strong Ru-trisbipy absorption, only a shoulder at 635 nm due to tetrahedral cobalt (II) can be observed. The strong absorption band of the Ru-trisbipy at 274 nm is attributed to a ligand-centred $\pi\text{-}\pi^*$ transition,⁶ the absorption centred at 445 nm is due to a MLCT (core $^2t_2^6 \rightarrow ^2t_2^5\pi^*$)⁶ meanwhile the shoulder masking the cobalt octahedra absorption at 494 nm is interpreted as a spin-forbidden MLCT transition.^{4, 29}

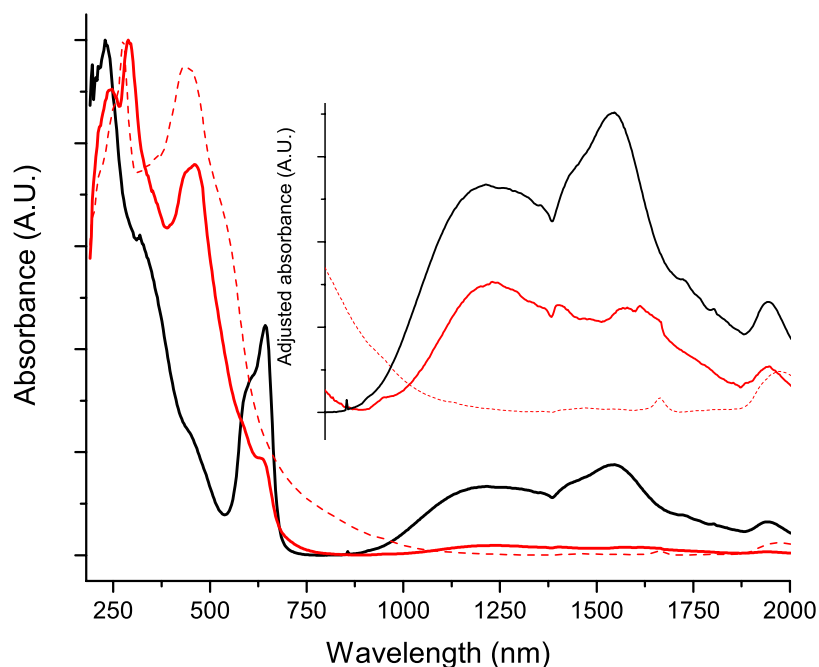


Figure 6 : Kubelka-Munk corrected absorbance of Cobalt hydroxydodecylsulfonate (black), Ru-trisbipy (dashed red) and Ru-trisbipy_CCo (red).

The magnified part of the graph indicates the presence of the two types of cobalt environments in Ru-trisbipy_CCo.

3.2. Pt-Salen_CCo

3.2.1. X-Ray Diffraction and Infrared Spectroscopy

As stated previously, the obtained compound has an interlamellar spacing of 22.0 Å (figure 7) and show traces of residual dodecylsulfonate. Whether the dodecylsulfonate is just on the surface or in the interlayer is this time impossible to know, indeed, the interlamellar spacing could be compatible with a very slightly co-inserted compound or with a pillaring arrangement of the molecule alone.

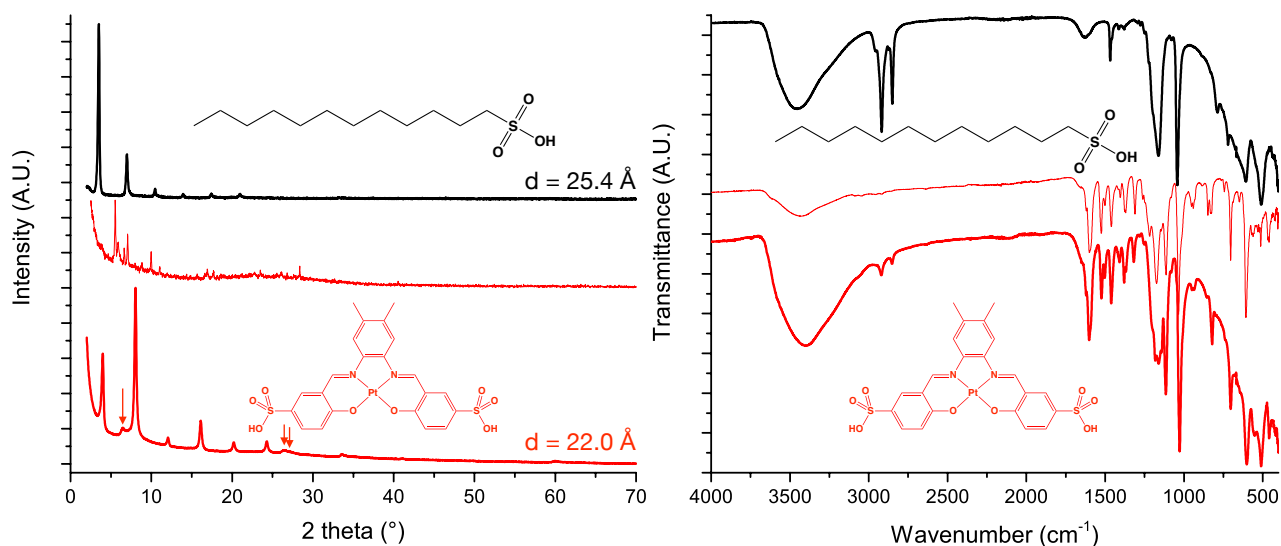


Figure 7 : XRD (right) and infrared spectra (left) of the starting compound (black), Pt-Salen alone (red thin line) and Pt-salenCo (red bold line).

The diffractogram of Pt-salenCo also exhibits several unknown peaks, the most intense is at $d = 13.6 \text{ \AA}$, the others being at 3.4 and 3.3 \AA . They are not corresponding to the molecule alone nor to cobalt oxides such as CoO or Co_3O_4 . The high angle peaks could correspond to in-plane reflections. The diffractogram also shows « anomalous » intensities for the 002/ peaks, this supports the introduction of a-Z element within the interlayer space. The infrared spectrum shows a clear signature of the salen as well as the remaining alkyl chains from the dodecylsulfonate.

3.2.2. Micro-analysis and UV/Vis spectroscopy of Pt-SalenCo

The results of the micro-analysis are presented in the table below :

Micro-analysis results measured (calculated)	Obtained formula
Co : 31.2 (30.94), C ; 18.3 (18.16), H : 3.56 (2.99) S : 3.9 (4.38), N : 1.58 (1.76), Pt : 12.3 (12.29)	Pt-SalenCo $\text{Co}_2(\text{OH})_{3.48}(\text{C}_{22}\text{H}_{16}\text{N}_2\text{O}_8\text{PtS}_2)_{0.24}(\text{DS}_0)_{0.04} \cdot 1.5\text{H}_2\text{O}$

Table 2 : Micro-analysis results of Pt-SalenCo.

These results are in agreement with the infrared spectroscopy indicating that some dodecylsulfonate is still present in the hybrid.

Due to the presence of the sulfonate as a grafting function for the complex, EDX could not be used to determine the co-insertion rate compared to previously intercalated molecules having a phosphonic acid as anchoring group.

The UV/Visible spectroscopy (figure 8) indicates that the absorptions of tetrahedral cobalt present at around 1550 nm and octahedral cobalt at around 1250 nm are still present. This is a good indicator to support the idea that the hydroxide has retained the tri-layer structure even after intercalation of the complex. For absorption bands at lower wavelength, due to strong Pt-salen absorption, only a shoulder at 643 nm due to tetrahedral cobalt (II) can be observed.

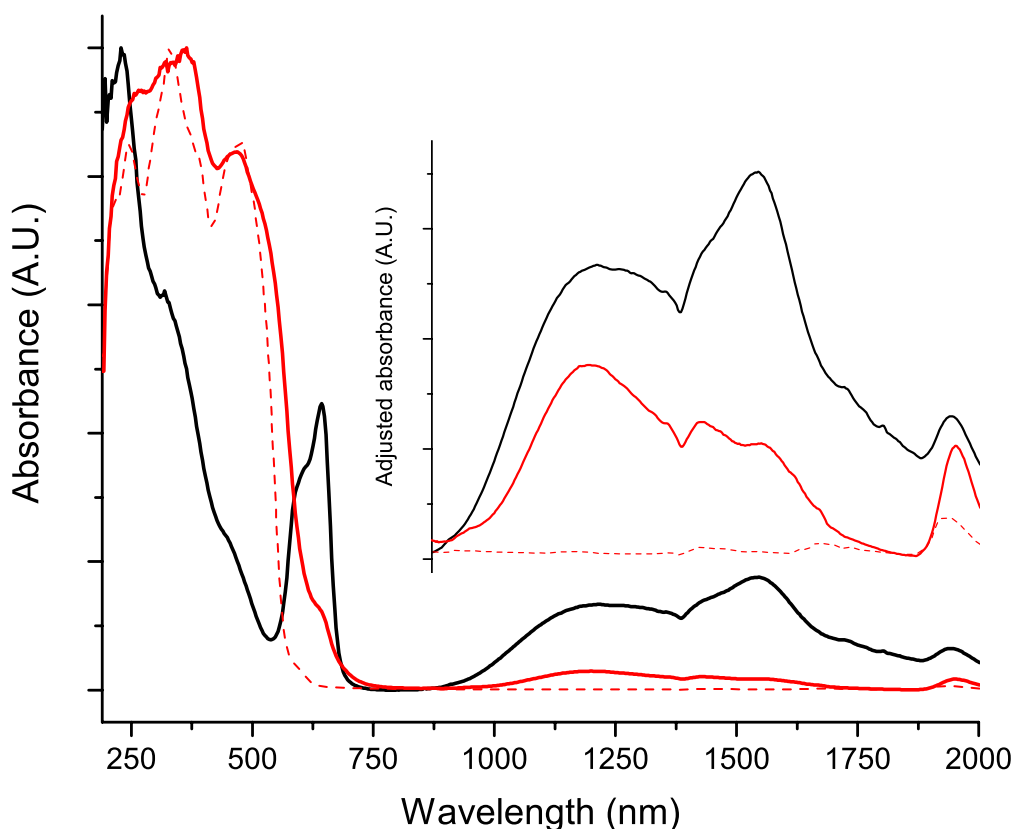


Figure 8 : Kubelka-Munk corrected absorbance of Cobalt hydroxydodecylsulfonate (black), Pt-Salen (dashed red) and Pt-salenCo (red).

The absorption bands visible at 1430 and 1950 nm are due to water that is present in our compound.³⁰ The absorption bands at 250 and 328 nm are attributed to $\pi\text{-}\pi^*$ transitions.²² The bands at 450-475 nm²² might be due to metal to ligand charge-transfer (MLCT) ($\text{Pt}(5d) \rightarrow \pi^*(\text{salen})$) mixed with intraligand charge-transfer ($\text{L}(\text{phenoxide}) \rightarrow \pi^*(\text{imine})$).

The magnified part of the graph indicates the presence of the two types of cobalt environments in our hybrids. Their relative intensities seem to be quite different, but it is unfortunately not possible to quantitatively assess this change. A hypothesis, the one we adopted throughout this PhD, would be that the tetrahedral content in the hybrid follows the insertion rate and number of grafting moieties *i.e.* 0.51 per formula unit in our case.

4. Magnetic and Luminescence Properties

As indicated in the introduction, the hybrids have been selected for their magnetic and luminescence properties, in this section both aspects of Ru-trisbipyCo and Pt-salenCo hybrid compounds will be discussed.

4.1. Magnetic Properties

4.1.1. Magnetic Properties of Ru-trisbipy₂Co

The measurements of the magnetic properties of Ru-trisbipy₂Co indicate that the magnetic behaviour is essentially maintained after functionalization, indicating that the structural integrity of the hydroxide is also preserved after such functionalization.

The magnetic properties of Ru-trisbipy₂Co are very classical. Ru-trisbipy₂Co presents a ferrimagnetic ordering at $T_c = 8.3$ K (figures 9 and 10). Yet, the value of the Curie constant ($4.34 \text{ emu}\cdot\text{K}\cdot\text{mol}^{-1}$) which is too low compared to the expected value of at least $5.1 \text{ emu}\cdot\text{K}\cdot\text{mol}^{-1}$. Considering the characterizations of the compound, showing absence of detectable impurity, and considering the otherwise very classical and expected magnetic behaviour, this discrepancy of the measured Curie constant might be due to an error on the mass of the sample measured in the squid (less than 2 mg of sample were used). New measurements on a larger batch are programmed.

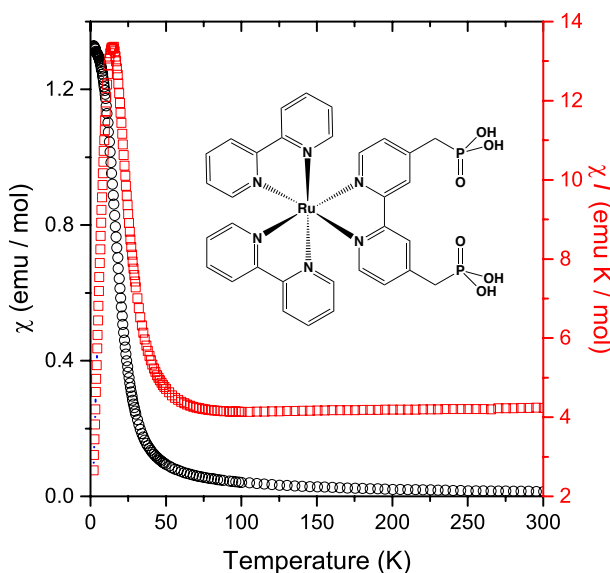


Figure 9 : χ and χT products of Ru-trisbipy₂Co measured at 5000G.

The ac susceptibility measurements (figure 10) allow to determine the ordering temperature, 8.3 K. These measurements evidence a more complicated behaviour, with other magnetic phases around 17 and 14K, likely due to the existence of phases with slightly different hydration level, or to an intrinsic behaviour of the hybrid compound. Ac susceptibility measurements after drying the sample thoroughly, and/or with a different ac frequency are planned to get more data about this behaviour.

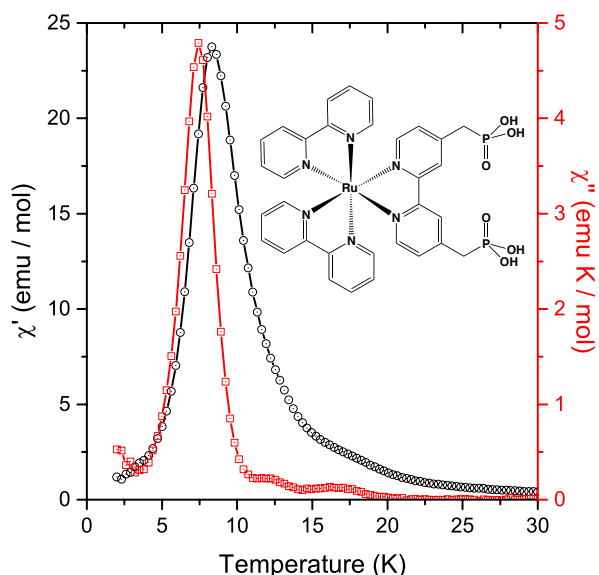


Figure 10 : ac susceptibility measurement of Ru-trisbipyCo ($f = 89$ Hz, $\mu_0 H_{ac} = 0.2$ mT).

For Ru-stribipyCo, due to an inadequate blocking of the powder for magnetization versus field measurement, no hysteresis opening was observed (figure 11). New measurements will be performed with the sample properly blocked in eicosane. The magnetization value at high field ($2.21 \mu_B$ at 5 T) is in line with the expected value for a ferrimagnetic behaviour (figure 11).

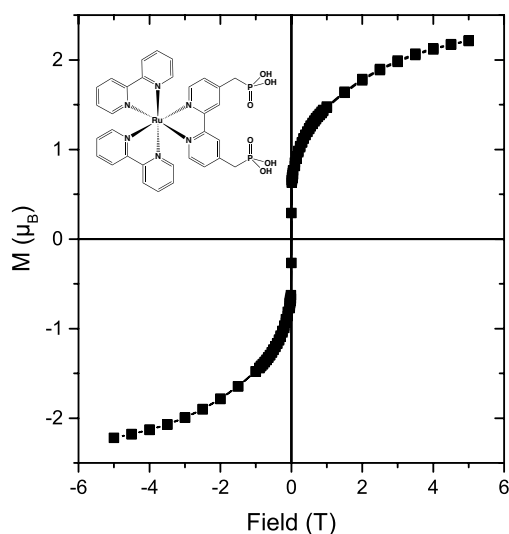


Figure 11 : Magnetization vs. field curve of Ru-trisbipyCo measured at 1.8 K.

Even if additional measurements are required to complete the magnetic characterization of the hybrid whenever possible, the magnetic properties are rather classical for cobalt hydroxide-based hybrid. Unfortunately, magnetic measurements performed on Pt-salenCo present the same problems.

4.1.2. Magnetic Properties of Pt-salen_cCo

The measurements of the magnetic properties of Pt-salen_cCo indicate similar behaviour. The hybrid compound behaves as a ferrimagnet, as well with $T = 7.4$ K. There again, and probably for the same reasons Curie constant is determined at $4.44 \text{ emu}\cdot\text{K}\cdot\text{mol}^{-1}$ is too low compared to the expected one.

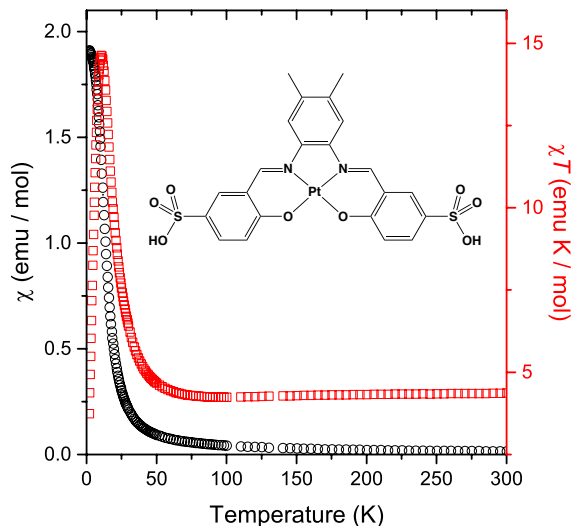


Figure 12 : χ and χT products of Pt-salen_cCo measured at 5000G.

The ac susceptibility measurements (figure 13) allow to determine the ordering temperature (7.4 K). These measurements also evidence the presence of a small amount of another magnetic phase, with an ordering temperature of around 21 K. As stated in the other chapters, the existence of more than one magnetic phase is relatively frequent for layered hybrid magnetic materials, and might be due to difference in the hydration level, or to an intrinsic behaviour of layered hybrid magnetic materials.³¹⁻³³

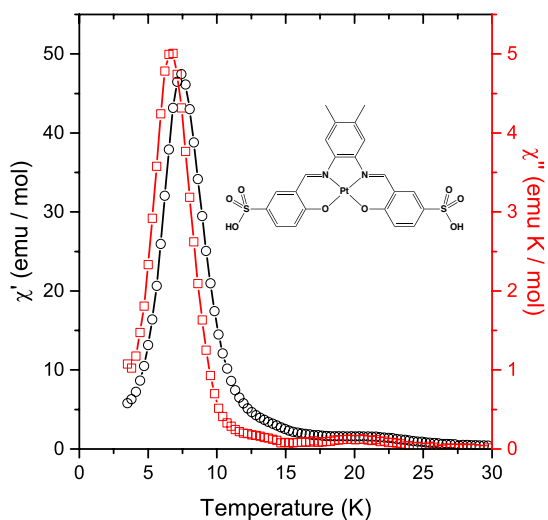


Figure 13 : ac susceptibility measurement of Pt-salen_cCo ($f = 89$ Hz, $\mu_0 H_{ac} = 0.2$ mT).

As described before, due to an inadequate blocking of the powder for magnetization versus field measurement, no hysteresis opening was observed (figure 14). New measurements will be performed with the sample properly blocked in eicosane. The moment value at high field (5 T) is measured at 2.36 μB which is in agreement with the ferrimagnetic behaviour of the hydroxide.

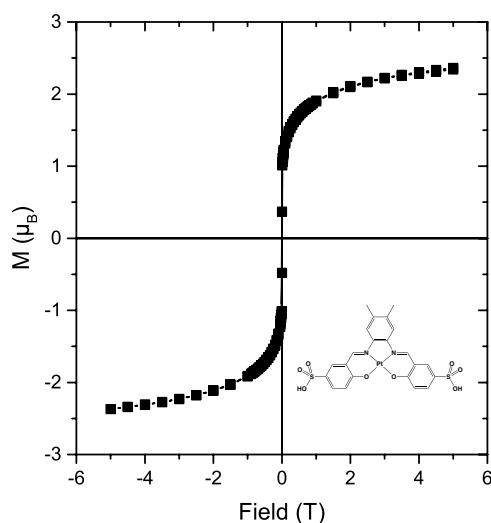


Figure 14 : Magnetization vs. field curve of Pt-salenCo measured at 1.8 K.

4.2. Luminescence Properties

We studied the luminescent properties of Ru-trisbipyCo and Pt-salenCo in the solid state with a laser excitation ($\lambda = 320 \text{ nm}$ and energy around 2.5 mW).

4.2.1. Luminescence Properties of Ru-trisbipyCo

The luminescence of Ru-trisbipy complexes has been widely studied, but its source at room temperature is more coming from a manifold of spin-orbit states rather than a specific spin triplet electronic state.⁶ We indeed observe (figure 15) a wide emission band centred around 690 nm which is in good agreement with observations in the literature⁶ and for similar systems as well with the previously described Mg/Al with intercalated tris(4,7-diphenyl-1,10-phenanthroline)ruthenium(II).¹⁰

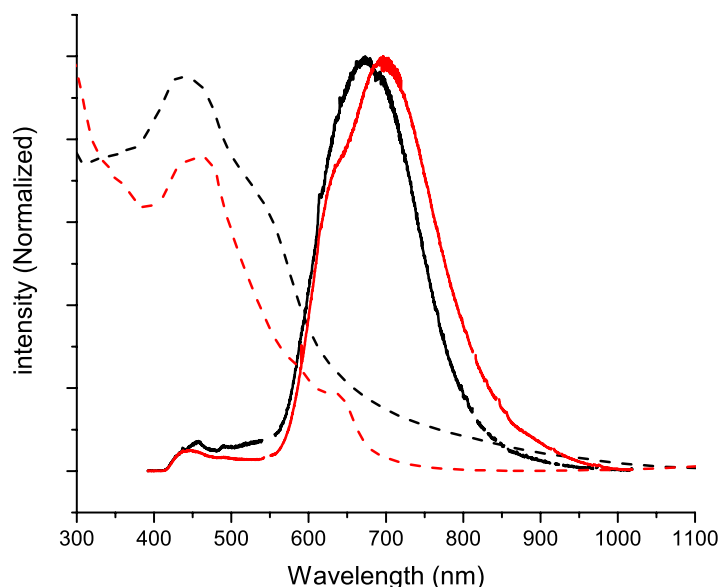


Figure 15 : Normalized absorptions (dashed lines) and emissions (full lines) of Ru-trisbipy (black) and Ru-trisbipy@Co (red).

The shoulder-like effect observed at 630 nm is very probably due to the reabsorption *via* the tetrahedral cobalt of the inorganic matrix (${}^4A_2(F) \rightarrow {}^4T_1(F)$ transition at 635 nm). This result also shows that the luminescence is preserved once intercalated inside the hydroxide, without any quenching.

4.2.2. Luminescence Properties of Pt-salen@Co

The luminescence of Pt-salen@Co shows two distinct features : one emission band centred at 627 nm and another at 705 nm. These correspond to transitions from the lowest excited triplet states *i.e.* intraligand charge-transfer (L(phenoxide) \rightarrow π^* (imine)) and MLCT (Pt(5d) \rightarrow π^* (Schiff base)) to the singlet ground state (figure 16).²²

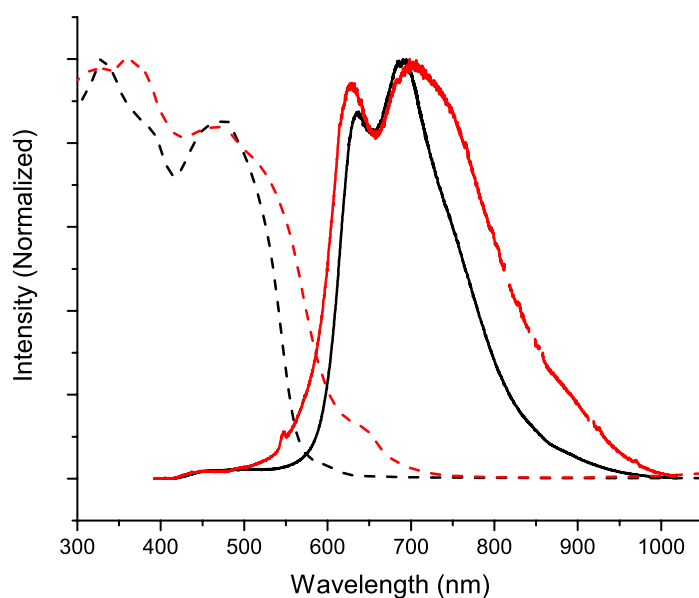


Figure 16 : Normalized absorptions (dashed lines) and emissions (full lines) of Pt-salen (black) and Pt-salen@Co (red).

There are almost no change in the luminescence features between the molecule alone and once inserted in the hybrid, which is expected as the absorption of the inorganic matrix is rather weak in this region. This lack of changes indicates the usefulness of the phosphonic acid as an « insulating » moiety to avoid electronic transfer to the inorganic matrix.

5. Conclusions

This section has shown that it is possible to functionalize cobalt layers hydroxide with various transition metal complexes and even when these are relatively big (around 12 Å sphere for Ru-trisbipy) and bulky.

This study shows that both the magnetic and luminescent properties of the inorganic matrix and the transition-metal complex are preserved.

Further studies of luminescence lifetimes and luminescence under cooling and under a magnetic field could be also interesting to further investigate the interactions between the two sub-networks (if any). The interplay between the magnetic ordering and the luminescence properties have been previously demonstrated on a fluorescent molecule (an oligophenylenevinylene) (*i.e.* emitting from a singlet state). In that case, the luminescence wavelength is modified upon magnetic ordering of the material.³⁴ The hybrid compounds obtained in this chapter are good candidates to exhibit a larger interplay between the properties, since intuit case, the emitting state is a mutliplet, so *a priori* more likely to be directly influenced by the magnetic ordering of the material.

6. Bibliography

1. S. Eyele-Mezui, Ph.D. Thesis, Université de Strasbourg, 2011.
2. R. Bourzami, S. Eyele-Mezui, E. Delahaye, M. Drillon, P. Rabu, N. Parizel, S. Choua, P. Turek and G. Rogez, *Inorganic Chemistry*, 2014, **53**, 1184-1194.
3. S. Eyele-Mezui, P. Vialat, C. Higy, R. Bourzami, C. Leuvrey, N. Parizel, P. Turek, P. Rabu, G. Rogez and C. Mousty, *The Journal of Physical Chemistry C*, 2015, **119**, 13335-13342.
4. F. E. Lytle and D. M. Hercules, *Journal of the American Chemical Society*, 1969, **91**, 253-257.
5. R. W. Harrigan and G. A. Crosby, *The Journal of Chemical Physics*, 1973, **59**, 3468-3476.
6. K. Kalyanasundaram, *Coordination Chemistry Reviews*, 1982, **46**, 159-244.
7. M. G. Sasso, F. H. Quina and E. J. H. Bechara, *Analytical Biochemistry*, 1986, **156**, 239-243.
8. E. H. Yonemoto, G. B. Saupe, R. H. Schmehl, S. M. Hubig, R. L. Riley, B. L. Iverson and T. E. Mallouk, *Journal of the American Chemical Society*, 1994, **116**, 4786-4795.
9. Q. Sun, S. Mosquera-Vazquez, L. M. Daku, L. Guenee, H. A. Goodwin, E. Vauthey and A. Hauser, *Journal of the American Chemical Society*, 2013, **135**, 13660-13663.
10. E. P. Giannelis, D. G. Nocera and T. J. Pinnavaia, *Inorganic Chemistry*, 1987, **26**, 203-205.
11. J. L. Colon, C. Y. Yang, A. Clearfield and C. R. Martin, *The Journal of Physical Chemistry*, 1990, **94**, 874-882.
12. Q. Wang, D. Yu, Y. Wang, J. Sun and J. Shen, *Langmuir*, 2008, **24**, 11684-11690.
13. E. Delahaye, S. Eyele-Mezui, M. Diop, C. Leuvrey, P. Rabu and G. Rogez, *Dalton Transactions*, 2010, **39**, 10577-10580.
14. S. Eyele-Mezui, E. Delahaye, G. Rogez and P. Rabu, *European Journal of Inorganic Chemistry*, 2012, **2012**, 5225-5238.
15. G. A. Crosby and J. N. Demas, *Journal of the American Chemical Society*, 1970, **92**, 7262-7270.
16. R. J. Watts and G. A. Crosby, *Journal of the American Chemical Society*, 1972, **94**, 2606-2614.
17. Q. Sun, S. Mosquera-Vazquez, L. M. Daku, L. Guenee, H. A. Goodwin, E. Vauthey and A. Hauser, *Journal of the American Chemical Society*, 2013, **135**, 13660-13663.
18. R. Caspar, L. Musatkina, A. Tatosyan, H. Amouri, M. Gruselle, C. Guyard-Duhayon, R. Duval and C. Cordier, *Inorganic Chemistry*, 2004, **43**, 7986-7993.
19. J. Zhang, F. Zhao, X. Zhu, W.-K. Wong, D. Ma and W.-Y. Wong, *Journal of Materials Chemistry*, 2012, **22**, 16448-16457.
20. P. Wu, D. L. Ma, C. H. Leung, S. C. Yan, N. Zhu, R. Abagyan and C. M. Che, *Chemistry*, 2009, **15**, 13008-13021.
21. W. Wu, J. Sun, S. Ji, W. Wu, J. Zhao and H. Guo, *Dalton Transactions*, 2011, **40**, 11550-11561.
22. C.-M. Che, C.-C. Kwok, S.-W. Lai, A. F. Rausch, W. J. Finkenzeller, N. Zhu and H. Yersin, *Chemistry - A European Journal*, 2010, **16**, 233-247.
23. C. M. Che, S. C. Chan, H. F. Xiang, M. C. Chan, Y. Liu and Y. Wang, *Chemical Communications*, 2004, **0**, 1484-1485.
24. S. M. Borisov, R. Saf, R. Fischer and I. Klimant, *Inorganic Chemistry*, 2013, **52**, 1206-1216.
25. E. F. Reid, V. C. Cook, D. J. Wilson and C. F. Hogan, *Chemistry*, 2013, **19**, 15907-15917.
26. M. Montalti, S. Wadhwa, W. Y. Kim, R. A. Kipp and R. H. Schmehl, *Inorganic Chemistry*, 2000, **39**, 76-84.

27. M. Botsivali, D. F. Evans, P. H. Missen and M. W. Upton, *Journal of the Chemical Society, Dalton Transactions*, 1985, **0**, 1147.
28. E. Delahaye, S. Eyele-Mezui, M. Diop, C. Leuvre, D. Foix, D. Gonbeau, P. Rabu and G. Rogez, *European Journal of Inorganic Chemistry*, 2012, **2012**, 2731-2740.
29. F. Zuloaga and M. Kasha, *Photochemistry and Photobiology*, 1968, **7**, 549-555.
30. G. A. Carter and D. C. McCain, *Remote Sensing of Environment*, 1993, **46**, 305-310.
31. E. Coronado, J. R. Galan-Mascaros, C. J. Gomez-Garcia and V. Laukhin, *Nature*, 2000, **408**, 447-449.
32. F. Bellouard, M. Clemente-León, E. Coronado, José R. Galán-Mascarós, Carlos J. Gómez-García, F. Romero and Kim R. Dunbar, *European Journal of Inorganic Chemistry*, 2002, **2002**, 1603-1606.
33. A. Demessence, G. Rogez and P. Rabu, *Chemistry of Materials*, 2006, **18**, 3005-3015.
34. J.-M. Rueff, J.-F. Nierengarten, P. Gilliot, A. Demessence, O. Cregut, M. Drillon and P. Rabu, *Chemistry of Materials*, 2004, **16**, 2933-2937.

General Conclusion and Prospects

General Conclusion and Prospects

This PhD work dealt with several aspects of layered hybrid materials chemistry : synthesis, structural characterization and physical properties.

Foremost, the work done during this PhD allowed us to develop many synthetic procedures to obtain new hybrid compounds based with copper and cobalt hydroxides by using a phosphonic acid as a novel grafting moiety. An alternate pre-intercalation technique has been developed, highlighting the role of the packing of the molecules in the interlamellar spacing for ion exchange reactions. We have been able to synthesize a large number of hybrids functionalized by various molecules with different rigid platforms and lateral functionalizations (these molecules were provided by the group of Paul-Alain Jaffrès, CEMCA, Brest).

Fluorene, benzene and (bis) thiophene bearing phosphonic acid anchoring groups have thus been successfully inserted into copper and cobalt layered hydroxides. We showed that despite some difficulties, the insertion of phosphonic acid molecules is in general easier than the one of the corresponding carboxylate. We have shown how more or less subtle variations of the reaction conditions (starting material, ratio between the reactants, temperature, duration of the reaction or post-synthesis treatment) enable the formation of the desired compounds. In most cases the formation of coinserted compounds (single-phase compounds functionalized by both the starting dodecylsulfate or dodecylsulfonate and the molecule of interest) has been avoided.

The peculiar design of the chosen molecules (a rigid aromatic platform bearing one or two phosphonate anchoring groups) led, in the absence of lateral functionalization, to a seldom encountered arrangement of the molecules within the interlamellar spacing *i.e.* almost parallel to the inorganic layers. For the insertion of molecules possessing two anchoring phosphonate groups into copper hydroxide, we evidenced experimentally that a stable phase in which only one out of the two anchoring groups is coordinated to one layer, the other being in interaction with the metal ions *via* a network of H-bonded molecules of water. This surprising non-pillaring arrangement was confirmed by theoretical structural simulations using First Principles Molecular Dynamics performed by the simulation team of our Department (Z. Chaker, G. Ori, M. Boero and C. Massobrio)

Another goal of this work was indeed to precise the understanding of the structure of the hybrids. The initial idea was to try to synthesize new hybrid by performing single-crystal-to-single-crystal reactions. Unfortunately, this idea did not lead to the desired results. Yet it enabled to elaborate a new easy and very reproducible method to synthesize single crystals of the starting copper hydroxi-dodecylsulfate $\text{Cu}_2(\text{OH})_3(\text{DS})$. The previously unknown structure of this compound was solved from single-crystal diffraction data (collaboration with Olivier Pérez and Nicolas Barrier, CRISMAT, Caen). Interestingly this compound crystallizes in a non-centrosymmetric space group, which makes it one the relatively rare example of chiral compounds obtained from achiral building blocks

During the optimization of the synthetic pathway to obtain single crystals of layered $\text{Cu}_2(\text{OH})_3(\text{DS})$, we manage to isolate and fully characterize a ribbon-like compound of formula $\text{Cu}_3(\text{DS})_2(\text{CH}_3\text{COO})_2(\text{OH})_2(\text{H}_2\text{O})_2$ in which both acetate and dodecylsulfate are present. The structure of this compound is very similar to the one obtained by Fujita *et al.* for a newly obtained series of carboxylate-sulfonate ribbon-like compounds.¹ In this thesis, considering the synthesis pathway we used, we propose that $\text{Cu}_3(\text{DS})_2(\text{CH}_3\text{COO})_2(\text{OH})_2(\text{H}_2\text{O})_2$ is indeed an intermediate in the formation of $\text{Cu}_2(\text{OH})_3(\text{DS})$ from $\text{Cu}(\text{OAc})_2$.

Unfortunately, the same approach applied to the cobalt related starting compound was not successful. Therefore efforts were made to precise the structure of the layered cobalt hydroxide layers by means of Pair Distribution Function analysis. This study was performed in close collaboration with C. Taviot-Guého (Institut de Chimie de Clermont-Ferrand). We first managed to validate the use of the bidimensional X-Pad Detector for PDF acquisition on the CRISTAL beamline at SOLEIL synchrotron. This allowed to acquire data for PDF analysis more than ten times faster than when the multianalyzer detector is used.

The results of the PDF treatment on carboxylate functionalized cobalt hydroxide layered hybrid then clearly showed that the scattering contrast between the inorganic part and the organic one is here too important to allow a direct observation of the organic moiety. Yet we evidenced that the functionalization of layered cobalt-hydroxide by insertion-grafting has strong influence on the structural deformation of the inorganic layers, not only on the tetrahedral sites but also on the nearby octahedral ones. In addition, we showed that this deformation is influenced not only by the grafting (formation of a coordination bond) but also by the intermolecular interactions within the interlamellar space.

The functionalized hybrid systems obtained in this work have been studied first for their magnetic properties. While the copper hydroxide derivatives present a antiferromagnetic behaviour, the cobalt hydroxide derivatives show a ferrimagnetic with T_C around 15 K. In that sense the functionalization by phosphonic acid bearing molecules does not drastically modify the behaviour observed on compounds functionalized more “classically” by carboxylates or sulfonates. Whereas the potential ferroelectric character of the compounds could not be evidenced unambiguously, we observed an interesting magnetoelectric effect, unprecedented in this kind of compounds, and which extends well into the paramagnetic phase (collaboration with Alain Pautrat, from CRISMAT in Caen).²

The precise origin of this magnetoelectric coupling has not yet been understood, even though it is likely due to magnetoelastic driven interactions. We hope that the full study (very time consuming) of the dielectric properties of the various series of compounds obtained (fluorene mono or biphosphonic with shorter or longer lateral alkyl chains, benzene derivatives with more or less polar side group or (bis)thiophenes bearing a large and polarizable heteroatom) will provide some interesting hints on the source of this magnetoelectric effect. In that respect, the very different arrangement observed for some molecules, almost parallel to the inorganic layers, is very promising to study the role of the organic moiety on the magnetoelectric effect.

A side aspect of this study concerned the fluorescent properties of the obtained hybrids. We showed the usefulness of the phosphonic acid with respect to carboxylate to limit the quenching of the luminescence of the inserted fluorophore. In addition we managed to insert very large luminescent complexes, in a reproducible way and with no co-insertion. Future work on this aspect will deal with luminescence measurements at low temperature and under a magnetic field to hopefully evidence the effect of a magnetic ordering on the luminescence characteristics.

As for the dielectric properties, this work will hopefully allow to get a better understanding of the origin of the magneto-electric properties that has been observed in various hybrids. Indeed, the variations of aromatic centre, polarizabilities/polarization of the lateral moieties and mono versus bi grafting functionality could help us rationalize the origin of this magnetoelectric effect. This could help us to design the most effective molecules to insert to get the biggest magnetoelectric effect.

The effort made in the characterization of the cobalt hydroxide has proven to give an accurate description of the system. The model obtained allowed us to make a much more realistic

starting point that will be used by the simulation team, while previous attempts have proven unsuccessful due to lack of accurate description of the system.

Some other tests on the improvements of the synthesis of cobalt hydroxy-acetate could also be made with cobalt sources ranging from metallic cobalt to β -phase cobalt hydroxide *via* hydrothermal method. Indeed, an aspect that could not be done during my PhD due to lack of time is to develop hydrothermal method similar to those used in Effenberger work³ where metallic copper, concentrated copper nitrate and high temperature and pressure hydrothermal vessels are used to synthesize $\text{Cu}_2(\text{OH})_3(\text{NO}_3)$ crystals. The possible very slow release of cobalt of the β -phase in an aqueous medium saturated with cobalt acetate could lead to the formation of similar crystals in hydrothermal conditions.

Nonetheless, the obtained improvements in the characterizations and syntheses of the starting compounds are also opening new doors for the shaping of these materials. Indeed, improvements made on copper hydroxide are desirable to obtain objects such as high aspect ratio nanoplatelets, opening a new surface chemistry that is very well developed for graphene, MoS_2 , titanium oxides or even perovskites nanosheets. It could be possible to do measurements on crystals instead of powders even if the copper hydroxide possesses less interesting magnetic properties.

Efforts on the shaping of these materials could also be made with deposition on substrates, attempts to exfoliate them by minimizing intermolecular interactions with short hydrophobic molecules for example. This exfoliation would then pave the way to several shaping methods ranging from the classical layer-by-layer method to flocculation attempts to generate other complex hybrid systems.

This PhD being made in the scope of an ANR funding that will end one year after my PhD ends, measurements of the magnetoelectric properties will be carried on to complete the different series. Once all the hybrids of interest will be measured, it would be interesting to see what helps inducing the observed magnetoelectric effect and what could inhibit it. This knowledge would be very useful to design other molecules with an optimized configuration to maximize the magnetoelectric effect.

Further interesting measurements could be done with our compounds, the first one would be to apply the methodology developed with PDF characterization described in chapter II to the hybrids synthesized in the other chapters. Indeed if the presence of acetate molecule proved to be too light for X-ray scattering to effectively locate the organic molecules, the presence of phosphorous, heavy halogens or transition metals such as platinum or ruthenium could improve significantly the possible localization of the organic molecules. These measurements could also be made upon cooling below the first magnetoelectric effect is observed, indeed it would be interesting to see if we are able to observe a phase transition of the layers upon the appearance of this magnetoelectric effect. These measurements could also be followed with measurements of the luminescence upon cooling, where this could be used as another probe of a potential phase transition. Additionally, coupling the previous measurements with very low temperature specific heat measurements under field could help observe and identify the potential phase transitions.

Finally, another aspect of this PhD developed in collaboration with the group of Yann Garcia at Louvain La Neuve University in Belgium and that has not been described in this thesis is that we demonstrated that the insertion of thermochromic molecules into the interlamellar spacing was possible and that we were able to subsequently modify the interlamellar spacing upon heating and cooling cycles. This aspect is also very promising for opening other ways to bring new properties to the layered cobalt hydroxide.

Bibliography

1. W. Fujita, A. Tokumitsu, Y. Fujii and H. Kikuchi, *CrystEngComm*, 2016, **18**, 8614-8621.
2. Q. Evrard, Z. Chaker, M. Roger, C. M. Sevrain, E. Delahaye, M. Gallart, P. Gilliot, C. Leuvrey, J.-M. Rueff, P. Rabu, C. Massobrio, M. Boero, A. Pautrat, P.-A. Jaffrès, G. Ori and G. Rogez, *Advanced Functional Materials*, 2017, DOI: 10.1002/adfm.201703576, 1703576.
3. H. Effenberger, *Zeitschrift für Kristallographie*, 1983, **165**, 127-135.

Appendixes

Appendix I : Theory About Total Scattering and Pair Distribution

Function Extraction

Appendix II : Complete IR Tables

Appendix III : Published Results

Appendix IV : Experimental Protocols

Appendix I : Theory About Total Scattering and Pair Distribution Function Extraction

Adapted from Olivier Durand Thesis made at Limoges University from the « Laboratoire de Sciences des Procédés Céramiques et de Traitement des Surfaces » the 4th July 2006.

The starting point of the pair distribution function extraction is the measurement of the scattered intensity as a function of the diffusion vector \vec{Q} . In our case, the scattered intensity is measured as :

$$Q = \frac{4\pi \sin \theta}{\lambda}$$

Q being the value of the diffusion vector, λ is the wavelength of the incident X-Rays and θ half of the diffusion angle 2θ . For clarity reasons, the inelastic scattering will be neglected in the following equations.

The amplitude of the scattered wave in the Q direction is written as :

$$A(\vec{Q}) = \sum_{j=1}^N b_j e^{i\vec{Q} \cdot \vec{r}_j}$$

Where N is the number of atoms in the sample and b_j and \vec{r}_j are the average diffusion length and the position vector of the j atom. The elastic differential cross section measured along \vec{Q} is then given by the squared average of the scattered amplitude.

$$\frac{d\sigma}{d\Omega} = I(\vec{Q}) = \langle A(\vec{Q}) A^*(\vec{Q}) \rangle = \sum_{j=1}^N \sum_{k=1}^N b_j b_k^* \langle e^{i\vec{Q} \cdot (\vec{r}_j - \vec{r}_k)} \rangle$$

The average $\langle \dots \rangle$ is done over time. We can already note that the intensity doesn't give direct informations on the atomic positions but rather on the interatomic vectors $\vec{r}_j - \vec{r}_k$.

When an average cristalline structure (a cristalline network) can be defined and when only the displacement disorder is taken into account, it is convenient to split the position vector of the j atom as :

$$\vec{r}_j = \vec{R}_j + \vec{\delta}_j$$

where R_j corresponds to the average atom j position in the structure and $\vec{\delta}_j$ is the difference compared to this ideal position. The equation then becomes :

$$I(\vec{Q}) = \sum_j \sum_k b_j b_k^* e^{i\vec{Q} \cdot (\vec{R}_j - \vec{R}_k)} \langle e^{i\vec{Q} \cdot (\vec{\delta}_j - \vec{\delta}_k)} \rangle$$

In our case (isotropic sample) the scattering signal gives only \vec{Q} modulus and not its direction. The equation of the scattered intensity can be simplified as the Debye scattering equation :

$$I(Q) = \sum_j \sum_k b_j b_k^* \frac{\sin(Qr_{jk})}{Qr_{jk}}$$

If $j \neq k$ the equation then becomes :

$$I(Q) = \sum_j \sum_{k \neq j} b_j b_k^* \frac{\sin(Qr_{jk})}{Qr_{jk}} + \sum_j |b_j|^2$$

The second part of this equation is the incoherent scattering (often called self-scattering). The first part generates interferences and defines the structure factor of the total statistic scattering $F(Q)$ as :

$$F(Q) = \frac{1}{N} \left(I(Q) - \sum_j |b_j|^2 \right) = \frac{1}{N} \sum_j \sum_{k \neq j} b_j b_k^* \frac{\sin(Qr_{jk})}{Qr_{jk}}$$

This structure factor of the total scattering represents the scattered intensity by atom in the sample and contains the information about interatomic distances.

The structure factor of the total normalized scattering $S(Q)$ is defined as :

$$S(Q) = \frac{F(Q)}{\left(\sum_j b_j \right)^2} + 1$$

Indeed, the structure factor of the total normalized scattering $S(Q)$ defined in the reciprocal space is linked *via* a fourrier transform to a function called $G(r)$ defined in real space.

$$S(Q) - 1 = \rho_0 \int_0^{Q_{\max}} 4\pi r^2 (G(r) - 1) \frac{\sin(Qr)}{Qr} dr$$

$$G(r) - 1 = \frac{1}{(2\pi)^3 \rho_0} \int_0^{Q_{\max}} 4\pi Q^2 (S(Q) - 1) \frac{\sin(Qr)}{Qr} dQ$$

with ρ_0 the atomic density (atoms per \AA^3)

$$\begin{array}{l} S(Q) \xrightarrow{Q \rightarrow 0} 0 \quad S(Q) \xrightarrow{Q \rightarrow \infty} 1 \\ G(r) \xrightarrow{r < r_c} 0 \quad G(r) \xrightarrow{r \rightarrow \infty} 1 \end{array}$$

With r_c being the value of the shortest interatomic distance in the material.

This $G(r)$ function is the normalized PDF. It represents the probability to find in the structure a pair of atoms at an r distance of each other. It is a monodimensional function that possess Dirac peaks for values of r equal to interatomic distances. In reality, given the huge amount of atoms as well as their thermal vibration, $G(r)$ is continuous. Its value below the shortest interatomic length is null and when $r \rightarrow \infty$, $G(r)$ is oscillating around 1. Theses oscillations are due to the fact that the order is still present at these correlation distances.

Appendix II : Complete IR Tables

	Fluorene Skeleton	P-Fluo-H	P ₂ -Fluo-H	P-Fluo-C	P ₂ -Fluo-C	P ₂ -Fluo-C ₈	P-Fluo-CN	P ₂ -Fluo-C ₄
			1697					
		1606	1607	1603	1606	1604	1609	1603
C-C ring stretch	1575	1579/ 1567/ 1555(w)	1574/ 1557	1583/ 1567	1577	1577	1574/ 1562(w)	1575
C-C ring stretch	1478	1482/ 1464	1475/ 1464	1470/ 1462	1461	1463	1476/ 1464	1461
C-C ring stretch	1447	1452/ 1437(w) 1427(w)	1449	1456/ 1446	1444	1440	1447	1445
							1422	1415
C-C ring stretch	1402	1411	1409	1405	1405	1404	1409	1404
	1384	1397/ 1390(w)	1391		1383	1376	1398/ 1382(w)	1376
		1363	1361(w)	1361	1363			1363(w)
PO ₃ as stretching (1330)	1311	1334	1333	1340	1337	1339	1332(w)	1343(w)
	1300	1303	1306	1302	1304	1301	1303	1303
C-H inplane bending		1284	1283	1278			1289	1268(w)
	1234	1265(w) 1239	1244	1255	1261(w)		1250	1230
C-H inplane bending	1192	1208/ 1195/ 1184 P=O/ 1171	1198/ 1180 P=O/ 1160	1203 P=O 1158(w)	1161 P=O	1162	1212/ 1206/ 1193	1205
C-H inplane bending		1146	1140	1148	1140		1180	1185/ 1168
C-H inplane bending		1126	1121	1133	1124	1128	1145/ 1132	1138
PO ₃ s stretching (1110)	1108	1103	1106	1115	1109		1115	1128/ 1117(vw)
	1092	1091	1095	1088	1086	1094	1098	1095
		1064	1072	1073	1073(w)		1057	
	1019	1022	1028(w)			1039	1021	1021
	1000	1001	1001	1011/ 1005	993	(1010) 991	1009/ 995	1007(w)/992
	953	975/ 953	965/ 949		950		957	976/ 971
		944/ 936		939	940		941	949
		929	927		931			926
				922	920	924	913	905
	862	887 877	905(w) 869	905 873	897		894(w) 875	870
		856	848		851	842	867/ 845	846
		834/ 820	832/825	835	825	820	821	824/ 813
		790(w)	768	783	789/776			793
		767	758	759		756	765/ 757	773/ 756
	738	750/ 737		739	737			746
		728				722	702/ 692	725
	698	701	705	665	692	689		697(vw)/687
	634/ 624	675/ 639	667	620	620	661/612		661/ 634/ 622
PO ₃ s déformation (605)			604	598	609/601	596	594	614/ 597
		588	590/ 565	574/569			583	571
		558/ 542	545/ 537	555	551		552	547
		523	526	538	529	533	530/ 525	535/ 526
PO ₃ as déformation (510)		505	504/ 500					500

	CoOAc	CoDSo	P-Fluo-C _c Co	P-Fluo-CN _c Co	P ₂ -Fluo-H _c Co	P ₂ -Fluo-C _c Co	P ₂ -Fluo-C _{4c} Co	P ₂ -Fluo-C _{8c} Co
		1626		1651			1628	
C-C ring stretch			1633/ 1607	1611	1601	1643/ 1604	1604	1633/ 1604
C-C ring stretch	1563			1574/ 1558/ 1540/ 1506	1571/ 1556/ 1540/ 1517/ 1504	1575		
C-C ring stretch	1557	1467	1469	1477/ 1463	1488/ 1472/ 1461	1481/ 1460	1460	1460
C-C ring stretch		1456	1457/ 1446			1446		
	1392/ 1385	1413			1403			
			1399	1408		1401	1395	
		1379	1382	1397/ 1394	1384	1382	1380	1377
			1361	1362(w)	1359(w)	1360		
PO3 as stretching (1330)			1339	1334(w)		1337		
		1293	1299	1302	1300	1299	1299	1297(w)
C-H inplane bending		1277	1275	1289	1277	1274	1264	
		1249/ 1223/ 1195(w)	1259	1245(w)	1260/ 1237		1228	
C-H inplane bending		1159	1216/ 1205	1211/ 1200/ 1187		1218/ 1207	1206	1166
C-H inplane bending			1143	1181	1200/ 1179		1183	
C-H inplane bending			1126	1137(w)	1123(w)	1121	1138(w)	1126
PO3 s stretching (1110)		1104(w)	1112	1111(w)	1097		1125	
				1092		1081	1090	1090
		1079	1073					
	1047	1042	1039	1037		1045	1041	1038
	1016			1005			1006	
			961	964		961	979(w)/ 961	959
			933	943(w)				
							904	
				870(w)		907		905(w)
		888(w)	877		880	878		878(w)
		831(w)	833	820	831	822	822	822
		786	785	774			790	
		756	760	762	760		774	
			739			745	751	720(w)
		719		703/ 689	712	693		690
			667		686	666	690	
	656		624			630		
PO3 s déformation (605)	608	606	601	600	618(w)	602	599	598
			577/562	583/ 565(w)	573	572		
			534	556				547(w)
		536		546	539			
PO3 as déformation (510)		503	513	529/ 525/ 518/ 515	516		514	511

	CuOAc	CuDS	P-Fluo-HcCu	P-Fluo-CcCu	P-Fluo-CNcCu	P ₂ -Fluo-HcCu	P ₂ -Fluo-CcCu	P ₂ -Fluo-C ₈ cCu
	1695				1638			
C-C ring stretch	1667		1631/ 1609	1633/ 1604	1610	1634	1633/ 1574	1633/ 1573
C-C ring stretch	1547		1570/ 1561(w)		1572/ 1535	1575/ 1557		
C-C ring stretch		1471	1462	1469/ 1458	1476/ 1462	1462	1461	1459/ 1438(w)
C-C ring stretch		1456	1450	1446	1436(w)		1444	
		1394			1424			
	1408		1407	1402	1408/ 1396	1407	1402	1398
		1378	1395(w)	1383			1384	1377
	1345			1360		1364(w)	1362	
PO3 as stretching (1330)		1313	1338	1339	1332	1337	1339	
		1286	1299	1299	1301	1299	1299	1299
C-H inplane bending		1274	1276	1275	1286	1275/ 1265	1262	1262(w)
		1259	1233(w)	1259	1243/ 1234(w)	1240(w)	1217	
C-H inplane bending		1234	1198/ 1188/ 1171	1217/ 1207	1210(w)/ 1201/ 1188	1200/ 1179	1208	
C-H inplane bending		1186		1145				1162
C-H inplane bending				1127	1133(w)/ 1110(w)		1120	1126
PO3 s stretching (1110)		1096	1103	1112		1099		
			1087		1092		1082	1092
				1074			1070(w)	
	1047	1043	1039	1036	1044	1038	1044	1042
	1023	1011		1023(w)	1008		1010	1009
		980	970	967	966		964	960
	947	957		933	943(w)			
			928(w)					
		890		905(w)			906(w)	
	870			875(w)	868		877(w)	881
							848(w)	
			832/ 818	834	819		824	823
	795			785/ 777	784(w)/ 776(w)			
		770	770	760	762			
			751/ 736	738	744(w)		745	749/ 723(w)
		719		717	721(w)/ 704/ 690		694	691
		697	700/ 678	667			667	667
	649	627	641	626			631	
PO3 s déformation (605)	612		592	602	599		603	600
		578/571	581	580/570	583		569	562
	545		543		558			
				534(w)				
PO3 as déformation (510)		511			525			
				490(w)	499(w)		500	500(w)
	478				478(w)			
	451	462		457/446/				
				436/425	423		427	429
	406	403		417				

	Benzene Skeleton	P-Bz-F	P-Bz-FcCu	P-Bz-FcCo	P-Bz-Cl	P-Bz-ClcCu	P-Bz-ClcCo
			1631	1626	1634	1633	1622
C-C ring stretch		1608			1588		
C-C ring stretch	1528	1583	1579	1579/ 1558/ 1539	1565/ 1540/ 1506	1562	1560/ 1540/ 1505
C-C ring stretch	1479	1480/ 1462	1477	1474/ 1472	1471	1469/ 1457	1488/ 1465
C-C ring stretch		1448(w) 1425	1420	1420/ 1418			
	1393				1399	1397	1397
			1379 (w)				
PO3 as stretching (1330)		1306			1337		
							1299(w)
C-H inplane bending		1270	1265	1265	1273		1260
		1231	1220	1218	1237		
C-H inplane bending		1162	1159	1160		1207	
C-H inplane bending	1176				1171/ 1158/ 1147	1142	1169(w)/ 1140
C-H inplane bending							
PO3 s stretching (1110)		1117	1105	1105	1097	1095	1092
			1084		1084		
		1062	1062	1077		1072	
	1036		1042	1042	1045	1040	1044
		1011/ 1001	1005	1004	1007/ 994	1000	1000
		952	968	969		966	964
		941			945(w)/ 932		
					923		
		911			892		
		878	879	880		888(w)	
							830(w)
		796		791	792	783	785
		770	788				
			733				
			688	687	718/ 690	689	689
	674	691/ 682	666		683/ 667	667	667
			626				
PO3 s déformation (605)			604				
		586/ 576	594/ 569	592	563	566	561
		563/ 545		564	555		
		523			541		543
PO3 as déformation (510)				518			506
		478/ 463	483		467		
					454/ 442		
		427			428/ 422	423	
		415	417		414		

	P-Bz-Br	P-Bz-Br _c Cu	P-Bz-Br _c Co	P-Bz-I	P-Bz-I _c Cu	P-Bz-I _c Co	P-Bz-C4N	P-Bz-C4N _c Cu	P-Bz-C4N _c Co
		1625	1629		1622	1626	1656	1658/ 1648	1656
C-C ring stretch							1594	1591	1591s
C-C ring stretch	1556/ 1505	1557/ 1539/ 1505	1556/ 1540/ 1505	1550/ 1505	1551/ 1505	1550/ 1505	1577	1574 /1549	1574/ 1557
C-C ring stretch	1488/ 1464	1465	1462	1462	1463/ 1455	1455	1485/ 1471	1487s/ 1471	1471
C-C ring stretch	1436							1442	1442
							1420	1416	1415
	1399	1395	1393	1393	1389	1387	1393	1393s	1397s
			1360				1358(w)	1356(w)	1364(w)
PO3 as stretching (1330)	1338			1339			1322	1314	1312
	1300(w)	1297(w)	1296(w)	1300(w)/ 1288	1297(w)	1296(w)			
C-H inplane bending	1287/ 1262	1261	1261	1261	1261	1262	1288	1284	1284
							1239	1233	1234
C-H inplane bending	1198			1187			1195(w)	1196s	1197s
C-H inplane bending	1168/ 1143	1171(w)	1168(w)	1174	1170	1170(w)	1165	1164(w)	1163(w)
C-H inplane bending	1126(w)/ 1112	1136	1134	1139/ 1107	1133	1133	1127	1116s	1118
PO3 s stretching (1110)	1086	1092	1091	1086	1088	1090	1091(w)	1090s	1089s
	1070	1067	1061	1061	1059	1059			
		1037	1044(w)		1044	1046	1047	1041	1037
	1002(w)/ 994	999	997	1003/ 991/ 980(w)	1011/ 996	1012(w)/ 996	1002/ 988	1001	999
		962	964		963	963	965	968	966
	950			950				953	951
	920			918			923		
	895			896				904	
							876		879(s)
		889(w)					860(w)		
	862			956					
			830(w)	810(w)					
	793	782	785	789	791(w)/ 786(w)/ 782	784	788	788	789
	768	762	760					756(w)	
				753	749	748			
	723/ 684	687	688	720(w)/ 684	707(w)/ 688	687			
		667	667	668	667	667	700s/ 688	694	691
	655	655	655	649	648	648			
PO3 s déformation (605)					596(w)	597	607	604s	602
		561		578			588	568	562
	554		559	557	559	558			
	546			543(w)/ 539			535		544
PO3 as déformation (510)			518			515			523s/ 519

	Squelette Thiophene	P ₂ -thio	P ₂ -Thio + CoOleic	P ₂ -Thio+ CuOleic	P ₂ -Thio-C	P ₂ -Thio-C _c Cu	P ₂ -Thio-C _c Co	P ₂ -diThio	P ₂ -dithio _c Cu	P ₂ -dithio _c Co
	1687/ 1666		1635	1637		1635	1635	1620	1630	1636
C-C ring stretch			1597	1558			1558/ 1539			
C-C ring stretch		1504	1505	1506	1520	1527	1522/ 1505	1499	1500	1501
C-C ring stretch		1460	1467/ 1455	1466/ 1456	1456	1467/ 1456	1470/ 1455			1454
C-C ring stretch										
	1408	1423			1420		1411	1427	1427	1427/ 1416
			1370	1378	1382	1381	1380			
					1347				1377(w)	1381
PO3 as stretching (1330)						1335	1336		1339(w)/ 1317	1336/ 1315
		1299								
C-H inplane bending	1251		1286	1284			1276	1277	1274	1272
		1233/ 1214	1234/ 1202	1235/ 1208		1237	1222	1232	1215	
C-H inplane bending		1188			1201	1197		1197	1199	1213/ 1198
C-H inplane bending					1169		1154			
C-H inplane bending		1119/ 1104			1119			1127		
PO3 s stretching (1110)	1081	1081	1086	1090	1086			1094		1118(w)
		1056	1060	1050	1060	1068	1071		1077	1072
	1034	1047/ 1020	1040	1038		1052	1045		1048	
		988	1008	1011	1009			1015	1016	1008
				982	981			987		959
		930	957	954		951	955		959	
					933/ 914		919	939		
										904
	871			870				898		873
					862			877	874	
				845	857					
	834	831	818		813			813		800
							787	798	799	
		768								
		750		732				742	745	742
	714	721	717		718	728	718			
		676			668				693(w)/ 673(w)/ 666(w)	
					625			648	652	647
PO3 s déformation (605)					610/ 597	605	605			
		589/ 581	586	595				564	574/ 566	
		566	564	568	565/ 552	571	566	556		559
		541/ 530			546/ 535			535		
PO3 as déformation (510)			513		525		514	515/ 509		524/514
		490			490			491	498(w)	
					475	481				
	467	447			436			454		
		415		417	421	419		420	421	

Layered Simple Hydroxides Functionalized by Fluorene-Phosphonic Acids: Synthesis, Interface Theoretical Insights, and Magnetoelectric Effect

Quentin Evrard, Ziyad Chaker, Mélissa Roger, Charlotte M. Sevrain, Emilie Delahaye, Mathieu Gallart, Pierre Gilliot, Cédric Leuvrey, Jean-Michel Rueff, Pierre Rabu, Carlo Massobrio, Mauro Boero, Alain Pautrat, Paul-Alain Jaffrès, Guido Ori,* and Guillaume Rogez*

Copper- and cobalt-based layered simple hydroxides (LSH) are successfully functionalized by a series of fluorene mono- and diphosphonic acids, using anionic exchange reactions and a preintercalation strategy. The lateral functionalization of the fluorene moieties has only little impact on the overall structure of the obtained layered hybrid materials but it influences the organization of the molecules within the interlamellar spacing. For bulky fluorene (9,9-dioctyl derivative), luminescence is preserved when inserted into copper and cobalt hydroxides, whereas it is completely quenched for the other fluorenes. Detailed characterization of the internal structure and chemical bonding properties for copper- and cobalt-based hybrids is performed via ancillary experimental techniques. For the copper-based LSH class, for which more elusive findings are found, first-principles molecular dynamics simulations unravel the fundamental stabilizing role of the H-bonding network promoted within the local environments of the fluorene mono- and diphosphonic acids. The cobalt series of compounds constitute a new class of hybrid magnets, with ordering temperatures ranging from 11.8 to 17.8 K and show a clear magnetoelectric effect. This effect appears above a threshold magnetic field, which is null below the magnetic ordering temperature, and it persists in the paramagnetic regime till about 110 K.

1. Introduction


The field of multiferroic materials (i.e., materials in which at least two of electric, magnetic, and elastic orders coexist) is currently mainly covered by oxides, but hybrid and molecule-based materials are recently emerging.^[1,2] Among molecule-based materials, one may quote coordination polymers and metal-organic frameworks^[3,4] or the series of compounds $[(\text{CH}_3)_2\text{NH}_2]\text{[M}(\text{HCOO})_3]$ (with $\text{M} = \text{Mn}, \text{Co}, \text{Ni}, \text{Fe}$) which illustrates the most studied achievements in the MOFs approach to multiferroics.^[5,6] The non-collinear magnetic ordering occurring below $T_N = 8.5$ to 35.6 K, depending on the transition metal ion,^[7,8] coexists with an antiferroelectric order, which develops at higher temperature (170 K).^[5] The central cation can also be modified to tune the properties and ordering temperatures.^[9] Moreover, it has been shown that some of these compounds could offer an electric control of the magnetization which should be very attractive for advanced memory devices.^[10]

Another example of hybrid multiferroic compound has been obtained by taking advantage of the hosting behavior and magnetic properties of oxalate-bridged 2D networks.^[11] This material is ferromagnetic below $T_C = 3.9$ K and ferroelectric in the whole temperature range. No magnetoelectric coupling could be evidenced in this material.

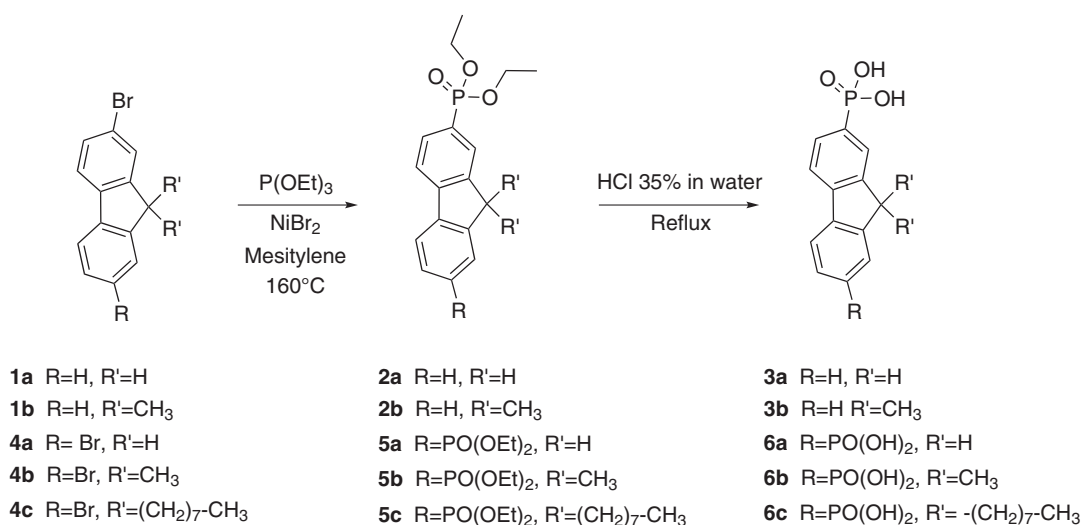
Finally, the last family of multiferroic hybrid compounds is built on layered perovskites, which are excellent candidates because they combine structural flexibility with robust magnetic and electrical properties.^[12–14] The study of CuCl_4 -based hybrids, with ethyl ammonium or phenyl-ethyl ammonium counter ions, reveals that these systems present a coexistence of ferromagnetic ordering below 9 and 13 K, respectively, originating from the inorganic part, and improper ferroelectric ordering below 247 and 340 K, respectively, originating from the hydrogen-bond (H-bond) ordering of the organic part.^[15,16]

It therefore appears that the still scarcely explored chemical hybrid approach to multiferroics and magnetoelectrics may

Q. Evrard, Z. Chaker, Dr. E. Delahaye, Dr. M. Gallart, Dr. P. Gilliot, C. Leuvrey, Dr. P. Rabu, Dr. C. Massobrio, Dr. M. Boero, Dr. G. Ori, Dr. G. Rogez
Institut de Physique et Chimie des Matériaux de Strasbourg
Université de Strasbourg
CNRS UMR 7504, F-67034 Strasbourg Cedex 2, France
E-mail: guido.ori@ipcms.unistra.fr; guillaume.rogez@ipcms.unistra.fr
Dr. M. Roger, Dr. C. M. Sevrain, Prof. P.-A. Jaffrès
CEMCA
CNRS UMR 6521
Université de Brest
IBSAM, 6 Avenue Victor Le Gorgeu, 29238 Brest, France
Dr. J.-M. Rueff, Dr. A. Pautrat
CRISMAT
CNRS UMR 6508
ENSICAEN
6 bd du Maréchal Juin, 14050 Caen Cedex, France

 The ORCID identification number(s) for the author(s) of this article can be found under <https://doi.org/10.1002/adfm.201703576>.

DOI: 10.1002/adfm.201703576



Scheme 1. Synthesis of the fluorenyl mono- and diphosphonic acids used in this work.

present various advantages with respect to the solid state chemistry approach, in terms of synthesis and possibility to modulate rather easily the structures and properties. Moreover, hybrid materials, where the two subnetworks responsible for the magnetic and electric properties are deeply interwoven, are a priori more likely to present magnetoelectric coupling compared to nanostructured composite materials, the potential magnetoelectric coupling being essentially tied to the interface.^[17–19]

In this respect, layered insertion compounds are particularly worthy of interest. Many works about multifunctional hybrids concerned layered bimetallic trioxalatometalates,^[20,21] hexathiohypodiphosphates,^[22] or magnetic layered double hydroxides,^[23] because they can be functionalized with various ligands via versatile reactions. Striking results were recently reported concerning combination of magnetism with chirality,^[24] ferroelectricity,^[11] superconductivity,^[23] or nonlinear optics.^[25]

Most of the preceding layered functional materials are characterized by weak bonds between subnetworks, which may limit synergy between properties. An alternative approach consists in the insertion and grafting of functional organic molecules into magnetic layered transition-metal hydroxides $M_x(\text{OH})_{2x-ny}(\text{X}^{n-})_y$ ($M(\text{II}) = \text{Co}$ or Cu and $\text{X}^- = \text{carboxylate}$, sulfate, or sulfonate anion). The X^{n-} anion located in the interlayer space may be substituted by a large variety of molecules via anionic exchange reaction.^[26–31] Whereas various organic molecules and coordination complexes bearing carboxylic or sulfonic acid anchoring functions have been successfully inserted into these layered simple hydroxides (LSH), to the best of our knowledge, phosphonic acid anchoring groups have never been used in such systems. As for the related compounds layered double hydroxides, $[\text{M}_{1-x}^{2+}\text{M}'_x^{3+}(\text{OH})_2]^{x+}(\text{X}^{n-})_{x/n} \cdot m\text{H}_2\text{O}$ without anchoring of X^- anions onto the layers, only a few works on the intercalation of molecules bearing phosphonic acids have been reported.^[32,33]

Phosphonic acids, due to their coordination properties, are widely employed to prepare crystalline hybrid materials^[34] that are studied for their porosity,^[35,36] ionic conduction,^[37,38] magnetic,^[39,40] or fluorescent^[41,42] properties or for their bactericidal effects.^[43]

Over the recent years, efforts were made on the use of rigid phosphonic acids for the solvothermal one-pot synthesis of hybrid compounds,^[44] with the aim to assess the consequences of this rigidity on the topology of the obtained systems.^[45] The rigidity results from a direct connection of the phosphonic acid on an aromatic^[46] or heteroaromatic ring^[47] acting as a rigid molecular platform. When low symmetrical phosphonic acid compounds like 3-phosphonobenzoic acid (which features an aromatic ring with prochiral faces) are reacted with copper salts in solvothermal conditions non-centrosymmetric crystals are obtained.^[48] Interestingly, non-centrosymmetric crystals can also be produced with diphosphonic acid as organic precursors.^[47] These earliest results motivated the further exploration of diphosphonic acids as precursors of hybrid materials. The choice of the rigid platform is another important parameter. In this respect, fluorene stands as an interesting rigid platform in which the presence of the five-membered ring breaks the symmetry of the compound.^[49,50]

In this paper, we extend the use of fluorene-based compounds proposing novel mono- and diphosphonic acids, with various alkyl chains in position 9 of the fluorene unit ($-\text{H}$, $-\text{CH}_3$ or $-(\text{CH}_2)_7\text{CH}_3$) (**Scheme 1**), to foster, so far unexplored, magnetoelectric phenomena into Cu and Co layered simple hydroxides. We address this challenge discussing in the following the synthesis, characterization, structural modeling, and magnetic and dielectric properties of new layered hybrid compounds, which will be referred to as **ACM**, where **A** is the mono- or diphosphonic acid fluorene and **M** denotes Co or Cu hydroxide layers.

2. Results and Discussion

2.1. Synthesis of the Organic Molecules

The synthesis of the fluorenyl-(di)phosphonic acids **3a–b** (monophosphonic acids) and **6a–c** (diphosphonic acids) (**Scheme 1**) was performed in a two-step sequence that starts

from the commercially available monobromofluorene (2-bromofluorene **1a**), dibromofluorene (2,7-dibromofluorene **4a**) or its 9,9-dimethyl analogue **1b** and **4b** or the 9,9-dioctyl-2,7-dibromofluorene **4c**. A nickel assisted Arbuzov reaction (Tavs's reaction) was selected to achieve the P–C bond as it is adapted to prepare aryl-mono or polyphosphonates.^[51] This reaction requires a careful addition of triethylphosphite on a solution composed of the selected (di)bromofluorenyl derivative **1a-b** (**4a-c**), nickel bromide and mesitylene, heated at 160 °C. After a purification step, the (di)phosphonates **2a-b** (**5a-c**) were isolated in 63% to 83% yields in a multigram scale. Then, the hydrolysis of the diethyl phosphonate functions into phosphonic acid was efficiently achieved by using concentrated HCl water solution (35% in water). The final products **3a-b** (**6a-c**) were isolated as white solids with good yields (>92%) and were fully characterized (see the Experimental Section and the Supporting Information).

2.2. Synthesis and Characterization of the Hybrid Compounds

2.2.1. Synthesis

The synthesis of the hybrid compounds was carried out following a generally used procedure consisting in dissolving an excess of the organic molecule in water at relatively high pH (≈ 8); then an equivalent volume of ethanol is added along with the starting materials $\text{Cu}_2(\text{OH})_3(\text{DS})$ and $\text{Co}_2(\text{OH})_{3.5}(\text{DS}_0)_{0.5}$, respectively (DS⁻ is dodecylsulfate and DS₀⁻ is dodecylsulfonate).^[26–30] Such kind of preintercalation strategy is often used for the functionalization of layered materials, hexathiohypodiphosphates (MPS₃),^[52,53] zirconium phosphate,^[54–56] layered double hydroxides (LDH),^[57] or layered oxides.^[58–60] It consists in prefunctionalizing the starting compound by a molecule which is further removed to allow the insertion of the desired species. In the case of LSH, we have developed the prefunctionalization by dodecylsulfate or dodecylsulfonate, which is very efficient to allow the insertion-grafting of bulky or fragile molecules.^[27,28,30]

In the present case, the attempts to insert-graft directly the fluorenyl-mono or diphosphonic acids into $\text{Cu}_2(\text{OH})_3(\text{OAc})$ or $\text{Co}_2(\text{OH})_{3.2}(\text{OAc})_{0.8}$ were unsuccessful, leading to unreacted compounds, multiphase, badly crystallized compounds, or oxides. The temperatures and durations of the reactions performed with preintercalated compounds $\text{Cu}_2(\text{OH})_3(\text{DS})$ or $\text{Co}_2(\text{OH})_{3.5}(\text{DS}_0)_{0.5}$ were adapted to obtain single-phase materials, while optimizing the crystallinity and avoiding the formation of oxides (Table 1). The successful and complete insertion necessitates the use of an excess of desired molecules, as already observed in the case of carboxylate and sulfonate anchoring functions.^[26,27] In the present case, with phosphonic acid anchoring groups, we used a ratio $R = n_{\text{PO}_3} / n_{\text{startinghydroxide}} = 2$ for monophosphonic acids and copper-based hydroxide (1.4 for cobalt-based hydroxides) and 4 (2.8) for diphosphonic acids. It is worth noticing that for the nonsubstituted fluorenes **3a** and **6a** it is necessary to use twice the amount of molecule, and to use a slightly higher pH. For their insertion into copper hydroxide, it was necessary to limit drastically the reaction time (15 min) to avoid formation of oxides. In addition, it has not

Table 1. Reaction conditions for the synthesis of the hybrid compounds.

	Starting hydroxide	$R^a)$	pH ^{b)}	T	T [h]
3a-cCu	$\text{Cu}_2(\text{OH})_3(\text{DS})$	4	8.8	Reflux (82 °C)	0.25
3b-cCu	$\text{Cu}_2(\text{OH})_3(\text{DS})$	2	8.3	RT	70
3b-cCo	$\text{Co}_2(\text{OH})_{3.5}(\text{DS}_0)_{0.5}$	1.4	8.3	RT	24
6a-cCu	$\text{Cu}_2(\text{OH})_3(\text{DS})$	8	8.8	Reflux (82 °C)	0.25
6b-cCu	$\text{Cu}_2(\text{OH})_3(\text{DS})$	4	8.3	Reflux (82 °C)	1
6b-cCo	$\text{Co}_2(\text{OH})_{3.5}(\text{DS}_0)_{0.5}$	2.8	8.3	Reflux (82 °C)	2
6c-cCu	$\text{Cu}_2(\text{OH})_3(\text{DS})$	4	8.3	70 °C	2
6c-cCo	$\text{Co}_2(\text{OH})_{3.5}(\text{DS}_0)_{0.5}$	2.8	8.3	Reflux (82 °C)	1.5

^{a)} $R = n_{\text{PO}_3} / n_{\text{startinghydroxide}}$; ^{b)} pH is the pH of the starting fluorene phosphonic acid aqueous solution before the addition of ethanol.

been possible to insert **3a** and **6a** into layered cobalt hydroxide, probably because of the acidity of the proton in position 9 of the fluorene motif.

2.2.2. Characterization

The powder X-ray diffraction patterns of the hybrid compounds are presented in Figure 1 along with one of the starting hydroxides. At low angles, the diagrams show the intense 00*l* diffraction peaks, up to at least the fourth harmonic, which clearly underlines the lamellar character of the hybrid compounds and provides the basal spacing (Table 2). No diffraction peak coming from the starting compounds is evidenced, and no sulfur atom is detected in elemental analysis (see the Experimental Section), which indicates the completeness of the exchange reaction. The cobalt compounds exhibit similar features in the high 2θ region (in-plane diffraction lines) with characteristic asymmetrical peaks at $2\theta = 33.46^\circ$ and $2\theta = 59.90^\circ$ which suggests a similar turbostratic disorder.^[27,61]

The abrupt change of the interlamellar spacing for the hybrid compounds with respect to the starting hydroxides $\text{Cu}_2(\text{OH})_3(\text{DS})$ or $\text{Co}_2(\text{OH})_{3.5}(\text{DS}_0)_{0.5}$ is in agreement with the insertion of the fluorene phosphonic acid molecules. Considering the length of the fluorene monophosphonic acids (about 1 nm) and the thickness of the inorganic sheets (about 0.2 nm for the sheets of copper hydroxide,^[62] and 0.7 nm for the triple-deck sheets of cobalt hydroxide,^[63–65]), the interlamellar spacing of the cobalt or copper-based hybrid compounds obtained with fluorene monophosphonic acids is coherent with a double layer arrangement of the molecules, with some possible interpenetration depending on the inclination angle. For the fluorene diphosphonic acids (length of about 1.2 nm), the observed interlamellar spacing obtained for cobalt-based compounds is coherent with a pillaring arrangement of the diphosphonic acids, almost perpendicular to the inorganic layers. Yet, for copper-based compounds the hypothesis of a bigrafting of the molecules onto the inorganic layers would lead to an interlamellar spacing of about 1.4 nm, much smaller than the observed one.

In order to solve this apparent discrepancy and to shed light on the molecular arrangement of fluorene mono- and diphosphonic acids in the interlayer environment for such systems we

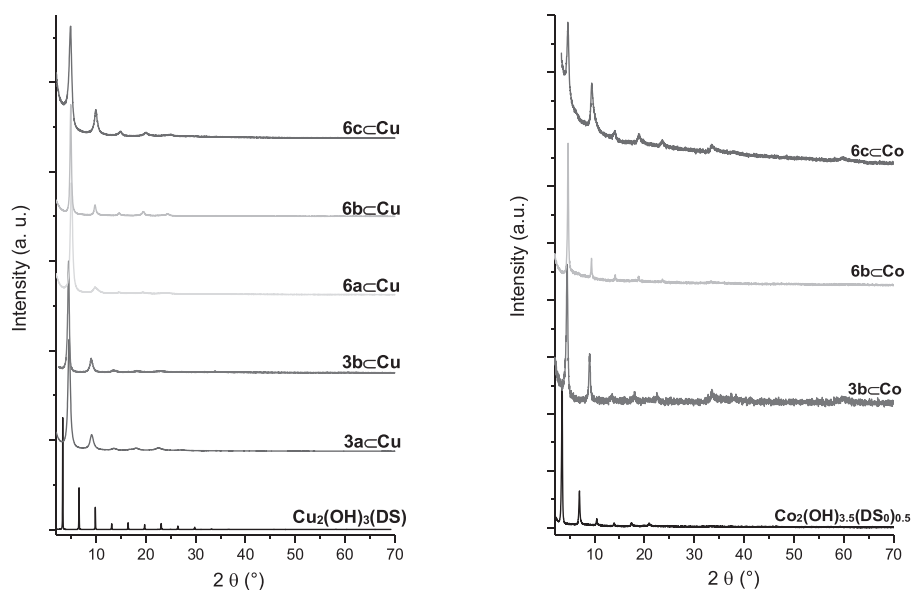


Figure 1. Powder XRD patterns of the Cu-based hybrids (left), and the Co-based hybrids (right).

made use of first-principles molecular dynamics simulations (FPMD) within the density functional theory (DFT) framework to investigate the structure, the chemical bonding, and the related dynamic properties of hybrid systems. This computational tool allowed us to unveil the interlayer chemical arrangements for **3aCu** and **6aCu**, providing support to the picture of a tilted orientation of **3a** in copper hydroxide, a detail elusive to experimental probes. Such a tilted arrangement for **3a** induces a slightly interdigitation of the fluorene moieties linked to opposite copper hydroxide layers and results consistent with the measured interlayer distance (1.9 nm). Instead, for **6aCu** a more complex arrangement is found, with the fluorene diphosphonic acid chemically anchored to the copper hydroxide layer through one phosphonate group (Cu–O_{6a} distance in the range of 0.26–0.32 nm) and the remaining one at a greater interatomic distance (Cu–O_{6a} distance of about 0.55 nm) with respect to the opposite inorganic layer. This arrangement allows for the coordination of a water molecule by the copper atoms, replacing the stabilizing role of the phosphonic acid groups. In Section 2.3, the chemical bonding properties and structural organization involved in the interlayer environments

of **3aCu** and **6aCu** are detailed and discussed, as well as the fundamental role of water molecules and the H-bonding network they promote.

Unfortunately, the precise structure of the inorganic layers for layered cobalt hydroxide is still unknown due to static disorder of the α -Co(OH)₂ inorganic layers.^[66,67] This prevents performing the same kind of approach for the analysis of the interaction between the phosphonic acid groups and the cobalt hydroxide layers. Yet, it is worth underlining that in the case of cobalt-based hybrids functionalized by fluorene diphosphonic acids, the experimental interlamellar distance is compatible with a pillaring arrangement of the molecules, the phosphonic acid moieties being coordinated to tetrahedral cobalt sites.

The Scanning Electron Microscopy (SEM) images of compounds **3bCu** and **6cCo** are shown in Figure S25 (Supporting Information) and are representative of all the hybrid compounds described here. The materials are obtained as thin platelets, in agreement with their lamellar structure.

The insertion rates, determined from elemental analysis (Table 2), are comprised between 0.34 and 0.5 molecule per formula unit in the case of monophosphonic acids and between 0.10 and 0.29 molecule per formula unit in the case of diphosphonic acids. In terms of phosphonic groups per formula unit, the insertion rates are thus very similar between monophosphonic acids and diphosphonic acids. It is nevertheless worth remarking that the insertion rate is significantly smaller for the bulky fluorene **6c**, bearing long lateral alkyl chains, than for fluorenes bearing only –H or –CH₃ groups in position 9. This observation, and the fact that the insertion rates deviate significantly from 1.0 phosphonic group per formula unit for copper-based hybrids and from 0.5 phosphonic group per formula unit for cobalt-based hybrids indicate that the exchange process is likely not topotactic, but rather processes via dissolution–recrystallization.^[68,69]

Table 2. Formula and interlamellar spacing of the hybrid compounds.

	Formula	<i>d</i> [nm]
3aCu	Cu ₂ (OH) _{3.56} (C ₁₃ H ₁₁ O ₃ P) _{0.44} ·2.7H ₂ O	1.96
3bCu	Cu ₂ (OH) _{3.5} (C ₁₅ H ₁₃ O ₃ P) _{0.50} ·2.3H ₂ O	1.93
3bCo	Co ₂ (OH) _{3.66} (C ₁₅ H ₁₃ O ₃ P) _{0.34} ·1.3H ₂ O	1.96
6aCu	Cu ₂ (OH) _{3.54} (C ₁₃ H ₁₀ O ₆ P ₂) _{0.23} ·3.5H ₂ O	1.80
6bCu	Cu ₂ (OH) _{3.6} (C ₁₅ H ₁₂ O ₆ P ₂) _{0.20} ·2.7H ₂ O	1.82
6bCo	Co ₂ (OH) _{3.42} (C ₁₅ H ₁₃ O ₆ P ₂) _{0.29} ·1.7H ₂ O	1.88
6cCu	Cu ₂ (OH) _{3.68} (C ₂₉ H ₄₂ O ₆ P ₂) _{0.16} ·2.5H ₂ O	1.78
6cCo	Co ₂ (OH) _{3.8} (C ₂₉ H ₄₂ O ₆ P ₂) _{0.10} ·2.9H ₂ O	1.88

Infrared spectra of all hybrid compounds exhibit a band at 1600 cm^{-1} ascribed to the P(O)(OH) group^[70] as well as a band around 1220 cm^{-1} corresponding to the P=O band (Figure S26, Supporting Information).^[33,71,72] It is however extremely difficult to assign precisely the other bands in the neighboring region ($900\text{--}1250\text{ cm}^{-1}$) with respect to the phosphonic acid group vibrational modes, and even more difficult to attempt to ascertain the grafting mode of the phosphonates. Such an attribution can be performed relatively easily in the case of carboxylate anchoring functions,^[73,74] and with more difficulties in the case of sulfonate anchoring functions.^[75–78] In the case of phosphonic acids, the attribution of the IR bands is the subject of various contradictory assertions in the literature.^[70–72,79–82] In the present case, it is all the more complicated due to the large number of bands present in this region of the spectra. It is however possible to spot the fingerprint of each molecule in the corresponding hybrid compound with bands such as the ones present at 1604 , 1469 , 1446 , and 1402 cm^{-1} that likely correspond to the C–C rings stretching modes in the fluorene moieties.^[83,84] Other bands present in the $1280\text{--}1000\text{ cm}^{-1}$ region and corresponding to the C–H inplane bending of the fluorenes^[9] cannot be told apart from each other due to the presence of multiple other peaks.

Finally, the UV–vis reflectance spectra of **6cCu** and **6cCo** are presented in Figure S27 of the Supporting Information (after Kubelka–Munk correction), along with the spectra of the starting fluorene. They are representative of the spectra of all hybrid compounds described here. The spectra of the copper hydroxide-based compounds are dominated by the O → Cu charge transfer band (which overlaps with the intense absorption of the fluorene moiety) and the weaker d–d band at 710 nm , responsible for the blue color of the compounds. For the cobalt hydroxide-based compounds, the UV part of the spectra is also dominated by the O → Co charge transfer band and the $\pi \rightarrow \pi^*$ bands of the fluorene moiety. At lower energies, two series of bands can be observed. The bands observed at 1550 , 635 , and 592 nm can be attributed respectively to $^4A_2(F) \rightarrow ^4T_2(F)$, $^4A_2(F) \rightarrow ^4T_1(F)$, and $^4A_2(F) \rightarrow ^4T_1(P)$ transitions of high spin d^7 Co(II) in tetrahedral sites, whereas the bands observed at 1250 and 494 nm can be attributed respectively to $^4T_{1g}(F) \rightarrow ^4T_{2g}(F)$ and $^4T_{1g}(F) \rightarrow ^4T_{1g}(P)$ transitions of high spin d^7 Co(II) in octahedral sites,^[85] in accordance with the proposed structure^[27,66,67,86] and with the magnetic behavior (see below).

Despite all fluorene derivatives used here (**3a**, **3b**, **6a**, **6b**, and **6c**) are luminescent (emission around 385 nm when excited at 340 nm), only hybrids containing the fluorene bearing the longest lateral chains (**6cCu** and **6cCo**) are still luminescent, the fluorene luminescence in the other hybrid compounds being totally quenched. This suggests that the quenching is essentially due to intermolecular interactions between fluorene moieties in the interlamellar spacing, as already observed for oligothiophenes^[86] and oligophenylenevinyls.^[87] For the hybrids containing the bulky fluorene **6c**, the density and arrangement of the inserted molecules is probably more favorable to avoid quenching of the luminescence. Yet the luminescence intensity is quite small, an important part of the incident light being absorbed by the inorganic host. Finally, for **6cCu** the luminescence occurs at the same wavelength as **6c** alone (385 nm), whereas **6cCo** fluoresces at a slightly larger

wavelength (405 nm) which suggests different host–guest interactions (Figure S28, Supporting Information).

2.3. Interlayer Chemical Bonding and the Role of Water

Computer simulations resorting to advanced theoretical methods provide useful information and complement experiments on layered materials, such as LSH, by unveiling the interplay between molecular architecture and electronic properties for this class of hybrid materials. In particular, DFT-based FPMD provides a reliable description of atomic forces, thereby making possible the assessment of the bonding interactions of multicomponent systems. FPMD has come to a full maturity in terms of technical developments and efficiency, being ready to be exploited on composite systems where an accurate description of the chemical bonding is a necessary requirement to shed light on their structure-property correlations.^[26] Herein, we take full advantage of a thoughtful, well-established simulation methodology benchmarked over a wealth of results for copper hydroxide acetate, a prototypical system for the present class of LSH materials.^[88–90] Recently, such methodology has been fostered to disentangle the role of 2D/3D spin-polarization interactions in copper hydroxide acetate.^[91]

This type of dynamical simulations has been used here to identify the local molecular organization of the interlayer environment of **3aCu** and **6aCu** systems. Figure 2a shows a typical stable structure of **3aCu**. For such system, the fluorene monophosphonic acid is found to be chemically anchored to the copper hydroxide layer through the interaction of three Cu atoms and one O atom of the phosphonate group within an equilibrium distance in the range of $0.26\text{--}0.32\text{ nm}$. Several local chemical scenarios have been explored for the phosphonate group, finding the mono-protonated form (fluorene- PO_3H^-) the most stable one. The optimized system, equilibrated at finite temperature for about 5 ps , shows the fluorene moieties homogeneously tilted with respect to the plane of copper hydroxide by an angle of $\approx 66^\circ$, which induces a partial interpenetration of the aromatic parts (Figure 2b).

For **6aCu**, we found the fluorene diphosphonic acids to be stably anchored to the copper hydroxide layer through one phosphonate group, chemically interacting with Cu atoms similarly as for the **3aCu**. However, the second phosphonic group (oppositely attached to the fluorene moiety) remains at a larger distance with respect to the opposite Cu layer at an interatomic distance of 0.55 nm (Figure 2c). Such structure allows a water molecule to fit the space in-between the phosphonate group and the copper layer and to be coordinated by the three Cu atoms with distances of $0.23\text{--}0.27\text{ nm}$. Contrary to **3aCu**, in the case of **6aCu** the fluorene moieties are not homogeneously tilted with respect to the Cu layer and the tilting angle can range from 60° to 75° . This structural difference can be explained by the larger free interlayer volume of **6aCu**, having $\frac{1}{2}$ of the fluorene moieties within the interlayer with respect to **3aCu**. This factor allows **6a** to have a greater mobility within the interlayer environment.

We also investigated the role of water molecules within the interlayer and for both systems we found common observations. To investigate the role of water we have analyzed the H-bonding network in terms of its electronic structure. To

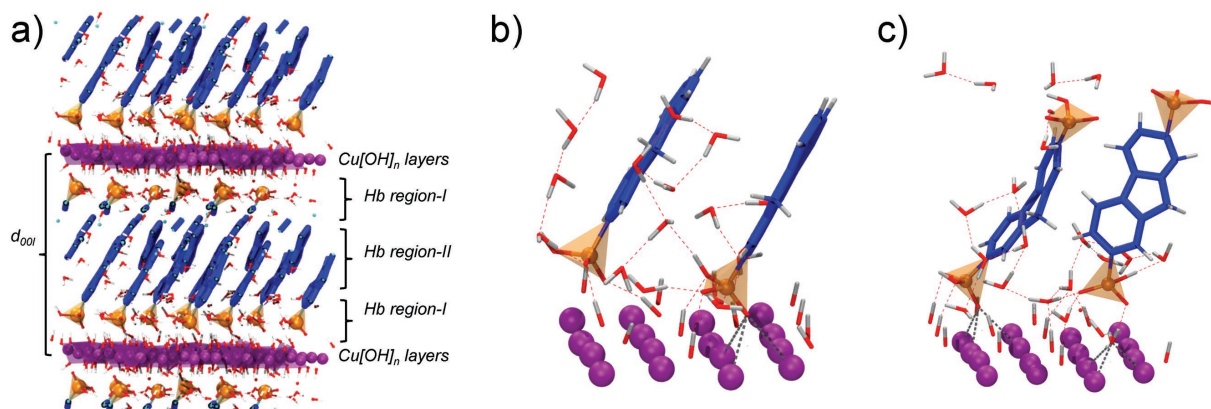


Figure 2. a) Typical structure of **3aCCu** obtained via FPMD simulations (visualized supercell replicated $2 \times 2 \times 2$ along x , y and z for clearness). The interlamellar distance (d_{001}), copper hydroxide layers ($\text{Cu}[\text{OH}]_n$) as well as the regions corresponding to H-bonding type-I and type-II are also indicated. Color legend: Cu atoms, purple; P atoms and polyhedra, orange; C skeleton of fluorene groups, blue; O atoms, red; and H atoms, gray. The local bonding environments surrounding the phosphonate groups ($-\text{PO}_3\text{H}$) for **3aCCu** and **6aCCu** are visualized in (b) and (c), respectively. The interaction between Cu atoms with the O atoms of the $-\text{PO}_3\text{H}$ groups and the O atoms of the water molecules are indicated as gray dashed lines. The H-bonding network is highlighted in red dashed lines.

this aim, maximally localized Wannier functions (WFCs) have been proven to provide a powerful tool to rationalize the electronic structure of water^[92,93] as well complex disordered systems.^[94,95] The center of the charge density associated with

a Wannier orbital can be thought of as representing an electron pair. Each oxygen atom is surrounded by four such centers (see **Figure 3a**). Two are at a longer distance (0.48–0.52 Å) from the oxygen, along the O–H bond axis, and can be interpreted as

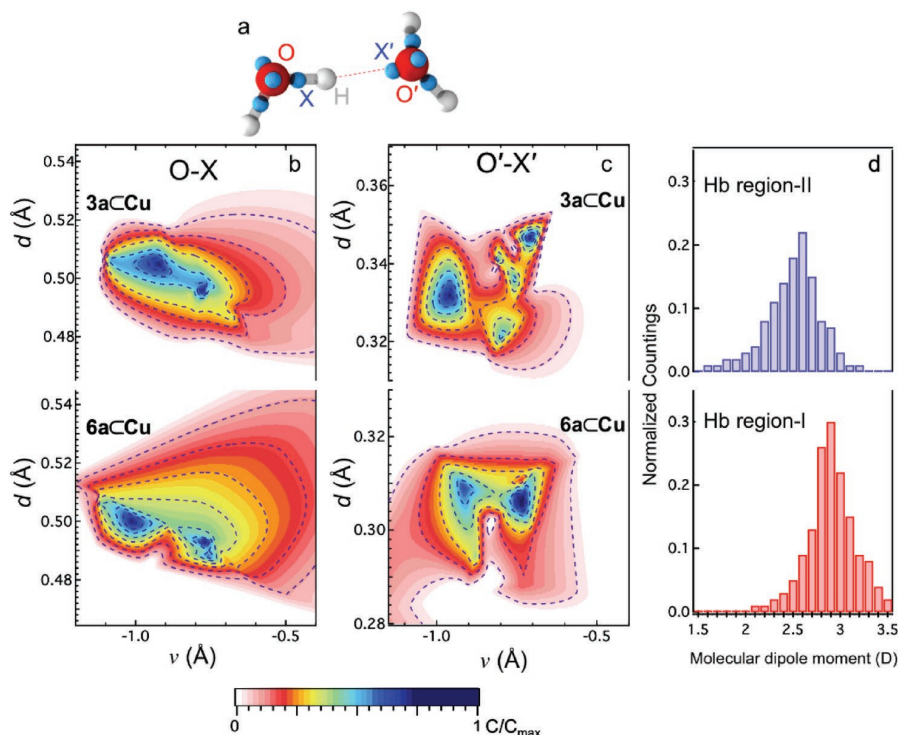


Figure 3. a) Schematic representation of a typical hydrogen bond promoted by two water molecules. The oxygen (O), hydrogen (H), and WFCs (X) are indicated in red, gray, and cyan, respectively. The acceptor oxygen and one of its lone pair WFCs are indicated as O' and X' , respectively. b,c) Joint probability distributions of the proton-transfer coordinate $\nu = d(\text{O}-\text{H}) - d(\text{O}'-\text{H})$ and of the distances of these oxygen atoms (O-X in b) and $\text{O}'-\text{X}'$ in c)) with their corresponding Wannier centers. The upper and lower plots correspond to the data analyzed for **3aCCu** and **6aCCu**, respectively. d) Normalized distributions of the modulus of the molecular dipole of water molecules in the central (Hb region-II in the upper part of 3-d) and the interface (Hb region-I, lower part of 3-d) regions of the interlayer hydrogen bonding network for **3aCCu**.

the σ -bonding pairs of the water molecule, whereas the other two are located at a shorter distance (0.30–0.34 Å) from the O atom and correspond to the lone pairs.

Within the interlayer regions of **3aCu** and **6aCu**, water molecules are found to be interacting with both the hydroxide groups of the copper hydroxide layers as well as the phosphonates groups by promoting an extended network of H-bonds. In these systems, a hydrogen bond involves three atoms: the hydrogen H, the oxygen atom O to which it is covalently bound and the acceptor oxygen O', being one of the neighboring water molecules or of the phosphonate groups. The proton transfer coordinate $\nu = d(\text{O}-\text{H}) - d(\text{O}'-\text{H})$ provides a convenient structural order parameter to characterize the H-bonding network.^[96] Values of $\nu > -1.25$ Å indicate the occurrence of a “well-formed” H-bonding.^[96] Figure 3b,c shows the joint probability distributions of the proton-transfer coordinate and one of the distances of the WFCs to the corresponding oxygen (O and O', respectively). This analysis of the positions of the WFCs as a function of the proton-transfer coordinate ν demonstrates unambiguously that the local fluctuations of the H-bonding are associated with major rearrangements of the electron density. These results show that both **3aCu** and **6aCu** interlayers are characterized by an extended H-bonding network. Both systems show two main peaks in terms of ν (within –1.1 to 0.9 Å) and within ν (–0.8 to –0.7 Å), respectively, for similar d_{OX} ($d_{\text{OX}'}$) distances. These two slightly different H-bonding interactions are ascribed to the H-bonds promoted by water molecules with the oxygen atoms of the phosphonate groups and with other neighboring water molecules (and hydroxide groups coordinating the Cu layers), respectively.

These results show that both **3aCu** and **6aCu** interlayers are characterized by an extended H-bonding network that stabilizes the interlayer arrangement of both fluorene mono- and diphosphonic acids. In fact, in the completely dehydrated systems both **3a** and **6a** were not found stable along our FPMD simulations. Such behaviors can be ascribed to the low interlayer density of the phosphonic acids leaving a large empty interlayer space. Indeed, a test with a higher density of fluorene monophosphonic acid ($\text{C}_{12}(\text{OH})_3(\text{C}_{13}\text{H}_{11}\text{O}_3\text{P}) \cdot 3\text{H}_2\text{O}$) resulted in a stable structure. However, such larger density has not been obtained by synthesis.

Considering the stoichiometries experimentally obtained, we can further split the interlayer environment of **3aCu** and **6aCu** in two different regions: (i) the first region located within 0.6 nm from the Cu atoms plane and the center of the interlayer and (ii) the second region at distances larger than 0.6 nm from the Cu layers. The H-bonds networks within the two different regions are characterized by different properties. Specially, in region-I the H-bonding network is promoted by the involvement of water molecules, hydroxide groups, and phosphonates groups, whereas in region-II the H-bonding is promoted uniquely by the water molecules. This difference can be made more quantitative by analyzing the electric molecular dipole moment of H_2O molecules. Figure 3d shows the water molecular dipole computed employing the analysis of the WFCs. The dipole moment of water molecules within the center of the interlayer (within the fluorene moieties environment) is slightly lower than the dipole of water molecules in the proximity of the copper hydroxide layers and phosphonate

groups (2.6 vs 2.9 D). This is indicative of the fact that the electric field induced by surrounding molecules enhances the dipole moment of the single water molecule.^[92,97]

2.4. Magnetic Properties

The magnetic behaviors of the copper compounds **3aCu**, **3bCu**, **6aCu**, **6bCu**, and **6cCu** are similar (Table 3; Figures S29 and S30, Supporting Information). The inverse of the susceptibility (not shown) varies linearly with the temperature (above 200 K) and can be fitted by the Curie–Weiss law, giving $C = 0.72, 0.94, 0.76, 0.71,$ and 0.95 emu K mol^{–1} for **3aCu**, **3bCu**, **6aCu**, **6bCu**, and **6cCu**, respectively, in the expected range for two Cu(II) ions.^[27,98] The χT products decrease regularly when decreasing the temperature, indicating an overall antiferromagnetic behavior, without any magnetic ordering down to the lowest accessible temperature (1.8 K).

The magnetic behaviors of the cobalt compounds **3bCo**, **6bCo**, and **6cCo** are also similar to each other (Table 3, Figure S31; Figures 4 and 5). The Curie constants range between 5.95 and 6.09 emu K mol^{–1}, in agreement with a mixture of tetrahedral and octahedral high spin Co(II) ions, with $C_{\text{tetra}} = 2.2$ to 2.8 emu K mol^{–1} for one Co(II) ion, and $C_{\text{octa}} = 2.8$ to 3.4 emu K mol^{–1}.^[98,99] Upon cooling, the χT products of the three cobalt hybrids go through a minimum around 80 K. This small decrease is well understood on the basis of spin–orbit coupling and/or antiferromagnetic interactions between the Co(II) moments (Figure S31, Supporting Information).^[100] Below this minimum, the observed steep increase of the χT products can be related to the occurrence of long-range ferrimagnetic order, supported by the occurrence of an out of phase signal in the imaginary part of the AC susceptibility, χ'' (Figure 4). The ordering temperatures were determined from the maximum of the real part of the AC susceptibility ($f = 95$ Hz, $\mu_0 H_{\text{ac}} = 0.3$ mT) (Figure 4 and Table 3).

The fact that the ordering temperatures hardly change when changing the inserted fluorene (the interlamellar distance remaining almost unchanged) is in agreement with an interlayer coupling via dipolar interactions.^[30,101] Finally, it should be noted that the AC peaks are relatively large, or, for **6cCo** show two peaks at 17.8 and 11.0 K and a small shoulder around 6.3 K for

Table 3. Summary of the magnetic characteristics of the hybrid compounds.

	C [emu K mol ^{–1}]	θ [K]	T_C [K]	M_{7T} at 1.8 K [μ_B]	$\mu_0 H_C$ at 1.8 K [T]
3aCu	0.72	–12.9	–	0.39	–
3bCu	0.94	–31.7	–	0.49	–
6aCu	0.76	–30.1	–	0.30	–
6bCu	0.71	–3.3	–	0.50 ^{a)}	–
6cCu	0.95	–19.9	–	0.57	–
3bCo	6.09	–21.7	11.8	2.43	0.20
6bCo	5.95	–22.4	11.9	2.43	0.33
6cCo	6.02	–13.6	17.8/11.0/6.3	2.92	0.22

^{a)} $\mu_0 H = 5$ T.

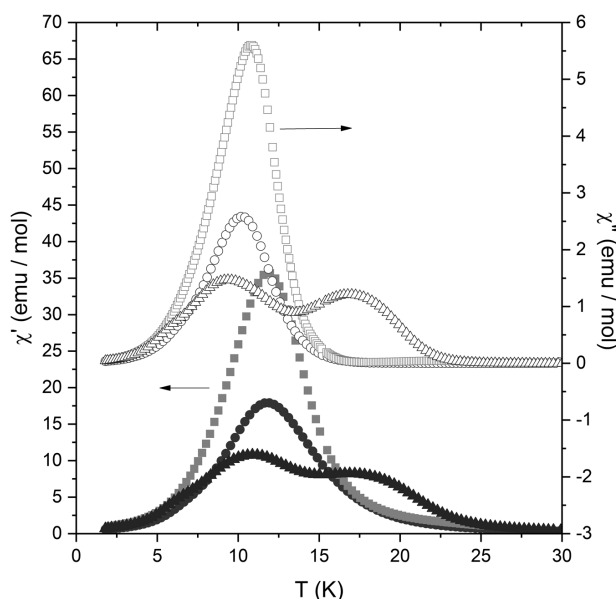


Figure 4. In phase (χ') (full symbols) and out of phase (χ'') (open symbols) magnetic susceptibilities measured in an AC field of 0.3 mT at 95 Hz for **3bCoCo** (circles), **6bCoCo** (squares), and **6cCoCo** (triangles). For the sake of clarity, only 20% and 25% of the experimental points are displayed for χ' and χ'' respectively.

χ' (17.0, 9.3, and 5.8 K for χ''). This suggests a distribution of ordering temperatures, not unusual for layered magnets.^[86,102,103]

The ferromagnetic-type ordering of cobalt-based hybrids is further confirmed by the magnetization versus field curves at low temperature (Figure 5), which shows the presence of hysteresis loops, with coercive fields ranging from 0.20 T for **3bCoCo** to 0.33 T for **6bCoCo** (Table 3).

The low value of the moments at high field ($M(7\text{ T}) = 2.4$, 2.4, and 2.9 μ_B for **3bCoCo**, **6bCoCo**, and **6cCoCo**, respectively, at 1.8 K) compared to the expected value for a total alignment of the moments (4–6 μ_B for two Co(II)) confirms a ferrimagnetic ordering, resulting from an unbalanced antiparallel alignment of the moments lead by tetrahedral and octahedral cobalt ions.^[100] Indeed, considering for octahedral $S = 3/2$, $L = 1$ Co(II) a magnetization saturation value $M_S = 2.87 \mu_B$ found in $\text{Co}_2(\text{OH})_3(\text{NO}_3)$, which contains exclusively octahedral sites,^[104] and for a tetrahedral $S = 3/2$ Co(II) ion $M_S = 3 \mu_B$, we can calculate a site ratio Oh:Td $\approx 76:24$ for **3bCoCo** and **6bCoCo** and 68:32 for **6cCoCo**, in good agreement with what was found from the chemical formulations.

2.5. Magnetoelectric Behavior

2.5.1. 6cCoCo

The magnetocapacitance was measured for two different geometries, i.e., $E_{ac} // B$ and $E_{ac} \perp B$. The most complete data set has been recorded for $E_{ac} // B$. Figure S32 (Supporting Information) shows the variation of C_p as function of temperature in the low temperature range and measured at different isotherms when warming the sample. Within our experimental resolution, no dielectric

anomaly was detected that would correspond to the temperature of long-range magnetic ordering. However, as shown in **Figure 6**, we do observe a positive magnetocapacitance ($ME = C_p(B)/C_p(0) - 1 = 0.16\%$ at 10 K and 7 T). Its variation as function of temperature is reported in **Figure 7**. Quite interestingly, this magnetocapacitance effect persists up to relatively large temperature, around 110 K. Two other characteristic temperatures can be observed, 50 K where the magnitude of the magnetoelectric effect changes by a factor of 2.6 and 17 K where a smaller but quite clear anomaly can be seen. By comparing with the thermal variation of magnetic susceptibility, some similarities can be noted. The highest temperature corresponds to the departure from a pure Curie–Weiss susceptibility (Figure S33, Supporting Information) and to the appearance of short-range magnetic correlations, which apparently trigger the magnetoelectric effect in this compound. The two other characteristic temperatures correspond respectively to the change of dimensionality of the magnetic behavior of the hybrid compound, from 2D to 3D short-range magnetic correlations (around 50 K) (unfortunately, due to the existence of a distribution of ordering temperatures (Figure 4), it was not possible to perform an accurate dimensionality analysis of the magnetic behavior, but the expected transition from 2D to 3D behavior is indeed expected in this temperature range^[105,106]), and to the occurrence of long-range magnetic ordering (around 17 K). Finally, it is worth noting that the magnetic threshold field necessary for the magnetoelectric effect to appear becomes zero below the magnetic ordering temperature of the compound (**Figure 8**)

For the second geometry, $E_{ac} \perp B$, we still observe a magnetocapacitance effect, but with opposite sign and a lower magnitude. This is clearly seen in Figure S34 (Supporting Information) where the magnetoelectric effects measured at the same temperature for both geometries are shown. This anisotropic effect is likely related to a preferred local orientation of microcrystalline platelets that compose the pellets. This will be studied in more detail in future, and may give important information on the intrinsic mechanism of spin–charge coupling in this sample.

2.5.2. 6bCoCo

For this sample, the magnetoelectric properties were only measured for $E_{ac} \perp B$ configuration. We measure a small negative magnetocapacitance with the same order of magnitude than for **6cCoCo**, which goes to zero at a temperature close to 60 K (Figures S35 and S36, Supporting Information). Here, a dielectric anomaly is evidenced at the temperature where the magnetocapacitance appears. This anomaly is observed both when sweeping the temperature and after a long time stabilization at different isotherms (Figure S37, Supporting Information). Then, a clear magnetoelectric coupling can be inferred, emerging at a temperature $T \lesssim 60$ K. Again, this temperature is much larger than the temperature where the magnetic long-range ordering takes place ($T_N \approx 11$ K) and rather corresponds to the temperature where short-range magnetic correlations occur.

It is worth noting that the emergence of magnetoelectricity in a paramagnetic state has been only rarely reported. A first example was the piezoelectric paramagnet $\text{NiSO}_4 \cdot 6\text{H}_2\text{O}$ where a small magnetoelectric effect was reported and principally

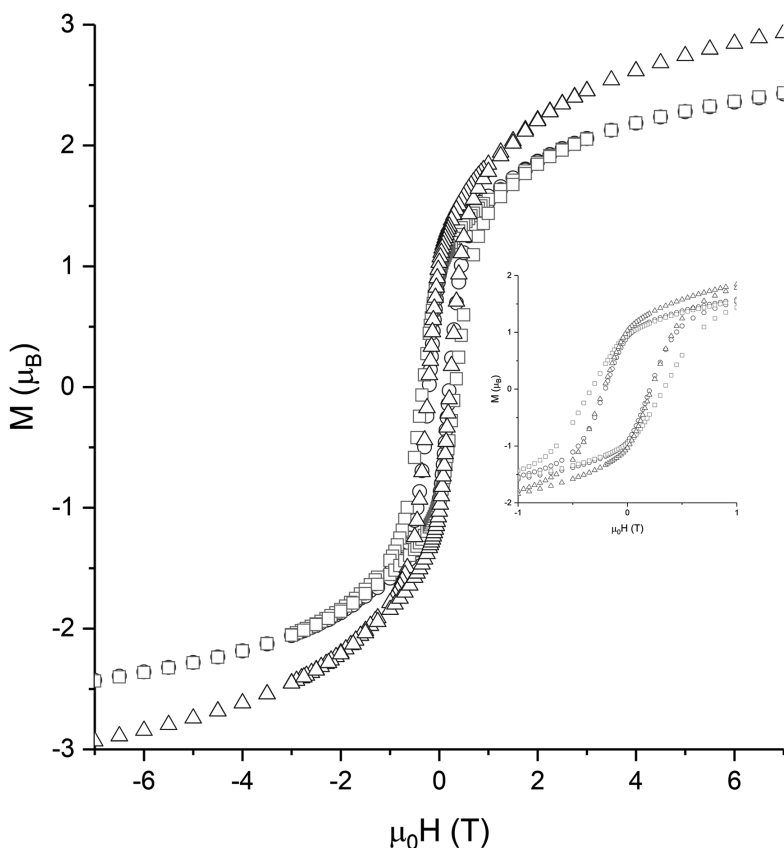


Figure 5. Magnetization versus field at 1.8 K for **3bcCo** (circles), **6bcCo** (squares), and **6ccCo** (triangles).

attributed to crystal field splitting.^[107] More recently, a nonlinear magnetoelectric effect was shown to survive in the paramagnetic regime in CsCuCl_3 .^[108] The coincidence of magnetoelectric effect starting precisely at the temperature where short-range magnetic correlation can be deduced from the Curie–Weiss susceptibility is all the more scarce. To the best of our knowledge, it has only been reported for the metal–organic framework $[(\text{CH}_3)_2\text{NH}_2]\text{Mn}(\text{HCOO})_3$.^[109] In general, such a change in absence of long-range magnetic ordering implies a local spin–lattice interaction where elastic energy plays a significant role. This indicates that a magnetoelastic-driven interaction is likely the driving force of the measured magnetoelectric effects.

3. Conclusion

In the present work, we demonstrated that mono- and diphosphonic acids bearing fluorene motif can be effectively grafted into copper- and cobalt-based hydroxides to create novel hybrid layered simple hydroxides. We addressed the detailed assessment of the internal structure and bonding nature for both classes of transition metals via a thorough set of characterization techniques.

For the copper-based LSH class, for which more elusive experimental findings are found, we employed first-principles

molecular dynamics simulations to disentangle the interlayer arrangement of both mono- and diphosphonic acids as well as the stabilizing role of the H-bonding network promoted within the surrounding of the phosphonate groups. In particular, taking advantage of the Wannier centers analysis we elucidated the complex interplay between the electric field induced by local electron density fluctuations and the interlayer inhomogeneous H-bonding network.

For the cobalt-based class in addition to quantify its ferromagnetic behavior, with ordering temperatures around 15 K, we reveal a clear magnetoelectric effect: application of a magnetic field to the material significantly modifies its capacitance. This effect appears above a threshold magnetic field, which is null below the magnetic ordering temperature, and it persists in the paramagnetic regime, which is very rare.

These findings pave a novel way to fill the critical need for a deeper understanding of the influence of the organic and inorganic subcomponent interactions for innovative magnetoelectric hybrid compounds with potential ferroelectric properties.

4. Experimental Section

General: All organic compounds were fully characterized by ^1H (500.13, 400.133, or 300.135 MHz) and ^{13}C (125.773 or 75.480 MHz) and ^{31}P (162 or 121.5 MHz) NMR spectroscopy (Bruker AC 300, Avance DRX 400, and Avance DRX 500 spectrometers). Coupling constants J were given in hertz. The following abbreviations were used: s for singlet, d for doublet, t for triplet, q for quadruplet, qt for quintuplet, sx for sextuplet, m for multiplet, and dt for doublet of triplets. The electrospray ionization (ESI) mass spectra were recorded with a Shimadzu LCMS-2020 instrument with samples in MeOH or in CH_3CN . The IR spectra of the organic compounds were recorded with a Nicolet Nexus FTIR spectrometer working in the transmittance mode in the $\tilde{\nu} = 200 - 4000 \text{ cm}^{-1}$ range. Powder X-ray diffraction (XRD) patterns were collected with a Bruker D8 diffractometer ($\text{Cu K}\alpha_1 = 0.1540598 \text{ nm}$) equipped with a LynxEye detector discriminating in energy. FTIR spectra of the hybrid compounds were collected in Attenuated Total Reflectance mode (ATR) on a SpectrumII spectrometer (PerkinElmer). UV/vis/NIR studies were performed with a Perkin-Elmer Lambda 950 spectrometer (spectra recorded in the reflection mode, using a 150 mm integrating sphere, with a resolution of 2 nm and a mean sampling rate of 200 nm min^{-1}). Elemental analyses for Co, Cu, C, H, and P were performed by the Analytische Laboratorien, Lindlar, Germany. The SEM images were obtained with a JEOL 6700F microscope equipped with a field emission gun, operating at 3 kV in the Secondary Electron Imaging mode (SEI). The magnetic studies were carried out with a SQUID magnetometer (Quantum Design MPMS3) covering the temperature and field ranges 2–300 K and $\pm 7 \text{ T}$, respectively. Magnetization versus field measurements at room temperature confirms the absence of ferromagnetic impurities. Data were corrected for the sample holder, and diamagnetism was estimated from Pascal constants.

The sample for magnetodielectric measurements were prepared as pellets of typical thicknesses 200 and 140 μm for **6bcCo** and **6ccCo**, respectively. Electrodes of surface $S \approx 0.5 \text{ cm}^2$ were painted using

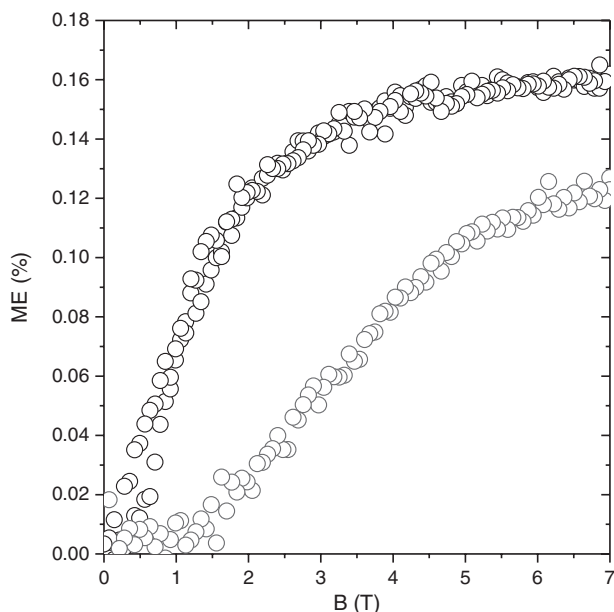


Figure 6. Relative magnetocapacitance of **6cCo** as a function of the magnetic field at 10 K (open black circles) and 35 K (open gray circles) (measured with field ramping up and down, $B//E_{ac}$).

silver paste Dupont 4929, which has advantages of large viscosity and of possible curing at room temperature. Special care was taken and preliminary tests were made to ensure that the paste does not diffuse and/or react with the materials. The complex impedance was measured as function of temperature and magnetic field in a Physical Property Measurement System (PPMS) (Quantum Design) using the 4282 Agilent LCR meter and a home made sample holder. The typical AC voltage was 300 mV (linear response) and the frequency was swept from 20 Hz to 800 KHz to analyze the complex impedance. Within

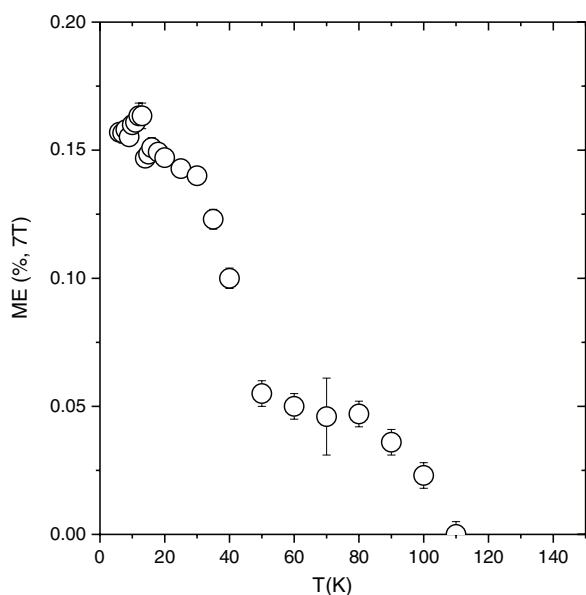


Figure 7. Relative magnetocapacitance of **6cCo** at 7 T ($B//E_{ac}$) as a function of temperature.

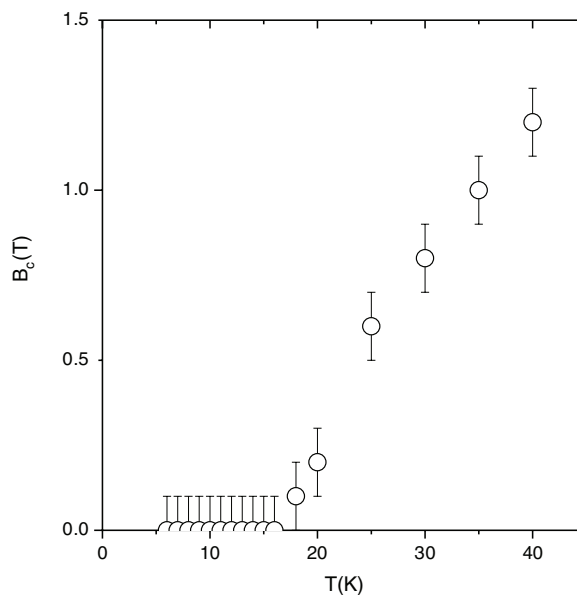


Figure 8. Magnetolectric threshold field for **6cCo** as a function of temperature ($B//E_{ac}$).

resolution, the frequency response was that of a simple parallel $R-C$ circuit in the quasi-insulating limit ($1/R \rightarrow 0$, phase angle $\theta \approx -\pi/2$). The capacitance was then deduced and its variation versus field and temperature extracted.

The detailed synthesis of the organic molecules and of the hybrid compounds is described in the Supporting Information.

Theoretical Methods: FPMD simulations were conducted in the framework of the DFT^[110] to elucidate structural and bonding properties of the targeted hybrid systems. In particular, the modeling framework of references was exploited^[88–91] to carry out FPMD simulations of two representative hybrid systems: **3aCu** and **6aCu**. The Car–Parrinello approach^[111] and the Becke–Lee–Yang–Parr functional^[112,113] were adopted to describe the exchange–correlation interactions. Valence electrons were treated explicitly, whereas norm-conserving pseudopotentials of the Troullier and Martins type^[114] accounted for the core–valence interaction. For Cu semicore states were included in the plane-wave (PW) expansion.^[114] The wave functions were expanded on a PW basis set with an energy cutoff of 90 Ry and the Brillouin zone sampling of the supercell was limited to the Γ point. Van der Waals interactions, fundamental in the systems, were included according to the empirical formulation of Grimme.^[115] Yet, since no adjustable parameter was required, its inclusion did not affect at any stage the Kohn–Sham equations, thus preserving the first-principles character of the electronic structure calculations.

The **3aCu** and **6aCu** hybrid systems were initially built starting from the optimized structure of the copper hydroxide acetate^[91] and setting the c lattice parameter to experimental values. The initial acetate groups were substituted with the **3a** and **6a** molecules in accordance with the structural formula experimentally determined and by introducing the correct amount of water molecules. In doing so, two models of 252 and 206 total atoms were obtained for the **3aCu** and **6aCu** systems ($\text{Cu}_2(\text{OH})_{3.5}(\text{C}_{13}\text{H}_{11}\text{O}_3\text{P})_{0.5} \cdot 3\text{H}_2\text{O}$ and $\text{Cu}_2(\text{OH})_{3.5}(\text{C}_{13}\text{H}_{10}\text{O}_6\text{P}_2)_{0.25} \cdot 3\text{H}_2\text{O}$), respectively. Energy optimization via a conjugate gradient algorithm was used to fully relax the system. Then, a damped FPMD was performed to quench the surface model at $T = 0$ K. To allow the local environments of the phosphonic acids to rearrange at finite temperature, FPMD simulations were performed to gradually increase the temperature up to 50 K constraining the Cu atoms and the hydroxide groups to their equilibrium position during the initial 1 ps.

The ionic temperature was controlled by Nosé–Hoover thermostat in all the canonical simulations. The hydroxide groups were then released by all constraints and the systems were equilibrated for additional 5 ps. The analysis of the interlayer structures was performed averaging the data computed along these last 5 ps. The electronic properties of the water molecules and interlayers were analyzed by averaging over 25 uncorrelated configurations taken along the trajectory of 5 ps and computing the maximally localized Wannier functions.

Following the former works,^[88–91] to explore ground states differing in the local spin densities, different initial random values were assigned to the fictitious electronic degree of freedom. Specifically, several initial randomizations per magnetization state were performed. Further details about the procedure employed can be found in ref. [91]. This procedure allows for the exploration of multiple-minima landscapes resulting from the existence of different spin configurations for a given value of the imposed multiplicity. Each multiplicity corresponds to a total value S for the projection along the z -direction of the total spin. In this way, one obtains different local intralayer spin configurations and associated values Σ ($\Sigma = 0$ or $\Sigma \neq 0$) corresponding to an identical multiplicity for the whole system. Herein, both limiting cases of total spin multiplicity $2S + 1$ corresponding to values equal to 1 ($S = 0$) and 33 ($S = 16$) were considered. The structure and the electronic properties discussed in this paper refer to the ground antiferromagnetic states ($S = 0$) for both **3aCu** and **6aCu** systems as being the most energetically stable states in the simulated conditions.

Supporting Information

Supporting Information is available from the Wiley Online Library or from the author.

Acknowledgements

Q.E. and Z.C. contributed equally to this work. The authors thank the CNRS, the Université de Strasbourg, the ENSICAEN, the Agence Nationale de la Recherche (Contract No. ANR-14-CE07-0004-01 (HYMN)), and the Labex NIE (ANR-11-LABX-0058_NIE within the Investissement d'Avenir program ANR-10-IDEX-0002-02) for financial support. The authors acknowledge computational facilities provided by HPC Equipe@MESO and the Idex program "Investissements d'Avenir" (2015–2016) of the University of Strasbourg.

Conflict of Interest

The authors declare no conflict of interest.

Keywords

first-principles molecular dynamics, fluorene phosphonic acids, layered simple hydroxides, magnetoelectric effects

Received: June 29, 2017

Revised: July 27, 2017

Published online:

[1] R. Ramesh, *Nature* **2009**, 461, 1218.

[2] G. Rogez, N. Viart, M. Drillon, *Angew. Chem. Int. Ed.* **2010**, 49, 1921.

[3] H.-R. Wen, Y.-Z. Tang, C.-M. Liu, J.-L. Chen, C.-L. Yu, *Inorg. Chem.* **2009**, 48, 10177.

- [4] S. Ohkoshi, H. Tokoro, T. Matsuda, H. Takahashi, H. Irie, K. Hashimoto, *Angew. Chem. Int. Ed.* **2007**, 46, 3238.
- [5] P. Jain, V. Ramachandran, R. J. Clark, H. D. Zhou, B. H. Toby, N. S. Dalal, H. W. Kroto, A. K. Cheetham, *J. Am. Chem. Soc.* **2009**, 131, 13625.
- [6] P. Jain, N. S. Dalal, B. H. Toby, H. W. Kroto, A. K. Cheetham, *J. Am. Chem. Soc.* **2008**, 130, 10450.
- [7] X.-Y. Wang, L. Gan, S.-W. Zhang, S. Gao, *Inorg. Chem.* **2004**, 43, 4615.
- [8] X.-Y. Wang, Z.-M. Wang, S. Gao, *Chem. Commun.* **2008**, 281.
- [9] M. Mączka, A. Gaĝor, M. Ptak, W. Paraguassu, T. A. da Silva, A. Sieradzki, A. Pikul, *Chem. Mater.* **2017**, 29, 2264.
- [10] A. Stroppa, P. Jain, P. Barone, M. Marsman, J. M. Perez-Mato, A. K. Cheetham, H. W. Kroto, S. Picozzi, *Angew. Chem. Int. Ed.* **2011**, 50, 5847.
- [11] E. Pardo, C. Train, H. Liu, L.-M. Chamoreau, B. Dkhil, K. Boubekeur, F. Lloret, K. Nakatani, H. Tokoro, S. Ohkoshi, M. Verdaguier, *Angew. Chem. Int. Ed.* **2012**, 51, 8356.
- [12] D. B. Mitzi, in *Progress in Inorganic Chemistry* (Ed: K. D. Karlin), John Wiley & Sons, Inc., Weinheim, Germany **1999**, pp. 1–121.
- [13] D. B. Mitzi, in *Functional Hybrid Materials* (Eds: P.-G. Romero, C. Sanchez), Wiley-VCH, Weinheim, Germany **2004**, pp. 347–390.
- [14] D. B. Mitzi, *J. Chem. Soc. Dalton Trans.* **2001**, 1.
- [15] A. O. Polyakov, A. H. Arkenbout, J. Baas, G. R. Blake, A. Meetsma, A. Caretta, P. H. M. van Loosdrecht, T. T. M. Palstra, *Chem. Mater.* **2012**, 24, 133.
- [16] B. Kundys, A. Lappas, M. Viret, V. Kapustianyk, V. Rudyk, S. Semak, C. Simon, I. Bakaimi, *Phys. Rev. B* **2010**, 81, 224434.
- [17] R. Ramesh, N. A. Spaldin, *Nat. Mater.* **2007**, 6, 21.
- [18] M. Trassin, J. D. Clarkson, S. R. Bowden, J. Liu, J. T. Heron, R. J. Paull, E. Arenholz, D. T. Pierce, J. Unguris, *Phys. Rev. B* **2013**, 87, 134426.
- [19] V. Gorige, R. Kati, D. H. Yoon, P. S. A. Kumar, *J. Phys. Appl. Phys.* **2016**, 49, 405001.
- [20] M. Clemente-León, E. Coronado, C. Martí-Gastaldo, F. M. Romero, *Chem. Soc. Rev.* **2011**, 40, 473.
- [21] C. Train, M. Gruselle, M. Verdaguier, *Chem. Soc. Rev.* **2011**, 40, 3297.
- [22] R. Clément, A. Léaustic, in *Magnetism: Molecules to Materials II. Molecule-Based Materials* (Eds: J. S. Miller, M. Drillon), Wiley-VCH, Weinheim, Germany **2001**.
- [23] E. Coronado, C. Martí-Gastaldo, E. Navarro-Moratalla, A. Ribera, S. J. Blundell, P. J. Baker, *Nat. Chem.* **2010**, 2, 1031.
- [24] C. Train, R. Gheorghe, V. Krstic, L.-M. Chamoreau, N. S. Ovanesyan, G. L. J. A. Rikken, M. Gruselle, M. Verdaguier, *Nat. Mater.* **2008**, 7, 729.
- [25] P. G. Lacroix, I. Malfant, S. Bénard, P. Yu, E. Rivière, K. Nakatani, *Chem. Mater.* **2001**, 13, 441.
- [26] G. Rogez, C. Massobrio, P. Rabu, M. Drillon, *Chem. Soc. Rev.* **2011**, 40, 1031.
- [27] É. Delahaye, S. Eyele-Mezui, J.-F. Bardeau, C. Leuvrey, L. Mager, P. Rabu, G. Rogez, *J. Mater. Chem.* **2009**, 19, 6106.
- [28] É. Delahaye, S. Eyele-Mezui, M. Diop, C. Leuvrey, P. Rabu, G. Rogez, *Dalton Trans.* **2010**, 39, 10577.
- [29] S. Eyele-Mezui, E. Delahaye, G. Rogez, P. Rabu, *Eur. J. Inorg. Chem.* **2012**, 2012, 5225.
- [30] R. Bourzami, S. Eyele-Mezui, E. Delahaye, M. Drillon, P. Rabu, N. Parizel, S. Choua, P. Turek, G. Rogez, *Inorg. Chem.* **2014**, 53, 1184.
- [31] O. Palamarciuc, E. Delahaye, P. Rabu, G. Rogez, *New J. Chem.* **2014**, 38, 2016.
- [32] V. Prévot, C. Forano, J. P. Besse, *Appl. Clay Sci.* **2001**, 18, 3.
- [33] H. Nijs, A. Clearfield, E. F. Vansant, *Microporous Mesoporous Mater.* **1998**, 23, 97.

- [34] *Metal Phosphonate Chemistry: From Synthesis to Applications* (Eds: A. Clearfield, K. D. Demadis), RSC Publishing, Cambridge, UK **2011**.
- [35] B. S. Gelfand, R. P. S. Huynh, R. K. Mah, G. K. H. Shimizu, *Angew. Chem., Int. Ed.* **2016**, *55*, 14614.
- [36] M. Taddei, F. Costantino, F. Marmottini, A. Comotti, P. Sozzani, R. Vivani, *Chem. Commun.* **2014**, *50*, 14831.
- [37] S. Pili, S. P. Argent, C. G. Morris, P. Rought, V. García-Sakai, I. P. Silverwood, T. L. Easun, M. Li, M. R. Warren, C. A. Murray, C. C. Tang, S. Yang, M. Schröder, *J. Am. Chem. Soc.* **2016**, *138*, 6352.
- [38] J. M. Taylor, R. K. Mah, I. L. Moudrakovski, C. I. Ratcliffe, R. Vaidhyathanan, G. K. H. Shimizu, *J. Am. Chem. Soc.* **2010**, *132*, 14055.
- [39] S. Chausson, J.-M. Rueff, M. B. Lepetit, O. Perez, R. Retoux, C. Simon, L. Le Pluart, P.-A. Jaffrès, *Eur. J. Inorg. Chem.* **2012**, *2012*, 2193.
- [40] C. Bloyet, M. Roger, J.-M. Rueff, B. Raveau, J.-F. Lohier, G. Rogez, P.-A. Jaffrès, *Eur. J. Inorg. Chem.* **2016**, *2016*, 4643.
- [41] J.-M. Rueff, N. Barrier, S. Boudin, V. Dorcet, V. Caignaert, P. Boullay, G. B. Hix, P.-A. Jaffrès, *Dalton Trans.* **2009**, 10614.
- [42] B. Mutelet, S. Boudin, O. Pérez, J. M. Rueff, C. Labbé, P. A. Jaffrès, *Dalton Trans.* **2014**, *44*, 1186.
- [43] M. Berchel, T. L. Gall, C. Denis, S. L. Hir, F. Quentel, C. Elléouet, T. Montier, J.-M. Rueff, J.-Y. Salaün, J.-P. Haelters, G. B. Hix, P. Lehn, P.-A. Jaffrès, *New J. Chem.* **2011**, *35*, 1000.
- [44] J.-M. Rueff, V. Caignaert, S. Chausson, A. Leclaire, C. Simon, O. Perez, L. Le Pluart, P.-A. Jaffrès, *Eur. J. Inorg. Chem.* **2008**, *2008*, 4117.
- [45] J.-M. Rueff, O. Perez, V. Caignaert, G. Hix, M. Berchel, F. Quentel, P.-A. Jaffrès, *Inorg. Chem.* **2015**, *54*, 2152.
- [46] J.-M. Rueff, O. Perez, A. Leclaire, H. Couthon-Gourvès, P.-A. Jaffrès, *Eur. J. Inorg. Chem.* **2009**, *2009*, 4870.
- [47] J.-M. Rueff, O. Perez, A. Pautrat, N. Barrier, G. B. Hix, S. Hernot, H. Couthon-Gourvès, P.-A. Jaffrès, *Inorg. Chem.* **2012**, *51*, 10251.
- [48] J.-M. Rueff, V. Caignaert, A. Leclaire, C. Simon, J.-P. Haelters, P.-A. Jaffrès, *CrystEngComm* **2009**, *11*, 556.
- [49] N. Hugot, M. Roger, J.-M. Rueff, J. Cardin, O. Perez, V. Caignaert, B. Raveau, G. Rogez, P.-A. Jaffrès, *Eur. J. Inorg. Chem.* **2016**, *2016*, 266.
- [50] C. Bloyet, J.-M. Rueff, V. Caignaert, J.-F. Lohier, J. Cardin, P.-A. Jaffrès, B. Raveau, *Z. Anorg. Allg. Chem.* **2017**, *643*, 250.
- [51] G. B. Hix, V. Caignaert, J.-M. Rueff, L. Le Pluart, J. E. Warren, P.-A. Jaffrès, *Cryst. Growth Des.* **2007**, *7*, 208.
- [52] T. Coradin, R. Clément, P. G. Lacroix, K. Nakatani, *Chem. Mater.* **1996**, *8*, 2153.
- [53] P. G. Lacroix, R. Clément, K. Nakatani, J. Zyss, I. Ledoux, *Science* **1994**, *263*, 658.
- [54] J. L. Colon, C. Y. Yang, A. Clearfield, C. R. Martin, *J. Phys. Chem.* **1988**, *92*, 5777.
- [55] J. L. Colon, C. Y. Yang, A. Clearfield, C. R. Martin, *J. Phys. Chem.* **1990**, *94*, 874.
- [56] Q. Wang, D. Yu, Y. Wang, J. Sun, J. Shen, *Langmuir* **2008**, *24*, 11684.
- [57] G. Huang, S. Ma, X. Zhao, X. Yang, K. Ooi, *Chem. Commun.* **2009**, 331.
- [58] A. Shimada, Y. Yoneyama, S. Tahara, P. H. Mutin, Y. Sugahara, *Chem. Mater.* **2009**, *21*, 4155.
- [59] S. Akbarian-Tefaghi, E. T. Veiga, G. Amand, J. B. Wiley, *Inorg. Chem.* **2016**, *55*, 1604.
- [60] Y. Wang, E. Delahaye, C. Leuvrey, F. Leroux, P. Rabu, G. Rogez, *Inorg. Chem.* **2016**, *55*, 4039.
- [61] V. Laget, S. Rouba, P. Rabu, C. Hornick, M. Drillon, *J. Magn. Magn. Mater.* **1996**, *154*, L7.
- [62] S. Švarcová, M. Klementová, P. Bezdička, W. Łasocha, M. Dušek, D. Hradil, *Cryst. Res. Technol.* **2011**, *46*, 1051.
- [63] V. Laget, *Ph.D. Thesis*, Université Louis Pasteur, Strasbourg, France **1998**.
- [64] M. Louër, D. Louër, D. Grandjean, *Acta Crystallogr. Sect. B* **1973**, *29*, 1696.
- [65] M. Kurmoo, *Philos. Trans. R. Soc. London, Ser. A* **1999**, *357*, 3041.
- [66] J. R. Neilson, J. A. Kurzman, R. Seshadri, D. E. Morse, *Chem. - Eur. J.* **2010**, *16*, 9998.
- [67] J. R. Neilson, B. Schwenzer, R. Seshadri, D. E. Morse, *Inorg. Chem.* **2009**, *48*, 11017.
- [68] V. Laget, C. Hornick, P. Rabu, M. Drillon, *J. Mater. Chem.* **1999**, *9*, 169.
- [69] S. Si, A. Taubert, A. Manton, G. Rogez, P. Rabu, *Chem. Sci.* **2012**, *3*, 1945.
- [70] K. D. Demadis, S. D. Katarachia, *Phosphorus Sulfur Silicon Relat. Elem.* **2004**, *179*, 627.
- [71] G. Guerrero, P. H. Mutin, A. Vioux, *Chem. Mater.* **2001**, *13*, 4367.
- [72] C. S. Kim, R. J. Lad, C. P. Tripp, *Sens. Actuators, B* **2001**, *76*, 442.
- [73] C. Dendrinou-Samara, G. Tsotsou, L. V. Ekateriniadou, A. H. Kortsaris, C. P. Raptopoulou, A. Terzis, D. A. Kyriakidis, D. P. Kessissoglou, *J. Inorg. Biochem.* **1998**, *71*, 171.
- [74] V. Robert, G. Lemerrier, *J. Am. Chem. Soc.* **2006**, *128*, 1183.
- [75] S.-H. Park, C. H. Lee, C. E. Lee, H.-C. Ri, S. Y. Shim, *Mater. Res. Bull.* **2002**, *37*, 1773.
- [76] S.-H. Park, C. E. Lee, *J. Phys. Chem. B* **2005**, *109*, 1118.
- [77] C. Bauer, P. Jacques, A. Kalt, *Chem. Phys. Lett.* **1999**, *307*, 397.
- [78] M. Kurmoo, P. Day, A. Derory, C. Estournès, R. Poinsot, M. J. Stead, C. J. Kepert, *J. Solid State Chem.* **1999**, *145*, 452.
- [79] G. R. Williams, D. O'Hare, *Solid State Sci.* **2006**, *8*, 971.
- [80] R. Luschinetz, G. Seifert, E. Jaehne, H.-J. P. Adler, *Macromol. Symp.* **2007**, *254*, 248.
- [81] S. Yagyu, M. Yoshitake, N. Tsud, T. Chikyow, *Appl. Surf. Sci.* **2009**, *256*, 1140.
- [82] S. Shori, P. J. Pellechia, H.-C. zur Loye, H. J. Ploehn, *J. Colloid Interface Sci.* **2015**, *437*, 97.
- [83] A. Bree, R. Zwarich, *J. Chem. Phys.* **1969**, *51*, 912.
- [84] S. Y. Lee, B. H. Boo, *J. Phys. Chem.* **1996**, *100*, 8782.
- [85] A. B. P. Lever, *Inorganic Electronic Spectroscopy*, 2nd ed., Elsevier, Amsterdam, The Netherlands **1984**.
- [86] A. Demessence, G. Rogez, P. Rabu, *Chem. Mater.* **2006**, *18*, 3005.
- [87] A. Demessence, A. Yassar, G. Rogez, L. Miozzo, S. D. Brion, P. Rabu, *J. Mater. Chem.* **2010**, *20*, 9401.
- [88] F. Yang, M. Boero, C. Massobrio, *J. Phys. Chem. C* **2010**, *114*, 20213.
- [89] F. Yang, M. Boero, P. Rabu, C. Massobrio, *C. R. Chim.* **2012**, *15*, 202.
- [90] F. Yang, C. Massobrio, M. Boero, *J. Phys. Chem. C* **2014**, *118*, 18700.
- [91] Z. Chaker, G. Ori, M. Boero, C. Massobrio, *Beilstein J. Nanotechnol.* **2017**, *8*, 857.
- [92] M. Boero, K. Terakura, T. Ikeshoji, C. C. Liew, M. Parrinello, *Phys. Rev. Lett.* **2000**, *85*, 3245.
- [93] M. Sharma, R. Resta, R. Car, *Phys. Rev. Lett.* **2005**, *95*, 187401.
- [94] G. Ori, C. Massobrio, A. Bouzid, M. Boero, B. Coasne, *Phys. Rev. B* **2014**, *90*, 045423.
- [95] A. Bouzid, S. Le Roux, G. Ori, M. Boero, C. Massobrio, *J. Chem. Phys.* **2015**, *143*, 034504.
- [96] M. Ceriotti, J. Cuny, M. Parrinello, D. E. Manolopoulos, *Proc. Natl. Acad. Sci. USA* **2013**, *110*, 15591.
- [97] R. Scipioni, D. A. Schmidt, M. Boero, *J. Chem. Phys.* **2009**, *130*, 024502.
- [98] R. L. Carlin, *Magnetochemistry*, Springer-Verlag, Berlin **1986**.

- [99] O. Kahn, *Molecular Magnetism*, VCH Publishers, New York **1993**.
- [100] J. R. Neilson, D. E. Morse, B. C. Melot, D. P. Shoemaker, J. A. Kurzman, R. Seshadri, *Phys. Rev. B* **2011**, *83*, 094418.
- [101] M. Drillon, P. Panissod, *J. Magn. Magn. Mater.* **1998**, *188*, 93.
- [102] F. Bellouard, M. Clemente-León, E. Coronado, J. R. Galán-Mascarós, C. J. Gómez-García, F. Romero, K. R. Dunbar, *Eur. J. Inorg. Chem.* **2002**, *2002*, 1603.
- [103] E. Coronado, J. R. Galán-Mascarós, C. J. Gómez-García, V. Laukhin, *Nature* **2000**, *408*, 447.
- [104] P. Rabu, S. Angelov, P. Legoll, M. Belaiche, M. Drillon, *Inorg. Chem.* **1993**, *32*, 2463.
- [105] J. Souletie, P. Rabu, M. Drillon, in *Magnetism: Molecules to Materials V* (Eds: J. S. Miller, M. Drillon), Wiley-VCH, Weinheim, Germany **2005**.
- [106] P. Rabu, J. M. Rueff, Z. L. Huang, S. Angelov, J. Souletie, M. Drillon, *Polyhedron* **2001**, *20*, 1677.
- [107] S. L. Hou, N. Bloembergen, *Phys. Rev.* **1965**, *138*, A1218.
- [108] A. I. Kharkovskiy, Y. V. Shaldin, V. I. Nizhankovskii, *J. Appl. Phys.* **2016**, *119*, 014101.
- [109] W. Wang, L.-Q. Yan, J.-Z. Cong, Y.-L. Zhao, F. Wang, S.-P. Shen, T. Zou, D. Zhang, S.-G. Wang, X.-F. Han, Y. Sun, *Sci. Rep.* **2013**, *3*, srep02024.
- [110] W. Kohn, L. J. Sham, *Phys. Rev.* **1965**, *140*, A1133.
- [111] R. Car, M. Parrinello, *Phys. Rev. Lett.* **1985**, *55*, 2471.
- [112] A. D. Becke, *Phys. Rev. A* **1988**, *38*, 3098.
- [113] C. Lee, W. Yang, R. G. Parr, *Phys. Rev. B* **1988**, *37*, 785.
- [114] N. Troullier, J. L. Martins, *Phys. Rev. B* **1991**, *43*, 1993.
- [115] S. Grimme, *J. Comput. Chem.* **2006**, *27*, 1787.

Appendix IV : Experimental Protocols

Synthesis of compounds made in chapter I

$\text{Cu}_2(\text{OH})_3\text{OAc}$ « classical »

Copper (II) acetate (3.992g, 20 mmol) is dissolved in 100 mL of water, the solution is then heated at 70°C under argon a solution of 1.2g (30 mmol) of NaOH solubilized in 150 mL of water is then added drop-wise during 30 minutes under constant bubbling. At the end of the addition, the blue solid is then washed with water and ethanol and dried under vacuum.

$\text{Cu}_2(\text{OH})_3\text{OAc}$ « one pot »

Copper (II) acetate (3.992g, 20 mmol) is dissolved in a mixture of 90 mL water and 10 mL ethanol, the mixture is then heated for 72h at 60°C without stirring. The obtained blue/green crystals are filtered and washed with water and ethanol. Yield : 5-10%

$\text{Cu}_2(\text{OH})_3(\text{DS})$ « classical »

Sodium dodecylsulfate (3.908g, 14.6 mmol) is dissolved in a mixture of 90 mL water and 60 mL ethanol with 15 minutes of argon bubbling. $\text{Cu}_2(\text{OH})_3\text{OAc}$ (520 mg, 2 mmol) is then added to the solution. This dispersion is maintained under argon and thermostated at 30°C for 72h. The blue powder is then washed with water and ethanol and dried under vacuum.

$\text{Cu}_2(\text{OH})_3(\text{DS})$ « one pot »

Sodium dodecylsulfate (1.332g, 5 mmol) is dissolved in a mixture of 70 mL water and 30 mL ethanol. Copper (II) acetate (1.999g, 10 mmol) is then added to the solution. The mixture is then heated to 60°C for 72h. The blue crystals are washed with water and ethanol then dried under vacuum. Yield : 40%

$\text{Cu}_3(\text{C}_{12}\text{H}_{25}\text{SO}_4)_2(\text{CH}_3\text{COO})_2(\text{OH})_2(\text{H}_2\text{O})_2$

Copper (II) acetate is added to 0.5 equivalent of a solution (0.05M) of sodium dodecylsulfate in mixture of 70 mL of water and 30 mL of ethanol and stirred vigorously during 1h at room temperature. The mixture is then allowed to evaporate without stirring for 3 days where needles form within a few days. Yield : 30%

Synthesis of compounds made in chapter II

$\text{Co}_2(\text{OH})_{3.2}(\text{OAc})_{0.8}$ or compound (1)

Cobalt acetate (4.98g, 20 mmol) was dissolved in 200 mL of distilled water. The obtained solution is then argon bubbled for 30 minutes and heated at 70°C. In this solution is then added drop-wise an NaOH solution (0.6g, 15mmol) in a mixture of 180 mL of water and 120 mL of ethanol during one hour while keeping the bubbling. After the addition, the heating, stirring and bubbling is maintained for 15 minutes. The round bottom flask is then allowed to cool for 15 minutes in the oil bath and with an additional 15 minutes in air. The blue suspension is then filtered and washed with water and ethanol. Yield : 30%

$\text{Co}_2(\text{OH})_{3.5}(\text{DSO})_{0.5}$

Sodium dodecylsulfonate (1.634g, 6 mmol) is dissolved in a mixture of 90 mL water and 60 mL ethanol and put under argon bubbling for 15 minutes. The $\text{Co}_2(\text{OH})_{3.2}(\text{OAc})_{0.8}$ (491 mg, 2 mmol) is added to the mixture. After 30 minutes of ultrasonication, the mixture is thermostated at 40 °C for 72 hours in an argon atmosphere. The green powder is filtered and washed with water then ethanol. Yield : 93%

$\text{Co}_2(\text{OH})_{3.35}(\text{4-NH}_2\text{-BzAc})_{0.65}$ or compound (2)

4-Aminobenzoic acid (4-NH₂-BzAc) (822 mg, 6 mmol) was dissolved in water (160 mL) and the pH was adjusted to 8 using NaOH (0.2 mol L⁻¹). At this stage, $\text{Co}_2(\text{OH})_{3.2}(\text{OAc})_{0.8}$ (496 mg, 2 mmol) was added along with 40 mL of ethanol. The mixture was stirred under argon at room temperature for 48 h. The dark green powder was collected by filtration, washed with water and ethanol, and dried under vacuum. $\text{Co}_2(\text{OH})_{3.35}(\text{4-NH}_2\text{-BzAc})_{0.65} \cdot 2.4 \text{ H}_2\text{O}$: $\text{Co}_2\text{C}_{4.55}\text{H}_{7.25}\text{N}_{0.65}\text{O}_{4.65} \cdot 2.4 \text{ H}_2\text{O}$ (M = 306.55 g/mol) found (%): Co, 37.92; C, 17.47; H, 3.29; N, 2.62; calcd: Co, 38.45; C, 17.83; H, 3.96; N, 2.97. Yield: 85%

$\text{Co}_2(\text{OH})_{3.57}(\text{AcBz-NQCH-C}_5\text{H}_{11})_{0.43}$ or compound (3)

Compound (2) (153 mg, 0.5 mmol), hexanal (150 mg, 1.5 mmol) and 20 mL of absolute ethanol were introduced in a 30 mL sealed microwave vessel. The mixture was placed under microwave irradiation (30 W) for 10 min. The dark green powder was collected by filtration, washed with ethanol and dried under vacuum. Yield: 80%. Anal. for $\text{Co}_2(\text{OH})_{3.57}(\text{AcBz-NQCH-C}_5\text{H}_{11})_{0.43} \cdot 2.3 \text{ H}_2\text{O}$: $\text{Co}_2\text{C}_{5.59}\text{H}_{10.45}\text{N}_{0.43}\text{O}_{4.43} \cdot 2.3 \text{ H}_2\text{O}$ (M = 313.87 g/mol) found (%): Co, 37.29; C, 21.32; H, 3.83; N, 1.95; calcd: Co, 37.55; C, 21.39; H, 4.83; N, 1.92. Yield : 80%

Synthesis of compounds made in chapter III

(P-Fluo-C)₂Cu

P-Fluo-C (91 mg, 0.33 mmol) was dissolved in 12 mL of water by adding 0.2M NaOH until reaching pH=8.3. Then 12 mL of ethanol was added in the solution along with $\text{Cu}_2(\text{OH})_3(\text{DS})$ (70 mg, 0.15 mmol). The suspension was stirred under argon during 70 h at room temperature. The light blue solid was then filtered, washed with water and ethanol then dried under vacuum. Analysis calculated for $\text{Cu}_2(\text{OH})_{3.5}(\text{C}_{15}\text{H}_{13}\text{O}_3\text{P})_{0.5} \cdot 2.3\text{H}_2\text{O}$, $\text{Cu}_2\text{C}_{7.5}\text{H}_{14.6}\text{O}_{7.3}\text{P}_{0.5}$ (M=364.2 g/mol): Cu : 34.91; C : 24.74; H : 4.18; P : 4.26. Found : Cu : 34.64; C : 24.72; H : 4.03; P : 3.82. Yield : 50%

(P-Fluo-C)₂Co

P-Fluo-C (91 mg, 0.33 mmol) was dissolved in 12 mL of water by adding 0.2M NaOH until a pH=8.3 was reached. Then 12 mL of ethanol was added in the solution along with $\text{Co}_2(\text{OH})_3(\text{DSO})$ (70 mg, 0.16 mmol). The suspension was stirred under argon during 24h at room temperature. The green-bluish solid was then filtered, washed with water and ethanol then dried under vacuum. Analysis calculated for $\text{Co}_2(\text{OH})_{3.66}(\text{C}_{15}\text{H}_{13}\text{O}_3\text{P})_{0.34} \cdot 1.3\text{H}_2\text{O}$, $\text{Co}_2\text{C}_{5.1}\text{H}_{10.7}\text{O}_{6.0}\text{P}_{0.34}$ (M=296.0 g/mol): Co : 39.82; C : 20.69; H : 3.75; P : 3.56. Found : Co : 39.53; C : 21.01; H : 3.63; P : 3.73. Yield : 90%

P₂-Fluo-C₈Cu

P₂-Fluo-C₈ (180 mg, 0.33 mmol) was dissolved in 12 mL of water by adding 0.2M NaOH until a pH=8.3 was reached. Then 12 mL of ethanol was added in the solution along with $\text{Cu}_2(\text{OH})_3(\text{DS})$ (76 mg, 0.16 mmol). The suspension was stirred under argon at 70°C during 2h. The light blue solid was then filtered, washed with water and ethanol then dried under vacuum. $\text{Cu}_2(\text{OH})_{3.68}(\text{C}_{29}\text{H}_{42}\text{O}_6\text{P}_2)_{0.16} \cdot 2.5\text{H}_2\text{O}$, $\text{Cu}_2\text{C}_{4.64}\text{H}_{15.4}\text{O}_{7.14}\text{P}_{0.32}$ (M=321.4 g/mol): Cu : 39.54; C : 17.34; H : 4.83; P : 3.09. Found : Cu : 39.11; C : 17.32; H : 3.86; P : 3.94. Yield : 70%

P₂-Fluo-C₈Co

P₂-Fluo-C₈ (181 mg, 0.30 mmol) was dissolved in 12 mL of water by adding 0.2M NaOH until a pH=8.3 was reached. Then 12 mL of ethanol was added in the solution along with $\text{Co}_2(\text{OH})_3(\text{DSO})$ (70 mg, 0.16 mmol). The suspension was stirred under argon and refluxed for 1h30. The green solid was then filtered, washed with water and ethanol then dried under vacuum. Analysis calculated for $\text{Co}_2(\text{OH})_{3.8}(\text{C}_{29}\text{H}_{42}\text{O}_6\text{P}_2)_{0.1} \cdot 2.9\text{H}_2\text{O}$, $\text{Co}_2\text{C}_{2.9}\text{H}_{13.8}\text{O}_{7.3}\text{P}_{0.2}$ (M=288.9 g/mol): Co : 40.79; C : 12.06; H : 4.81; P : 2.15. Found : Co : 40.35; C : 12.13; H : 3.58; P : 2.67. Yield : 90%

P₂-Fluo-C₂Cu

P₂-Fluo-C (118 mg, 0.33 mmol) was dissolved in 12 mL of water by adding 0.2M NaOH until a pH=8.3 was reached. Then 12 mL of ethanol was added in the solution along with Cu₂(OH)₃(DS) (77 mg, 0.16 mmol). The suspension was stirred under argon and refluxed for 1 hour. The light blue solid was then filtered, washed with water and ethanol then dried under vacuum. Analysis calculated for Cu₂(OH)_{3.6}(C₁₅H₁₂O₆P₂)_{0.2}·2.7H₂O, Cu₂C₃H_{11.4}O_{9.3}P_{0.4} (M=307.0 g/mol): Cu : 41.4; C : 11.74; H : 3.74; P : 4.04. Found : Cu : 40.8; C : 12; H : 3.17; P : 3.23.
Yield : 80%

P₂-Fluo-C₂Co

P₂-Fluo-C (118 mg, 0.33 mmol) was dissolved in 12 mL of water by adding 0.2M NaOH until a pH=8.3 was reached. Then 12 mL of ethanol was added in the solution along with Co₂(OH)₃(DSO) (70 mg, 0.16 mmol). The suspension was stirred under argon and refluxed for 2 hours. The green solid was then filtered, washed with water and ethanol then dried under vacuum. Analysis calculated for Co₂(OH)_{3.42}(C₁₅H₁₃O₆P₂)_{0.29}·1.7H₂O, Co₂C_{4.35}H_{10.59}O_{6.86}P_{0.58} (M=308.2 g/mol): Co : 38.24; C : 16.95; H : 3.37; P : 5.83. Found : Co : 38.01; C : 17.47; H : 3.53; P : 4.65.
Yield : 70%

P-Fluo-H₂Cu

P-Fluo-H (163 mg, 0.66 mmol) was dissolved in 12mL of water by adding 0.2M NaOH until a pH=8.8 was reached. Then 12 mL of ethanol was added in the solution along with Cu₂(OH)₃(DS) (77 mg, 0.16 mmol). The suspension was stirred under argon and refluxed for 15 minutes. The light blue solid was then filtered, washed with water and ethanol then dried under vacuum. Analysis calculated for Cu₂(OH)_{3.56}(C₁₃H₁₁O₃P)_{0.44}·2.7H₂O, Cu₂C_{5.72}H_{13.8}O_{7.58}P_{0.44} (M=344.6 g/mol): Cu : 36.88; C : 19.94; H : 4.04; P : 3.95. Found : Cu : 36.8; C : 20.15; H : 3.63; P : 3.79.
Yield : 90%

P₂-Fluo-H₂Cu

P₂-Fluo-H (215 mg, 0.66 mmol) was dissolved in 12 mL of water by adding 0.2M NaOH until a pH=8.8 was reached. Then 12 mL of ethanol was added in the solution along with Cu₂(OH)₃(DS) (77 mg, 0.16 mmol). The suspension was stirred under argon and refluxed for 15 minutes. The light blue solid was then filtered, washed with water and ethanol then dried under vacuum. Analysis calculated for Cu₂(OH)_{3.54}(C₁₃H₁₀O₆P₂)_{0.23}·3.5H₂O, Cu₂C_{2.99}H_{12.84}O_{8.42}P_{0.46} (M=323.5 g/mol): Cu : 39.29; C : 11.1; H : 4; P : 4.41. Found : Cu : 38.99; C : 11.18; H : 3.03; P : 4.19.
Yield : 90%

P₂-Fluo-C₄Co

Fluoren-C₄-P₂ (143 mg, 0.33 mmol) was dissolved in 12 mL of water by adding NaOH until a pH=8.5 was reached. Then 12 mL of ethanol was added in the solution along with Co₂(OH)_{3.5}(DSO)_{0.5} (70 mg, 0.16 mmol). The suspension was stirred under argon and refluxed for 2h30. The green solid was then filtered, washed with water and ethanol then dried under vacuum. Analysis calculated for Co₂(OH)_{3.64}(C₂₁H₂₆O₆P₂)_{0.18}·1.5H₂O, Co₂C_{3.78}H_{11.32}O_{6.22}P_{0.36} (M=285.3 g/mol): Co : 41.31; C : 15.91; H : 4.00; P : 3.91. Found : Co : 40.8; C : 15.74; H : 4.24; P : 3.36. Yield : Close to 100%

Synthesis of compounds made in chapter IV

P-Bz-F₂Cu

P-Bz-F (64.2 mg, 0.33 mmol) was dissolved in 12 mL of water by adding NaOH until reaching pH=8.8. Then 12 mL of ethanol was added in the solution along with Cu₂(OH)₃(DS) (76 mg, 0.16 mmol). The suspension was stirred under argon during 3 h at 70°C. The light grayish-blue powder was then filtered, washed with water and ethanol then dried under vacuum. Analysis calculated for

$\text{Cu}_2(\text{OH})_{3.7}(\text{C}_6\text{H}_5\text{FO}_3\text{P})_{0.25}(\text{DS})_{0.05}\cdot 1\text{H}_2\text{O}$, $\text{Cu}_2\text{C}_{2.1}\text{H}_{8.2}\text{O}_{5.654}\text{P}_{0.25}\text{F}_{0.25}$ (M=265.1 g/mol): Cu : 47.95; C : 9.52; H : 2.76; P : 2.92; F : 1.79 . Found : Cu : 48.80; C : 9.71; H : 3.12; P : 2.80; F : 1.88. Yield : 95%

P-Bz-ClCu

P-Bz-Cl (64.2 mg, 0.33 mmol) was dissolved in 12 mL of water by adding NaOH until reaching pH=8.8. Then 12 mL of ethanol was added in the solution along with $\text{Cu}_2(\text{OH})_3(\text{DS})$ (76 mg, 0.16 mmol). The suspension was stirred under argon during 3 h at 70°C. The light grayish-blue powder was then filtered, washed with water and ethanol then dried under vacuum. Analysis calculated for $\text{Cu}_2(\text{OH})_{3.63}(\text{C}_6\text{H}_5\text{ClO}_3\text{P})_{0.37}\cdot 1.1\text{H}_2\text{O}$, $\text{Cu}_2\text{C}_{2.22}\text{H}_{14.6}\text{O}_{5.84}\text{P}_{0.37}\text{Cl}_{0.37}$ (M=279.5 g/mol): Cu : 45.47; C : 9.54; H : 2.77; P : 4.10; Cl : .3.69 Found : Cu : 45.70; C : 9.41; H : 3.12; P : 3.76; Cl : 4.35. Yield : 80%

P-Bz-BrCu

P-Bz-Br (78.2 mg, 0.33 mmol) was dissolved in 12 mL of water by adding NaOH until reaching pH=8.8. Then 12 mL of ethanol was added in the solution along with $\text{Cu}_2(\text{OH})_3(\text{DS})$ (76 mg, 0.16 mmol). The suspension was stirred under argon during 3 h at 70°C. The light grayish-blue powder was then filtered, washed with water and ethanol then dried under vacuum. Analysis calculated for $\text{Cu}_2(\text{OH})_{3.63}(\text{C}_6\text{H}_5\text{BrO}_3\text{P})_{0.32}(\text{DS})_{0.05}\cdot 1.6\text{H}_2\text{O}$, $\text{Cu}_2\text{C}_{2.52}\text{H}_{9.68}\text{O}_{6.39}\text{P}_{0.32}\text{Br}_{0.32}$ (M=306.4 g/mol): Cu : 41.47; C : 9.88; H : 3.18; P : 3.23; Br : 8.34. Found : Cu : 42.30; C : 10.37; H : 2.83; P : 2.86; Br : 8.75. Yield : 96%

P-Bz-ICu

P-Bz-I (77.2 mg, 0.33 mmol) was dissolved in 12 mL of water by adding NaOH until reaching pH=8.9. Then 12 mL of ethanol was added in the solution along with $\text{Cu}_2(\text{OH})_3(\text{DS})$ (76 mg, 0.16 mmol). The suspension was stirred under argon during 3 h at 70°C. The light grayish-blue powder was then filtered, washed with water and ethanol then dried under vacuum. Analysis calculated for $\text{Cu}_2(\text{OH})_{3.61}(\text{C}_6\text{H}_5\text{IO}_3\text{P})_{0.39}\cdot 1.5\text{H}_2\text{O}$, $\text{Cu}_2\text{C}_{2.34}\text{H}_{8.56}\text{O}_{4.78}\text{P}_{0.39}\text{I}_{0.39}$ (M=325.9 g/mol): Cu : 39.0; C : 8.62; H : 2.65; P : 3.71; I : 15.19. Found : Cu : 37.8; C : 10.3; H : 2.73; P : 2.58; I : 10.68. Yield : Close to 100%

P-Bz-OC₄NcCu

P-Bz-OC₄N (84.0 mg, 0.35 mmol) was dissolved in 12 mL of water by adding NaOH until reaching pH=8.6. Then 12 mL of ethanol was added in the solution along with $\text{Cu}_2(\text{OH})_3(\text{DS})$ (76 mg, 0.16 mmol). The suspension was stirred under argon during 1h30 at 90°C. The light grayish-blue powder was then filtered, washed with water and ethanol then dried under vacuum. Analysis calculated for $\text{Cu}_2(\text{OH})_{3.67}(\text{C}_{10}\text{H}_{11}\text{NO}_4\text{P})_{0.33}\cdot 1.5\text{H}_2\text{O}$, $\text{Cu}_2\text{C}_{3.3}\text{H}_{10.36}\text{O}_{6.49}\text{P}_{0.33}\text{N}_{0.33}$ (M=295.8 g/mol): Cu : 42.97; C : 13.40; H : 3.51; P : 3.46; N : 1.56. Found : Cu : 42.9; C : 13.26; H : 3.32; P : 2.09; N : 1.04. Yield : 96%

P-Bz-FcCo

P-Bz-F (64.2 mg, 0.33 mmol) was dissolved in 12 mL of water by adding NaOH until reaching pH=8.8. Then 12 mL of ethanol was added in the solution along with $\text{Cu}_2(\text{OH})_3(\text{DS})$ (76 mg, 0.16 mmol). The suspension was stirred under argon during 3 h at 70°C. The green powder was then filtered, washed with water and ethanol then dried under vacuum. Analysis calculated for $\text{Co}_2(\text{OH})_{3.63}(\text{C}_6\text{H}_5\text{O}_3\text{PF})_{0.37}\cdot 1\text{H}_2\text{O}$, $\text{Co}_2\text{C}_{2.22}\text{H}_{7.48}\text{O}_{5.74}\text{P}_{0.37}\text{F}_{0.37}$ (M=262.4 g/mol): Co : 47.95; C : 9.52; H : 2.76; P : 2.92; F : 1.79 . Found : Co : 48.80; C : 9.71; H : 3.12; P : 2.80; F : 1.88. Yield : 70%

P-Bz-Cl₂Co

P-Bz-Cl (64.3 mg, 0.33 mmol) was dissolved in 12 mL of water by adding NaOH until reaching pH=8.3. Then 12 mL of ethanol was added in the solution along with Co₂(OH)_{3.5}(DSo)_{0.5} (70 mg, 0.16 mmol). The suspension was stirred under argon during 2 h at 90°C. The green powder was then filtered, washed with water and ethanol then dried under vacuum. Analysis calculated for Cu₂(OH)_{3.63}(C₆H₅ClO₃P)_{0.37}·1.1H₂O, Cu₂C_{2.22}H_{14.6}O_{5.84}P_{0.37} (M=X g/mol): Co : x; C : x; H : x; P : x; Cl : .x Found : Co : x; C : x; H : x; P : x; Cl : x. Yield : X%45.9mg

P-Bz-Br₂Co

P-Bz-Br (79.5 mg, 0.33 mmol) was dissolved in 12 mL of water by adding NaOH until reaching pH=8.6. Then 12 mL of ethanol was added in the solution along with Co₂(OH)_{3.5}(DSo)_{0.5} (70 mg, 0.16 mmol). The suspension was stirred under argon during 1 h at 90°C. The green powder was then filtered, washed with water and ethanol then dried under vacuum. Analysis calculated for Co₂(OH)_{3.71}(C₆H₅O₃PBr)_{0.29}, Co₂C_{1.74}H_{5.16}O_{4.58}P_{0.29}Br_{0.29} (M=249.4 g/mol): Co : 47.3; C : 8.38; H : 2.09; P : 3.60; Br : 9.29. Found : Co : 47.7; C : 8.65; H : 2.95; P : 2.92; Br : 7.69. Yield : Close to 100%48.5mg

P-Bz-I₂Co

P-Bz-I (77.2 mg, 0.27 mmol) was dissolved in 12 mL of water by adding NaOH until reaching pH=8.6. Then 12 mL of ethanol was added in the solution along with Co₂(OH)_{3.5}(DSo)_{0.5} (70 mg, 0.16 mmol). The suspension was stirred under argon during 1 h at 90°C. The green powder was then filtered, washed with water and ethanol then dried under vacuum. Analysis calculated for Co₂(OH)_{3.65}(C₆H₅O₃PI)_{0.35}·0.7H₂O, Co₂C_{2.1}H_{6.8}O_{5.4}P_{0.35}I_{0.35} (M=291.6 g/mol): Co : 40.4; C : 8.65; H : 2.35; P : 3.72; I : 15.23. Found : Co : 41.8; C : 8.59; H : 2.95; P : 3.16; I : 7.53. Yield : Close to 100%

P-Bz-OC₄N₂Co

P-Bz-OC₄N (81.0 mg, 0.34 mmol) was dissolved in 12 mL of water by adding NaOH until reaching pH=8.6. Then 12 mL of ethanol was added in the solution along with Co₂(OH)_{3.5}(DSo)_{0.5} (70 mg, 0.16 mmol). The suspension was stirred under argon during 4h at 90°C. The green powder was then filtered, washed with water and ethanol then dried under vacuum. Analysis calculated for Co₂(OH)_{3.6}(C₁₀H₁₁NO₄P)_{0.4}·1.5H₂O, Co₂C₄H₁₁O_{6.7}P_{0.44}N_{0.4} (M=302.2 g/mol): Co : 39.01; C : 15.9; H : 3.67; P : 4.10; N : 1.85. Found : Co : 41.8; C : 15.8; H : 3.36; P : 2.48; N : 1.04. Yield : 96%

Synthesis of compounds made in chapter V

P₂-Thio-C₂Cu

P₂-Thio-C (63.9 mg, 0.25 mmol) was dissolved in 12 mL of water by adding NaOH until reaching pH=8.9. Then 12 mL of ethanol was added in the solution along with Cu₂(OH)₃(DS) (76 mg, 0.16 mmol). The suspension was stirred under argon during 6h at 90°C. The grayish-blue powder was then filtered, washed with water and ethanol then dried under vacuum. Analysis calculated for Cu₂(OH)_{3.56}(C₅H₆O₆P₂S)_{0.22}·1H₂O, Cu₂C_{1.1}H_{6.88}O_{5.88}P_{0.44}S_{0.22} (M=262 g/mol): Cu : 48.51; C : 5.04; H : 2.65; P : 5.20; S : 2.69. Found : Cu : 50.6; C : 6.00; H : 3.11; P : 4.25; S : 1.87. Yield : 88%

P₂-diThioCu

P₂-diThio (55.9 mg, 0.17 mmol) was dissolved in 12 mL of water by adding NaOH until reaching pH=8.8. Then 12 mL of ethanol was added in the solution along with Cu₂(OH)₃(DS) (76 mg, 0.16 mmol). The suspension was stirred under argon during 4h at 90°C. The grayish-blue powder was then filtered, washed with water and ethanol then dried under vacuum. Analysis calculated for Cu₂(OH)_{3.46}(C₈H₆O₆P₂S₂)_{0.27}·1.5H₂O, Cu₂C_{2.16}H_{8.08}O_{6.58}P_{0.54}S_{0.54} (M=300.5 g/mol): Cu : 42.3; C : 8.63; H : 2.71; P : 5.57; S : 5.76. Found : Cu : 43.4; C : 8.89; H : 2.87; P : 3.39; S : 3.38. Yield : 93%

P₂-Thio-CCo

P₂-Thio-C (42.9 mg, 0.165 mmol) was dissolved in 12 mL of water by adding NaOH until reaching pH=8.8. Then 12 mL of ethanol was added in the solution along with Co₂(OH)_{3.5}(DSO)_{0.5} (70 mg, 0.16 mmol). The suspension was stirred under argon during 4h at 90°C. The green powder was then filtered, washed with water and ethanol then dried under vacuum. Analysis calculated for Co₂(OH)_{3.7}(C₅H₆O₆P₂S)_{0.1}(DSO)_{0.1}·1H₂O, Co₂C_{6.3}H_{6.8}O_{4.6}P_{0.2}S_{0.2} (M=249.4 g/mol): Co : 47.27; C : 8.19; H : 3.56; P : 2.48; S : 2.57. Found : Co : 58.8; C : 7.94; H : 3.59; P : 2.11; S : 2.2. Yield : Close to 100%

P₂-diThioCo

P₂-diThio (54.7 mg, 0.168 mmol) was dissolved in 20 mL of water by adding NaOH until reaching pH=8.7. Then 12 mL of ethanol was added in the solution along with Co₂(OH)_{3.5}(DSO)_{0.5} (69 mg, 0.16 mmol). The suspension was stirred under argon during 3h15 at 90°C. The green powder was then filtered, washed with water and ethanol then dried under vacuum. Analysis calculated for Co₂(OH)_{3.66}(C₈H₆O₆P₂S₂)_{0.17}·1.1H₂O, Co₂C_{1.36}H_{6.88}O_{5.78}P_{0.34}S_{0.34} (M=262.2 g/mol): Co : 44.94; C : 6.23; H : 2.95; P : 4.02; S : 4.16. Found : Co : 57.1; C : 6.24; H : 3.03; P : 2.41; S : 3.00. Yield : Close to 100%

OleylCu

Sodium oleyl sulfate (122 mg, 0.33 mmol) was dissolved in 15 mL of water. Then 10 mL of ethanol was added in the solution along with Cu₂(OH)₃(OAc) (40.8 mg, 0.16 mmol). The suspension was stirred under argon during 6h at 60°C. The light blue powder was then filtered, washed with water and ethanol then dried under vacuum. Analysis calculated for Cu₂(OH)_{4-x}(C₁₈H₃₅O₄S)_x·1.5H₂O, Cu₂C_xH_xO_xS_x (M=X g/mol): Cu : X; C : X; H : X; P : X; S : X. Found : Cu : X; C : X; H : X; P : X; S : X. Yield : %

OleylCo

Sodium oleyl sulfate (122 mg, 0.33 mmol) was dissolved in 15 mL of water. Then 10 mL of ethanol was added in the solution along with Co₂(OH)_{3.2}(OAc)_{0.8} (40.6 mg, 0.16 mmol). The suspension was stirred under argon during 6h at 60°C. The green powder was then filtered, washed with water and ethanol then dried under vacuum. Analysis calculated for Co₂(OH)_{4-x}(C₁₈H₃₅O₄S)_x·1.5H₂O, Co₂C_xH_xO_xS_x (M=X g/mol): Co : X; C : X; H : X; P : X; S : X. Found : Co : X; C : X; H : X; P : X; S : X. Yield : %

P₂-ThioCo

P₂-Thio (41.5 mg, 0.170 mmol) was dissolved in 12 mL of water by adding NaOH until reaching pH=8.3. Then 12 mL of ethanol was added in the solution along with Co₂(OH)_{4-x}(Oleyl)_x (19.2 mg, X mmol). The suspension was stirred under argon during 1h at 90°C. The green powder was then filtered, washed with water and ethanol then dried under vacuum. Analysis calculated for Co₂(OH)_{3.7}(C₄H₄O₆P₂S)_{0.1}·1H₂O, Co₂C_{6.3}H_{6.8}O_{4.6}P_{0.2}S_{0.2} (M=X g/mol): Co : X; C : X; H : X; P : X; S : X. Found : Co : X; C : X; H : X; P : X; S : X. Yield : X%13.1mg

P₂-ThioCu

P₂-Thio (41.8 mg, 0.171 mmol) was dissolved in 12 mL of water by adding NaOH until reaching pH=8.3. Then 12 mL of ethanol was added in the solution along with Cu₂(OH)_{4-x}(Oleyl)_x (23.3 mg, X mmol). The suspension was stirred under argon during 1h at 90°C. The green/grey powder was then filtered, washed with water and ethanol then dried under vacuum. Analysis calculated for Cu₂(OH)_{3.7}(C₄H₄O₆P₂S)_{0.1}·1H₂O, Cu₂C_{6.3}H_{6.8}O_{4.6}P_{0.2}S_{0.2} (M=X g/mol): Cu : X; C : X; H : X; P : X; S : X. Found : Cu : X; C : X; H : X; P : X; S : X. Yield : X%8.3mg

Synthesis of compounds made in chapter VI

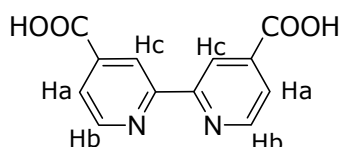
All the following syntheses are adapted from 1 and 2.

Synthesis of the ruthenium complex:

dcbpy

This ligand is obtained by oxidation of dimethylbipyridine by potassium dichromate. 5g (20.5 mmol) of 4,4'-dimethyl-2,2'-bipyridine is added under stirring to 125 mL of sulfuric acid (98%). While maintaining a temperature between 60 and 80°C 24g (81.5 mmol) of K₂Cr₂O₇ is carefully added to the solution. Upon completion of the addition, the reaction mixture must be cooled down to 40°C. The solution is then transferred in a 800 mL beaker containing a mixture of water and ice. The yellow solid obtained is then washed with water. This solid is purified by dissolution in 170 mL of 50% nitric acid (reflux during 4 hours). After the reflux the mixture is transferred in a liter of a mixture of water and ice. The obtained solid is then washed with water (5 x 50 mL) then with acetone (2 x 50 mL). The final product is white.

Yield : 94%

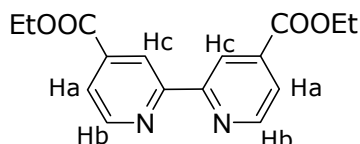


¹H-RMN (300 MHz DMSO-d₆): 7,6-7,66 ppm (2H_b, m); 8,16 ppm (2H_c, s), 8,55-8,56 ppm (2H_a, d).

4,4'-diethoxycarbonyl-2,2'-bipyridine (1) :

To a suspension of 4-4'-dicarboxypyridine (5.0g, 20.5 mmol) is placed in 400 mL of ethanol, with 5 mL of sulfuric acid. The mixture is then heated during 80 hours to obtain a clear solution which is then cooled to room temperature. 400 mL of water is then added and ethanol is discarded under vacuum. The pH is adjusted at 7 *via* the addition of a solution of NaOH, the obtained precipitate is filtered and washed with water then dried to give the solid.

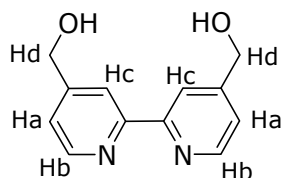
Yield : 90%



¹H-RMN (300 MHz CDCl₃) : 1,44 ppm (6H (CH₃), t, J = 7,2Hz), 4,43-4,5 ppm (4H (CH₂), q, J = 7,2Hz), 7,9-7,93 ppm (2H_b, dd, J₁ = 1,53Hz, J₂ = 5,04Hz); 8,86-8,89 ppm (2H_a, dd), 8,55-8,56 ppm (2H_c, m).

4,4'-Bis(hydroxymethyl)-2,2'-bipyridine (2) : NaBH₄ (8.2g) is added to a solution of (1) (3.0 g, 10.0 mmol) in 200 mL of EtOH. The mixture is refluxed during 3 hours then cooled to room temperature. A saturated solution of ammonium chloride is added to decompose the excess of NaBH₄. The solvent is then discarded with vacuum. The precipitate is dissolved in a minimum amount of water. The resulting solution is extracted with ethyl acetate (5 x 200 mL), dried with Na₂SO₄ then the solvent is evaporated to obtain the desired solid.

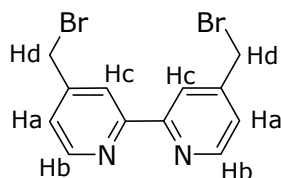
Yield : 79%



¹H-RMN (300 MHz CDCl₃) : 1,44 ppm (6H (CH₂), t, J = 7,2Hz), 4,43-4,5 ppm (4H (CH₂), q, J = 7,2Hz), 7,9-7,93 ppm (2Hb, dd, J₁ = 1,53Hz, J₂ = 5,04Hz); 8,86-8,89 ppm (2Ha, dd), 8,55-8,56 ppm (2Hc, m).

4,4'-Bis(bromomethyl)-2,2'-bipyridine (3): A suspension of (2) (0.90 g, 4.2 mmol) is dissolved in a mixture of 48% HBr (20 mL) and concentrated sulfuric acid (6.7 mL). The solution is then refluxed for 6 hours then cooled to room temperature when 40 mL of water is added. The pH is adjusted to 7 *via* the addition of an NaOH solution and the precipitate is filtered, washed with water and dried under vacuum. The obtained product is purified with dissolution in 40 mL of chloroform and then filtered. The solution is dried with MgSO₄ and dried under vacuum until a white powder is obtained.

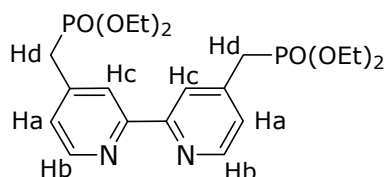
Yield : 85%



¹H-RMN (300 MHz CDCl₃) : 4,5 ppm (4Hd (CH₂), s), 7,28 ppm (2Ha, s); 8,49 ppm (2Hc, d), 8,7 ppm (2Hb, m).

4,4'-Bis(diéthylmethylphosphonate)-2,2'-bipyridine (4) ; A solution of (3) (1.5g, 4.4 mmol) in 10 mL of chloroform and 15 mL of diethylphosphite is refluxed for 3 hours under inert atmosphere. The phosphite excess is discarded with vacuum and the remaining solid is purified *via* column chromatography on silica gel. (eluant ethyl acetate/methanol 80/20)

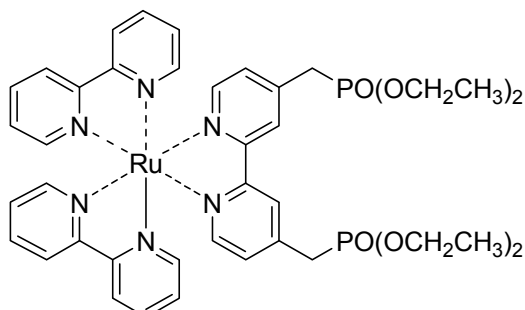
Yield : 80%



¹H-RMN (300 MHz CDCl₃) : 1,24-1,31 ppm (12H (CH₃), t, J = 7,02 Hz), 3,22 ppm (4Hd, d, J = 22 Hz), 4,02-4,12 ppm (8H (CH₂), J = 7Hz), 7,37 ppm (2Ha, m); 8,42 ppm (2Hc, s), 8,7 ppm (2Hb, d, J = 7,02 Hz).

[Ru(bpy)₂(4,4'-(CH₂PO₃Et₂)₂bpy)]Cl₂ (5) : A solution of (4) (0.13 g, 0.29 mmol) and *cis*-[Ru(bpy)₂Cl₂]₂·2H₂O (0.1g, 0.18 mmol) is mixed in a 40 mL DMF solution then refluxed under inert atmosphere and covered from light during 5 hours. The reactive medium is then evaporated and the solid is purified *via* column chromatography on sephadex LH20. The choice of methanol as eluant allows to obtain the desired product in the form of an orange powder.

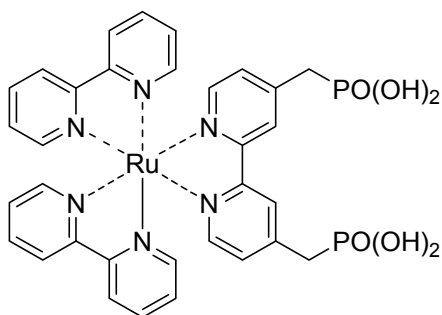
Yield : 72%



¹H-RMN (300 MHz D₂O) : 0,8 ppm (12H expected 6 observed, (CH₃), t, J = 7 Hz), 2,7 ppm (4H, (CH₂P), d, J = 22 Hz), 3.37 ppm (8H expected 4 observed, (CH₂), J = 7Hz), 7,24 (4H, m), 7,5 (2H, s), 7,8 (10H, m), 8,3 (6H, m). (NMR shows a partial hydrolysis of the ester moieties, typical for this type of compounds.)

[Ru(bpy)₂(4,4'-(CH₂PO₃H₂)₂bpy)]Cl₂ (6) : A solution of (5) (0.10 g, 0.013 mmol) in 20 mL of an aqueous solution of HCl (18%) is refluxed for 8 hours. The remaining solvent is then dried under vacuum to obtain the desired complex.

Yield : 90%



¹H-RMN (300 MHz D₂O) : 2,75 ppm (4H, (CH₂P), d, J = 22 Hz), 7,24 (4H, m), 7,5 (2H, s), 7,8 (10H, m), 8,3 (6H, m).

Total yield : 30%

Synthesis of the platinum complex :

- N-phenylsalicylideneimine (A)

Salicylaldehyde (17.5 mL, 164 mmol) and aniline (14.9 mL, 164 mmol) were introduced in a round-bottomed flask. The orange mixture was heated at 120°C for one night without condenser. The mixture was cooled to room temperature until precipitation of an orange solid. The solid was filtered and recrystallized with isopropanol (40-50 ml).

Yield = 90-95 %.

Anal. for A : C₁₃H₁₁NO (*M* = 197.08 g / mol) : Found (Calc.) (%) : C, 79.20 (79.16); H, 5.53 (5.62); N, 7.03 (7.10). ¹H NMR (CDCl₃) : 8.62 (s, 1H), 7.43 (m, 4H), 7.31 (m, 3H), 7.05 (d, 1H), 6.96 (m, 1H). IR (KBr pellet, cm⁻¹) : 3055 w, 2885 w, 2741 w, 1950 w, 1801 w, 1679 w, 1614 s, 1570 s, 1482 s, 1453 s, 1399 s, 1359 m, 1275 s, 1185 s, 1149 s, 1073 m, 1026 m, 979 m, 895 m, 822 m, 755 s, 687 m, 547 m, 519 m, 492 w, 432 w.

- N-phenylsalicylideneimine-5-sulfonic acid (B)

A (15.5 g, 56 mmol) was added to concentrated sulfuric acid (95%) (43 mL). The mixture was heated and stirred for 2 hours at 100°C with a condenser. The red-brown solution was allowed to cool to room temperature. Then, the solution was poured onto ice (300 g) and a yellow lumbering solid formed. The solid was filtered and recrystallized in hot water. After cooling, a yellow powder was filtered.

Yield = 50-55 %.

Anal. for B·2H₂O : C₁₃H₁₁NO₄S·2H₂O (*M* = 313.04 g / mol) : Found (Calc.) (%) : C, 50.43 (49.84); H, 4.65 (4.79); N, 4.35 (4.47). ¹H NMR (DMSO-d₆) : 10.24 (s, 1H), 9.07 (s, 1H), 8.02 (s, 1H), 7.65 (m, 1H), 7.45 (m, 4H), 7.35 (m, 1H), 6.95 (d, 1H). IR (KBr pellet, cm⁻¹) : 3395 m, 3134 w, 3061 m, 1652 s, 1601 s, 1498 w, 1441 w, 1394 m, 1363 w, 1299 m, 1223 s, 1189 s, 1114 s, 1034 s, 910 w, 872 m, 1759 w, 714 m, 660 w, 596 m, 548 w, 510 m.

- 5-sulfonatosalicylaldehyde sodium salt (C)

B (9.09 g, 32.8 mmol) was dissolved in 60 mL of an aqueous solution of Na₂CO₃ (0.9 mol / L). The solution was heated at 110°C in an open beaker for 2.5 h with replacement of the evaporated water. Glacial acetic acid (12 mL) and ethanol (12 mL) were added to the cooled solution. The solution was cooled in an ice bath and a solid precipitated. The off white crystalline solid was filtered, washed with ethanol and dried in vacuum.

Yield = 75-80%

Anal. for C·1.5H₂O : C₇H₅SO₅Na·1.5H₂O (*M* = 251.19 g / mol) : Found (Calc.) (%) : C, 33.53 (33.47); H, 2.98 (3.21); S, 13.20 (12.77). ¹H NMR (DMSO-d₆) : 10.24 (s, 1H), 7.88 (d, 1H), 7.69 (d*d, 1H), 6.91 (d, 1H). IR (KBr pellet, cm⁻¹) : 3526 s, 3425 s, 3389 s, 3097 w, 3058 w, 2897 m, 1654 s, 1576 m, 1468 s, 1423 vw, 1371 m, 1319 m, 1288 m, 1218 s, 1174 s, 1137 m, 1105 s, 1038 s, 912 w, 851 m, 760 m, 673 m, 594 m, 559 w, 538 w, 507 w, 461 w, 446 w.

-Salen complex (D)

C (2.0 g, 8.85 mmol) is dissolved in 25 mL of methanol. Upon complete dissolution of C, the 4,5-dimethylbenzene-1,2-diamine (0.61 g, 4.42 mmol) in 20 mL of methanol is slowly added to the solution of C. After addition, the mixture is then refluxed for two hours with an inclined condenser to get rid of water content. The bright yellow precipitate is filtered and is the desired salen compound.

Yield : 33%

-Platinum insertion in the salen complex (E)

D (0.197 g, 0.36 mmol) along with sodium acetate (60 mg, 0.73 mmol) are solubilized in 10 mL of DMSO by heating up to 80°C. Upon complete dissolution, potassium tetrachloroplatinate (II) (0.150 g, 0.36 mmol) is added, the orange solution turns red. The mixture is then heated at 110°C with a reflux condenser overnight. The solution is then allowed to cool to room temperature where orange crystals are formed. These crystals are filtered and washed with 5 mL of DMSO and 10 mL of EtOH and dried under vacuum overnight.

Yield : 50%

Ruthenium complex (6)⊂Co :

(6) (110 mg, 0.148 mmol) is solubilized in 12 mL of water *via* addition of NaOH up to pH = 8.6. Co₂(OH)_{3.5}(DSo)_{0.5} (30 mg, 0.073 mmol) is added along with 12 mL of EtOH in the solution of (6) and bubbled with argon for 15 minutes. The dispersion is helped with 1 minute of ultrasonication and then heated to 80°C for 15 hours under argon and protected from light. The obtained red/green product is then filtered and washed with water then ethanol.

Analysis calculated for Co₂(OH)_{3.8}(C₃₂H₂₈N₆O₆P₂Ru)_{0.1}•1H₂O, Co₂C_{3.2}H_{8.6}O_{5.4}P_{0.2}N_{0.6}Ru_{0.1} (M=276.1 g/mol): Co : 42.69; C : 13.92; H : 3.14; P : 2.24; N : 3.04; Ru : 3.66. Found : Co : 42.4; C : 13.83; H : 3.54; P : 2.41; N : 2.64; Ru : 0.79.

Yield : 65%

Platinum complex (E)⊂Co :

(E) (130 mg, 0.185 mmol) is solubilized in 12 mL of water. Co₂(OH)_{3.5}(DSo)_{0.5} (70 mg, 0.165 mmol) is added along with 12 mL of EtOH in the solution of (E) and bubbled with argon for 15 minutes. The dispersion is helped with 1 minute of ultrasonication and then refluxed at 90°C for 24 hours under argon and protected from light. The obtained red/green product is then filtered and washed with water then ethanol.

Analysis calculated for Co₂(OH)_{3.48}(C₂₂H₁₆N₂O₈PtS₂)_{0.24}(DSo)_{0.04}•1.5H₂O, Co₂C_{5.76}H_{11.32}O_{7.02}S_{0.48}Pt_{0.24} (M=381.0 g/mol): Co : 30.94; C : 18.16; H : 2.99; S : 4.28; N : 1.76; Pt : 12.29. Found : Co : 31.2; C : 18.3; H : 3.56; S : 3.9; N : 1.58; Pt : 12.3.

Yield : close to 100%

Experimental measurements conditions :

Butterfly CuDS morphology:

The Powder X-Ray Diffraction (PXRD) diagram of $\text{Cu}_2(\text{OH})_3(\text{C}_{12}\text{H}_{25}\text{SO}_4)$ was measured in transmission geometry on a PANalytical Xpert-pro diffractometer equipped with a focusing mirror ($\text{Cu-}\lambda\text{K}\alpha_{\text{moy}}$) and a PIXcel detector. The polycrystalline sample was loaded in a capillary of 0.3 mm diameter. The PXRD diagram was recorded at room temperature between 3 and $60^\circ(2\theta)$ with a step size of $\sim 0.013^\circ(2\theta)$ for 2 hours.

The Rietveld refinements were performed with the JANA2006 program³ to check the composition of the polycrystalline sample of $\text{Cu}_2(\text{OH})_3(\text{C}_{12}\text{H}_{25}\text{SO}_4)$. Assuming the crystal structure model obtained from the single crystal X-ray data only the scale, unit cell and profile parameters were refined. The low R factors ($R_{\text{obs}} = 7,01$; $R_{\text{Bobs}} = 13,15$; $R_{\text{wp}} = 8,43$, $\text{gof} = 1,80$) and the absence of any extra peaks testify that the polycrystalline sample correspond to a single-phase sample of $\text{Cu}_2(\text{OH})_3(\text{C}_{12}\text{H}_{25}\text{SO}_4)$.

Mono crystal setup for CuDS platelets and Ribbon-like structure :

X-ray diffraction measurements were performed using Mo $K\alpha$ radiation produced with a micro focus Incoatec $1\mu\text{s}$ sealed X-ray tube on a KappaCCD (Bruker-Nonius) four circles diffractometer equipped with a Apex2 bi-dimensional detector (CCD: charge coupled device). Crystals of suitable crystalline quality were selected for single crystal XRD; details of the data collection are given in Table 1. Data were corrected from absorption using Sadabs program developed for scaling and absorption corrections of area detector data. The structure was determined with Superflip⁴ using charge-flipping algorithm and introduced in the program Jana2006.¹⁴⁶

Chemical formula	$\text{Cu}_3(\text{C}_{12}\text{H}_{25}\text{SO}_4)_2(\text{CH}_3\text{COO})_2(\text{OH})_2(\text{H}_2\text{O})_2$	$\text{Cu}_2(\text{OH})_3(\text{C}_{12}\text{H}_{25}\text{SO}_4)$
Molecular weight ($\text{g}\cdot\text{mol}^{-1}$)	905.5	444.5
Space group	$P\bar{1}$	$P2_1$
a (Å)	5.602(2)	5.591(10)
b (Å)	8.314(3)	6.108(11)
c (Å)	21.283(8)	26.96(5)
α (°)	83.02(2)	90
β (°)	85.87(2)	92.76(3)
γ (°)	81.85(2)	90
Cell volume (Å ³)	972.4(7)	920(3)
Z	1	2
Density ($\text{g}\cdot\text{cm}^{-3}$)	1.546	1.6053
μ (mm^{-1})	1.798	2.452
wavelength (Å)	0.71069	0.71069
scan strategy / D_x (mm)	ω/ϕ scan / 50	ω/ϕ scan / 50
θ max	29.17	29.03

Reflections index limit	-6 ≤ h ≤ 7 -10 ≤ k ≤ 11 -27 ≤ l ≤ 28	-7 ≤ h ≤ 7 -8 ≤ k ≤ 8 -36 ≤ l ≤ 36
unique reflections with I ≥ 3σ(I)	1199	1093
Absorption correction	multi-scan / SADABS	multi-scan / SADABS
Internal R value before / after correction (%)	15.1% / 6.2%	15.3% / 4.9%
# refinement parameters	119	78
ρ _{min} / ρ _{max} (e/Å ³)	-1.72/1.21	-2.43/1.19
F(000)	473	460
Reliability factors %	9.95%	6.98%

Table 1 : Details of single crystal data collection parameters.

Powder X-ray diffraction (XRD) patterns were collected with a Bruker D8 diffractometer (Cu Kα1 = 0.1540598 nm) equipped with a LynxEye detector discriminating in energy in Bragg-Brentano geometry.

FT-IR spectra of the hybrid compounds were collected in ATR mode on a SpectrumII spectrometer (PerkinElmer).

TGA-TDA experiments were performed using a TA instrument SDT Q600 (heating rates of 5°C·min⁻¹ under air stream, using Pt crucibles).

The SEM images were obtained with a JEOL 6700F microscope equipped with a field emission gun, operating at 3 kV in the SEI mode and with a ZEISS GeminiSEM 500 microscope, operating at 1 kV or 5kV in secondary electron imaging mode.

The magnetic studies were carried out with a SQUID magnetometer (Quantum Design MPMS3) covering the temperature and field ranges 2–300 K and ± 7 T, respectively. Magnetization versus field measurements at room temperature confirm the absence of ferromagnetic impurities. Data were corrected for the sample holder, and diamagnetism was estimated from Pascal constants.

Non-Linear Optical (NLO) activity was evaluated by detecting the Second-Harmonic Generation (SHG) process. SHG measurements have been performed with an inverted microscope (Olympus IX71). The SHG process is induced by focusing in the sample a pulsed laser beam at 900 nm (Spectra Physics, Tsunami) with ultrashort pulse durations (100 fs at 80 MHz) and input power of 50 mW. Samples in powder form deposited onto a microscope slide are excited by this laser beam using a low-aperture microscope objective (Olympus, SLMPlan, X20, N.A. = 0.35). The SHG signal emitted at 450 nm is separated from the excitation beam by a dichroic mirror and collected during 1 s in reflection mode using a spectrometer (Acton research SP2300) coupled with a CCD camera (Princeton Instruments PIXIS400). For SHG imaging, a micrometric displacement stage is combined with a photon photomultiplier in counting mode (Hamamatsu, H7421).

Bibliography

1. A. R. Oki and R. J. Morgan, *Synthetic Communications*, 1995, **25**, 4093-4097.
2. I. Gillaizeau-Gauthier, F. Odobel, M. Alebbi, R. Argazzi, E. Costa, C. A. Bignozzi, P. Qu and G. J. Meyer, *Inorganic Chemistry*, 2001, **40**, 6073-6079.
3. S. H. Park, M. H. Jung, Y. J. Lee and Y. D. Huh, *Dalton Transactions*, 2017, **46**, 3363-3368.
4. V. Petříček, M. Dušek and L. Palatinus, *Zeitschrift für Kristallographie - Crystalline Materials*, 2014, **229**.

Résumé de la thèse de doctorat Quentin Evrard

Hydroxydes Simples Lamellaires multifonctionnels : investigations structurales, fonctionnalisations et propriétés

Le domaine de la science des matériaux est extrêmement vaste et a toujours suscité un fort intérêt de la première taille d'un silex au procédé de photolithographie sur des monocristaux de silicium. Si les outils à notre disposition ont bien évidemment fortement évolué au fil des années, le principe fondamental est resté identique. Par exemple combiner la résistance à la compression du béton avec la résistance à l'élongation de l'acier permet d'obtenir un matériau qui est à la fois résistant à la compression mais aussi à l'élongation, permettant de construire des ponts ou des bâtiments élevés. Il s'agit ici d'une exemple à l'échelle macroscopique, mais il faut savoir que ce principe reste valable à l'échelle nanométrique.

Les matériaux ainsi obtenus sont appelés matériaux hybrides, où la combinaison à l'échelle nanométrique d'au moins deux matériaux différents permet l'obtention d'un matériau final possédant un mélange des propriétés de ces composants initiaux ou de nouvelles propriétés intrinsèques dues à des effets de synergie entre les deux composants.

Un des exemples les plus commun de ce type de matériaux sont les matériaux hybrides dits organiques/inorganiques. En effet, le concept de mélanger des matériaux organiques et inorganiques est déjà présent dans les cultures pré-Colombiennes avec le bleu Maya, un mélange d'argiles (palygorskite et montmorillonite) avec une molécule organique (l'indigotine obtenue à partir de feuilles d'añil),¹ permettant à la molécule organique relativement fragile d'être préservée bien plus longtemps (Figure 1). En effet, son inclusion dans l'argile la protège des acides, des bases ou bien de la biodégradation, la rendant stable pour plusieurs siècles. Néanmoins, même aujourd'hui, être capable de concevoir ce type de matériaux de façon rationnelle reste un défi qui soulève un grand intérêt dans un grand nombre de domaines allant des membranes séparatrices² ou de propriétés optiques intéressantes³ tels qu'un colorant laser à l'état solide,⁴⁻⁶ des diodes électroluminescentes⁷ ou bien encore du transport de trous.⁸



Figure 1. Image impliquant du bleu Maya dans la salle 3 du temple de Bonampak (Mexique) datant de 791 après J.-C.⁹

Ces matériaux hybrides ont été séparés en deux classes distinctes,¹⁰ la classe I regroupe les matériaux hybrides possédant une faible cohésion entre ses deux composants (liaison hydrogène, Van der Waals ou électrostatique) tandis que les matériaux dits de classe II possèdent une plus forte cohésion (liaison covalence ou de coordination par exemple...). La raison de cette classification est principalement liée au fait qu'une interaction plus forte entre les composants du matériaux hybride peuvent permettre plus d'interactions physiques entre eux, favorisant la présence d'effet de synergie tels qu'une capacitance électrochimique plus élevée¹¹ ou une plus forte luminescence¹² même si cette condition n'est pas nécessaire pour toutes les propriétés comme la catalyse¹³ ou la luminescence.¹⁴

La plupart de ces matériaux hybrides ont aussi l'avantage de pouvoir être obtenus via des conditions de réaction chimique/physique douces et de faciliter ainsi leur synthèse à plus faible cout environnemental.

Dans le cas du bleu Maya, la propriété recherchée était l'amélioration de la stabilité de la molécule organique, cependant, il est possible de rechercher de nombreuses autres propriétés. Il existe dans la littérature de nombreux exemples où les matériaux hybrides montrent des propriétés de luminescence,^{12, 14-16} magnétiques,¹⁷⁻¹⁹ optiques,^{3, 5, 6} électroniques,²⁰⁻²² photo²³ ou electro²⁴⁻²⁶ catalytiques. Dans certains cas²⁷⁻³⁰ il est possible d'obtenir des matériaux multifonctionnels.

Les Hydroxydes Simples Lamellaires (HSL) de métaux de transition ont pour formule générale $M_2(OH)_3X$ ($M^{II} = Co, Cu, Ni, Mn$ et $X^- = NO_3^-, Cl^-,$ carboxylate, sulfonate, sulfate ou phosphonate) (Fig. 2).

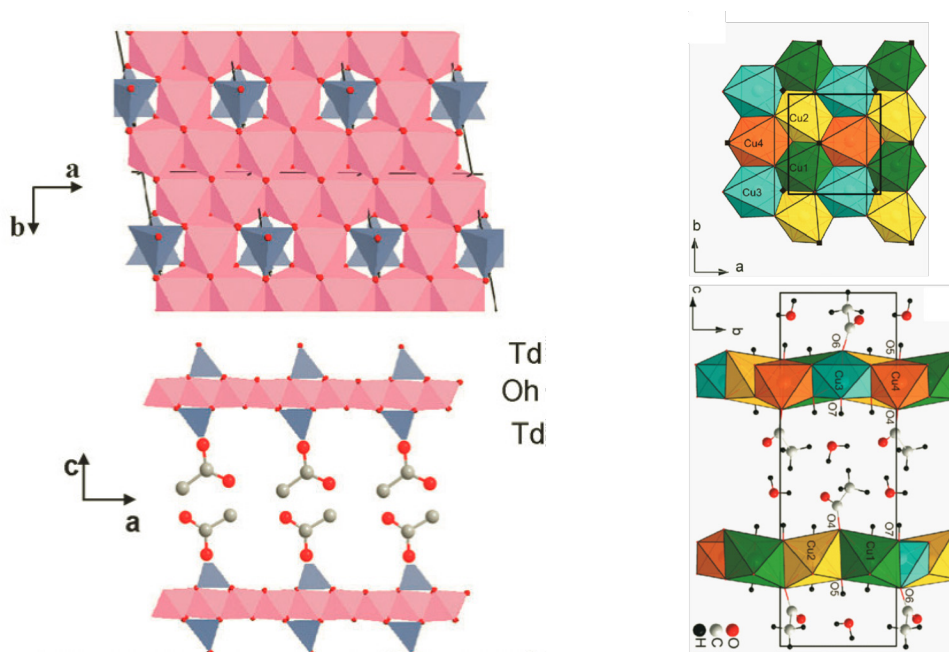


Figure 2. Vue de la structure modèle de $Co_2(OH)_3(OAc) \cdot H_2O$ (gauche) (Hexagonal : $a = b = 3,13 \text{ \AA}$, $c = 12,7 \text{ \AA}$ ³¹ et de $Cu_2(OH)_3(OAc) \cdot H_2O$ (droite) (Monoclinique ($P12_11$) $a = 5,58 \text{ \AA}$, $b = 6,07 \text{ \AA}$, $c = 18,51 \text{ \AA}$ $\beta = 91,80^\circ$).³²

Une caractéristique remarquable de ces systèmes est que l'anion présent dans l'espace interlamellaire est en général coordiné aux métaux de la couche inorganique. Dans quelques cas, il peut n'être relié aux couches inorganiques que par liaisons hydrogène.³³ Cet anion, ligand acétate par exemple, peut-être substitué par un grand nombre de molécules possédant une fonction "d'accrochage", sulfonate, carboxylate ou phosphonate notamment, *via* une réaction d'échange anionique. L'espèce ainsi intercalée peut servir de pilier voire de connecteur entre les couches inorganiques. Dans de tels systèmes, la covalence de la liaison entre espèce intercalée et sous-réseau inorganique peut favoriser l'éventuelle interaction entre propriétés.³⁴

Parmi les résultats marquants obtenus au laboratoire, le greffage d'alkyl-carboxylates de longueurs variées a permis de moduler l'espace inter-feuillets et de mettre en évidence le rôle du couplage dipolaire dans l'établissement d'un ordre magnétique à longue distance.³⁵ En outre, un système présentant un ordre antiferromagnétique canté avec un très grand champ coercitif (5,9 T à 4,2 K) a pu être obtenu dans le cas d'un système hybride hydroxyde de Co^{II} lamellaire / téréphthalate (obtenu par synthèse hydrothermale).¹⁷ Le rôle des électrons π des di-carboxylates insaturés greffés entre les couches sur l'interaction magnétique entre celles-ci (et donc l'ordre magnétique à longue distance) a également été mis en évidence sur des systèmes d'hydroxyde lamellaire de Cu^{II} ou de Co^{II}.³⁶

Ce travail de thèse s'inscrit dans la lignée des travaux réalisés au laboratoire ayant pour objet la fonctionnalisation d'hydroxydes simple lamellaires de cuivre et de cobalt (Fig. 2) par un certain nombre de molécules organiques et de complexes de métaux de transition (Fig. 3) afin d'apporter une propriété nouvelle au matériau ainsi obtenu. Les propriétés additionnelles recherchées sont à la fois la luminescence, la thermo commutation et surtout la ferroélectricité en vue d'obtenir un matériau hybride multiferroïque intrinsèque.

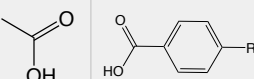
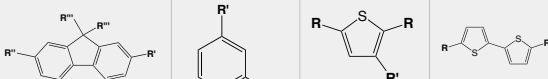
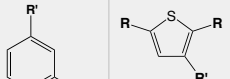
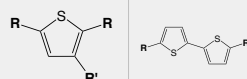
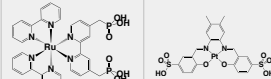
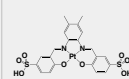
Objectif	Analyse structurale	Effet magnétodieléctrique			Luminescence			
Fonction de greffage	-COOH	-PO(OH) ₂ ou -COOH	-PO(OH) ₂	-PO(OH) ₂	-PO(OH) ₂	-SO ₂ (OH)		
Plateforme rigide								
Functionalisation	Aucune	R = NH ₂ , -N(CH)(CH ₂) ₂ CH ₃ , -N(CH)(CH ₂) ₃ CH ₃ , -N(CH)(CH ₂) ₄ CH ₃ , -N(CH)(CH ₂) ₁₀ CH ₃ ou 4-(iminométhyl) benzonnitrile	R' = PO(OH) ₂ R'' = PO(OH) ₂ , COOH ou H R''' = H, CH ₃ , -(CH ₂) ₃ -CH ₃ , ou -(CH ₂) ₇ -CH ₃	R' = COOH ou PO(OH) ₂ X = F, Cl, Br, I, O(CH ₂)CN ou O(CH ₂) ₃ CN	R = PO(OH) ₂ R' = H ou CH ₃	R = PO(OH) ₂	Aucune	Aucune
Chapitre	II	III	IV	V	VI			

Figure 3. Tableau des molécules insérées dans les hydroxydes de cuivre et cobalt.

Il a été développé au laboratoire une technique dite de pré-intercalation permettant de fonctionnaliser ces hydroxydes avec des molécules complexes telles que celles indiquées ci-dessus. Cette technique est montrée dans la figure 4 ci-dessous, elle consiste à échanger l'acétate présent dans l'espace interfoliaire par du dodécylsulfate ou du dodécylsulfonate dans l'hydroxyde de cuivre et de cobalt respectivement.

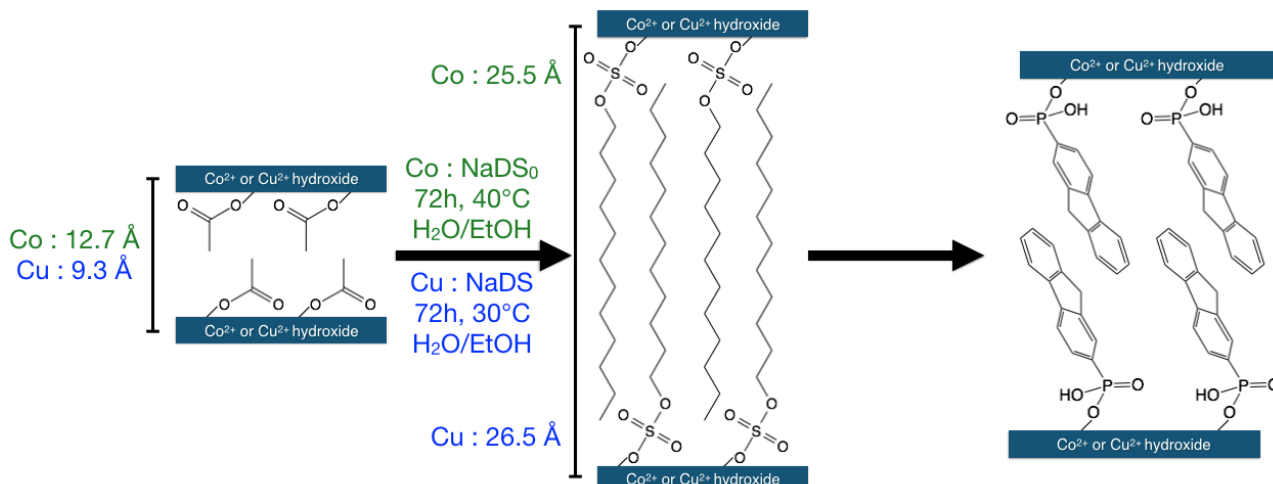


Figure 4. Schéma explicatif décrivant la méthode de pré-intercalation utilisée traditionnellement au laboratoire.

Cette technique de pré-intercalation, utilisée en conjonction avec l'optimisation des conditions d'insertion des différentes molécules a permis d'obtenir la plupart des hybrides avec une seule distance interlamellaire. Cependant, dans quelques cas, cette technique c'est avérée insuffisante et j'ai dû adapter cette technique via la pré-insertion d'oleyl sulfate. En effet, avec certaines molécules il a été noté que l'arrangement ordonné des chaînes alkyl présent dans les hybrides à base de dodécylsulfate/dodécylsulfonate et les interactions alkyl/alkyl en résultant étaient un facteur limitant à l'insertion. L'oleyl sulfate a été choisi par la présence d'une insaturation au milieu de la chaîne, cette insaturation permettant d'augmenter le désordre de l'empilement des chaînes de façon suffisante pour permettre l'insertion totale des molécules ne s'insérant pas par voie classique (Fig 5.).

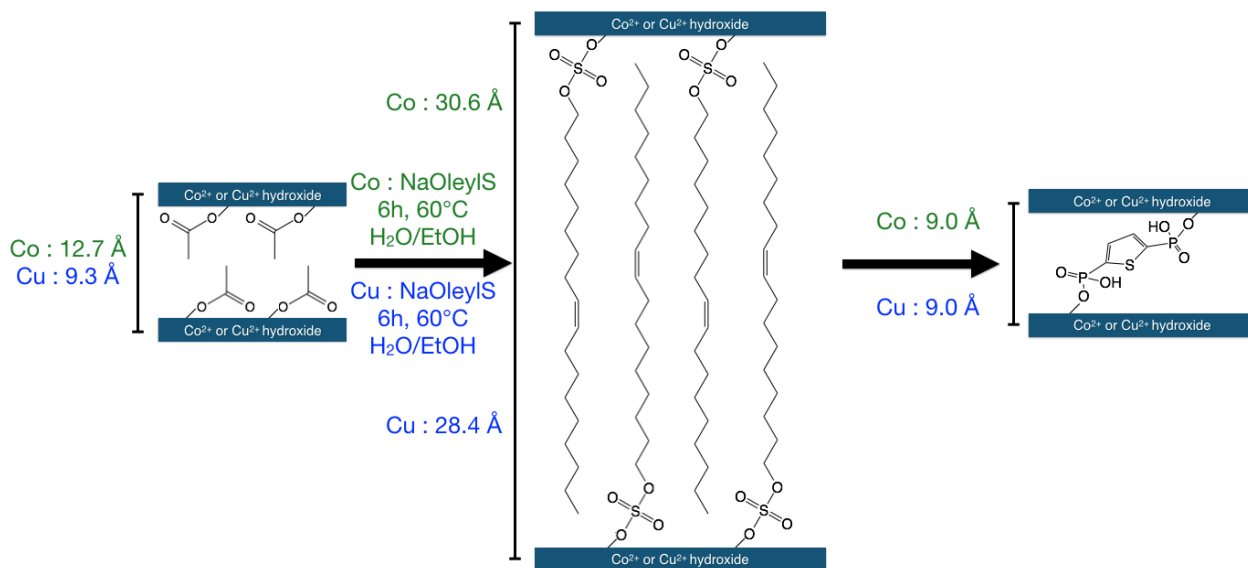


Figure 5. Schéma explicatif décrivant la méthode de pré-intercalation modifiée utilisée dans le cas de certaines molécules difficiles.

Ma thèse s'est articulée autour de trois axes principaux :

- L'optimisation des conditions de synthèse des produits de départ pour obtenir des cristallites de la taille la plus grande possible afin à la fois d'obtenir des mono-cristaux pour connaître la structure des composés de départ ainsi que de faciliter d'éventuelles mesures diélectriques sur un seul cristal au lieu d'une poudre polycristalline. Ces mono-cristaux pouvant ensuite être fonctionnalisés par différentes molécules.
- L'optimisation des conditions de synthèse pour l'insertion de différentes molécules dans l'espace interlamellaire possédant des fonctions d'accroche acide phosphonique ainsi que quelques molécules possédant des fonctions d'accroche carboxylate et sulfonate. Ainsi que la caractérisation des composés ainsi obtenus via des techniques de diffraction des rayons X, de spectroscopie infrarouge et UV-visible, d'analyse élémentaire ou bien encore par microscopie électronique à balayage couplée à une analyse dispersive en énergie.
- Les mesures des propriétés magnétiques, diélectriques, de luminescence ainsi que de thermo commutation des différents hybrides obtenus.

L'optimisation de la cristallinité des produits de départ pour l'hydroxyde de cuivre a mené à l'augmentation de la taille des cristallites d'un facteur 30 (Fig. 6), et a permis de résoudre la structure sur monocristal de l'hydroxyde de cuivre dans lequel est inséré le dodécylsulfate tout en gardant une morphologie plaquettaire.

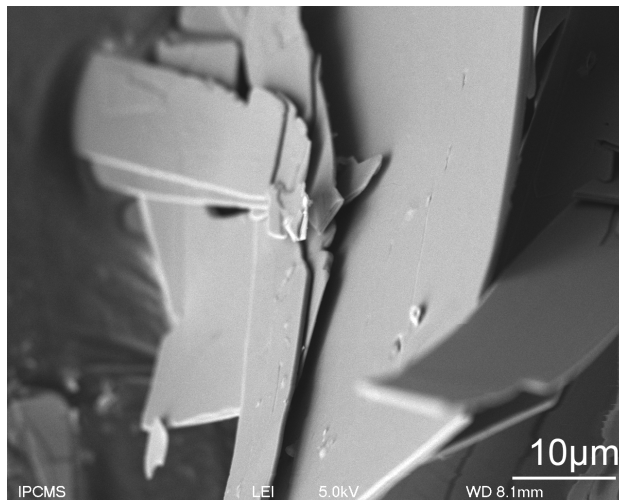
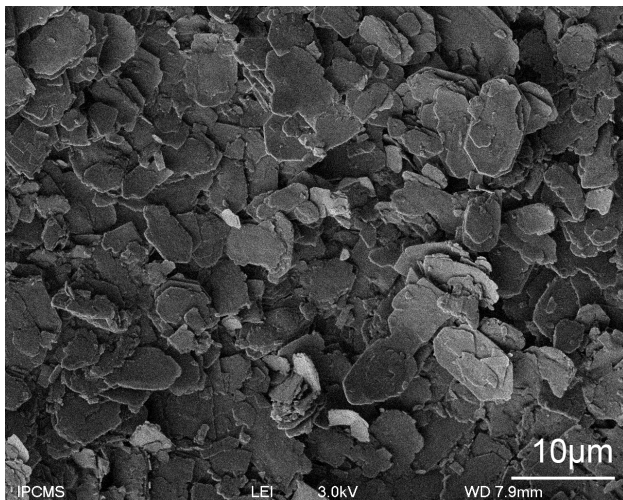
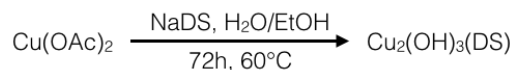
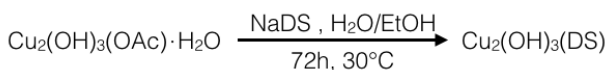
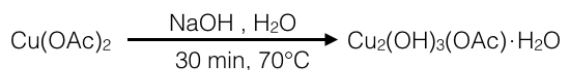


Figure 6. Images en microscopie à balayage électronique des tailles de cristallites de $\text{Cu}_2(\text{OH})_3\text{DS}$ obtenues par échange via $\text{Cu}_2(\text{OH})_3(\text{OAc})$ (gauche) et via optimisation des conditions de synthèse en une étape (droite) et conditions de synthèse permettant de les obtenir (haut).

Ces avancées dans la cristallisation des produits de départ ont permis de résoudre la structure mono-cristal de ce composé jusqu'alors inconnue. La structure est donnée dans la figure 7 ci-dessous.

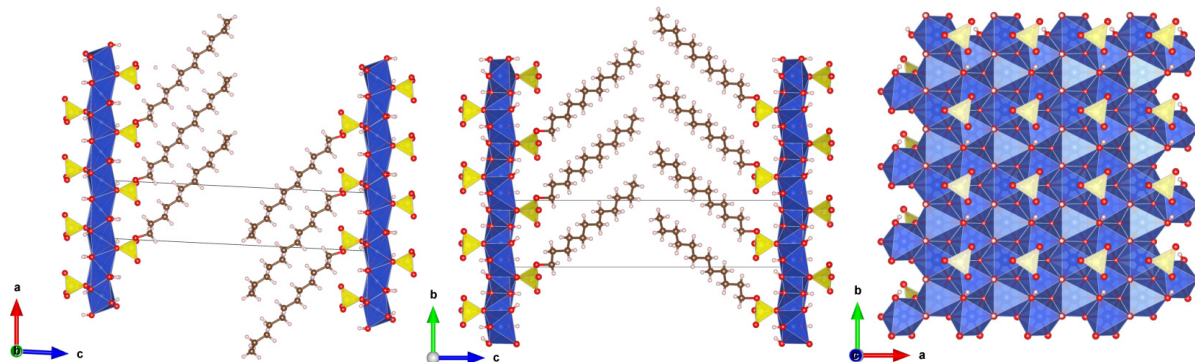


Figure 7. Structure de $\text{Cu}_2(\text{OH})_3(\text{DS})$, groupe d'espace $P2_1$, paramètres de maille : $a = 5.591(10) \text{ \AA}$, $b = 6.108(11) \text{ \AA}$, $c = 26.96(5) \text{ \AA}$, $\alpha = \gamma = 90^\circ$ $\beta = 92.76(3)^\circ$, R -factor : 7%.

Comme indiqué dans la figure ci-dessus, l'arrangement particulier des chaînes alkyl entre les feuillets de type brucite font cristalliser ce composé dans un groupe d'espace non-centrosymétrique. Nous avons donc voulu confirmer cette non-centrosymétrie en effectuant des mesures de génération de seconde harmonique. Ces mesures ont montré une forte anisotropie de réponse de l'échantillon en fonction de la polarisation du laser ainsi qu'une différence d'intensité de réponse en fonction de l'épaisseur de la cristallite (Fig 8). Le laser utilisé pour exciter l'échantillon est un laser pulsé à 900 nm, avec une durée de pulse de l'ordre de 100fs.

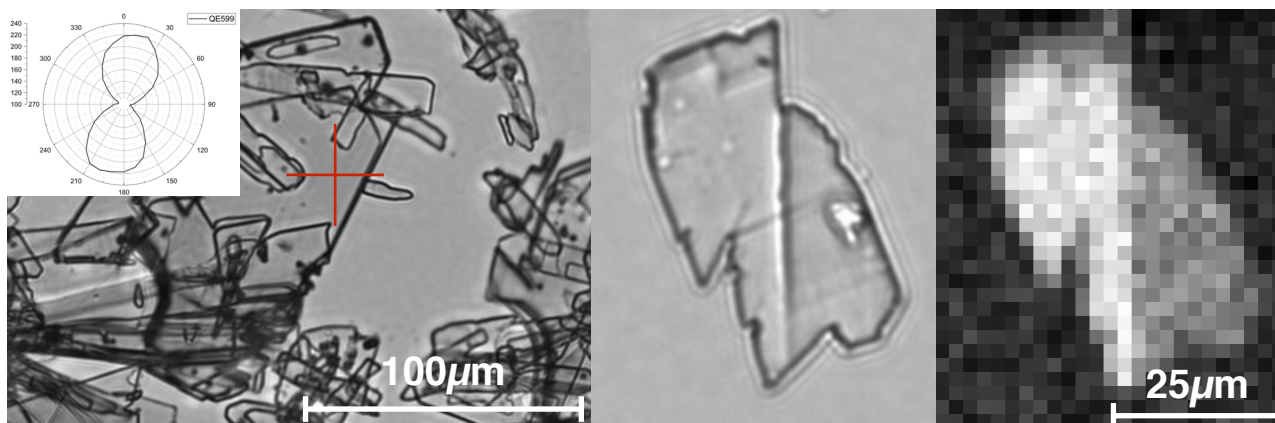


Figure 8. Image optique d'un cristal de $\text{Cu}_2(\text{OH})_3(\text{DS})$ (réponse selon la polarisation de l'échantillon en insert) (gauche) image optique (centre) et cartographie de la réponse de génération de seconde harmonique (droite).

Ces expériences ont permis d'obtenir des composés de départ possédant des tailles de cristallites de dimensions latérales importantes. Durant cette optimisation des conditions de synthèse, il a été observé qu'il était possible, via d'autres conditions de synthèse, de contrôler de la morphologie des composés obtenus, de plaquettes à « papillon ».

Il est à noter que cette méthode n'a pas pu être appliquée sur les composés au cobalt, qui restent beaucoup moins bien cristallisés. Cependant, la structure de l'hydroxide de cobalt a pu être grandement précisée par des études cristallographiques utilisant la diffusion totale des rayons X, par la Fonction de Distribution de Paires (FDP). En effet, les différentes mesures effectuées en collaboration avec Erik Elkaïm le coordinateur de la ligne et Christine Taviot-Guého sur la ligne Cristal au synchrotron Soleil a permis d'extraire les fonctions de distribution de paires de différents composés d'hydroxides de cobalt fonctionnalisés (Fig 9).

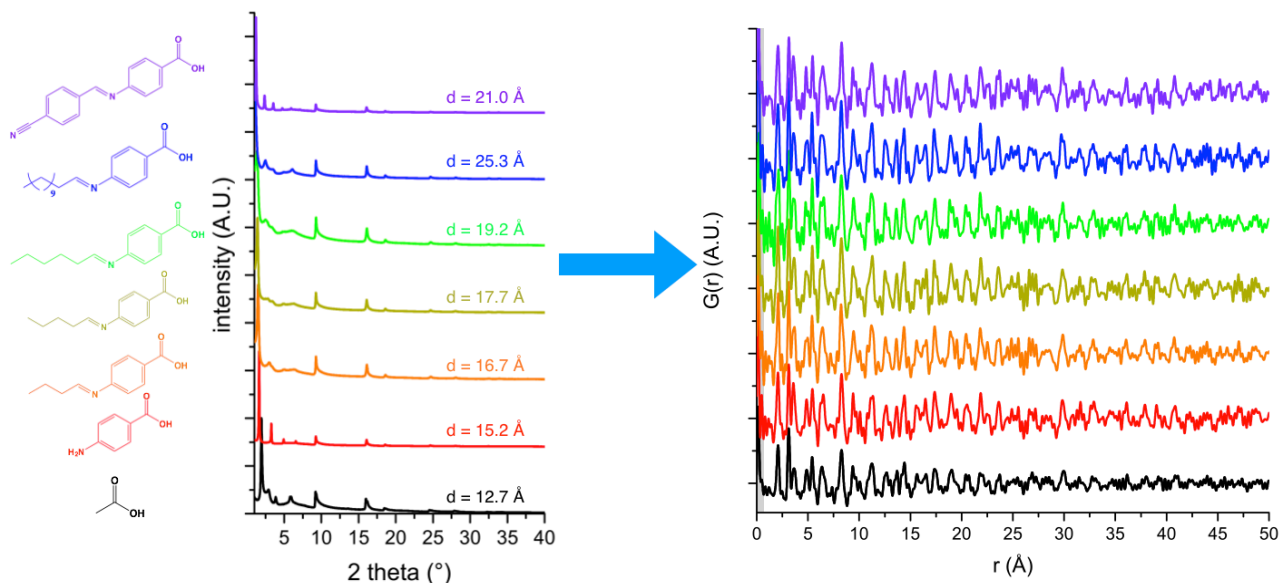


Figure 9. Diffractogrammes d'hydroxides de cobalt hybrides fonctionnalisés avec différentes molécules (gauche) et leur fonction de distribution de paires respectives (droite).

L'étude des FDP sur ces composés hybrides n'a pas permis de localiser la partie organique, dû à la différence importante de facteur de diffusion entre le cobalt et les éléments plus légers tels que le carbone ou l'azote. Cette étude a cependant permis de préciser la structure de l'hydroxide de cobalt et de confronter notre structure aux deux modèles proposés dans la littérature sur un système similaire.^{37, 38} Parallèlement, cette étude sur différents hybrides a permis de démontrer et d'observer les effets du greffage de différentes molécules sur la structuration des hydroxides eux-mêmes (Fig 10).

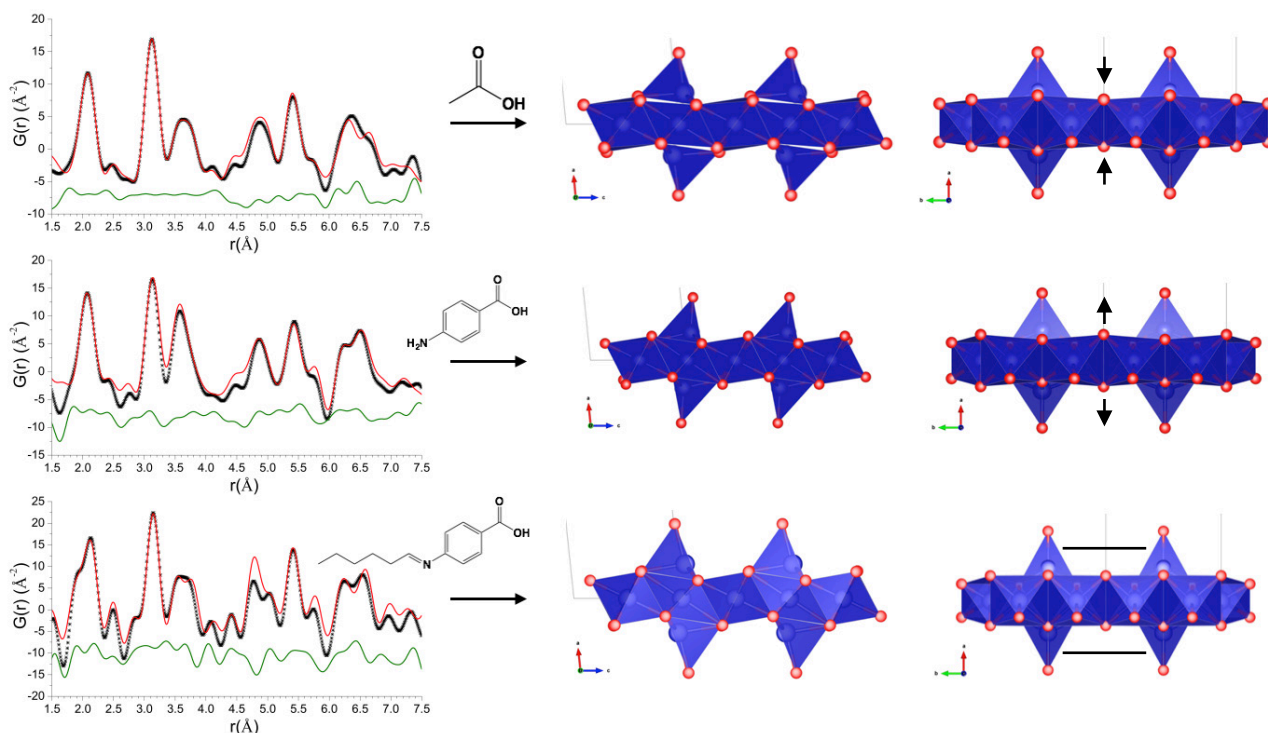


Figure 10. FDP expérimentales (noir) calculées (rouges) et différence (vert) et les structures affinées obtenues.

Une fois la cristallinité des produits de départ à base de cuivre optimisée et la structure de l'hydroxide de cobalt précisée, il a ensuite fallu démontrer la faisabilité du greffage d'acide phosphonique sur ces feuillets inorganiques. Les molécules dérivées de fluorènes ont fait partie de la première série de molécules insérées dans les hydroxydes de cuivre (Fig. 11) et de cobalt (Fig. 14).

Ces premières insertions ont permis de mettre en exergue la différence de réactivité entre les différentes molécules. En effet, les conditions d'insertion allant de 70 heures à température ambiante à 15 minutes à reflux (82°C) nous indiquent que la présence d'acide phosphonique n'est pas le seul facteur conditionnant l'insertion totale et le remplacement des alkyl-sulfonates/sulfates présents dans le produit de départ.

La série d'hybrides obtenus dans l'hydroxide de cuivre montre plusieurs choses. La première est que, selon les spectres infrarouges, l'échange du dodecylsulfate se fait de manière complète avec les différentes molécules de fluorène. La seconde est visible au niveau des distances interlamellaires qui sont, dans le cas des hybrides possédant une fonction de greffage acide phosphonique compatible avec le greffage d'une molécule avec légère inter-digitation.

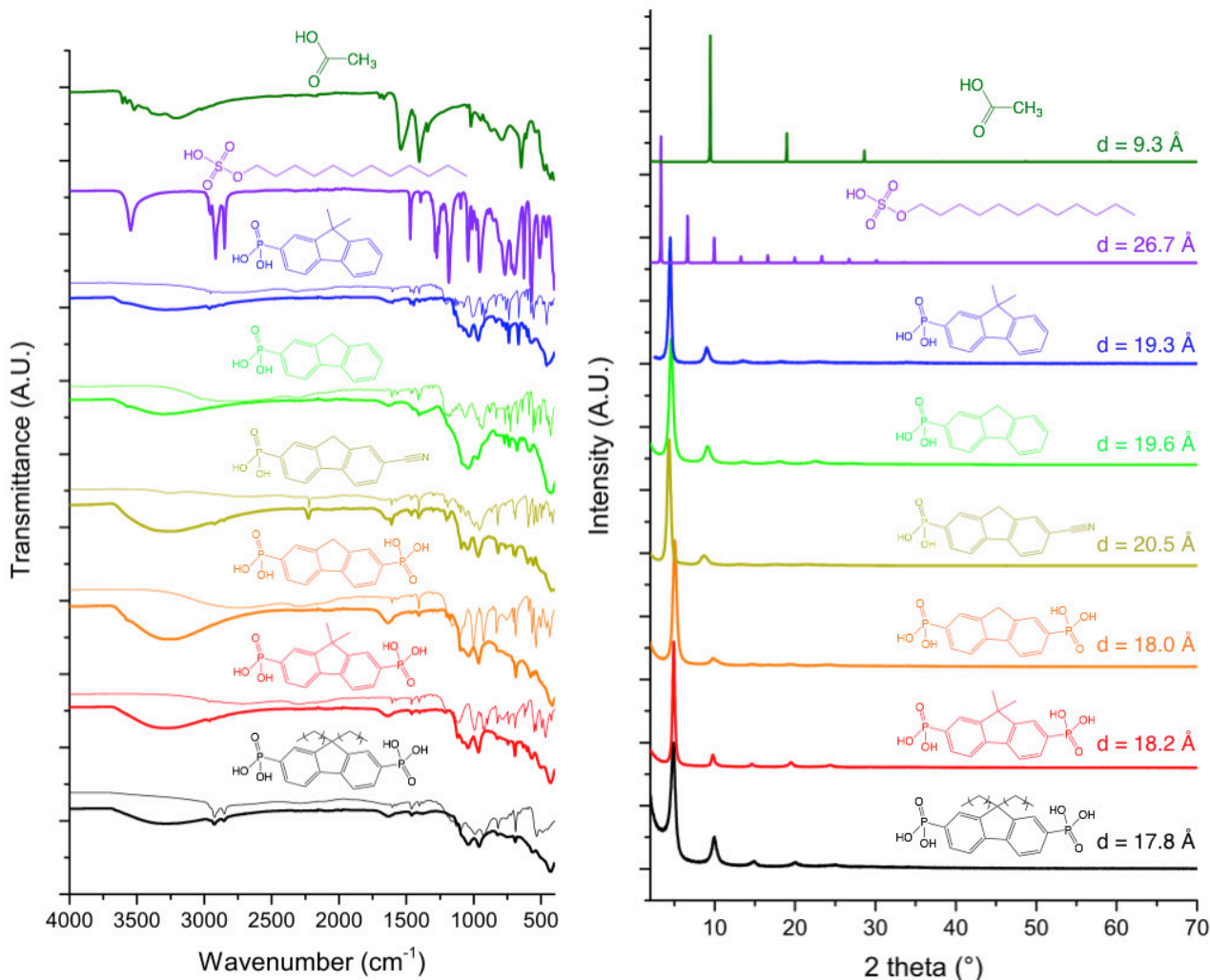


Figure 11. Diffractogrammes (droite) et spectres infrarouge (gauche) des hybrides (gras) et molécules insérées (traits fins) obtenus dans le cas de l'hydroxyde de cuivre.

Le cas des hybrides obtenus à partir de molécules possédant deux fonctions de greffage indique que pour la distance interlamellaire observée (de l'ordre de 18 Å) un greffage pontant des deux fonctions d'accroche au sein du feuillet n'est pas réalisable. Afin d'analyser plus finement ce comportement, en collaboration avec l'équipe de simulation de notre département, des simulations de nos systèmes par une approche Car-Parrinello de dynamique moléculaire ont été effectuées (Fig. 12).

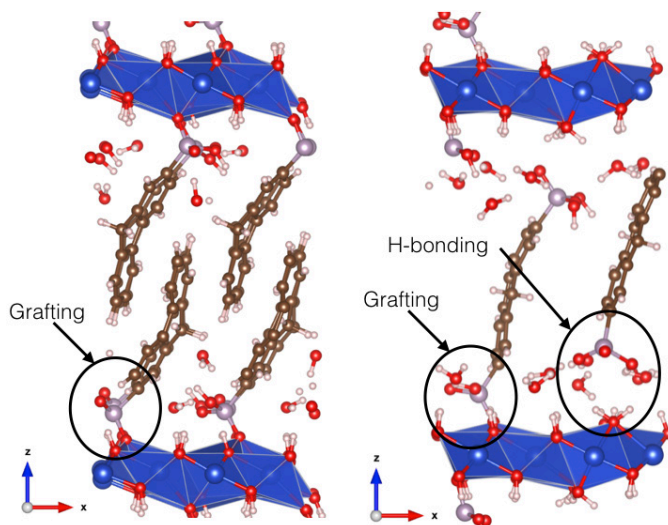


Figure 12. Simulations d'un hybride dans l'hydroxyde de cuivre fonctionnalisés avec un fluorène mono-phosphonique (gauche) et bi-phosphonique (droite).

On peut observer dans la figure 12 ci-dessus que, si le cas des fluorènes mono-phosphonique montre bien un greffage avec une interdigitation des molécules de fluorène, le cas des fluorènes di-phosphoniques montre clairement la coexistence d'un greffage d'un côté et de la formation d'un réseau de liaisons hydrogène via des molécules d'eau de l'autre. Ce comportement souligne l'importance de la présence d'eau au sein du milieu interfoliaire. Il a été possible de combiner expérience et simulations afin de tenter d'obtenir un bis-greffage au sein des feuillets. Les résultats de cette analyse combinée sont présentés dans la figure 13 ci dessous.

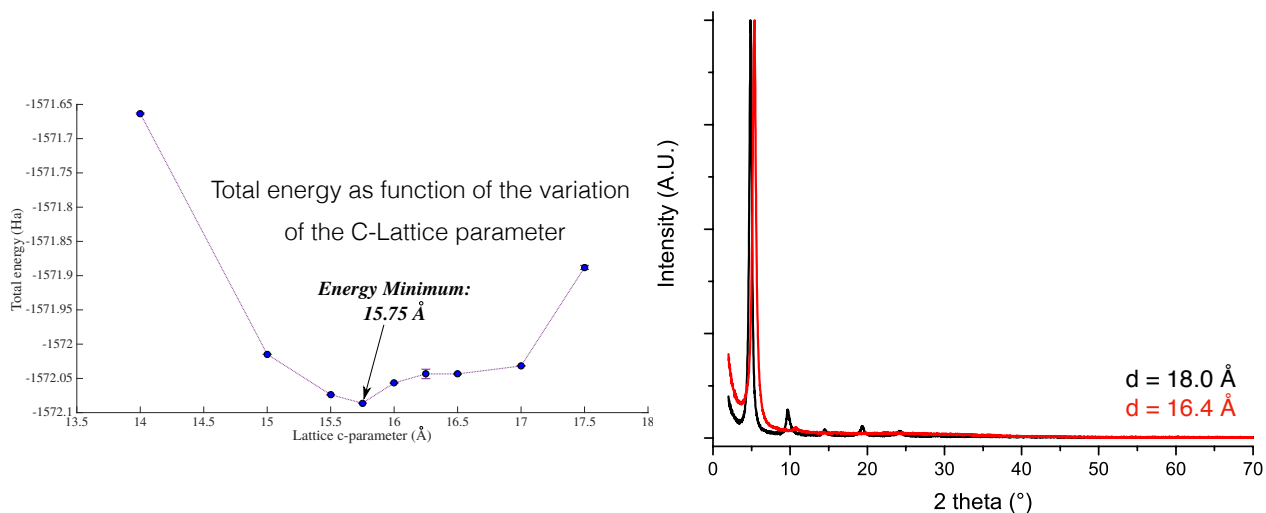


Figure 13. Simulations montrant le minimum d'énergie pour un système bis-greffé dans l'hydroxide de cuivre (gauche) et diffractogrammes obtenus sur le système original (noir) et après chauffage à 140°C pendant 2 heures (rouge).

Le chauffage de l'hydroxide obtenu nous a permis de modifier la distance interlamellaire de 18.0 Å à 16.4 Å, cette distance est en bon accord avec la distance théorique de minimum d'énergie pour une structure anhydre et bis-greffée. Ce comportement ouvre la voie à une étude en température plus complète des différents hybrides obtenus. Le rôle de l'eau étant primordial pour la réactivité (l'eau est nécessaire pour effectuer la réaction d'insertion) ainsi que sa forte présence au sein de l'espace interfoliaire (stabilisation du greffage de l'acide phosphonique sur l'hydroxide).

Fort de cette expérience, l'insertion des composés dérivés de fluorène dans les hydroxides de cobalt a été effectuée de la même façon (Fig. 14). Comme observé sur la série avec l'hydroxide de cuivre, la spectroscopie infrarouge nous indique que le dodécylsulfonate est entièrement échangé par les molécules de fluorène. La diffraction des rayons X nous indique quant à elle trois types de comportements.

Les premiers sont les produits avec une distance interlamellaire de l'ordre de 19-20 Å qui est obtenue avec les fluorènes possédant une seule fonction de greffage, les deuxièmes sont les hybrides obtenus avec deux fonctions de greffage acide phosphonique et qui possèdent un encombrement latéral, la distance interlamellaire est de 18.8 Å ce qui, contrairement à ce qui a été obtenu dans l'hydroxide de cuivre, est en bon accord avec un greffage pontant des molécules sur les feuillets. Une troisième catégorie d'hybrides a été obtenue, il s'agit cette fois-ci d'hybrides possédant une distance interlamellaire très courte (11.8 Å) avec la molécule possédant deux fonctions de greffage et un faible encombrement latéral. Cette très faible distance interlamellaire conjuguée au faible taux d'insertion mesuré (0.17 molécules par unité de formule contre 0.29 pour le fluorène possédant des méthyles en position latérale par exemple) nous a indiqué qu'il était possible que les molécules de fluorène soient présentes quasiment à plat dans l'espace interfoliaire comme présenté dans l'illustration ci dessous (Fig. 15).

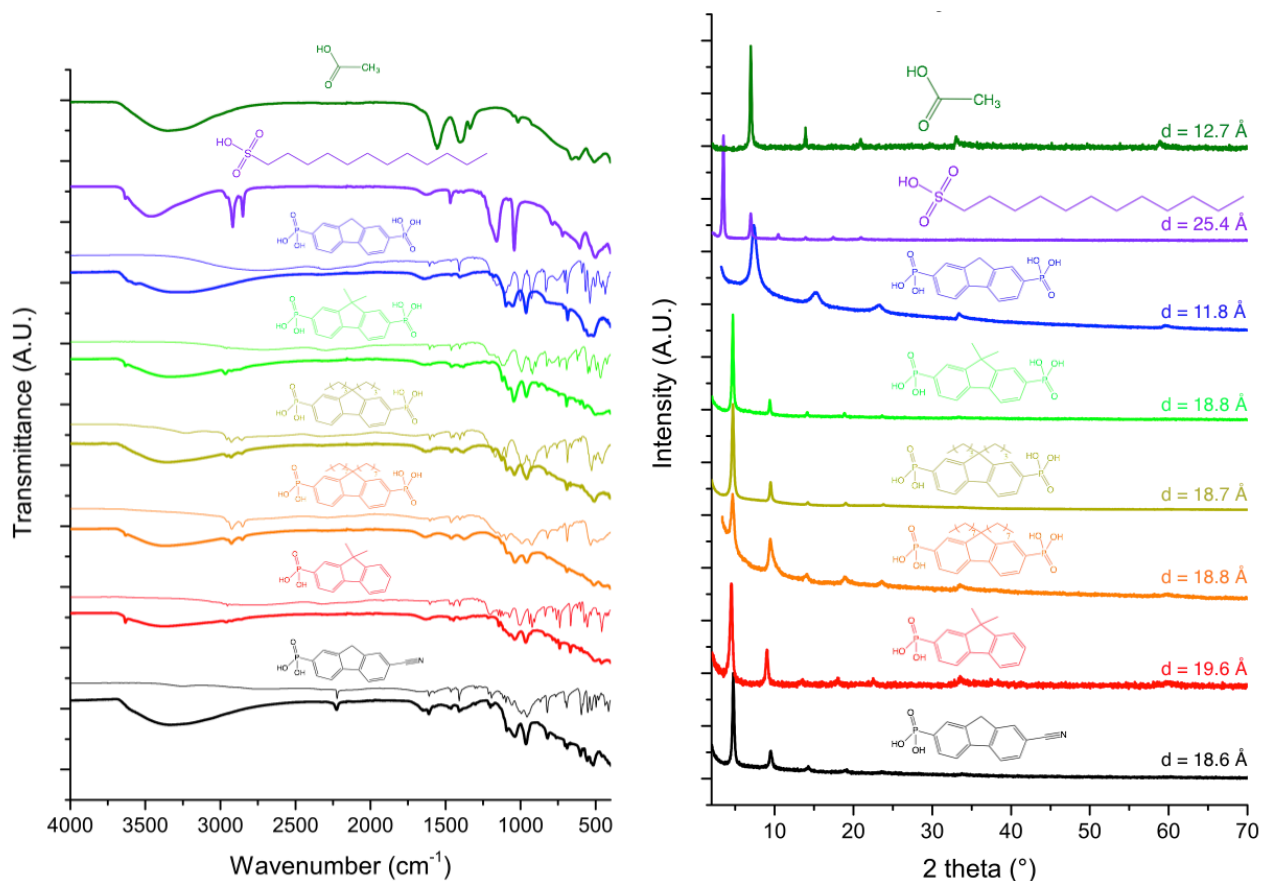


Figure 14. Diffractogrammes (droite) et spectres infrarouge (gauche) des hybrides (gras) et molécules insérées (traits fins) obtenus dans le cas de l'hydroxyde de cobalt.

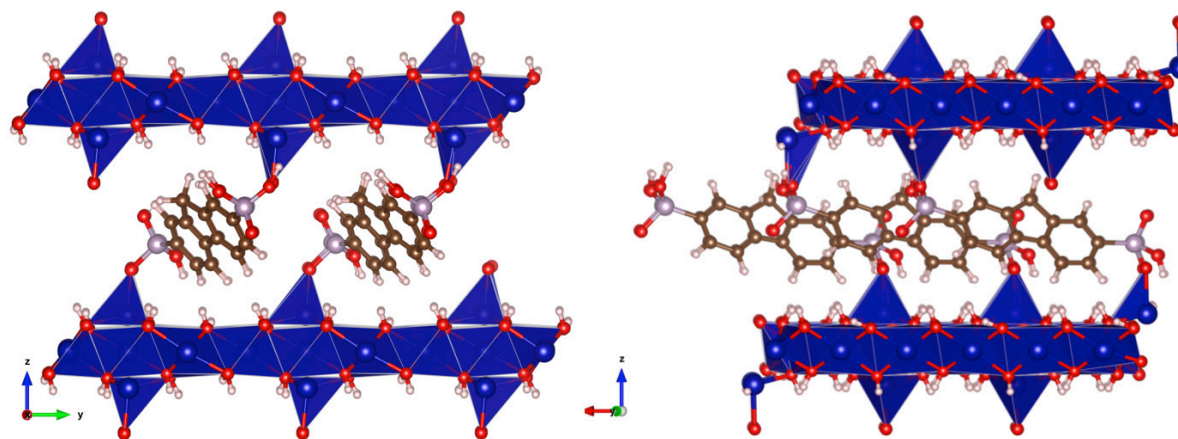


Figure 15. Illustration de l'arrangement possible des molécules de fluorène au sein de l'hydroxyde de cobalt.

Une fois les différentes molécules de fluorène insérées, il a été important de pouvoir analyser la morphologie et les taux d'insertion des différents hybrides obtenus. Les résultats sont présentés dans le tableau suivant :

Molécule insérée	Reference	Ratio PO ₃ :DS (1 = 0.165 mmol)	pH	Temperature	Time (h)
	P-Fluo-HCCu	4:1	8.8	Reflux (82°C)*	0.25
	P-Fluo-CCCu	2:1	8.3	R.T.	70

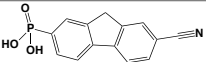
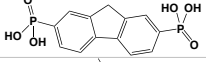
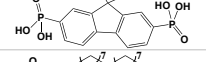
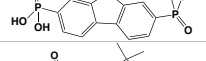
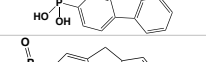
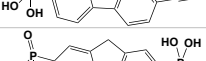
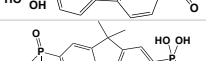
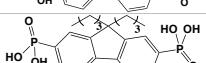
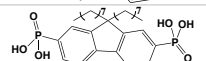

Molécule inserted	Reference	Ratio PO ₃ :DS (1 = 0.165 mmol)	pH	Temperature	Time (h)
	P-Fluo-CN<Cu	2:1	8.3	Reflux (82°C)*	4
	P ₂ -Fluo-H<Cu	8:1	8.8	Reflux (82°C)*	0.25
	P ₂ -Fluo-C<Cu	4:1	8.3	Reflux (82°C)*	1
	P ₂ -Fluo-C ₈ <Cu	4:1	8.3	70°C	2
	P-Fluo-C<Cu	1.4:1	8.3	R.T.	24
	P-Fluo-CN<Co	1.4:1	8.8	Reflux (82°C)	2
	P ₂ -Fluo-H<Co	2.8:1	8.6	Reflux (82°C)	1
	P ₂ -Fluo-C<Co	2.8:1	8.3	Reflux (82°C)	2
	P ₂ -Fluo-C ₄ <Co	2.8:1	8.5	Reflux (82°C)	2.5
	P ₂ -Fluo-C ₈ <Co	2.8:1	8.3	Reflux (82°C)	1.5

Figure 16. Conditions de synthèse après optimisation utilisées pour obtenir des hybrides possédant une seule distribution de distances interlamellaire.

De façon générale les conditions optimisées pour l'obtention des différents hybrides font ressortir plusieurs tendances. Le premier étant qu'il est nécessaire d'augmenter le ratio PO₃:DS₀ dans le cas des molécules comptant deux fonctions d'accroche acide phosphonique. Le deuxième étant le contrôle du pH de la solution de départ qui est grandement dépendant de la solubilité de la molécule d'intérêt. En effet, les molécules de fluorène avec des fonctions latérales par exemple, ne sont pas solubles dans l'eau sans ajout de soude pour augmenter le pH. Les conditions de température et de temps de réaction quant à elles ne suivent pas de tendance précise. Pour les fluorènes possédant des fonctions latérales méthyle, les conditions de température ambiante et temps long sont suffisantes, en revanche, pour tous les autres hybrides, un chauffage est nécessaire avec des temps de réaction très variables en fonction de chaque molécule.

La morphologie des différents hybrides obtenus peut-être observée dans les figures 17 et 18 ci-dessous, on peut observer que pour les hybrides obtenus avec l'hydroxyde de cuivre, la morphologie plaquettaire typique pour ce type de matériaux est bien conservée après fonctionnalisation malgré un changement de la texturation à la surface des plaquettes (Fig. 17).

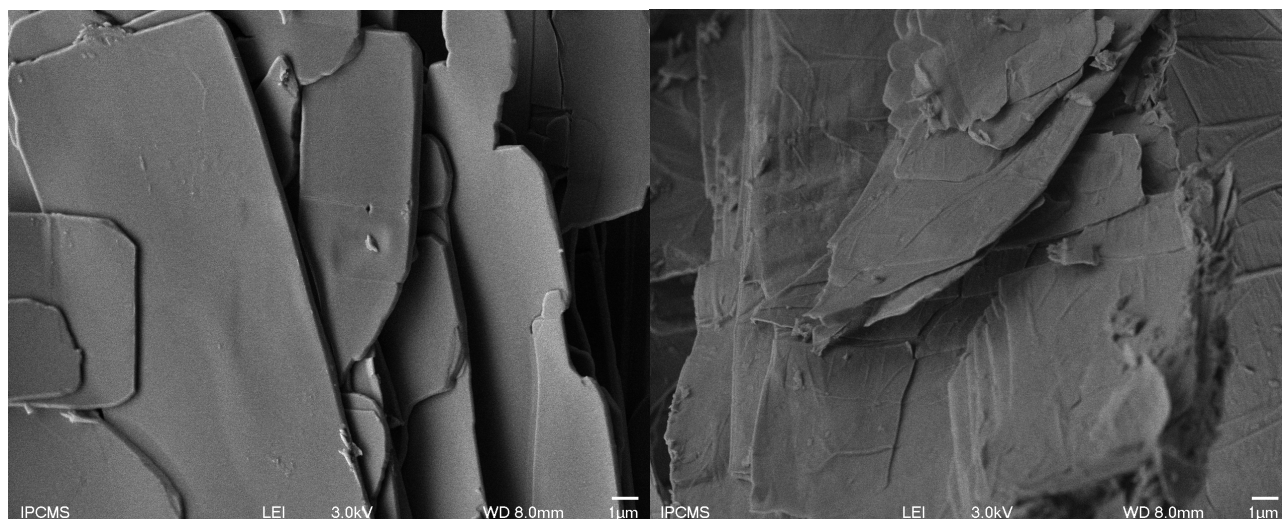


Figure 16. Morphologies de Cu₂(OH)₃DS (gauche) et des hybrides obtenus à base d'hydroxyde de cuivre (droite).

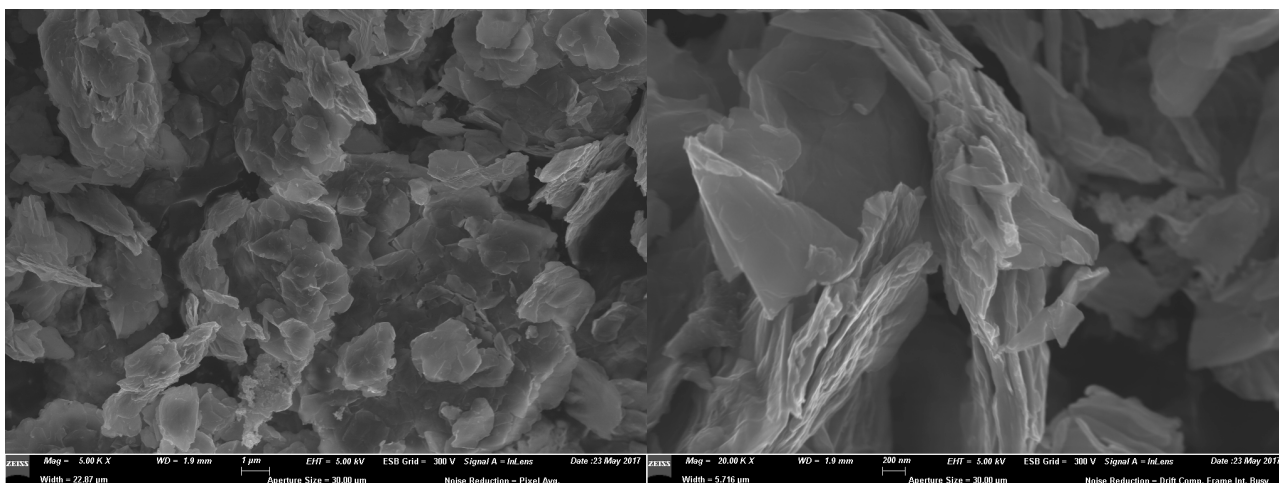


Figure 17. Morphologies de $Co_2(OH)_{3.5}(DSO)_{0.5}$ (gauche) et des hybrides obtenus à base d'hydroxyde de cobalt (droite).

Il est possible de voir sur la figure ci-dessus que, si la morphologie plaquettaire est conservée avec l'hydroxyde de cobalt, les dimensions latérales de ces plaquettes sont bien inférieures à celles obtenues dans l'hydroxyde de cuivre avec des dimensions de l'ordre du micromètre de diamètre pour moins d'une centaine de nanomètre d'épaisseur.

Une fois la morphologie des différents composés étudiée, il a été important d'étudier les différents taux d'insertions obtenus dans les hydroxydes de cuivre et de cobalt. Ces résultats sont condensés dans la figure 18 ci-dessous :

Contenu en eau (ATG mesuré (calculé))	Ratio Cu:P via EDX mesuré (calculé)	Résultats de Micro-analyse mesuré (calculé)	Formule obtenue
7.2% (19.7%)	6.35 (4.54)	Cu : 36.80 (36.88), C : 20.15 (19.94) H : 3.63 (4.04), P : 3.79 (3.95)	P-Fluo-HcCu $Cu_2(OH)_{3.56}(C_{13}H_{10}O_3P)_{0.44} \cdot 2.7H_2O$
13.6% (11.3%)	3.85 (4.00)	Cu : 34.64 (34.91), C : 24.72 (24.74) H : 4.03 (4.18), P : 3.82 (4.26)	P-Fluo-CcCu $Cu_2(OH)_{3.5}(C_{15}H_{14}O_3P)_{0.5} \cdot 2.3H_2O$
9.0% (7.7%)	5.39 (4.76)	C : 23.95 (23.61), H : 3.22 (3.44), N : 1.57 (1.69)	P-Fluo-CNcCu $Cu_2(OH)_{3.5}(C_{14}H_8O_3PN)_{0.42}(DS)_{0.08} \cdot 1.5H_2O$
9.5% (19.4%)	4.99 (4.34)	Cu : 38.99 (39.29), C : 11.18 (11.1) H : 3.03 (4.00), P : 4.19 (4.41)	P ₂ -Fluo-HcCu $Cu_2(OH)_{3.54}(C_{13}H_{10}O_6P_2)_{0.23} \cdot 3.5H_2O$
17.0% (15.8%)	5.97 (10.00)	Cu : 41.4 (40.80), C : 11.74 (12.00) H : 3.74 (3.17), P : 4.04 (3.23)	P ₂ -Fluo-CcCu $Cu_2(OH)_{3.6}(C_{15}H_{14}O_6P_2)_{0.2} \cdot 2.7H_2O$
9,2% (14,0%)	3.80 (6.25)	Cu : 39.11 (39.54), C : 17.32 (17.34) H : 3.86 (4.83), P : 3.94 (3.09)	P ₂ -Fluo-C ₈ cCu $Cu_2(OH)_{3.68}(C_{29}H_{42}O_6P_2)_{0.16} \cdot 2.5H_2O$
10.7% (8.0%)	5.43 (5.88)	Co : 39.53 (39.82), C : 21.01 (20.69) H : 3.63 (3.75), P : 3.73 (3.56)	P-Fluo-CcCo $Co_2(OH)_{3.66}(C_{15}H_{13}O_3P)_{0.34} \cdot 1.3H_2O$
12.1% (11.4%)	4.32 (5.40)	Co : 45.9 (37.35), C : 19.77 (19.71) H : 3.38 (3.50), P : 2.24 (3.63)	P-Fluo-CNcCo $Co_2(OH)_{3.63}(C_{14}H_8O_3PN)_{0.37} \cdot 2H_2O$
-	6.50 (5.88)	C : 10.61 (10.53) H : 3.21 (2.94)	P ₂ -Fluo-HcCo $Co_2(OH)_{3.66}(C_{13}H_{10}O_6P_2)_{0.17} \cdot 1H_2O$
10.5% (10.0%)	5.97 (3.45)	Co : 38.24 (38.01), C : 16.95 (17.47) H : 3.37 (3.53), P : 5.83 (4.65)	P ₂ -Fluo-CcCo $Co_2(OH)_{3.42}(C_{15}H_{14}O_6P_2)_{0.29} \cdot 1.7H_2O$
-	-	Co : 40.80 (41.31), C : 15.74 (15.91) H : 4.24 (4.00), P : 3.36 (3.91)	P ₂ -Fluo-C ₄ cCo $Co_2(OH)_{3.64}(C_{21}H_{26}O_6P_2)_{0.18} \cdot 1.5H_2O$
10.0% (18,0%)	6.87 (10.00)	Co : 40.35 (40.79), C : 12.06 (12.13) H : 3.58 (4.81), P : 2.67 (2.15)	P ₂ -Fluo-C ₈ cCo $Co_2(OH)_{3.8}(C_{29}H_{42}O_6P_2)_{0.10} \cdot 2.9H_2O$

Figure 18. Taux d'insertions calculés à partir des résultats de micro-analyses et accord obtenu avec les analyses ATG/ATD et EDX entre les formules calculées et observées.

Les taux d'insertion (hormis le cas particulier de P₂-Fluo-HcCo où les molécules sont greffées à plat) sont en bon accord avec les résultats obtenus précédemment au laboratoire. Les taux d'insertion diminuent avec l'augmentation de l'encombrement de la molécule à insérer ainsi qu'avec le nombre de fonctions de greffage. De plus, à molécule comparable, les taux de greffage observés dans l'hydroxyde de cobalt sont plus faibles que dans l'hydroxyde de cuivre, ceci est probablement expliqué par le fait que le greffage se ferait au niveau du tétraèdre de cobalt uniquement.

Afin d'obtenir un maximum d'informations sur la configuration des différentes molécules dans l'espace interlamellaire, nous avons fait des mesure de luminescence sur ces composés (Fig. 19). En effet, le fluorène est une molécule reconnue pour sa luminescence, et la conservation de ses propriétés d'émission sont une observable indirecte de l'état d'empilement des molécules au sein de l'espace interfoliaire.

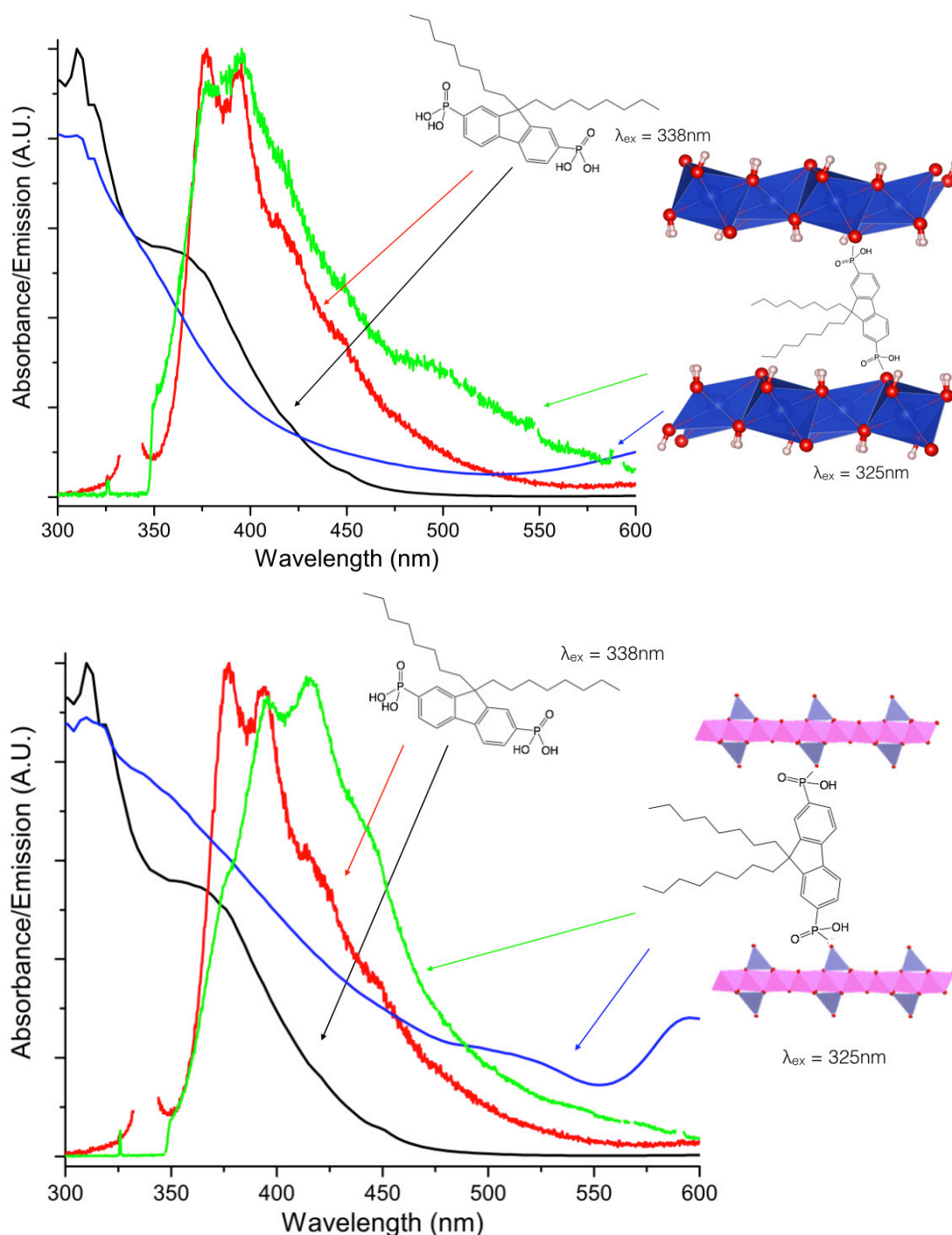


Figure 19. Mesures d'absorbtion (bleu et noir) et de luminescence (rouge et vert) à l'état solide de P₂-Fluo-C₈ et P₂-Fluo-C₈Cu (haut) et P₂-Fluo-C₈Co (bas)

Ces mesures de luminescence nous ont permis d'observer une conservation de la luminescence pour les hybrides avec les chaînes octyl, le léger décalage observé dans les mesures d'émission dans le cobalt est probablement dû à la réabsorption de la matrice inorganique qui est plus importante dans la région des 400 nm que pour l'hydroxyde de cuivre. De façon intéressante, cette luminescence n'est plus observée avec les hybrides de fluorènes possédant de plus courtes chaînes ou bien même des protons semblant indiquer un empilement des molécules plus important qui désactive leur luminescence. Des études plus poussées comme l'extraction de la FDP sur ces composés pourraient éventuellement permettre de pousser plus loin cette étude.

Forts de cette expérience acquise avec l'insertion de dérivés de fluorène, nous avons effectué l'insertion d'autres molécules utilisant un cycle benzénique ou un thiophène comme plateforme rigide. Le but étant toujours l'obtention d'une polarisation électrique dans le matériau final.

Les diffractogrammes et spectres infrarouges de la série effectuée avec des dérivés benzéniques est présentée ci-dessous :

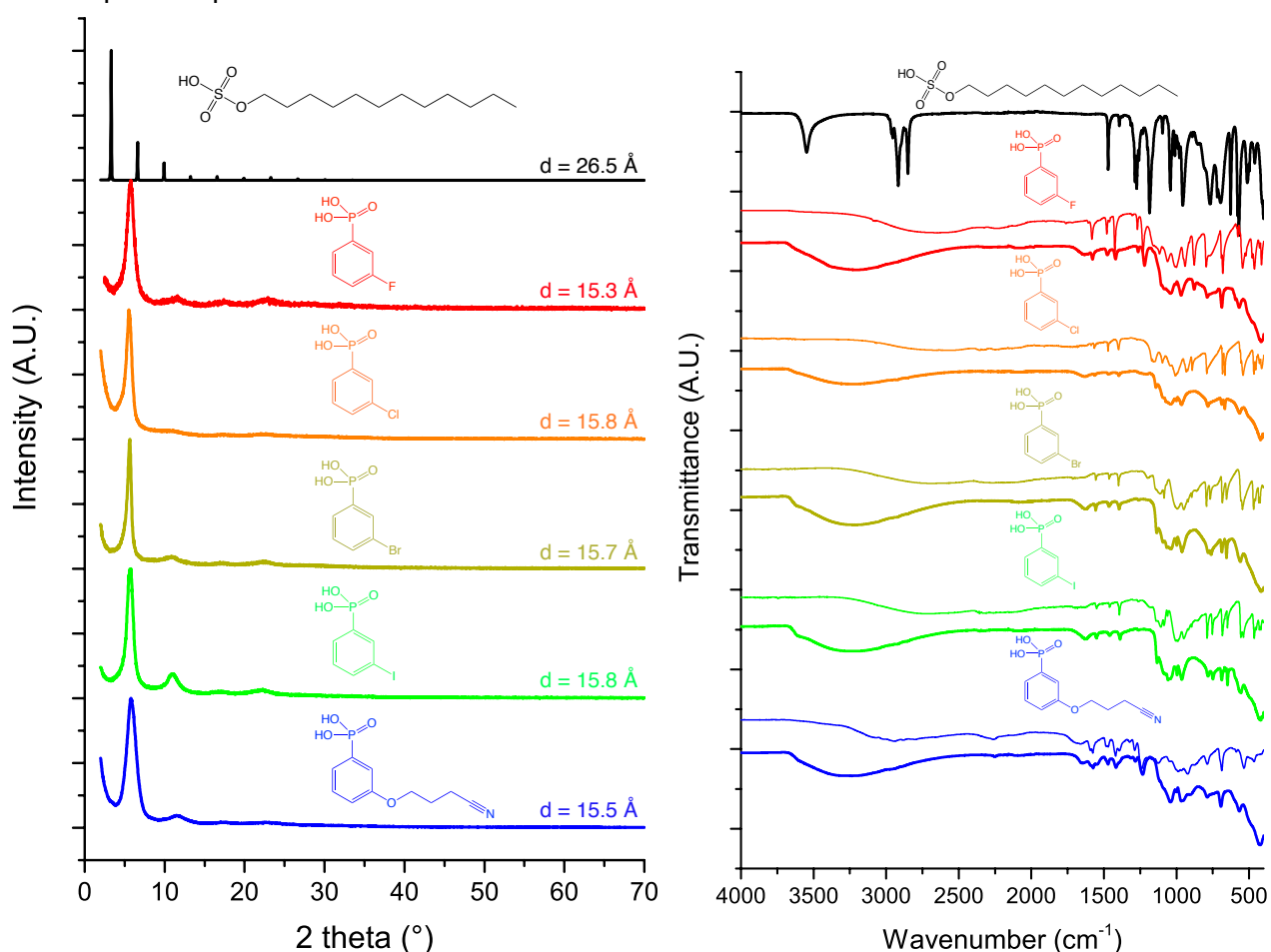


Figure 20. Diffractogrammes de rayons X sur poudre (gauche) et spectres infrarouges (droite) des différents hybrides obtenus dans l'hydroxyde de cuivre (trait épais) et des molécules organiques seules (trait fin).

Les spectres infrarouges des hybrides obtenus dans l'hydroxyde de cuivre indiquent bien le remplacement du dodecylsulfate par les différentes molécules d'intérêt. Les diffractogrammes indiquent une distance interlamellaire ne variant que d'environ 0,3 Å avec une distance interlamellaire moyenne de 15,6 Å, ces distances semblent conforter un arrangement similaire des molécules dans l'espace interfoliaire, supprimant une variable potentielle dans la détermination de l'origine des propriétés magnéto-capacitives observées. En effet, l'objectif principal de cette série est de montrer si la différence de polarisabilité/polarisation de la liaison C-X influe sur les propriétés magnéto-capacitives.

La figure ci-dessous montre les différents diffractogrammes et spectres infrarouges obtenus dans l'hydroxyde de cobalt.

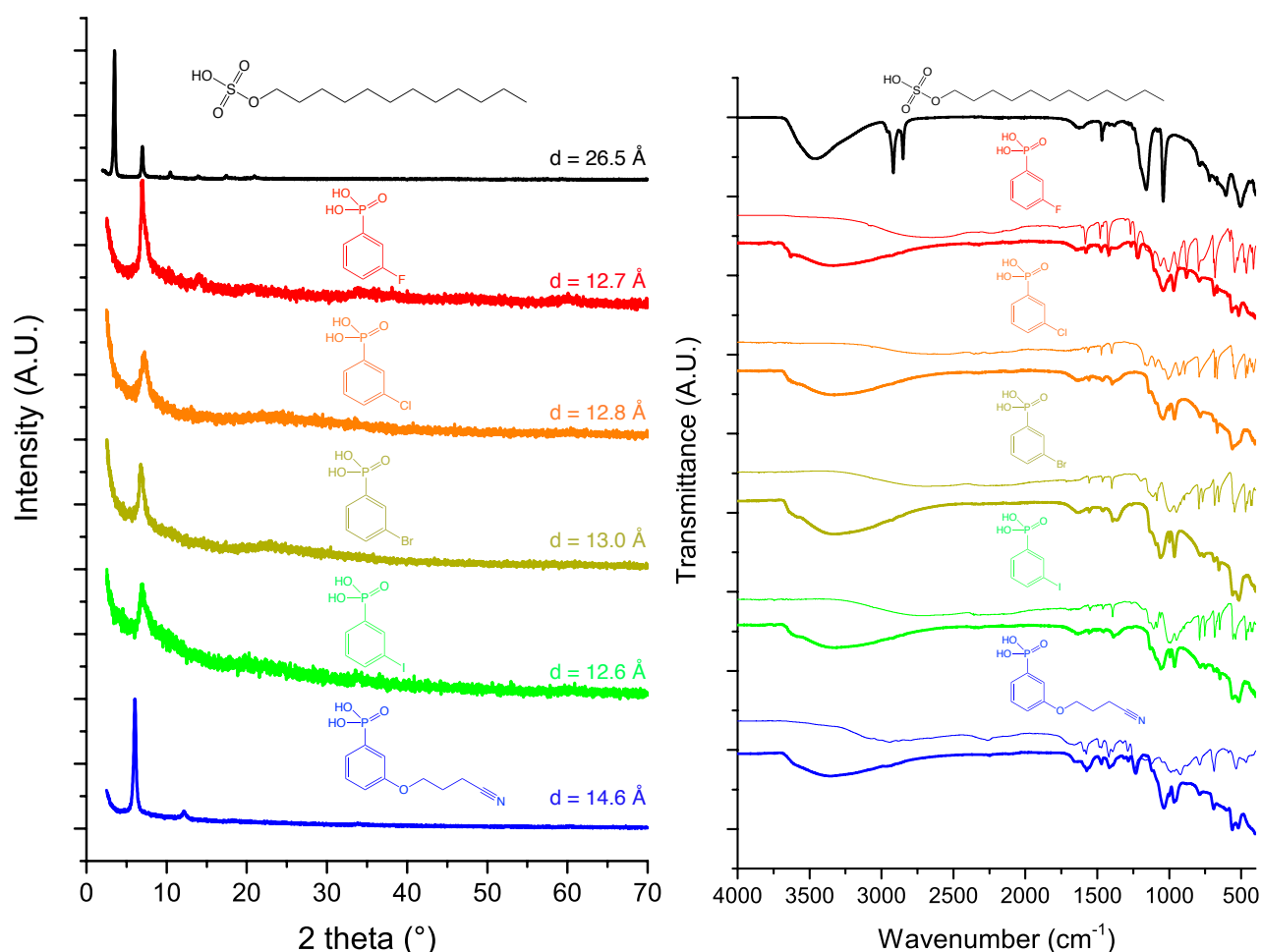


Figure 21. Diffractogrammes de rayons X sur poudre (gauche) et spectres infrarouges (droite) des différents hybrides obtenus dans l'hydroxyde de cobalt (trait épais) et des molécules organiques seules (trait fin).

Dans le cas de l'hydroxyde de cobalt, les cristallinités observées sont très faibles mais les distances inter lamellaires obtenues sont compatibles avec un arrangement quasi à plat des différentes molécules au sein de l'espace interlamellaire. La spectroscopie infrarouge indique quant à elle bien un échange entre le dodecylsulfonate et les différents dérivés benzéniques dont la signature caractéristique est présente de façon claire dans la gamme des 1300-1700 cm^{-1} notamment avec la signature des liaisons C-C du dérivé benzénique.

Comme dans le cas particulier de $\text{P}_2\text{-Fluo-HcCo}$, les molécules possédant des fonctions d'accroche acide phosphonique et étant quasiment plates semblent favoriser une mise à plat de la molécule dans l'espace interfeuillet. Les raisons précises sur les mécanismes menant à cette configuration restent cependant à étudier.

Un autre aspect important de ma thèse a consisté à la préparation et à la mesure des propriétés multiferroïques des échantillons. Dans un premier temps, les propriétés magnétiques des matériaux ont été mesurées de façon standard sur des poudres compactées dans des gélules scellées. Ces mesures ont donné les résultats suivants pour les hybrides de fluorènes obtenus dans des hydroxydes de cuivres :

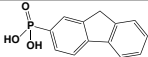
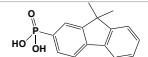
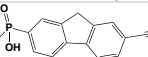
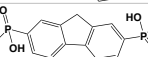
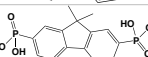
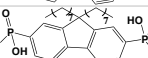
Molécule insérée	Constante de Curie ($\text{emu}\cdot\text{K}\cdot\text{mol}^{-1}$)	Température de Weiss θ (K)	Aimantation à 7 T (μ_B) (à 1,8 K)
	0,72	-12,9	0,39
	0,94	-31,7	0,49
	0,62	-11,1	0,32 ($\mu_0H = 5 \text{ T}$)
	0,76	-30,1	0,30
	0,71	-3,3	0,50 ($\mu_0H = 5 \text{ T}$)
	0,95	-19,9	0,57

Figure 22. Propriétés magnétiques des hybrides obtenus dans l'hydroxyde de cuivre.

De façon générale, tous les hybrides obtenus dans l'hydroxyde de cuivre ont un comportement général antiferromagnétique indiqué par une décroissance du produit de la susceptibilité magnétique et de la température en fonction de l'abaissement de la température (Fig. 23).

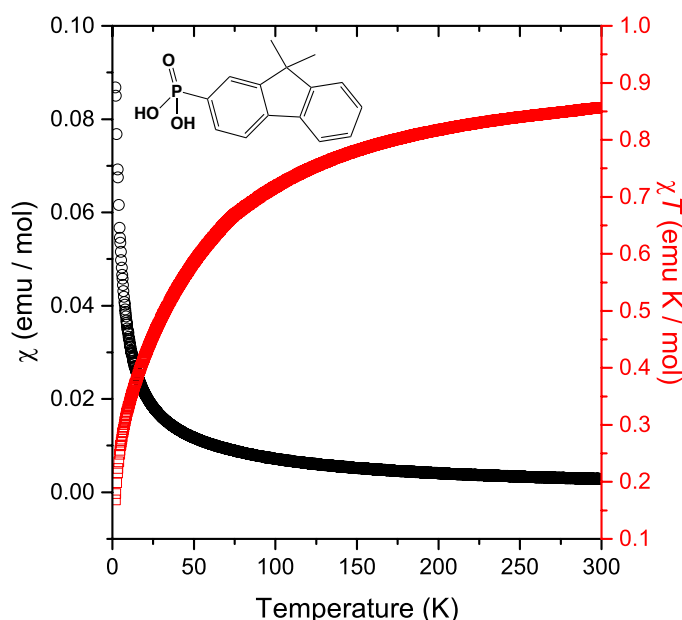


Figure 23. Susceptibilité magnétique et produit de la susceptibilité magnétique et de la température en fonction de la température, comportement typique de tous les hybrides obtenus dans l'hydroxyde de cuivre.

Aucune mise en ordre magnétique n'a pu être observée au delà de 2 K par des mesures de susceptibilité sous champ alternatif.

Le comportement magnétique des hybrides obtenus dans l'hydroxyde de cobalt est plus intéressant, en effet, un couplage antiferromagnétique entre les cobalt II en site tétraédriques et les cobalt II en site octaédriques existe et entraîne un moment résiduel non-nul dû à la non-compensation des spins des sites octaédriques par les sites tétraédriques.

Les résultats des mesures de comportement magnétiques pour les hybrides à base d'hydroxyde de cobalt ont été résumés dans le tableau suivant :

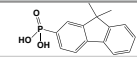
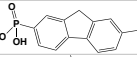
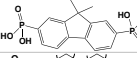
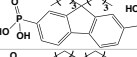
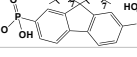
Molécule insérée	Constante de Curie (emu·K·mol ⁻¹)	Température de Weiss θ (K)	Température de Curie T_C (K)	Aimantation à 7 T (μ_B) (1,8 K)	Champ coercitif (T) (1,8 K)
	6,09	-21,7	11,8	2,43	0,20
	5,70	-31,4	8,5	2,46	0,10
	5,95	-22,4	11,9	2,43	0,33
	5,73	-63,4	13,5	1,95 (2 K, 5 T)	-
	6,02	-13,6	17,8/11,0/6,3	2,92	0,22

Figure 24. Propriétés magnétiques des hybrides obtenus dans l'hydroxyde de cobalt.

Ces données nous indiquent des constantes de Curie en accord avec un mélange de cobalt II tétraédriques et de cobalt II octaédriques, ainsi que des températures de mise en ordre magnétique d'environ 11 K avec des variations relativement importantes en fonction du fluorène inséré, en particulier avec P₂-Fluo-C₈Co qui possède plusieurs températures de mise en ordre magnétique, probablement dues à la présence de désordre important généré par les configurations des chaînes alkyl du fluorène entraînant une différence de configuration. Les faibles valeurs d'aimantation à 7 T couplées avec la remontée du produit χT à basse température (Fig. 25) nous indiquent que ces hybrides ont un comportement général ferrimagnétique.

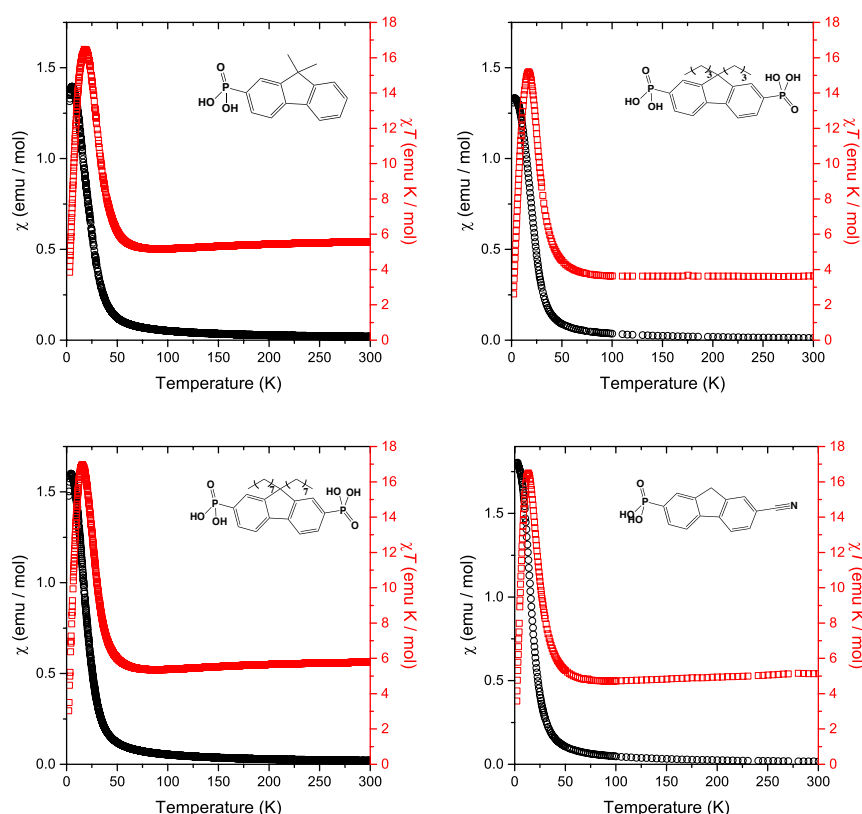


Figure 25. Susceptibilité magnétique et produit χT en fonction de la température, comportement typique de quelques hybrides obtenus à partir d'hydroxyde de cobalt.

Une fois les propriétés magnétiques des composés étudiés, il a fallu mesurer les propriétés diélectriques de ces matériaux. Comme décrit précédemment, ces composés sont sous formes de poudres qu'il a fallu pastiller par pressage à froid afin d'obtenir des pastilles de 5 mm de diamètre et d'une épaisseur typique de 50 à 100 μm . Des contacts à la laque d'argent ont été posés sur les deux faces des pastilles afin de former des électrodes, et ces contacts ont été assurés par des fils de cuivre directement reliés à l'impedancemètre (Fig. 26).

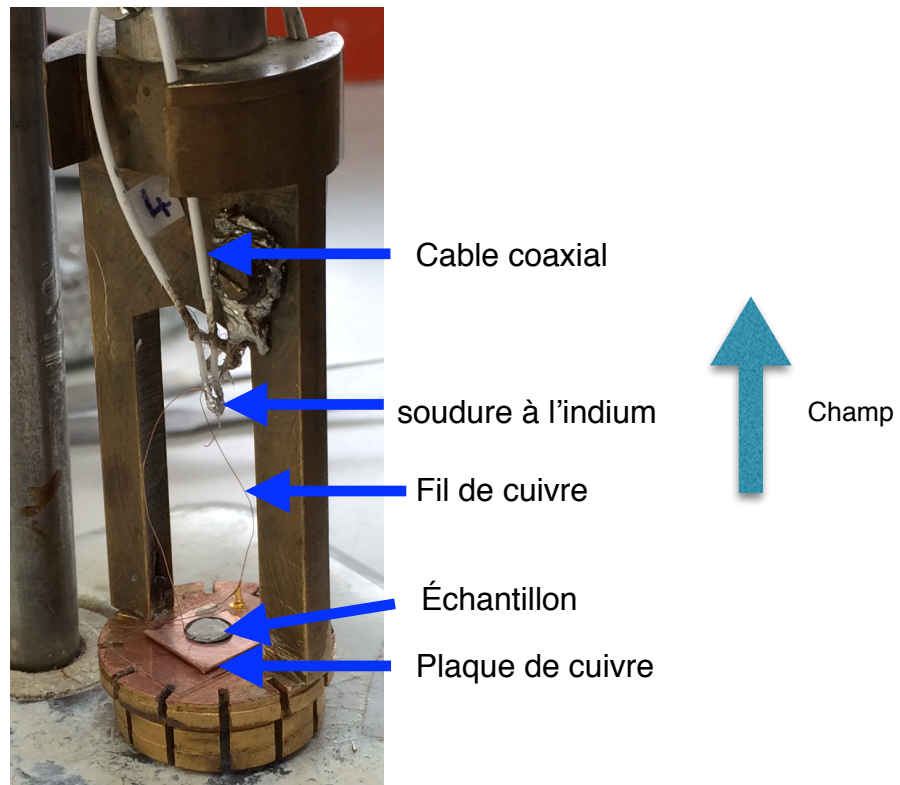


Figure 26. Image du montage de l'échantillon sur la cane de mesure.

Les premiers essais ont été effectués sur le montage indiqué en figure 26, mais n'a pas donné de résultats concluants, le montage a donc été simplifié avec des mesures sur des contacts d'argent des deux côtés de la pastille qui a permis l'obtention de mesures propres et de résultats démontrant un effet magnéto-capacitif de façon claire (Fig. 27) ainsi qu'un effet anisotrope (Fig. 28) rarement observé pour ce type de mesures.

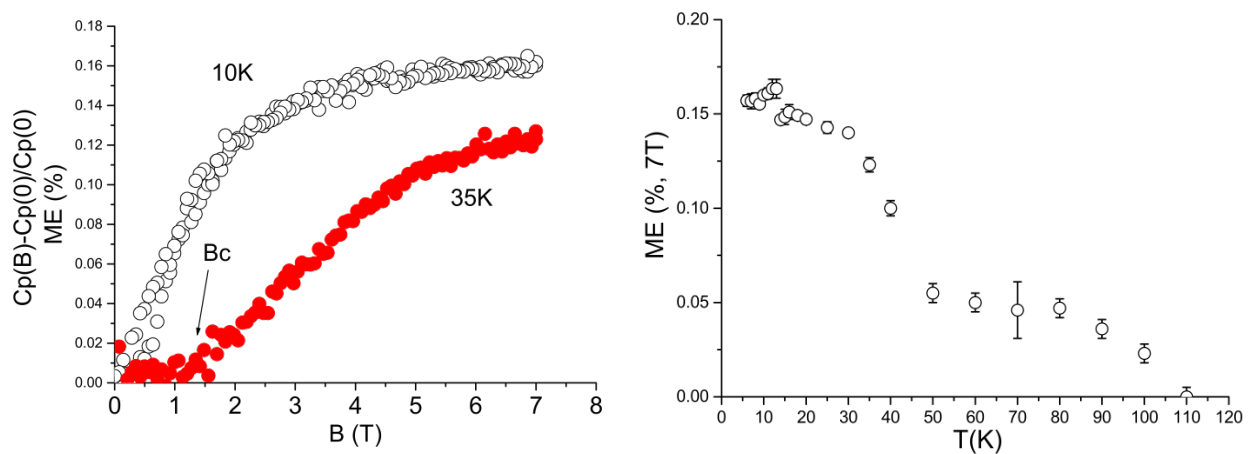


Figure 27. Mesures d'effet magneto-electrique en fonction du champ (gauche) et de la température (droite) dans un hydroxyde de cobalt avec du fluorène diphosphonique possédant des octyles en fonction latérale

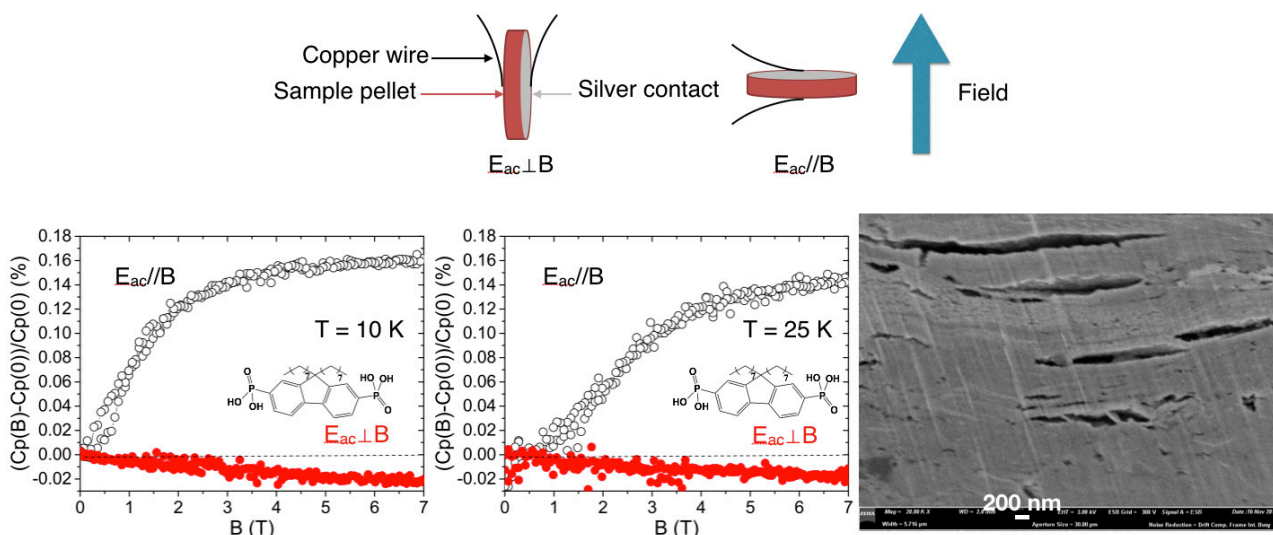


Figure 28. Mesures d'effet magneto-electrique en fonction du champ et de l'orientation (gauche) et coupe de la pastille montrant l'alignement des plaquettes selon une direction.

Un autre volet de cette thèse a été l'obtention d'hybrides avec des molécules synthétisées par des collègues de l'Université Catholique de Louvain (Dr. Yann Garcia et Varun Kumar). Ces molécules ont l'intérêt d'être photo/thermo commutables de façon réversible à l'état solide.³⁹ Ces capacités de thermo commutation sont conservées une fois les molécules insérées dans l'hydroxyde de cobalt, des mesures de diffraction en température avec une référence interne au silicium ont été effectuées. Elles montrent bien la variation de l'espacement interlamellaire avec la température.

Enfin, une dernière partie de ma thèse a été consacrée à l'ajout de propriétés de luminescence à ces hydroxydes par l'insertion de complexes de métaux de transition. Parmi les complexes retenus, deux ont été insérés, un dérivé de salen-platine possédant des fonctions d'accroche sulfonate ainsi qu'un complexe de ruthénium-tris-bipyridine possédant des fonctions d'accroche acide phosphonique. L'enjeu était de voir si les propriétés de luminescence étaient conservées une fois les complexes insérés ainsi que de voir si des modifications d'émission avaient lieu une fois le greffage effectué. Le dépouillement complet des mesures est en cours actuellement.

Ces mesures sont très prometteuses puisqu'elles montrent qu'il est possible d'observer un couplage magnétoélectrique (Fig. 27-28) pour un composé hybride au cobalt dans lequel ont été insérées des molécules de fluorène. Ces mesures ont été effectuées à partir de pastilles pressées à froid et nous avons aussi pu observer un intéressant effet géométrique de l'échantillon peu décrit dans la littérature. En effet, le couplage magnétoélectrique apparaît plus fort et positif quand $E_{ac} // B$ alors qu'il apparaît faible et négatif lorsque $E_{ac} \perp B$. De plus, une fois toutes les séries analysées, il sera possible de déterminer sur la force de ce couplage magnétoélectrique :

- L'effet de la fonction latérale du fluorène
- L'effet du mono ou bis-greffage du fluorène
- L'effet de la polarisation de la chaîne latérale dans la série des benzènes halogénés

Enfin, il sera intéressant d'effectuer des mesures de transition de phase sur ces composés, il est en effet remarquable d'obtenir un effet magnétoélectrique persistant aux alentours de 100K, température très supérieure à la température de mise en ordre magnétique 3D de notre matériau. Phénomène très rarement observé dans la littérature et expliqué par la persistance de couplages magnéto-élastiques bien au delà de la mise en ordre magnétique de notre matériau.

Bibliographie

1. A. Doménech, M. T. Doménech-Carbó, M. Sánchez del Río, M. L. Vázquez de Agredos Pascual and E. Lima, *New Journal of Chemistry*, 2009, **33**, 2371.
2. P. Kumar and V. V. Guliyants, *Microporous and Mesoporous Materials*, 2010, **132**, 1-14.
3. C. Sanchez, B. Lebeau, F. Chaput and J.-P. Boilot, *Advanced Materials*, 2003, **15**, 1969-1994.
4. Y. Kobayashi, Y. Kurokawa and Y. Imai, *Journal of non-crystalline solids*, 1988, **105**, 198-200.
5. B. Dunn and J. I. Zink, *Journal of Materials Chemistry*, 1991, **1**, 903-913.
6. M. Casalboni, F. De Matteis, P. Proposito and R. Pizzoferrato, *Applied Physics Letters*, 1999, **75**, 2172-2174.
7. T. Dantas de Morais, F. Chaput, K. Lahlil and J.-P. Boilot, *Advanced Materials*, 1999, **11**, 107-112.
8. T. Dantas de Morais, F. Chaput, J.-P. Boilot, K. Lahlil, B. Darracq and Y. Lévy, *Advanced materials for optics and electronics*, 2000, **10**, 69-79.
9. A. Espinosa, Mexico, 1987.
10. C. Sanchez, B. Julián, P. Belleville and M. Popall, *Journal of Materials Chemistry*, 2005, **15**, 3559-3592.
11. J. Xu, K. Wang, S. Z. Zu, B. H. Han and Z. Wei, *ACS Nano*, 2010, **4**, 5019-5026.
12. L. Liu, Q. Wang, C. Gao, H. Chen, W. Liu and Y. Tang, *The Journal of Physical Chemistry C*, 2014, **118**, 14511-14520.
13. K. Zhou, Y. Zhu, X. Yang and C. Li, *Electroanalysis*, 2009, **22**, 259-264.
14. X. Gao, M. Hu, L. Lei, D. O'Hare, C. Markland, Y. Sun and S. Faulkner, *Chemical communications*, 2011, **47**, 2104-2106.
15. E. Káfuňková, K. Lang, P. Kubát, M. Klementová, J. Mosinger, M. Šlouf, A.-L. Troutier-Thuilliez, F. Leroux, V. Verney and C. Taviot-Guého, *Journal of Materials Chemistry*, 2010, **20**, 9423.
16. D. Yan, Y. Zhao, M. Wei, R. Liang, J. Lu, D. G. Evans and X. Duan, *RSC Advances*, 2013, **3**, 4303.
17. Z.-L. Huang, M. Drillon, N. Masciocchi, A. Sironi, J.-T. Zhao, P. Rabu and P. Panissod, *Chemistry of Materials*, 2000, **12**, 2805-2812.
18. P. Rabu*, J. M. Rueff, Z. L. Huang, S. Angelov, J. Souletie and M. Drillon*, *Polyhedron*, 2001, **20**, 1677-1685.
19. M. Drillon, P. Panissod, P. Rabu, J. Souletie, V. Ksenofontov and P. Gülich, *Physical Review B*, 2002, **65**.
20. A. García-Fernández, J. M. Bermúdez-García, S. Castro-García, R. Artiaga, J. López-Beceiro, M. A. Señaris-Rodríguez and M. Sánchez-Andújar, *Polyhedron*, 2016, **114**, 249-255.
21. X.-H. Lv, W.-Q. Liao, P.-f. Li, Z.-X. Wang, C.-Y. Mao and Y. Zhang, *Journal of Materials Chemistry C*, 2016, **4**, 1881-1885.
22. S. Chaouachi, B. Hamdi and R. Zouari, *Synthetic Metals*, 2017, DOI: 10.1016/j.synthmet.2016.11.030, 122-131.
23. X. Li, Y. Zhong, Q. Li and L. Wang, *Journal of colloid and interface science*, 2013, **405**, 226-232.
24. Y. Liang, Y. Li, H. Wang and H. Dai, *J Am Chem Soc*, 2013, **135**, 2013-2036.
25. A. L. Wang, H. Xu, J. X. Feng, L. X. Ding, Y. X. Tong and G. R. Li, *J Am Chem Soc*, 2013, **135**, 10703-10709.

26. S. Eyele-Mezui, P. Vialat, C. Higy, R. Bourzami, C. Leuvrey, N. Parizel, P. Turek, P. Rabu, G. Rogez and C. Mousty, *The Journal of Physical Chemistry C*, 2015, **119**, 13335-13342.
27. R. Marangoni, L. P. Ramos and F. Wypych, *Journal of colloid and interface science*, 2009, **330**, 303-309.
28. E. Coronado, C. Marti-Gastaldo, E. Navarro-Moratalla, A. Ribera, S. J. Blundell and P. J. Baker, *Nature chemistry*, 2010, **2**, 1031-1036.
29. B. W. Li, M. Osada, Y. Ebina, S. Ueda and T. Sasaki, *J Am Chem Soc*, 2016, **138**, 7621-7625.
30. Y.-L. Liu, D.-H. Wu, Z. Wang and Y. Zhang, *New Journal of Chemistry*, 2017, DOI: 10.1039/C6NJ03973A.
31. M. Louër, D. Louër and D. Grandjean, *Acta Crystallographica Section B Structural Crystallography and Crystal Chemistry*, 1973, **29**, 1696-1703.
32. S. Švarcová, M. Klementová, P. Bezdička, W. Łasocha, M. Dušek and D. Hradil, *Crystal Research and Technology*, 2011, **46**, 1051-1057.
33. M. Taibi, S. Ammar, N. Jouini, F. Fiévet, P. Molini and M. Drillon, *Journal of Materials Chemistry*, 2002, **12**, 3238-3244.
34. G. Rogez, C. Massobrio, P. Rabu and M. Drillon, *Chemical Society reviews*, 2011, **40**, 1031-1058.
35. V. Laget, M. Drillon, C. Hornick, P. Rabu, F. Romero, P. Turek and R. Ziessel, *Journal of Alloys and Compounds*, 1997, **262-263**, 423-427.
36. C. Hornick, P. Rabu and M. Drillon, *Polyhedron*, 2000, **19**, 259-266.
37. R. Ma, Z. Liu, K. Takada, K. Fukuda, Y. Ebina, Y. Bando and T. Sasaki, *Inorganic chemistry*, 2006, **45**, 3964-3969.
38. J. R. Neilson, J. A. Kurzman, R. Seshadri and D. E. Morse, *Chemistry*, 2010, **16**, 9998-10006.
39. P. L. Jacquemin, K. Robeyns, M. Devillers and Y. Garcia, *Chemical communications*, 2014, **50**, 649-651.

Quentin EVRARD

Hydroxydes Simples



Lamellaires multifonctionnels : investigations structurales, fonctionnalisations et propriétés



Résumé

Le but de cette thèse est l'obtention de matériaux multiferroïques par l'insertion de molécules organiques dans une matrice magnétique d'hydroxide simple lamellaire. Durant cette thèse a été démontré la faisabilité de la fonctionnalisation d'hydroxydes simples lamellaires de cuivre et de cobalt par des molécules possédant des fonctions d'accroche acide phosphonique. Le développement des techniques de pré-fonctionnalisation a permis de fonctionnaliser ces hydroxydes simple lamellaire par une variété importantes de molécules (fluorènes, benzènes, thiophènes et complexes de métaux de transition) afin d'apporter une propriété additionnelle au magnétisme de l'hydroxyde. Les premières mesures ont permis de mettre en évidence un couplage entre température d'ordre magnétique et anomalie diélectrique. La complexité de la mesure des propriétés diélectriques avec ces échantillons (sur poudre pastillées à froid) ont mis en lumière la nécessité d'obtenir des tailles de cristallites plus importantes. Des efforts sur la taille des cristallites ont donc été effectués et ont permis d'obtenir des monocristaux d'hydroxydodécylsulfate de cuivre.

Mots-clés: Hydroxide simple lamellaire, chimie douce, matériaux hybrides, couplage magnétoélectrique

Abstract

The main goal of this thesis is to obtain multiferroic materials via the intercalation of organic molecules in a magnetic inorganic matrix made of layered simple hydroxide. The possibility to use phosphonic acid as grafting moiety for the functionalization of layered simple hydroxides has been demonstrated during this thesis. Pre-functionalization techniques has allowed the functionalization of layered simple hydroxides of copper and cobalt with a wide variety of molecules (fluorenes, benzenes, thiophenes or transition-metal complexes) to bring an additional property to the magnetic properties of the layered hydroxide. The first measurements revealed a coupling between magnetic ordering temperature and dielectric anomaly. The dielectric properties measurements proved to be difficult with the samples (on cold-pressed pellets) and shown the usefulness of developing new methods to improve the crystallite size. To that end, new syntheses procedures led to the obtention of mono crystals of copper-hydroxidodecylsulfonate allowing to get additional structural informations.

Keywords : Layered simple hydroxide, chimie douce, hybrid materials, magnetoelectric coupling